AD-A077 167 ILLINOIS UNIV AT URBANA-CHAMPAIGN ELECTROMAGNETICS LAB F/G 17/9
PROCEEDINGS OF THE ANTENNA APPLICATIONS SYMPOSIUM (1979) HELD 2--ETC(U)
SEP 79 F19628-79-M-0015
UNCLASSIFIED NL

1 OF 6
ADA 077167

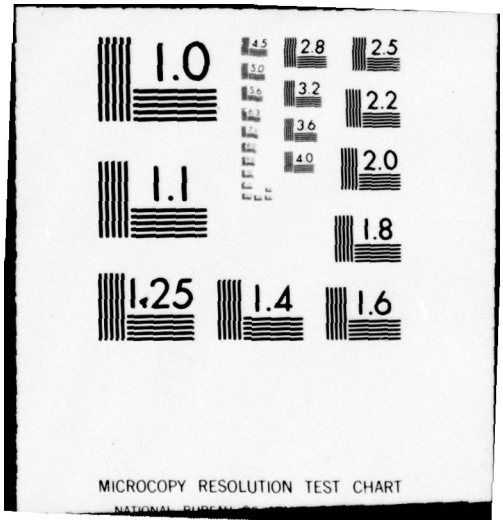
1.0
1.1
1.25
1.4
1.6
1.8
2.0
2.2
2.5
2.8
3.2
3.6
4.0
4.5
5.0
5.6
MICROCOPY RESOLUTION TEST CHART

AD A072162

Proceedings of the 1979 ANTENNA APPLICATIONS SYMPOSIUM

Sponsored by

ELECTROMAGNETIC SCIENCES DIVISION
ROME AIR DEVELOPMENT CENTER
USAF SYSTEMS COMMAND
AND
ELECTROMAGNETICS LABORATORY
UNIVERSITY OF ILLINOIS
URBANA-CHAMPAIGN, ILLINOIS 61801

September 26, 27, 28, 1979
Robert Allerton Park

FILE COPY

"The views and conclusions contained in this document are those of the authors and should not be interpreted as necessarily representing the official policies or endorsements, either expressed or implied, of the Electromagnetic Sciences Division, Rome Air Development Center, USAF Systems Command."

AD A077167

DDC FILE COPY

REPORT DOCUMENTATION PAGE

READ INSTRUCTIONS BEFORE COMPLETING FORM

1. REPORT NUMBER: N/A	2. GOVT ACCESSION NO.
3. RECIPIENT'S CATALOG NUMBER	
4. TITLE (and Subtitle): Proceedings of the 1979 Antenna Applications Symposium	5. TYPE OF REPORT & PERIOD COVERED: Final Rept. 26-28 September 1979
	6. PERFORMING ORG. REPORT NUMBER
7. AUTHOR(s): N/A	8. CONTRACT OR GRANT NUMBER(s): F19628-79-M-0015
9. PERFORMING ORGANIZATION NAME AND ADDRESS: Electromagnetics Laboratory, University of Illinois, Urbana - Champaign, IL 61801	10. PROGRAM ELEMENT, PROJECT, TASK AREA & WORK UNIT NUMBERS: 62702F, Project 06DM, 9994SYMP
11. CONTROLLING OFFICE NAME AND ADDRESS: Electromagnetic Sciences Division, RADC/EE, Hanscom AFB, MA 01731	12. REPORT DATE: September 1979
	13. NUMBER OF PAGES: 516
14. MONITORING AGENCY NAME & ADDRESS (if different from Controlling Office): 523	15. SECURITY CLASS. (of this report): UNCLASSIFIED
	15a. DECLASSIFICATION/DOWNGRADING SCHEDULE

16. DISTRIBUTION STATEMENT (of this Report)

Approved for Public Release; Distribution Unlimited

(1979)

17. DISTRIBUTION STATEMENT (of the abstract entered in Block 20, if different from Report)

(6) Proceedings of the Antenna Applications Symposium held 26-28 September 1979 at Robert Allerton Park, University of Illinois.

18. SUPPL

DDC RECEIVED NOV 21 1979 E

19. KEY WORDS (Continue on reverse side if necessary and identify by block number)

Antenna Symposium
Tactical Radar Antennas
Antenna Arrays
Antenna Measurements
Microstrip Antennas
Low Sidelobe Antennas

20. ABSTRACT (Continue on reverse side if necessary and identify by block number)

The proceedings volume is composed of papers presented at the 1979 Antenna Applications Symposium, cosponsored by Univ. of Illinois and RADC Electromagnetic Sciences Division. Topics in low sidelobe radar antennas, tactical radar antennas, antenna measurements, antenna array design and antenna analysis are covered in thirty-six technical papers.

DD FORM 1 JAN 73 1473 EDITION OF 1 NOV 65 IS OBSOLETE

UNCLASSIFIED

SECURITY CLASSIFICATION OF THIS PAGE (When Data Entered)

408102

PROCEEDINGS OF THE

1979

ANTENNA APPLICATIONS

SYMPOSIUM

Sponsored by

ELECTROMAGNETIC SCIENCES DIVISION

ROME AIR DEVELOPMENT CENTER

USAF SYSTEMS COMMAND

and

ELECTROMAGNETICS LABORATORY

UNIVERSITY OF ILLINOIS

URBANA-CHAMPAIGN, ILLINOIS 61801

September 26, 27, 28, 1979

Robert Allerton Park

University of Illinois

PROGRAM FOR 1979 ANTENNA APPLICATIONS SYMPOSIUM

WEDNESDAY, SEPTEMBER 26, 1979

ANTENNAS FOR TACTICAL RADAR - I

Welcome

Partial Contents:

"Air Force Requirements for Antenna Technology," Allan C. Schell, RADC/EEA, Hanscom AFB, MA.

"Low Sidelobe Reflector Antenna for Tactical Radars," R. M. Scudder and L. H. Yorinks, RCA, Moorestown, NJ.

* "Low Sidelobe Tactical Radar Antenna," Werner Gansz, Raytheon, Wayland, MA.

"Low Sidelobe Parabolic Cylinder Antenna for Surveillance Radars," Salvatore Milazzo and John Stangel, Sperry Gyroscope, Great Neck, NY.

"Near Field Blockage of an Ultralow Sidelobe Antenna," Stephen G. Winchell and Daniel Davis, Westinghouse, Baltimore, MD.

"A Wide-Band, Ultralow Sidelobe Antenna," Gary E. Evans and Stephen G. Winchell, Westinghouse, Baltimore, MD.

ANTENNAS FOR TACTICAL RADAR - II

"A Millimeter-Wave Scanning Antenna for Radar Application," O. B. Kesler, W. F. Montgomery and C. C. Liu, Texas Instruments, Dallas, TX.

"Sidelobe Level Control for Unequally Spaced Arrays," Charles F. Winter, Raytheon, Wayland, MA.

"Sidelobe Discrimination Technique," Paul Eberhardt and William McNaul, Cubic Corporation, San Diego, CA.

"A Low-Inertia Commutating Feed for Circular Arrays," R. I. Wolfson and C. F. Cho, ITT-Gilfillan, Van Nuys, CA.

next page

* "Cost Reduction Techniques for Phased Arrays," Ray Tang, Hughes, Fullerton, CA.

* "Systems Study of Overlapped, Sub-Arrayed, Scanning Antennas," Ron Fante, RADC/EEA, Hanscom AFB, MA.

"A Highly Thinned Array Using the Image Element Antenna," Raymond G. Immell and Bill H. Sasser, Motorola, Scottsdale, AZ.

---

*Not included in this volume

ession For
GRA&I
TAB
nounced
ification
ribution/
ilability Codes
Avail and/or
special

THURSDAY, SEPTEMBER 27, 1979

ARRAYS

"Computer-Aided Fault Determination for an Advanced Phased Array Antenna," Donald K. Alexander and Roger P. Gray, Jr., Westinghouse, Baltimore, MD.

"Resonance Phenomena on Multiple-Yagi Arrays," J. M. Tranquilla and G. B. Graham, University of New Brunswick, Fredericton, NB, Canada.

"Radiation from Conformal Dipole Arrays Mounted on Dielectrically-Clad Conducting Cylinders," K. S. Lee and G. Eichmann, City College of New York, New York, NY.

"Eight Element Printed Probe Array Antenna," R. N. Simons and D. T. Shahani, Indian Institute of Technology, New Delhi, India.

"A Microwave Power Transmission Antenna System for the Solar Power Satellite," Walter W. Lund, Jr., Boeing, Seattle, WA.

* "Solar Power Satellite Antenna," Charles Y. Tomita and Harold E. Foster, Rockwell, Anaheim, CA.

"A Variable Impedance Ratio Printed Circuit Balun," R. Y. Shimoda, Boeing, Seattle, WA.

ANTENNA ANALYSIS AND DESIGN

"Design and Theory of Circularly Polarized Microstrip Antennas," W. F. Richards, Y. T. Lo, and P. Simon, University of Illinois, Urbana, IL.

"Analysis and Design of Circular Microstrip Resonator Antennas," A. van de Capelle, B. van den Mooter, H. Verbiest, and J. Vandensande, Katholieke Universiteit Leuven, Heverlee, Belgium.

"A Unified Approach to the Solution of Microstrip Antenna Problems," Edgar L. Coffey, III, The BDM Corp., Albuquerque, NM.

"A Common Aperture S- and X-Band Feed for the Deep Space Network," W. F. Williams and J. R. Withington, JPL, Pasadena, CA.

"The Look Through Antenna," D. Killion and W. McNaul, Cubic Corporation, San Diego, CA.

"Air Launch Cruise Missile Instrumentation Antennas," R. E. Lantagne, J. P. Grady, and G. E. Miller, Boeing, Seattle, WA.

"Sectoral Scalar Horns for Precise Beam Control," W. A. Schneider, T. L. Blakney and V. J. Zanella, Boeing, Seattle, WA. → next page

* "Design Concepts for Omnidirectional VHF and UHF Communications Antennas," A. R. Sindoris, North Carolina State University, Raleigh, NC, D. H. Schaubert and F. G. Farrar, Harry Diamond Labs, Adelphi, MD.

FRIDAY, SEPTEMBER 28, 1979

ANTENNA MEASUREMENTS

"Near Field Pattern Measurement Facility," C. E. Kirchhoff, Martin Marietta, Denver, CO.

* "Automated Near Field Antenna Test Set for Phased Array Antenna Production," David Stalman, RCA, Moorestown, NJ.

* "Some Recent Near Field Antenna Measurements at NBS," Carl Stubenrauch, NBS, Boulder, CO.

"Planar Near Field Measurements for Aircraft Antenna Applications," Jerome D. Hanfling, Raytheon, Bedford, MA.

"Series 1580 Antenna Pattern Recorder," Joseph H. Pape, Scientific-Atlanta, Atlanta, GA.

* "Digital Antenna Data Collecting System for MIL-A-87136 Testing," Joseph H. Pape, Scientific-Atlanta, Atlanta, GA.

"Conceptual Analysis of Measurement on Compact Ranges," Richard C. Johnson, Georgia Tech, and Doren W. Hess, Scientific-Atlanta, Inc., Atlanta, GA.

"A Safe Test Method for Effective Radiated Power Measurement," George J. Monser, Raytheon, Goleta, CA.

IN MEMORIAM

A meeting predecessor to this symposium, held at Allerton House each Fall, was organized by E. M. Turner for sixteen years while he was Head of the Antenna and Radomes Group at Wright-Patterson Air Force Base. He encouraged the revival of this gathering and, although retired, presented papers at the First and Second Symposia in 1977 and 1978.

Many of us, particularly the "old timers," will long remember the irrepressible enthusiasm and unabashed humor that always marked his presence here. For the first time in many, successive repetitions of this occasion, Ed will not be here. Our sense of loss at the death of a colleague and friend, whose contributions to the profession were numerous and widespread, is tempered by the assurance that his impatient spirit is lingering near, beseeching us to get on with solving whatever problems confront us.

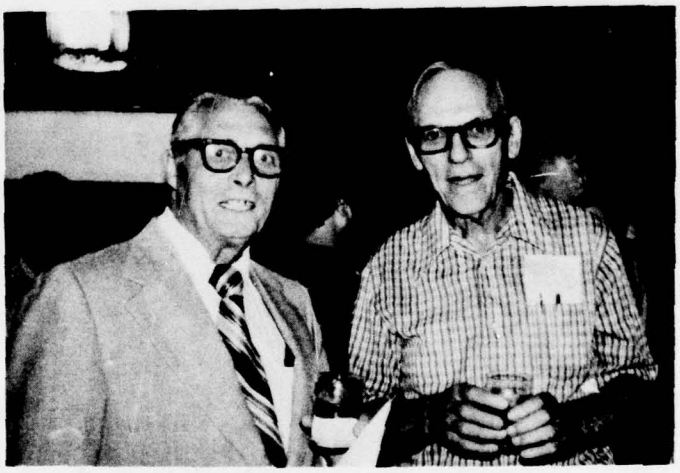

Ed Turner (right) with Ed Jordan at the 1978 Antenna Applications Symposium.

AIR FORCE REQUIREMENTS FOR ANTENNA TECHNOLOGY

Allan C. Schell

Electromagnetic Sciences Division
Rome Air Development Center
Hanscom AFB, MA 01731

I. INTRODUCTION

Air Force requirements for advanced space, missile, aircraft and ground systems have led to a continuing development of antennas with improved performance. The threats perceived under current scenarios have identified weaknesses of presently fielded equipment that require substantial upgrades in the antenna area. There are many programs at the research, exploratory development, and advanced development levels that are dedicated to addressing these needs. The anticipated improvements can be summarized as leading to antennas with high efficiency, low sidelobe patterns over a wide band; to antennas in which the pattern characteristics, especially nulls, can be controlled; and to antennas that are of lower cost per unit area.

II. CURRENT ISSUES AFFECTING AIR FORCE FUNCTIONS

The mission area of command, control, and communications encompasses the functions necessary for a commander to determine the various aspects of the military situation under his cognizance, and to convey his decision in an effective manner to those under his command. Within the C^3 mission area, the principal functional areas that involve antenna technology are tactical surveillance, strategic surveillance, tactical communications, strategic communications, navigation, and aircraft control. For each of these functions, there is a differing set of issues involving system performance. In general, the common issues are vulnerability, accuracy, coverage or capacity, reliability, physical and mechanical attributes, and cost. However, among the functional areas, the priorities of these issues differ considerably. In Table I is shown a list of the functional areas and the principal issues associated with them. In the following sections, these are related to equipment performance.

TABLE I

ISSUES FOR AIR FORCE C^3 FUNCTIONAL AREAS

AIR FORCE FUNCTION	ISSUE
Tactical Surveillance	Vulnerability of radars to jamming and antiradiation missiles Data rate Mobility, availability Cost
Strategic Surveillance	Coverage of northern hemisphere against low altitude targets Precision assessment of ICBM's, RV's Radar vulnerability Reliability, maintainability
Tactical Communications	Channel capacity Vulnerability to jamming Increase in aircraft weight, drag Cost
Strategic Communications	Vulnerability to damage, jamming Message rate Post-attack performance Reliability
Navigation and Aircraft Control	Accuracy Portability Cost of tactical equipment Ease and speed of operation

Tactical Surveillance

Current tactical radars employ mechanically rotating antennas for air surveillance. The vulnerability of these radars to intense distributed jamming and to anti-radiation missiles has led to efforts to provide new tactical radar antennas with low sidelobes and a null steering capability. This antenna performance will be required over a wide instantaneous bandwidth. Earlier sidelobe cancellers are anticipated to be replaced by flexible adaptive nulling equipment.

A need for increased data rates on high speed targets and a desire to combine track with scan functions are motivating a drive to incorporate phased array technology in future tactical radars, assuming that the mobility requirements on size and weight can be met. Because there are many tactical radars in the inventory, cost is an important factor, and will play a determining role in choices between array and reflector antennas.

Table II summarizes the principal issues and performance factors for tactical radar.

TABLE II

TACTICAL SURVEILLANCE

ISSUE	TECHNICAL PERFORMANCE FACTOR
Jamming Vulnerability	Wide Bandwidth Null Steering Capability
ARM Vulnerability	Low Sidelobes
Data Rate on Multiple Targets	Beam Agility
Mobility	Radar (Antenna) Size and Weight
Availability	Redundance, Parts Quality
Cost	Number of Elements, Array vs Reflector

Strategic Surveillance

The impact of currently envisaged threats and needs in the strategic surveillance radar area has been to prompt examinations of widely diverse techniques. The detection of aircraft and cruise missiles flying at low altitudes requires that the antenna minimize the effects of multipath and clutter. An alternative technique to

ground based radars that is receiving considerable attention is spaceborne radar. Significant advances in technology, particularly in the area of lightweight transceiver modules, are needed to produce an affordable, large, and operationally flexible spaceborne array.

Radar plays an important role in accurately assessing the characteristics of strategic weaponry heading toward the U.S. Improvements in attack assessment may necessitate increased antenna bandwidth and gain. For over-the-horizon radars operating in the high frequency band, the properties of the ionosphere play a crucial role in both the accuracy and the availability of the equipment.

All strategic equipment is measured by its vulnerability to attack. Thus structural hardness, fail safe modes, and redundancy are dominant considerations; and low cost, while always desirable, is lower in priority, partly because of the fewer number of systems deployed. Table III summarizes the strategic surveillance issues relating to antennas.

TABLE III

STRATEGIC SURVEILLANCE

ISSUE	TECHNICAL PERFORMANCE FACTOR
Low Altitude Target Detection	Overcoming Effects of Multipath, Screening, and Clutter
Precision Assessment of Launched Weapons	Bandwidth, Gain & Aperture-to-Medium Coupling
Vulnerability	Structural Hardness, Redundancy
Reliability	Redundancy, Propagation
Maintainability	Modularity, Fault Indication and Fault Tolerance

Tactical Communications

Communications satellites, both military and commercial, are an important part of Air Force communications. In order to provide high data rate communications within existing frequency bands, it is desired to use channels simultaneously at several locations. This leads to antenna requirements of decoupled spot beams and dual polarization beams with low cross polarization.

As in the case of radar, jamming vulnerability is reduced by low sidelobes and by steering nulls, or by forming patterns that adapt to the maximum desired signal and minimum interference for the total environment. When this technology is applied to aircraft, there is the additional requirement to minimize the weight, size, and number of

antennas. As is usually the case in tactical equipment, cost is an important factor for antennas that are to be widely deployed. This has led to increased emphasis on microstrip and similar lightweight antenna technology. These issues are listed in Table IV.

TABLE IV

TACTICAL COMMUNICATIONS

ISSUE	TECHNICAL PERFORMANCE FACTOR
Channel Capacity	Frequency Reuse by Angular or Polarization Diversity
Jamming Vulnerability	Null Steering Capability Wide Bandwith
Arm Vulnerability	Low Sidelobes
Aircraft Weight and Drag Increase	Antenna Conformality and Size Number of Antennas
Cost	Number of Elements and Control Devices

Strategic Communications

The Air Force is deploying AFSATCOM, a satellite strategic communications system. Emphasis will continue on the reduction of the vulnerability of satellite systems to jamming, and this will require antennas for these systems with wideband null forming capability.

For emergency essential message communication, transmission at very low frequencies is effective under extremely severe conditions. VLF communications requires very large antennas, and has prompted the development of long trailing wires for aircraft, and large ground arrays. At these frequencies, bandwidth is at a premium, and there are periodic revisitations to the analyses of high Q antennas. Novel methods of rapid or broadband tuning of these antennas are important. These same issues are of concern in the design of strategic communications antennas for the HF bands.

An aspect of strategic VLF, LF or HF communications that is paramount is the effect of the propagation medium. VLF waves propagate in the earth-ionosphere waveguide, and are affected by changes in ionospheric composition and height. High frequency waves are severely dependent on ionospheric changes, and effective HF communications requires thorough knowledge in real time of propagation conditions. New modes of HF propagation, such as ducted HF, may lead to requirements for HF antennas with significantly increased directionality. Table V

lists some of the issues and the relevant performance factors for strategic communications.

TABLE V

STRATEGIC COMMUNICATIONS

ISSUE	TECHNICAL PERFORMANCE FACTOR
Vulnerability	Hardness, Anti-jam Capability
Message Rate	Frequency Band, Q, Tuning
Post-attack Performance	Propagation Medium Recovery
Reliability	Diversity, Medium Effects

Navigation and Aircraft Control

Many of the issues that pertain to communications satellite terminals on aircraft are germaine to the development of aircraft antennas for the Global Positioning Satellite System. Loran is a navigation system in use by the Air Force. One of the more important needs for the Loran system is rapidly deployable antennas for tactical operations.

The Air Force has procured new aircraft landing systems for air bases and for tactical use. The nomenclature for these are GPN-22 and TPN-19, and they employ phased arrays for track and scan by the precision approach radars. Because the phased arrays are part of the limited scan feed for the main reflector, the beam steering commands are not as simple as for planar arrays; however, the antenna is capable of very accurate beam pointing over a limited sector. These radars are good illustrations of how imaginative phased array technology can be applied to tactical needs. Table VI contains a few of the issues that pertain to this area.

TABLE VI

NAVIGATION AND AIRCRAFT CONTROL

ISSUE	TECHNICAL PERFORMANCE FACTOR
Accuracy	Precision Beam Forming and Monopulse
Cost (Tactical Equipment)	Number of Radiating and Control Elements
Portability	Antenna Size and Weight
Ease of Operation	Simplicity, Antenna Set-up Time

III. CURRENT RESEARCH & DEVELOPMENT OF ADVANCED ANTENNA TECHNOLOGY

There are many efforts underway to address the projected needs for improved antenna technology. In the tactical surveillance area, competitive designs will be evaluated for a low sidelobe, wideband phased array antenna for an agile beam radar. Alternative approaches using wide bandwidth lenses are to be studied. New initiatives on low cost phase shifters and electronically variable delay lines are planned.

For strategic surveillance, two approaches to the design of light weight, efficient transceiver modules are underway for spaceborne radar. Studies of the feed design and for techniques to steer nulls by feed array control are being initiated. Problems of interelement coupling within the enormous lens face of the planned spaceborne antenna are to be analyzed. For ground based arrays, the applicability of circular array technology has been assessed for both strategic and tactical radars, and this technology has been found to have many desirable features, although low sidelobe level does not seem to be one of them.

A planned voice communication system between tactical fighter aircraft will incorporate null steering antennas as a primary means of protection against jamming. Microstrip antennas are viewed as key elements of avionics, and there will be continuing efforts to improve bandwidth and to include more control elements on the printed circuit board.

Satellite communications will emphasize multibeam technology, null steering, and dual polarization. The satcom terminals on aircraft will have more uniform gain coverage over a hemisphere, leading to smaller antennas than are presently needed from planar structures with gain varying nearly as cos θ. Conformality to the aircraft surface will continue to be a very desirable feature.

In addition to the further development of satellite antennas cited above, the strategic communications area will see the development of aircraft antennas capable of sensing both transverse electric and transverse magnetic modes of VLF waves. Pop-up antennas using balloons are candidates for rapid deployment of tactical Loran stations.

IV. SUMMARY

The primary driving force behind current antenna development is the intense electronic jamming environment that is envisaged for any future conflict. This is leading to an emphasis on low sidelobes and adaptive pattern formation as integral parts of future surveillance and communications antennas. A second issue is the need for increased capability, and the desire to incorporate multiple functions through a single aperture. Mobility, measured in size and weight, and the standard constraint of cost will continue to play dominant roles. To summarize, the trends of future antenna development are focused on cleaner patterns, meaning low sidelobes and greater efficiency over a wider band; smarter antennas, meaning the ability to steer nulls or

to adaptively form patterns in response to the electromagnetic environment; and lower cost antennas, meaning the development of less expensive element control, and further development and application of microstrip technology, including the incorporation of gigabit logic on the antenna boards.

LOW SIDELOBE REFLECTOR ANTENNA FOR TACTICAL RADARS

R.M. Scudder, L.H. Yorinks
Government Systems Division
Missile and Surface Radar
Moorestown, NJ 08057

INTRODUCTION

This paper describes a preliminary development of a paraboloidal reflector antenna system for S-band tactical surveillance radars. The work was supported in part by RADC Contract F30602-76-C-0290.

Figure 1 is a sketch of a radar system showing the antenna as it would appear in use. The antenna is intended for mounting on a pedestal of the type used for the existing AN/TPS-43 radars. The pedestal rotates the antenna for azimuth scan while the antenna rapidly steps its beam electronically across 20 degrees of elevation scan. Suitable for a radar using only a single-channel wideband signal processor, the antenna achieves reduced vulnerability interference through reduction in the magnitude and extent of its radiation sidelobes.

Because reflector antennas for the earliest radars were designed to operate in an environment of much less electromagnetic interference than is currently the case, design emphasis on extremely low sidelobe level was not required. Antenna design in the past has been guided by the policy of maximizing aperture efficiency while limiting round-trip sidelobes to a level just low enough to limit false radar detections on passive targets. The practical consequence of this policy has been to fill the US military inventory with radars of superior clear-search capability but limited usefulness in present-day tactical environments. The sidelobe performance of existing radar antennas is more the result of this design policy than the result of a technology limitation inherent in any specific approach. The development results reported herein show that, by the application of design techniques specifically oriented toward sidelobe suppression, excellent sidelobe performance can be achieved with a reflector-antenna configuration.

The design of the antenna was guided by RADC, Hanscom AFB, and by concurrent RCA radar system analysis. Additional radar logistic parameters used in the system analysis were based on the parameters of the AN/TPS-43 radar.

The antenna configuration described here is compatible with the constraints associated with present-day tactical radar operating environments, including electromagnetic interference and natural clutter. General design goals of the antenna include the following:

- Very low azimuth sidelobes, and low average sidelobes.
- Wide-band capability necessary for compatibility with the most effective interference-rejecting radar waveforms.

- Minimal hardware implementation of polarization diversity necessary for all-weather operation.
- A basically simple structure to ensure minimum acquisition and life-cycle costs.
- Stepped beam in elevation with mechanical rotation in azimuth to provide volumetric search using a single wide-band signal-processing channel.
- Reliability and maintainability for operation in tactical environments.
- Simplicity of converting into and out of the transport configuration.
- A lightweight structure for air transport.
- All of the above in a low-cost, transportable assembly compatible with tactical operational environments, following the general logistic philosophy of the AN/TPS-43 configuration.

Key performance requirements include the following:

- Azimuth sidelobes,

1st	< -35 dB
2nd	<-38 dB
3rd	<-41 dB
Other	<-50 dB

- Instantaneous Bandwidth, >200 MHz
- Polarization Diversity

PHYSICAL DESCRIPTION OF THE ANTENNA

Major components shown above the pedestal in Figure 1 include (1) the reflector structure with edge-mounted shields (absorber panels), and (2) the vertical array of dual-polarized feed-horns and associated waveguide interfaces with the transmitter and RF receiving equipment.

Other equipments located on the rotating structure include the unit containing the transmitter polarization switching and beam steering controls, the RF power distribution network, the circulator/TR limiter group, and the RF/IF preamplifier group. All these items are located within the RF equipment housing structure, which also supports the feed and reflector structures in both the operating and transport configurations. As shown, a separate IFF antenna assembly is mounted at the top edge of the radar reflector.

Major parameters of the antenna configuration are shown in Table 1.

The stepped-beam antenna system uses a combination of the orthogonal beam matrices, phase shifters, and power-distribution networks to provide both elevation beam steering and independent control of transmit and receive polarization modes.

TABLE 1. PARAMETERS OF STEPPED-BEAM REFLECTOR ANTENNA

Aperture Size	20 Feet Wide, 12 Feet High
Reflector Structure	Aluminum Monocoque
Focal Length	6.5 Feet
Surface Mfg. Tolerance	0.020 Inch, RMS
Number of Feedhorns	7
Feedhorn Configuration	Corrugated
Number of Beams	7
Beam Step Control	Phase Shift
Polarization	Horiz., Vert., Circular (Switchable)
Transport Package Size	188 Inches Long, 88 Inches Wide, 100 Inches High
Transport Package Weight	4570 Pounds

Figure 2 shows the microwave subsystem in block diagram form. Stepped-beam steering in elevation is accomplished by commanded phase tapers that are identical for the orthogonal polarization paths. The polarization mode is selected by command of a mean phase difference between the two groups of eight phase shifters. Duplexing isolation between the transmit and receive paths is implemented by a 180-degree phase difference between the two groups of phase shifters, set immediately after the time of the transmit pulse to effectively 'switch' the antenna from the transmitter channel to the receive path. The power-distribution network provides amplitude weighting on various horns in the seven-horn group as a function of elevation beam steering position. The first two horns are driven for the lowest beam, three horns for each of the next three elevation beams starting with the lowest three and working up to the middle three horns, and one horn for each of the three highest elevation beams. See Table 2.

Although the transmit and receive paths largely share common circuitry, they branch at a point where operation of the elevation beam-steering phase shifters can permit those phasers to perform a transmit-receive duplexing function. The antenna group includes low-noise RF and IF amplification of signals for external single-channel wideband processing.

Complete receiver protection is provided by the transmit/receiver-limiter assembly.

A sketch of the feedhorn assembly mounted on the RF network structure (Figure 3) shows the angular and focal positioning of the seven horns. This positioning is based on the elevation and azimuth pattern performance in combination with the radar elevation coverage requirements. The horns are corrugated rectangular structures designed to handle the dual polarization and wide instantaneous bandwidth parameters of the radar; the dual polarization mode transducers are indicated in the figure. For transport, the uppermost six horns are removed as a unit from the RF network and stowed to permit the reflector structure to fold flat on the pallet housing of the RF network.

TABLE 2. FORMATION OF THE SEVEN ELEVATION BEAMS BY SEVEN FEED HORNS

Feed-Horn No.	Elevation Beam No. and Elevation (Deg.)						
	1	2	3	4	5	6	7
	0.7	2.0	3.8	5.9	7.9	12.3	19.2
1	X	X	-	-	-	-	-
2	X	X	X	-	-	-	-
3	-	X	X	X	-	-	-
4	-	-	X	X	-	-	-
5	-	-	-	X	X	-	-
6	-	-	-	-	-	X	-
7	-	-	-	-	-	-	X

Note:The X marks identify the horns used for each beam.

For transport, the antenna and sections of the reflector are unlatched from the center section and stowed flat on the base. The center section hinges down so that it, too, lies flat. The resulting transport configuration is a pallet-like assembly compatible with all modes of transportation, including C-130 cargo aircraft.

PERFORMANCE OF THE ANTENNA

Radiation Patterns

The antenna feed system was configured to provide peak azimuth sidelobes 40 dB down while achieving the elevation beamshape required for precise target height estimation. The patterns of the antenna design were calculated by using the RCA computer program DISH.

The feed configuration sketched in Figure 3 shows seven horns located with the centers of their apertures on a straight line. That line makes an angle of 65.77 degrees with the axis of the paraboloid.

Elevation patterns using the feed were calculated and are shown in Figures 4 and 5. Figure 4 gives the elevation beam set at three frequencies overlaid for vertical polarization, while the horizontally polarized result appears in Figure 5. Patterns of Figure 5 were calculated for a frequency of 3.35 GHz. The four lowest beams are formed by exciting sets of three adjacent feed horns (the lowest beam is formed by exciting only two horns) in order to keep the elevation sidelobe levels below 24 dB and to obtain the beamwidths necessary for proper beam crossover levels. For example, to obtain the second lowest beam, horns 1, 2, and 3 are excited simultaneously, with horn 2 receiving about 92 percent of the power and the remainder evenly split between horns 1 and 3. Both the beam locations and crossover levels are dictated by the required radar accuracy for target height estimation.

Elevation performance is summarized in Figure 6 where relative gain and 6 dB beamwidth are plotted against the elevation angle of the beam. The points corresponding to the feed displacement are shown plotted on the figure. As expected,

maximum gains and minimum beamwidths correspond to beams radiating near the axis of the paraboloid. Table 3 summarizes the total set of elevation beam parameters.

Whereas the elevation beamwidth increases as the beam is scanned in elevation from the axis of the paraboloid, the azimuth beamwidth is virtually independent of elevation beam position. This is the result of positioning the feed along a line 65.77 degrees from the paraboloid axis, which is the azimuth focal locus. In addition, the illumination of the reflector is tailored to provide very low azimuth sidelobes as required for operation in an ECM environment. This constant beamwidth and low azimuth sidelobe performance is demonstrated in Figures 7, 8, and 9 which show calculated azimuth patterns corresponding to beams 2, 4, and 7.

Pattern Considerations Related to Performance

Operation of a radar antenna in an environment with high levels of interference demands that the antenna receive very little spurious energy, i.e., that the antenna have very low sidelobes. Two areas are of particular concern: (1) azimuth sidelobe levels must be low to minimize reception of interfering signals, and (2) any energy radiated into a cone 45 degrees from the zenith must be controlled so that the threat of anti-radiation missiles (ARMs) is minimized.

Low azimuth sidelobes near the main beam were obtained by designing the feed to heavily taper the reflector illumination toward the sides of the reflector. The edge illumination is typically -20 dB or less. This results in peak azimuth sidelobe levels of better than -40 dB in the absence of reflector errors or surface deformation. Since the reflector will be fabricated as a self-supporting monocoque or honeycomb structure, surface errors due to manufacture are expected to be random across the surface without periodic correlation intervals. The average sidelobe level due to a 0.020-inch RMS surface tolerance will be lower than -70 dB as will be shown in the following

TABLE 3. ELEVATION PERFORMANCE VERSUS FREQUENCY

	Elevation Angle (Rel. to Axis) (degrees)			Beam Width 6 dB Down (degrees)			Gain Over Isotropic (dBi)			Gain Beamwidth Product (X 10)		
Beam No.	3.1 GHz	3.35 GHz	3.7 GHz	3.1 GHz	3.35 GHz	3.7 GHz	3.1 GHz	3.35 GHz	3.7 GHz	3.1 GHz	3.35 GHz	3.7 GHz
1	-1.29	-1.28	-1.32	2.37	2.22	2.03	41.4	42.1	42.6	33.5	36.0	37.1
2	0	0	0	2.43	2.28	2.07	41.8	42.3	42.9	36.8	38.8	40.4
3	1.77	1.77	1.80	2.58	2.43	2.25	41.7	42.1	42.7	38.2	39.4	41.9
4	3.33	3.35	3.36	3.75	3.87	3.90	40.1	40.2	40.2	38.4	40.5	40.9
5	5.85	5.88	5.91	5.46	5.49	5.55	37.8	37.9	38.2	32.9	33.8	36.7
6	10.31	10.27	10.33	8.40	8.10	7.71	35.9	36.3	36.5	32.7	34.5	34.4
7	17.23	17.23	17.20	11.85	11.40	10.86	33.0	33.1	33.1	23.6	23.3	22.2

Notes: (1) The data is for vertical polarization.
(2) The gain-beamwidth product is the product of the gain and the 6-dB elevation beamwidth.

section. However, the reflector can become distorted due to wind forces on its surface, and these distortions may lead to increased sidelobe levels in the vicinity of the main beam. The reflector is stiff enough, however, so that the first sidelobe will be below -35 dB.

Aperture blockage by the feed is often an important source of close-in sidelobes in a reflector antenna. The offset geometry, however, minimizes this blockage and may be configured to eliminate it. In the case of this antenna design, the maximum blockage area is 6 x 8 inches which results in a sidelobe level of -60 dB. The blockage contribution to close-in sidelobes is therefore negligible.

The primary contributor to wide angle azimuth sidelobe energy is feed spill over past the edge of the reflector. The directivity of the feed is approximately 10 dBi. Since the intercept of the reflector is at least 20 dB below this, or -10 dBi, and the directivity of the reflector is about 40 dBi, the spillover sidelobe is no greater than -50 dB relative to the beam peak.

Extraneous energy in the conical region 45 degrees from the zenith is also caused by feed spillover. Reflector illumination in elevation is not tapered as much as in azimuth since the "close-in" sidelobe level in elevation is not as critical. Therefore, the top of the reflector intercepts the feed pattern below its 10 dB point. This would result in sidelobes of about -35 dB in the vicinity of the zenith. Much of this spillover energy is eliminated by placing an absorbing shield at the top of the reflector as shown in Figure 10. Adequate suppression of this spillover has been demonstrated experimentally as will be shown in Figure 26.

The shield also serves to isolate the aperture of the IFF antenna from that of the reflector so that scattering from the IFF antenna is minimized.

Since the reflector will be of the solid surface type, no direct feed-through will result in back lobes. Spillover energy below the bottom reflector is prevented by locating microwave absorbing material between the bottom of the reflector and the base plate of the pedestal. In addition, a similar layer of absorber material applied to the surface of the baseplate is also required.

STRUCTURAL AND ENVIRONMENTAL PARAMETERS AND THEIR EFFECTS

Both the manufacturing tolerances and deformation of the reflector due to environmental conditions affect the very low sidelobe levels desired from the antenna. Tolerances in feed fabrication and positioning have only a second-order effect on sidelobe levels, although they directly affect beam positions. Because of the relatively small size of the feed and rigidity of its mounting structure, such effects are easily controlled.

The reflector is a monocoque structure which is fabricated of 14-inch-high subpanels continuous across the width of the reflector within each reflector panel. Bowing or deformation along the height of each subpanel is controlled to less than ±0.005-inch peak. Relative locations of the subpanels and variations in the surface from the theoretical surface along their long dimensions is such that the RMS surface tolerance will be less than 0.020 inch. If the surface errors are assumed to be correlated

over regions 14 inches in diameter and to have an RMS variation of 0.020 inch, then from Ruze[1], the sidelobe power level due to random errors is given by

$$G_{max} = 1/\eta(2C/D)^2\bar{\delta}^2$$

where n is the aperture efficiency, C is the correlation radius, D is the aperture diameter, and $\bar{\delta}^2$ is the mean square aperture phase error in radians squared, which is no more than $(4\pi/\lambda)^2\bar{\Delta}^2$, where $\bar{\Delta}^2$ is the mean square surface error. Using 2C = 14, η =0.71, D =200 as an average diameter, and $\bar{\delta}^2 = 6.2 \times 10^{-3}$ (phase error at 3.7 GHz), the axial value of the scattered energy relative to the peak of the main beam is -44 dB. The sidelobes due to random errors will then tend to fall below -60 dB within 16 degrees of the main beam (see Figure 11) so that random errors make a very small contribution to wide angle sidelobes.

A similar analysis pertaining to elevation sidelobes due to correlated misa-lignment between the 14-inch high subpanels which span the width of the reflector gives a value of -33 dB. The sidelobe contribution due to such errors will fall to less than -50 dB above and below 16 degrees from the main beam and will be essentially confined to the width of that beam. Thus, the contribution to the elevation sidelobe level is no worse than -33 dB close to the beam where the diffraction lobes in this region are of the order of -25 dB. Contributions at wide angles are equally acceptable.

The average sidelobe level may be obtained by examining the gain reduction due to random errors. The ratio of the antenna gain with random errors to that in the absence of errors is at most $e^{-\bar{\delta}^2}$. The lost power averaged over all space is the average sidelobe level relative to an isotropic source. The average level relative to the peak of the pattern is given by

$$\overline{SLL}_{dB} = 10\ \log_{10}([1 - e^{-\bar{\delta}^2}]/4\pi) + G_o - 10\bar{\delta}^2\log_{10}e$$

where G_o is the gain antenna in dB in the absence of random errors. For the case at hand, G_o =43 dB at midband including aperture efficiency and $\bar{\delta}^2 = 6.2 \times 10^{-3}$. Therefore, the average sidelobe level will be lower than -70 dB, considering only the effects of random surface tolerances. This result is pessimistic since it neglects the fact that a substantial portion of the scattered energy due to surface tolerances overlaps the main beam. Since about 75 percent of the scattered power is contained in a 16-degree cone about the main beam, the average sidelobe level outside this cone is better than -80 dB.

Thus far, only the effects of manufacturing tolerances have been considered, and these have been treated statistically. When the antenna is deployed in the field, environmental factors will influence the antenna performance also. Since the antenna rotates at 6 RPM when it is operational, thermal distortions from uneven solar illumination of the reflector will not be a problem. Distortion of the reflector due to wind forces will occur for expected wind velocities. The dynamic wind conditions are very complex, especially since the reflector rotates. Some insight into the effects of reflector distortion has been obtained, however, by considering the more simple static situation of a head wind directly into the reflector and parallel to its axis. This type of wind loading results in a flattening of the curvature of the surface of the reflector.

Radiation Systems, Inc.* has analyzed the reflector using computerized structural analysis techniques assuming a 52 knot head wind. The structure, analyzed as shown in Figure 12, includes vertical trusses which extend 30 inches below the bottom of the reflector where they are fastened to the pedestal. The trusses provide support over the vertical extent of the reflector and serve as a means of mounting the reflector.

Figure 12 also shows the calculated deformation of the reflector as contours of constant displacement over the surface of the reflector. The displacements are parallel to the paraboloid axis. Similar contours for the simplified function for displacement, given by $z = -0.018x - 0.0035y + 0.027$ where x and y are in feet and z is in inches, are also shown in the figure. This simplified function gives greater displacements than those predicted over almost the entire reflector. Therefore, patterns calculated using this function should have slightly pessimistic results; i.e., sidelobe sensitivity to reflector surface displacement should be greater with the simplified function than with the predicted displacement.

Examination of the effect of the y-dependent displacement shows it to have no effect on the azimuth sidelobe levels. Its only effect is on elevation beam position. The x-dependent displacement directly affects azimuth sidelobe levels. Figure 13 shows a set of patterns calculated for values of maximum displacement at the extreme azimuthal edges of the reflector. For the magnitude of displacement expected from this reflector, 0.18 inch, the effect on sidelobe level is very slight. The reflector manufacturer indicates that the deflection of the reflector can be reduced and hence the sidelobe performance can be improved slightly, but at increased cost.

In summary, these results verify that the sidelobe performance of the antenna reflector design will meet the specified values, by using a monocoque structure of 10-inch depth, with a surface random tolerance of 0.020 inch, RMS.

PERFORMANCE GOALS vs COMPUTED AND/OR MEASURED RESULTS

Table 4 summarizes the major goals of the antenna design and development results. In addition to the results shown in Table 4, several parameters pertaining to basic surveillance radar detection and height finding performance are shown in the RF losses itemized in Table 5. These are shown for the low elevation, long range beams where losses are most critical.

Height Finding

Figure 14 shows the height estimation performance for the vertical beam configuration for vertical polarization. At 100 nmi range, the 1-sigma height estimation accuracy varies from 800 feet to 2500 feet. Averaged over altitude, the 1-sigma error is 1320 feet. For shorter ranges the error is generally less.

The angle estimation is the maximum likelihood estimate for amplitude comparison for Gaussian beams based on Hofstetter et al,[2] who developed the angle estimation formula for an amplitude comparison monopulse system using four product beams

*Private communication

TABLE 4. ANTENNA PERFORMANCE GOALS AND RESULTS

Parameter	Goal	Typical Result
Azimuth Sidelobes:		
1st	<-35 dB	<-38 dB
2nd	<-38 dB	<-44 dB
3rd	<-41 dB	<-50 dB
Other	<-50 dB	<-50 dB
Average Sidelobes	-	<-70 dB
Elevation Sidelobes, High Angle	-	<-42 dB
Elevation Sidelobes, Near	-	<-24 dB
Operating Frequency	-	3100 - 3700 MHz
Instantaneous Bandwidth	>200 MHz	600 MHz
Polarization Cancellation Ratio	-	15 dB
Az Angle Resolution (3 dB Beamwidth)	<1.5	<1.4
Ant System (Gain-Losses-Efficiencies):		
Transmit (Net Gain)	40 dB	40.4 dB
Receive (Net Gain)	40 dB	40.2 dB
Aperture Efficiency	-	69%
Spillover Efficiency	-	92%
RF Power Handling	-	180 kW Pk. 15 kW Average
Height Accuracy at 100 nmi	2,000 Ft	1320 Ft RSS to 80K Ft

TABLE 5. SUBSYSTEM RF LOSSES (LOW ELEVATION BEAMS)

	Receive (dB)	Transmit (dB)
Phase Shifters	1.1	1.1
Orthogonal Beam Network	0.4	0.4
Waveguide Distribution Networks	0.2	0.2
Rotary Joint	-	0.2
T/R Limiter Assembly	0.4	-
Total	2.1	1.9

ANTENNA GAIN

Uniform Aperture	44.4 dB
Aperture Efficiency (69%)	-1.7 dB
Spillover Efficiency	-0.4 dB
Total	42.3 dB

arranged on a rectangular grid. The results of that analysis were expanded to permit the beam parameters to differ in elevation.

The height estimation errors are primarily due to radar thermal noise limitations. Based on the parameters of Table 3, the peak errors shown in Figure 14 occur at elevation beam crossover angles shown in Figure 4.

EXPERIMENTAL PERFORMANCE SUBSTANTIATION

Antenna performance was verified by constructing a one-tenth scale model operating at Ka-band (31-36 GHz). Measurements were performed in an indoor antenna range 45 feet long which was equipped to measure both conventional antenna patterns and radiation contours.

Throughout the experimental program, the reflector was illuminated using several different types of feeds. Conical multimode feeds with essentially rotationally symmetric beams were used to verify the scanning performance of the antenna. These were ultimately replaced by an array of rectangular corrugated horns which were used to evaluate the antenna more realistically as a stacked beam system. The antenna configurations tested and the results from these tests are described in detail in the following paragraphs.

DESCRIPTION OF THE SCALE MODEL ANTENNA AND ANTENNA RANGE

The scale model antenna consists of a precision machined reflector, one of several feed systems, a precise positioning fixture for the various feed assemblies, and necessary structure to support the feed and reflector and mount to an antenna positioner.

The 10:1 scale model reflector is an offset section of a parabola with a focal length of 7.80 inches. The antenna aperture is an ellipse with a major axis measuring 24.0 inches and a minor axis of 14.40 inches. The reflector geometry is illustrated in the photograph of the scale model antenna, Figure 15.

The reflector was machined from a solid block of aluminum using a numerically controlled milling machine to obtain an accurate and stable reflecting surface. Subsequent measurements of the surface showed the actual surface to be within 0.0025 inch of theoretical with an RMS tolerance of 0.0013 inch. The maximum error occurred in one small region of the reflector due to a non-uniformity in the block of aluminum from which the reflector was machined. If this one region is neglected, the RMS error is less than 0.001 inch. Reflector surface tolerances will therefore make a negligible contribution to measured antenna sidelobes.

Several different feeds were considered and evaluated during the course of the program. The first type of feed used to illuminate the reflector was a dual mode conical horn feed shown in Figure 16. The feed was designed to have a rotationally symmetric radiation pattern such that the illumination distribution on the reflector would be independent of polarization. The dual mode feed was displaced from the focal point of the paraboloid to verify the scan performance of the offset reflector predicted by computer simulation.

Although the dual mode conical horn feed was useful for verifying the scan performance, it is not suited for use in a stacked beam antenna operating over a 15 percent bandwidth for two reasons. First, a dual mode horn cannot provide rotationally symmetric radiation patterns over a 15 percent band when the TM_{11} mode is generated by a step discontinuity in the waveguide diameter. Second, the conical horns are too large to place in an array which will properly place beams for elevation coverage and target height estimation. The dual mode horns did, however, provide very useful corroboration of the calculated antenna performance.

Stacked beam performance was evaluated using an array of rectangular waveguide horns with corrugated side walls. These provide illumination of the reflector with adequate polarization diversity, and also fit into the space available. Figure 17 is a photograph of the five horn test feed. The horns are in a staircase arrangement so that their phase centers are properly located to maintain scan independent azimuth beamwidths.

The antenna range used for all antenna pattern measurements was a tapered anechoic chamber. The distance from the source antenna, located at the apex of the chamber, to the antenna under test was approximately 45 feet. The chamber flares at a total included angle of about 30 degrees up to a cross section of 20 feet square. The test antenna was placed approximately in the center of the spherical quiet zone which is about 6 feet in diameter.

Detailed measurements of extraneous energy in the quiet zone of the anechoic chamber using the "Free Space VSWR" method demonstrated that such reflected energy was at least 60 dB below the direct path energy at frequencies of 10 and 18 GHz. In addition, the performance of the chamber improved with increasing frequency. These results were extrapolated to the 30 GHz band. The very low sidelobe levels obtained with the scale model antenna attest to the low levels of extraneous energy within the quiet zone of the chamber.

The length of the antenna range was 45 feet. In terms of multiples of the quantity D^2/λ , where D is the largest linear dimension of the antenna aperture, the range is $0.36D^2/\lambda$. Patterns calculated for this near field spacing of source and test antennas (Figure 18) show negligible differences in sidelobe levels but slight beam broadening. Slight refocusing of the feed brought the predicted near and far field patterns into very close correspondence, as shown in Figure 18. Hence, the antenna range used is fully expected to give results virtually identical to those which would have been obtained with a conventional far field range, but with the major advantage of low range reflections.

Measured Scale Model Patterns

The purpose of this paragraph is to illustrate a sampling of the measured pattern data accumulated in support of the analysis and computation done on this development. Some were done to gain confidence in simulated patterns; others, such as the azimuth patterns, were considered to be the most accurate evaluation of antenna performance, especially at wide angles from the main beam. All measured data was done in the anechoic chamber test range previously described.

Correlation of Computed and Measured Patterns

Figure 19 shows a comparison of pattern data of an elevation beam which was both computed and measured. This is one of a set which, when combined, spanned most of the elevation coverage of the antenna. The agreement between computed and measured patterns was more than adequate for purposes of evaluating the elevation beam characteristics.

Cross Polarized Patterns

Figure 20 is an example of cross-polarization performance characteristics of the antenna geometry, relative to the principal polarization pattern. This is an expanded scale pattern where the co-polarized response is shown in two segments, illustrating an inherent cross polarization response better than -15 dB relative to the main beam peak. Both computed and measured patterns confirmed that the cross polarized response is essentially everywhere lower amplitude than the co-polarized response. This is illustrated in Figure 21 which shows computed cross polarized and co-polarized contour patterns for a beam at 4 degrees elevation. Since the reflector vertex occurs at the lower edge of the reflector, only two cross-polarized principal lobes exist. This level of cross-polarization pattern response, combined with component tolerances within the RF feed networks, corresponds to an average integrated cancellation ratio of 15 dB for distributed clutter in the lower elevation beams.

Azimuth Patterns

The primary use of measured patterns was the development and verification of the low sidelobe characteristics of the azimuth patterns. Optimization of the basic reflector illumination distribution and the methods of controlling spurious reflections from structural areas were done experimentally.

Figures 22, 23, and 24 show three patterns measured with the corrugated horn feed array previously shown in Figure 15 and Figure 17 for the case of the 4.5 degree elevation beam. Two vertically polarized cases are shown at two frequencies in the operating band. The third shows the horizontally polarized equivalent at the midband frequency. The importance of isolating or shielding structural members associated with the reflector and feed supports was clearly estahlished in these pattern tests.

Vertical Plane Patterns

The vertical pattern cut, corresponding to the azimuth pattern of Figure 22, is shown in Figure 25. The asymmetrical distortion of the pattern at lower levels is due to interaction between the corrugated horns making up the feed array.

Suppression of High Elevation Angle Sidelobes

The pattern of Figure 26 is a wide elevation angle response of the antenna from below the horizon in the forward direction through the zenith and beyond. The purpose of the test is to evaluate the effectiveness of the shielding method at the upper edge of the reflector in limiting high angle radiation in the zone used by ARMs in the homing

phase of their flight path. A moderate amount of shielding provides adequate suppression. Three cases are illustrated in Figure 26: 1) no shielding, 2) a shield 3 feet deep; 3) a shield 5 feet deep. These data indicated that the antenna design should include a shield 3 feet deep and 10 feet wide at the upper edge of the reflector, in addition to shielding below the reflector to control feed spillover.

CONCLUSION

The overall result of this effort is an antenna design for tactical radar with: 1) wide instantaneous bandwidth (600 MHz at S-band); 2) low azimuthal sidelobes; 3) low sidelobes in a cone of 45 degree half-angle centered at the zenith; 4) polarization diversity, including orthogonal, linear, and circular; 5) electronically steered beam over 20 degrees in elevation compatible with wide bandwidth signal processing.

This study demonstrates that, by applying design techniques specifically directed at sidelobe suppression, very low sidelobe performance can be achieved with a reflector antenna. These techniques include: 1) much lower edge illumination than has been customary, at a modest sacrifice of aperture efficiency; 2) edge shielding to reduce the sidelobes caused by spillover at the edge of the reflector; 3) feed offset configurations that minimize blockage of the aperture by the feed structure; 4) shielding techniques that minimize high-angle radiation from the feedhorn structure.

REFERENCES

1. J. Ruze, "Antenna Tolerance Theory - A Review," *Proc. IEEE*, Vol. 54, No. 4, April 1966, pp. 633-640.

2. E. M. Hofstetter and D. G. Delong, Jr., "Detection and Parameter Estimation in an Amplitude Comparison Monopulse Radar," IEEE *Transactions on Information Theory*, Vol. IT-15, No. 1, Jan. 1969, pp. 22-30.

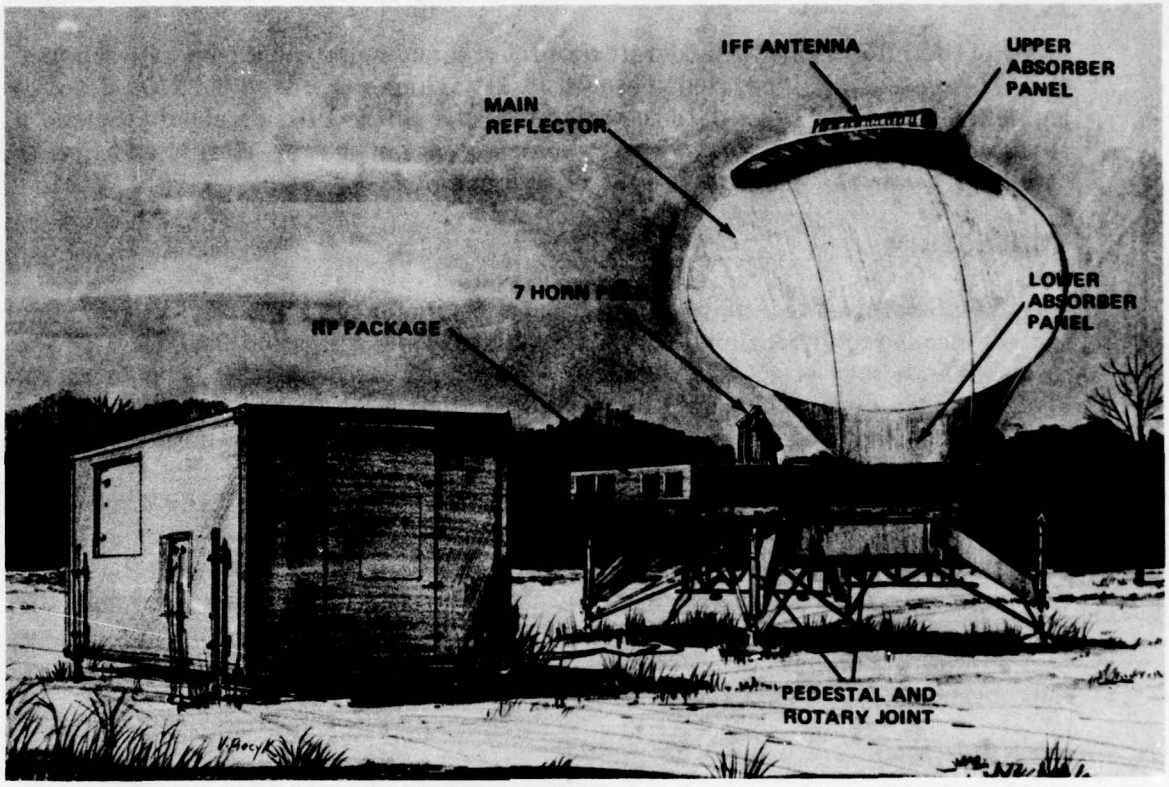

Figure 1. Sketch of Stepped-Beam Reflector Antenna Showing Location of Components

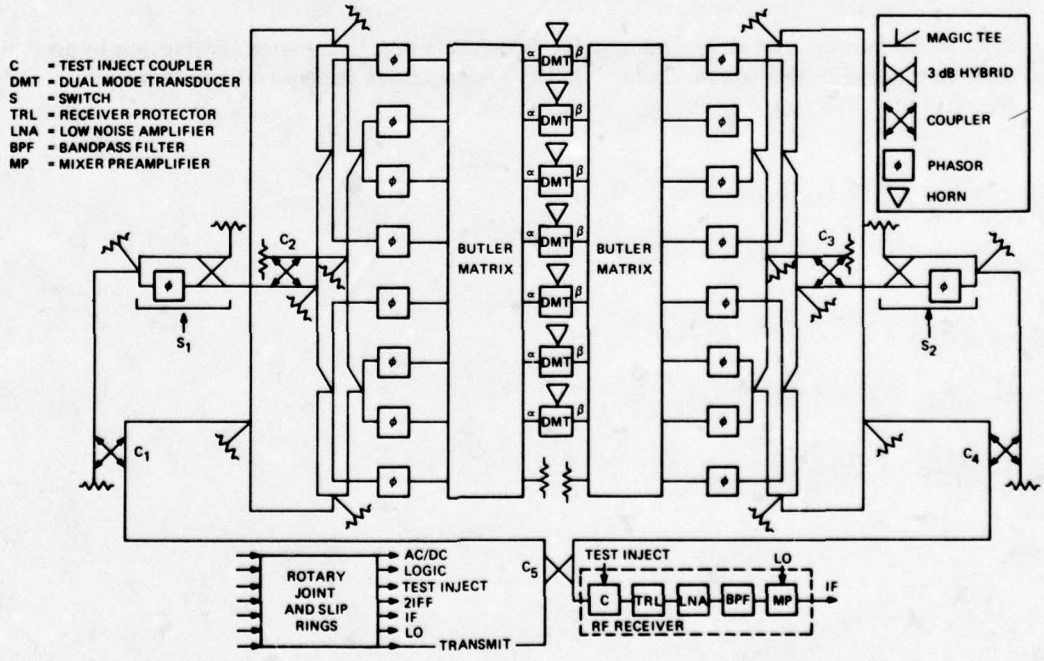

Figure 2. Block Diagram of Microwave Subsystem

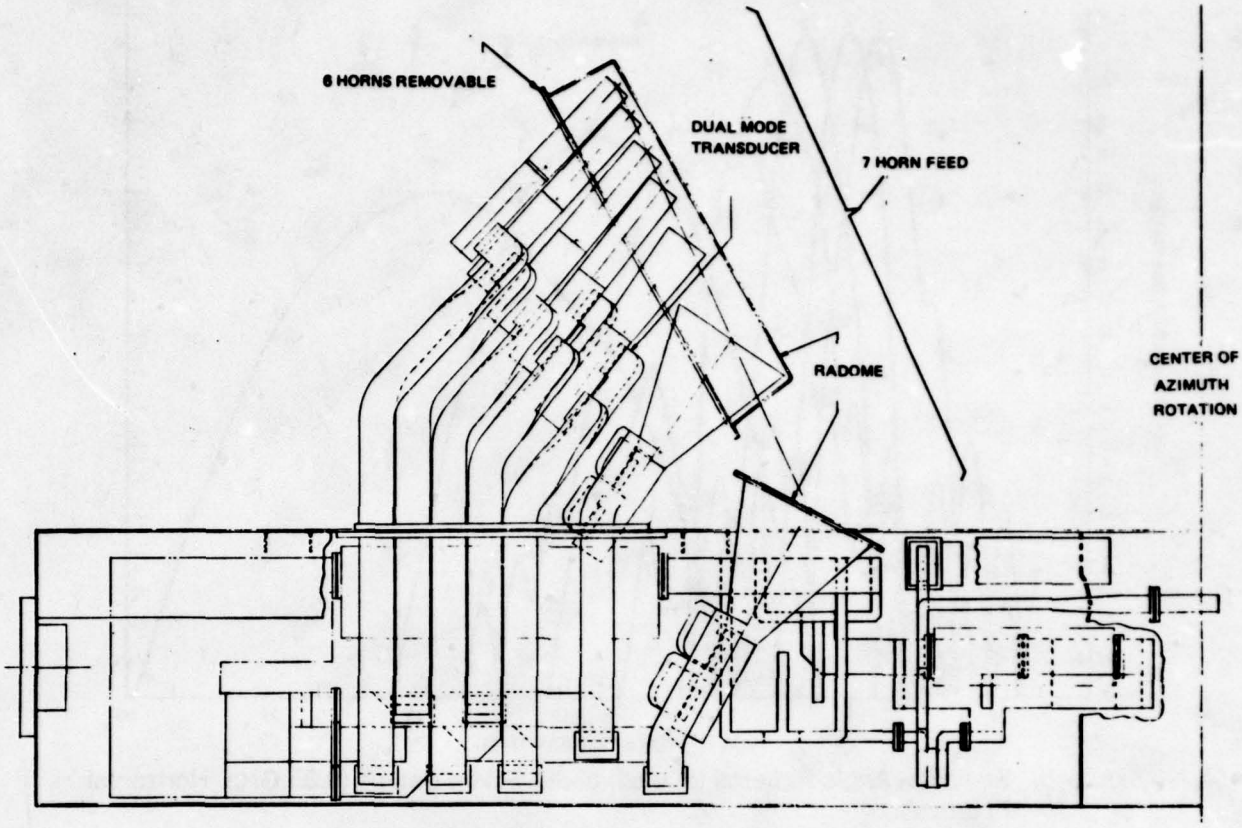

Figure 3. Configuration of the Seven-Horn Feed

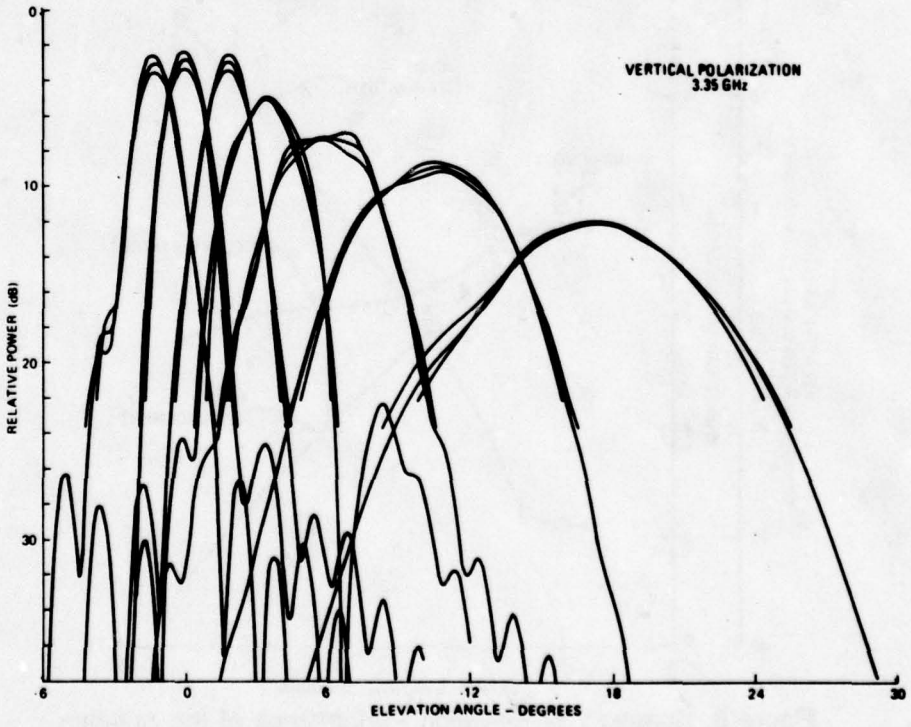

Figure 4. Calculated Elevation Patterns

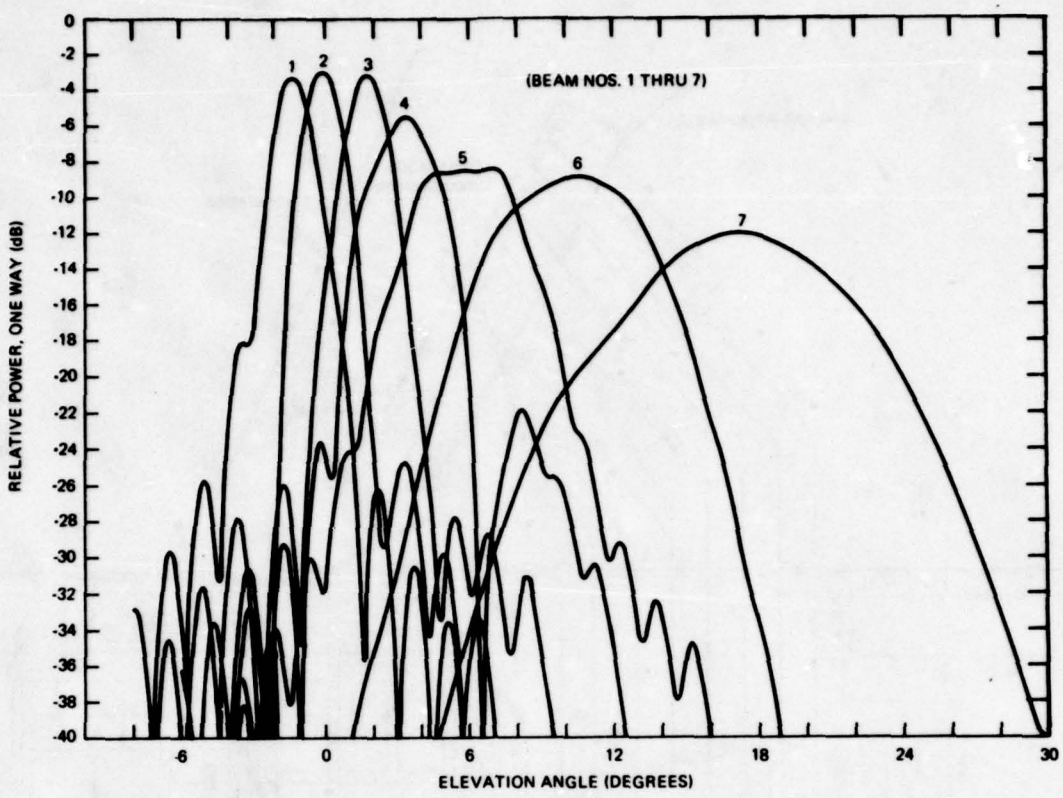

Figure 5. Elevation Angle Patterns for each of the Seven Beams (3.35 GHz, Horizontal Polarization)

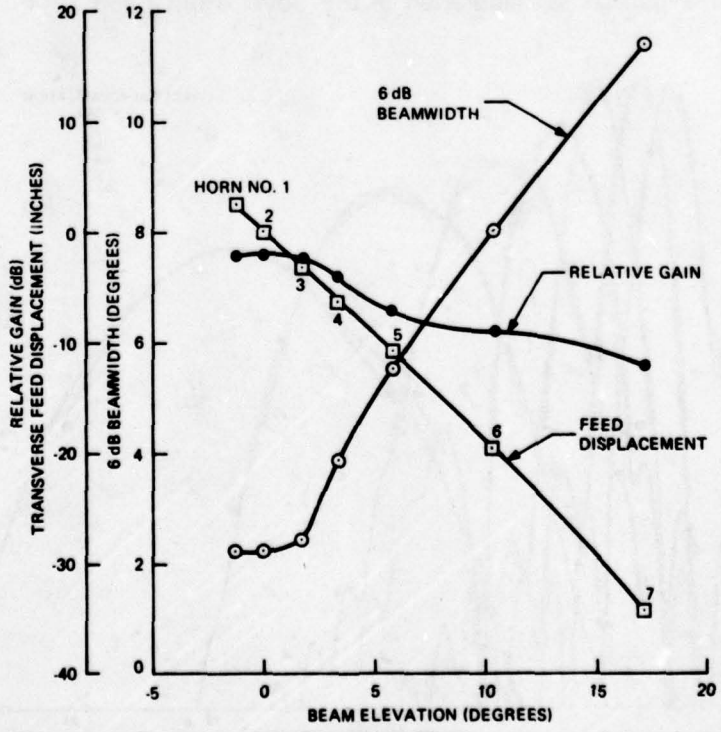

Figure 6. Summary of Elevation Performance of the Antenna

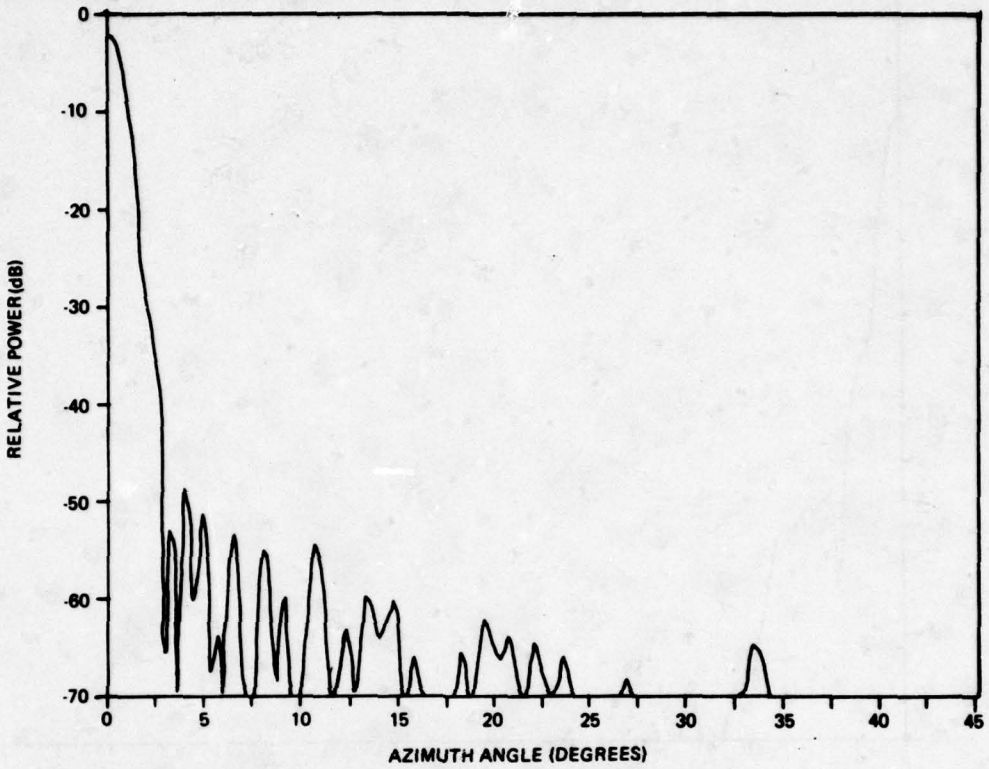

Figure 7. Azimuth Pattern of Baseline Antenna, Beam No. 2

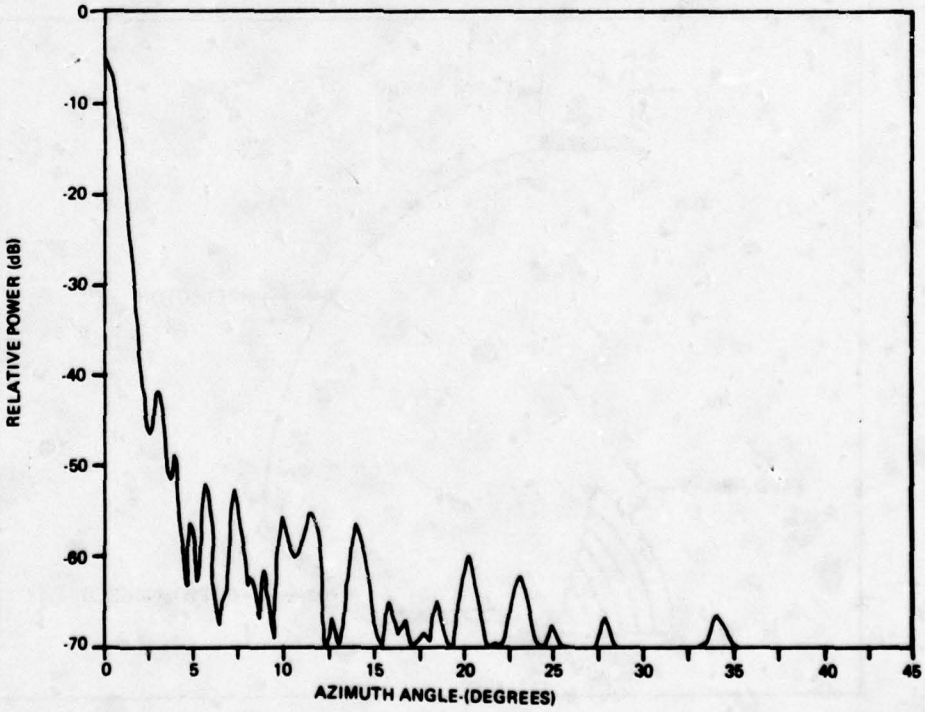

Figure 8. Azimuth Pattern of Baseline Antenna, Beam No. 4

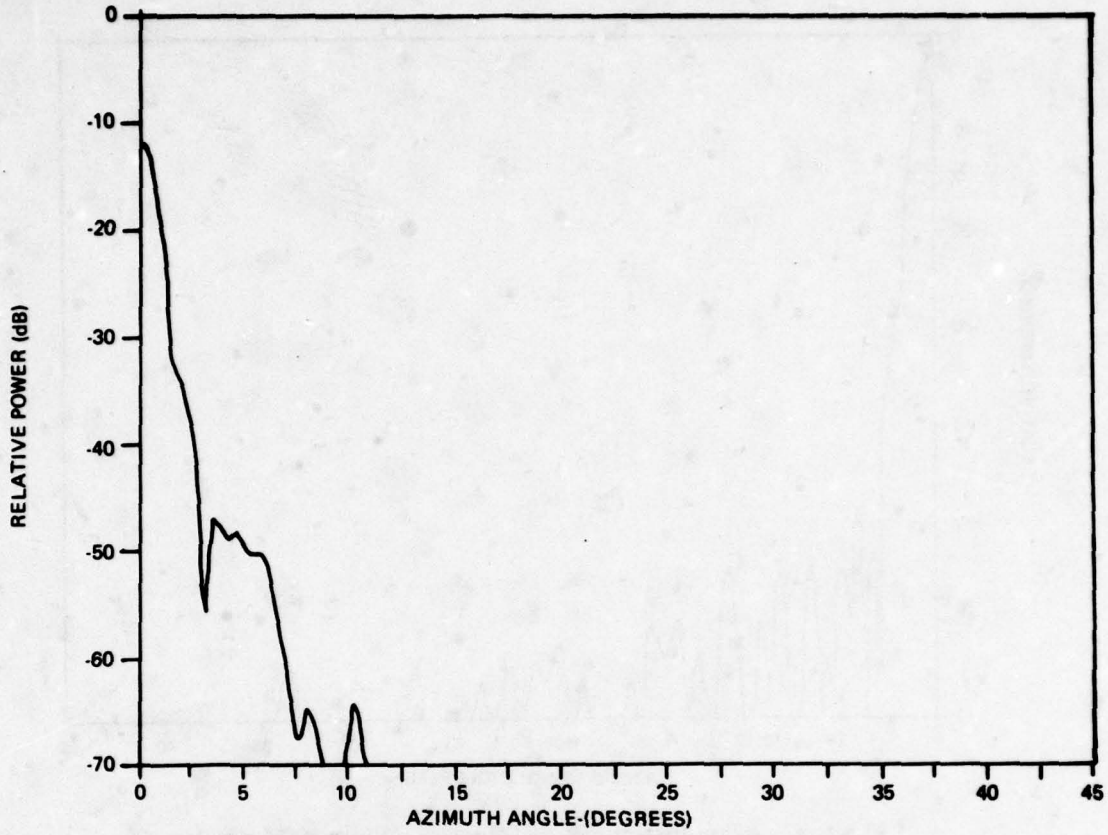

Figure 9. Azimuth Pattern of Baseline Antenna, Beam No. 7

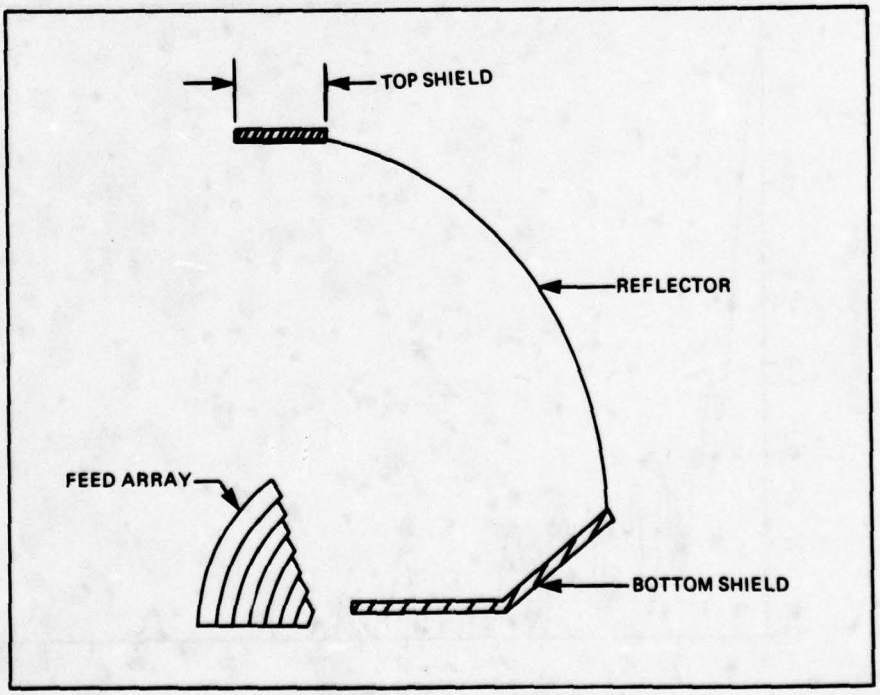

Figure 10. Side View of Reflector showing Location of Top and Bottom Absorber Panels

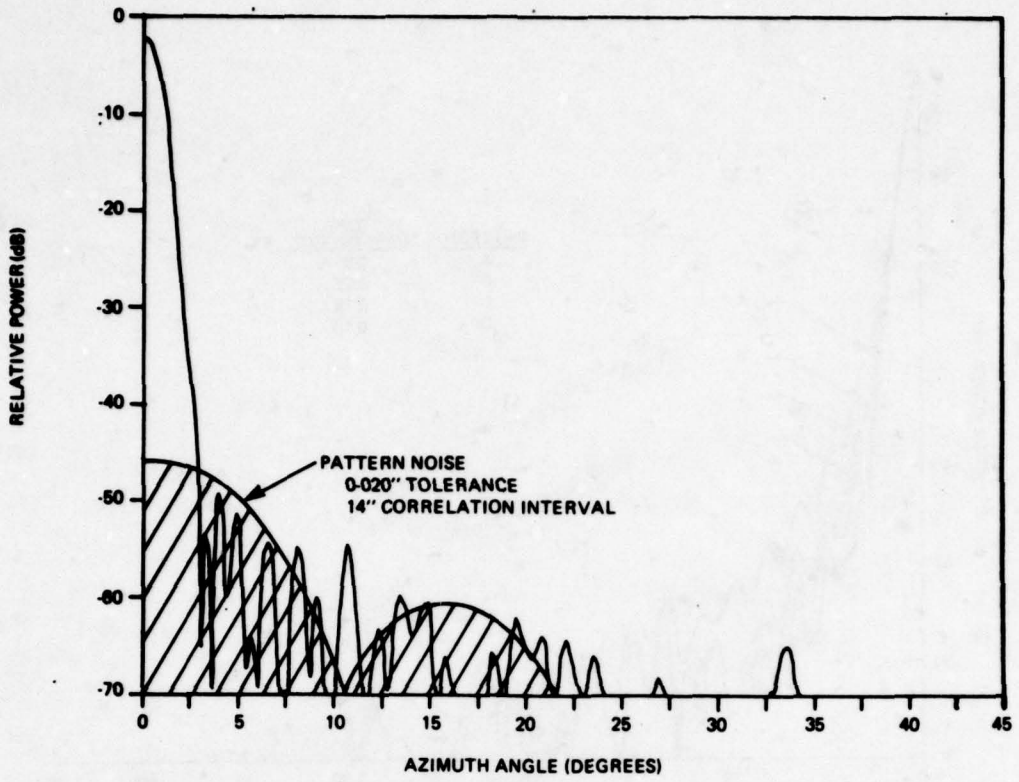

Figure 11. Pattern Effects of Reflector Random Surface Tolerances (Azimuth Pattern, Beam No. 2)

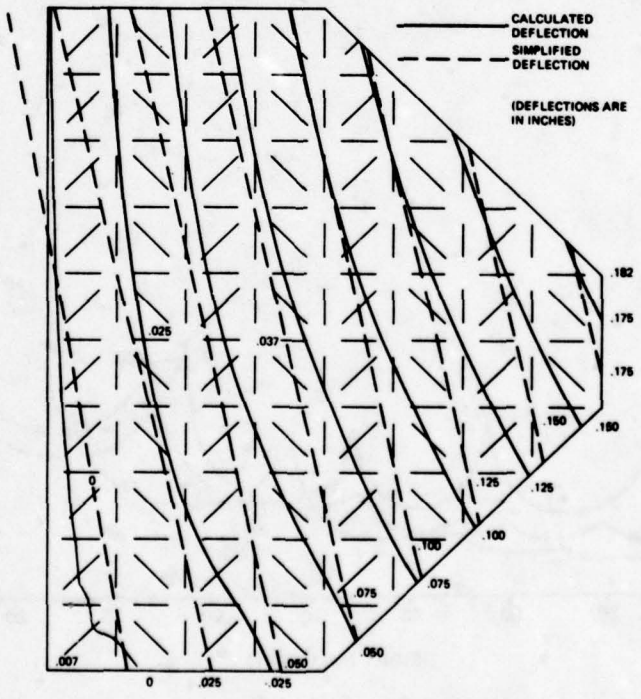

Figure 12. Reflector Configuration Used in Computerized Stress Simulations

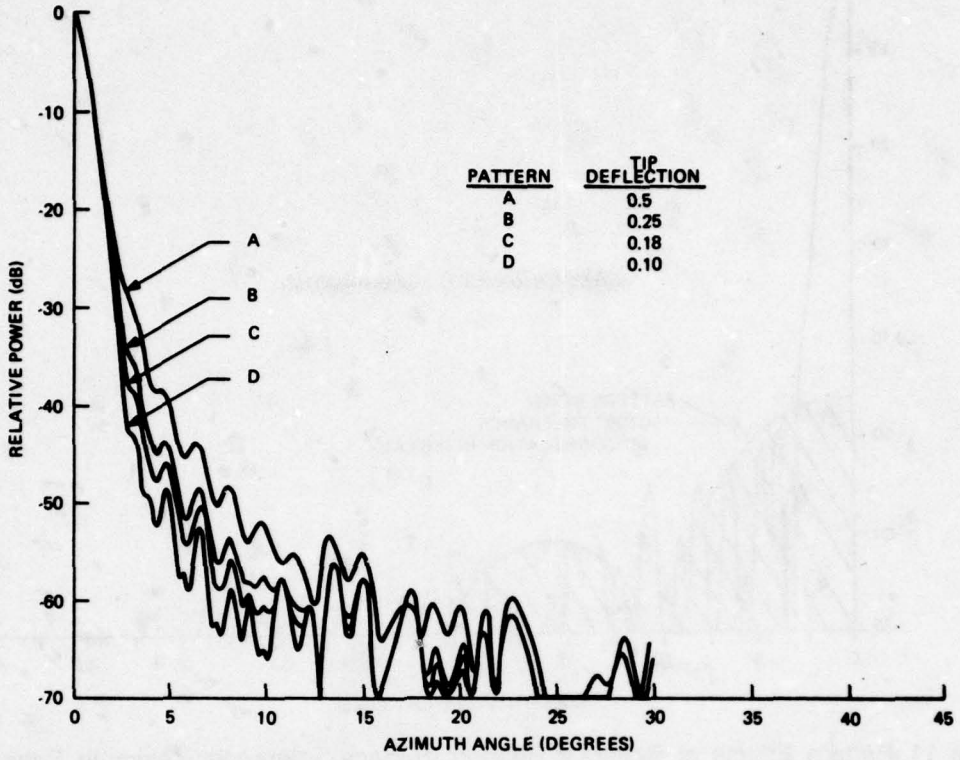

Figure 13. Effect of Maximum Reflector Deflection Due to Wind Loading (Linear Deflection Law)

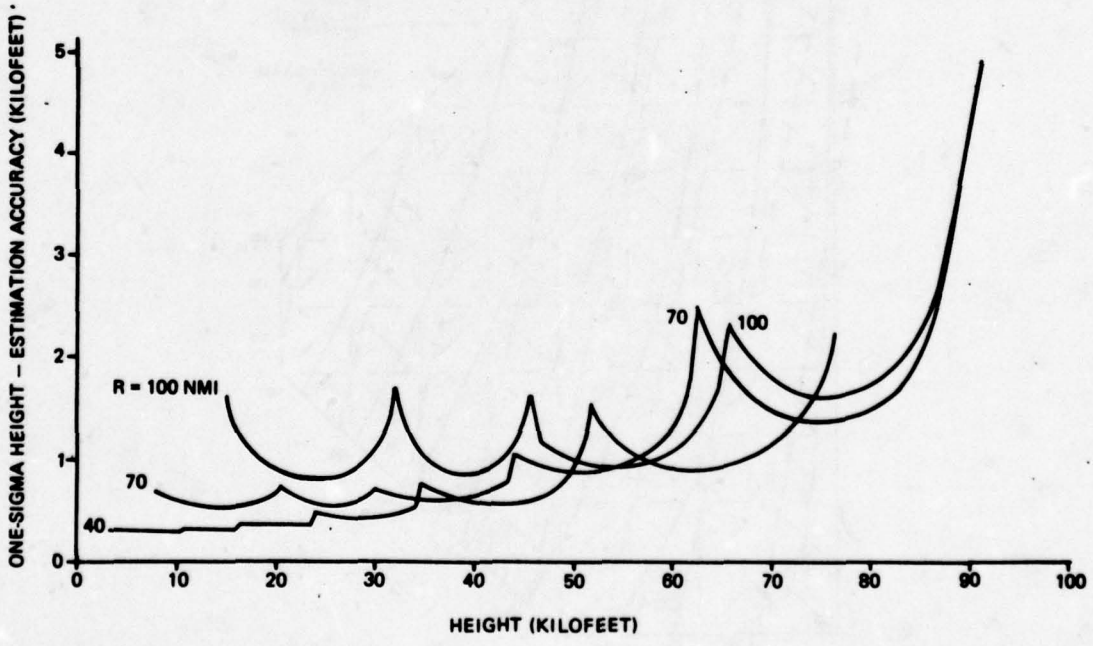

Figure 14. Height Estimation Performance, Vertical Polarization

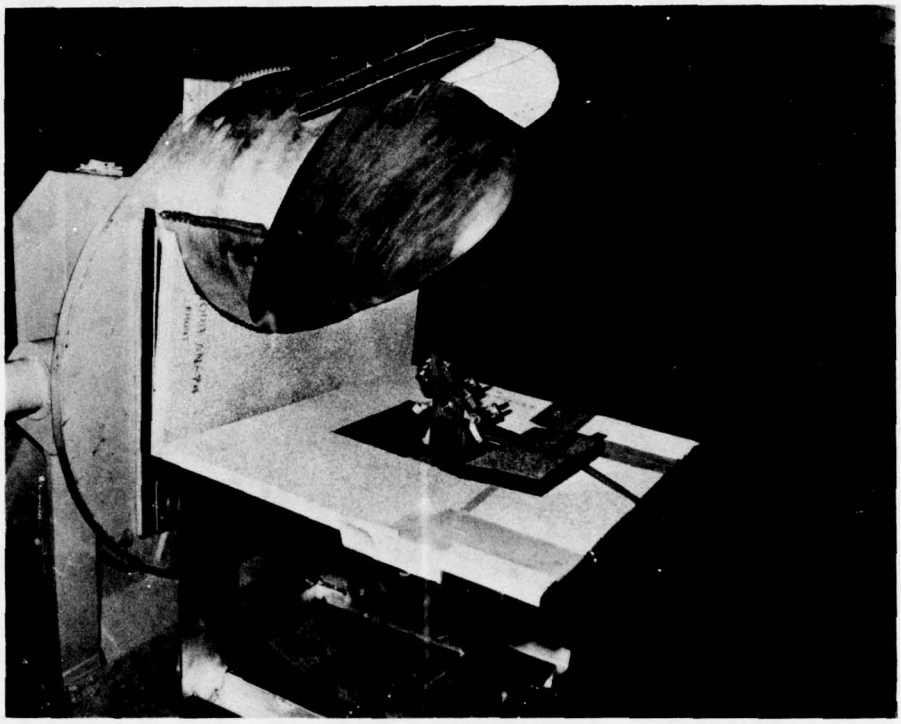

Figure 15. Scale Model Antenna

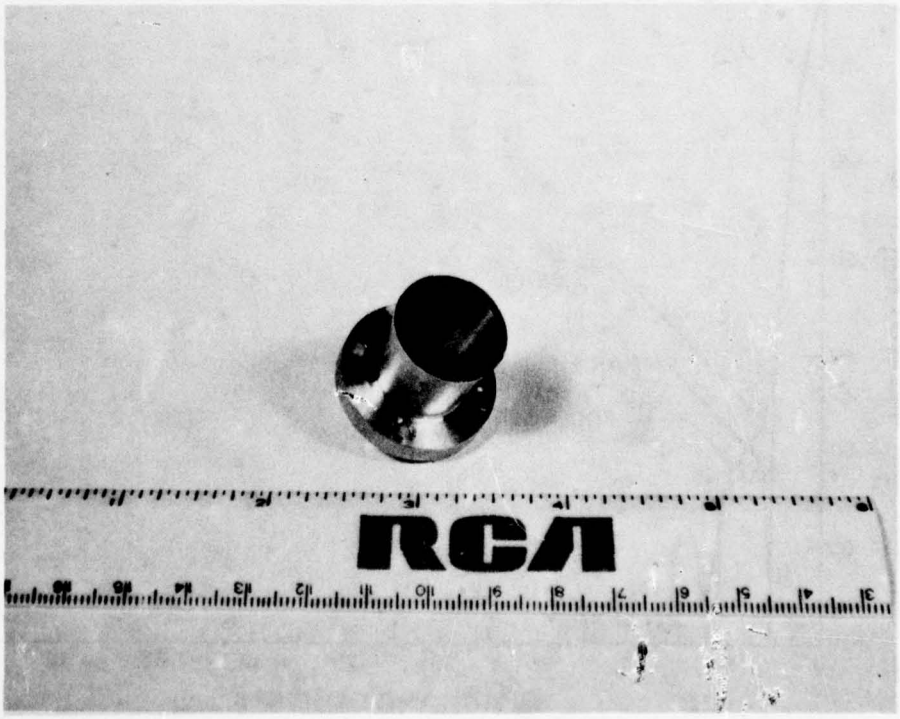

Figure 16. Dual Mode Conical Horn Feed

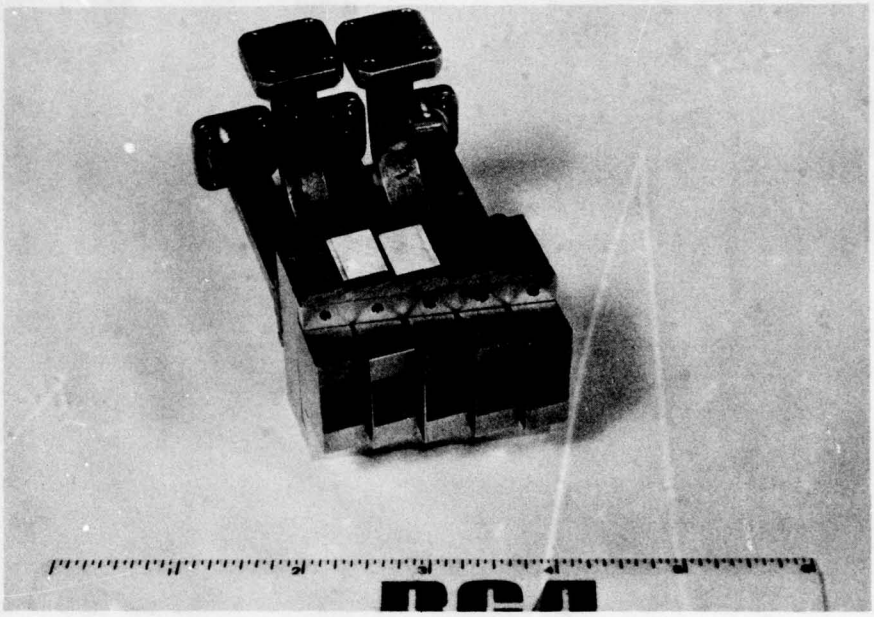

Figure 17. Five Horn Test Feed, showing Corrugated Rectangular Structure

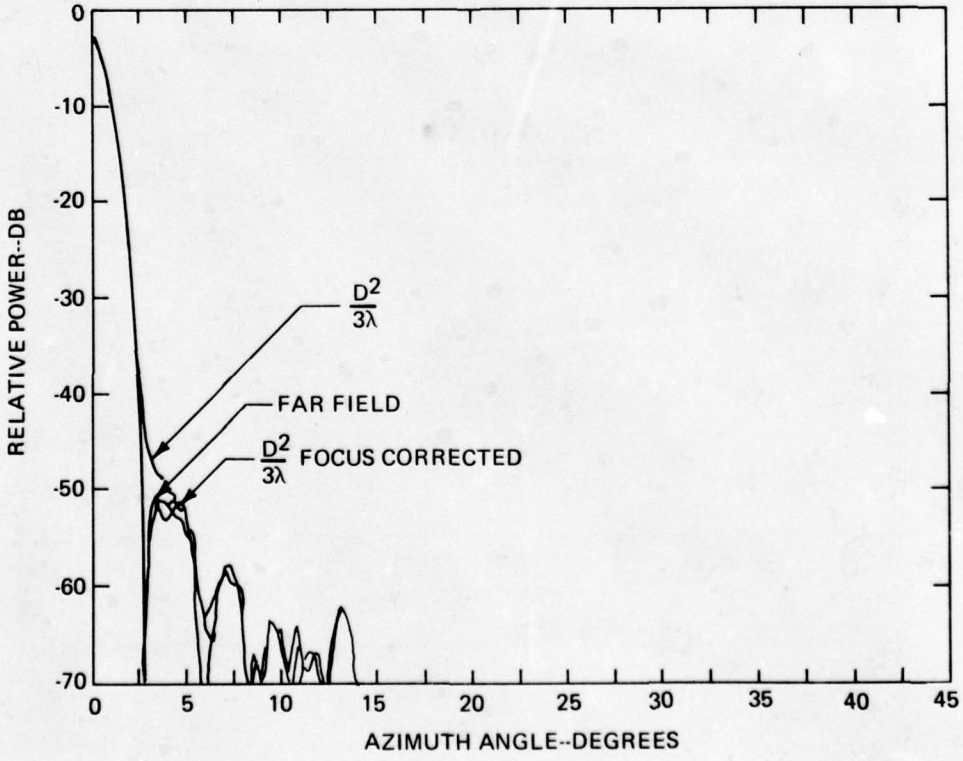

Figure 18. Computed Azimuth Pattern for Horizon Beam

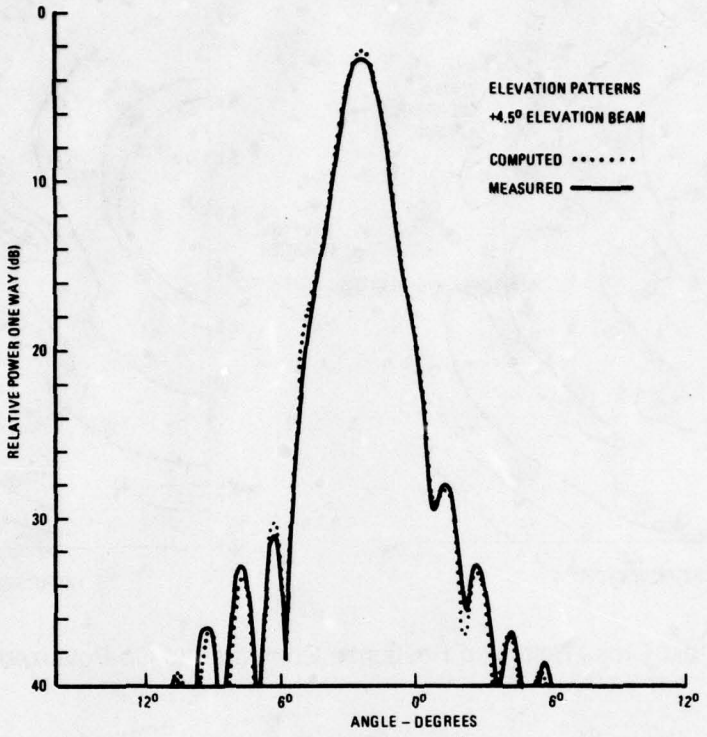

Figure 19. Comparison of Computed and Measured Patterns

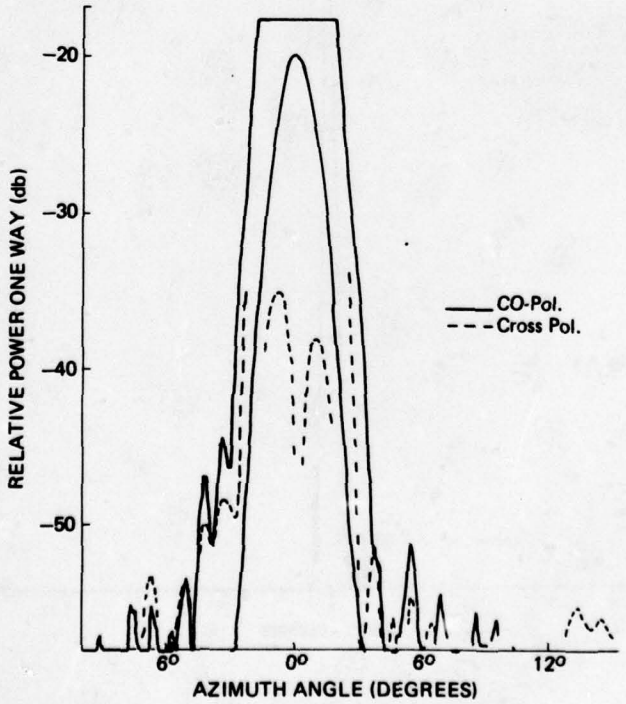

Figure 20. Measured Cross-Polarized Response Compared to Co-Polarized Response

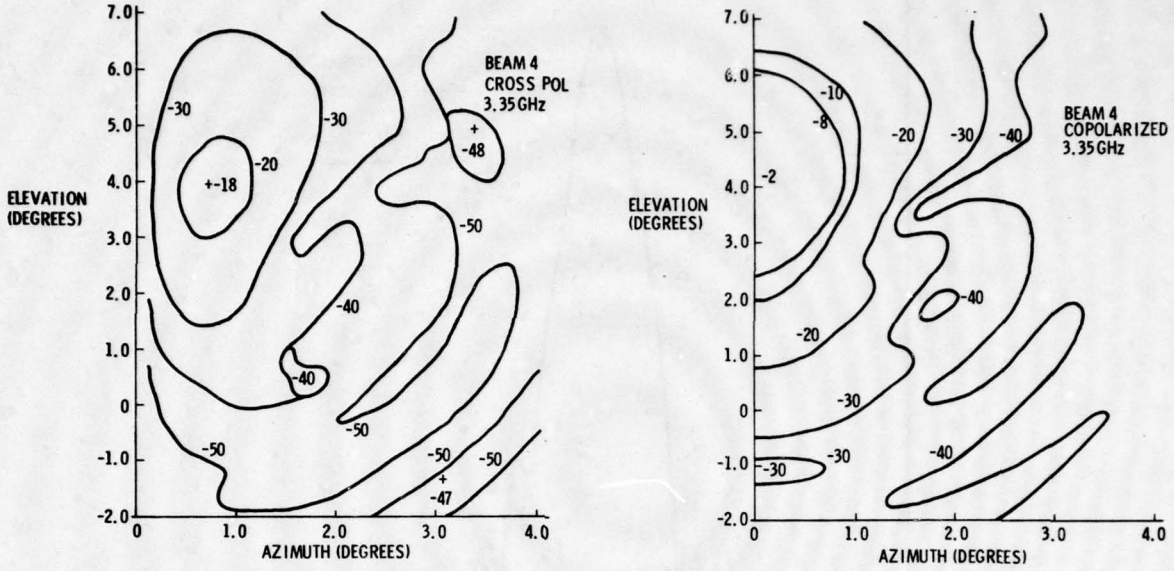

Figure 21. Computed Cross-Polarized Response Compared to Co-Polarized Response

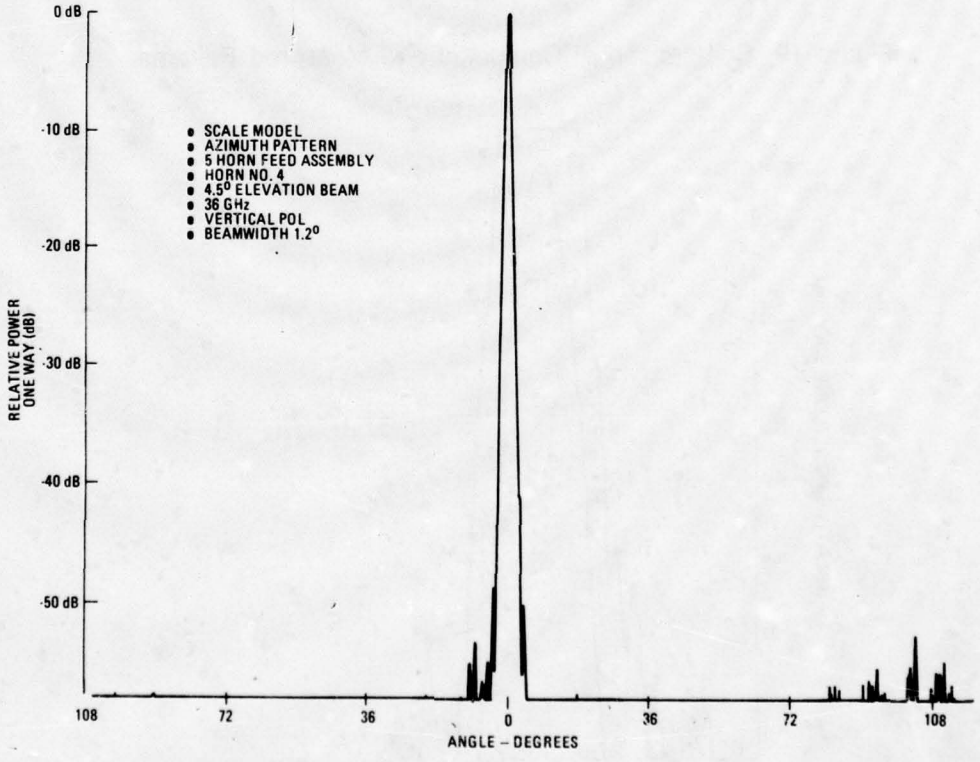

Figure 22. Azimuth Pattern, Vertical Polarization, at 36 GHz

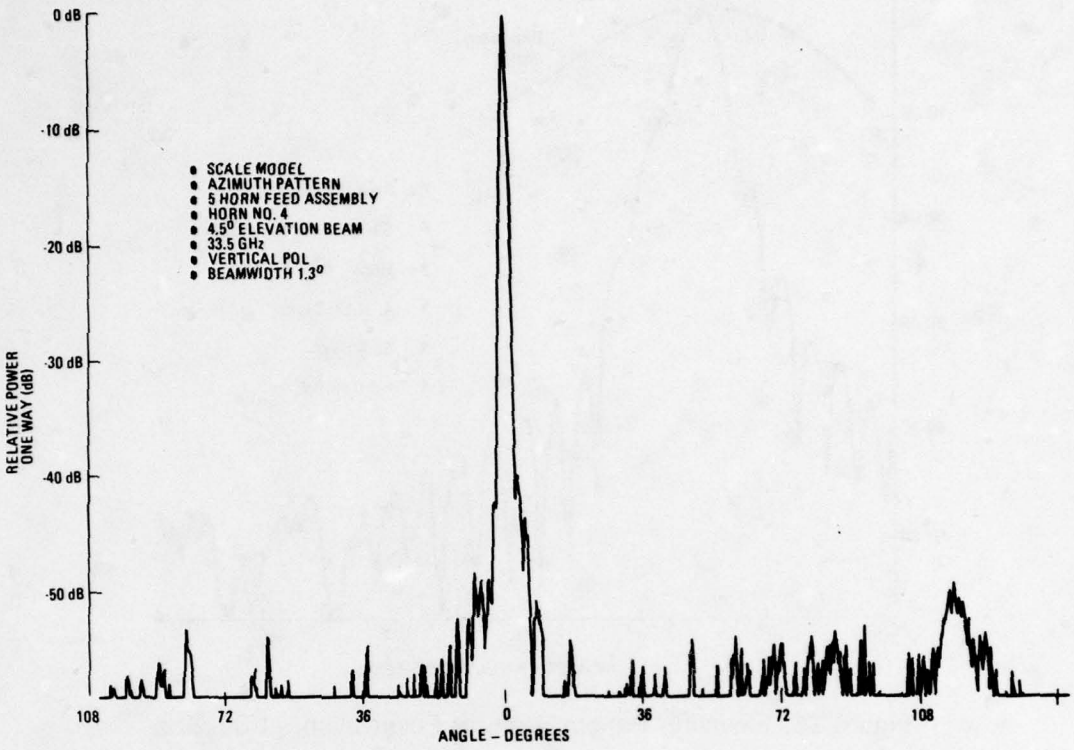

Figure 23. Azimuth Pattern, Vertical Polarization, at 33.5 GHz

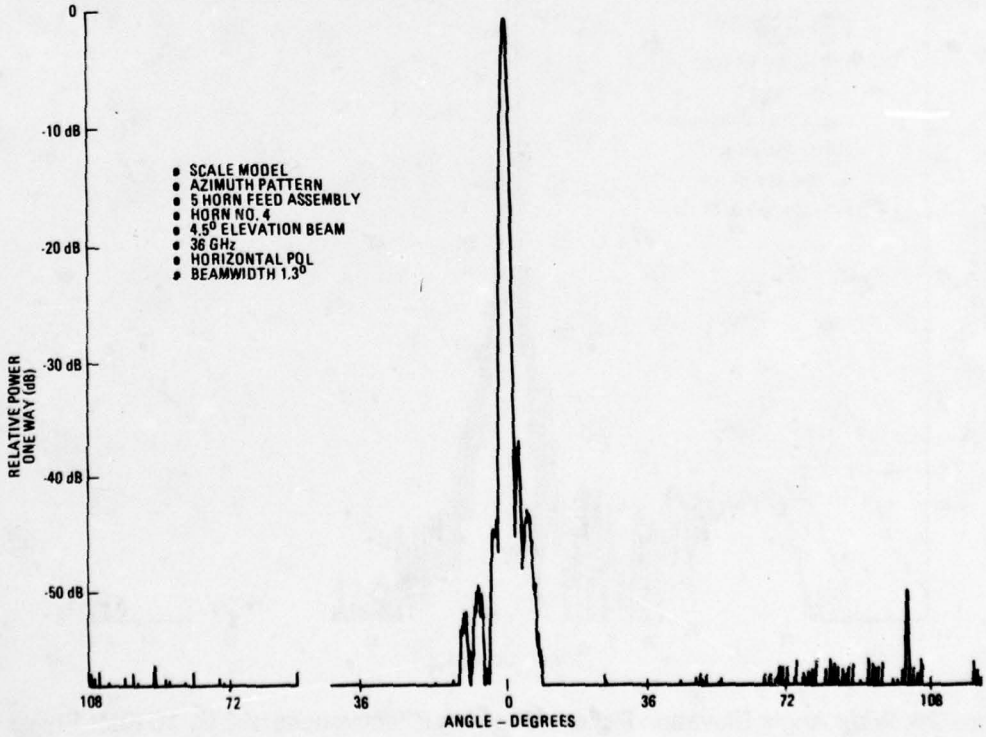

Figure 24. Azimuth Pattern, Horizontal Polarization at 33.5 GHz

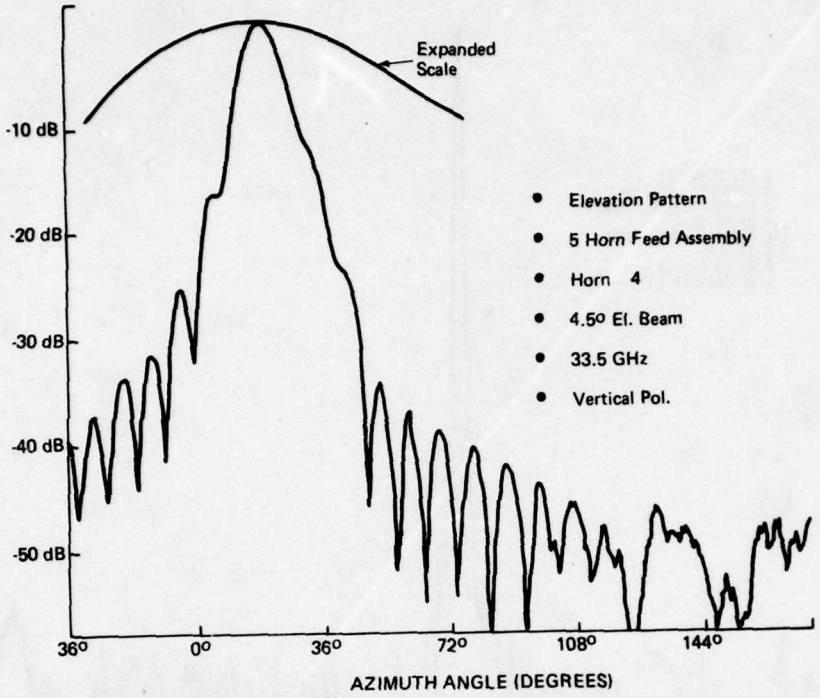

Figure 25. Elevation Pattern, Vertical Polarization, at 36 GHz

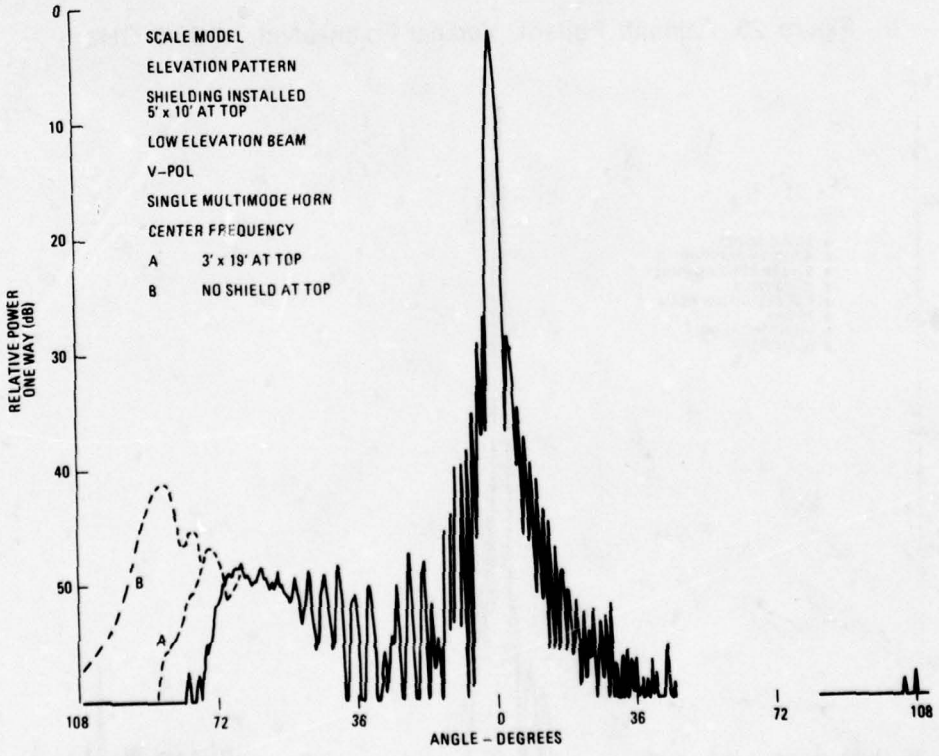

Figure 26. Wide Angle Elevation Pattern Showing Effectiveness of 3 by 10 Foot Shield at Top of Reflector vs 5 by 10 Foot Shield and No Shield

LOW SIDELOBE PARABOLIC CYLINDER ANTENNA FOR SURVEILLANCE RADARS*

by Salvatore Milazzo and John Stangel

Sperry Gyroscope

Sperry Rand Corporation

Great Neck, New York

Abstract - An antenna configuration consisting of a parabolic cylindrical reflector illuminated by an off-set line source feed is described. The antenna is mechanically rotated about the cylindrical axis for 360 degree azimuth coverage. Elevation coverage and height finding is achieved by electronic scanning using phase shifters in the line source feed. A novel imaging concept, which simplifies analysis and fosters better understanding of the principles of this design, is derived. Synthesis techniques for low sidelobe performance and for minimization of reflector size are presented.

* This work was supported in part by the U.S. Air Force, Rome Air Development Center under contract number F19628-78-C-0147.

1. Introduction

Tactical surveillance radars of the future must perform reliably in increasingly hostile and sophisticated ECM environments. These environments are characterized by severe active and passive jamming, anti-radiation missiles and a host of other advanced electronic warfare systems, which constitute formidable impediments to the operability and survivability of radar systems.

To effectively counter this threat, future tactical radars must be equipped with antennas which exhibit very low sidelobe radiation profiles. In addition, these antennas must be compatible with a variety of advanced ECCM techniques such as spread spectrum, wide-band frequency agility and polarization diversity. Furthermore, tactical radars must be rapidly transportable to facilitate the highly dynamic military operations envisioned in future hostilities. This will necessitate antenna configurations which are amenable to lightweight construction, low-volume packaging and rapid, reliable erection and tear-down.

This paper discusses an innovative parabolic cylinder antenna which is consistent with the above characteristics. The concept is described within the context of an S-band long range, three-dimensional surveillance radar whose primary mission is tactical ground control intercept. The antenna design approach, as depicted in figure 1, is comprised of a mechanically rotating parabolic cylindrical reflector which is illuminated by a line source array feed located at the focal line. The cylindrical axis and line source feed are substantially vertical and parallel to the axis of rotation. The reflector surface is off-set thus eliminating aperture blockage by the feed and facilitating the formation of beams with low sidelobes in both azimuth and elevation.

The elevation plane characteristics of the secondary patterns are dictated primarily by the amplitude and phase profile impressed on the line source feed. Electronic scanning and beam broadening in the elevation plane are accomplished by ferrite phase shifters at the feed elements. Sequential comparison of target returns on adjacent beams provides the radar with target altitude data. Excellent beam characteristics are preserved for all scanned beams by virtue of a unique property of this configuration which precludes phase, amplitude and polarization aberrations when linear phase gradients are imposed on the line source feed. Beam broadening is achieved by impressing a non-linear phase function on the feed in such a manner as to minimize the required reflector area.

A low sidelobe illumination in azimuth is realized by comprising each element of the line source feed as a transverse linear sub-array of several elements. The azimuth illumination on the reflector is then determined by the excitation of these elements.

The generic advantages of the parabolic cylinder antenna for advanced tactical radar applications were originally recognized by Rome Air Development Center, Deputy for Electronic Technology. The generally positive results of preliminary analyses and experiments conducted at RADC have been recently published (1, 2, 3). The present paper reports the initial results of concurrent studies performed at Sperry. These studies have generated a unique geometrical optics concept which lends greater insight into the principles of the parabolic cylinder antenna and simplifies the analysis and synthesis of optimized antenna systems for specific applications. In addition, several novel design techniques are described. These techniques relate to the realization of very low sidelobe performance and to the minimization of reflector size.

2. Geometrical Optics Theory

A parabolic cylindrical reflector fed by a line source is in many respects an ideal antenna configuration for advanced surveillance radars. As with all reflectors, the parabolic cylinder offers the potential for simple, light-weight implementation appropriate for a cost effective, transportable radar system. The parabolic cylinder reflector is unique in that its beam may be electronically scanned in direction of the cylindrical axis with theoretically no scanning aberrations. This scanning is readily accomplished by imposing a linear phase gradient on the line source feed. This property, as well as other unique properties, of the parabolic cylinder reflector antenna may be deduced from the following analytical development.

Consider the parabolic cylinder antenna in the coordinate system illustrated in figure 2. A line source of height, h, lies on the y-axis and illuminates an off-set sector of a parabolic cylinder. The y-axis is also the focus of the parabolic cylinder while the line, z = -f, is its apex. It is convenient to express some of the geometrical relationships in terms of the cylindrical coordinates, (ρ, ψ, y). Thus, the parabolic cylinder is given as:

$$\rho = \frac{2f}{1 + \cos\psi} \tag{1}$$

The transformation to the original Cartesian system is readily expressed as:

$$\begin{aligned} x &= \rho \sin\psi \\ y &= y \\ z &= -\rho \cos\psi \end{aligned} \tag{2}$$

Now consider a conical wave emanating from the line source. The propagation vector of such a wave is given by:

$$\bar{K}_I = K_o (\cos\alpha \hat{\rho} + \sin\alpha \hat{y}) \qquad (3)$$

where $(90 - \alpha)$ is the cone half-angle. This wave is generated by impressing a linear phase gradient on the line source according to the relationship:

$$\frac{d\gamma}{dy} = -K_o \sin\alpha \qquad (4)$$

where K_o is the free space propagation constant, $2\pi/\lambda$. The effect of reflection from the parabolic cylinder is to convert the radial component of the propagation vector to the z-directed component while leaving the y-component unaffected. Thus, the propagation vector of the conical wave after reflection is:

$$\bar{K}_R = K_o (\sin\alpha \hat{y} + \cos\alpha \hat{z}) \qquad (5)$$

This is a plane wave scanned at an angle α with respect to the z-axis. Therefore, the beam of an ideal parabolic cylinder antenna may be scanned without phase aberration by imposing a linear phase gradient on the line source feed.

The above relationships (3) and (5) may be used to deduce unique imaging properties which are applicable to the parabolic cylinder antenna. Referring again to figure 2, consider the radiation emitted from a point (0, y, 0) on the line source feed in a direction (ψ, α). The ray in this direction is one of the family of rays comprising the conical wave postulated above. Therefore, its direction after reflection from the parabolic cylinder is compatible with the propagation vector of equation (5). Perturbing this ray by $d\alpha$ will cause an equal perturbation $d\alpha$ for the reflected ray since substituting $(\alpha + d\alpha)$ for α in equation (3) will result in a replacement of $(\alpha + d\alpha)$ for α in equation (5). The virtual source of this ray is (x, y, -2f).

This is apparent by noting the equivalence of incident and reflected ray geometries in the ψ -plane and x-plane respectively. As illustrated in figure 2, the apparent locus of the reflected rays from the reflector to the apparent source point as projected to the x-z plane has a length ρ . This corresponds to the projected length of the incident rays from the line source to the reflector. This equality is readily observed by substituting z for ψ in the equation for the parabolic cylinder according to equation (2). Equation (1) then becomes:

$$\rho = 2f + z \tag{6}$$

For the sector illustrated in figure 2, z is negative.

If we now perturb the (ψ, α) ray through an angle $d\psi$ in the ψ -direction, we find that the locus of the virtual source is perturbed in the x-direction only by a length dx. The quantitative relationship between these differentials is derived as follows:

Substituting $x/\sin\psi$ for ρ in equation (1) and rearranging terms, we get:

$$x + x\cos\psi = 2f \sin\psi$$

Taking the total differential of both sides:

$$dx + dx \cos\psi - x \sin\psi d\psi = 2f \cos\psi \, d\psi$$

$$dx (1 + \cos\psi) = (x \sin\psi + 2f \cos\psi) \, d\psi$$

$$= 2f \left[\frac{\sin^2\psi}{1 + \cos\psi} + \cos\psi \right] d\psi$$

$$= 2f \left[\frac{\sin^2\psi + \cos\psi + \cos^2\psi}{1 + \cos\psi} \right] d\psi$$

The differential relationship thus reduces to:

$$dx = \frac{2f d\psi}{1 + \cos\psi} = \rho \, d\psi \tag{7}$$

Two points are noteworthy regarding equation (7) and its derivation.

First, since only total differentials were taken in the derivation, any differential dependencies of $d\psi$ on dy would have shown up in equation (7). The absence of such terms indicates that a perturbation of the ψ coordinate results only in a perturbation of the x-coordinate of the virtual source. This indicates that a point source located at y = y on the y-axis may be represented by a line source at y = y in the z = -2f plane upon reflection by a ideal, infinite parabolic cylindrical reflector as defined by equation (1). This implies that a different displacement, dy, of the source point on the line source feed will result in an equal displacement, dy, of the image line source in the z = -2f plane. Thus, a line source feed of height, h, on the y-axis may be represented by a planar source of height, h, in the z = -2f plane.

The second point regarding equation (7) is that the differential relationship between dx and $d\psi$ is a function of ψ only. Therefore, if the radiation of the line source feed can be written as a separable function in y and ψ, then the illumination in the image plane can likewise be represented as a separable function in y and x. The y-illumination of the line source is therefore directly transferable to the imaged plane aperture, while the x-illumination is obtained from the ψ-pattern of the feed via the transformation implied in equation (7). The second form of equation (7), showing linear ρ dependence, suggests that the necessary transformation is equivalent to the so-called space attenuation which must be used to properly design conventional paraboloidal reflector systems.

Although scalar field quantities have been predominently employed in the foregoing development, the imaging theorem substantially holds for

vector fields as well. In a vectorial development the reflection process is defined in terms of incident and reflected magnetic fields in a manner analogous to that employed by Fante[1]. Imaging then allows one to replace an actual infinitesimal current element with an equivalent current element at the image point. Thus, a y-directed linear magnetic current on the y-axis, which gives rise to a ψ polarized incident electric field, would be imaged into a y-directed magnetic current sheet in the z = -2f plane, which gives rise to an x-(horizontally) polarized electric field upon reflection. Sinilarly, a y-directed linear electric current element in the line source feed gives rise to a ψ polarized magnetic field. The resultant antenna characteristics may then be deduced by placing an equivalent y-directed electric current sheet in the z = -2f plane. The electric field of the antenna would then be predominently vertically polarized having y and z components only. The parabolic cylinder antenna is therefore substantially free of polarization anomalies. The absence of polarization problems is further reinforced by discussions in Silver[4], and Collin and Zucker[5], and by a precise computer simulation using vector diffraction theory as discussed in Section 3 of this paper.

3. Low Sidelobe Azimuth Pattern Synthesis

A primary advantage of the parabolic cylinder antenna for surveillance radar applications resides in its ability to produce low sidelobe azimuth patterns while maintaining the simplicity generic to this approach. To achieve this objective a low sidelobe synthesis procedure similar to that recently described by Stangel, Herper and D'Agostino[(6)] was devised. The principles of this procedure are briefly outlined below:

The far field pattern of a uniformly illuminated, perfectly collimating antenna and its focal plane distribution due to a single incoming plane

wave are perfect images of each other. To introduce the effect of a tapered aperture illumination, F(x,y) which yields a low sidelobe far field pattern for a realizable parabolic antenna, a set of plane waves with different incoming angles is assumed incident upon the antenna. (See figure 3). These are adjusted in magnitude and phase to yield the same illumination, F(x,y) on the antenna aperture. Further, the reflector focuses these plane waves and establishes a focal plane distribution, $\phi(\xi,\eta)$ which is no longer a perfect image of the desired far field pattern, but a distorted version due to aberrations in the antenna system. If however, a feed system is designed with an excitation which duplicates the complex conjugate $\phi^*(\xi,\eta)$ of the focal plane distribution, $\phi(\xi,\eta)$, then the low sidelobe far field pattern will result.

This technique has been simulated on a high speed computer. Calculations have been made of focal plane distributions and far field patterns for both horizontal and vertical polarizations. Since vector diffraction formulations are used, the calculations yield accurate predictions of major lobe and near-in sidelobe features in both the focal plane and the far field regions. The results indicate the effectiveness of a Woodward-type synthesis of far field patterns with low sidelobes. The line source feed-parabolic cylinder arrangement is shown in Figure 4. Note that the offset reflector extends from the focal line to the focal plane. Focal plane distributions due to three incident plane waves, weighted and properly angled to yield a far field pattern with -37 dB sidelobes, were first calculated at regular intervals along the line source. This was done to ensure that the line source was in the cylindrical wave zone of the cylindrical reflector. Figure 5 illustrates the results obtained. The patterns at different heights on the line source are all similar with almost

identical peak amplitudes except at the very ends of the line source where the peak value drops down about 2.5 dB. Thus the required cylindrical wave behavior between the line source and the reflector is present for the antenna dimensions shown in figure 4:

Figures 6 and 7 show more detail for the focal plane distributions obtained in a plane perpendicular to and at the center of the line source (the plane y = 0 in Figure 4). For each polarization, separate focal plane distributions due to each of the incident plane waves and to the sum of the plane waves are shown. In addition to satisfying the above requirement that the illumination function F(x,y) have low sidelobe characteristics, the angles between the plane waves can be chosen so that the resulting focal plane distributions intersect each other orthogonally in a perfectly collimating system. As shown in figures 6 and 7, the distributions are slightly assymmetrical and display small differences in major lobe widths and sidelobe characteristics due to aberrations of the offset parabolic system. This assymetry is a manifestation of the transformation implicit in equation (7) governing the relationship between the primary pattern of the feed and the equivalent illumination of the image aperture. The distributions however are still very nearly orthogonal to each other. That is, the three single plane wave distributions intersect each other so that where one has a peak amplitude, the other two distributions have nulls. This property is very useful in the design of a transverse feed consisting of several horn radiators.

Far field patterns were computed for the offset reflector using three horn feeds located at the peaks of the three individual focal plane distributions with amplitudes and conjugate phases matching those in the three distributions. An additional horn was placed on either side of the

three central horns. The amplitude and phase excitations for these outer horns were obtained from corresponding points in the sum focal plane distribution pattern. This procedure resulted in the far field patterns shown in figures 8 and 9, with -36 dB and -38 dB first sidelobes for vertical and horizontal polarizations, respectively.

An important parameter which is useful in calculating the positions of the feed horns is the beam deviation factor. This is the ratio of the angle by which the beam is scanned to the angle that the feed is displaced from the reflector axis. It is well known that this factor is a function of the f/D ratio where f is equal to the focal length and D is equal to the diameter or width of the reflector. In the above work a beam deviation factor of .76 was observed. Close agreement is obtained with earlier work reported in Silver[4] is the full diameter, D of the reflector is used in calculating the f/D ratio, rather than taking D equal to the width of the offset portion of the reflector. That is, Silver gives a value for beam deviation factor of .75 for f/D = .25 as is the case in figure 4 above. Similar results are reported by Mitra, et al[7].

4. Elevation Pattern Synthesis

The parabolic cylinder antenna incorporates a capability for electronically scanning its beam in elevation to ultimately provide target altitude data to the radar. Electronic scanning is accomplished by phase shifters located at the elements of the line source feed. The theory outlined in section 2 indicates that a linear phase gradient ideally effects elevation scan without aberration thus producing elevation pattern characteristics which are uniformly dictated by the vertical amplitude distribution on the line source feed. However, to realize this behavior the reflector must be sized sufficiently large to intercept the primary radiation for all scanning

conditions. Therefore, to minimize reflector area consistent with cost and transportability objectives, a judicious departure from linear phasing affords an optimum design.

A systematic study of the performance/configurational trade-offs afforded by the choice of phase function was conducted using the computer models discussed above. The type of phase function which was found to offer an excellent compromise is illustrated in figure 10. It consists of a combination of linear and spherical phasing such that all energy emanating from the line source feed impinges to first order on the reflector thus minimizing spillover radiation and hence wide-angle sidelobes.

The computed elevation beams for the design dimensioned in figure 4 extending from 0 to 20 degrees in elevation are shown in figure 11. The reflector/line source configuration is tilted back 8 degrees with respect to the zenith so that the lowest 0° elevation pattern represents a beam which is scanned minus 8° with respect to the z-axis (figure 2). The lowest beam results from a phase front which is linear except for a short spherical section at the bottom (figure 10A). By design, the lowest ray from the spherical section is horizontal in the figure and will strike the reflector, as will be the case for all other outgoing rays. The spherical section of the wavefront is gradually decreased as the scan angle increases up to 8 degrees elevation. The phase front is completely linear for the 8 degree beam. To scan further, the phasing shown in figure 10 B with spherical phasing at the top, is utilized. The net result is that a set of elevation beams is obtained with nearly constant beamwidth while the gain variation is less than 0.5 dB although only for the 8 degree beam is the total reflector irradiated. If beam broadening corresponding to lower gain is required at

the higher elevation angles, further defocussing can be applied. The pattern data reproduced in figure 11 predicts maximum elevation plane sidelobes of 33 dB for all except the highest elevation beam where sidelobes rise to 28 dB maximum.

5. Conclusion

The parabolic cylinder antenna represents a unique and comparatively simple design approach for generating and electronically scanning low sidelobe, aberration free pencil beams. These features will foster the application of this approach to future tactical surveillance radar systems. The analyses reported in this paper generally support these conclusions. These are the initial results of an analytical program currently in progress at Sperry under Rome Air Development Center sponsorship. The principle thrust of activities planned for the near future include parametric, economic and tolerance analyses leading to a complete conceptual design of a transportable low sidelobe parabolic cylinder antenna for an advanced tactical surveillance radar application.

Acknowledgements

The authors wish to express their gratitude to Carl Rothenberg, John Herper and Harry Perini of Sperry's Microwave Engineering Department who were involved in the initial evaluations of the concepts presented in this paper, and to Walter Rotman, Peter Franchi and Bill Mavroides of Rome Air Development Center, Deputy for Electronic Technology for many valuable suggestions during the performance of this work.

References

(1) Ronald L. Fante, Design of Parabolic Cylinder Reflector Systems with Low Sidelobes, Rome Air Development Center, Tech. Report No. RADC-TR-88-204, June 1977.

(2) Ronald L. Fante, Peter R. Franchi, Nicholas R. Kernweis and Lancer F. Dennett, A Parabolic-Cylinder Antenna with Very Low Sidelobes, 1979 International IEEE/AP-S Symposium, Seattle, WA, June 1979.

(3) Ronald L. Fante, Tolerance Errors for Very Low Sidelobe Antennas, Rome Air Development Center, Tech. Report No. RADC-TR-77-360, Oct. 1977.

(4) Samuel Silver, Microwave Antenna Theory and Design, Mc Graw-Hill, New York, N.Y. (1949), pp. 151-155, pp. 488.

(5) Robert E. Collin and Francis J. Zucker, Antenna Theory, Part II, Mc Graw-Hill, New York, N.Y. (1969), pp. 83-84.

(6) J.J. Stangel, J.C. Herper and J.V. D'Agostino, Low Sidelobe Transverse Feed Technique, 1979 International IEEE/AP-S Symposium, Seattle, WA, June 1979.

(7) Raj Mittra, Yahya Rahmat-Samii, Victor Galindo-Israel and R. Norman, An Efficient Technique for the Computation of Vector Secondary Patterns of Offset Paraboloid Reflectors, IEEE Trans. on Antennas and Propagation, Vol AP-27, No. 3, pp. 294-304, May 1979.

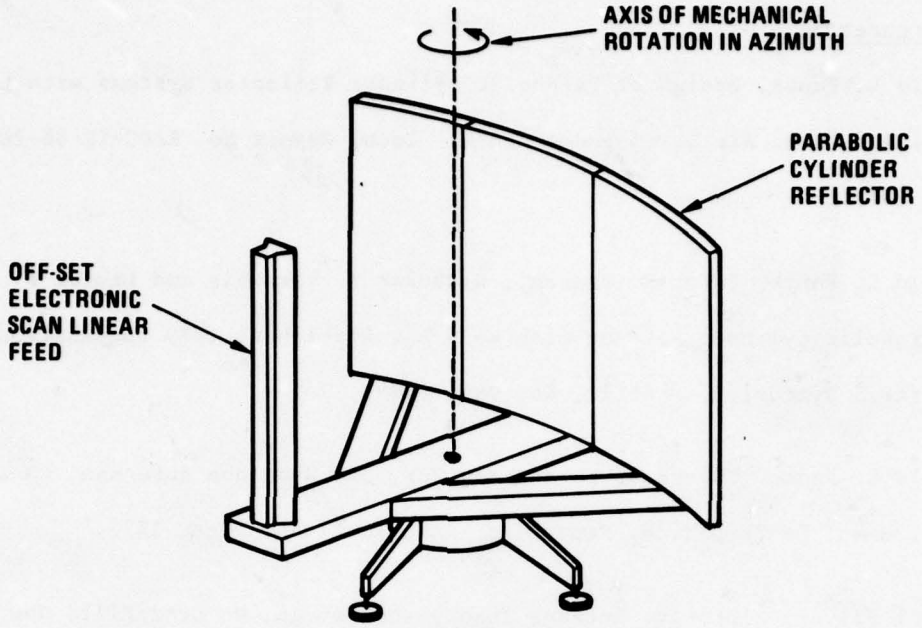

Figure 1. Parabolic Cylinder Antenna Configuration

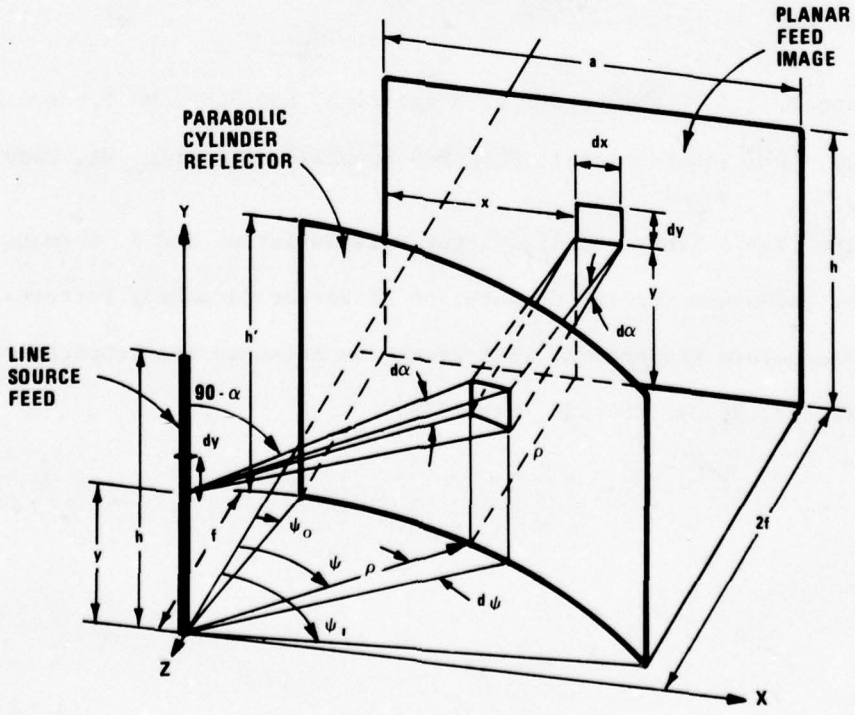

Figure 2. Image Plane Geometry

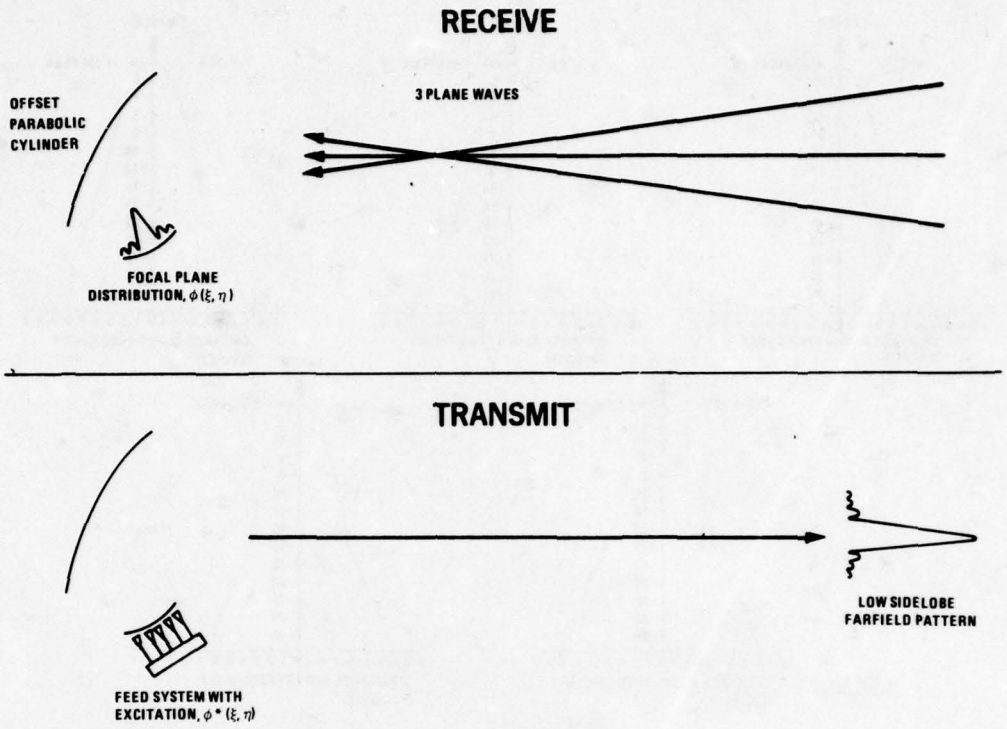

Figure 3. Far Field - Focal Plane Relationships

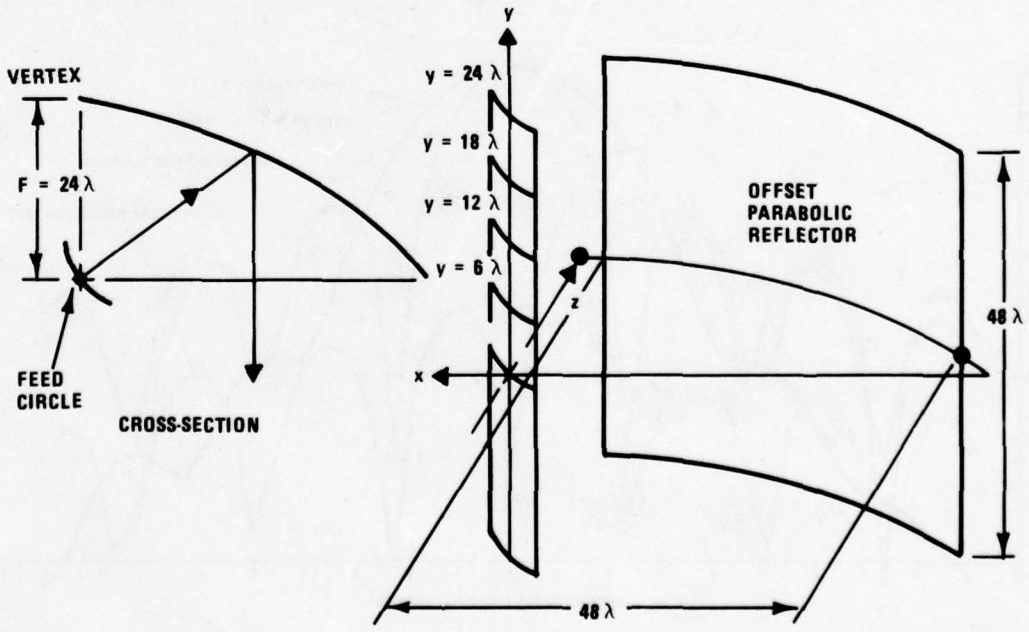

Figure 4. Coordinate System for Focal Plane Analysis

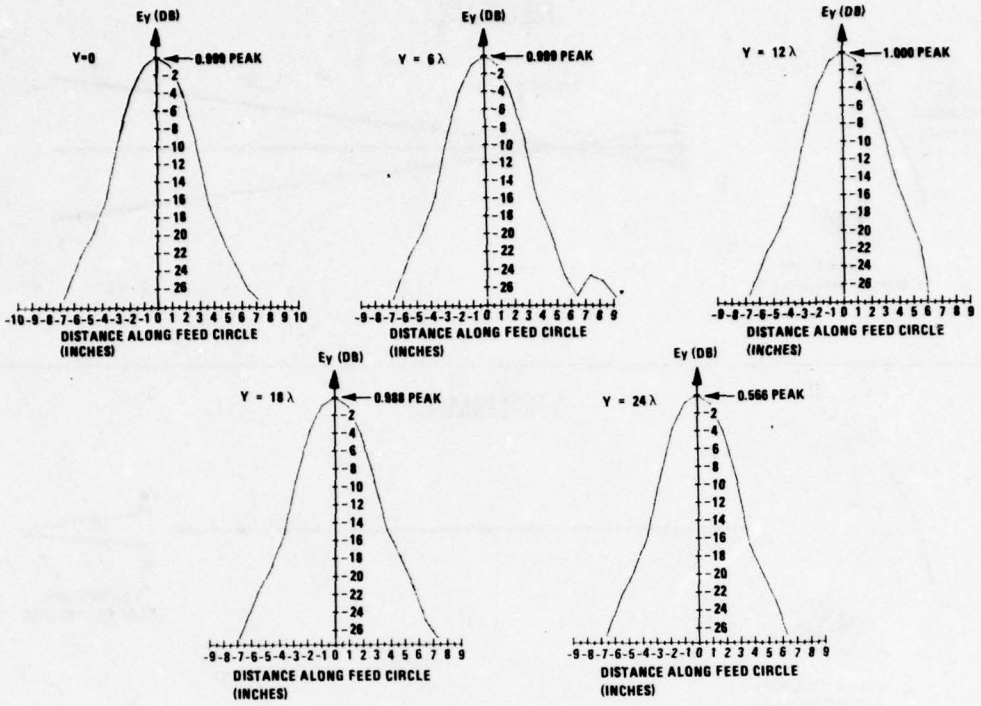

Figure 5. Focal Plane Distributions

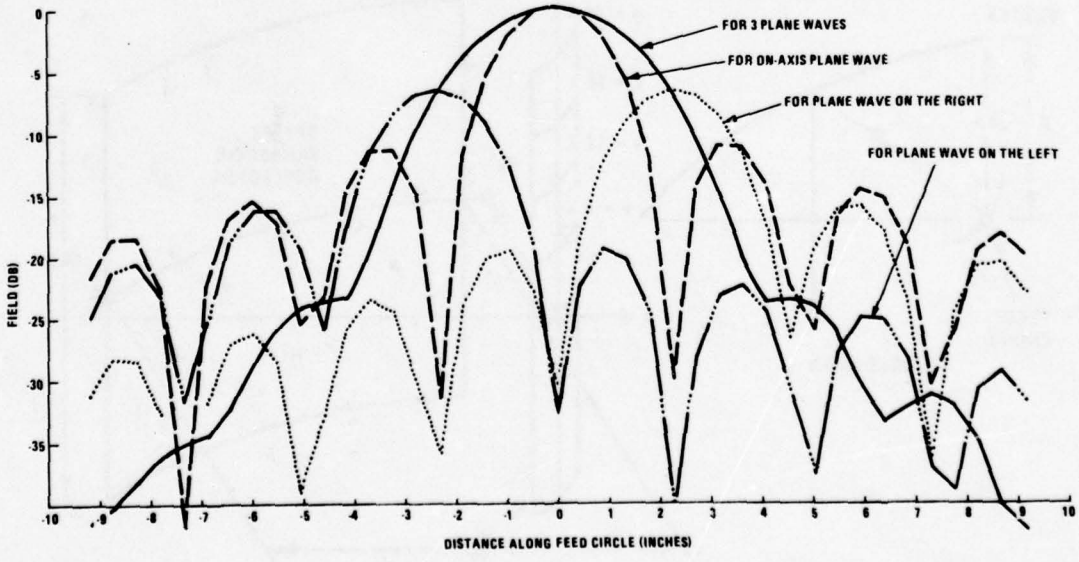

Figure 6. Focal Plane Distributions (Vertical Polarization)

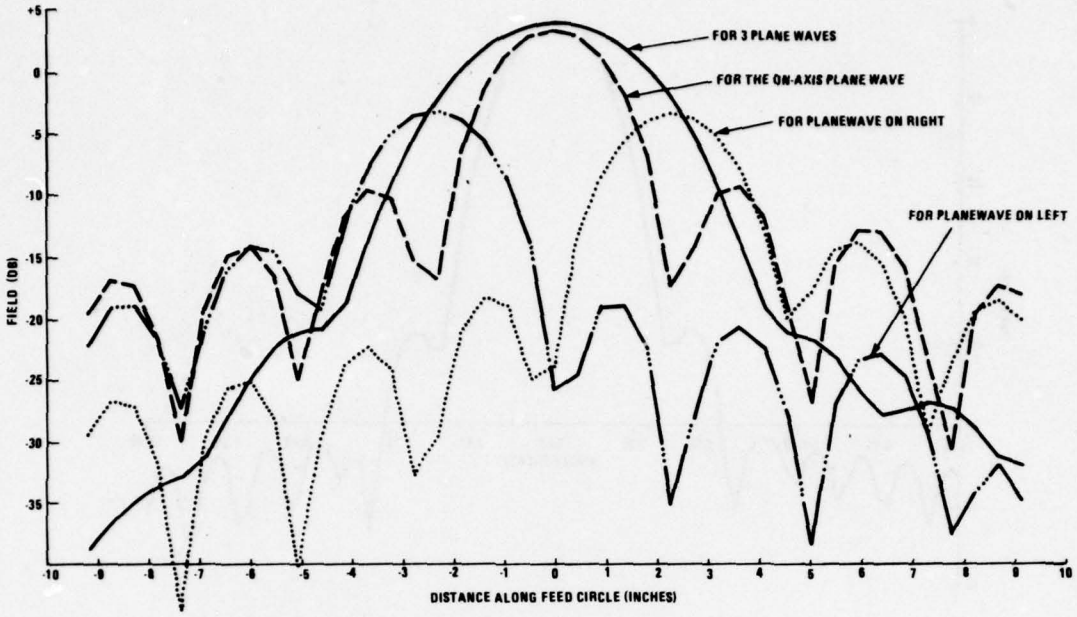

Figure 7. Focal Plane Distributions (Horizontal Polarization)

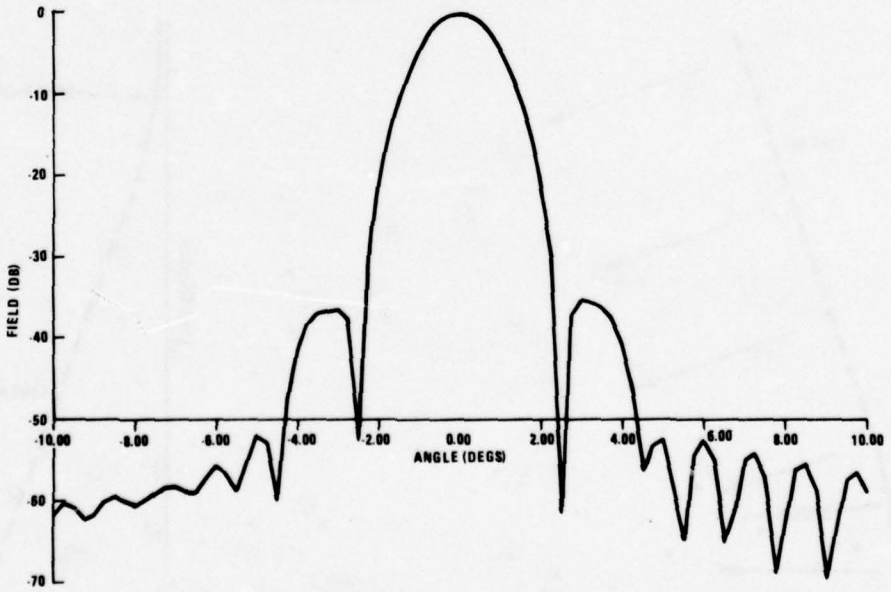

Figure 8. Far Field Azimuth Pattern Vertical Polarization 5 Horn Feed

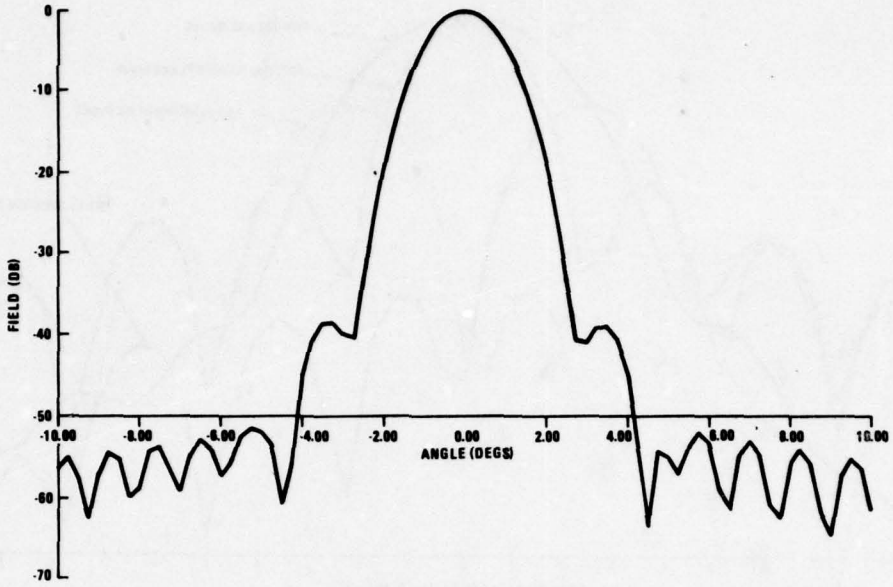

Figure 9. Far Field Azimuth Pattern Horizontal Polarization 5 Horn Feed

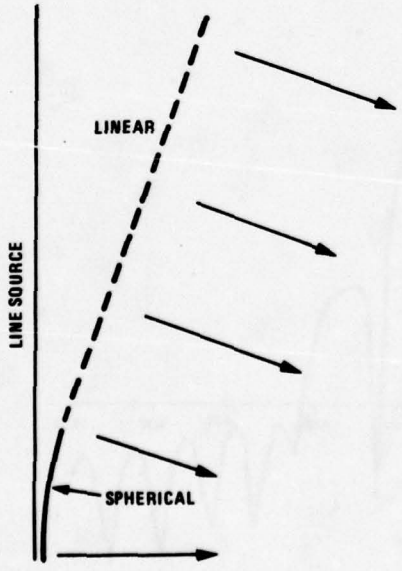

Figure 10A

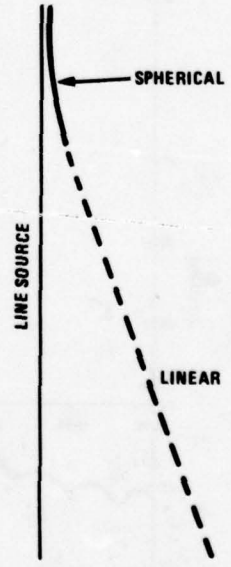

Figure 10B

Figure 10. Phase Functions

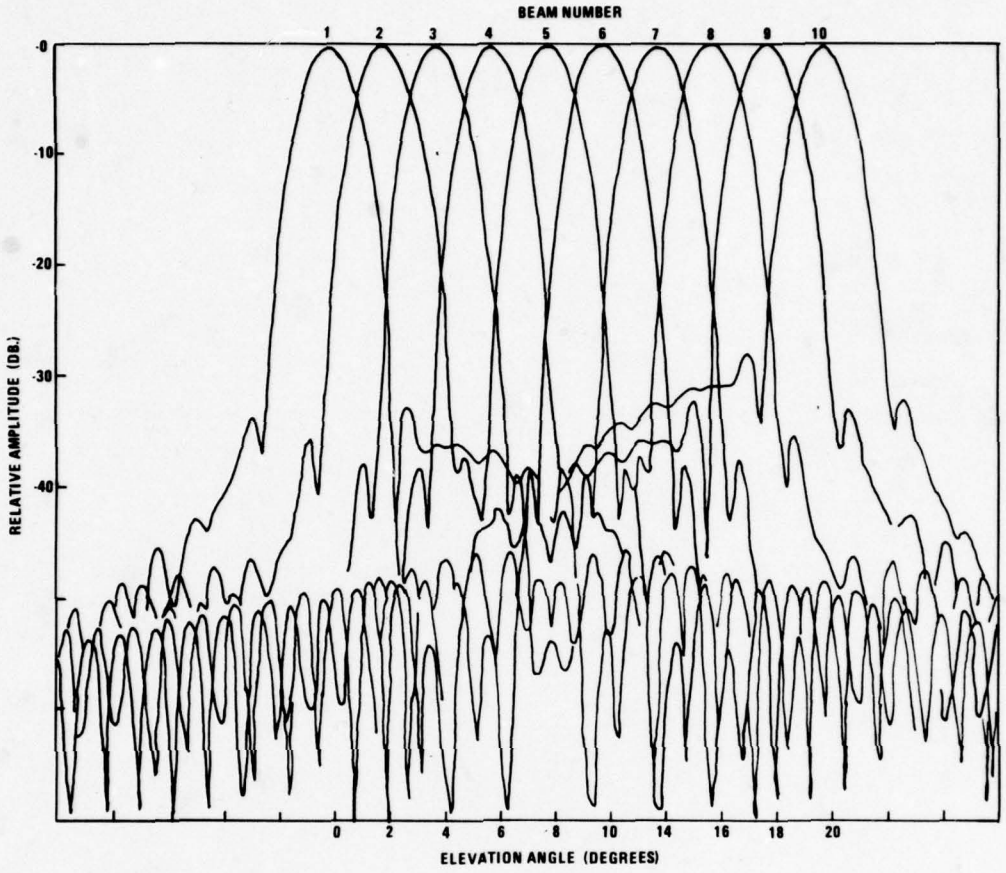

Figure 11. Elevation Coverage

NEAR FIELD BLOCKAGE OF AN ULTRALOW SIDELOBE ANTENNA

by
Stephen G. Winchell and Daniel Davis
Westinghouse Electric Corporation
Baltimore, Maryland U.S.A.

An analytical model is presented which describes the far field radiation pattern of an array antenna blocked by a vertical or horizontal metallic cylinder in the near field of the aperture. The implementation of this model as a generalized computer program has been completed, and the computed radiation patterns have been verified by extensive measurements on a low sidelobe, X-band slotted waveguide array. The effects of the blockage are summarized graphically for a wide range of obstacle sizes and distances, and for aperture illuminations ranging from conventional reflector-type distributions to ultralow sidelobe distributions. Using dielectric or absorptive coatings to improve the radiation pattern in the presence of cylindrical obstacles is proposed as a logical extension to the existing model.

Introduction

Near field blockage of ultralow sidelobe antennas by vertical and horizontal metallic cylinders has been studied both analytically and experimentally to determine how the radiation characteristics of a shipboard antenna are affected when blocked by a mast and yardarm just outside the turning radius of the antenna. An analytical model was developed to compute the principal plane azimuth pattern of an array blocked by these obstacles and has been verified experimentally.

The analytical model of the vertical cylinder is based on a two-dimensional Hankel function expansion of the radiated energy from each element of the array. Included in the model is the scattered energy from the cylinder which is reradiated by the array, adding a significant perturbation to the blocked radiation pattern of the antenna. The horizontal cylinder analysis is an original approach, incorporating the Hankel function expansion analysis in the elevation plane, in addition to an azimuth plane field integration from each element of the array over the finite length of the cylinder. Horizontally and vertically polarized radiation patterns were measured using an X-band slotted waveguide array blocked by horizontal and vertical cylinders of various diameters and distances from the antenna. These patterns provide the base of comparison between the analytical and experimental results.

Vertical Cylinder Blockage

To determine a closed form expression for the radiation pattern of an antenna blocked by a vertical metallic cylinder, the cylinder is assumed to be infinite in length. Furthermore, the antenna is assumed to be a planar array with separable vertical and horizontal illumination functions. By limiting the radiation patterns to principal plane azimuth patterns, the geometry can be simplified to a two-dimensional analysis as shown in figure 1. The horizontal aperture of the antenna is subdivided into N subapertures of such a size that the cylinder is in the far field of each subaperture.

For the case of a vertically polarized radiating element, the incident electric field is parallel to the axis of the cylinder and is propogating in the -x′ direction. Neglecting the time dependence, the plane wave from the mth radiating element can be expressed as $E_{inc} = A_m e^{ikx'}$, which can be rewritten in polar coordinates as

$$E_{inc} = A_m e^{ikr\cos(\theta - \theta_m)}$$
$$= A_m \left[\cos(kr\cos(\theta - \theta_m)) + i\sin(kr\cos(\theta - \theta_m))\right]$$

Using the two identities[1]

$$\cos(Z\cos\theta) = J_0(Z) + 2\sum_{k=1}^{\infty}(-1)^k J_{2k}(Z)\cos(2k\theta)$$

$$\sin(Z\cos\theta) = 2\sum_{k=0}^{\infty}(-1)^k J_{2k+1}(Z)\cos((2k+1)\theta)$$

the incident electric field can be rewritten as an infinite series of Bessel functions.

$$E_{inc} = A_m \sum_{n=0}^{\infty} \epsilon_n i^n J_n(kr)\cos(n(\theta - \theta_m)) \begin{cases} \epsilon_n = 1, & n = 0 \\ \epsilon_n = 2, & n \neq 0 \end{cases}$$

To fit the boundary conditions at the surface of the cylinder, an outward traveling cylindrical wave from the cylinder must be added of the form

$$E_{scat} = \sum_{n=0}^{\infty} B_n H_n^{(2)}(kr)\cos(n(\theta - \theta_m))$$

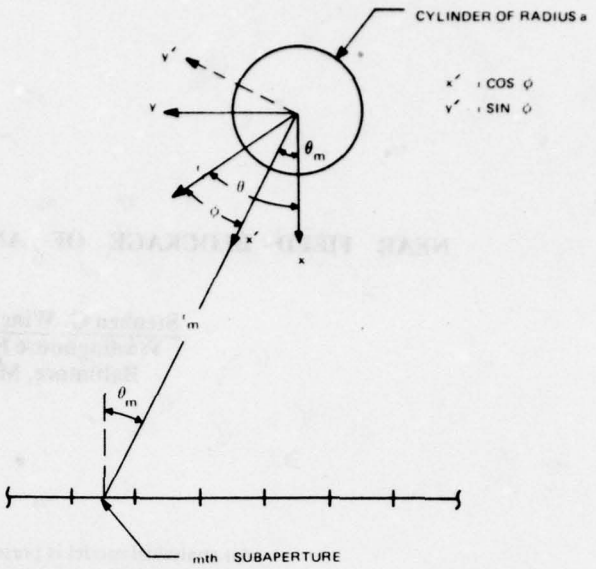

Figure 1. Horizontal Line Source Blocked by a Vertical Cylinder

Requiring the scattered wave to be equal and opposite to the incident wave at the surface of the cylinder, where r = a, allows the unknown coefficients of the Hankel function expansion to be determined.

$$B_n = -A_m \epsilon_n i^n \frac{J_n(ka)}{H_n^{(2)}(ka)}$$

The scattered wave can then be expressed as

$$E_{scat} = -A_m \sum_{n=0}^{\infty} \epsilon_n i^n \frac{J_n(ka)}{H_n^{(2)}(ka)} H_n^{(2)}(kr_m)\cos(n(\theta - \theta_m))$$

Repeating this analysis for each of the radiating subapertures, the total scattered field from the cylinder can be expressed as

$$E_{scat} = -\sum_{m=1}^{N} A_m \sum_{n=0}^{\infty} \epsilon_n i^n \frac{J_n(ka)}{H_n^{(2)}(ka)} H_n^{(2)}(kr_m)\cos(n(\theta - \theta_m))$$

For the case of horizontally polarized radiating elements, the magnetic field is parallel to the axis of the cylinder, and the boundary conditions at the surface of the cylinder require the circumferential components of the incident and scattered fields to cancel. Thus, for the horizontally polarized elements, the coefficients are determined by

$$B_n = -A_m \epsilon_n i^n \frac{J_n'(ka)}{H_n^{(2)'}(ka)}$$

The total scattered field from a cylinder illuminated by a line source of horizontally polarized radiating elements is then

$$H_{scat} = -\sum_{m=1}^{N} A_m \sum_{n=0}^{\infty} \epsilon_n i^n \frac{J_n'(ka)}{H_n^{(2)'}(ka)} H_n^{(2)}(kr_m)\cos(n(\theta - \theta_m))$$

The computer program developed to implement this mathematical model was based on the work done by A.J. Hissink.[2] While many modifications and additions were made to his computational model, the basic method of analysis and the associated geometry have been retained. Of particular interest in his model are several features which reduce the computational time required to determine the scattered field from the cylinder. These inlcude an efficient Bessel function generator, and the use of a skew-symmetric correction to the uniform illumination across each subaperture to minimize the number of subapertures required to obtain an accurate representation of the scattered field.

A major addition to the computational model, however, was the calculation of the energy scattered by the cylinder in the direction of the antenna, which is then reradiated to add a significant perturbation to the energy scattered by the cylinder. Note that due to the conical scattering properties of the cylinder, this phenomenon will only be observed in cases where the energy radiated by the antenna propogates in a direction normal to the axis of the cylinder. However, instead of computing the precise fluctuations of the resultant blocked radiation pattern, only the envelope is determined. This simplification is required for several reasons. First, the frequency of the resulting perturbation is a function of the distance between the antenna and the obstacle. As this distance is increased, the number of pattern angles required to describe the perturbations rapidly becomes impractical. Secondly, the phase of the reradiated energy from each element of the array cannot be determined without a detailed description of the power division network feeding the radiating elements, thus reducing the generality of the model.

Figure 2 shows a measured blocked radiation pattern superimposed over the maximum and minimum envelopes of the computed blocked radiation pattern for the case of a 1.022λ diameter vertical cylinder located 14λ away and directly in front of an 18.43λ wide aperture. Included in the figure, as a reference, is the computed free space radiation pattern of the test antenna - an X-band slotted waveguide array illuminated by a 42-dB Hamming function illumination.

Extensive measurements were conducted to confirm the validity of the computational model, of which figure 2 is a typical example. Not only were various obstacle sizes and distances included, but also several cylinder bearings relative to the antenna boresight were examined for each blockage configuration. A graphical summary of the results is presented in figure 3, where the rms sidelobe level of the blocked radiation

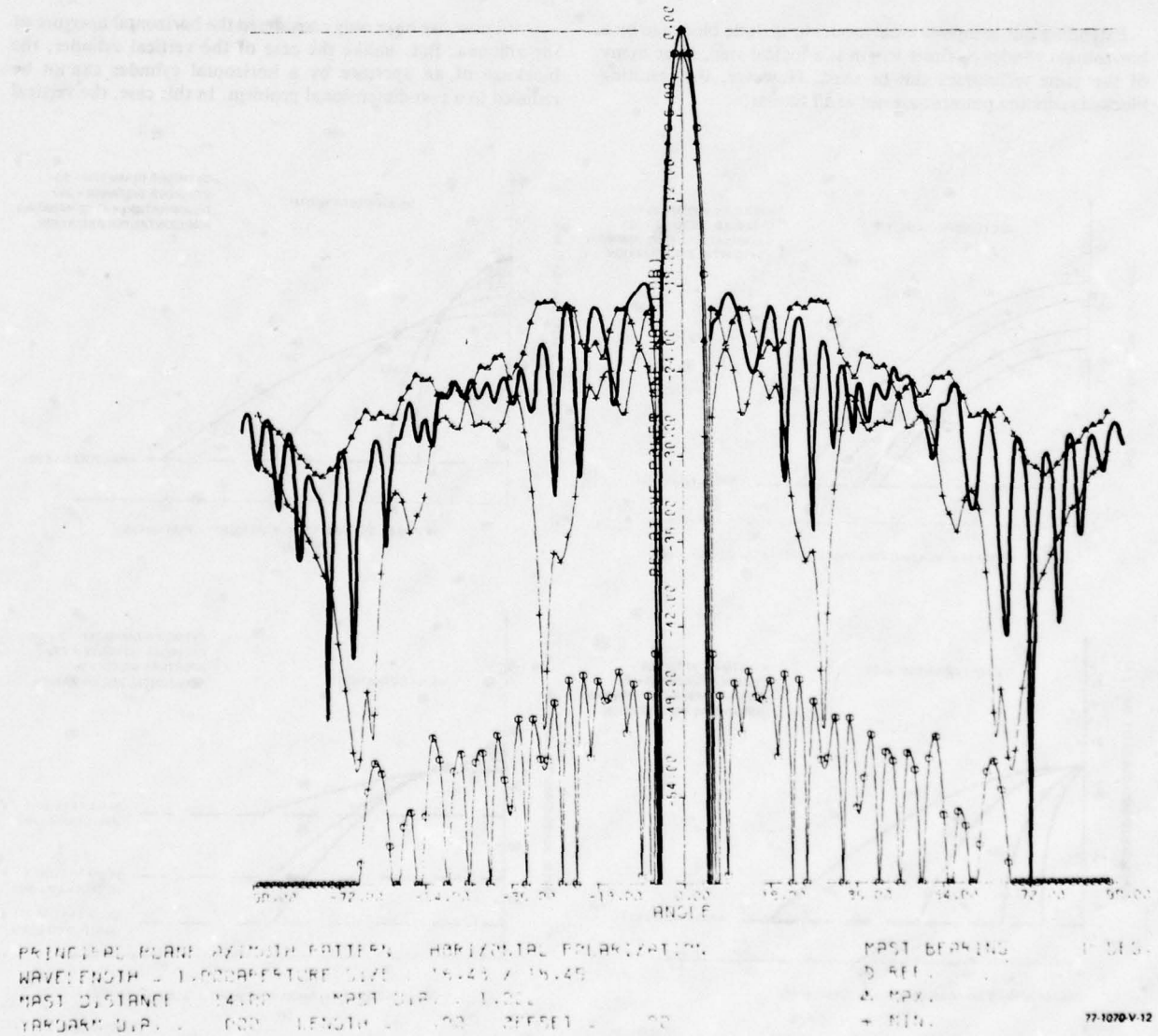

Figure 2. Aperture Blockage by a Vertical Cylinder

THIS PAGE IS BEST QUALITY PRACTICABLE
FROM COPY FURNISHED TO DDC

pattern is plotted as a function of the cylinder bearing from boresight for a wide range of configurations. Note that the bearing at which the effects of the cylindrical scattering become negligible can be approximated as

$$\theta = \pm \text{ASIN} \frac{\text{WDTH}}{2 * \text{DCYL}}$$

where WDTH is the aperture width, and DCYL is the distance to the cylinder.

Of particular interest in figure 3 is the dependence of the blocked radiation pattern on the aperture illumination of the antenna. When the cylinder is located directly in front of the antenna, the radiation pattern created by a low sidelobe distribution is degraded more than the pattern of a more conventional distribution. However, as the antenna rotates away from the obstacle, the sidelobe level of the low sidelobe antenna decreases much more rapidly than that of the conventional reflector-type antenna. The results summarized in figure 3 are for a horizontally polarized antenna. In general, the rms sidelobe levels for a vertically polarized antenna are 1.5 to 3.0 dB higher in magnitude.

Horizontal Cylinder Blockage

Extending our computational model to include blockage by a horizontal cylinder of finite length is a logical step, since many of the same techniques can be used. However, the resulting blocked radiation patterns are not at all similar.

When a horizontal cylinder is illuminated by a rectangular aperture oriented parallel to the axis of the cylinder, the scattered energy lies primarily in the plane perpendicular to the axis of the cylinder. But when the antenna has rotated to a position where it is no longer parallel to the cylinder, the scattered energy forms a cone as shown in figure 4. Effectively, in the principal azimuth plane, two beams are formed. The forward-scattering beam combines with the main beam of the antenna to determine the gain of the blocked aperture. The reflected beam, however, will show up as broad sidelobe (having approximately the same beamwidth as the unblocked aperture) at an angle of $180 - 2\theta$.

The distribution of fields along the cylinder, resulting from the horizontal illumination function of the aperture, determines the azimuth radiation pattern of the two scattered beams. As long as the cylinder extends completely across the projected horizontal aperture of the antenna, the cylinder will radiate an azimuth pattern identical to the unblocked pattern of the antenna. But as the antenna continues rotating to a position where the cylinder extends only partially across the projected aperture, the illumination on the cylinder no longer matches the illumination function of the antenna, and the azimuth pattern of the two scattered beams begins to deteriorate and exhibit rapidly decreasing gain.

Until now, we have only considered the horizontal aperture of the antenna. But, unlike the case of the vertical cylinder, the blockage of an aperture by a horizontal cylinder cannot be reduced to a two-dimensional problem. In this case, the vertical

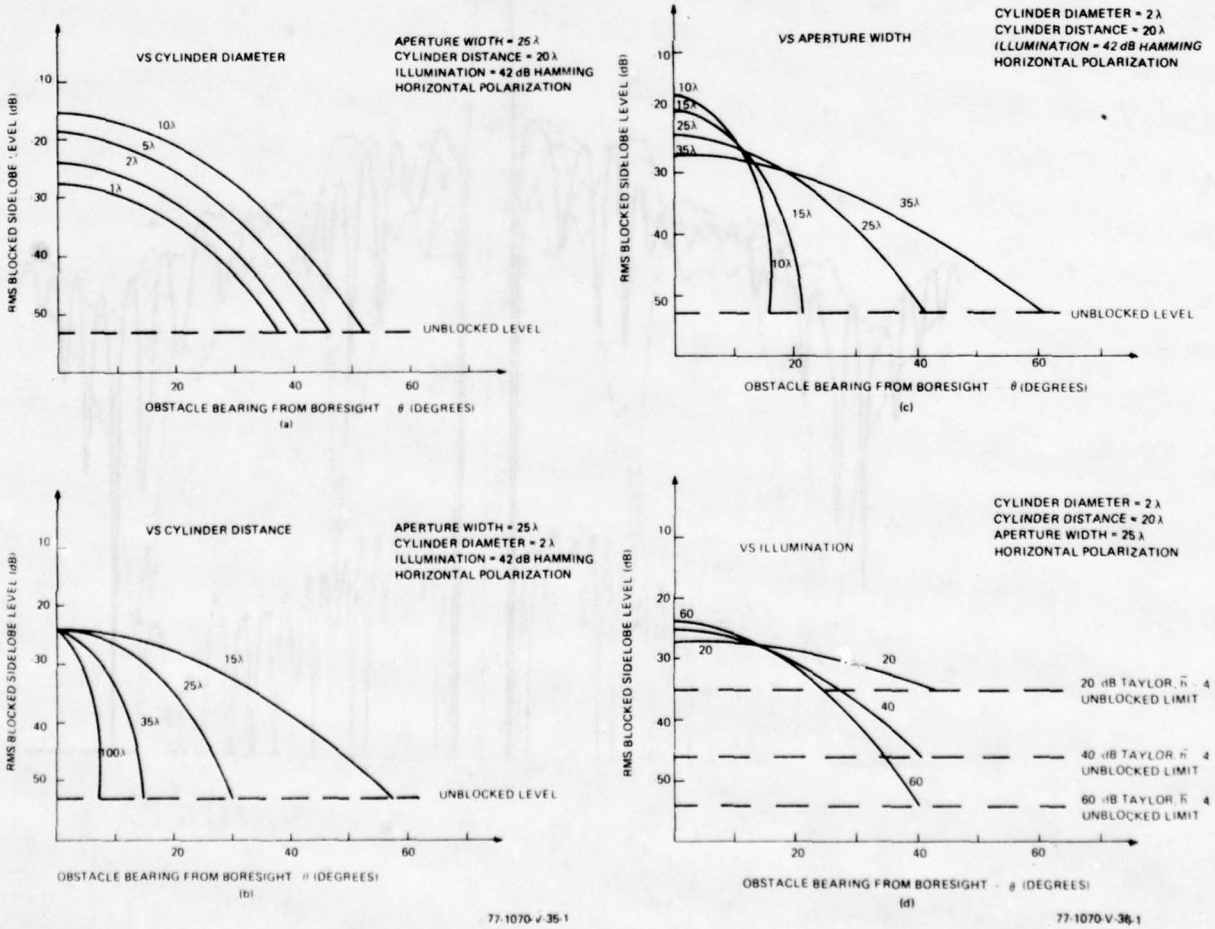

Figure 3. Vertical Cylinder Blockage Summary

aperture of the antenna and the relative location and size of the horizontal cylinder combine to produce a normalizing factor on the magnitude of the two scattered beams. The determination of these factors for the two scattered beams is straightforward, since in the vertical plane, the blockage configuration is identical to a horizontal array of radiating elements blocked by a vertical cylinder. But, in this case, the scattered field in the vertical plane need only be determined at two angles, 0 and 180 degrees, corresponding to the two scattered beams of figure 4.

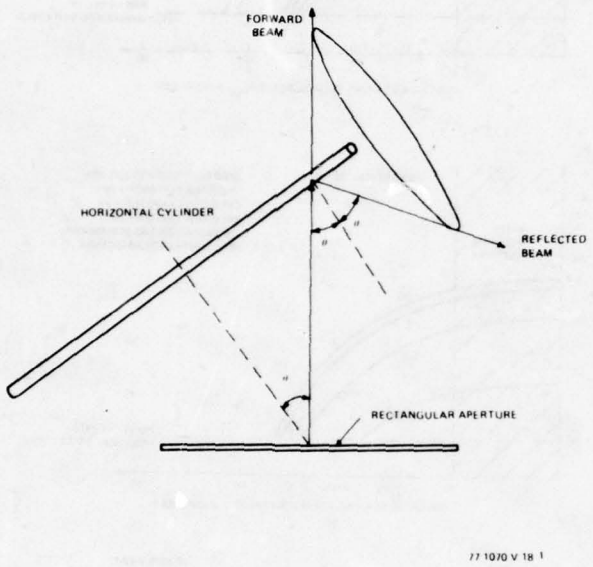

Figure 4. Geometry of Horizontal Cylinder Blockage

In summary, the computational model used to determine the radiation pattern of an antenna blocked by a horizontal cylinder consists of four parts: (1) normalization of the scattered beams due to the vertical aperture illumination, (2) summation of the total fields at each point along the cylinder due to the horizontal aperture illumination, (3) determination of the "dual-beam" azimuth pattern radiated by the cylinder, and (4) subtraction of the pattern of the cylinder from the free space radiating pattern of the antenna.

Figure 5 shows a measured radiation pattern of our X-band 42-dB Hamming function array blocked by a 0.409λ diameter horizontal cylinder located 14λ from the aperture. The obstacle bearing, corresponding to θ in figure 4, is 40 degrees. As predictd by our model, the pattern is identical to the free space radiation pattern of the antenna, except in the region around 100 degrees = 180 - 2θ, and at the peak of the beam, where the gain has been reduced.

For the case of blockage by a vertical cylinder, the parameter which best describes the blocked radiation pattern is the rms sidelobe level. However, the peak value of the reflected beam best describes the effects of aperture blockage by a horizontal cylinder. A graphical summary of the results is presented in figure 6, where the peak of the reflected beam is plotted as a function of the cylinder bearing from boresight for a wide range of configurations. Note that for small cylinder bearings from boresight the reflected beam is blocked by the aperture. Also, the magnitude of the reflected beam remains approximately constant for increasingly larger obstacle bearings from boresight, until the cylinder is no longer illuminated by the entire projected aperture of the antenna. As in the case of blockage by a vertical cylinder, the results presented in figure 6 are for a horizontally polarized array of elements. The peak level of the reflected beam for a vertically polarized antenna is approximately 3-dB lower in magnitude. As expected, this result is the opposite of the result noted for blockage by a vertical cylinder.

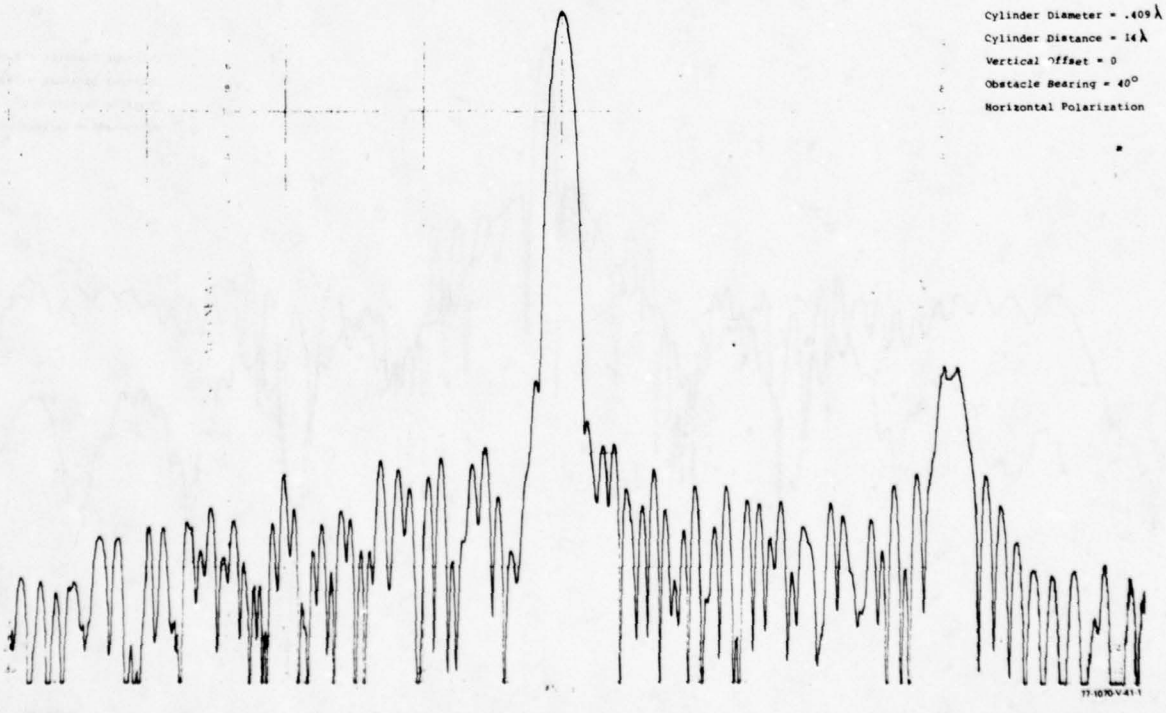

Figure 5. Measured Horizontal Cylinder Blockage, Obstacle Bearing = −40 degrees

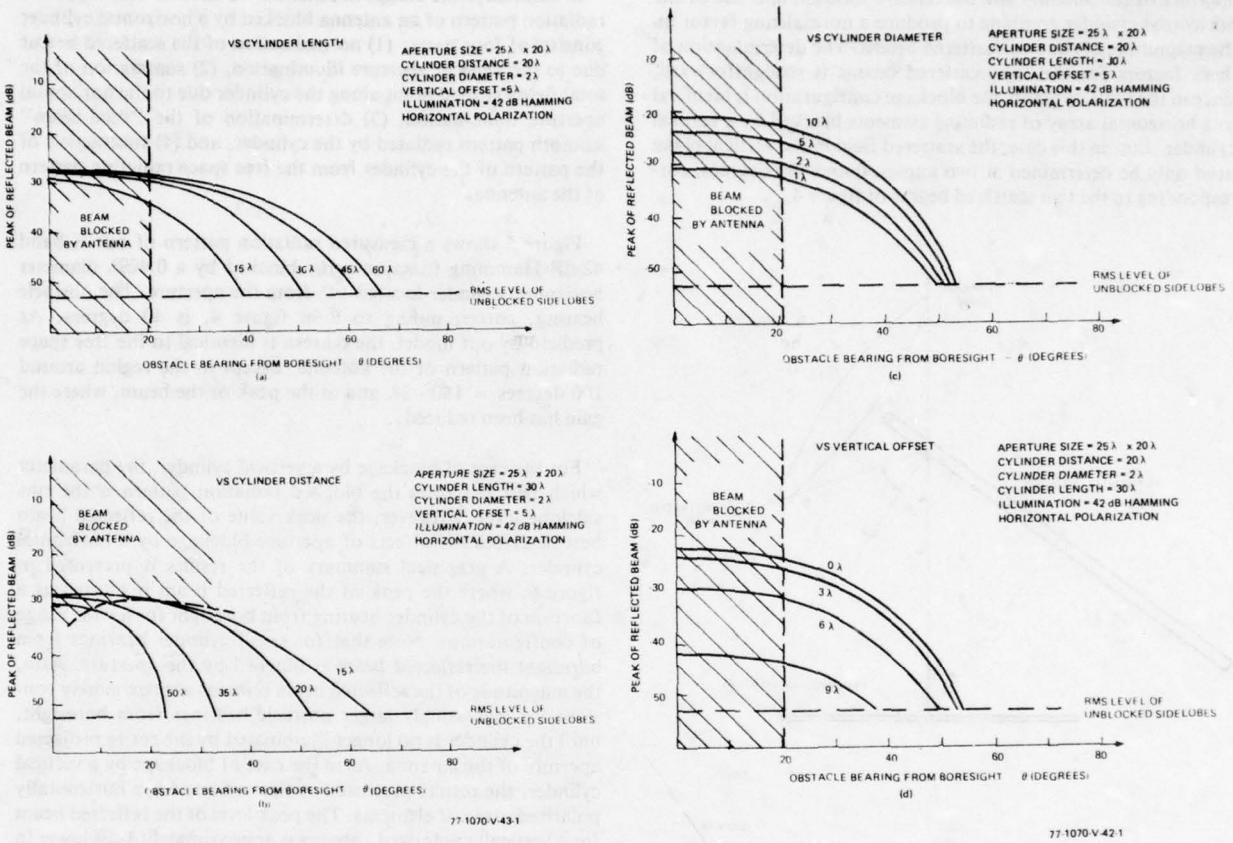

Figure 6. Horizontal Cylinder Blockage Summary

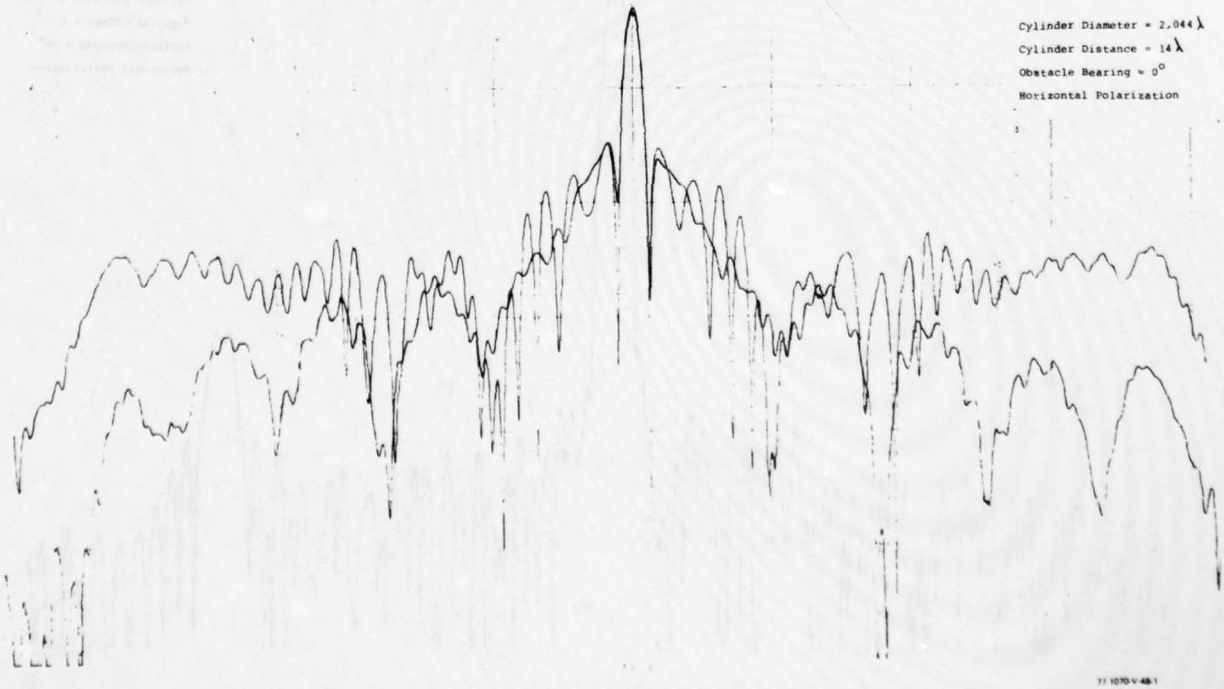

Figure 7. Blockage Reduction Due to Absorptive Coating

Summary and Recommendations

The analytical tools presented in this paper have been proven to be valid models in determining the effects of aperture blockage by both vertical and horizontal cylinders. While only a brief sample could be presented here, extensive experimental measurements were conducted over a wide range of obstacle sizes and distances to confirm the validity of these models. While valuable information has been gained concerning the effects of aperture blockage by these obstacles, the next step is to utilize these models to reduce these effects.

Investigations into the use of dielectric and absorptive coatings have been only briefly reported in the literature. However, measurements conducted during the experimental phase of our study show that significant improvements in the blocked radiation pattern can be achieved as shown in figure 7. Our analytical models are ideally suited for analyzing the effects of such coatings, since this amounts only to a change in the boundary conditions at the surface of the cylinder. The extension of these models to include various coatings could determine relatively inexpensive means of significantly improving the radiation patterns of shipboard antennas blocked in the near field by such obstacles as masts and yardarms.

Acknowledgements

The authors wish to thank the U.S. Naval Research Laboratory for sponsoring this study, and Mr. C.J. Miller for his many helpful suggestions during the course of the investigation.

References

1. Abramowitz, M., and Stegun, I.A. (Eds.) "Handbook of Mathematical Functions," Dover, N.Y., 1959, Section 9.1.

2. Hissink, A.J., "Radar Antenna with Near-Field Cylindrical Obstruction," *Proceedings of the I.E.E.E.*, Vol. 118, No. 2, Feb. 1971, pp 293-300.

A Wide-Band, Ultralow Sidelobe Antenna

by

Gary E. Evans and Stephen G. Winchell
Westinghouse Electric Corporation
Baltimore, Maryland U.S.A.

Abstract

A planar dipole array is described which operates from 1000 to 1400 MHz, limited only by the onset of grating lobes. Wide-angle sidelobes are typically −50 to −60 dB. Near the main beam, sidelobes reach −45 dB at the design frequency and −35 dB at the band edge. The 42-foot wide array contains eight rows of 64 dipoles to produce a 1.5- degree beamwidth and 32 dB gain. Construction methods and error considerations are discussed, and the extensive use of numerically controlled machinery is described.

Introduction

Ultralow sidelobes have become relatively common in slotted waveguide arrays, but a growing need exists for corporate-fed low sidelobe arrays. They do not have the squint or instantaneous bandwidth limitation of the slotted waveguides, yet they offer more beam flexibility than do reflectors. In the past, sidelobe reduction has been severely limited by material and manufacturing tolerances and by divider design. The array described here makes use of air- dielectric stripline and numerically-controlled machinery to eliminate most of these problems. This was demonstrated by the test of a 512-dipole L-band array having −50 to −60 dB wide-angle sidelobes and −35 to −45 dB worst sidelobes over the 1000 to 1400 MHz band. The array consisted of eight identical rows of 64 dipoles each, with each row further divided into eight subarrays.

Tolerances

Successful low-sidelobe arrays depend on the effective control of three types of errors: consistent errors due to design limitations, errors induced by coupling, and random manufacturing errors. The errors are necessarily small enough that we can consider a linear superposition of the several effects. Each is significant, but, for a wide- band array, the consistent errors predominate. Within each group, errors can further be classified by the size of the region that they influence. For example, an error between subarrays has almost eight times the effect of an equal error between dipoles, but the pattern effects decrease rapidly outside the main envelope of the subarray pattern. More specifically, to the extent that particular amplitude and phase errors α and ϵ affect a number N of identical regions, the overall error pattern can be factored as:

$$F_{error}(\theta) = F_{dipole}(\theta)\, F_{region}(\theta) \sum_{N\ regions} \alpha\, V_n e^{j2\pi\epsilon/\lambda}.$$

Referring to figure 1, we see that the several classes of error have larger effects over progressively smaller regions.

If an array is to be used over a 30 percent instantaneous bandwidth, it is essential that the line lengths to all radiators be equal. In that case, the minimum amount of physical line occurs for a corporate type of power

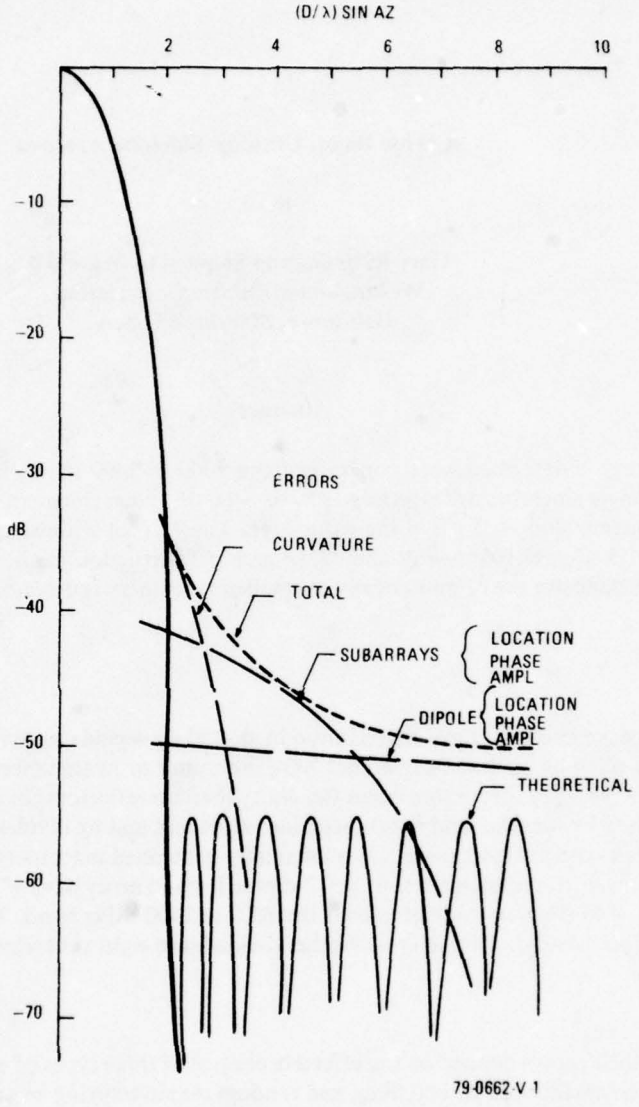

Figure 1. Sidelobe Contributions from Various Error Sources

divider distributed throughout the array. Such a divider behaves distinctly differently from a series-fed divider, such as the slotted waveguide. Figure 2a illustrates that consistent errors in the latter result in a gradual departure from the ideal taper and thus cause pattern distortions that are largely masked by the main beam. The corporate divider of figure 2b, however, produces directly observable scattered sidelobes that must typically be 10 to 20 dB lower to be acceptable. This has a major impact on the tolerances of the non-random errors in the array. Chief among these are the frequency variations of coupler phase and of power division, since these are repeated from row to row, as well as within a row, concentrating their pattern errors in specific directions in the principal azimuth plane.

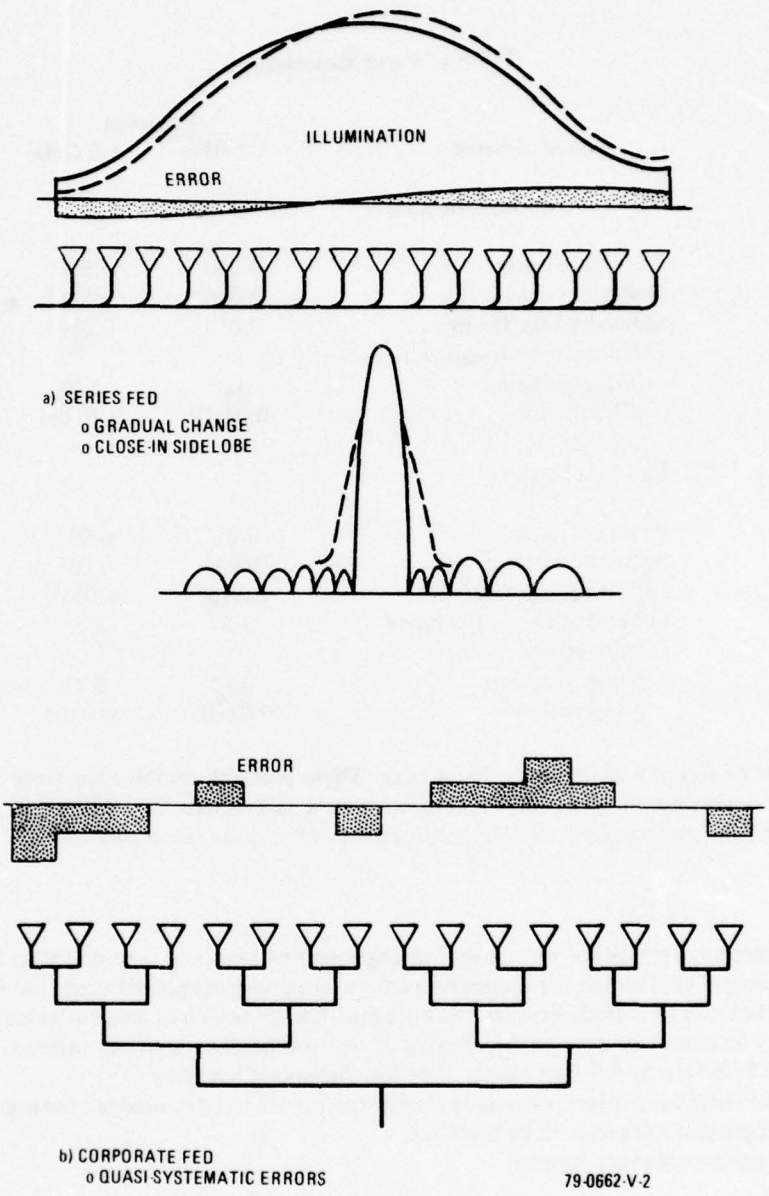

Figure 2. Comparison of Series and Corporate Errors

Coupling between dipoles has several significant results. First, it alters the effective distribution. This is predicted by computation and can be compensated for. Second, it varies with frequency. This would be a severe problem except that computations show the effect to be over 50 dB down. Third, it changes the impedance of the dipoles. This has influenced the decision to use isolated couplers throughout the divider, and it has been accounted for in the impedance matching. Fourth, it can induce currents in the structural elements in the array. This effect is minor for the polarization involved.

Random error tolerances determine the cost of the array. Starting with a -55 dB Tschebycheff distribution, the error allocations of table 1 were arrived at with the aid of pattern computation and balancing the relative cost of each variable. Evaluation of the final allocation results in the statistical pattern of figure 3 at

Table 1. Error Estimates

Source of Error	Errors at 1.3 GHz	Errors at 1.0 GHz
1. Non-random Row-to-Row		
Curvature error	0.030″	0.030″
Non-curved subarrays	0.056″	0.056″
Subarray edge fittings	0.010″	0.010″
Divider errors designed in		
phase/junction	0.3°	1.0°
dB/junction	0.03 dB	0.10 dB
2. Random Errors		
Panel position	0.01″	0.01″
Subarray within panel	0.03″	0.03″
Dipole within subarray	0.015″	0.015″
Subarray phase adjustment	3.5°	3.5°
Divider errors		
phase/junction	0.4°	0.4°
dB/junction	0.04 dB	0.04 dB

midband and that of figure 4 at the lower band edge. These patterns combine the fixed and random errors with the theoretical distribution and print the level which will not be exceeded 90 percent of the time. Subsequent development and patterns have shown the allocations to be quite reasonable.

Design

The required antenna uses 42-foot wide rows, which require 64 dipoles to avoid grating lobes through 1400 MHz. The most general application for the experiment required vertical polarization and frequency coverage down to 1000 MHz so as to include beacon transmission. Earlier tests had made it evident that about eight rows are necessary to allow accurate pattern testing at the low sidelobe levels of interest. These 512 dipoles were grouped into 5.25-foot by 4.5-foot panels of 64 for convenient handling.

The tolerances of table 1 are severe, especially if adjustments are to be minimized for manufacturability. To meet them, several ground rules seem to be essential:

a. Equal phase outputs at every coupler
b. No dielectric
c. A precisely reproducible manufacturing technique
d. Isolated power division
e. Absolute minimum of connectors
f. Mechanical adjustment at final assembly.

To accomplish these, the array was built entirely of air- dielectric stripline with ground planes and center conductors stamped on a numerically-controlled machine. The resulting lines are economical, are of low loss, have high power capacity and, most important, are precise. This is illustrated in figure 5 for two of the outputs for one of the subarrays.

The dipole is designed for a match in the radiating environment. Experimentally, the E-plane neighbors are readily simulated with ground planes at half the E-plane spacing. Lacking magnetic short circuits, accounting for the H-plane coupling requires building a small array. The entire process converges rapidly if the small array is nearly matched to start with. This is accomplished by computing impedances that include coupling.

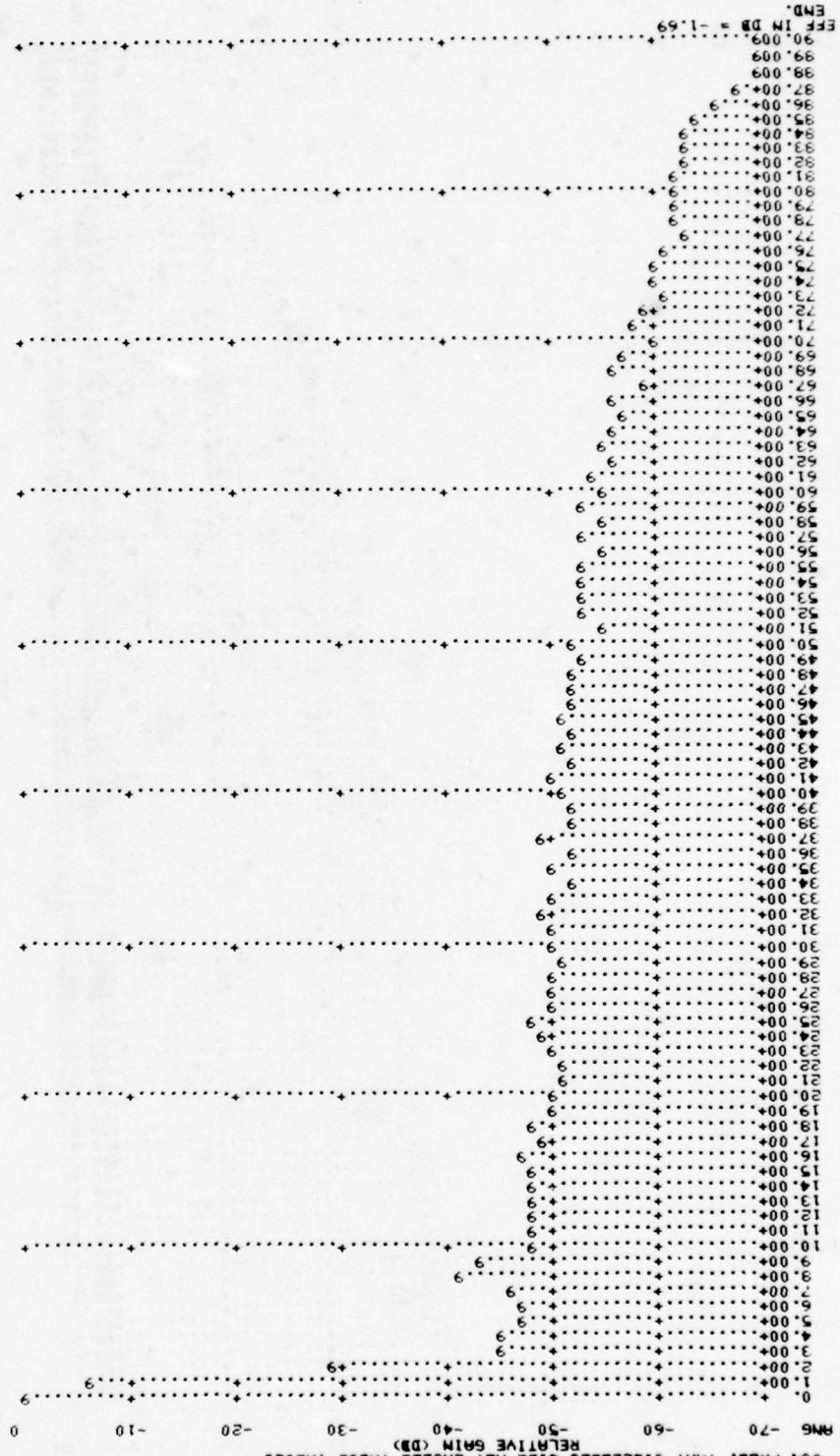

Figure 3. Sidelobe Calculations for the Errors of Table 1 at 1.3 GHz

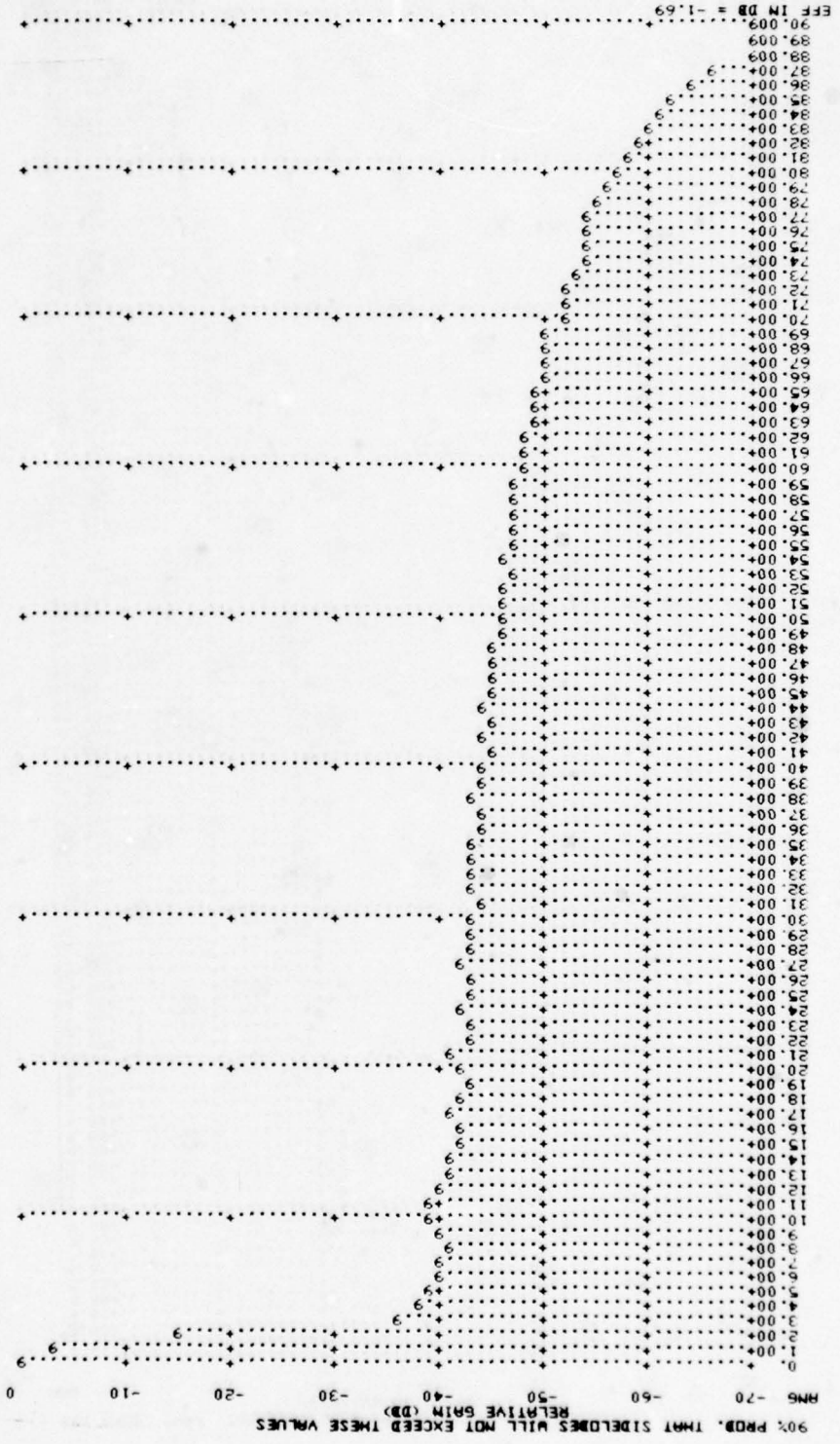

Figure 4. Sidelobe Calculations for the Errors of Table 1 at 1.0 GHz

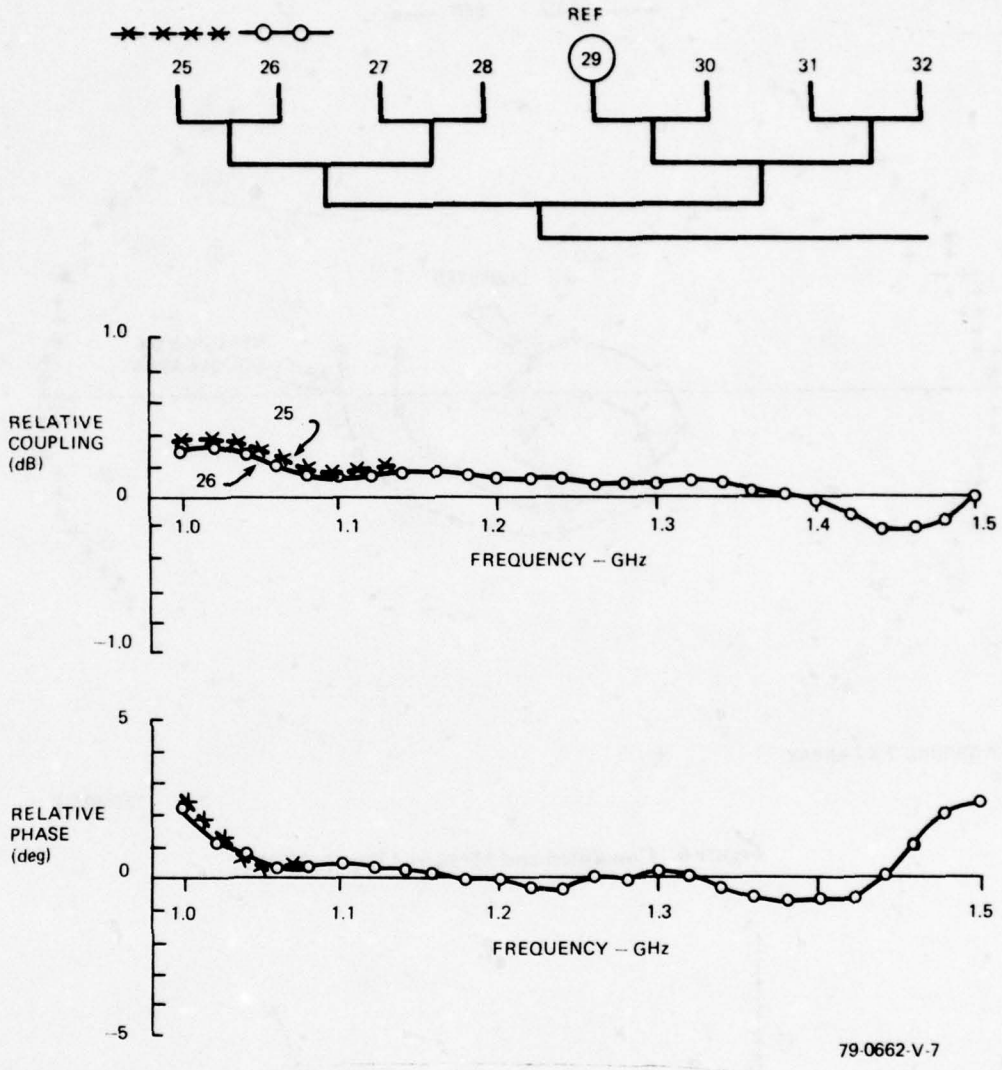

Figure 5. Measured Subarray Response

Figure 6 shows the computed and measured impedances for a dipole matched between ground planes but placed in a two-dimensional array. The correlation is good enough to anticipate the correction before constructing the test dipoles. Physically, the dipoles are formed as a part of the ground planes, so that they can be precisely stamped with the tape-controlled machinery and fed without connectors. VSWR of the final dipole is compared with that measured on the full array in figure 7.

The mechanical assembly of such a large, precise structure requires special consideration. The basic approach has been to start with a stiff, but inexact, structure and to precisely mount subunits to a contour. Even for the structural elements, extensive use was made of tape-controlled punching and drilling to assure uniformity between rows and within each subarray assembly. The power dividers with integral dipoles are assembled into the support frame to a positional tolerance of ± 0.010 inch through the use of prepunched locating holes in the support frame. The front face, with its wind-reducing holes, is similarly located to produce the complete subarray. Final precision alignment of the eight subarray panel assemblies is accomplished optically with

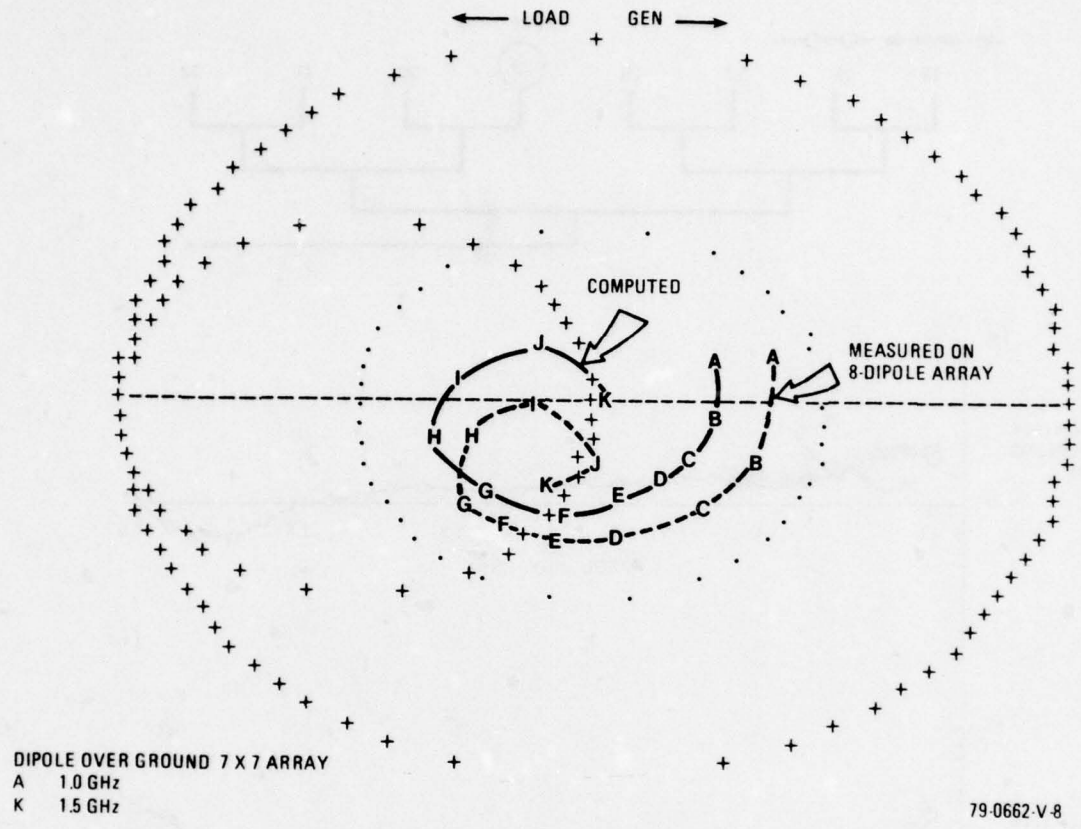

Figure 6. Computed and Measured Dipole VSWR

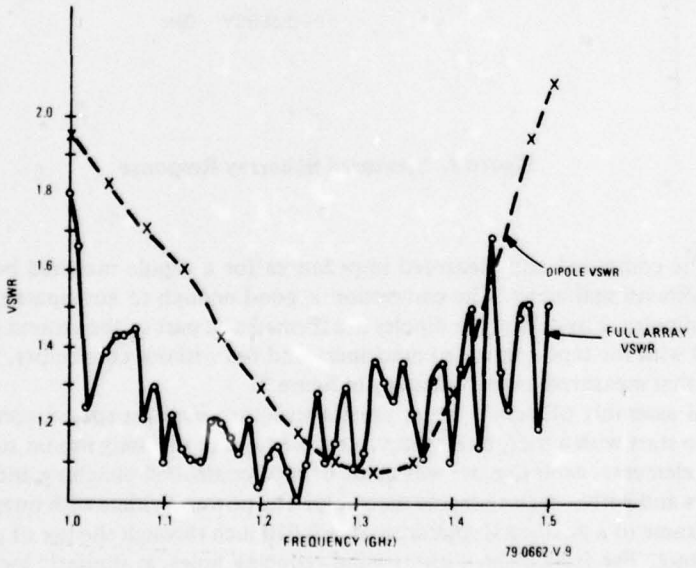

Figure 7. Measured Dipole and Array VSWR

the machined targets shown in figure 8. During this alignment, the face is set to a 1700-foot radius to account for the length of the ground range used to measure patterns. In forming the flat subarrays along such a curve, a residual scalloped phase error remains and a corresponding -40 dB sidelobe is formed at ± 8 degrees from broadside. This sidelobe is apparent in the patterns of figures 3 and 4.

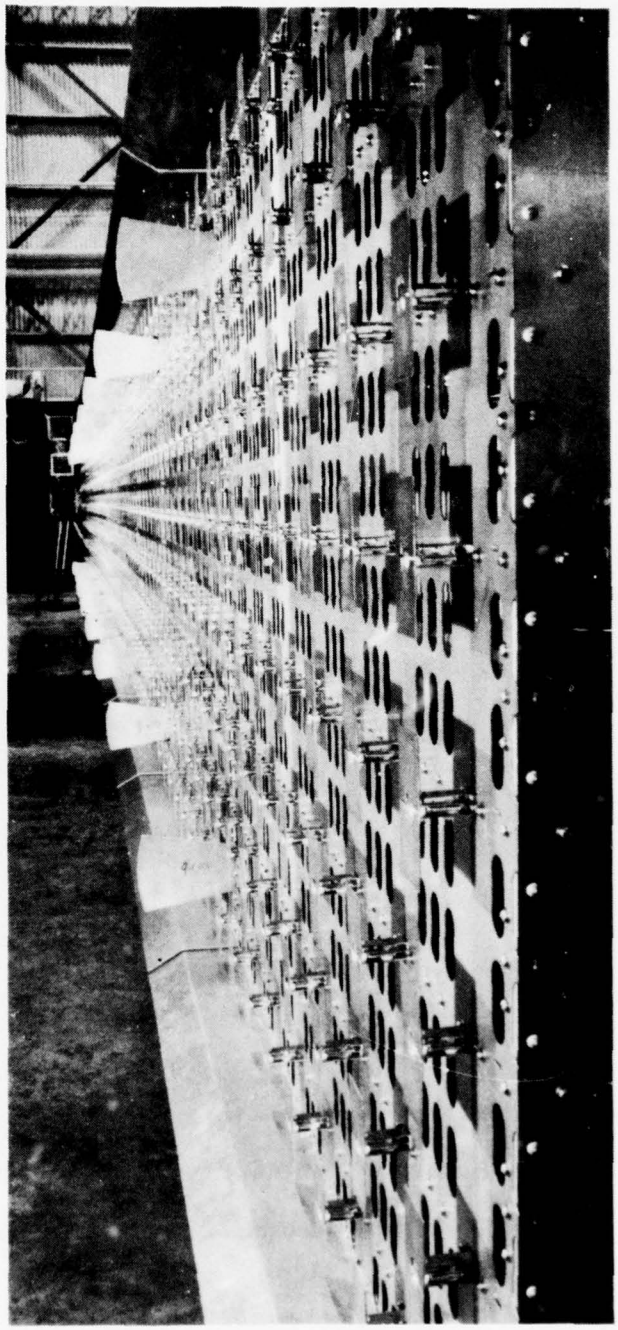

Figure 8. Optical Alignment

Patterns

The completed antenna was disassembled, shipped to the ground plane test range, reassembled, and tested on the pedestal shown in figure 9. The principal plane azimuth pattern at the design frequency of 1.3 GHz is shown in figure 10. It is significant that adjustments were not made, indicating a good potential for economical production. The characteristic falloff from broadside is evident, as anticipated by the corporate error analysis. The broad base of dipole errors is acceptably low, indicating acceptable random manufacturing errors. Close to the beam, moderate errors are apparent from larger regions of the array. The beam base itself would benefit from correction of the subarray-to-subarray phases. Patterns at other frequencies are shown in figures 11 to 14. Here again, the broad base of sidelobes is quite low, with the frequency response beginning to show up near the main beam. These numbers generally agree with the predictions of figures 3 and 4. The cross-polarized pattern of figure 11 verifies that no significant horizontal polarization radiates outside of the main beam. In patterns measured above 1.4 GHz, the anticipated grating lobe appears, but the basic sidelobes remain below -30 dB to at least 1.6 GHz.

The backlobe is somewhat higher than anticipated, but an after-the-fact analysis of the windage-hole leakage indicates that this is the source of that measured level. Figure 15 compares the measured data with that calculated for the hole pattern.

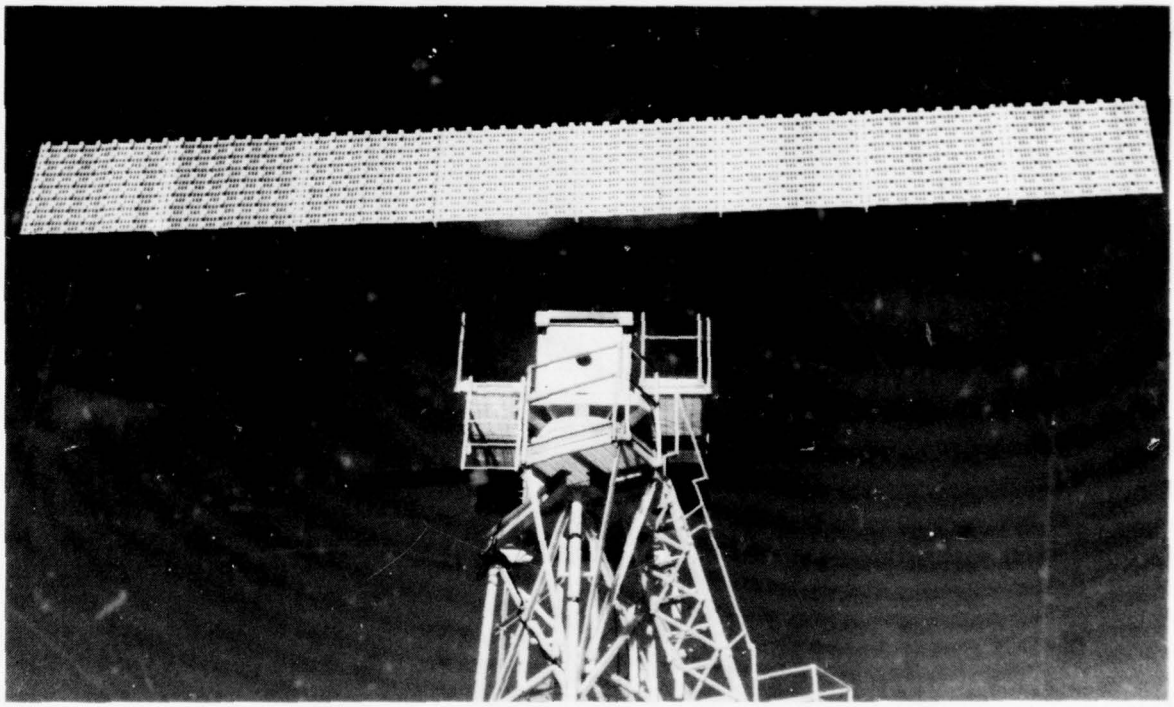

Figure 9. 42-Foot Array Mounted on Test Range Pedestal

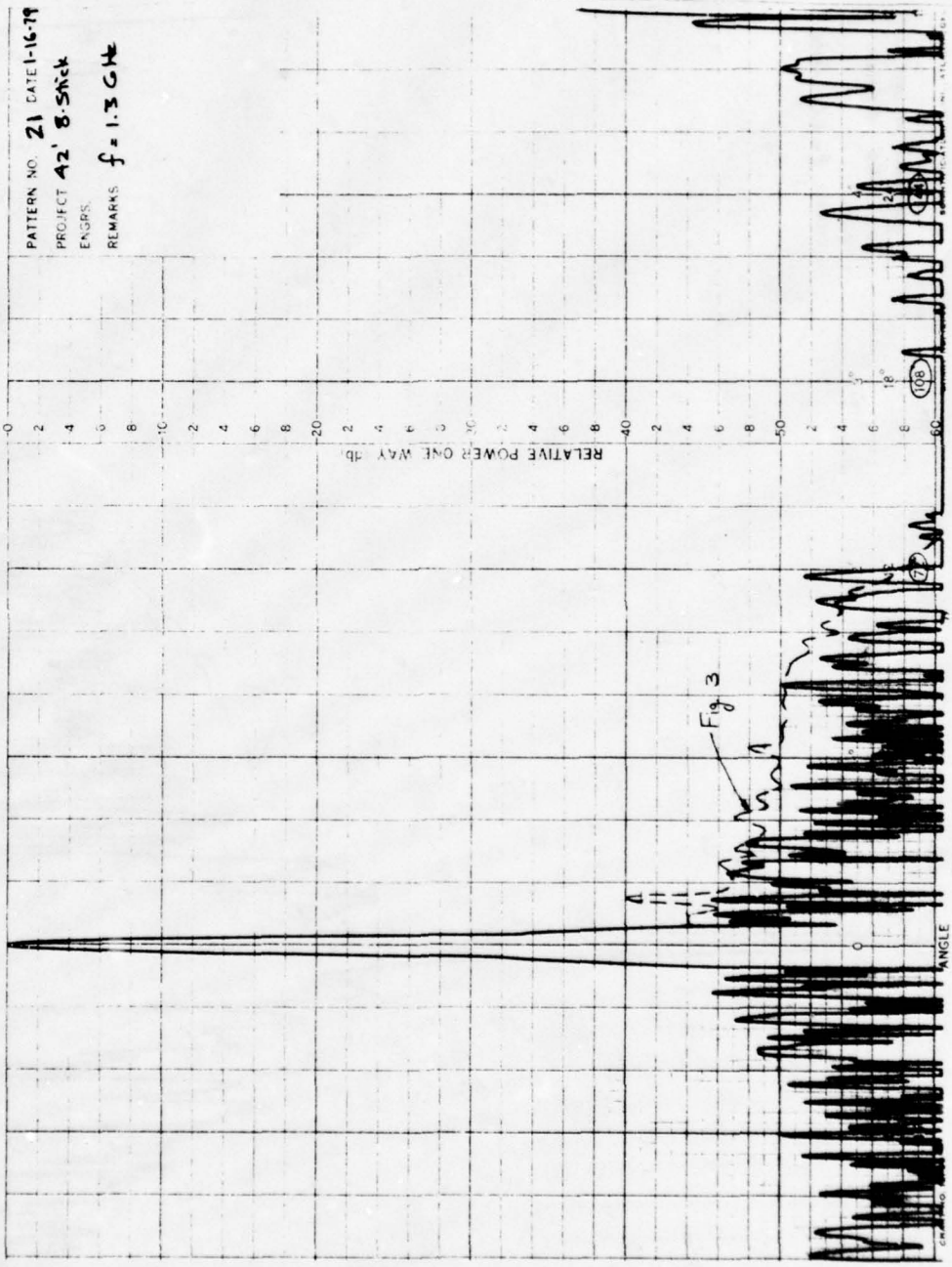

Figure 10. Azimuth Pattern at the Design Frequency of 1.3 GHz

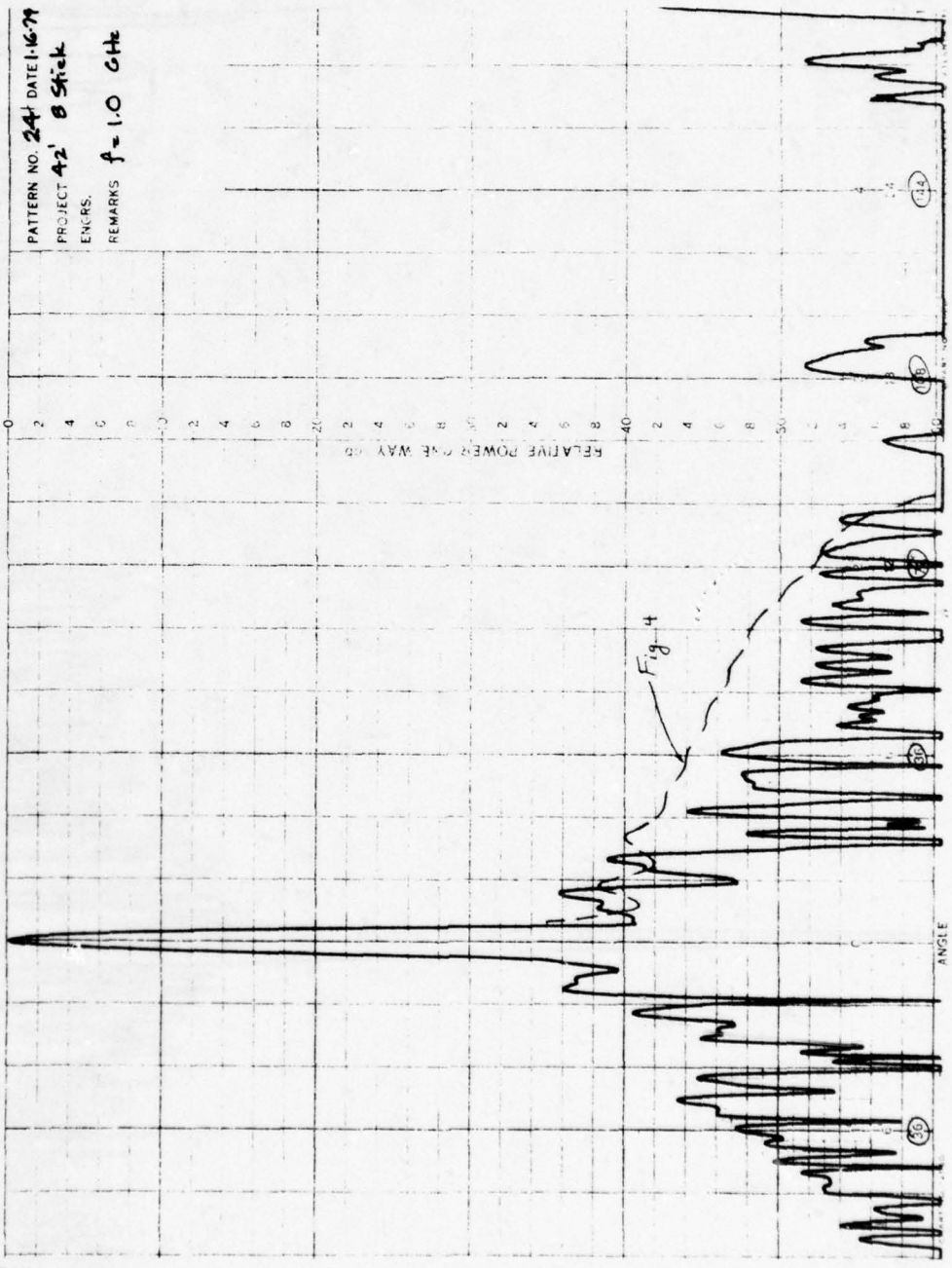

Figure 11. Measured Azimuth Pattern at 1.0 GHz

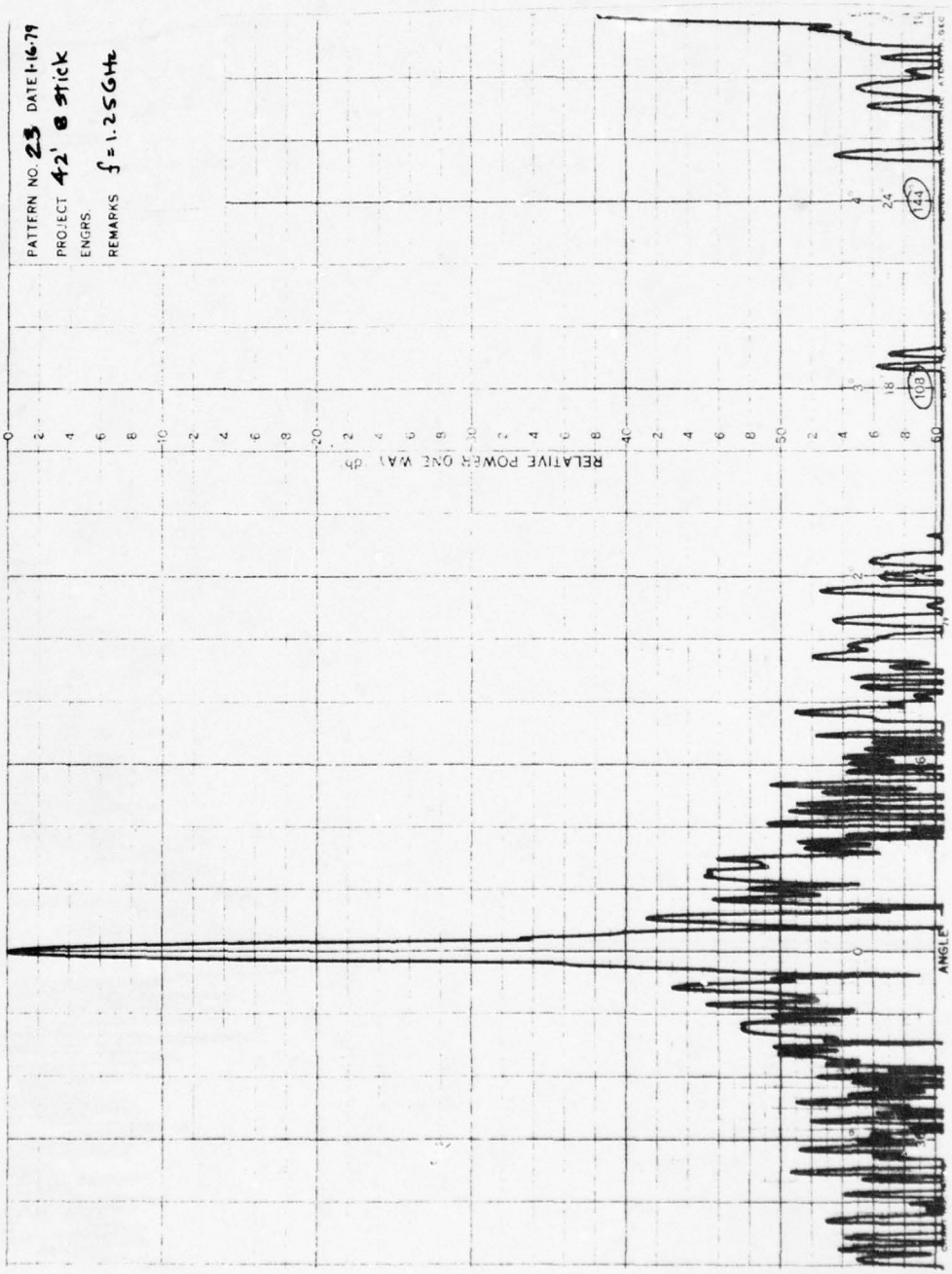

Figure 12. Measured Azimuth Pattern at 1.25 GHz

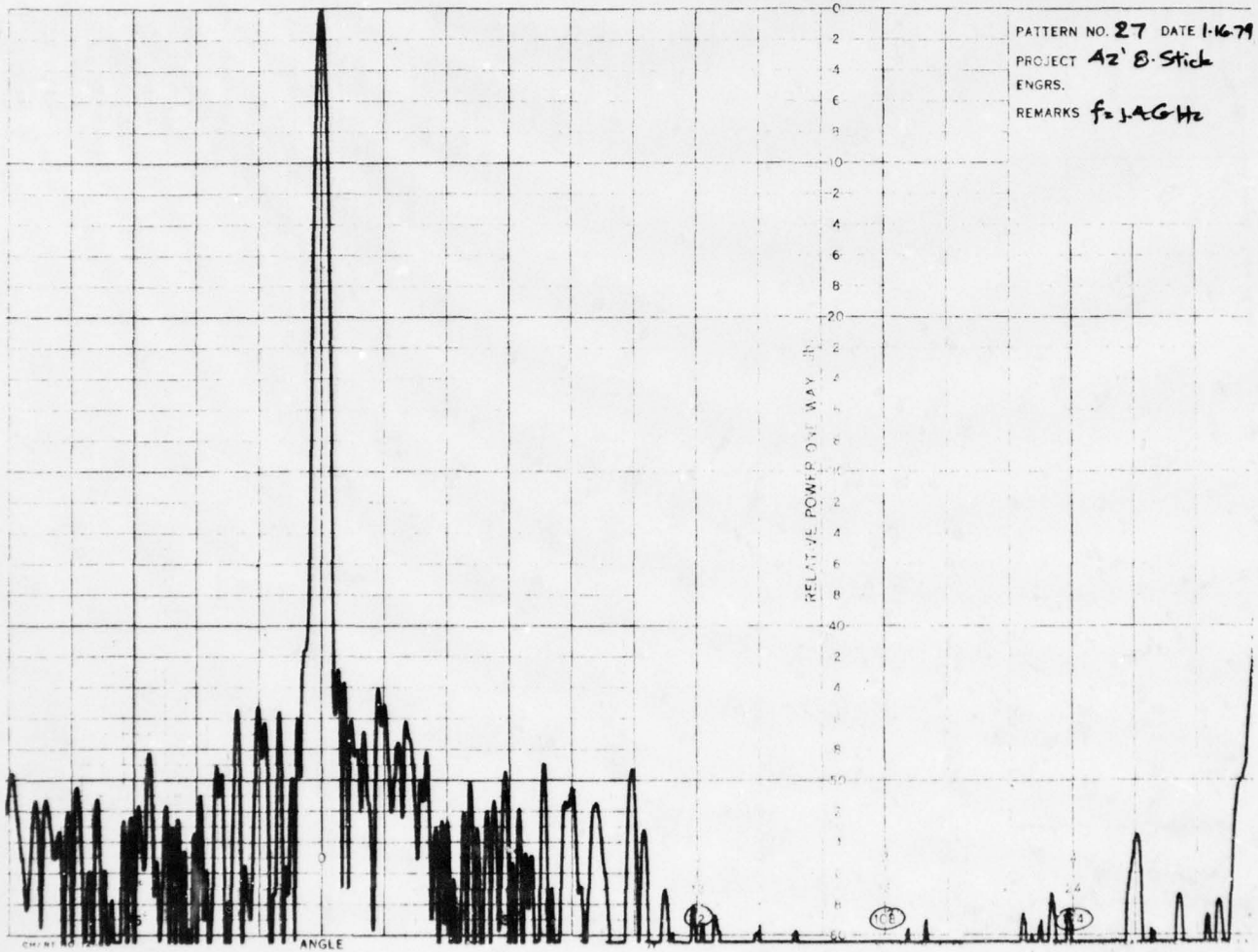

Figure 13. Measured Azimuth Pattern at 1.40 GHz

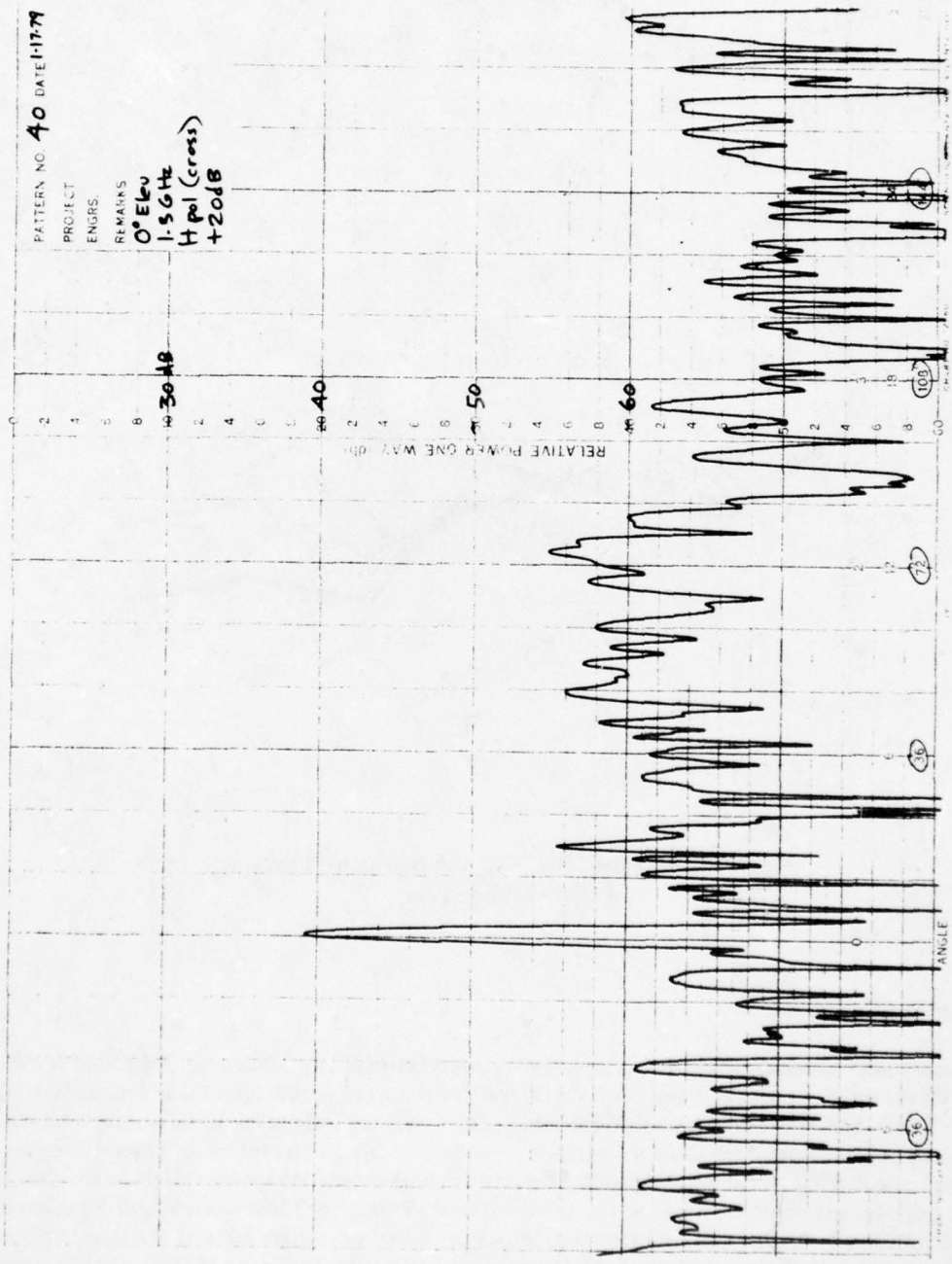

Figure 14. Measured Cross-Polarized Response at 1.3 GHz

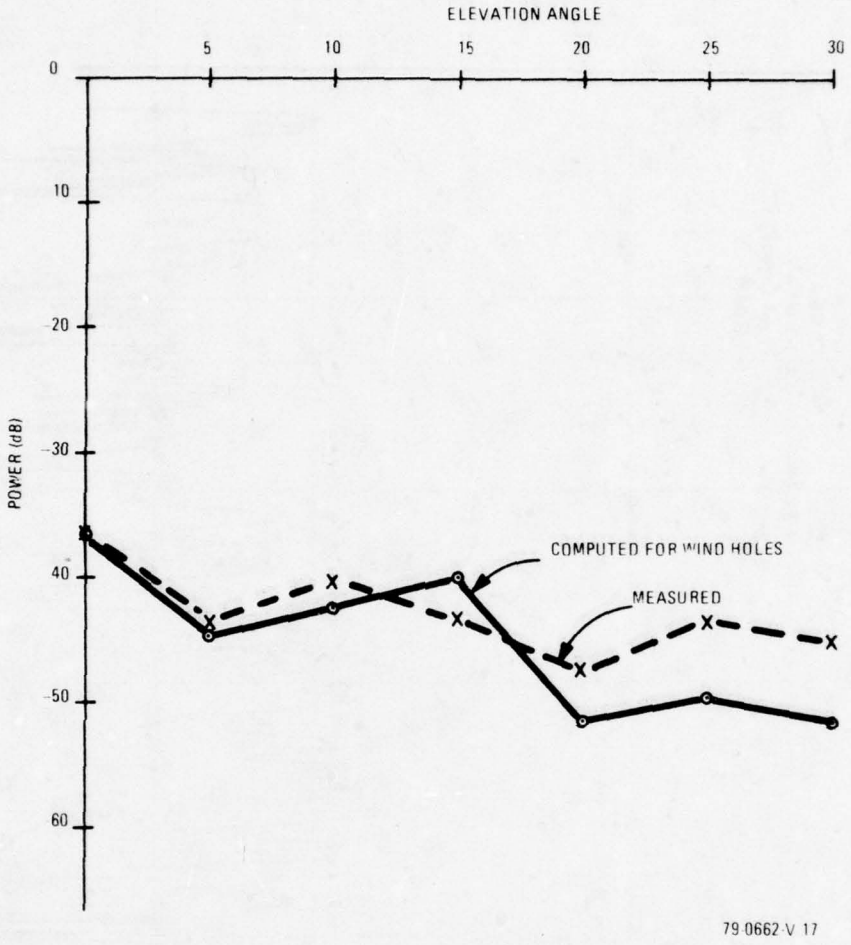

Figure 15. Measured Backlobe and Calculated Leakage Pattern Comparison

Summary and Conclusions

A primary goal of the experiment was to establish limits on structural, manufacturing, and component accuracy. Of the three, it appears that it is within the state of the art to hold structural and manufacturing errors to the -50 dB level at L-band for a full-size array. The frequency changes indicate a somewhat higher limit due to component design. A preliminary estimate is -40 dB over a 30 percent band. Several avenues are open for improvement. First, for more than eight rows, the random errors decrease inversely as the gain increases. Second, adjustments could be made at the subarray level. Third, for those cases requiring more accuracy, tape-controlled milling has been programmed. However, based on system tests of waveguide antennas, the limits of stamping are not much above the diffuse scatter and similar background effects of the environment, so that the wide-band array should be useful for many applications.

A MILLIMETER-WAVE SCANNING ANTENNA FOR RADAR APPLICATION

Oren B. Kesler, William F. Montgomery, and Charles C. Liu
Texas Instruments Incorporated
Equipment Group
Dallas, Texas 75266

Introduction

During certain tactical operations, such as tracking or acquisition of a target, a high gain antenna is required to rapidly scan through a volume in space. The polarization twist reflector antenna with the hardware realizations, using photo-lithographic processes, described in this paper presents an attractive solution at millimeter-wave frequencies. The rapid scanning feature of the polarization twist antenna is achieved by scanning only a light weight flat plate rather than an entire antenna/mount assembly having high inertia. By virtue of its reflection properties the flat reflection plate need only be scanned by half the angle that the antenna pattern is scanned in comparison to a 1:1 scan to beam skew ratio of other antennas. This allows a simple spherical bearing gimbal mechanism for a 45° conical sector scan. The antenna feed remains stationary, thereby eliminating the need for a rotary joint, which at millimeter-wave frequencies is unreliable, difficult to build, and very expensive. The antennas presented in this paper are truly low cost, efficient millimeter-wave and Ka-band antennas for radar application.

Discussion of Prior Art

Prior high gain millimeter-wave radar antennas are generally of the optical generic category, such as prime focus reflectors, Cassegain reflectors, and horns. These optical type antennas, as well as planar arrays are mechanically scanned by means of a gimbal system, and as a consequence require two expensive and often band-limiting rotary joints. When monopulse direction finding is used, each of the two rotary joints have three matched channels with high tolerances, particulary at 94 GHz frequency. The beam scanning rate of these mechanically scanned antennas are limited by the inertia of the antenna, gimbal, and rotary joint mechanisms.

In the millimeter frequency band the art of electronic scanned antennas is meager. Switched beam-scanned antennas using lens or reflectors can scan only small regions due to coma aberrations. Phased arrays above 90 GHz are virtually nonexistent, although there is no scientific reason why they are not possible. However, cost and power loss are certain to restrict phased arrays for years to come.

The millimeter-wave radar antenna described in this paper yields high performance with simplicity and low cost. In particular, the described millimeter-wave radar antenna combines all of the following attributes in a single practical millimeter antenna:

1. High gain
2. Low dissipative losses
3. Four-lobe monopulse
4. Low sidelobe difference patterns
5. Wide angle scanning
6. No rotary joints
7. Spherical bearing gimbal with low inertia for acceleration
8. Innovative photolithographic fabrication techniques
   - Capacitive and inductive tuned twist reflector for polarization twist
9. Low cross-polarization
10. Wide bandwidth

Description of Antenna

Figure 1 shows a sketch of a polarization twist antenna. The polarization of the feed horn in the sketch is vertical. Rays emanating from the feed horn are reflected by the parabolic surface since the dielectric material has vertical metallic lines on the inside surface. The rays are then reflected by a flat plate which also accomplishes a 90° polarization rotation. The rotation is accomplished with 45° lines on the surface of the flat plate and 180° phase difference between the reflected electric field components parallel and perpendicular to the lines. The ray is reflected at an angle 2θ to the horizontal, as shown in Figure 2, for a plate angle of θ with the vertical. The rays pass out through the parabolic surface since the E-field is now perpendicular to the metallic lines.

The polarization twist geometry has been explored as a candidate for a scanning antenna at lower frequencies by Martin and Schwartzman [1]. Houseman [2] describes an experimental 94 GHz model. Waineo and Konienczny [3] have demonstrated a 94 GHz flight test model with scanning capability. The antenna described here was designed to simulate a missile flyable antenna, however, precise adjustment mechanisms were installed so that design data could be gathered.

Hardware Realization

A six inch millimeter polarization twist antenna constructed by Texas Instruments is shown in Figure 2. Working models were built at 35 and 94 GHz. A 45.0^{o} conical sector of scan is possible with these antennas. Since the device pictured in Figure 2 was intended as an engineering model, many of the mechanisms were included for convenience and experimentation and could be eliminated in later models. Figure 3 shows these mechanisms. The middle micrometer moves the horn in and out relative to the parabolic surface. A screw adjustment moves the

flat reflecting surface in and out relative to the horn. The micrometers were installed on the scan mechanism to accurately determine scan angle. A millimeter mixer is shown attached to the back of the antenna.

Gimbal System

Since the polarization twist reflector must only rotate by 22.5° to give 45° of beam scan, it is possible to use the spherical bearing gimbal system shown in Figure 4. This use of the spherical bearing would not be possible on conventional antennas that must be rotated 45°. Blockage is reduced by the use of the spherical bearing since the distance between the transreflector and the pivot point is minimized. The precision spherial bearing is off the shelf and inexpensive. The push rod assemblies are also low cost since there are no critical tolerances involved in their construction. In Figure 3 the micrometers that set the scan for experimental purposes would be replaced by servomechanisms in an operating system.

Horn Feed

Preliminary tests were performed using a single horn feed on both the 94 GHz and 35 GHz models. The horns were designed to give a 10 dB edge taper, excluding space loss, for lower side lobes. The 94 GHz horn was formed by milling out the E-plane walls of the waveguide at a 10° flare angle after the H-plane walls had been removed. Brass was then used to replace the H-plane walls. The 94 GHz feed horn and flat polarization twisting plate are shown in Figure 5.

An E-plane monopulse feed was constructed for the 94 GHz model. A commercially available hybrid tee was used for the comparator circuitry. The two feed apertures were brought sufficiently close together by milling off the outside of the common walls of the two feeding waveguides. The total wall thickness between the feed apertures was .020 inches prior to flaring. In order to obtain the desired compromise between sum and difference channel illumination the apertures were flared by sharpening their common wall to a knife edge and milling out the inside of the other two walls at a 10° angle. The phase was adjusted in both channels, using phase trimmers, until the maximum null depth was obtained. A phase adjustment was required because of the extremely small mechanical tolerances necessary to maintain phase and amplitude matched channels at 94 GHz. It was not, however, necessary to resort to machining the feed from a single block. Figure 6 shows the sum and difference patterns of the E-plane feed.

Polarization Twist Reflector

The 94 GHz polarization twist reflector in Figure 5 is designed such that the sum of the inductive reflection coefficient and the capacitive reflection coefficient is zero for broadside incidence at the center frequency. Changing the line width and period of the grid

shown in Figure 7 changes the capacitance and inductance associated with them. Line widths and spacings were determined to satisfy the reflection coefficient requirement for a standard thickness laminate, that is close to one quarter wavelength. The use of a standard laminate thickness and an etching process make this design procedure highly desirable from the standpoints of low cost and reproducibility. Figure 8 shows the variation in line width versus period satisfying the reflection coefficient condition. The solid and dashed curves are respectively for a 20-mil thick stock piece of copper clad RT/Duroid* and a $\lambda/4$ (21.16-mil) substrate. Widths of 4.03 and 2.45 mils are respectively seen for the two cases with period A = 8 mils. The performance of the twist reflector depends upon the difference in phases of the inductive, Φ_I, and capacitive, Φ_C, reflection coefficients. A measure of the performance given by the ratio, in dB, of the untwisted to twisted components is $20 \log_{10} \cot|((\Phi_I - \Phi_C)/2)|$. The relative phase as a function of frequency at normal incidence is approximately the same for the two cases and is given in Figure 9. The figure shows that the relative phase error, deviation from 180 degrees, is less than 20 degrees over the 87 to 101 GHz band. Phase variations with scan angle in the planes parallel and perpendicular to the lines are given in Figure 10. The phase error is less than 9 degrees over twisting plate angle of 22.5 degrees or beam angle of 45 degrees.

Similar parametric design curves for a 35 GHz twist reflector are shown in Figure 11. The solid and dashed curves are respectively for 0.062 inch Duroid and $\lambda/4$ laminate. In this case a significantly wider period, A = 0.120 inches, was selected for the 35 GHz twist reflector shown in Figure 12. Figure 13 shows the relative phases of the inductive and capacitive reflection coefficients as a function of frequency. The phase variation is significantly different from the 94 GHz designs with low inductances. Here the inductance is considerably larger causing the different frequency behavior. The phase error is less than 30 degrees over the 31 to 40 GHz band for the $\lambda/4$ case. In the 0.062 inch case the band extends from 31 to 50 GHz. This shows that it can be advantageous to choose a higher inductance design and in doing so to decrease the tolerance and increase the bandwidth.

Transreflector

The parabolic dish shown in Figure 2 is a half-wavelength fiber glass structure. Epoxy resin and E-glass cloth were used for the fiber glass. The dish was formed by laying up pre-impregnated sheets on a male mold and curing in an autoclave. The dish was 29-mils thick for the 94 GHz model. A 2½-mil fiber glass laminate with copper on one side was etched with 3-mil lines and 8-mil spacings, gored, and carefully laid up on the inside of the dish. On a low cost production antenna the copper could be deposited directly on the inside of the parabolic surface and the lines could then be etched. The part of the

*Regulation trade mark Rogers Corporation

fiber glass structure that comes straight back toward the back of the antenna adds necessary phase shift to the rays passing through it when the beam is scanned.

As can be seen in Figure 1, the antenna aperture size is constant, independent of scan angle. Changes in beamwidth, gain, and beam steering with scan angle can be due in part to transreflector transmission effects. As a first order approximation of these effects a ray tracing computer program was written for the twist reflector geometry. Figure 14 shows the results of this program for beamwidth and gain at various scan angles. Figure 15 shows the beam steering and sidelobe results. The beamwidth increased by .02° and the gain decreased by 0.15 dB at 45° scan angle. The sidelobes increased by 1 dB and the beam steering is a maximum of 0.06° at 45° scan angle. From these results it can be seen that the effects of the transreflector should be minimal if fabrication errors do not play a significant role.

Test Results

Figure 6 demonstrates the high quality beam scanning capability of the 94 SGHz antenna out to 45 degrees. The 1.4 degree beamwidth broadens only slightly and the gain degrades less than 1 dB at 45 degrees. The measured relative gain versus scan angle is shown in Figure 17. Peak sidelobes are between -22.5 and -25 dB in the scan range. The antenna pattern integrity was maintained over a wide frequency bandwidth. The exact bandwidth determination was limited by measurement capability. Figure 18 shows the 35 GHz antenna being scanned in the H-plane. The 3.5° beamwidth varied only slightly with 45° of scan. Peak sidelobes are between -19 and -23 dB for this non-optimized engineering model. Expanded scale pattern in Figure 19 shows good pattern symmetry. The antenna has a high degree of polarization purity at 0 degree scan because the metallic lines in the parabolic surface act as a polarization filter. The cross-polarization is down more than 32 to 37 dB in the main beam. As scan is increased the polarization purity gradually degrades due to the changing orientation of the lines with scan. Figures 20 and 21 show antenna patterns at 39.89 and 30.21 GHz which demonstrate that the bandwidth is greater than 27 percent.

Figure 22 shows the 94 GHz monopulse sum and difference, H-plane patterns. The null in the difference pattern is 47.5 dB below the sum peak. The 1.8° sum beamwidth is broader than the single horn antenna beamwidth because of the non-optimum monopulse feed. The improved quality of this 94 GHz pattern when compared to the previous results reflects the aquisition of an improved measurement system.

Conclusions

The polarization twist antenna with hardware realizations described here using photolithographic processes, spherical bearing

gimbal, and standard laminates is indeed an attractive low cost, rapid scanning, monopulse, millimeter wave radar antenna. It has been shown that the use of a standard copper clad laminate with etched lines is a low cost, producible design technique for the twist reflector. Various choices of line widths and periods may be selected. The specific selection of parameters may be made trading off, bandwidth, tolerance, and performance with scan angle. The polarization twist reflectors fabricated demonstrate the essentially constant gain and beamwidth with scan angle predicted by geometrical optics and an analysis of transreflector effects. Deviations from constant gain may also be explained by degraded twist reflector performance at large scan angles. The fabrication of a high quality monopulse system is possible at 94 GHz using off the shelf components.

The basic millimeter-wave antenna described here can be used in many other applications where a scanning beam is required. For example, the paraboloidal transreflector may be synthesized or spoiled to give a cosecant type fan-beam pattern. Such a pattern could have a single plane monopulse and scanning capability.

References:

1 R. W. Martin and L. Schwartzman, "A Rapid Wide Angle Scanning Antenna With Minimum Beam Distortion," Proc. of East Coast A.N.E. Conference, pp. 47-51, 1958.

2 E.O. Houseman, "A Millimeter-Wave Polarization Twist Antenna," Proc. of International A.P. Conference, pp. 51-54, 1978.

3 D.K. Waineo and J. F. Konieczny, "A Millimeter Wave Monopulse Antenna With Rapid Scan Capability," Proc. of International A.P. Conference, pp. 477-480, 1979.

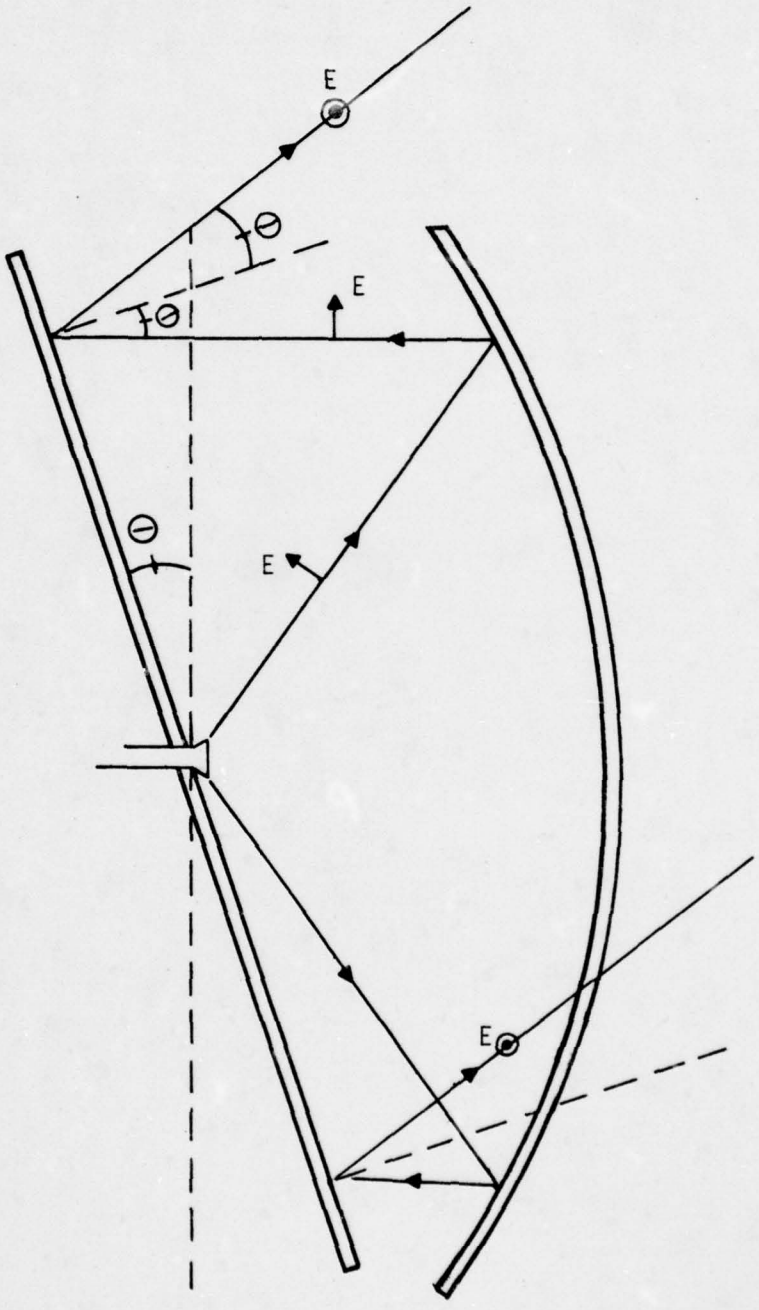

Figure 1. Polarization Twist Operation

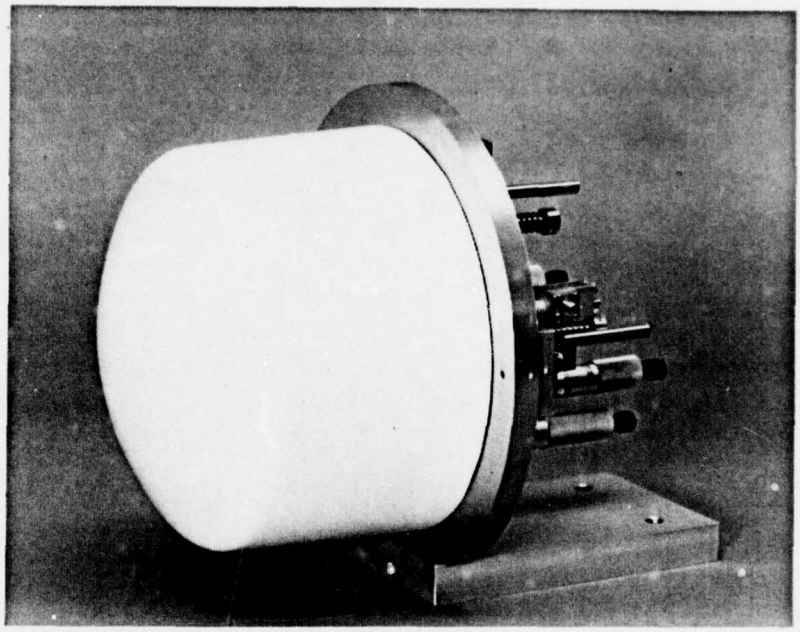

FIGURE 2. POLARIZATION TWIST REFLECTOR

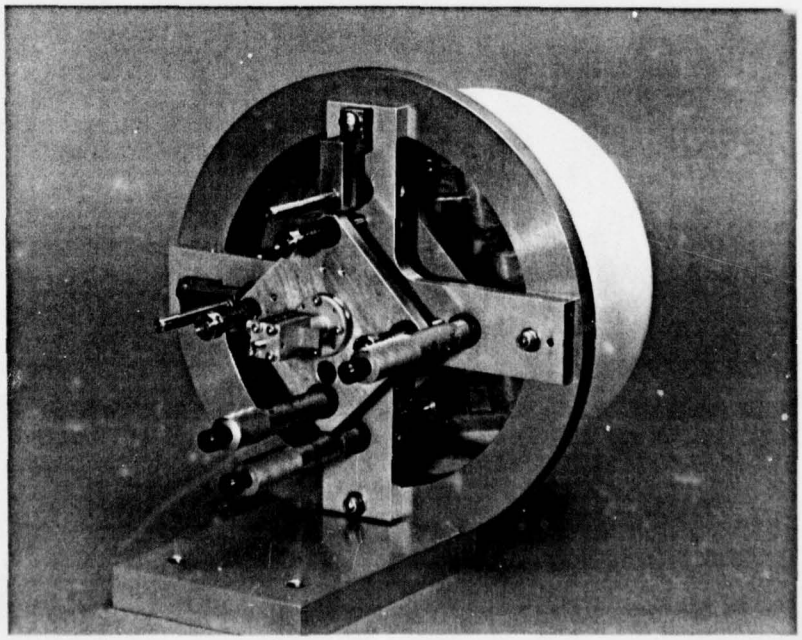

FIGURE 3. ADJUSTING MECHANISM

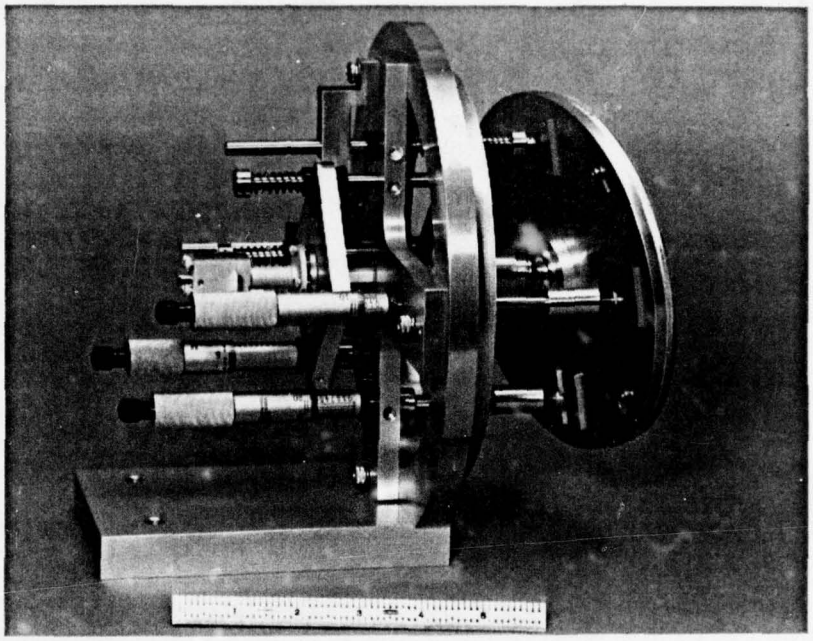

FIGURE 4. GIMBAL SYSTEM

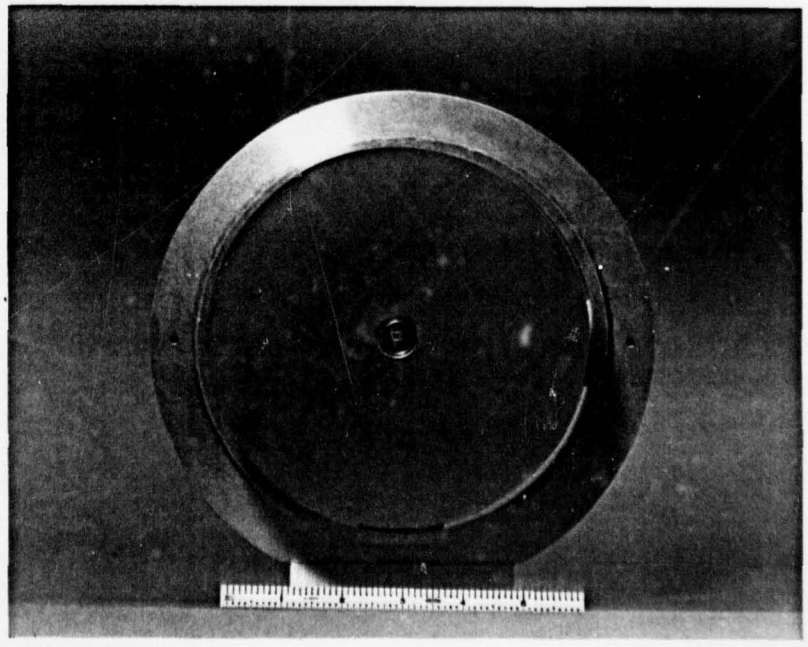

FIGURE 5. 94 GHz TWIST REFLECTOR AND HORN FEED

TEXAS INSTRUMENTS
INCORPORATED
DALLAS TEXAS

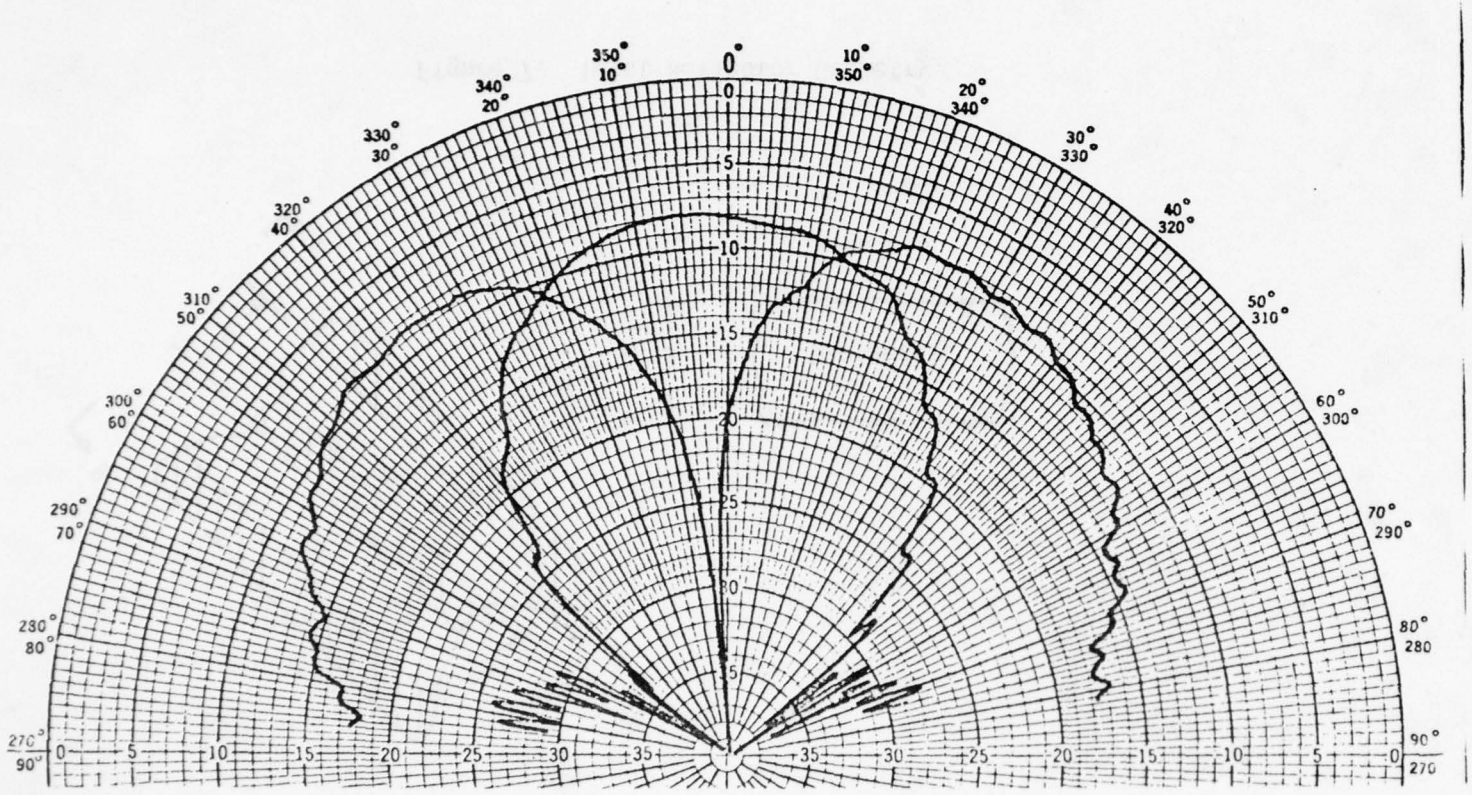

Figure 6. Monopulse Feed Pattern
Sum and Difference E-Plane

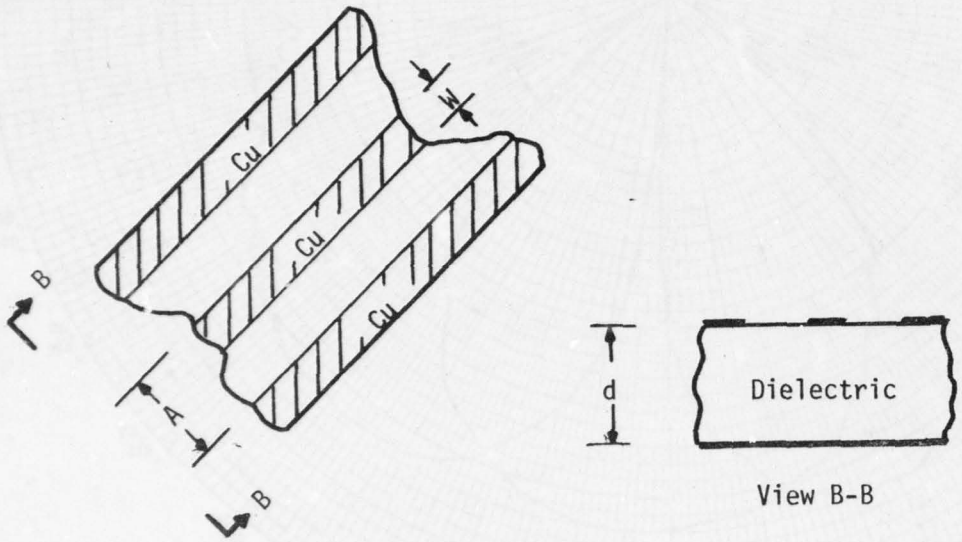

Figure 7. Twist Reflector Geometry.

AD-A077 167 ILLINOIS UNIV AT URBANA-CHAMPAIGN ELECTROMAGNETICS LAB F/G 17/9
PROCEEDINGS OF THE ANTENNA APPLICATIONS SYMPOSIUM (1979) HELD 2--ETC(U)
SEP 79 F19628-79-M-0015
UNCLASSIFIED NL

2 OF 6
ADA 077167

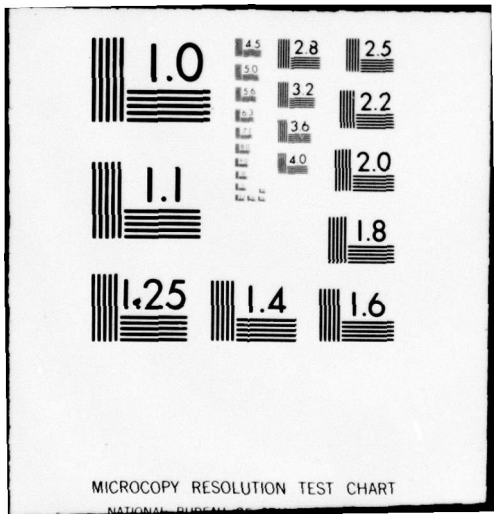
1.0
1.1
1.25
1.4
1.6
1.8
2.0
2.2
2.5
2.8
3.2
3.6
4.0
4.5
5.0
MICROCOPY RESOLUTION TEST CHART

ØØ ØØ A077167 (U) FIELD/GROUP ØØØØØØ

UNCLASSIFIED TITLE

PROCEEDINGS OF THE ANTENNA APPLICATIONS SYMPOSIUM (1979) HELD 26-28 SEPTEM
OF ILLINOIS.

ABSTRACT

(U) PARTIAL CONTENTS: LOW SIDELOBE REFLECTOR ANTENNA FOR TACTICAL RADARS;
SURVEILLANCE RADARS; NEAR FIELD BLOCKAGE OF AN ULTRALOW SIDELOBE ANTENNA;
APPLICATION; SIDELOBE LEVEL CONTROL FOR UNEQUALLY SPACED ARRAYS; A LOW-INE
MPUTER-AIDED FAULT DETERMINATION FOR AN ADVANCED PHASED ARRAY ANTENNA; RES
IATION FROM CONFORMAL DIPOLE ARRAYS MOUNTED ON DIELECTRICALLY-CLAD CONDUCT
ANTENNA SYSTEM FOR THE SOLAR POWER SATELLITE; A VARIABLE IMPEDANCE RADIO
IRCULARLY POLARIZED MICROSTRIP ANTENNAS; A COMMON APERTURE S- AND X-BAND F
UISE MISSILE INSTRUMENTATION ANTENNAS; SECTORAL SCALAR HORNS FOR PRECISE B
ACILITY; PLANAR NEAR FIELD MEASUREMENTS FOR AIRCRAFT ANTENNA APPLICATIONS;
D POWER MEASUREMENT.

INDEX TERMS ASSIGNED

ARRAYS
DEEP SPACE
ILLINOIS
RESONANCE
SOLAR ENERGY
RADAR
ANTENNAS
ULTRALOW FREQUENCY
CIRCULAR
NETWORKS
RADAR
ARTIFICIAL SAT
SEARCH RADAR
TACTICAL WARFA
SIDELOBES

TERMS NOT FOUND ON NLDB

ADVANCED PHASED ARRAY ANTENNA
AIRCRAFT ANTENNA APPLICATIONS
CIRCULARLY POLARIZED MICROSTRIP ANTENNAS
COMPUTER-AIDED FAULT DETERMINATION
LOW SIDELOBE PARABOLIC CYLINDER ANTENNA
LOW-INERTIA COMMUTATING FEED
MILLIMETER-WAVE SCANNING ANTENNA
NEAR FIELD BLOCKAGE
PLANAR NEAR FIELD MEASUREMENTS
RADIATED POWER MEASUREMENT
SCALAR HORNS
SPACED ARRAYS
X-BAND FEED
AIR LAUNCH CRU
ANTENNA APPLIC
COMMON APERTUR
CONFORMAL DIPO
LOW SIDELOBE R
MICROWAVE POWE
MULTIPLE-YAGI
NEAR FIELD PAT
PRECISE BEAM C
SAFE TEST
SIDELOBE LEVEL
VARIABLE IMPED

D 26-28 SEPTEMBER 1979 AT ROBERT ALLERTON PARK, UNIVERSITY

CTICAL RADARS; LOW SIDELOBE PARABOLIC CYLINDER ANTENNA FOR
LOBE ANTENNA; A MILLIMETER-WAVE SCANNING ANTENNA FOR RADAR
AYS; A LOW-INERTIA COMMUTATING FEED FOR CIRCULAR ARRAYS; CO
Y ANTENNA; RESONANCE PHENOMENA ON MULTIPLE-YAGI ARRAYS; RAD
Y-CLAD CONDUCTING CYLINDERS; A MICROWAVE POWER TRANSMISSION
PEDANCE RADIO PRINTED CIRCUIT BALUN; DESIGN AND THEORY OF C
- AND X-BAND FEED FOR THE DEEP SPACE NETWORK; AIR LAUNCH CR
FOR PRECISE BEAM CONTROL; NEAR FIELD PATTERN MEASUREMENT F
APPLICATIONS; AND A SAFE TEST METHOD FOR EFFECTIVE RADIATE

S ASSIGNED
CIRCULAR
NETWORKS
RADAR
ARTIFICIAL SATELLITES
SEARCH RADAR
TACTICAL WARFARE
SIDELOBES

UND ON NLDB
AIR LAUNCH CRUISE MISSILE INSTRUMENTATION ANTENNAS
ANTENNA APPLICATIONS SYMPOSIUM
COMMON APERTURE
CONFORMAL DIPOLE ARRAYS
LOW SIDELOBE REFLECTOR ANTENNA
MICROWAVE POWER TRANSMISSION ANTENNA SYSTEM
MULTIPLE-YAGI ARRAYS
NEAR FIELD PATTERN MEASUREMENT FACILITY
PRECISE BEAM CONTROL
SAFE TEST
SIDELOBE LEVEL CONTROL
VARIABLE IMPEDANCE RADIO PRINTED CIRCUIT BALUN

SSIFIED

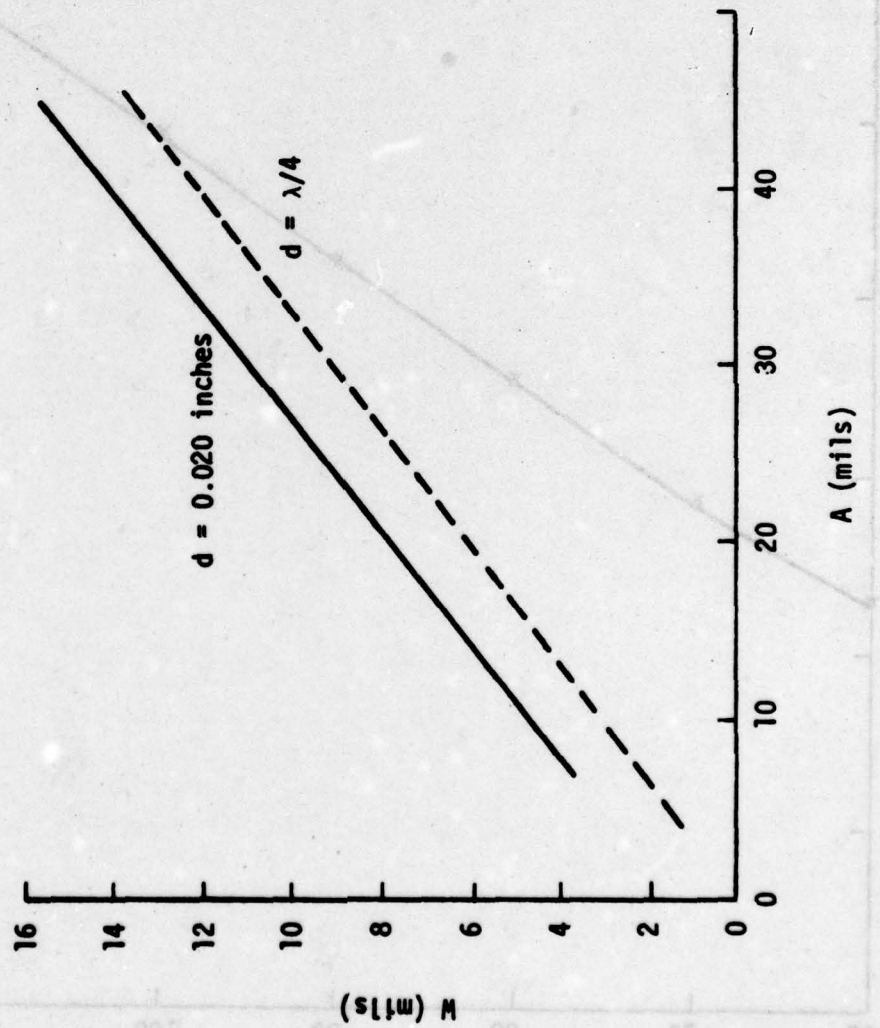

Figure 8. Line Width Versus Period for a 94 GHz Twist Reflector.

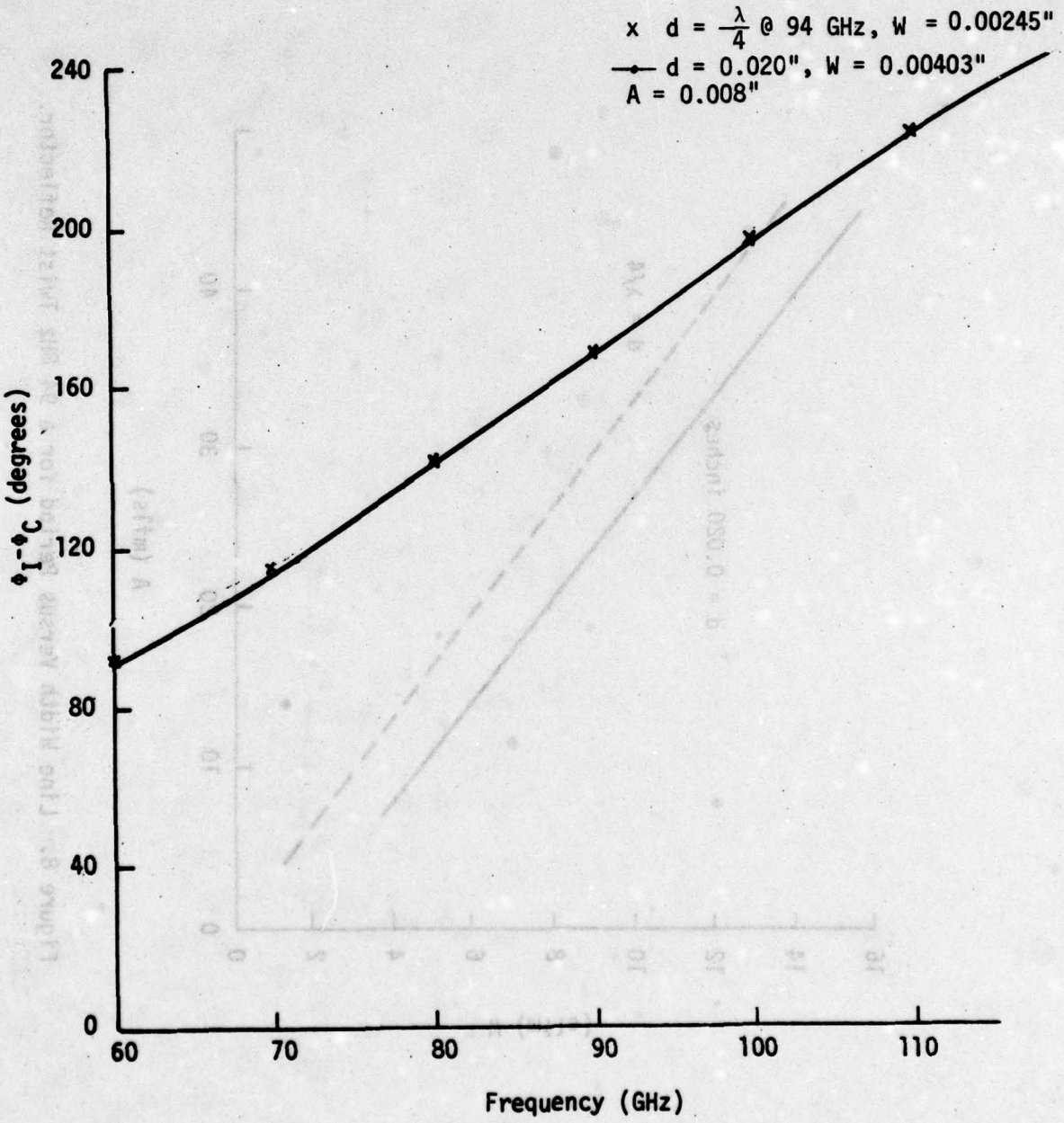

Figure 9. Phase Difference of Inductive and Capacitive Reflection Coefficients Versus Frequency.

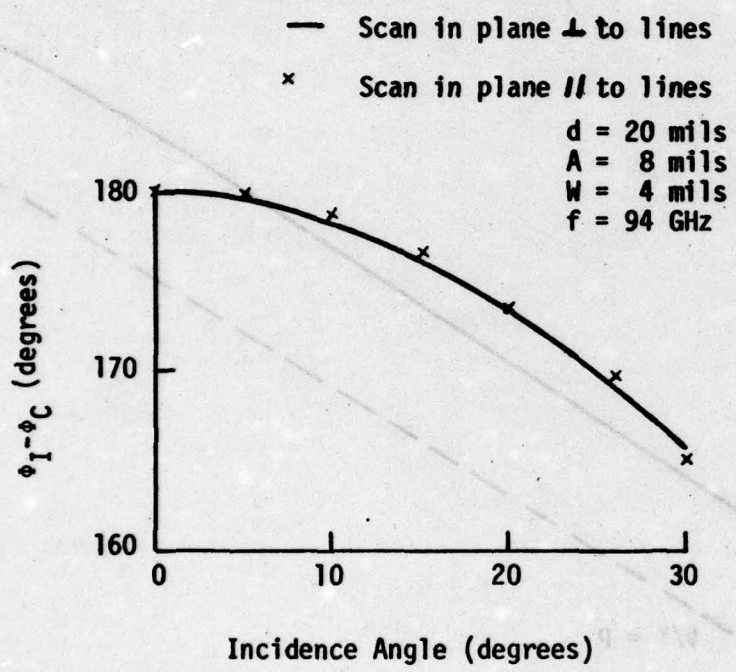

Figure 10. Phase Difference of Inductive and Capacitive Reflection Coefficients Versus Incidence Angle.

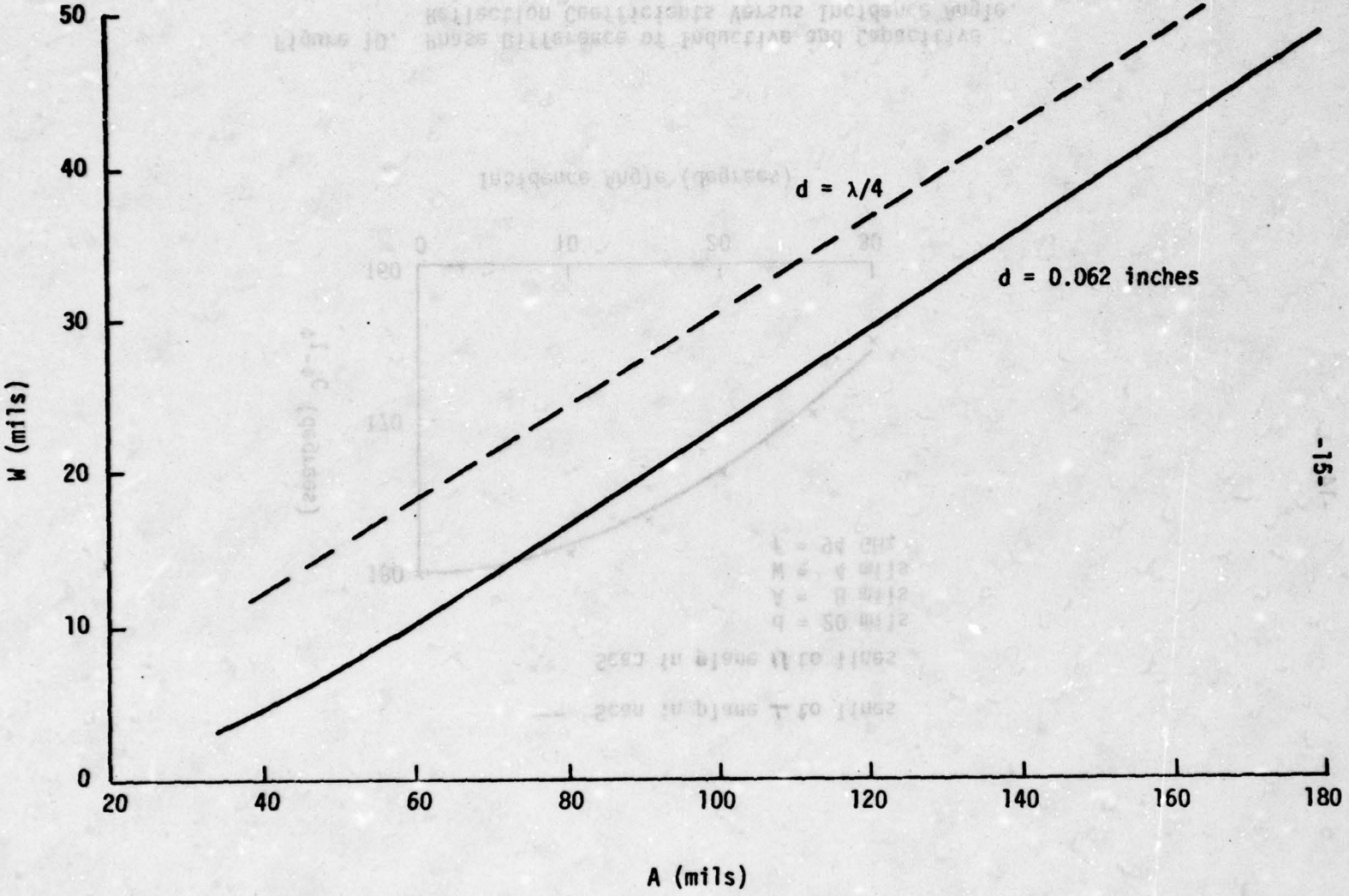

Figure 11. Line Width Versus Period for a 35 GHz Twist Reflector.

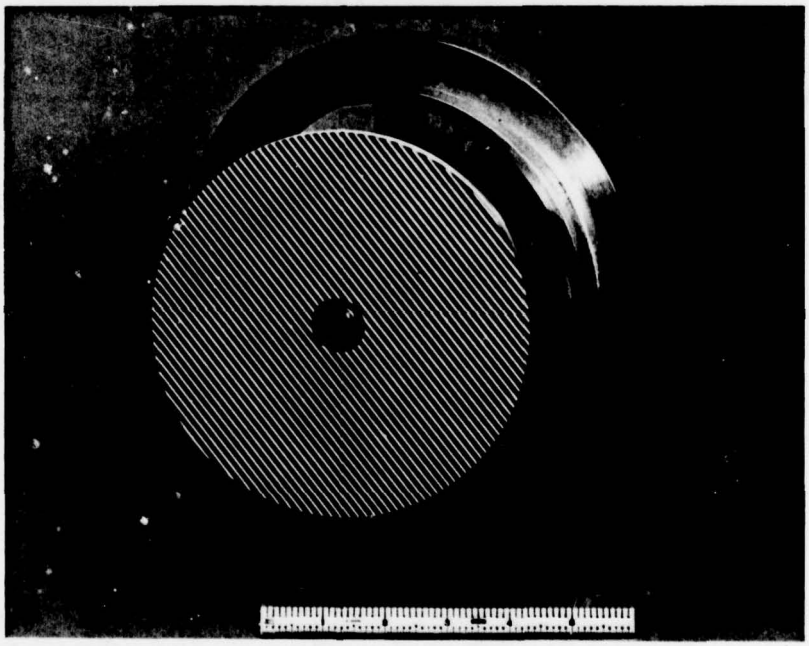

FIGURE 12. 35 GHz TWIST REFLECTOR AND HORN FEED

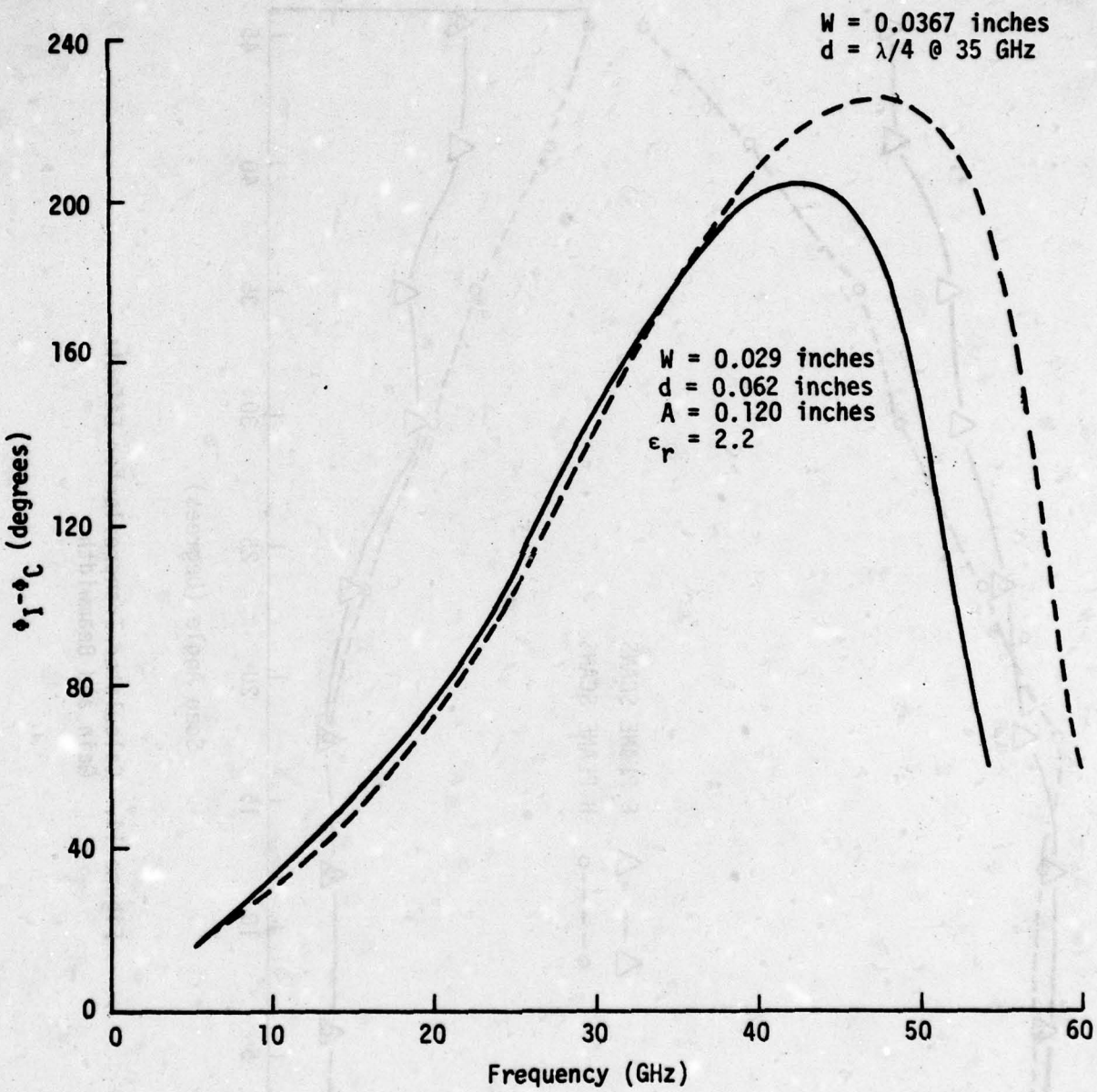

Figure 13. Phase Difference of Inductive and Capacitive Reflection Coefficients Versus Frequency.

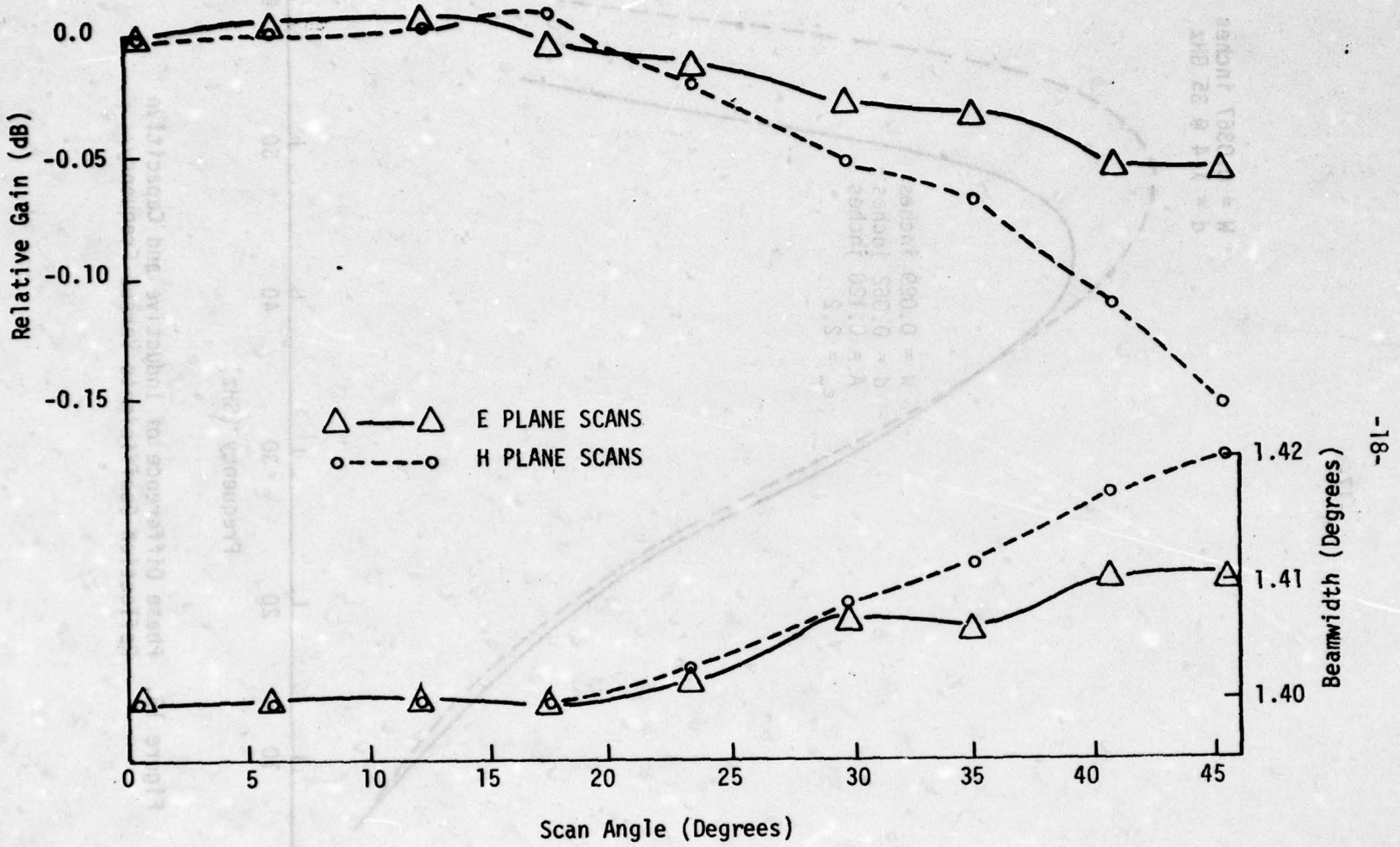

Figure 14. Calculated Transreflector Effects
Gain and Beamwidth

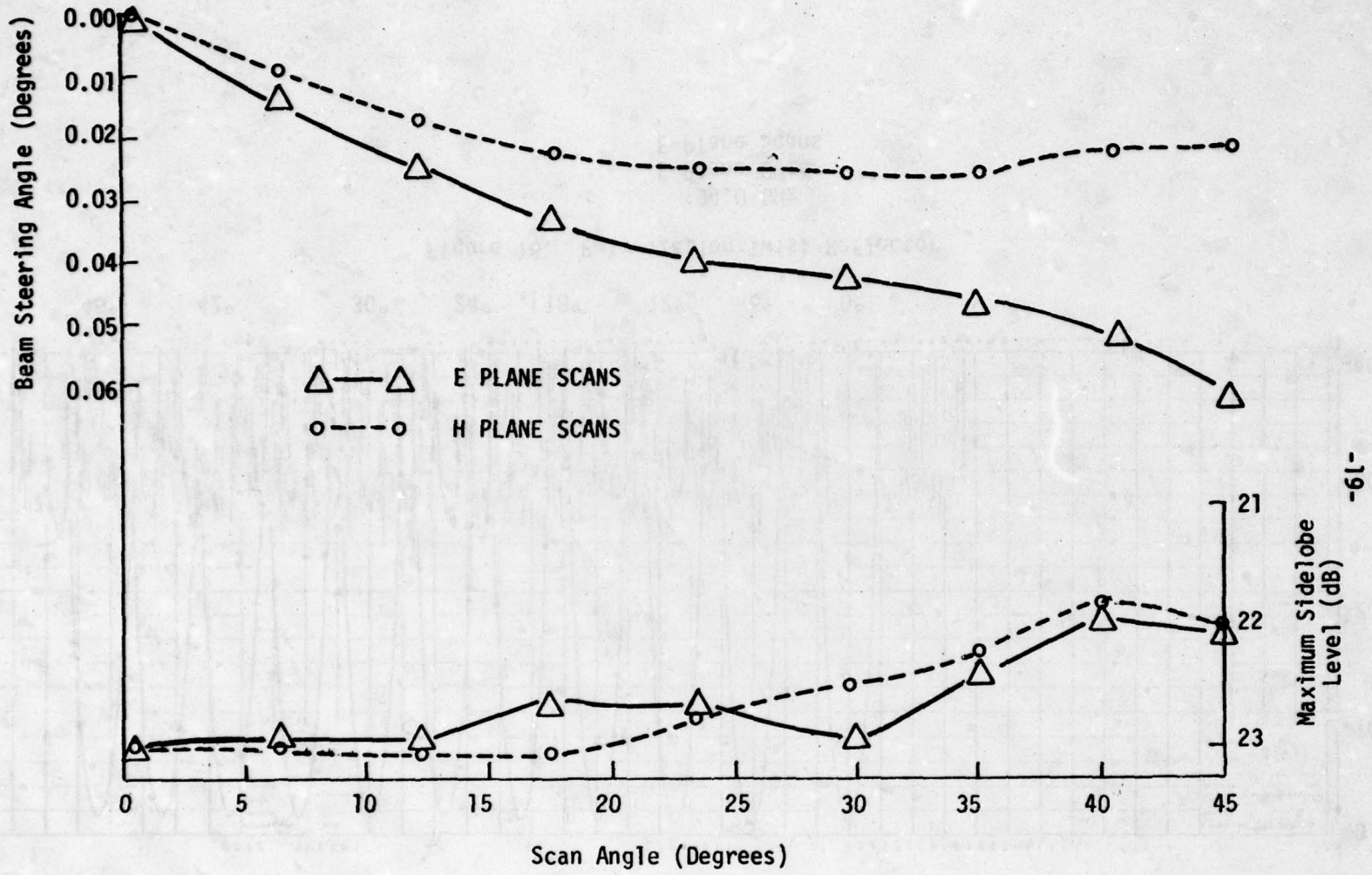

Figure 15. Calculated Transreflector Effects Beam Steering and Sidelobe Levels.

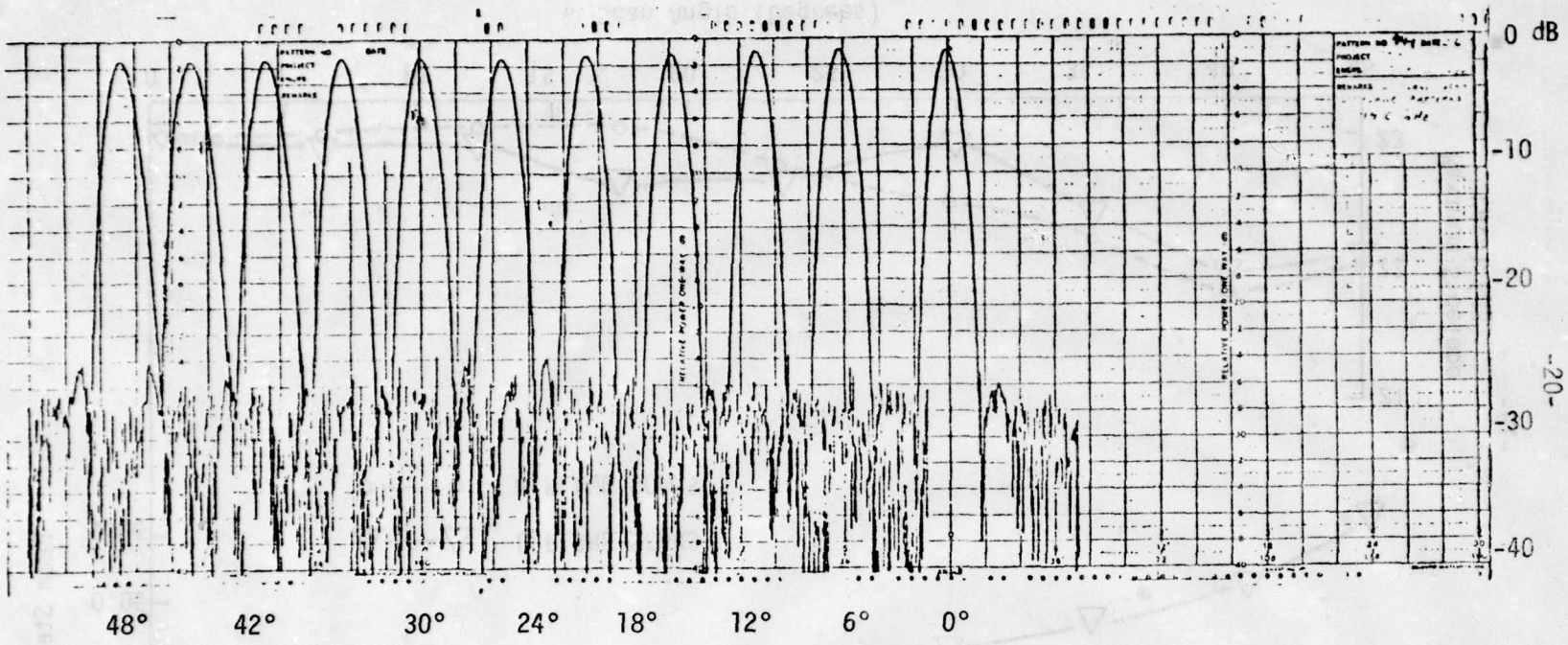

Figure 16. Polarization Twist Reflector

94.0 GHz
E-Plane Cuts
E-Plane Scans

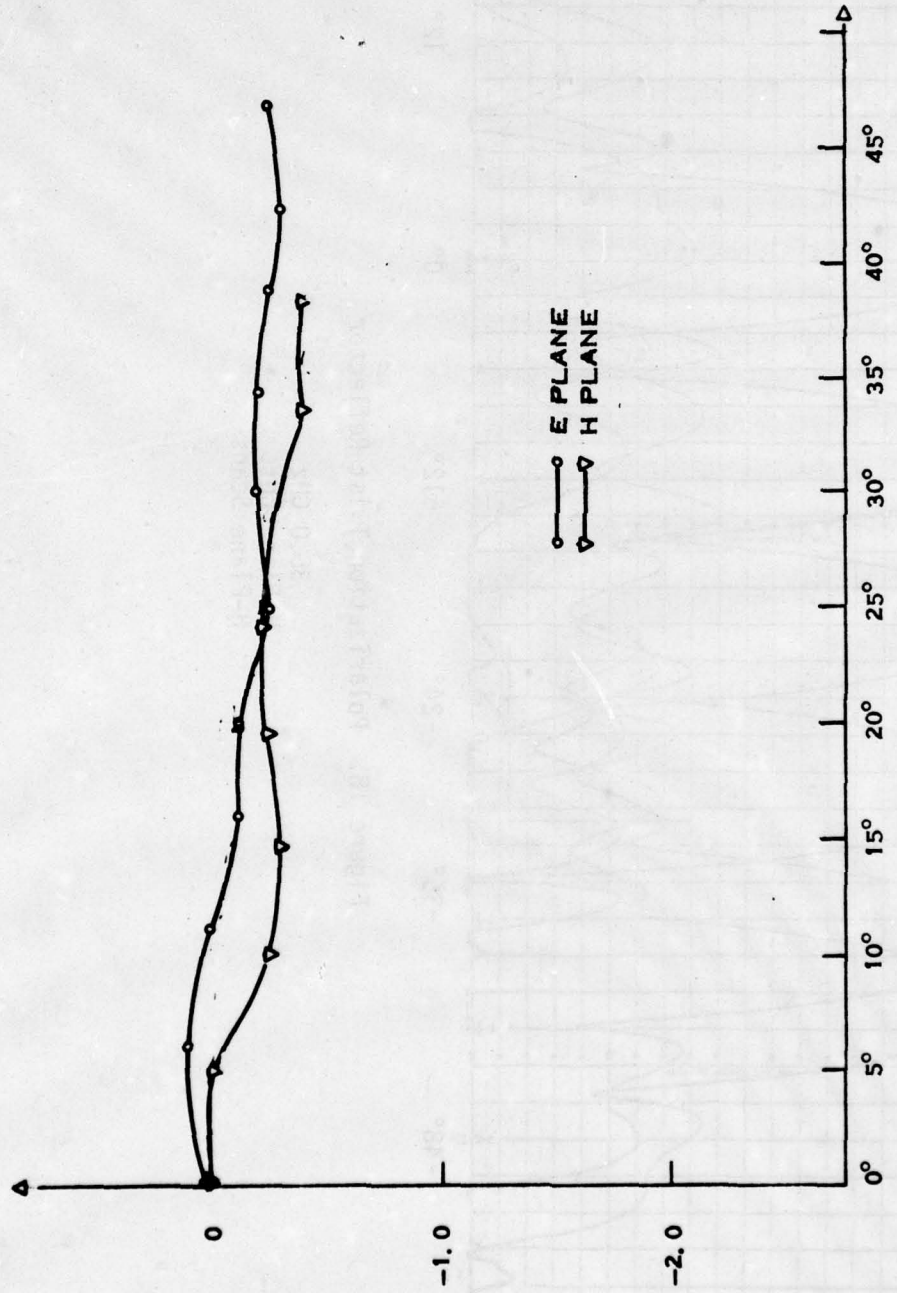

Figure 17. Measured Relative Gain (94 GHz)

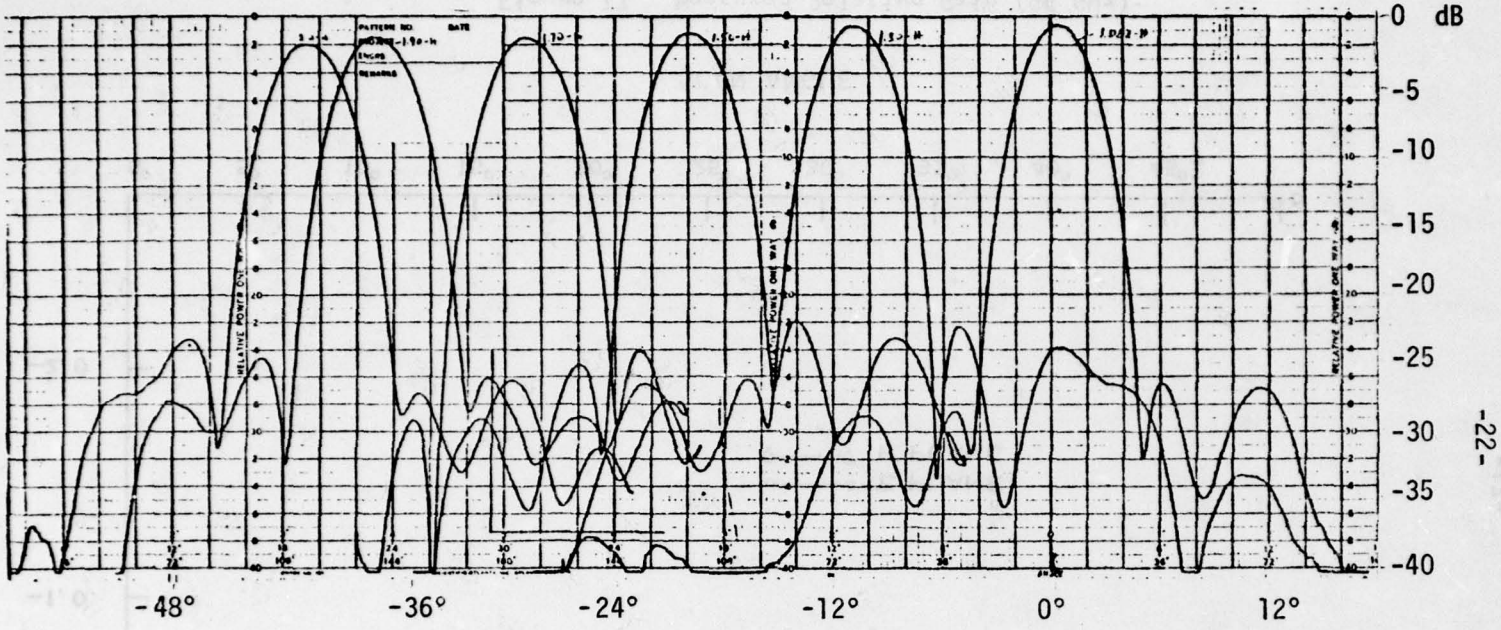

Figure 18. Polarization Twist Reflector

35.0 GHz
H-Plane Cuts
H-Plane Scans

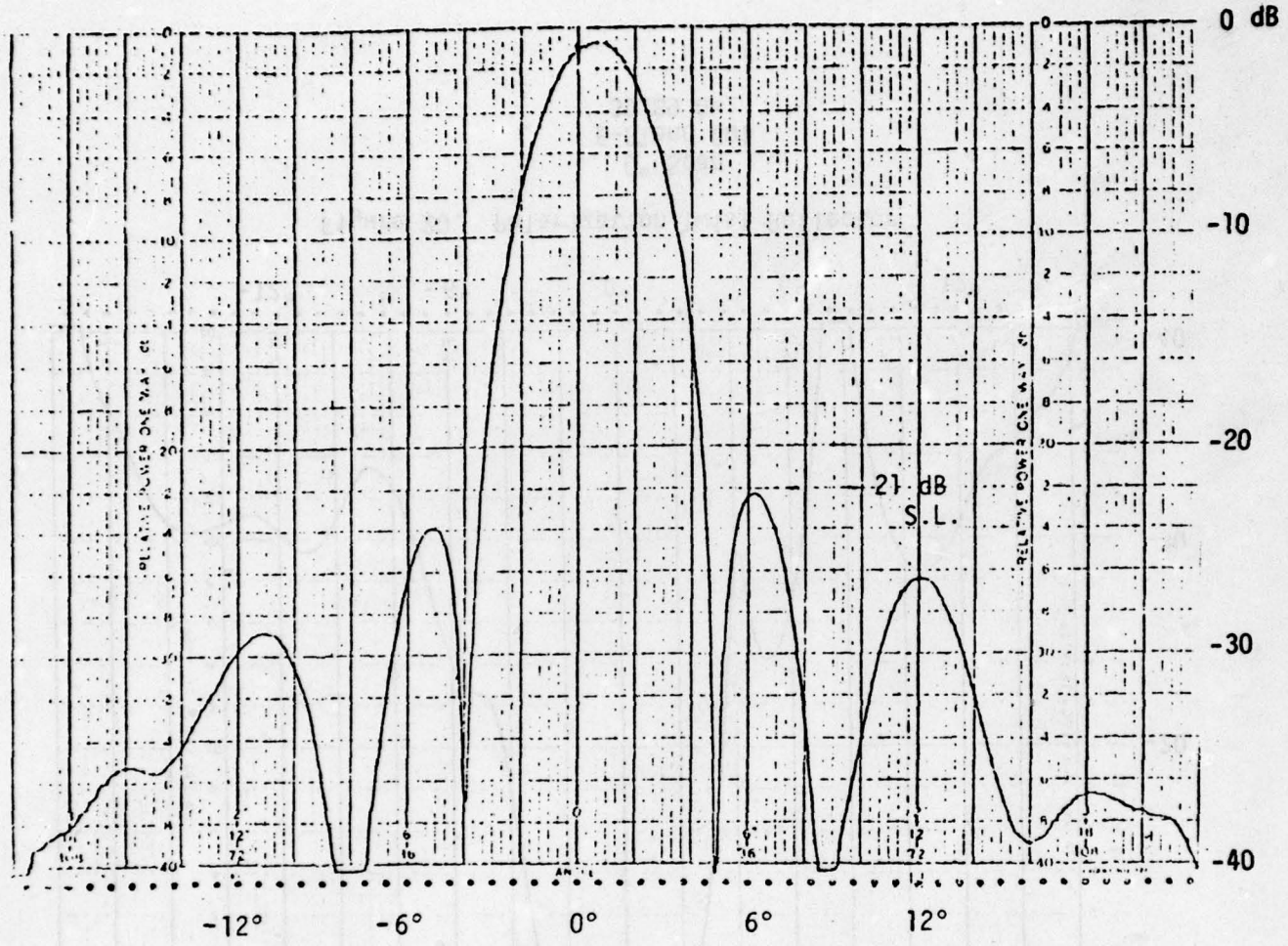

Figure 19. Polarization Twist Reflector

0° - Scan
E-Plane Cut
35.0 GHz

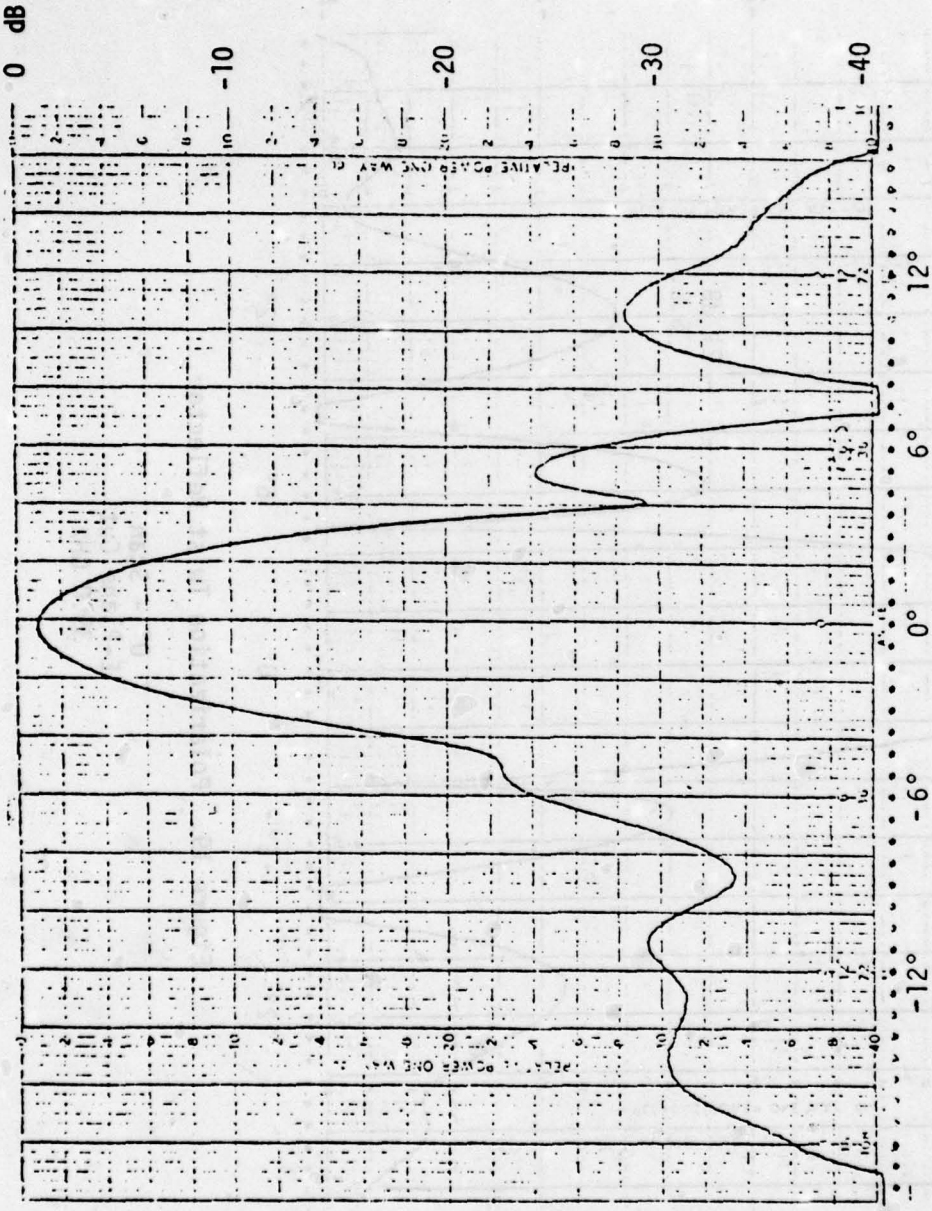

Figure 20. Polarization Twist Reflector
0° Scan
E-Plane Cut
39.89 GHz

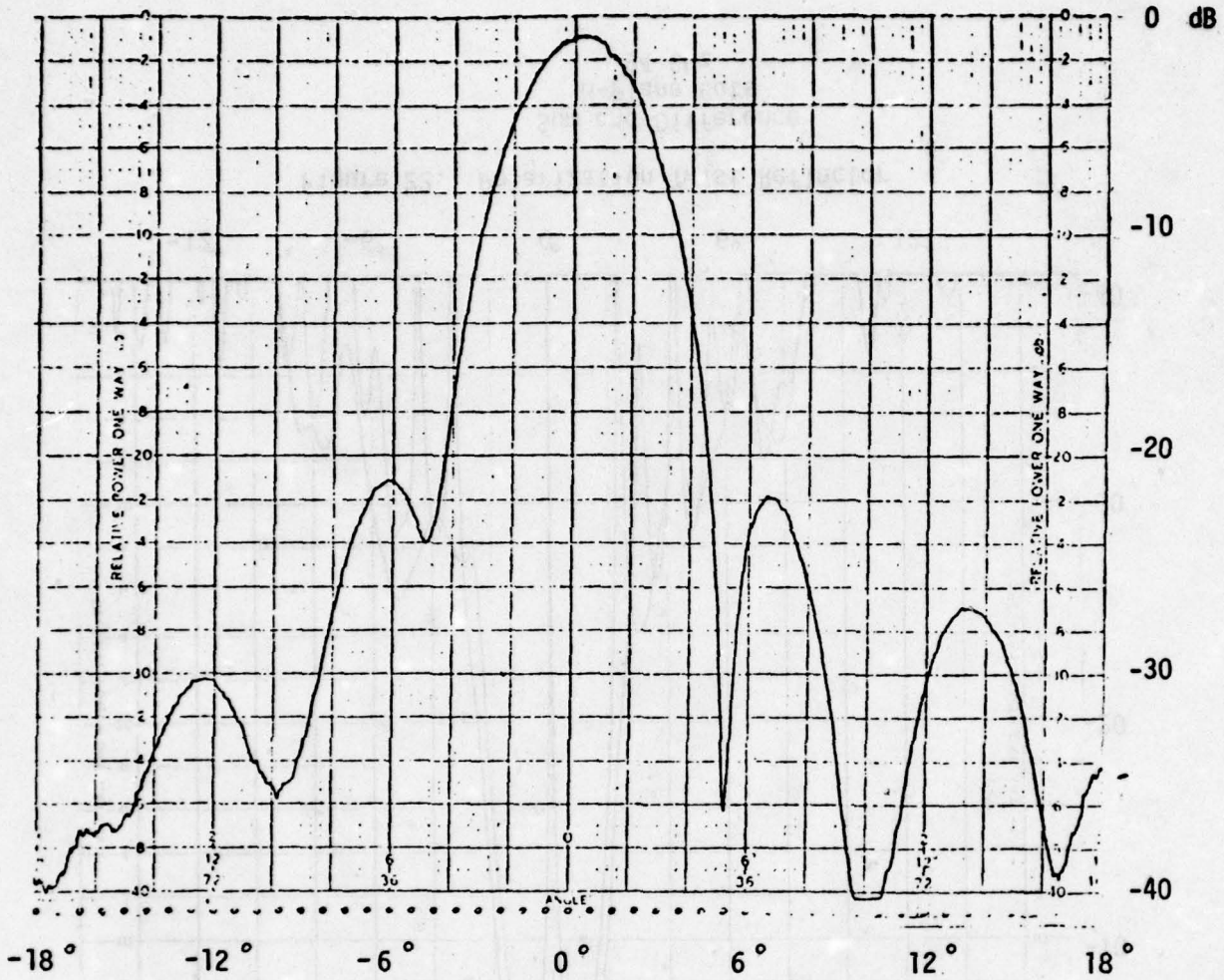

Figure 21. Polarization Twist Reflector

0° Scan
E-Plane Cut
30.21 GHz

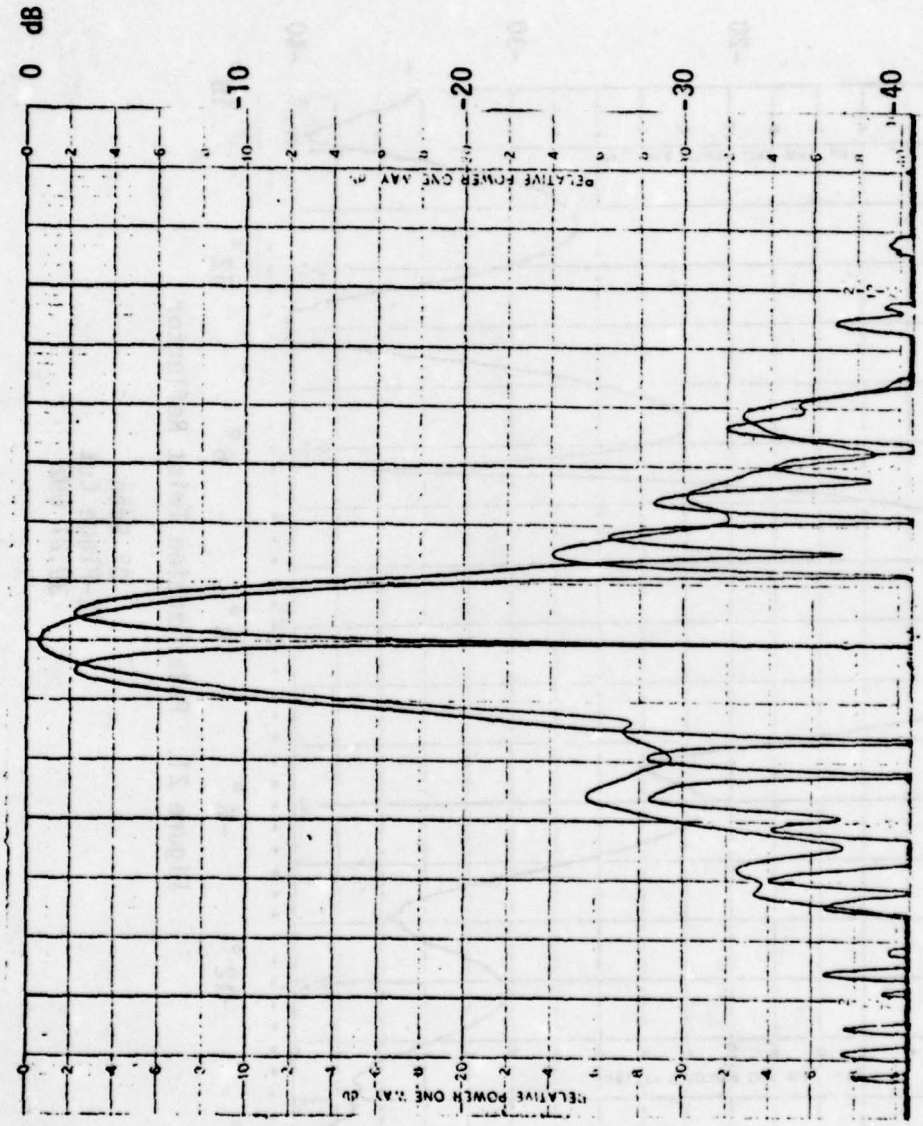

Figure 22. Polarization Twist Reflector
Sum and Difference
H-Plane Cuts
94 GHz

SIDELOBE LEVEL CONTROL
FOR UNEQUALLY SPACED ARRAYS

Charles F. Winter
Microwave/Antenna Department
RAYTHEON COMPANY
Wayland MA 01778

ABSTRACT

An iterative procedure is described for deriving the unequal element spacings required by a linear array of N equally excited, symmetrically disposed, isotropic radiating elements in order to generate a far-field antenna pattern having prescribed sidelobe levels. The procedure employs a Newton-Raphson technique applied to an error-squared function where element displacements away from the element positions of an equally spaced reference array are taken as the independent variables. The error function consists of the sum of the squares of the differences between calculated pattern sidelobe levels and desired sidelobe levels.

Examples are presented for prescribed control levels applied to selected antenna pattern sidelobes which can appear between the main beam peak and the first grating lobe position of the reference array when the pattern is calculated using an aperture-normalized (sine-space) variable. Since the number of sidelobes in this region is typically greater than the number of available element position displacements, the error function can be minimized to zero only if control of some sidelobes is sacrificed. For some applications it happens that the visible region (far-field theta-space) need include precisely the same number of sidelobes as the number of element displacements. In these cases a unique solution is obtained whenever the error function value goes exactly to zero.

When the application requires scanning the antenna pattern main beam peak away from the array broadside direction, calculation of the pattern with an aperture-normalized variable is easily interpreted in terms of the visible region limits and the total number of sidelobes which will occur in real (theta-) space under a maximum scan angle condition. Examples of several cases for given scan angles are presented in order to show the prescribed sidelobe level trade-offs which are associated with useful sets of array element spacings. A minimum element spacing of one-half wavelength severely limits the possible scan angle coverage.

Prepared for Presentation at the
1979 Antenna Applications Symposium
Allerton Park, Monticello, Illinois
September 26-28, 1979

SIDELOBE LEVEL CONTROL FOR UNEQUALLY SPACED ARRAYS

I. INTRODUCTION

Unequally spaced linear arrays are often considered when it is desired to have some degree of control over the antenna pattern sidelobe levels that result if equal excitations are required at all array elements. Methods of synthesizing unequally spaced arrays have typically concentrated upon (1) suppressing the close-in sidelobe levels [1] - [5] , (2) eliminating the periodic grating lobes associated with equally spaced arrays, and/or (3) minimizing the total number of array elements necessary for a specified pattern beamwidth [6] - [12] .

The purpose of this paper is to describe a modified iterative procedure [13] that has been found useful for establishing sets of linear array unequal element spacings which will theoretically control the suppression levels of selected sidelobes in the antenna pattern. In particular, those sidelobes that fall inside the far-field angle at which grating lobe (plateau) energy is about to enter the visible space region are considered. The application for the type of antenna associated with this procedure is a one-dimensional scanning radar system that uses a TR-module at each array element location. No effort will be made to utilize asymmetrical sets of element spacings [14] , to employ a non-linear array configuration [15] , nor to introduce the effects of mutual coupling between array elements [16] .

The iterative procedure described derives a set of unequal element spacings by minimizing an error function consisting of the sum of the squares of the differences between calculated sidelobe levels and desired sidelobe levels for selected sidelobes which can appear in visible space. This error function is minimized by the Newton-Raphson method [17] where the independent variables are position displacement terms applied to the innermost spacings of an N-element, equally spaced, reference linear array.

Section II describes the linear array parameter definitions to be employed. Section III contains a discussion of the pertinent characteristics associated with the equally spaced reference array. Section IV describes the iterative

procedure and some of its limitations. Section V gives examples of the procedure applied to Tchebychef-type sidelobe behavior for sidelobe positions close-in to the pattern main beam peak. Section VI gives examples of the procedure applied to an arbitrary fall-off rate for these close-in sidelobes. Section VII gives examples of the procedure applied to Tchebychef-type sidelobe behavior for the far-out sidelobe positions just inside the location of the first grating lobe region of the reference array pattern. Section VIII gives examples of the procedure applied to a situation where the error function being minimized need not converge to zero and non-unique sets of element spacings thus occur. Section IX discusses the problem of the minimum element spacing in the set typically being less than one-half wavelength. Section X then summarizes the results established by the examples presented.

II. PARAMETER DEFINITIONS AND EQUATIONS

Consider a linear array of N, equally excited, isotropic, radiating elements symmetrically disposed about the center point of the array axis. Figure 1 shows the geometry and indexing conventions utilized with respect to an odd number of array elements. No change in these conventions is required should N be an even number since, in this case, there would simply be no element at the aperture center point.

The cross-symbols along the axis indicate the locations of equally spaced elements of a reference array whose aperture coordinates are given by

$$(1) \qquad s_n = \frac{2n - N - 1}{2N} \qquad \text{for } 1 \leq n \leq N.$$

The circle-symbols indicate the nonuniform locations to which the set of N equally spaced elements can be shifted by displacement terms, c_i, subject to the restrictions (1) that the array end elements remain fixed in position and (2) that, if N is odd, the central element will also remain fixed. Fixing the end element locations normalizes the array aperture length at (essentially) unity and is, therefore, helpful in establishing limits for the visible region of pattern space.

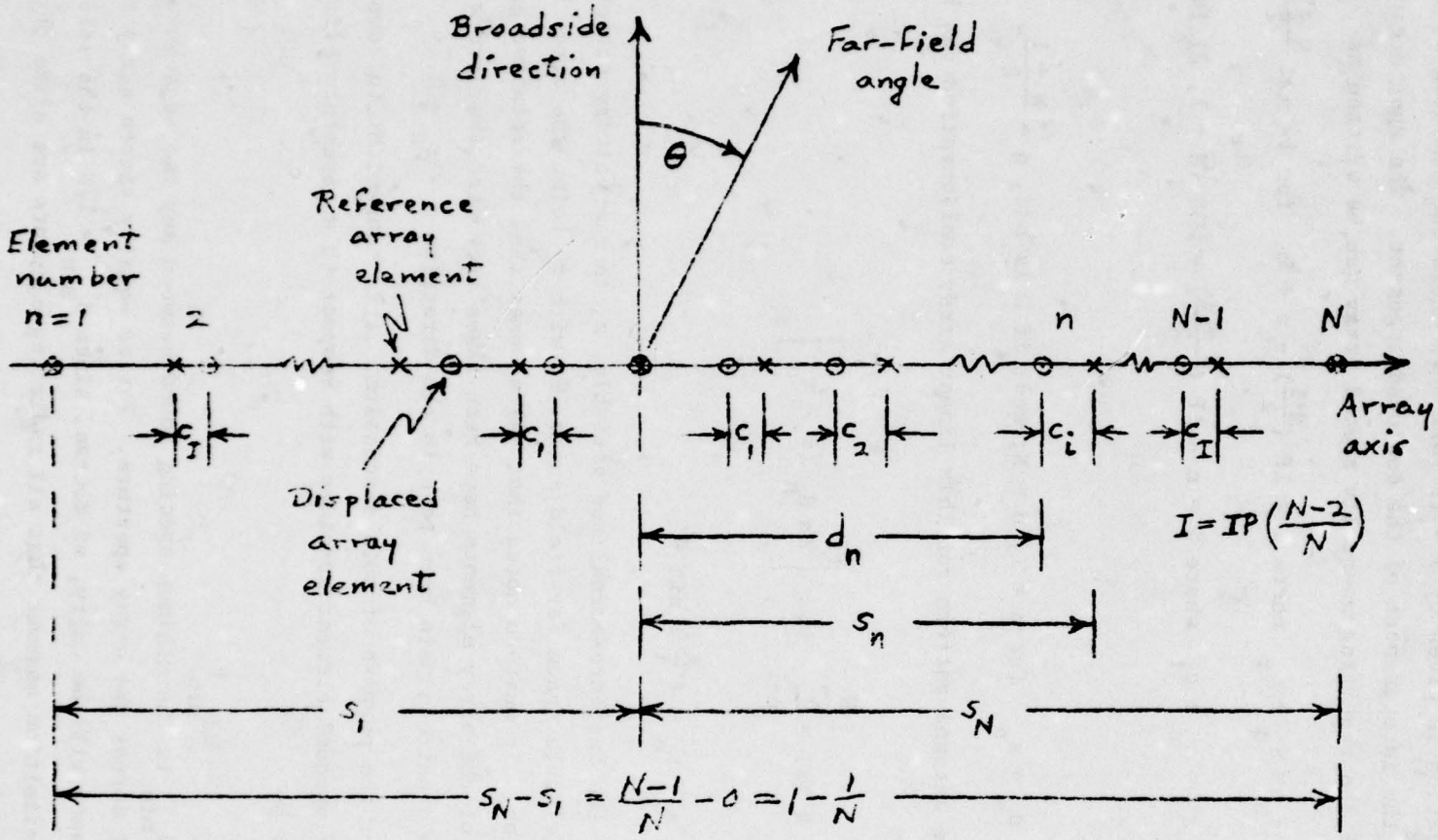

Figure 1. Linear Array Geometry and Indexing Conventions.

The number of possible displacement terms for this linear array configuration is given by I = IP (N/2 - 1) where the notation IP(*) indicates the integer part of the enclosed argument. The aperture coordinates of the resulting unequally spaced array can be written as

(3a) $$d_n = s_n + c_i \quad \text{where } i = IP\left(\frac{N+1}{2}\right) - n + 1 \quad \text{for } 1 < n < \frac{N+1}{2},$$

(3b) $$d_n = s_n + c_i \quad \text{where } i = n - IP\left(\frac{N+1}{2}\right) - MOD\,(N+1, 2) \quad \text{for } \frac{N+1}{2} < n < N,$$

and

(3c) $$d_n = s_n \quad \text{for } n = 1,\ n = N, \text{ and, if } N \text{ is odd, } n = \frac{N+1}{2}.$$

The antenna pattern for this linear array configuration can be approximated by

(4) $$R(z) = \sum_{n=1}^{N} \cos\left[2\pi d_n (z - z_o)\right]$$

where

(5) $$z - z_o = \left(\frac{A}{\lambda}\right) \sin\theta$$

relates the aperture-normalized variable, z, in the voltage pattern expression to the visible space far-field angle, θ, with z_o being the array broadside direction. It must be noted that (4) assumes that the relative excitation phases of the array elements have been taken such that they are all in-phase to form a pattern main beam peak in the direction $z - z_o = 0$.

For the purpose of this discussion, it is convenient to compare various sets of unequal element spacings with respect to an aperture efficiency value defined by

(6) $$\eta = N d_{min}$$

where d_{min} is the minimum spacing found between any two adjacent elements of the set across the array aperture. For an equally spaced array the aperture efficiency will be unity, of course, since $d_{min} = 1/N$ in the reference array. This definition assumes that all radiating elements are alike physically and have identical radiation patterns.

III. REFERENCE ARRAY PATTERN CHARACTERISTICS

The antenna pattern shape calculated by (4) is invariant in the z-space notation employed. That is, allowing z_o to vary is equivalent to scanning the pattern in visible space in agreement with (5). Figure 2 shows the pattern of a 12-element, uniformly excited, equally spaced, linear array plotted in dB down form. This pattern is seen to be periodic in z-space with a period of (N =) 12; - exactly equal to the number of array elements.

It is evident from (5) that the visible region of space can be limited by the z-values

$$(7a) \qquad z_L = z_o + \left(\frac{A}{\lambda}\right) \sin(-90^o) = z_o - \frac{A}{\lambda}$$

at the pattern left side and

$$(7b) \qquad z_R = z_o + \left(\frac{A}{\lambda}\right) \sin(90^o) = z_o + \frac{A}{\lambda}$$

at the right side.

Eliminating the array aperture broadside direction, z_o, from (7a) and (7b) gives

$$(8) \qquad \frac{A}{\lambda} = \frac{z_R - z_L}{2}$$

expressing the aperture length in terms of the visible region limits.

The scan angle of the array pattern main beam peak can be written in terms of the aperture length and the visible region limits using (5), (7a), (7b), and (8) as

$$(9) \qquad \theta_s = -\sin^{-1}\left[1 + \frac{z_L}{\left(\frac{A}{\lambda}\right)}\right] = \sin^{-1}\left[1 - \frac{z_R}{\left(\frac{A}{\lambda}\right)}\right] = \sin^{-1}\left[\frac{z_L + z_R}{z_L - z_R}\right].$$

In order to prevent any portion of the grating lobe (peaked at $z - z_o = -12$ in Figure 2) from entering visible space as the main beam peak (at $z - z_o = 0$) is scanned (in the positive sense of θ) away from the broadside direction, one might select a left hand limit of $z_L = -11$. For an aperture length of $A/\lambda = 6$ (based on an equal spacing of 0.5λ), a maximum scan angle (away from broadside at $z_o = -5$) of $\theta_{max} = \sin^{-1}(1 - 11/6) = 56.44^o$ is found possible. Since the right hand visible region limit occurs at $z_R = +1$, the main beam null on the outer side of the pattern has just reached the end of visible space. That is, the first sidelobe on this side of the pattern has moved into the invisible region.

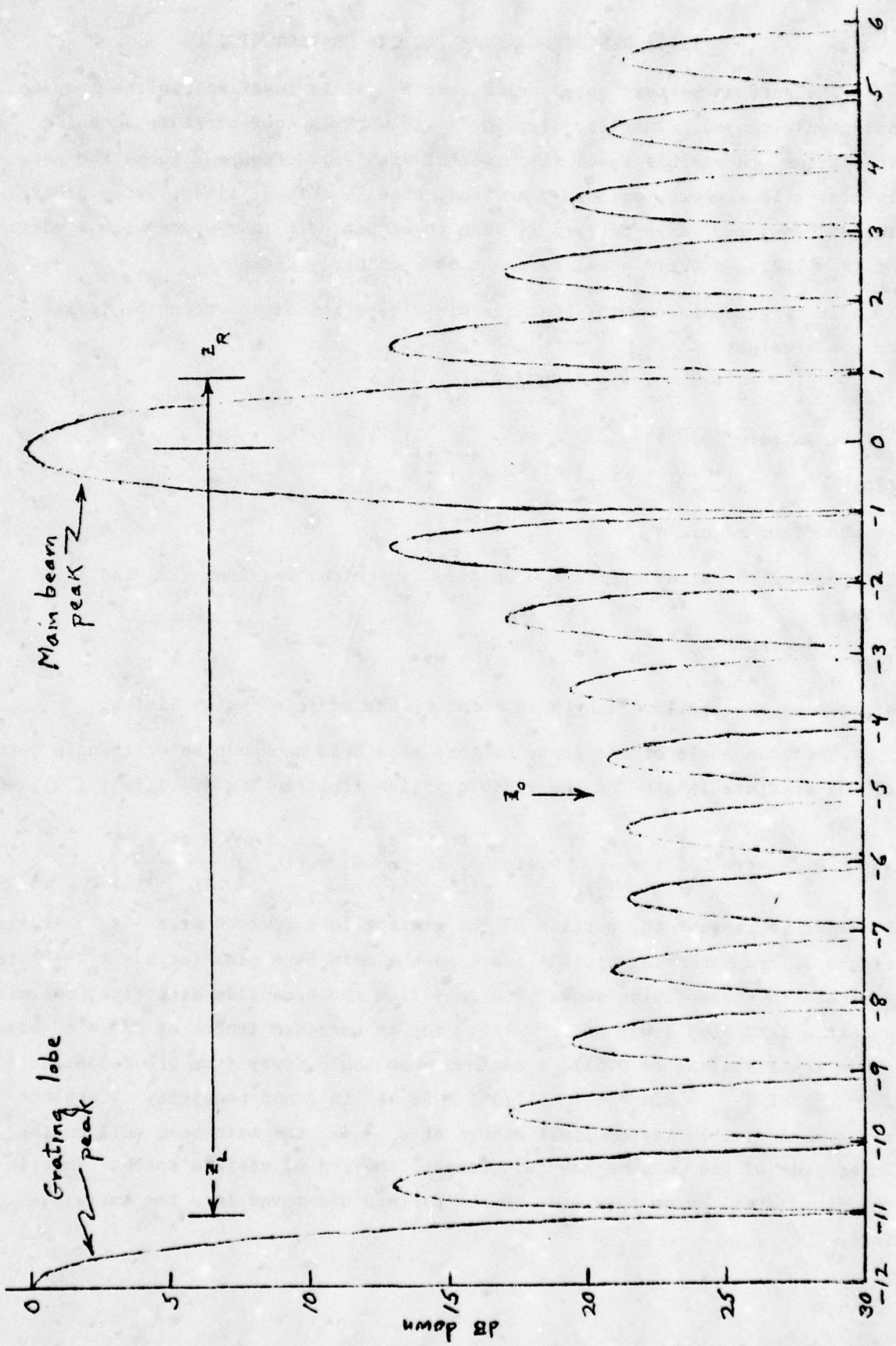

Figure 2. Pattern for Equally Spaced Reference Array of (N=) 12-Elements.

Figure 3 shows how the (maximum) scan angle as defined by (9) will increase with the number of elements for a uniformly excited, equally spaced (at 0.5 λ), linear array subject to the conditions that (1) the inner null of the left side grating lobe is at $z_L = -(N - 1)$ and (2) the outer main beam null is at $z_R = +1$. Note that a 60° maximum scan angle requirement takes at least (N =) 15 array elements.

Figure 4 shows how the aperture length varies with the number of elements at selected maximum scan angles for a uniformly excited, equally spaced, linear array subject to the condition that the innerside null of the left hand grating lobe is at $z_L = -(N - 1)$. A 12-element array scanned 60° uses a length of 5.895λ or an equal element spacing of 0.4912 λ. A portion of the right hand skirt of the main beam peak (>12 dB down) in Figure 2 would, of course, have moved into the invisible region for this situation.

When it is necessary to suppress the antenna pattern sidelobes which can appear in the visible region of space to levels more than those of the reference array pattern, it is of interest to examine whether or not the use of unequal element spacings might be helpful.

IV. ITERATIVE PROCEDURE EXPRESSIONS

The iterative procedure used herein accomplishes the adjustments of the d_n - spacings as follows.

a) Select an initial set of c_i - displacements for $1 \leq i \leq I$ which will all be zero if a starting equally spaced array is chosen.

b) Calculate the linear array element coordinates (3a), (3b), and (3c) for N elements.

c) Calculate the aperture-normalized antenna pattern (4) at a grid of z-points suitable for determining each sidelobe peak level, $P(z_k)$, in dB down throughout the range $z_{min} \leq z - z_o \leq z_{max}$.

d) Select a set of K desired sidelobe levels, L_k, in dB down and calculate an error function of form

$$E(c_i) = \sum_{k=1}^{K} \left\{ w_k \left[P(z_k) - L_k \right] \right\}^2 \tag{10}$$

where weightings, w_k, other than unity may be assigned when appropriate.

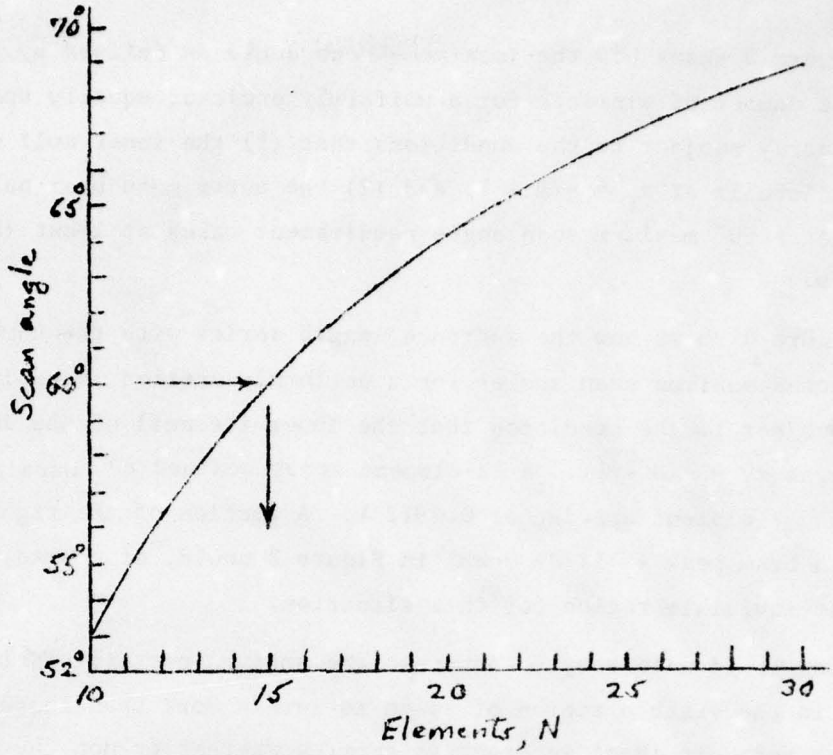

Figure 3. Maximum Scan Angle vs. Number of Elements.

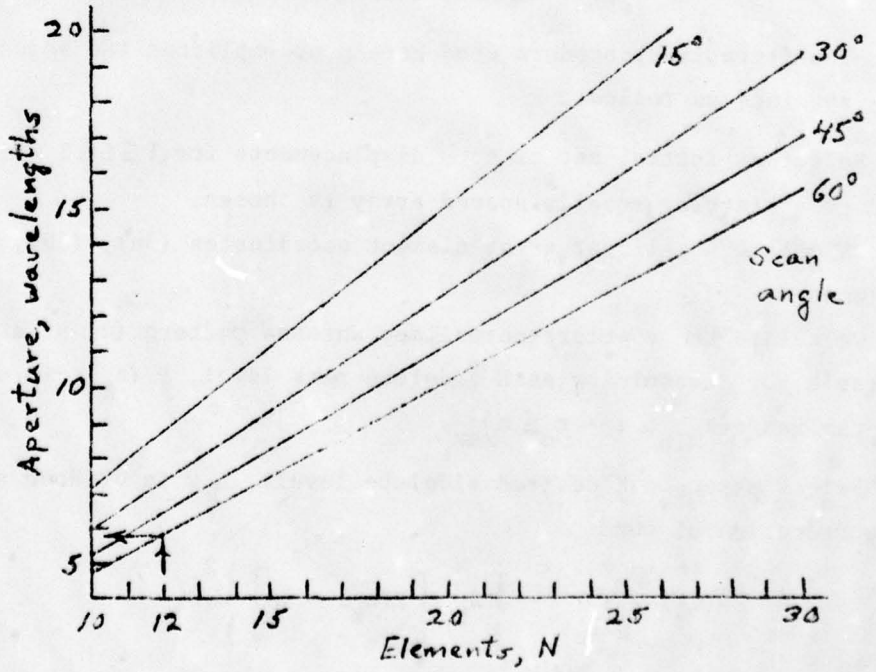

Figure 4. Aperture Length vs. Number of Elements.

e) Attempt to minimize this error function by the Newton-Raphson method [17] applied to the I simultaneous equations

$$\frac{\partial E(c_i)}{\partial c_j} = 0 \qquad j = 1, 2, \ldots, I. \tag{11}$$

f) Use the new set of displacements, c_i', from step e)

$$c_i' = c_i + \Delta c_i \qquad \text{for } 1 \leq i \leq I \tag{12}$$

and repeat steps b) through e) until one or more of the following criteria is satisfied:

1. The c_i terms are all less than some small tolerance.
2. The individual sidelobe errors are all less than some acceptable tolerance.
3. The error function reaches some minimum value.

In addition to providing protection for possible nonconvergence of the Newton-Raphson process, the iterative procedure as used herein guards against confusion in the counting indices (1) of the unequally spaced element locations and (2) of the antenna pattern sidelobe positions. In the first situation, the aperture efficiency value (6) turns negative if the element locations become transposed. When this occurs, the practical solution for the prescribed sidelobe level behavior leads to consideration of amplitude weighting at the array elements [18] using a reduced number of elements. The second situation arises when voltage zero crossings of the antenna pattern (4) disappear [13] and null-filled characteristics are found in the sidelobe structure. When this occurs, the procedure assigns a weight, w_k, of zero to be used in the error summation (10) for this k-value. Examples of these two situations are given below in Sections V and VIII, respectively.

V. CLOSE-IN TCHEBYCHEF-TYPE EXAMPLES

It is informative (for non-scanning applications, in particular) to observe how unequal element spacings might be used to obtain Tchebychef-type behavior by the close-in sidelobes of the antenna pattern. Since a 12-element array has (I =) 5 independent displacement term variables, examples were calculated for prescribed sidelobe levels of 14 dB to 21 dB by 1 dB increments for the first (K =) 5 close-in sidelobes of the pattern.

TABLE I lists the calculated levels of the ten sidelobes (or null-filled voltage minimums) in these patterns as matched up with the sidelobes of the reference array. The first five sidelobes, of course, are exactly at the prescribed levels because the iterative procedure error function value converged to zero for these cases. Substantial variations are seen to exist among the levels of the outermost sidelobes. However, the examples for levels of 15 dB to 17 dB show good suppression over the first eight successive sidelobes.

TABLE I
CALCULATED SIDELOBE LEVELS
CLOSE-IN TCHEBYCHEF-BEHAVIOR

	SIDELOBE POSITION									
PSLL	1	2	3	4	5	6	7	8	9	10
Ref.	13.06	17.22	19.56	20.89	21.51	21.51	20.89	19.56	17.22	13.06
14	14.0	14.0	14.0	14.0	14.0	12.8	12.7	( )	11.4	( )
15	15.0	15.0	15.0	15.0	15.0	16.7	(19.3)	19.2	(19.3)	7.8
16	16.0	16.0	16.0	16.0	16.0	27.6	47.3	35.6	12.8	5.7
17	17.0	17.0	17.0	17.0	17.0	(25.7)	20.2	19.7	9.2	4.8
18	18.0	18.0	18.0	18.0	18.0	(21.6)	13.0	16.0	7.4	4.9
19	19.0	19.0	19.0	19.0	19.0	(24.0)	9.8	14.5	6.5	5.9
20	20.0	20.0	20.0	20.0	20.0	39.1	9.3	12.4	6.5	6.9
21	21.0	21.0	21.0	21.0	21.0	14.6	15.2	8.2	7.8	8.4
	( ) indicates dB level of a filled-in pattern null.									

Figure 5 compares the d_n-element spacings for each of the prescribed sidelobes level cases with the reference array. The minimum element spacing location and the aperture efficiency (6) for each case are indicated. In general, the minimum spacing occurs between the first and second elements counted away from the array center. It appears that the best aperture efficiency value will occur for a prescribed sidelobe level very close to the 16 dB case.

Figure 6 shows the calculated antenna patterns for the prescribed sidelobe levels of 14 dB and 16 dB. Figure 7 shows the 18 dB and 20 dB cases. For the 16 dB pattern, if $z_L = -8.8$ and $z_R = 1.0$ are selected, all sidelobes in the

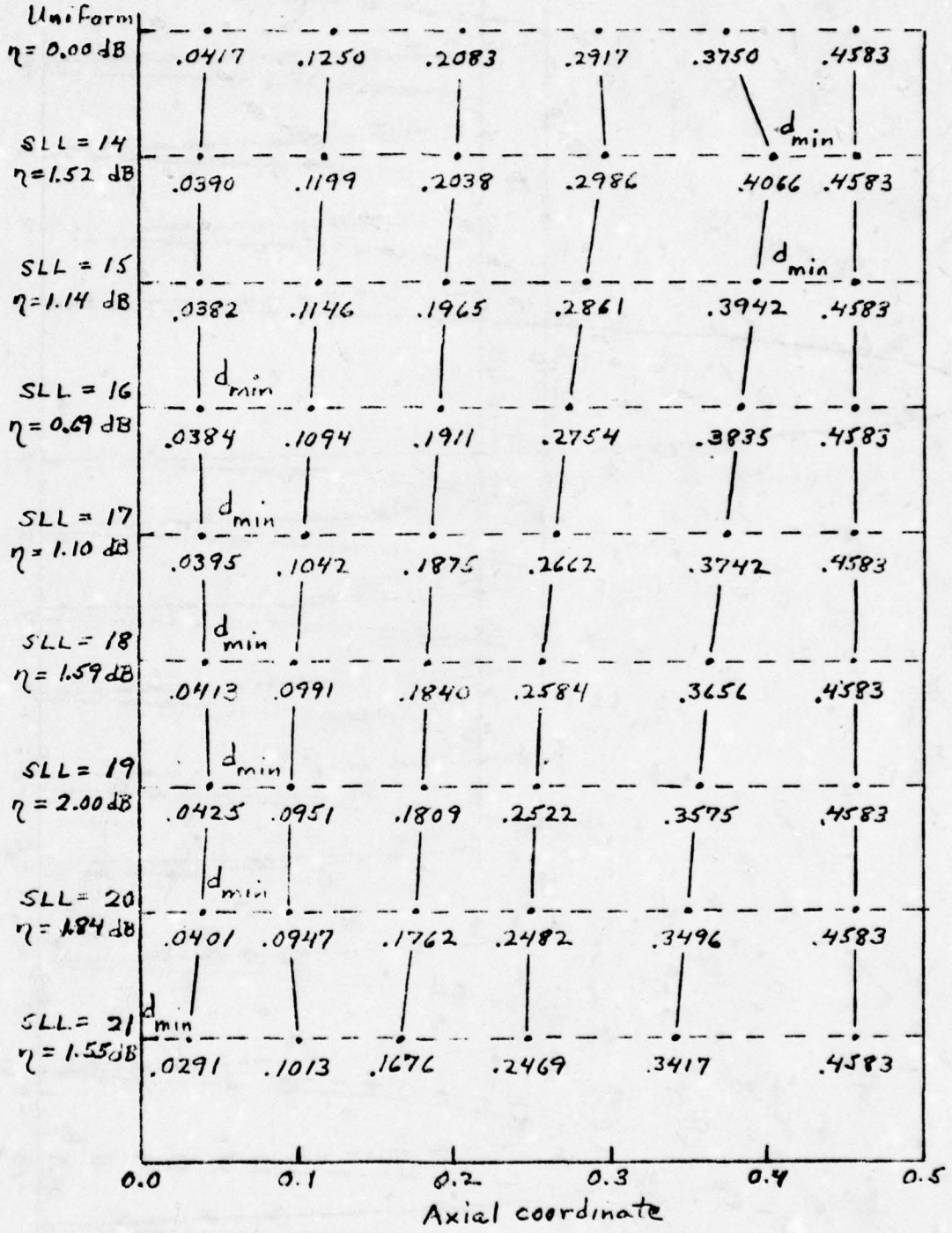

Figure 5. Element Spacings for Tchebychef-Type Close-In Examples.

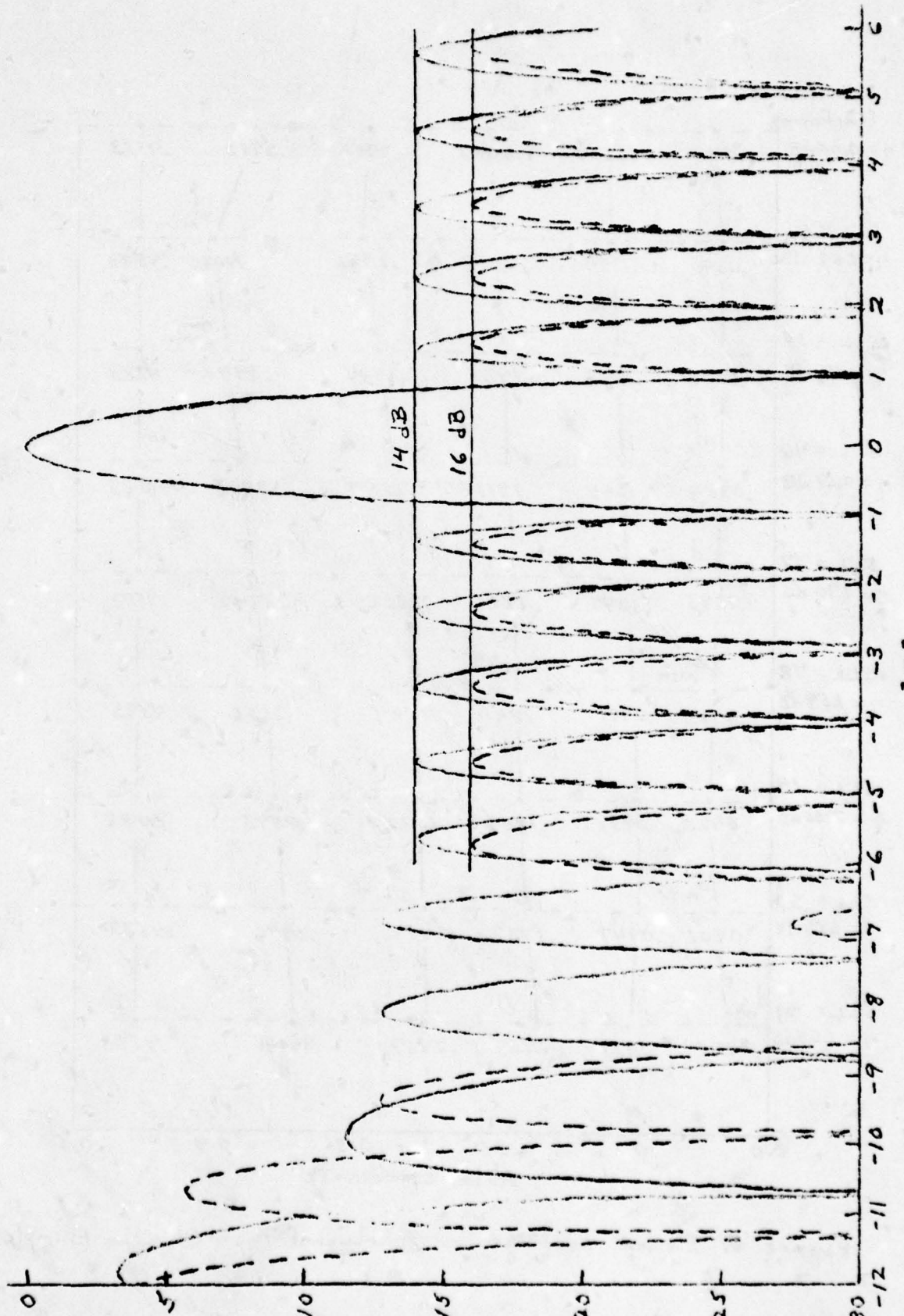

Figure 6. Patterns for 14 dB and 16 dB ($\kappa=5$) Close-In Sidelobe Levels.

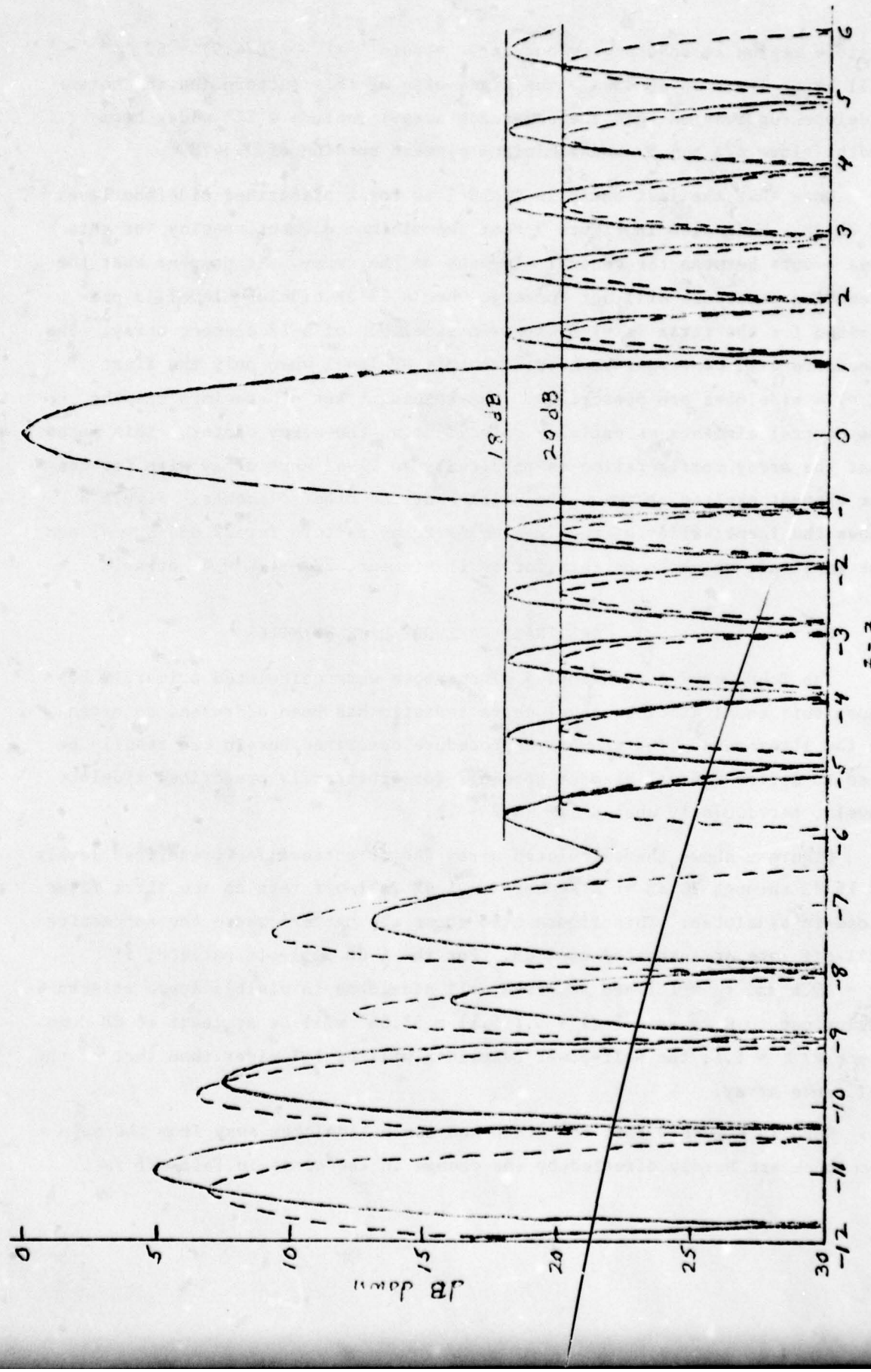

Figure 7. Patterns for 18 dB and 20 dB (K=5) Close-In Sidelobe Levels.

visible region at scan angles out to $\theta_s = -\sin^{-1}(1 - 8.8/4.9) = 52.74^\circ$ will be at least 16 dB down. The trade-offs of this pattern (having better sidelobe suppression than the reference array) include a 22% wider beamwidth (since $A/\lambda = 4.9$) and a minimum element spacing of 0.3478λ.

Note that the last entry in TABLE I is for a prescribed sidelobe level of 21 dB. Note also in Figure 5 that the minimum element spacing for this case occurs between the central elements of the array. It happens that the iterative procedure will not converge when a 22 dB sidelobe level is prescribed for the first (K =) 5 close-in sidelobes of a 12 element array. The procedure will converge, however, for this dB level when only the first (K =) 4 sidelobes are prescribed. The resultant set of spacings has the two central elements essentially coincident at the array center. This means that the array configuration is physically an 11-element array with its center element excited at twice the voltage of the other elements. Figure 8 shows the identicality of the 12-element array pattern for 22 dB (K = 4) and the amplitude weighted pattern for an 11-element, 22 dB (K = 4) array.

VI. ARBITRARY FALL-OFF RATE EXAMPLES

The Tchebychef-type examples given above were calculated primarily because this equal sidelobe level characteristic has been addressed so often in the literature. The iterative procedure described herein can readily be used to derive unequal element spacings for arbitrarily prescribed sidelobe levels, particularly when $K \leq IP\ (N/2 - 1)$.

Figure 9 shows the calculated array factor pattern for prescribed levels of 16 dB through 20 dB at a successive 1 dB fall-off rate on the first five close-in sidelobes. This figure also shows the pattern where the successive fall-off rate is increased to 2 dB. For the 1 dB fall-off pattern, if $z_L = -9.1$ and $z_R = 1.1$ are selected, all sidelobes in visible space at scan angles out to $\theta_s = -\sin^{-1}(1 - 9.1/5.1) = 51.66^\circ$ will be at least 16 dB down. Since $A/\lambda = 5.1$, the half-power beamwidth will be 18% wider than that of the reference array.

Note in Figure 9 that the ninth and tenth sidelobes away from the main beam peak are hardly effected by the change in the close-in fall-off rate.

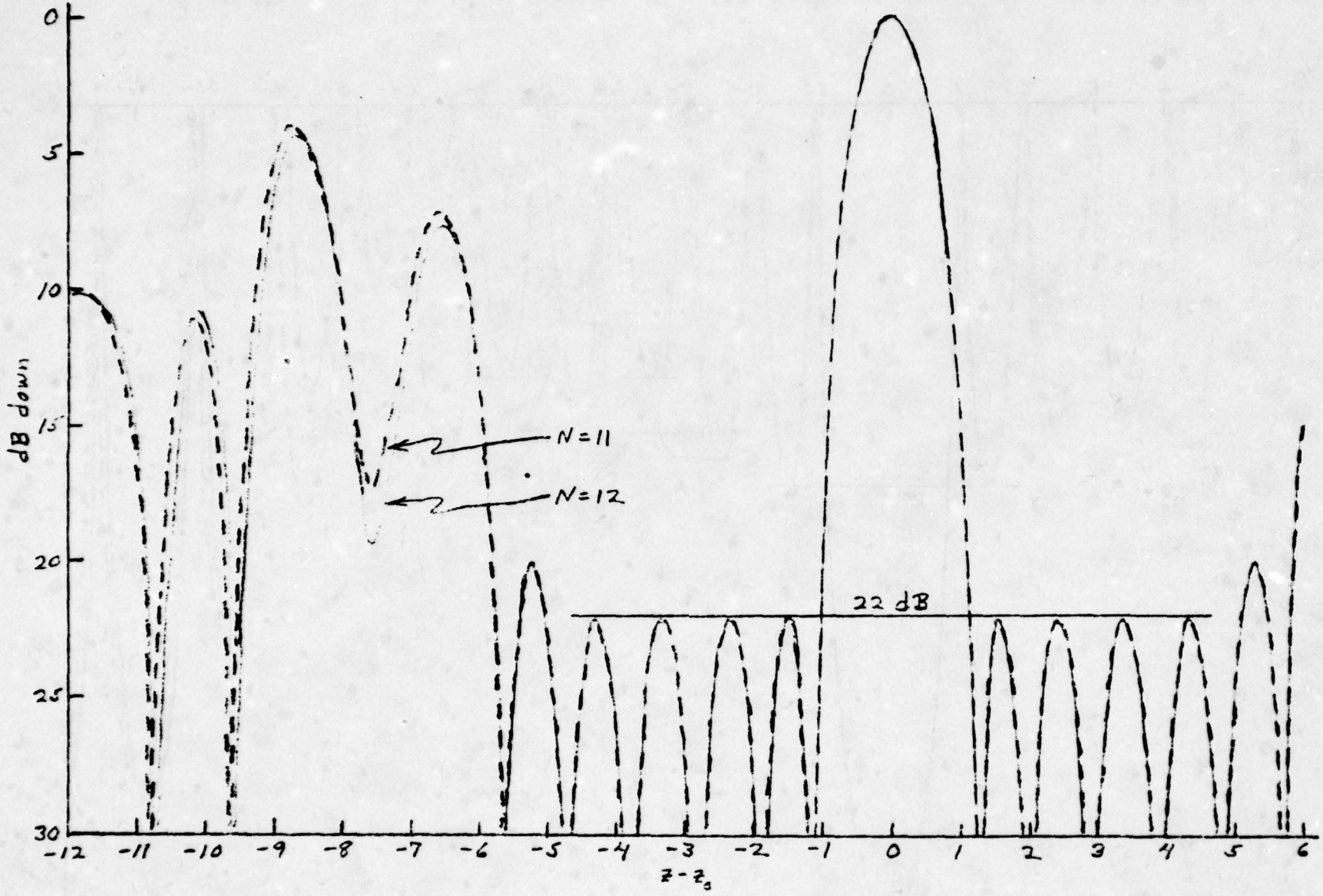

Figure 8. Patterns for 22 dB (K=4) Close-In Sidelobe Levels with N = 11 and 12.

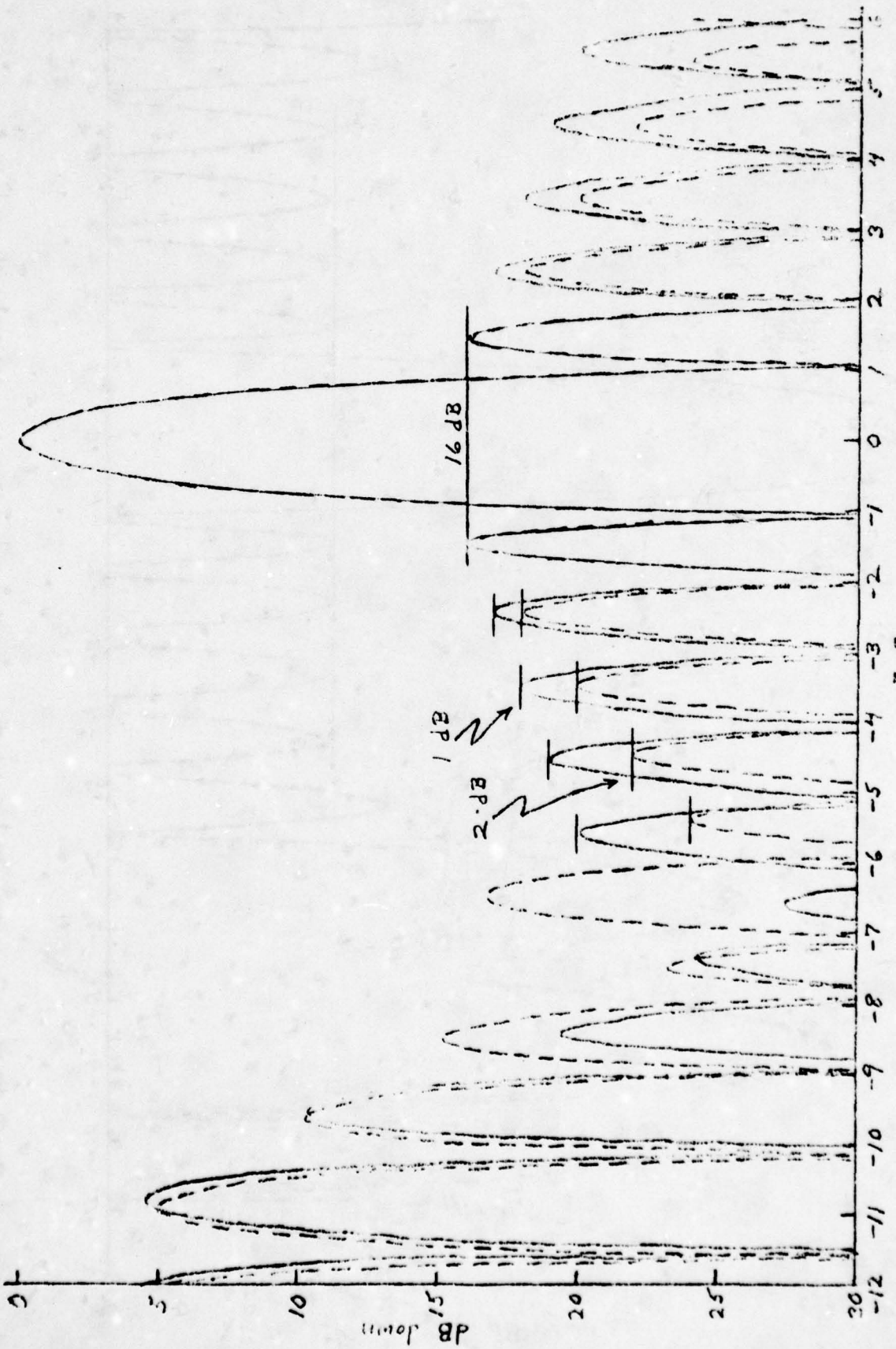

Figure 9. Patterns for 1 dB and 2 dB Fall-Off Rates of (K=5) Close-In Sidelobes.

This situation suggests that it may be difficult to suppress these far-out sidelobes to levels of 15 dB down or better when the first several close-in sidelobes are also required to be at this level or more in dB down.

VII. FAR-OUT TCHEBYCHEF-TYPE EXAMPLES

When scanning applications are involved, it is sometimes the far-out sidelobes that are of most importance. That is, the first sidelobe away from the main beam peak might be acceptable near a 13 dB level while the more remote sidelobes are to be substantially suppressed. Examples were calculated for prescribed sidelobe levels of 18 dB to 30 dB by 2 dB increments for the (K =) 5 far-out sidelobes just inside the first grating lobe position of the reference array pattern.

TABLE II lists the calculated levels of the ten sidelobes for these patterns as they match up with the sidelobes of the reference array pattern. The last five sidelobes are exactly at the prescribed levels because the iterative procedure error function converged to zero. Substantial variation of the close-in sidelobes is seen to exist only for the fifth one which rises to 9.5 dB down when the far-out sidelobes are suppressed to 30 dB down.

TABLE II
CALCULATED SIDELOBE LEVELS
FAR-OUT TCHEBYCHEF BEHAVIOR

	SIDELOBE POSITION									
PSLL	1	2	3	4	5	6	7	8	9	10
Ref.	13.06	17.22	19.56	20.89	21.51	21.51	20.89	19.56	17.22	13.06
16	12.9	17.6	21.6	25.3	25.9	16.0	16.0	16.0	16.0	16.0
18	12.6	16.8	19.9	22.7	26.3	18.0	18.0	18.0	18.0	18.0
20	12.5	16.4	18.9	21.0	23.6	20.0	20.0	20.0	20.0	20.0
22	12.4	16.2	18.4	19.9	20.4	22.0	22.0	22.0	22.0	22.0
24	12.3	16.1	18.1	19.2	17.2	24.0	24.0	24.0	24.0	24.0
26	12.2	16.0	17.9	18.9	14.5	26.0	26.0	26.0	26.0	26.0
28	12.2	15.9	17.7	19.0	12.0	28.0	28.0	28.0	28.0	28.0
30	12.0	15.7	17.5	19.7	9.5	30.0	30.0	30.0	30.0	30.0

Figure 10 compares the d_n-element spacings for these prescribed far-out sidelobe level cases. The minimum element spacing for these cases is always near the edge of the array. It appears that the best aperture efficiency value would occur for a prescribed sidelobe level within a few tenths of a dB of the 20 dB case.

Figure 11 shows the calculated antenna patterns for the prescribed sidelobe levels of 18 dB and 22 dB. Figure 12 shows the 26 dB and 30 dB cases. For the 22 dB pattern, if $z_L = -10.7$ and $z_R = 1.0$ are selected, the five close-in sidelobes are all approximately 1 db higher than those of the reference array while the five far-out sidelobes are suppressed to 22 dB. A maximum scan angle of $\theta_s = -\sin^{-1}(1 - 10.7/5.85) = 56.0^o$ is possible. The half-power beamwidth is 2.6% wider than that of the reference pattern. The minimum element spacing is $0.4486\,\lambda$.

VIII. NON-ZERO ERROR FUNCTION EXAMPLES

The examples given above were cases where the number of prescribed sidelobe levels, K, was equal to the number of possible displacement terms, I. The error function (10) coverged (if it did) to zero and a unique set of unequal element spacings resulted. Consider now the situation where the number of prescribed levels is taken to be greater than the number of displacements, i.e., $K > I$. The 16 dB close-in pattern of Figure 6 and the 1 dB fall-off rate pattern of Figure 9 both showed that a peak sidelobe level of 16 dB down could be maintained out to $z - z_o \simeq \pm 9.0$. That is, eight successive sidelobe positions might be involved with prescribed levels of approximately 16 dB.

Figure 13 shows two calculated patterns for a prescribed 17 dB sidelobe level on the $K = 8$ close-in sidelobes of a 12-element ($I = 5$) array. For one case the initial displacement values, c_i, of the iterative procedure were those of the 17 dB ($K = 5$) close-in Tchebychef example. For the other case the initial displacements were from the 18 dB ($K = 5$) far-out Tchebychef example. Observe the latter case has a filled-in pattern null at $z - z_o = 6.5$, hence, only seven sidelobe peaks contribute to the error function (10). All seven of these sidelobes are approximately 17 dB down with one, the fourth

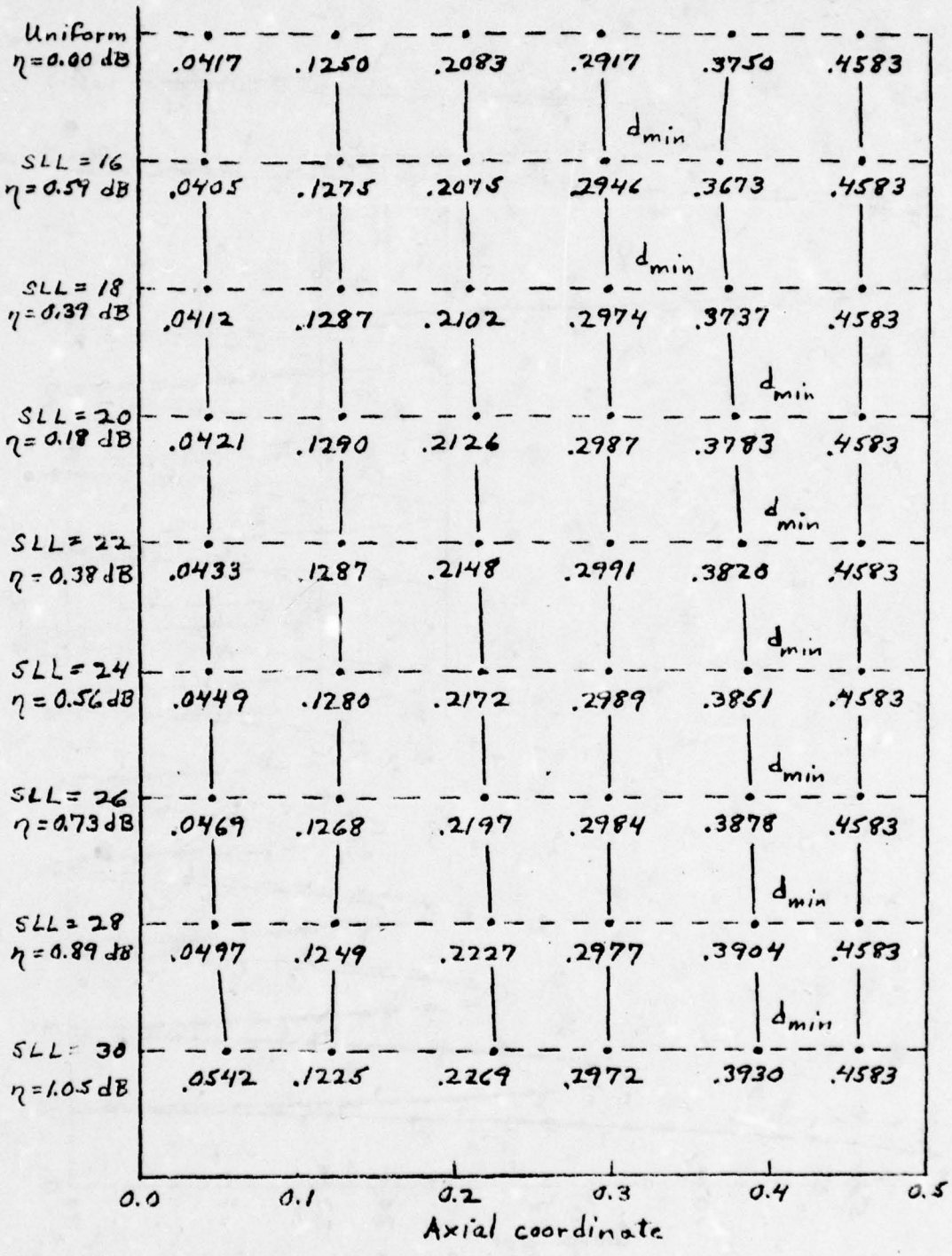

Figure 10. Element Spacings for Tchebychef-Type Far-Out Examples.

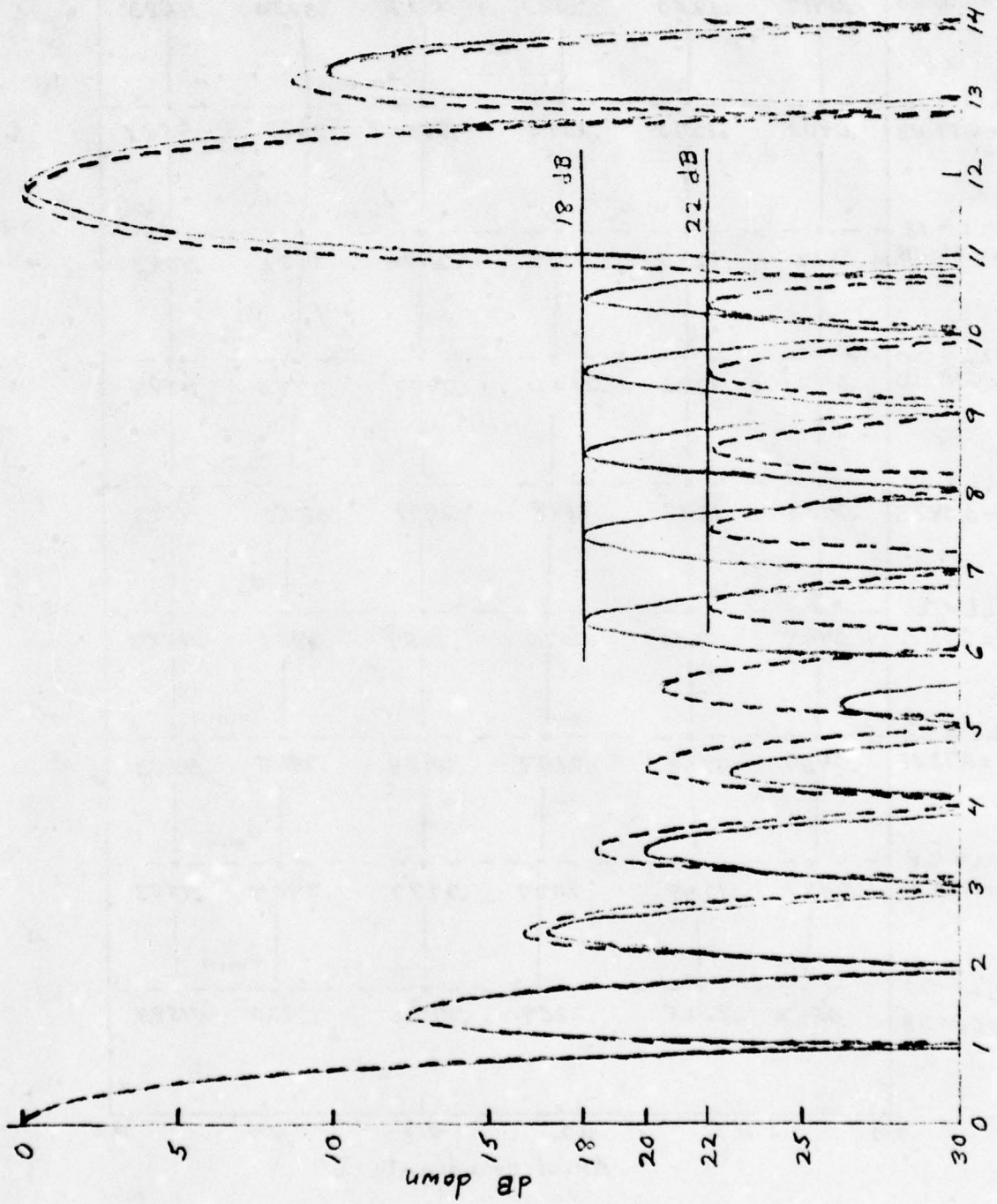

Figure 11. Patterns for 18 dB and 22 dB (K=5) Far-Out Sidelobe Levels.

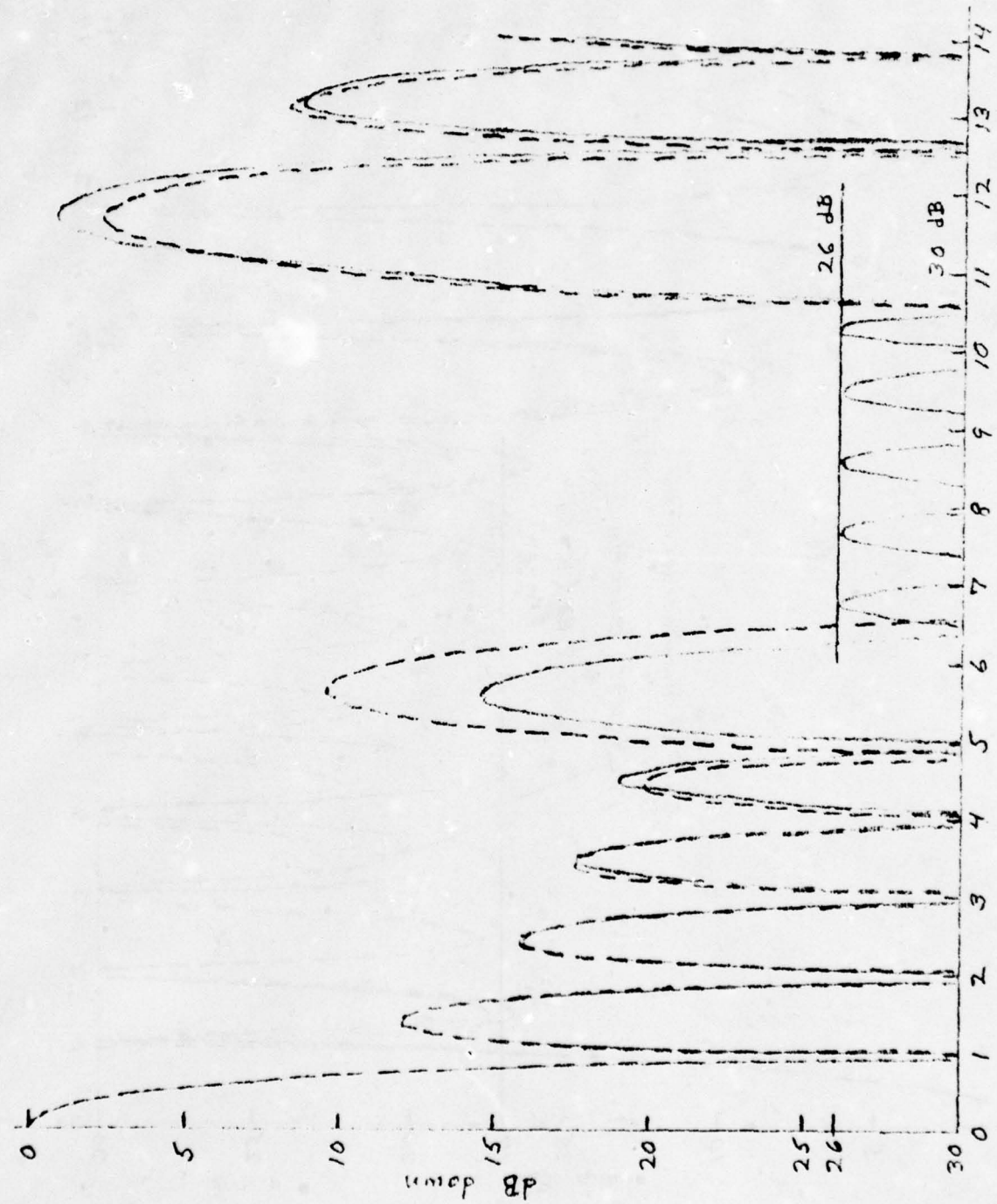

Figure 12. Patterns for 26 dB and 30 dB (K=5) Far-Out Sidelobe Levels.

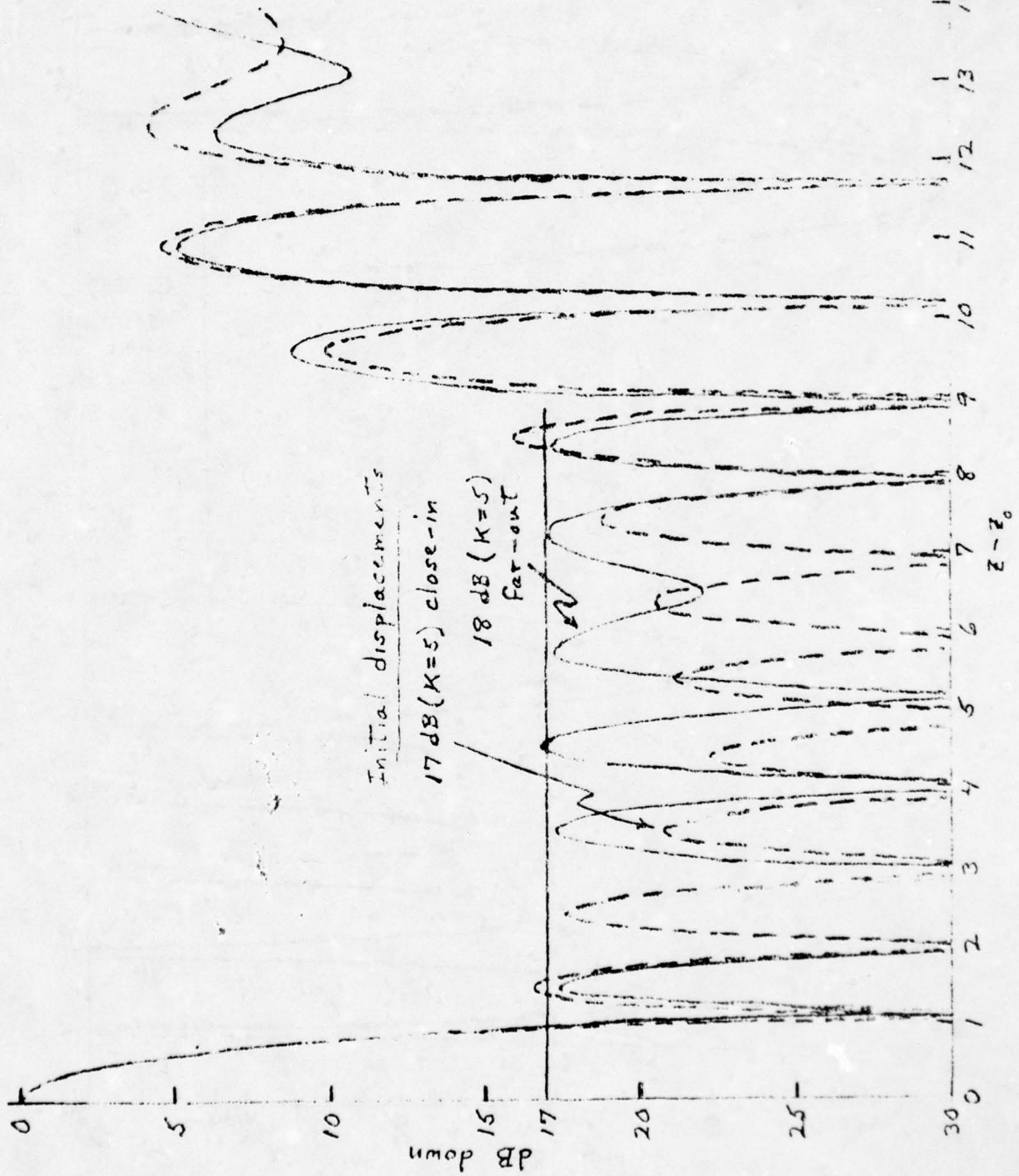

Figure 13. Patterns for 17 dB (K=8) Close-In Sidelobe Levels.

away from the main beam peak, being 16.81 dB down. The former case maintains 8 distinct sidelobes in the prescribed region with two of them, the first at 16.56 dB and the eighth at 15.96 dB, being less than 17 dB down. For both of these patterns, a maximum scan angle of $\theta_s = -\sin^{-1}(1 - 8.9/5.0) = 51.26^o$ results if $z_L = -8.9$ and $z_R = 1.1$ are selected.

Other sets of starting displacement values, c_i, were used in the iterative procedure and convergence to one of these two patterns always occurred when the process converged. Additional approximating solutions could undoubtedly be found by varying the summation weightings.

Figure 14 shows calculated patterns for prescribed sidelobe levels of 16 dB and 18 dB on the K = 8 close-in sidelobes (starting from the displacements of the 17 dB null filled pattern). The 16 dB case shows one sidelobe, the fourth at 15.57 dB down, less than the prescribed level. The 18 dB case shows five sidelobes less than the prescribed level with the highest being at 17.22 dB down. The maximum scan angle conditions for these patterns are essentially the same as for the 17 dB (K = 8) cases.

IX. MINIMUM ELEMENT SPACING CONSIDERATIONS

A basic difficulty in using an unequally spaced array for a suppressed-sidelobe, scanning-radar, system application is associated with the minimum spacing found in the set of displaced element locations. That is, a physically realizable radiating element must be compatible with this spacing.

The 18 dB (K = 8) case shown in Figure 14 has its minimum element spacing between the first and second elements counted away from the array center point. Under the visible region limit selection ($z_L = -8.8$ and $z_R = 1.1$) mentioned in Section VIII, this spacing is only 0.3141λ ; - quite a small spacing for typical radiators. The minimum spacing (and the aperture length), of course, can be scaled to a larger value at the expense of a reduced maximum scan angle. Figure 15 exposes this relationship subject to a left hand limit of $z_L = -8.8$. Note that a half-wavelength element spacing dimension allows a scan to just $\pm 6.70^o$ before the ninth sidelobe of the 18 dB (K = 8) pattern will start to move into visible space. For a non-scanning system application, of course, a minimum element spacing of 0.5584λ would probably be quite acceptable.

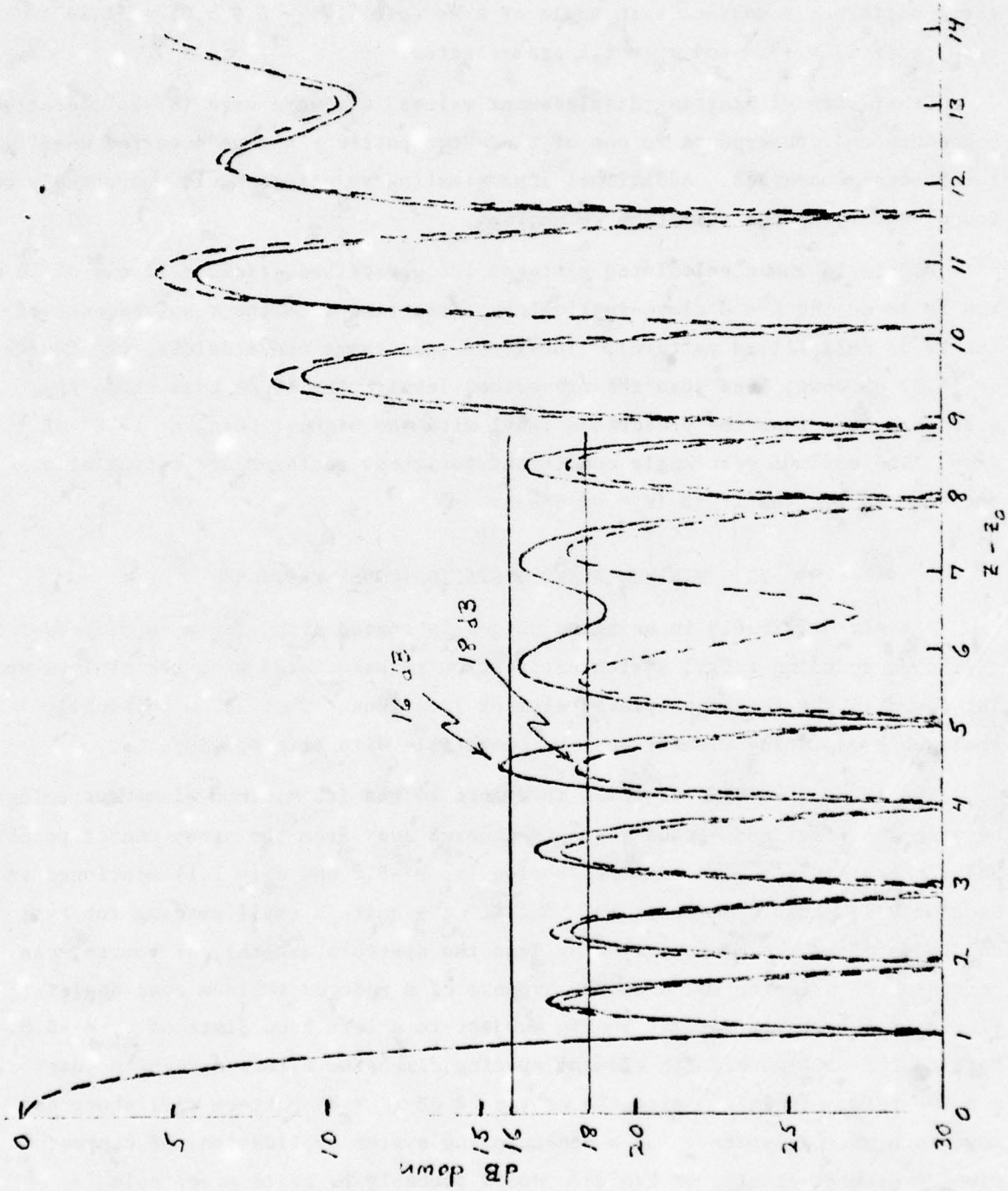

Figure 14. Patterns for 16 dB and 18 dB (K=8) Close-In Sidelobe Levels.

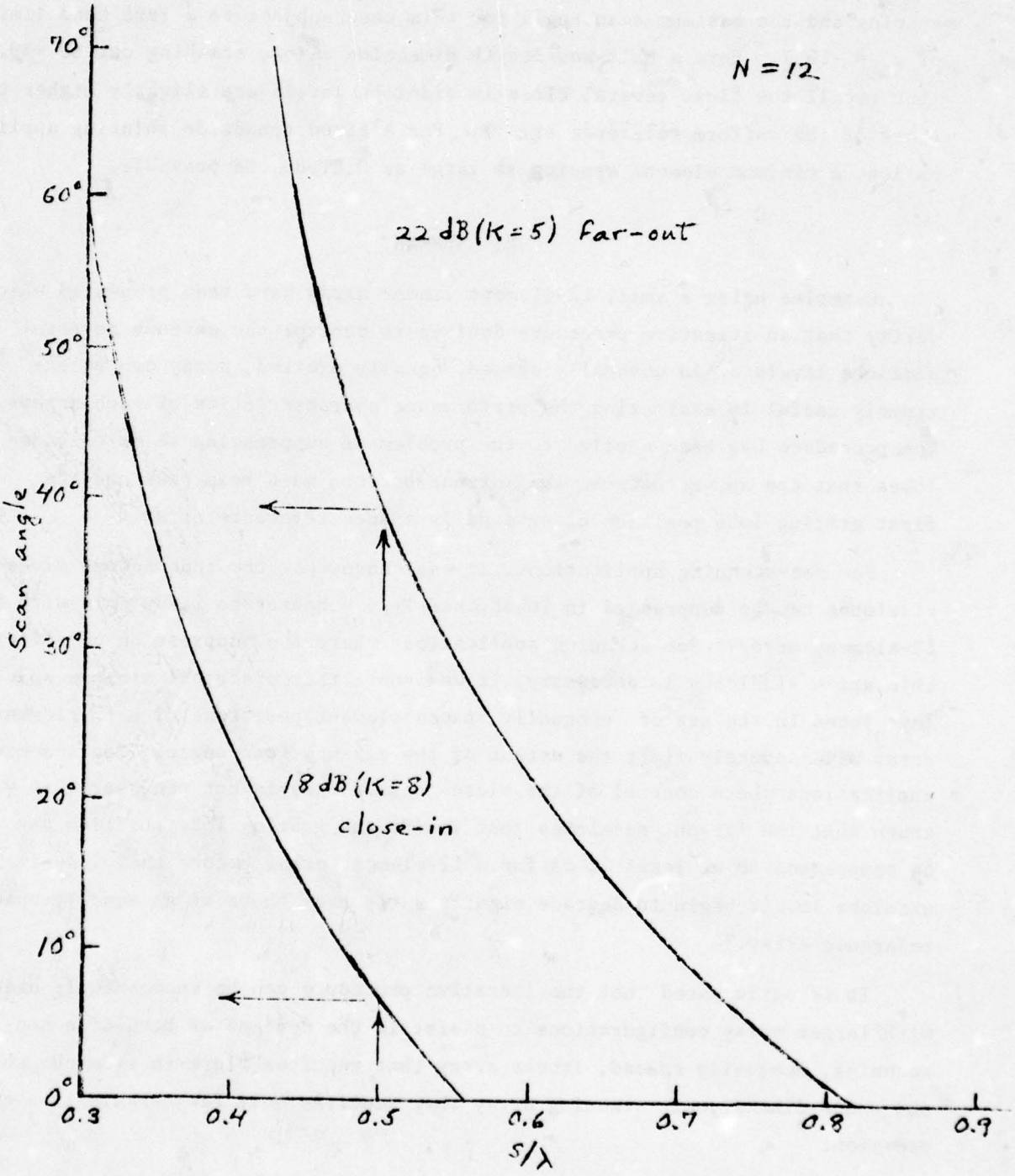

Figure 15. Maximum Scan Angle vs. Minimum Element Spacing.

The 22 dB (K = 5) far-out Tchebychef sidelobe case shown in Figure 11 has its minimum element spacing between the outermost two elements of the array. Figure 15 shows the relationship between a scaled minimum element spacing and the maximum scan angle for this case subject to a left hand limit of $z_L = -10.7$. Here a half-wavelength dimension allows scanning out to $\pm 39.32^o$ (but recall the first several close-in sidelobe levels are slightly higher than those of the uniform reference array). For a fixed broadside pointing application, a minimum element spacing as large as 0.8168λ is possible.

X. SUMMARY

Examples using a small 12-element linear array have been presented which verify that an iterative procedure devised to control the antenna pattern sidelobe levels of an unequally spaced, equally excited, array can be extremely useful in estimating the performance characteristics of such arrays. The procedure has been applied to the problem of suppressing selected sidelobes that can appear between the antenna pattern main beam peak and the first grating lobe position of an equally spaced reference array.

For non-scanning applications, it was shown that the independent close-in sidelobes can be suppressed in Tchebychef-Type behavior to 21 dB down with a 12-element array. For scanning applications where the suppression of all visible space sidelobes is necessary, it was shown that practical minimum spacings found in the set of unequally spaced element positions of a 12-element array will severely limit the extent of the maximum scan angle. For scanning applications where control of the close-in sidelobes is not necessary, it was shown that the far-out sidelobes just inside the grating lobe position can be suppressed to at least 22 dB for a 12-element array before the close-in sidelobe levels begin to degrade significantly from those of an equally spaced reference array.

It is anticipated that the iterative procedure can be successfully used with larger array configurations to assist in the designs of both of a non-scanning, unequally spaced, linear array that requires close-in sidelobe suppression and a one-dimensional, scanning array that requires only far-out sidelobe suppression.

REFERENCES

[1] R. F. Harrington, "Sidelobe Reduction by Nonuniform Element Spacing," IRE Trans. Antennas Propagat., Vol. AP-9, pp. 187-192, March 1961.

[2] Ye. V. Baklanov, V. L. Pokrovskiy, and G. I. Surdutovich, "A Theory of Linear Arrays with Unequal Spacing," Radio Engineering and Electronic Physics, No. 6, pp. 905-913, June 1962.

[3] A. L. Snover and A. J. Ferraro, "An Investigation of the Properties of Synthesized Nonuniformly Spaced Antenna Arrays," IEEE Trans. Antennas Propagat., Vol. AP-12, pp. 132-133, January 1964.

[4] J. Galejs, "Minimization of Sidelobes in Space Tapered Linear Arrays," IEEE Trans. Antennas Propagat., Vol. AP-12, pp. 497-498, July 1965.

[5] C. H. Tang, "On a Design Method for Nonuniformly Spaced Arrays," IEEE Trans. Antennas Propagat., Vol. AP-13, pp. 642-643, July 1965.

[6] D. D. King, R. F. Packard, and R. K. Thomas, "Unequally-Spaced, Broad-Band Antenna Arrays," IRE Trans. Antennas Propagat., Vol. AP-8, pp. 380-384, July 1960.

[7] A. L. Maffett, "Array Factors with Nonuniform Spacing Parameter," IRE Trans. Antennas Propagat., Vol. AP-10, pp. 131-136, March 1962.

[8] M. G. Andreason, "Linear Arrays with Variable Interelement Spacings," IRE Trans. Antennas Propagat., Vol. AP-10, pp. 137-143, March 1962.

[9] M. I. Skolnik, G. Nemhauser, and J. W. Sherman, III, "Dynamic Programming Applied to Unequally Spaced Arrays, "IEEE Trans. Antennas Propagat., Vol. AP-12, pp. 35-43, January 1964.

[10] A. Ishimaru and Y-S. Chen, "Thinning and Broadbanding Antenna Arrays by Unequal Spacings," IEEE Trans. Antennas Propagat., Vol. AP-13, pp. 34-42, January 1965.

[11] Y. T. Lo and S. W. Lee, "A Study of Space-Tapered Arrays," IEEE Trans. Antennas Propagat., Vol. AP-14, pp. 22-30, January 1966.

[12] B. D. Steinberg, "Comparison Between the Peak Sidelobe of the Random Array and Algorithmically Designed Aperiodic Arrays," IEEE Trans. Antennas Propagat., Vol. AP-21, pp. 366-370, May 1973.

[13] C. F. Winter, "Using Continuous Apertures Illuminations Discretely," IEEE Trans. Antennas Propagat., Vol. AP-25, pp. 695-700, September 1977.

[14] R. P. Dooley, "The Optimum Design of Small Nonuniformly Spaced Arrays," IEEE Trans. Antennas Propagat., Vol. AP-20, pp. 636-637, September 1972.

[15] V. Galindo, "Nonlinear Antenna Arrays," IEEE Trans. Antennas Propagat., Vol. AP-12, p. 782, November 1964.

[16] J. L. Allen, "A Simple Model for Mutual Coupling Effects on Patterns of Unequally Spaced Arrays," IEEE Trans. Antennas Propagat., Vol. AP-15, pp. 530-533, July 1967.

[17] P. A. Stark, Introduction to Numerical Analysis. New York: MacMillan, 1970, pp. 130-133.

[18] H. K. Schuman and B. J. Strait, "On the Design of Unequally Spaced Arrays with Nearly Equal Sidelobes," IEEE Trans. Antennas Propagat., Vol. AP-16, pp. 493-494, July 1968.

SIDELOBE DISCRIMINATION TECHNIQUE

by

Paul Eberhardt

and

William McNaul

CUBIC CORP.
DEFENSE SYSTEMS DIVISION
SAN DIEGO, CALIFORNIA

1.0 INTRODUCTION

Sidelobe suppression is an important consideration in directive antenna system design. In direction finding or ELINT data collection, spurious signals arriving on sidelobes must be suppressed. A variety of systems have been devised to differentiate between signals on sidelobes and signals arriving on an antenna main beam. A number of these techniques are found in the literature[1]. Schemes employing separate main antenna and omni guard channel comparisons are most common.

Without exception, these methods result in increased system cost and complexity. Often an additional price is paid in significantly reduced RF performance (gain, sensitivity, etc.). Efforts are continually underway to develop antennas with reduced sidelobes to ease the burden on the selected sidelobe discrimination (SLD) system and to provide false or spurious response rates below acceptable limit levels. In the high density scenarios of today's EW environment, this often leads to a series of conflicting and equally undesirable engineering tradeoffs.

The technique presented here offers a new solution to the SLD problems of the past. This method is highly effective, yet relatively simple and inexpensive (in both dollars and negative RF effects). Simply stated, a method has been established to distinctly and clearly label -- rather than suppress -- signals arriving on sidelobes. This labeling is then used to differentiate between legitimate and spurious RF signals. Immediate blanking or selective processing may then be performed as desired.

The basic idea is still very much in its infancy as far as practical realization of a deployed system is concerned. This paper includes a conceptual discussion as well as experimental results for a number of implementation techniques.

2.0 THEORETICAL BACKGROUND

According to diffraction theory, the distribution of power radiated from an aperture may be defined in terms of the current distribution over the aperture and its particular edge discontinuities[2]. During the development of a number of reflector type antennas, general trends for aperture effects have been observed. These trends are also discussed in the literature[2,3]:

(1) Sidelobe levels are more sensitive to slight defocusing than the main beam.

(2) Scattering due to blockage tends to affect the sidelobe levels more than the main beam level.

(3) Sidelobes are more sensitive to perturbations to the aperture distribution than is the main beam.

The third observation provides the key for sidelobe identification --namely, a characteristic that makes a signal arriving on a sidelobe distinctly different from the same signal arriving on the antenna main beam. The technique may be described as follows:

> The introduction of a modulation or disturbance in the aperture distribution of an antenna generates corresponding modulations in both sidelobe and main beam signals. However, modulation on the sidelobe is measurably greater than that on the main beam. The sidelobe modulation is useful in flagging signals arriving on the sidelobes. The resulting "flagged" signals may be selectively processed.

The pattern shown in Figure 2-1, which will be discussed later in more detail, shows sidelobe modulation and indicates the potential of this technique.

3.0 PRACTICAL CONSIDERATIONS

Thus far, it has been postulated that perturbations in the sidelobes that are absent from the main lobe can be beneficial for sidelobe signal rejection. Further investigations

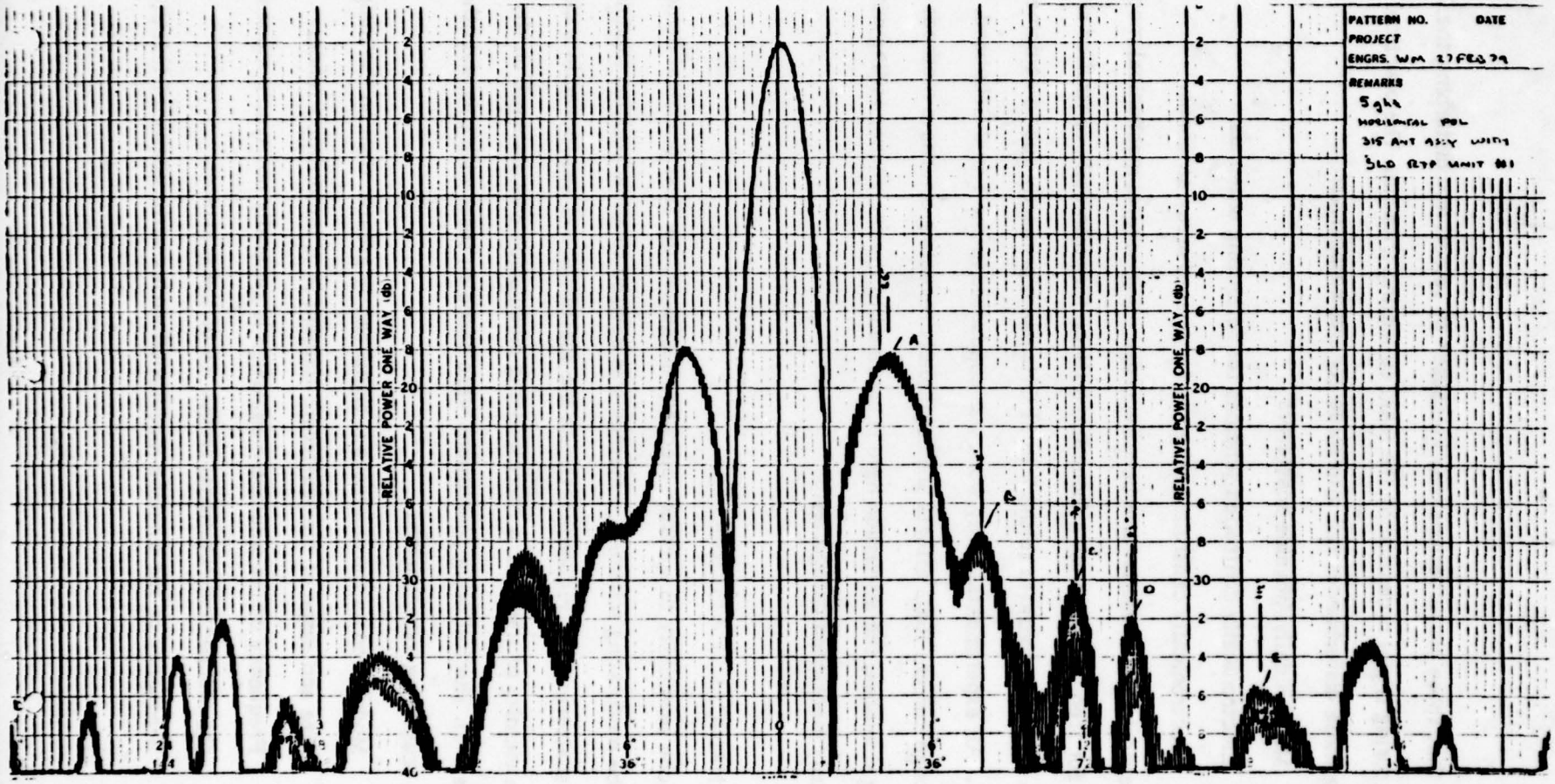

FIGURE 2-1.
MECHANICALLY MODULATED AZIMUTH PATTERN (5 GHz)

established that these perturbations may be caused by selectively disturbing the RF signal path during signal reception by the main collecting antenna. The practical means of providing these disturbances fall into three general categories:

(1) Mechanically movable scatterers

(2) Electronically controlled schemes for reflecting antennas

(3) Electronically controlled schemes for phased array antennas.

Promising experimental results have been recorded using several mechanical modulation techniques for frequencies ranging from 3 to 8 GHz. Electronically controlled sidelobe modulation work was confined to the 7 to 11 GHz band, primarily due to equipment limitations. All experimental array work was conducted in the 1 to 2 GHz band.

Although current R&D efforts are continually revealing alternate methods for modulating sidelobes, the discussion here is confined to the techniques falling within the previously mentioned categories.

3.1 MECHANICAL SCATTERER

Sidelobe sensitivity to aperture blockage suggested the first practical demonstration of a sidelobe modulating scheme. A method was devised to allow position modulation of a short scattering rod (Figure 3.1-1). As the scattering rod was moved in a circular path in the vicinity of the feed, a corresponding modulation was observed on the pattern (see Figure 2-1). The following conclusions were based on tests with this and other related mechnical scattering experiments:

(1) Modulation on the sidelobes is significantly greater than on the mainlobe.

(2) Size and shape of the scattering element is of minor importance.

(3) Frequency of the sidelobe modulation is generally not synchronous with the mechanical rotational frequency of the scatterer.

(4) Frequency of the sidelobe modulation varies with received RF frequency.

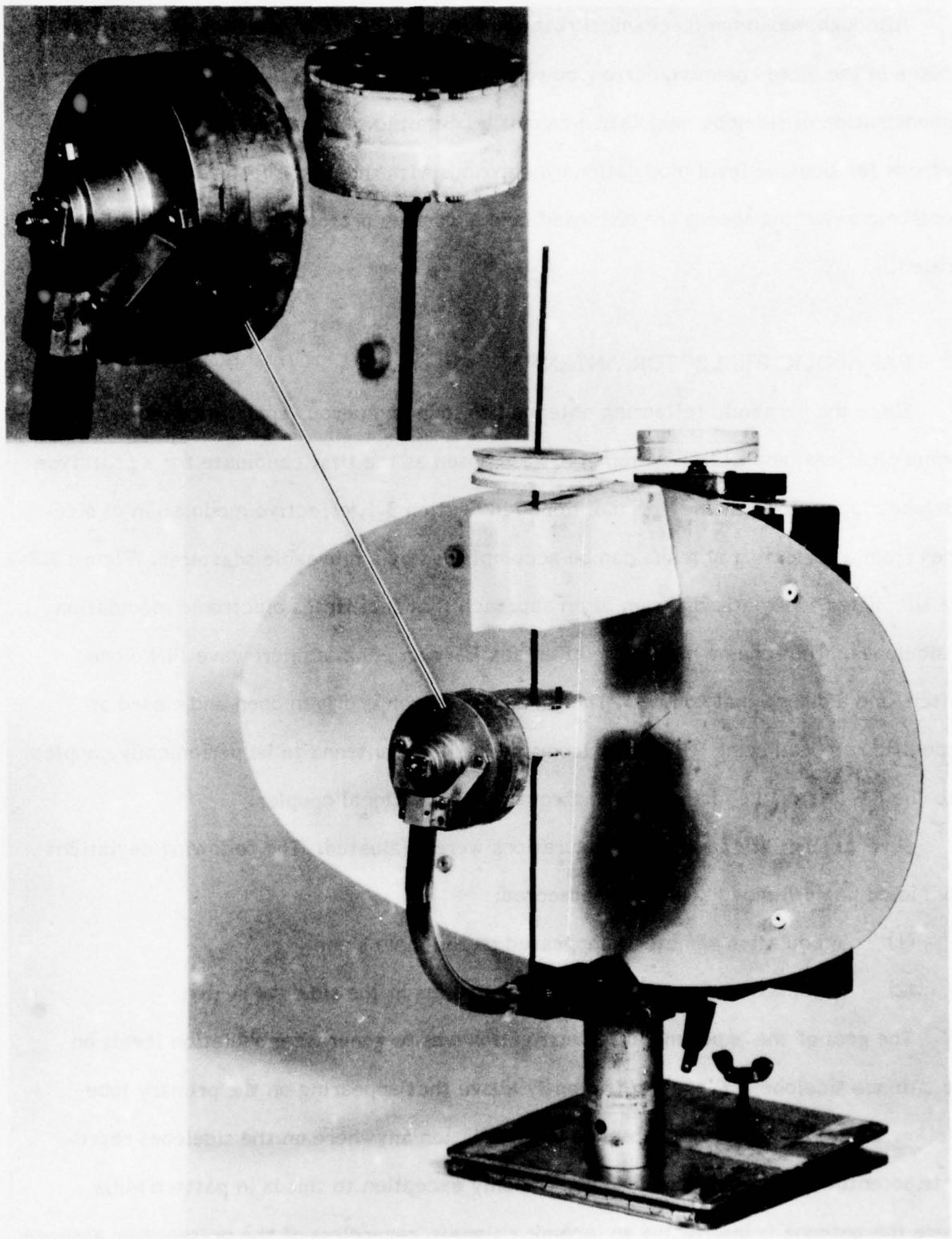

FIGURE 3.1-1
POSITION MODULATION OF SHORT SCATTERING ROD

Although maximum mechanical rotation rates set limits on the usefulness of this scheme in the more common, narrow pulsewidth applications, its usefulness as a practical demonstration of sidelobe modulation cannot be disputed. In the following two sections, methods for sidelobe level modulation synchronous with the perturbations at higher electronic switching speeds are discussed, and a working prototype detector is demonstrated.

3.2 PARABOLIC REFLECTOR ANTENNAS

Since the parabolic reflecting antenna has found numerous applications in radar, communications, and ELINT systems, it was chosen as the first candidate for a prototype sidelobe modulation scheme. As mentioned in Section 3.1, effective modulation of sidelobes from a reflecting antenna can be accomplished by a moveable scatterer. Figure 3.2-1 is a simplified schematic diagram of an approach that facilitates electronic modulation of sidelobes. The scheme makes use of an auxiliary antenna, a microwave PIN diode switch, and a directional coupler. The PIN diode switch is driven open and closed at a specific rate, allowing RF energy from the auxiliary antenna to be periodically coupled into the RF line of the main antenna through the directional coupler.

Several auxiliary antenna configurations were evaluated. The following deviations from ideal pattern modulation were observed:

(1) Modulation sometimes appeared on the main beam

(2) Modulation disappeared at various points in the sidelobe region.

The goal of the experimental investigation was to generate modulation levels on the antenna sidelobes at levels sufficiently above that appearing on the primary lobe to allow threshold detection. Absence of modulation anywhere on the sidelobes represents potential false alarm conditions. The only exception to this is in pattern nulls where the antenna is insensitive to incoming signals, regardless of the presence or absence of modulation.

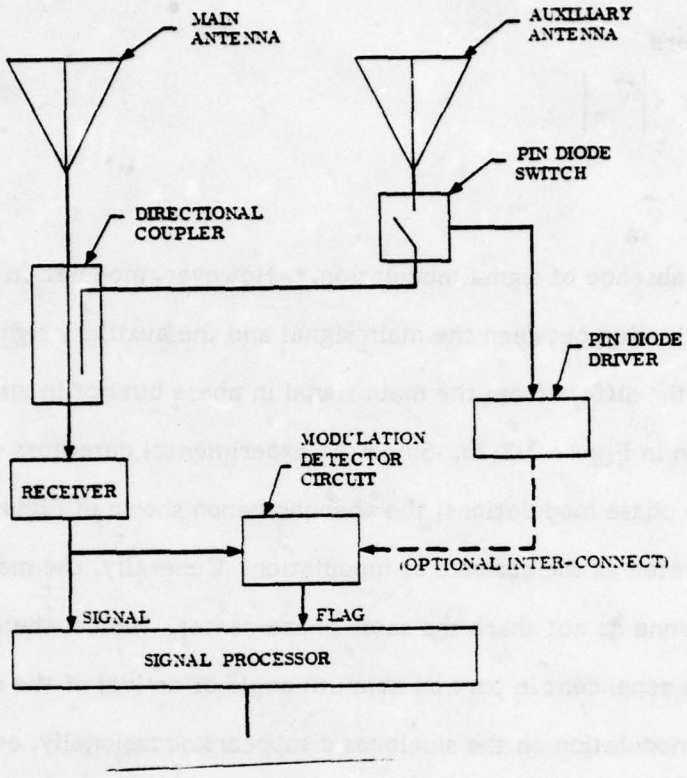

Figure 3.2-1
AUXILIARY ANTENNA SCHEME

In the auxiliary antenna scheme, sidelobe modulation results from the vector addition of the main antenna signal voltage and the auxiliary signal voltage (see Figure 3.2-2a).

The resultant voltage is given by

$$\vec{V}_r = \vec{V}_m + \vec{V}_a \qquad (1)$$

where $\vec{V}_m$ = main antenna signal voltage vector

$\vec{V}_a$ = auxiliary antenna signal voltage vector

$\vec{V}_r$ = resultant signal voltage vector.

As shown in Figure 3.2-2a, switching the auxiliary signal in and out will cause both amplitude and phase modulation of the resultant vector. The amplitude change is expressed as:

$$\Delta V = \left|\vec{V}_r\right| - \left|\vec{V}_m\right| \qquad (2)$$

The condition where

$$\left|\vec{V}_a\right| << \left|\vec{V}_m\right|$$

such that

$$\vec{V}_r \rightarrow \vec{V}_m$$

will result in the absence of signal modulation.* However, modulation will also disappear if the phase relationship between the main signal and the auxiliary signal is such that the resultant vector differs from the main signal in phase but not in amplitude. This condition is shown in Figure 3.2-2b. Since the experimental detectors described here are insensitive to phase modulations, the phenonomenon shown in Figure 3.2-2b will always be interpreted as the absence of modulation. Generally, the main antenna and the auxiliary antenna do not share the same phase center. Hence, the angle Θ (see Figures 3.2-2a and -2b) is dependent in part on azimuth angle of arrival of the modulated signal. For this reason, modulation on the sidelobes disappears occasionally, even though the condition of equation (3) is not met.

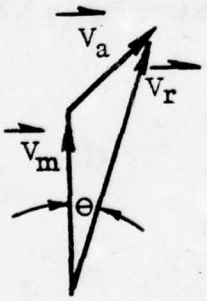

Figure 3.2-2a

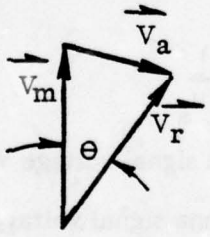

Figure 3.2-2b

* It has been found that values of $\left|\vec{V}_a\right| \approx \left|\frac{\vec{V}_m}{10}\right|$ are sufficient to produce modulation.

Vector addition analysis of the sidelobe modulation technique reveals the importance of auxiliary antenna pattern characteristics. The following observations may be made:

(1) Equation (2) suggests the advantage of an auxiliary antenna pattern with a null coinciding with the mainlobe of the main antenna.

(2) Broad uniform coverage by the auxiliary antenna outside the region of the main beam is necessary to modulate sidelobes. Nulls in this region will result in the absence of modulation in the direction coinciding with each null.

(3) The auxiliary antenna need not cover the main pattern sidelobes, as in more conventional systems, but only be close to the same levels. To optimize performance, auxiliary antenna patterns can be "tailored" to the shape of the main antenna pattern as shown in Figure 3.2-3.

(4) The auxiliary antenna polarization should be selected to ensure that auxiliary voltage vectors are always present to interact with the sidelobe signal vectors of the main antenna.

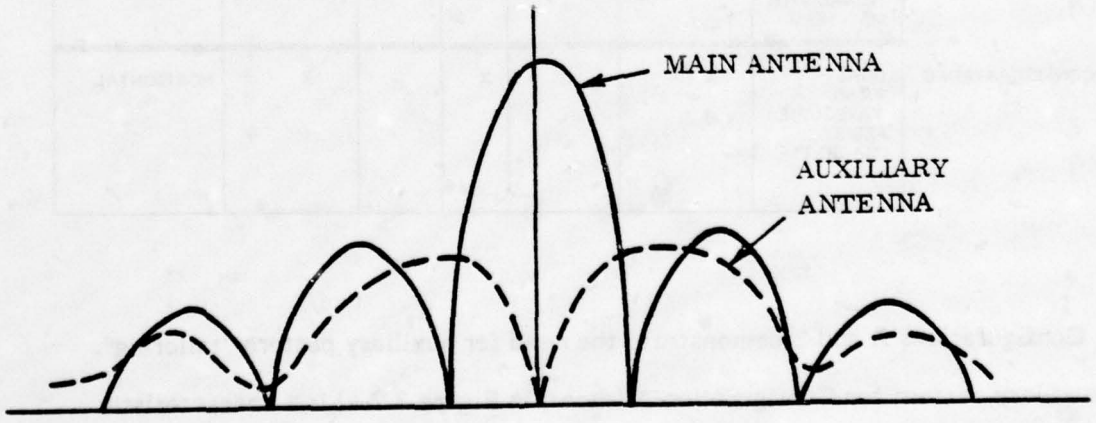

Figure 3.2-3
"TAILORING" OF AUXILIARY PATTERN

Several auxiliary antenna configurations were investigated. Three schemes showing particular promise are summarized in Table 3.2-1. These auxiliary antenna parameters were found to be useful criteria for determining the value of a particular modulation scheme:

(1) Pattern type

(2) Polarization

(3) Physical type.

TABLE 3.2-1
AUXILIARY ANTENNA PARAMETERS

	PHYSICAL TYPE			PATTERN TYPE			POLARIZATION
	DESCRIPTION	REFLECTOR FEED	SEPARATE ANTENNA	NULL ON AXIS	BROAD	DIRECTIONAL	
CONFIGURATION A	SINGLE LOG PERIOD DIPOLE CODIRECTIONAL WITH MAINBEAM		X		X		HORIZONTAL
CONFIGURATION B	DUAL PLANAR SPIRALS 180° OUT OF PHASE CO DIRECTIONAL WITH MAINBEAM		X	X	X		CIRCULAR
CONFIGURATION C	DUAL WR 90 WAVEGUIDE FED BY "MAGIC T"	X		X		X	HORIZONTAL

Configurations A and B demonstrate the need for auxiliary pattern "tailoring". The auxiliary pattern for Configuration A (shown in Figure 3.2-4) is a characteristic log periodic dipole E-plane cut with its inherent nulls at 90 degrees. The main antenna pattern was recorded with the auxiliary antenna switched at 1 Hz. Note that the trace broadening, which indicates signal modulation, nearly disappears in the region of $\pm$ 90 degrees azimuth. Further beam "tailoring" was used to orient a null on the main beam

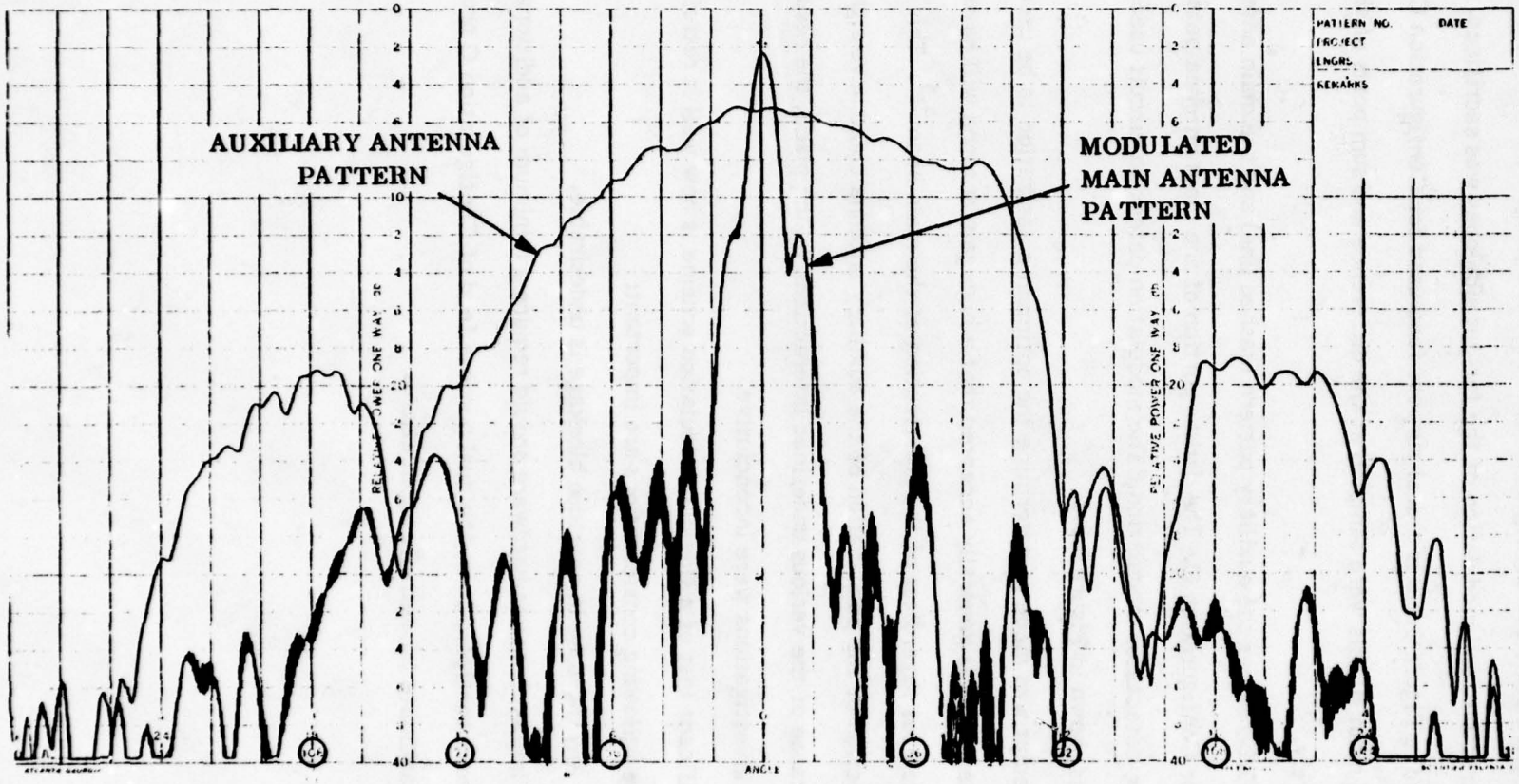

FIGURE 3.2-4
AUXILIARY PATTERN FOR CONFIGURATION A

as shown in Figure 3.2-5 for Configuration B. The dual planar spiral array, however, proved too directive, and modulation of the far-out sidelobes was sacrificed.

Pictured in Figure 3.2-6 is a dual purpose feed used for Configuration C. The auxiliary and main signals were sampled at the difference and sum ports of the magic "T" respectively.

Figure 3.2-7 shows the auxiliary pattern (dashed line) and the main antenna pattern (solid line) for Configuration C. The darker portion of the main antenna pattern indicates a region of no detectable modulation. The modulation detection circuit used to generate this pattern is shown in Figure 3.2-8.

An attempt was made to determine the optimum polarization to be used for the auxiliary antenna. It is generally accepted that a high gain antenna will have randomly polarized sidelobes regardless of the polarization of the main beam[4,5]. This would indicate that the selection of the polarization of the auxiliary antenna could have significant effects. Because of the various undefined interactions taking place, the results of polarization investigations were inconclusive.

A significant test of a sidelobe modulation scheme is how well it retrofits to existing systems. The following considerations are important:

(1) Any increase in aperture blockage is undesirable.

(2) Implementation hardware should require a minimum of additional space and weight.

In light of these considerations, the dual purpose feed of Configuration C promises to be a likely candidate for retrofit applications.

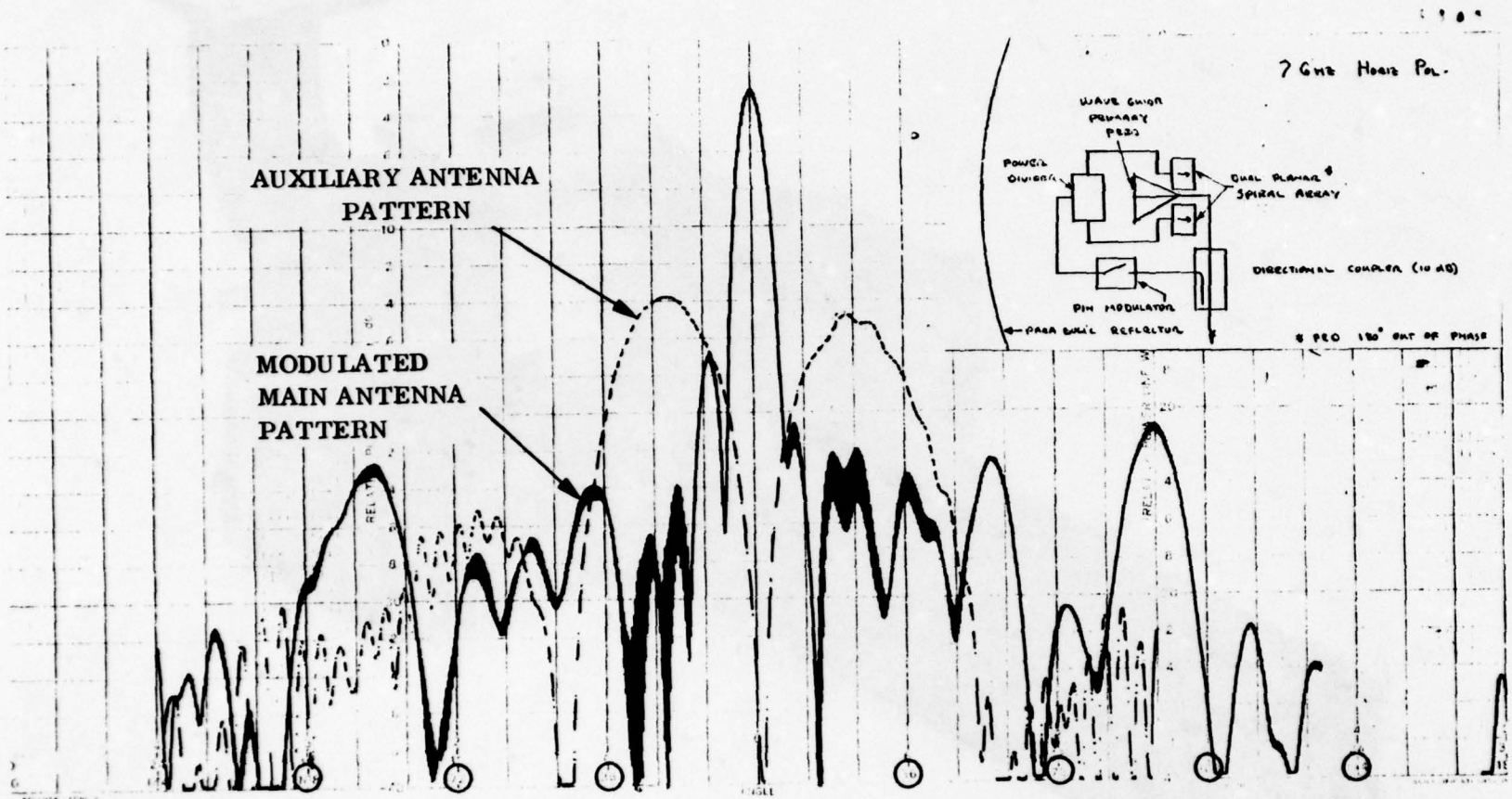

FIGURE 3.2-5
CONFIGURATION B/NULL ON MAIN BEAM

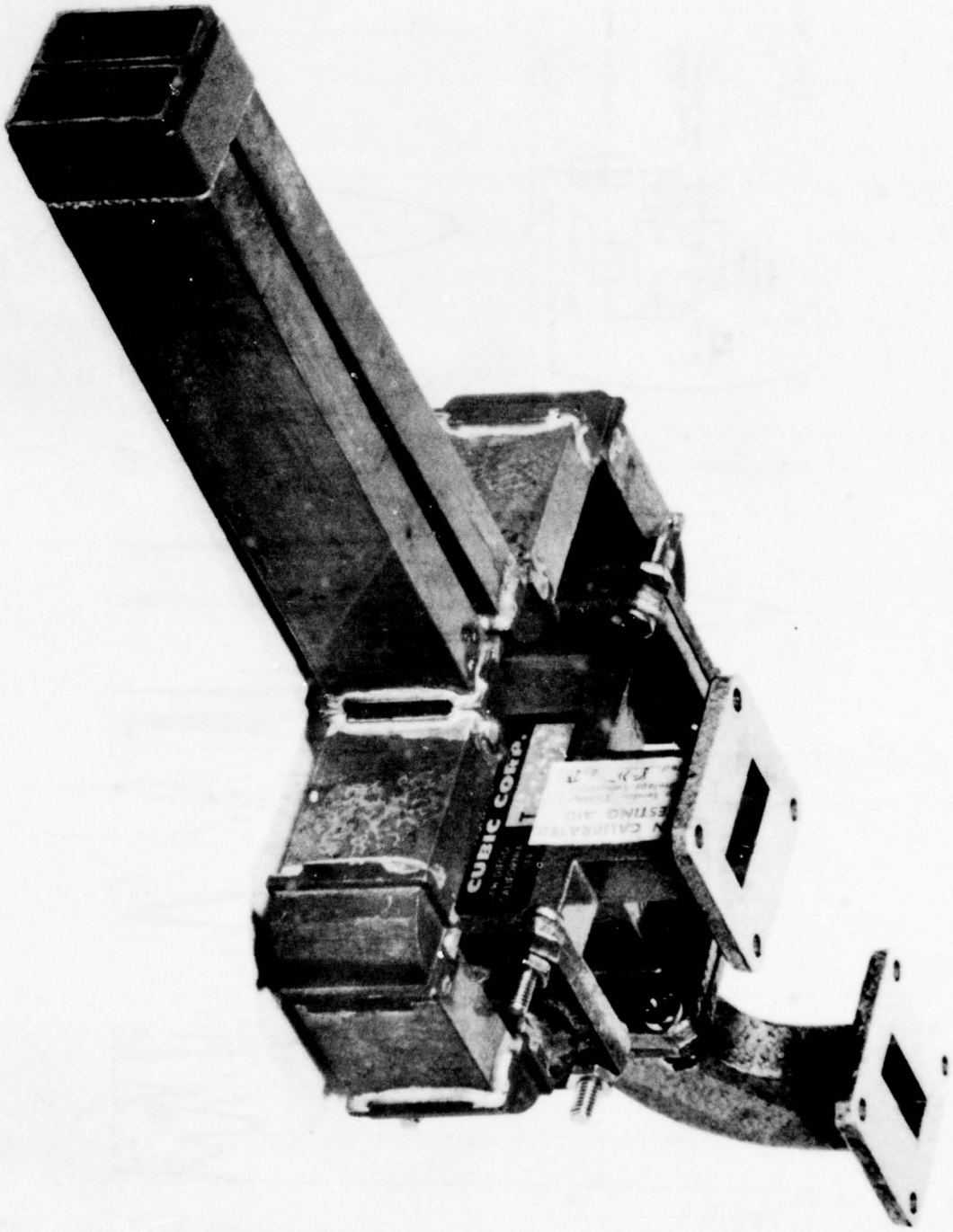

FIGURE 3.2-6
DUAL PURPOSE FEED/CONFIGURATION C

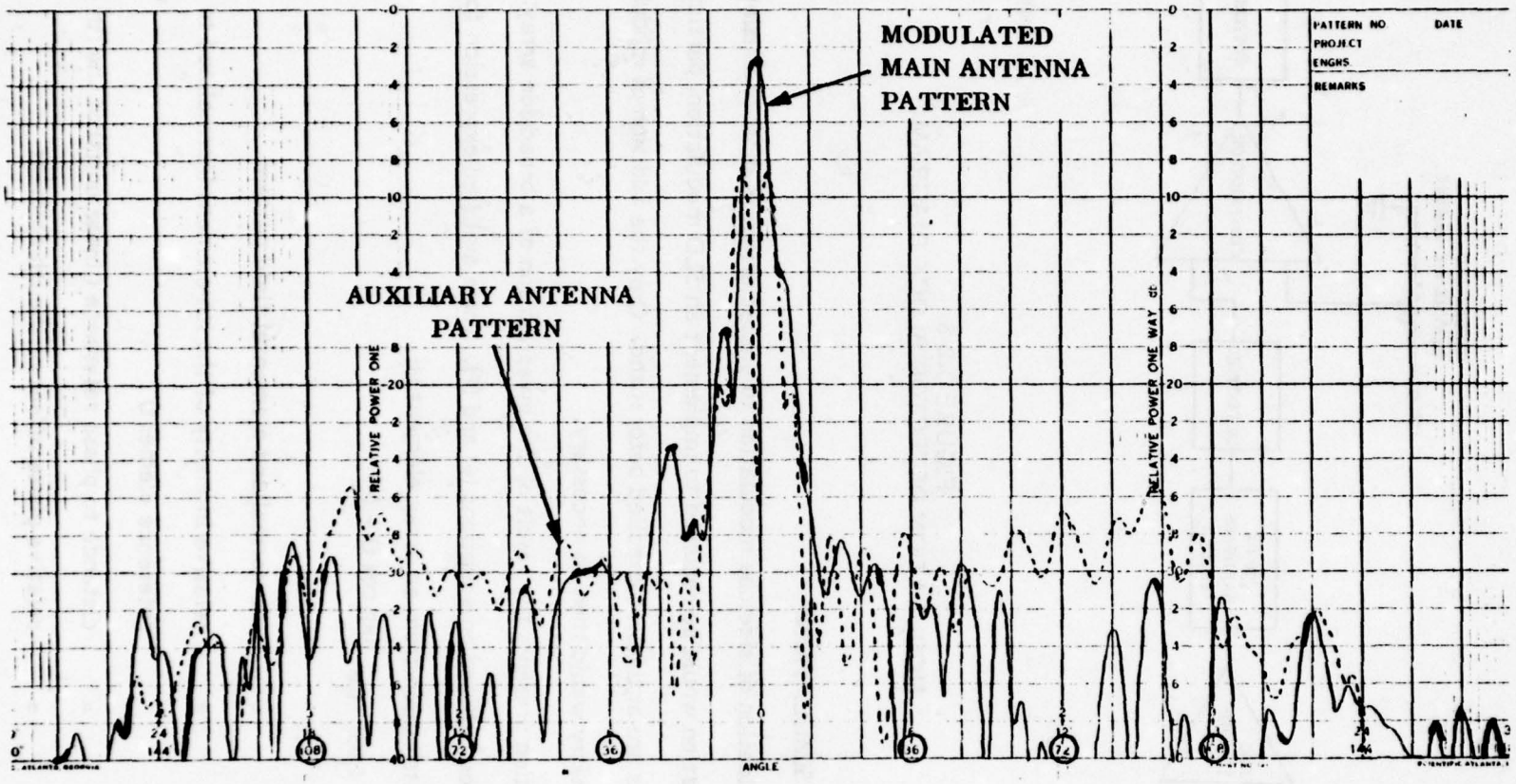

FIGURE 3.2-7
AUXILIARY & MAIN ANTENNA PATTERN/CONFIGURATION C

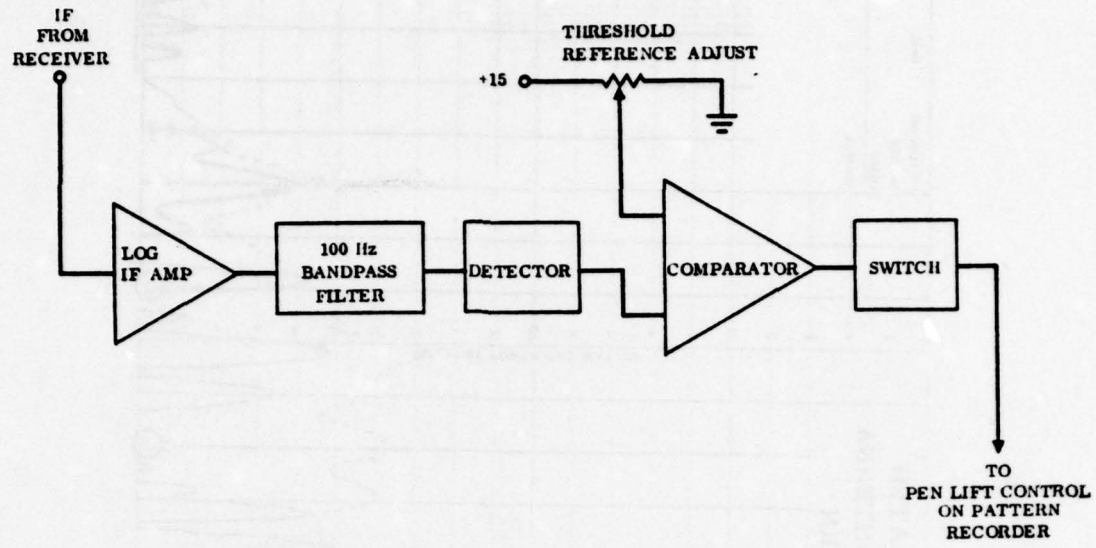

FIGURE 3.2-8
MODULATION DETECTOR BLOCK DIAGRAM

3.3 ARRAY SIMULATION

The application of sidelobe modulation to phased arrays is most promising. Little if any modification would be required to implement an SLD modulation, particularly if the elements are actively controlled beforehand. Only the addition of modulation detection circuitry would then be necessary.

This section presents the result of the investigation of a broadside array. The array simulation is based on equations (6) and (7). The simplified expression for the total field contribution from an array element is:

$$E_i(\Theta) = f_i(\Theta)\ I_i e^{\,j(kr_i \cos\Theta + \delta_i)} \qquad (4)$$

where

$f_i(\Theta)$ = the normalized elemental field pattern

I_i = relative intensity of the ith element (normalized to an arbitrary reference element)

r_i = distance to phase reference (linear units) of the ith element

δ_i = relative phase offset of the ith element

k = $2\pi/\lambda$ (λ in the same linear units are r_i).

For an isotropic element, the pattern reduces to:

$$f_i(\Theta) = 1 \tag{5}$$

Thus, the total field pattern may be written as

$$E(\Theta) = \sum_{i=1}^{N} I_i \, e^{j(kr_i \cos \Theta + \delta_i)} \tag{6}$$

where

N = number of array elements.

The far field power pattern, which is useful in evaluating measured data, is given by:

$$P(\Theta)_{dB} = 20 \log\left(\frac{E(\Theta)}{E_{max}}\right) \tag{7}$$

where $P(\Theta)_{dB}$ is the relative far field power density distribution for the array.

Figure 3.3-1 provides an overview of the coordinate system. Mutual interaction of the elements has been ignored.

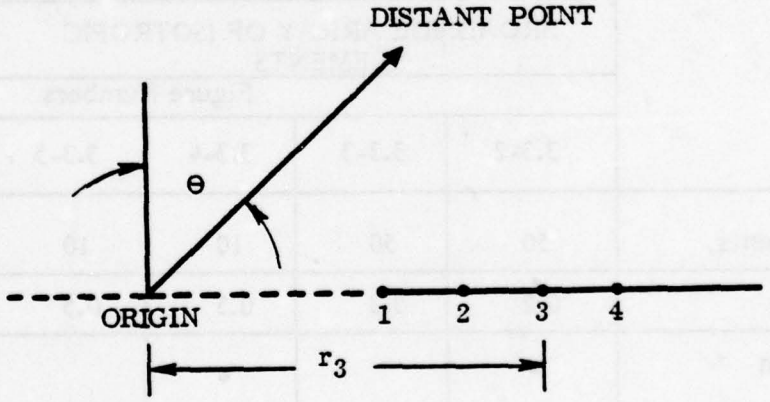

FIGURE 3.3-1
LINEAR ARRAY OF ISOTROPIC RADIATORS

Sample computed azimuth patterns showing sidelobe modulation of a uniform linear array of isotropic radiators are presented in Figures 3.3-2 through 3.3-5. The patterns plotted were generated by modulating either I_i or δ_i for a single element of a selected array.

The computer simulation results for a large array, a smaller array, and a three-element LPD array are discussed in the following paragraphs; measured data and simulation patterns are presented as Figures 3.3-2 through -5 and Figures 3.3-7 through -10. Table 3.3-1 indexes this data to aid in comparisons.

Contrasting the phase modulated pattern shows that this type of modulation produces a less regular and ordered disturbance of the sidelobe structure (see Figures 3.3-2 and -4). Amplitude modulation, on the other hand, causes less drastic and more regular pattern perturbations (see Figures 3.3-3 and -5). When pattern modulation resulting from small phase shifts are contrasted with patterns from larger amplitude perturbations of an element, similar results are observed. This makes the distinction between the two methods of introducing sidelobe modulations less distinct.

TABLE 3.3-1
INDEX OF COMPUTER SIMULATIONS

	BROADSIDE ARRAY OF ISOTROPIC ELEMENTS				LPD ARRAY*	
	Figure Numbers					
	3.3-2	3.3-3	3.3-4	3.3-5	3.3-9*	3.3-10*
Number of Elements	50	50	10	10	3	3
Element Spacing	0.2	0.2	0.5	0.5	0.4λ**	0.6λ**
Phase Modulation	•		•		•	•
Number of Increments	11		6		1	1
Phase Increment	33°		66°		22°	22°
Amplitude Modulation		•		•		
Number of Pattern Traces		11		6		
Amplitude Increment		10%		20%		
Modulation of Element	5	5	2	2	1	1

* Measured data also provided for identical configuration.
** Separation is frequency dependent; this value approximate.

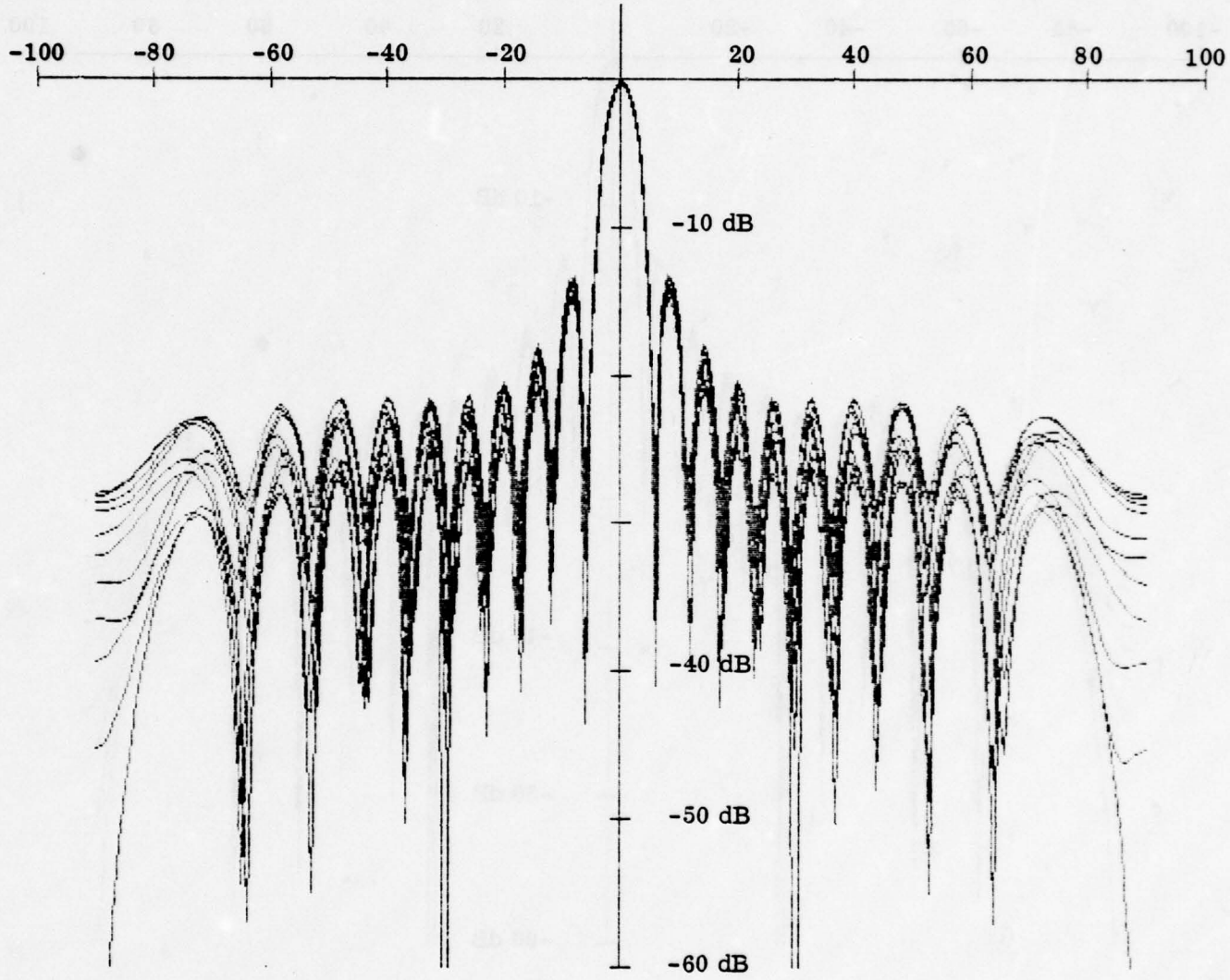

FIGURE 3.3-2
10λ ARRAY SIMULATION: PHASE MODULATION

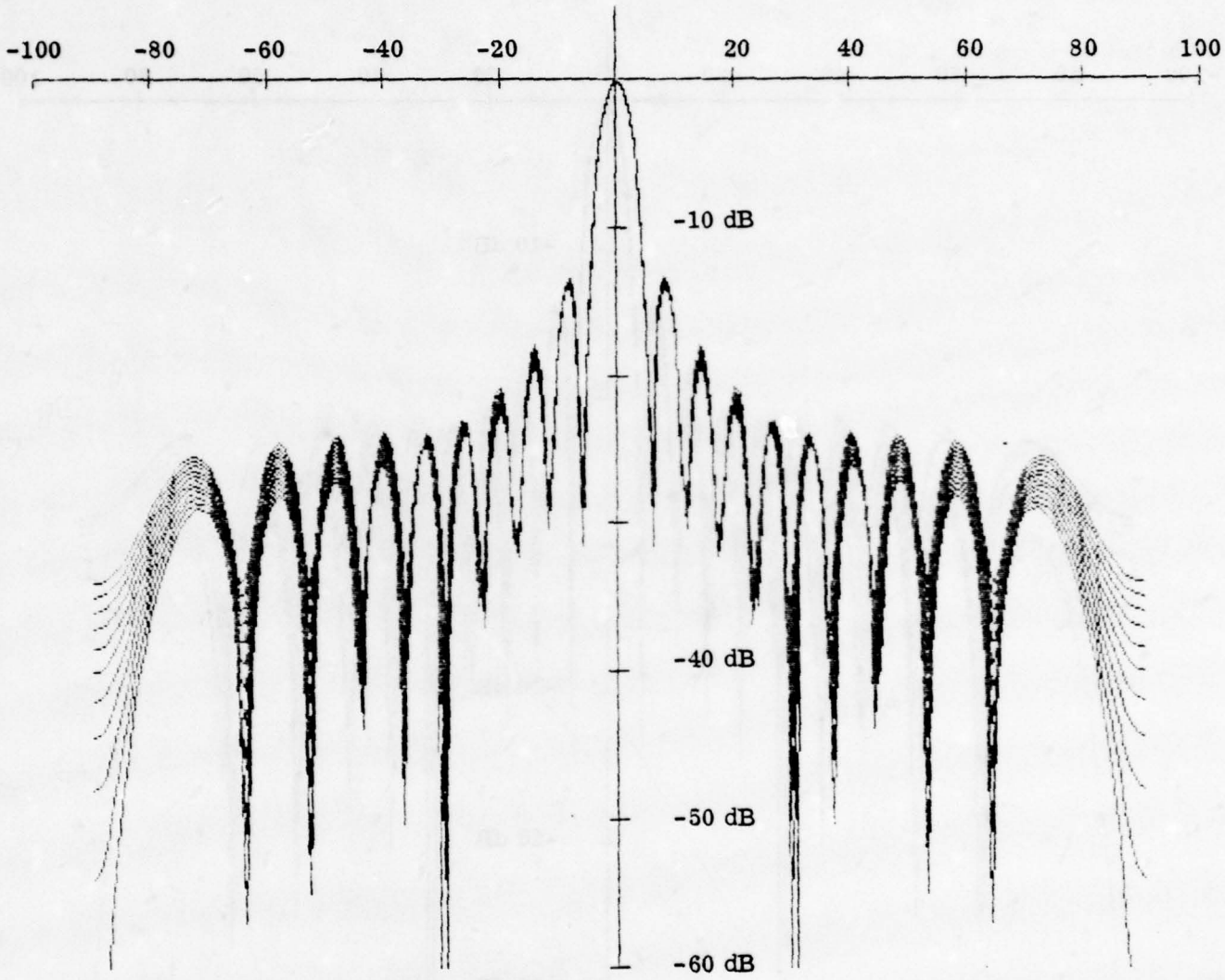

FIGURE 3.3-3
10λ ARRAY SIMULATION: AMPLITUDE MODULATION

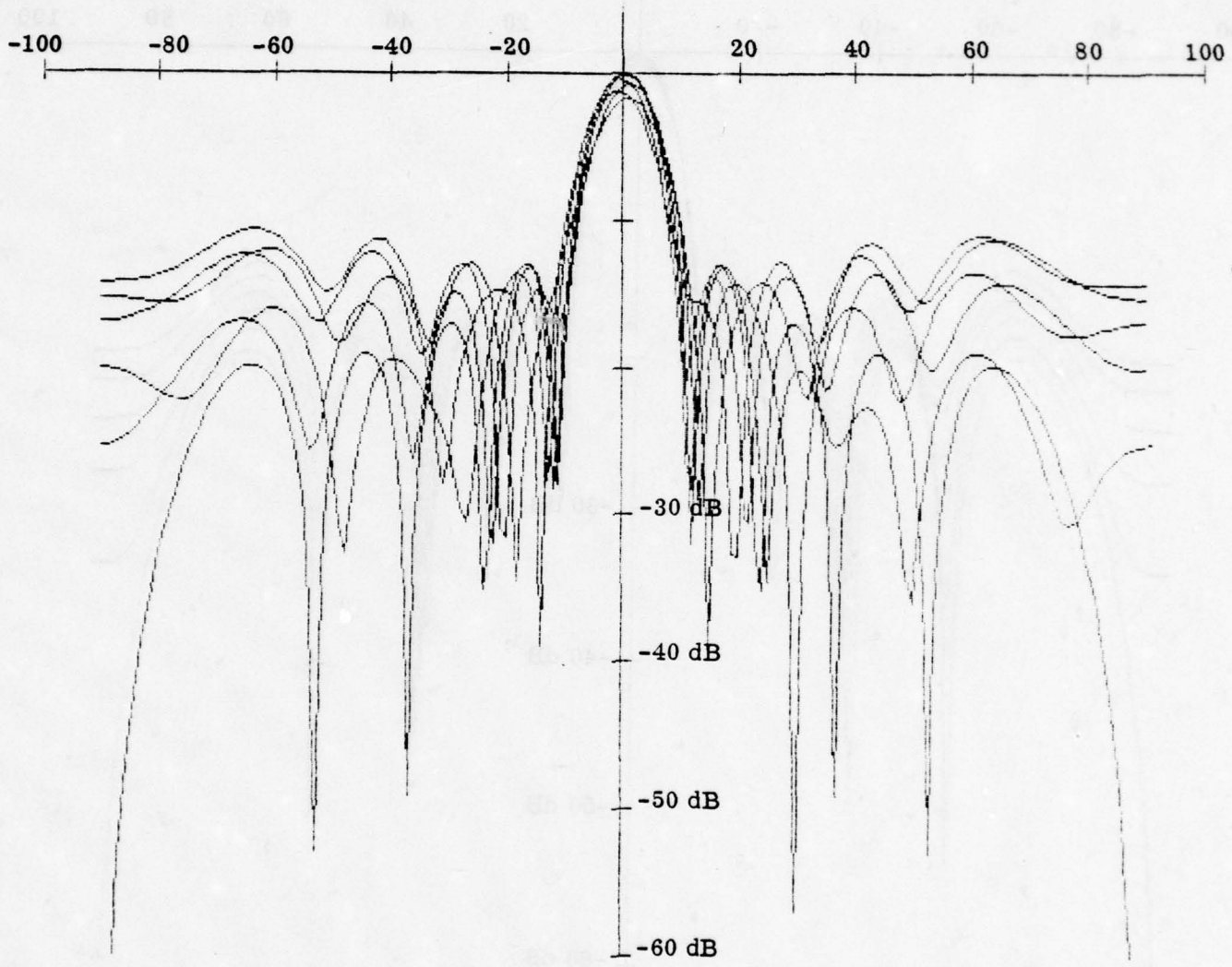

FIGURE 3.3-4
5λ ARRAY SIMULATION: PHASE MODULATION

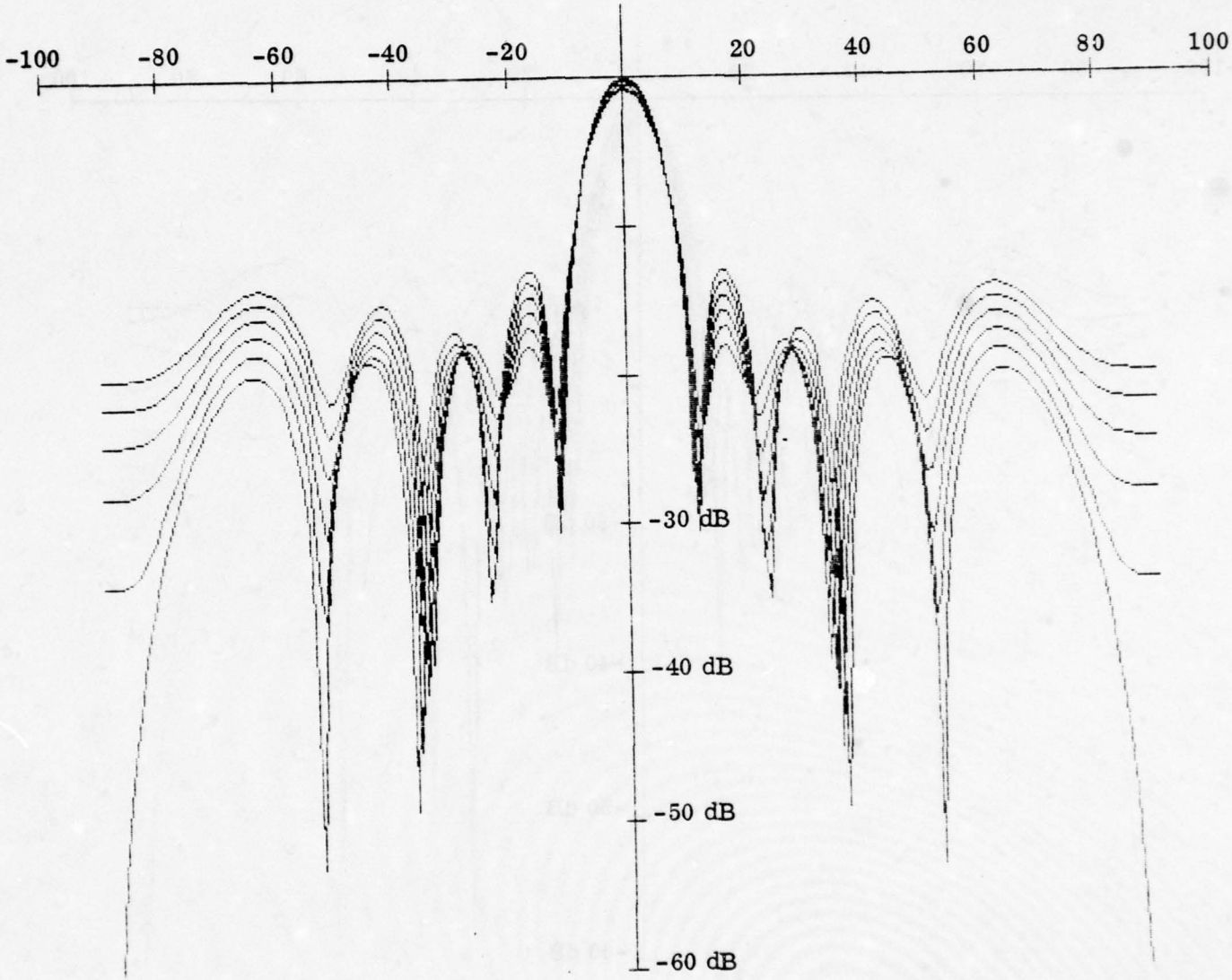

FIGURE 3.3-5
5λ ARRAY SIMULATION: AMPLITUDE MODULATION

A second difference between the two modulations is simply this: The introduction of a nonsymmetrical phase taper on an aperture will cause some degree of beam squint. Beam squint is translated as increased modulation on the main beam and, hence, is an undesirable effect.

A fundamental weakness can be seen in each of the simulation patterns to varying degrees; namely, for certain angles of arrival, sidelobe modulation level is less than the main beam modulation level. These areas are identified as intersections or tangencies in adjacent patterns. Signals arriving in one of these regions cannot be differentiated from a signal arriving on the antenna main beam.

The implementation models of the sidelobe identification techniques thus far have all used a binary (i.e., on/off) type of perturbation, because binary (phase or amplitude) modulation is relatively easy to mechanize.

In order to verify these general conclusions experimentally, a three element array of log periodic dipole (LPD) elements was measured (see Figure 3.3-6). One element feed was phase modulated, while the phase of the other two remained stationary. The amplitude of all elements was equal.

Full patterns were taken with approximately a 1-Hz phase modulation rate. The duty cycle of the modulation was adjusted so the "on and off" conditions could be discriminated on the patterns.

Experimentally measured patterns were made for the array modulation scheme shown in Figure 3.3-6. A delay line-type phase shifter capable of introducing either 0 or 22 degrees of phase shift was used.

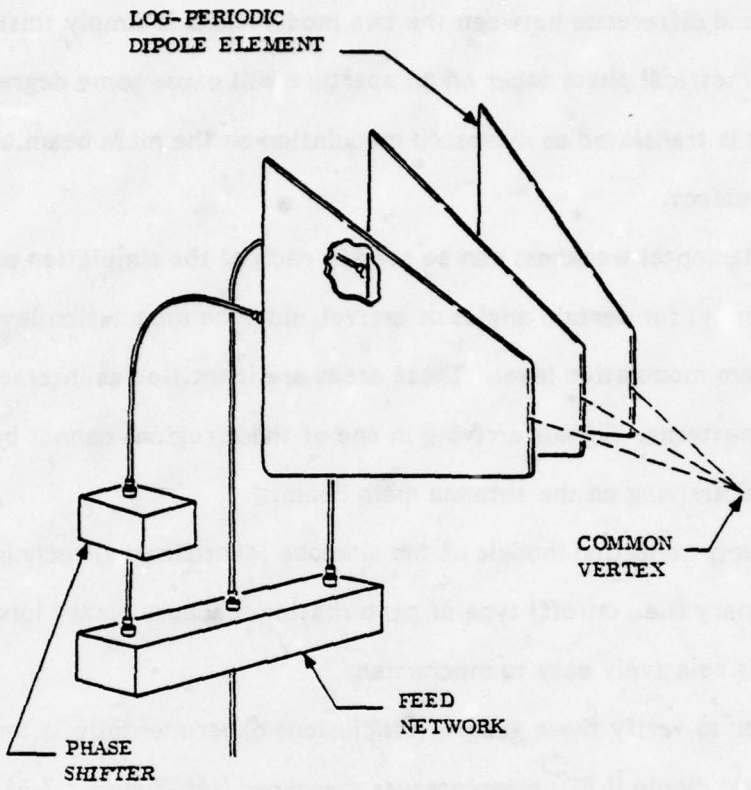

FIGURE 3.3-6
LOG PERIODIC ARRAY

A computer simulation of this selected experimental data set was performed using the technique outlined earlier, with the following modifications:

(1) The array elements were squinted relative to each other and were directive (+8 dBi typically).

(2) Actual measured antenna element patterns were entered and utilized in the array calculations.

Figures 3.3-7 and 3.3-8 are the measured patterns with a binary phase-modulated edge element. Corresponding computer runs were made (see Figures 3.3-9 and -10). Reasonable similarities between the patterns are evident in the position of the first null, beamwidth, sidelobe levels, and modulation.

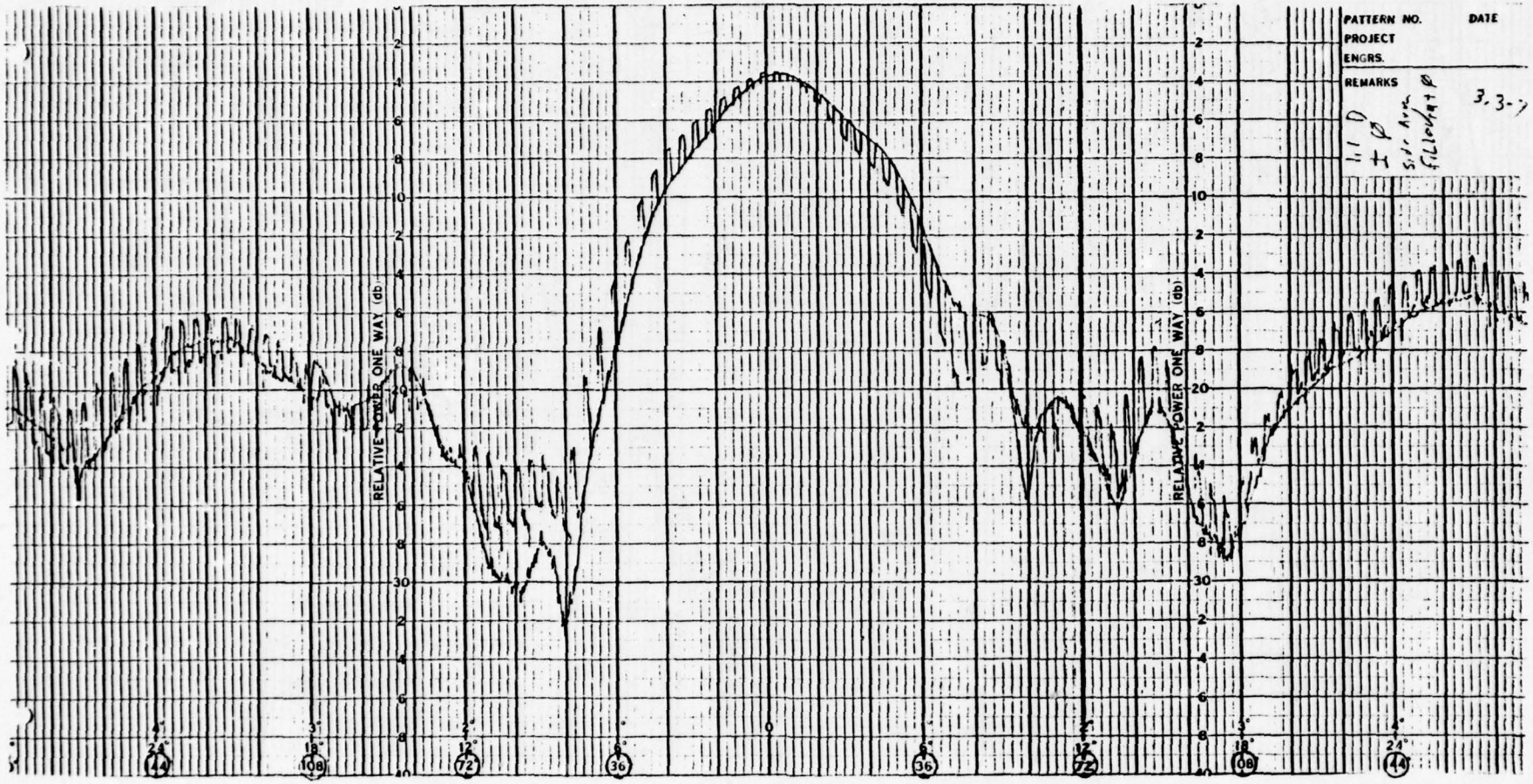

FIGURE 3.3-7
AZIMUTH PATTERNS (1.1 gHz) measured

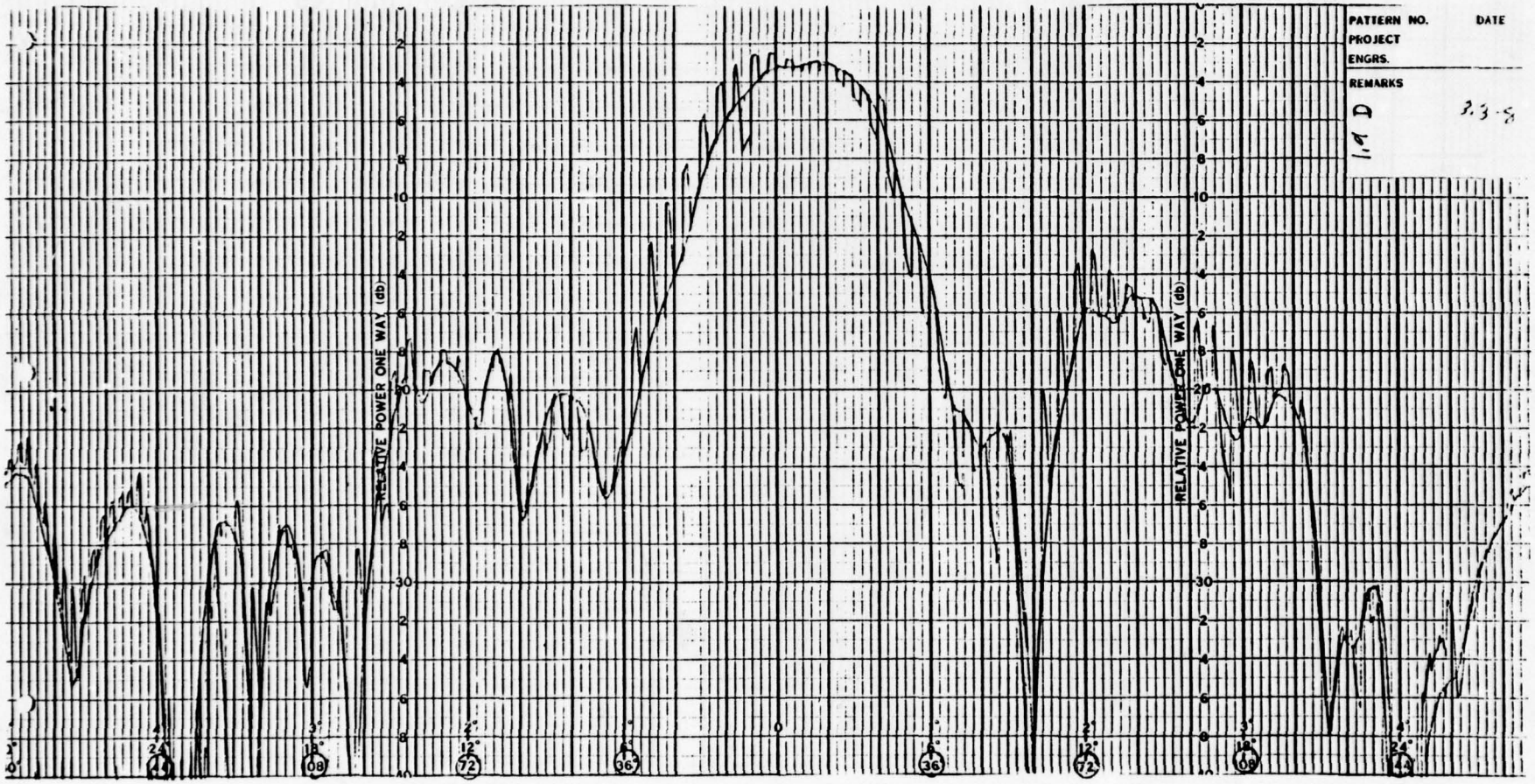

FIGURE 3.3-8
MODULATED 3 ELEMENT ARRAY AZIMUTH PATTERNS (1.9 gHz)

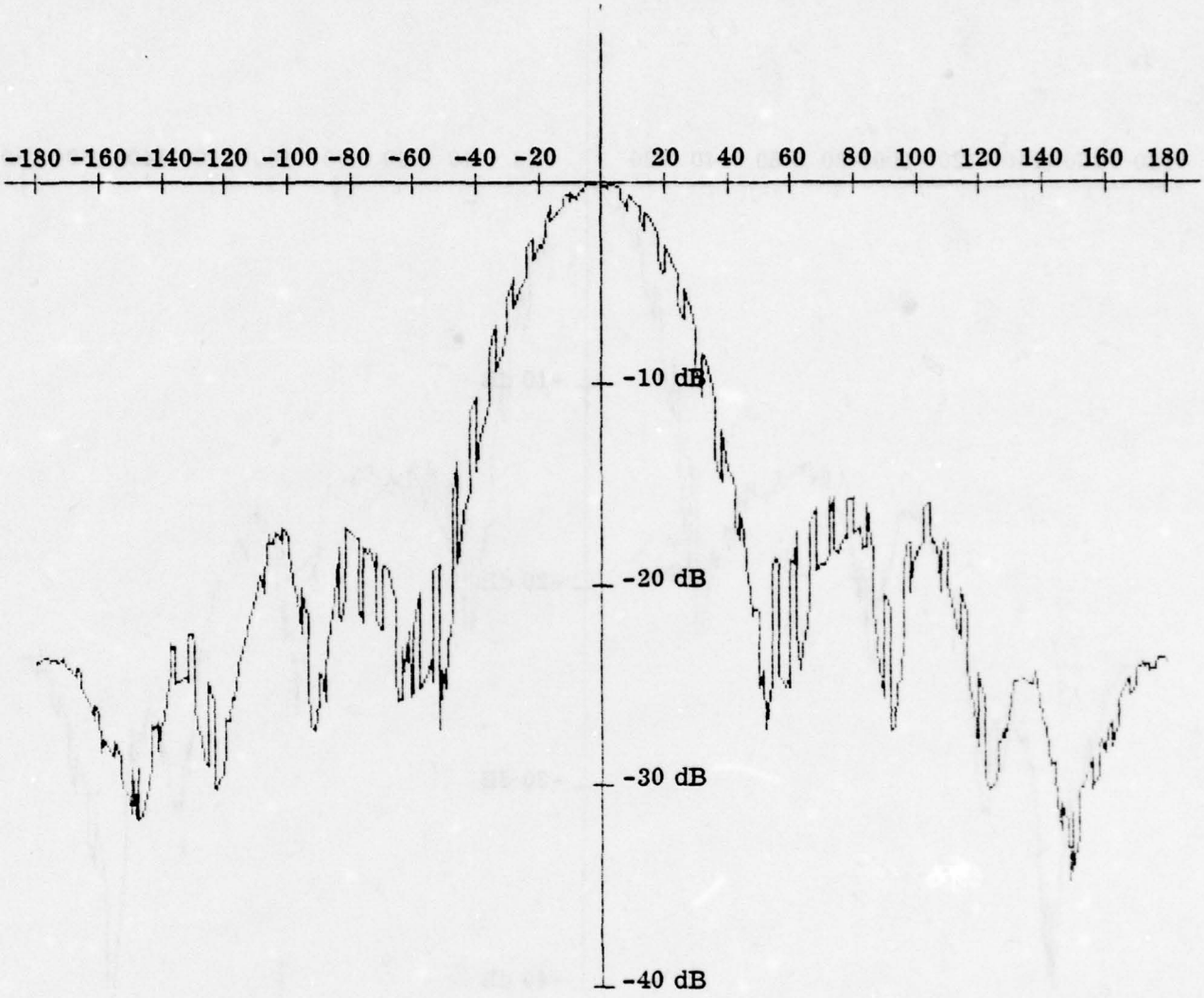

FIGURE 3.3-9
1.1-GHz THREE-ELEMENT LPD ARRAY SIMULATION

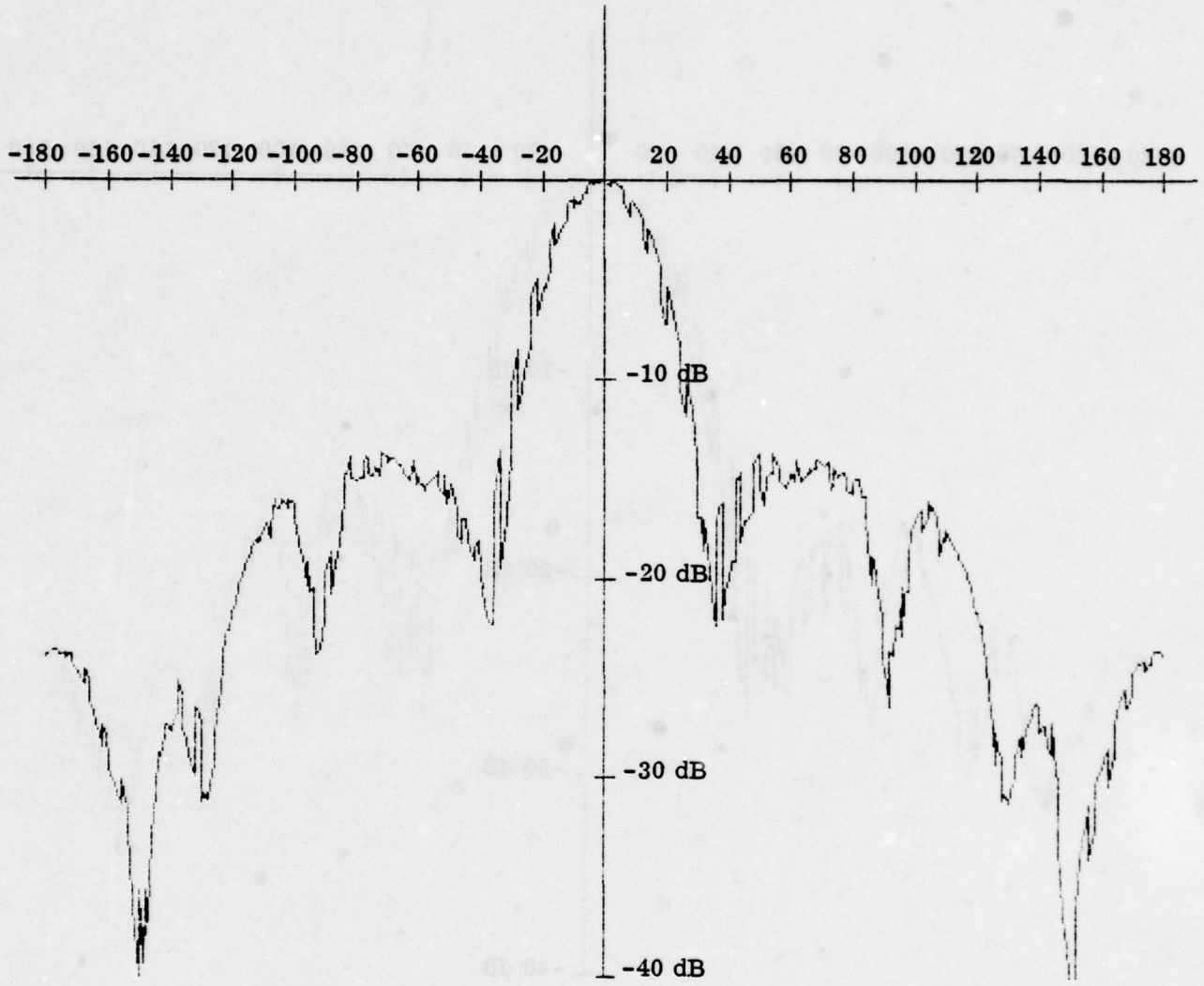

FIGURE 3.3-10
1.9-GHz THREE-ELEMENT LPD ARRAY SIMULATION

4.0 CONCLUSION

Although still in the conceptual stage, the sidelobe identification technique discussed here promises to add a new dimension to the art of sidelobe suppression. An attempt has been made to point out the advantages as well as potential shortcomings of this new technique. Table 4-1 summarizes the general conclusions, including predicted performance tradeoffs, advantages, and disadvantages of the modulating scheme investigated thus far. Ongoing R&D efforts will serve to clarify the design parameters of this technique and explore its potential applications.

TABLE 4-1
SUMMARY OF CONCLUSIONS

	ADVANTAGES	DISADVANTAGES
MECHANICAL SCATTERER	•EXCELLENT MODULATION DISTRIBUTION	•MAXIMUM MODULATION FREQUENCY RELATIVELY LOW
AUXILIARY ANTENNA	•FLEXIBLE/EASILY RETROFITTED CAN BE TAILORED TO INDIVIDUAL SIDELOBE CONFIGURATIONS •FAST	•INCREASED BLOCKAGE AND WEIGHT •RELATIVE PHASE CO-LOCATION PREFERRED •PERIODIC ABSENCE OF MODULATION OF SIDELOBES
ARRAY AMPLITUDE MODULATION	•EXISTING ACTIVE ARRAYS NEED MINIMAL MODIFICATION •REGULAR DISTRIBUTION OF MODULATION •NO MAIN BEAM SCAN •PERFORMANCE INCREASES WITH NUMBER OF ELEMENTS •BEST FOR HIGHLY DIRECTIVE SYSTEMS	•NO LARGE MODULATION VALUES WHEN COMPARED TO PHASE MODULATION
PHASE MODULATION	•EXISTING ACTIVE ARRAYS NEED MINIMAL MODIFICATION •USEFUL FOR LOW AND MEDIUM GAIN ARRAYS •CAUSES LARGE MODULATION IN SOME REGIONS	•MORE DIFFICULT TO IMPLEMENT THAN AMPLITUDE MODULATION •CAUSES BEAM SQUINT, LIMITED HIGH GAIN APPLICATION •MODULATION OCCASIONALLY DISAPPEARS

REFERENCES

1. Weeks, Walter LeRoy, Antenna Engineering. McGraw-Hill, New York: 1968.

2. Silver, S., Microwave Antenna Theory and Design. Radiation Laboratory Series, Vol. 12. McGraw-Hill Book Company Inc., New York: 1950.

3. Kraus, J.D., Antennas. McGraw-Hill Book Co. Inc., New York: 1950.

4. Watson, Peter A., and Samie I. Ghobrial, "Off-Axis Polarization Characteristics of Cassegrainian and Front-Fed Paraboloidal Antennas", IEEEE Trans. Antennas and Propagation, Vol. AP-20 pp. 691, November 1972.

5. Chu Ta-Shing and Turring R.H., "Polarization Properties of Offset Reflector Antennas", IEEEE Trans Antennas and Propagation, Vol. AP-21, No. 3 pp 339-345, May 1973.

*A LOW-INERTIA COMMUTATING FEED FOR CIRCULAR ARRAYS**

by

R.I. Wolfson and C.F. Cho
ITT Gilfillan, Van Nuys, California 91409

* The work described herein was supported by the United States Air Force, Electronic Systems Division, Hanscom AFB, through Contract No. F19628-79-C-0034 and under the direction of Mr. Walter Rotman and Lt. Gregory Cruz.

ABSTRACT

This paper describes the development of a low-inertia commutating feed for azimuth steering the beam of a circular array. In addition to superior electrical performance over that of an electronic system, the commutator offers improvements in reliability and life-cycle cost (LCC). It can be accessibly located where maintenance actions are more easily carried out than in an electronically-scanned system or a conventional rotating antenna. Noncontacting loop couplers achieve low-loss transfer and distribution of RF energy, with precise control of amplitude and phase that is needed to realize low sidelobe levels. This method of coupling is preferable to the capacitive coupling used in existing electromechanical commutating feeds, where illumination flutter results in unacceptable MTI performance. To obtain multiple beam groups in elevation, two or more commutators may be stacked on a common drive shaft.

Section I

INTRODUCTION

An electronically-scanned circular array antenna is advantageous for applications where 360-degree azimuth scan is required, and where the characteristics of the beam must remain unchanged for every azimuth angle. Electronically scanning a set of three or more planar phased arrays can provide the required 360 degrees of coverage, but results in beam distortion as the angle varies. Mechanically rotating antennas provide the required beam characteristics, but usually do not have the required data rate.

Existing all-electronic circular arrays also have disadvantages. In a practical configuration, they require many active subassemblies with an unacceptably large amount of loss, and they require frequent maintenance. In addition, variations in subassembly characteristics due to component differences may cause small variations in the beam characteristics with azimuth scan angle, as well as high sidelobes. The existing Wullenweber electromechanical commutating feed has the desirable low drive power and high reliability, as it uses a low-inertia mechanically rotating feed. In that device, the power is capacitively coupled from a rotating to a stationary transmission line that connects to the large circular array elements. However, the capacitive coupling used causes unacceptable loss and flutter, or fluctuations in the radiated beam with rotational angle.

Large-scale parallel-plate combiner/dividers have been developed by ITT Gilfillan that make use of a magnetic loop coupler. This device derives its properties from both the waveguide loop coupler and the -3 dB quarter-wave directional coupler. In the waveguide version, matched coupling to the dominant mode is obtained by proper quarter-wave transformation of the waveguide impedance to that of the coaxial input. Wide bandwidth is ensured by coupling to the fields in a manner that minimizes impedance change, thereby reducing the Q of the network. The use of magnetic loop couplers in a commutating feed provides low RF loss and inertia while limiting flutter to the narrow range of angles where the rotor loops pass over small gaps between adjacent stator loops.

One of several antenna concepts being considered for systems such as the Unattended Radar (UAR) is a circular array, shown in Figure 1. The principal motivations for such an approach over a conventional rotating antenna are reduced drive power, improved reliability, and availability of simplified maintenance. Over the past decade, numerous purely electronic scan concepts for circular arrays have been developed. All of these approaches have been plagued by high loss and poor reliability due to the large number of components in series, and poor sidelobe performance due to large amplitude and phase errors.

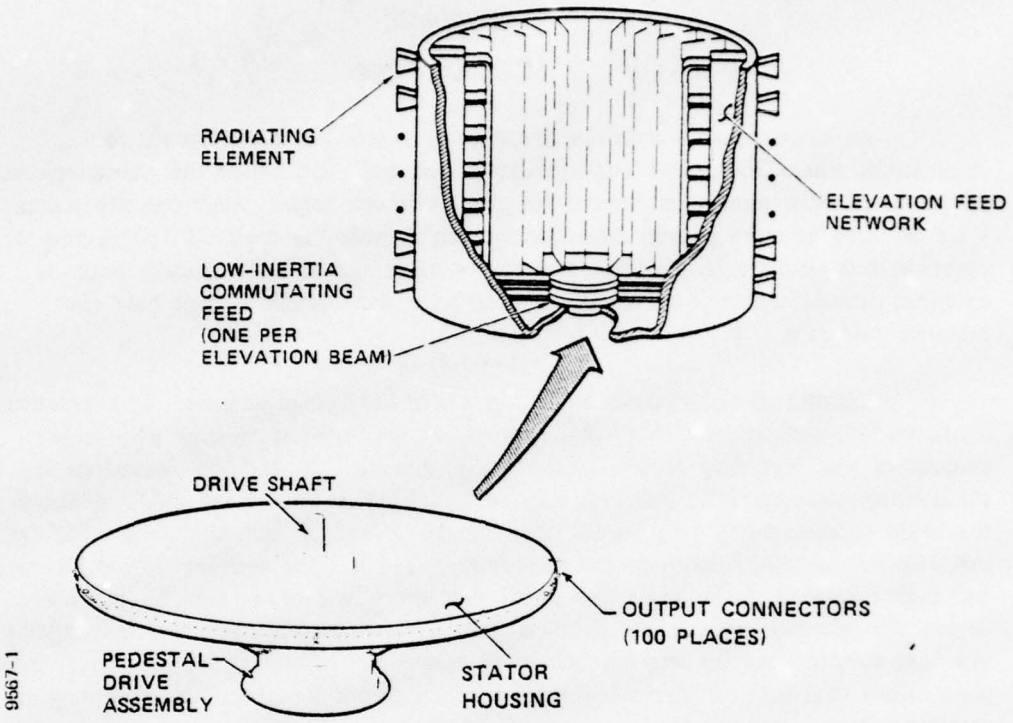

Figure 1. Circular Array Antenna with Low-Inertia Commutating Feed

To address these problems, the Department of the Air Force, Electronic Systems Division, has funded ITT Gilfillan to develop, construct and evaluate a Commutating Feed Assembly for steering the beam of a circular array. The advantages of such an approach are simplicity, low cost, and low drive power. Properly designed, such a commutator offers superior electrical performance over an electronic system and significant improvements in reliability and LCC.

Table I presents a summary of the requirements for the Commutating Feed Assembly. Significant mechanical requirements include a drive power of below 50 watts, and the ability to stack two or more commutators for systems with multiple beams. In addition, the system concept should be readily extendable to a circular array with approximately 200 outputs, with as many as one-third of these excited at one time. Other important considerations are the environmental conditions encountered in the Arctic, as well as the extremely high MTBF required for unattended operation. For high-performance radar operation, low phase and amplitude variations are required for good MTI performance.

TABLE I. COMMUTATING FEED ASSEMBLY REQUIREMENTS

Frequency Band	1.2 to 1.4 GHz
Number of Output Ports	100
Number of Excited Ports	26
Excited Sector	90°
Aperture Illumination	Consistent with -20 dB sidelobes
VSWR	
Input	1.3:1 maximum
Output Ports	1.3:1 maximum
Insertion Loss	1.0 dB maximum
Power Capacity	
Peak	10 kW
Average	500W
Rotation Rate	15 rpm
Drive Power	50W maximum
Environment	-35°F to +100°F minimum (as encountered in Arctic)
Reliability	Consistent with Unattended Radar operation
Stacking	2 or more Commutators
Growth	200 Outputs 68 Excited

Section II

ANTENNA DESIGN CONSIDERATIONS

A. PATHLENGTH COMPENSATION

In order to obtain a planar wavefront from a circular array of radiating elements, it is necessary to compensate for unequal pathlengths that occur in space due to curvature of the array. The geometry for this situation is illustrated in Figure 2. The differential pathlengths, relative to the edge elements, that are required for a planar wavefront are given by the equation

$$\Delta\ell_n = \frac{R(\cos\phi_n - \cos\phi_{max})\cos\theta}{\sqrt{\epsilon_r}}$$

where:

R	=	radius of circular array,
ϕ_{max}	=	one-half of sector angle,
ϕ_n	=	angle of nth element relative to center of sector,
θ	=	desired elevation scan angle for zero phase error, and
ϵ_r	=	*relative dielectric constant of stripline feed.*

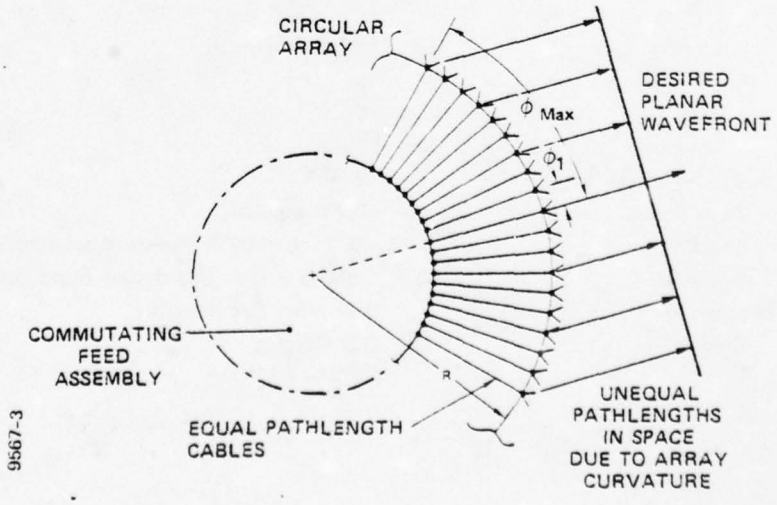

Figure 2. Pathlength Variations in Circular Array

Note that the differential pathlengths, $\Delta\ell_n$, required for a planar wavefront are a function of elevation scan angle, θ. Thus, the circular array can be compensated exactly only at one preselected value of elevation scan angle. A value of 15 degrees is assumed, as this angle is the maximum value of θ for which there is essentially no degradation in beamwidth and sidelobe performance at the horizon. As $\Delta\ell_n$ is independent of frequency, this configuration is inherently broadband.

B. ILLUMINATION FUNCTION

Three types of illumination functions were considered for this application: Taylor, Chebyshev, and a modified (sin u)/u. The Taylor illumination produces a determined number of near-in sidelobe pairs at the design level, after which the sidelobe structure gradually decays to the level established by random errors. For the model circular array of 100 elements, a -29 dB, $\bar{N} = 4$ Taylor function is chosen because it results in the best compromise between sidelobe level and aperture efficiency, and in practice, the element-coupling values are readily achievable.

Azimuth patterns were computed at 1.4 GHz for the 100-element model array with diameters of 180, 160, and 135 inches. As shown in Figure 3, high grating lobes appear in the two arrays with the largest interelement spacings, 0.67 and 0.60 wavelength at this frequency. The exact level of grating lobe is influenced appreciably by the azimuth pattern of the individual elements. Figure 3 was computed assuming a cosine element power pattern.

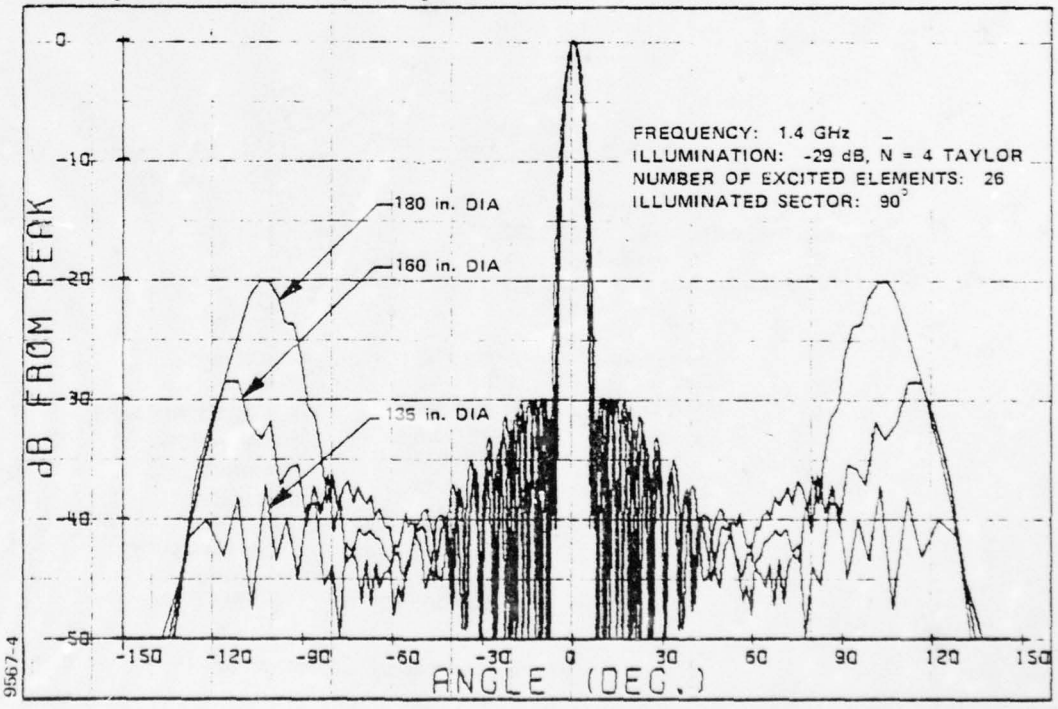

Figure 3. Computed Azimuth Patterns of 100-Element Circular Array Antenna

Section III

COMMUTATOR DESIGN

A simplified block diagram of the commutator is shown in Figure 4. The annular rotary coupler is a special design that provides two equal-amplitude, in-phase RF output signals.

The rotating stripline feed network consists of a center-fed array of directional couplers, delay lines for phase compensation, phase trimmers, and printed-circuit rotor coupling loops.

The stationary housing includes the support structure, pedestal drive assembly, bearings, RF chokes, stator coupling loops, and output connectors.

A. STRIPLINE FEED NETWORK

Several types of array feed networks were considered for this application. Parallel or corporate-feed approaches were rejected because of their high sensitivity to coupling errors, difficulty in realizing the required illumination with a reasonable range of coupling values, and excessive size. Center-fed equal-pathlength (before phase compensation) series array feeds were selected for their low loss, wide bandwidth, relative insensitivity to coupling errors, and compact form factor. A layout of the stripline feed network is shown in Figure 5. Note that the two halves are identical mirror images of one another.

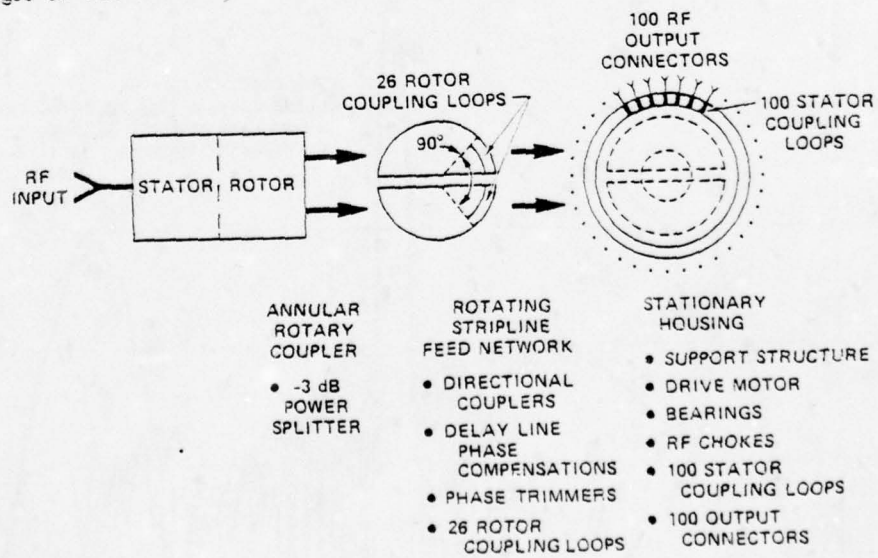

Figure 4. Block Diagram of Commutator

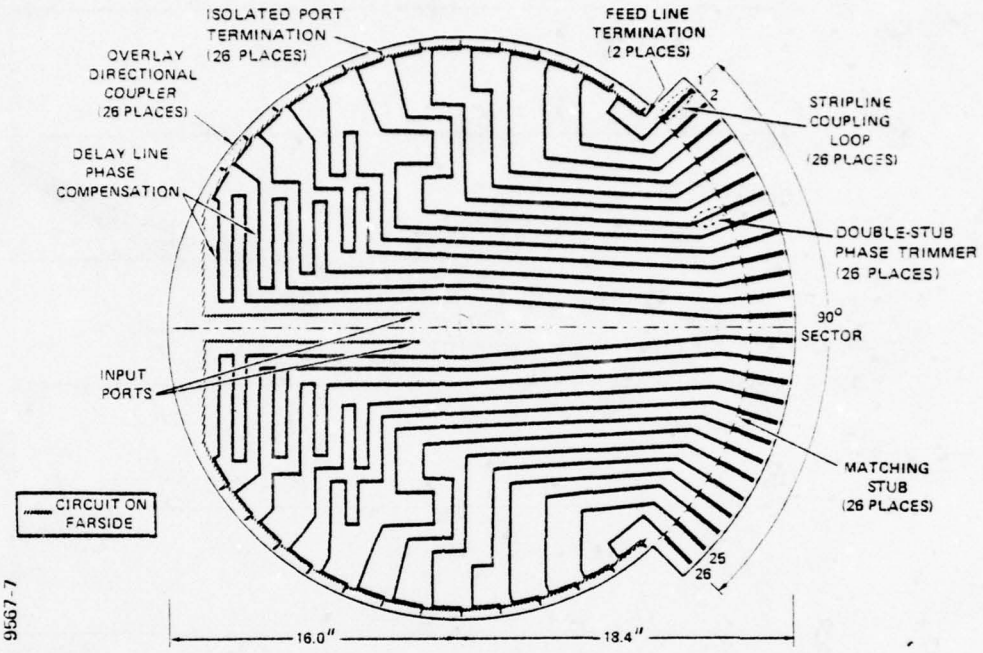

Figure 5. Stripline Feed Network

A tradeoff study was made of key parameters for the commonly used stripline coupler configurations. The $\lambda/4$ overlap directional coupler was selected because the required values of coupling are easily achieved, and coupling flatness, VSWR, isolation, and phase runout are excellent over wide operating bandwidths. One drawback of this type coupler, however, is that a three-layer construction with accurate front-to-back registration is required.

Design information for the overlap directional coupler is described in the literature;[1] however, a modified configuration with the isolated-port arm crossing over the main feedline was developed so that the terminating resistor of each coupler could be externally located for accessibility.

A tradeoff exists in the design of a series feed network between the range of element coupling factors and the amount of power dissipated in the mainline load termination. This is illustrated in Figure 6, for a 13-element series feed with -29 dB, $\bar{N} = 4$ Taylor illumination. It can be seen that with no power into the end load, a wide range of coupling factors is required: 0 dB to -7.47 dB. With 3 percent power into the end load, which represents an additional insertion loss penalty of only 0.13 dB, a more viable range of design coupling factors is obtained: -5.56 dB to -7.60 dB. The use of nearly equal coupling factors also gives better element-to-element amplitude and phase tracking, so that array performance at the operating band edges is only minimally affected.

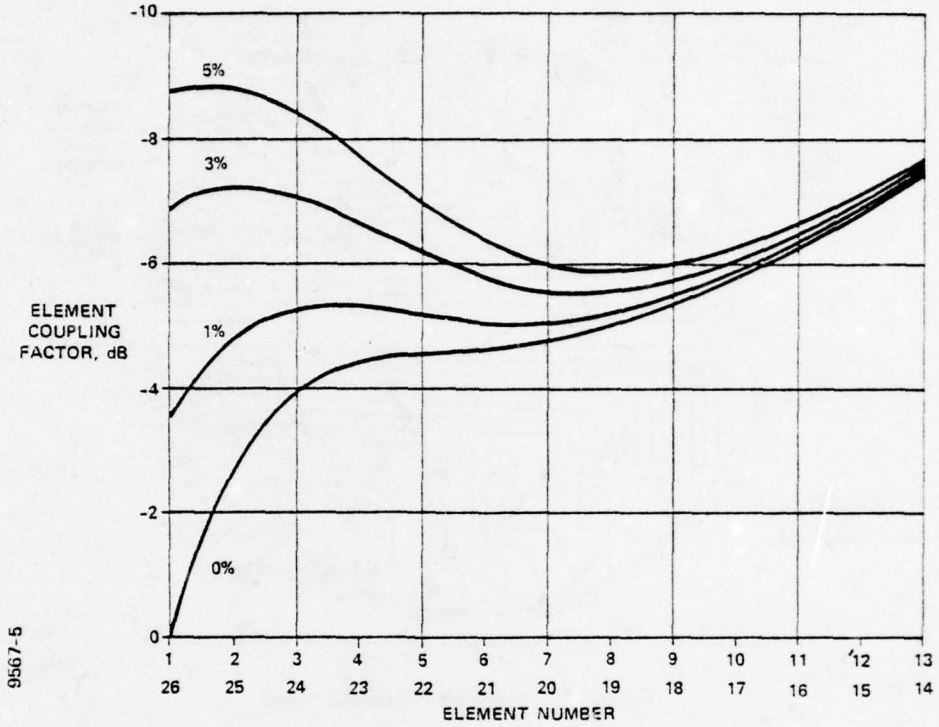

Figure 6. Element Coupling Factor vs Element Number for various percents Power into End Load

USE OR DISCLOSURE OF PROPOSAL DATA IS SUBJECT TO THE
RESTRICTION ON THE TITLE PAGE OF THIS PROPOSAL

The two stripline assemblies, each consisting of a central 0.020-inch thick etched circuit board and two 0.125-inch thick dielectric sheets, are bonded under heat and pressure to form rugged, trouble-free units. These "unitized" stripline assemblies are then mechanically mounted between a pair of 0.063-inch thick aluminum ground planes, approximately three feet in diameter, to form the rotating feed network, which is shown mounted in the stationary housing in Figure 7.

The rotor loops are fabricated by etching them directly on the stripline circuit board, and grounding the ends of the loops to the ground plane by means of shorting pins. This solves the problem of how to attach the rotor loops both mechanically and electrically to the stripline feed network in an inexpensive and reliable fashion.

B. MAGNETIC LOOP COUPLER

The magnetic loop coupler can be considered a conventional $\lambda/4$ directional coupler, modified to produce a zero-dB coupler as illustrated in Figure 8. The approximate performance of this configuration can be described by modifying the analytical expressions for broadside coupled lines.[2]

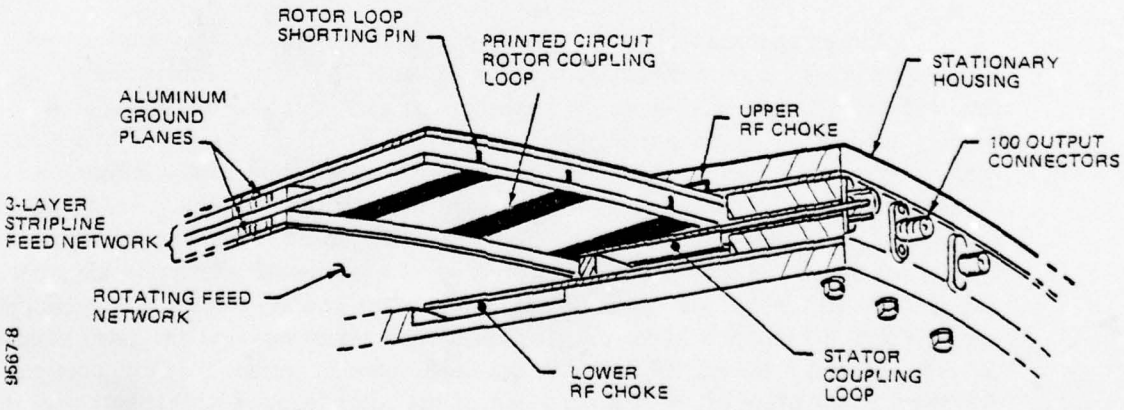

Figure 7. Rotating Feed Network mounted in Stationary Housing

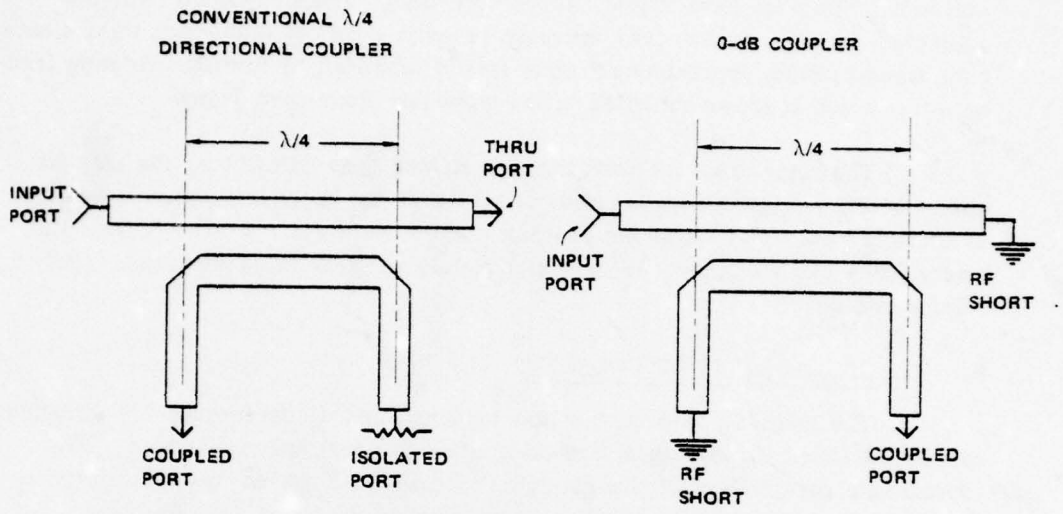

Figure 8. Conventional λ/4 Directional Coupler modified to Obtain 0-dB Coupler

Proper operation of the magnetic loop couplers requires that the quarter-wavelength loops are terminated in a reliable, low-loss RF short. This is easily accomplished for the stator loops by means of the aluminum shorting bar that is used to support the grounded end of each loop. The problem is more complicated for the rotor loops, which continually move relative to the commutator housing. A contacting short is undesirable from the standpoint of loss, reliability, wear and the generation of electrical contact noise. Therefore, RF chokes of the standard double quarter-wavelength design are used to provide noncontacting RF shorts for the rotor loops. Two RF chokes are required: one in the lower housing surface that produces an RF short in the plane where the stripline ground planes end and the rotor coupling loop begins; and a second RF choke in the upper housing surface that produces an RF short in the plane of the grounded end of the rotor loop. Each choke cavity is made by machining an annular groove in the inner housing surface, and then using a washer-shaped ring to form the folded quarter-wavelength sections.

To achieve highly-efficient, wideband, power transfer there exists a multitude of parameters that must be optimized experimentally: the length, width and ground-plane spacing of both the rotor and stator loops, the gap between adjacent stator loops, and most critically, the separation between rotor and stator loops.

Section IV

EXPERIMENTAL RESULTS

A. MODIFIED OVERLAP DIRECTIONAL COUPLER

After several iterations, the design of the modified (isolated-port arm "flipped") overlap directional coupler was optimized for three coupling values over the desired range: -5.0, -6.5, and -8.0 dB. Measured data were used to generate the design curves shown in Figures 9 and 10. The measured coupling, isolation, and VSWR for the nominal -6.5 dB coupler design are shown in Figures 11 and 12. Although this coupler was intended for the 1.2 to 1.4 GHz band only, note the excellent performance of the device over the extended band, 1.0 to 1.6 GHz.

B. LOOP COUPLER TEST FIXTURE

The design of the rotor and stator loops was optimized with the use of several test fixtures, one of which is shown in Figure 13. Five rotor loops of different widths from 0.2 to 0.4 inch can be seen. This test fixture is constructed such that the ground-plane spacing of the rotor loops, as well as the separation between rotor and stator loops, can be varied.

The measured swept-frequency insertion loss for the 0.25-inch wide rotor loop, positioned directly over a stator loop, is shown in Figure 14.

The coupling performance varies somewhat as the rotor loops pass over the stator loops. These variations are minimized in magnitude and duration by using narrow rotor loops and much wider stator loops. Of course, during the interval when the rotor loop is over the gap region between adjacent stator loops, it couples equally to these two stator loops; hence, the coupling falls below -3 dB. This effect is seen in Figure 15, which was measured at 1.3 GHz for the 0.25-inch wide rotor loop. The impact of this large amplitude change on the array pattern can be avoided either by staggering the relative location of rotor and stator loops so that all nulls do not occur simultaneously, or by transmitting and receiving only when loops are well engaged.

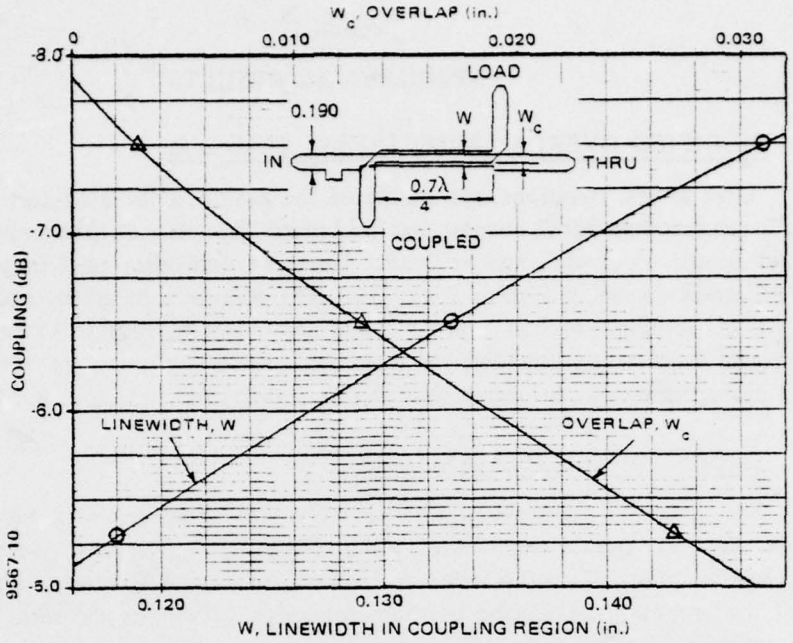

Figure 9. Design Curve for modified λ/4 Overlap Directional Coupler

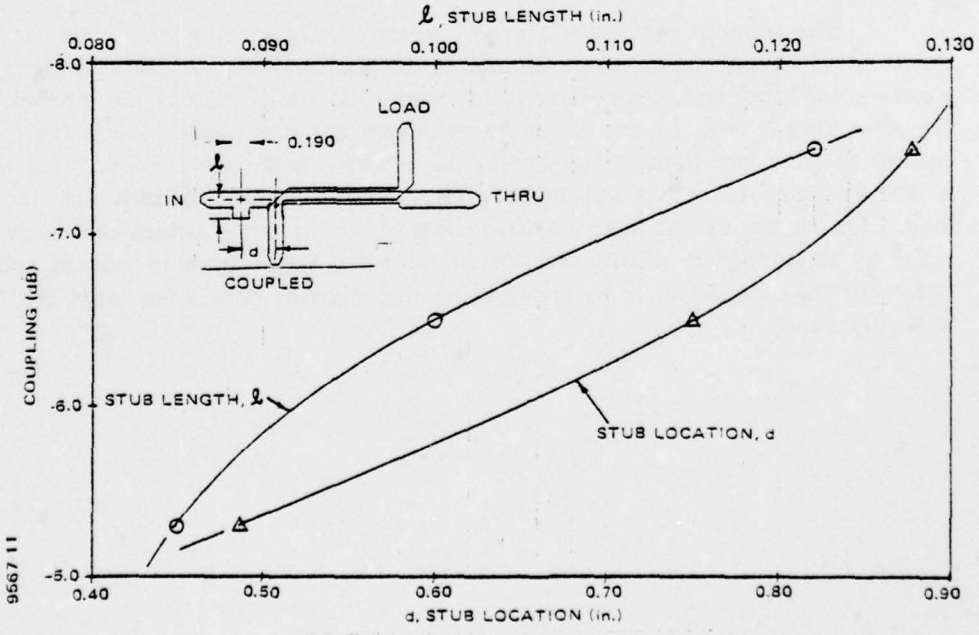

Figure 10. Matching Stub Length and Location

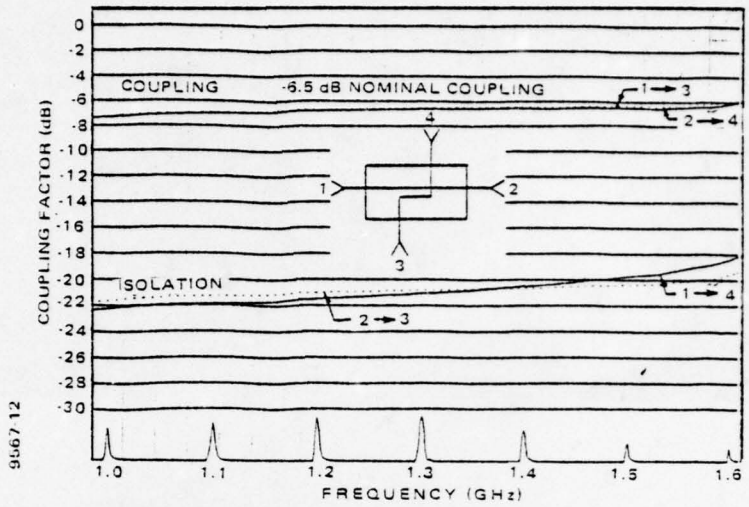

Figure 11. Measured Coupling and Isolation vs Frequency of modified λ/4 Overlap Directional Coupler

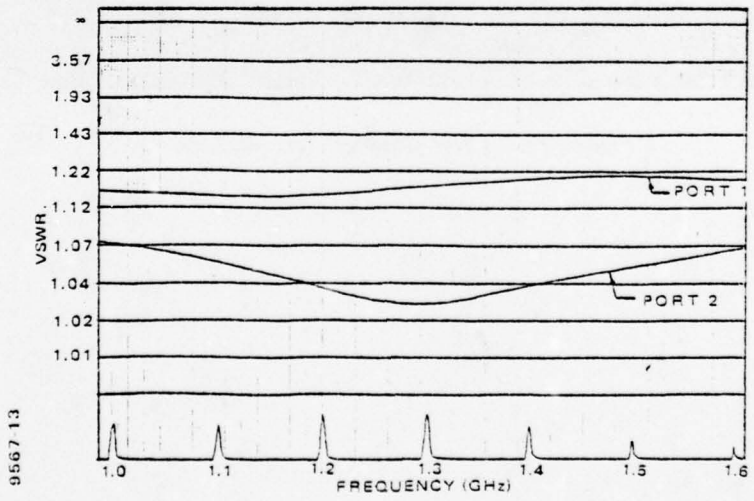

Figure 12. Measured VSWR vs Frequency of modified λ/4 Overlap Directional Coupler

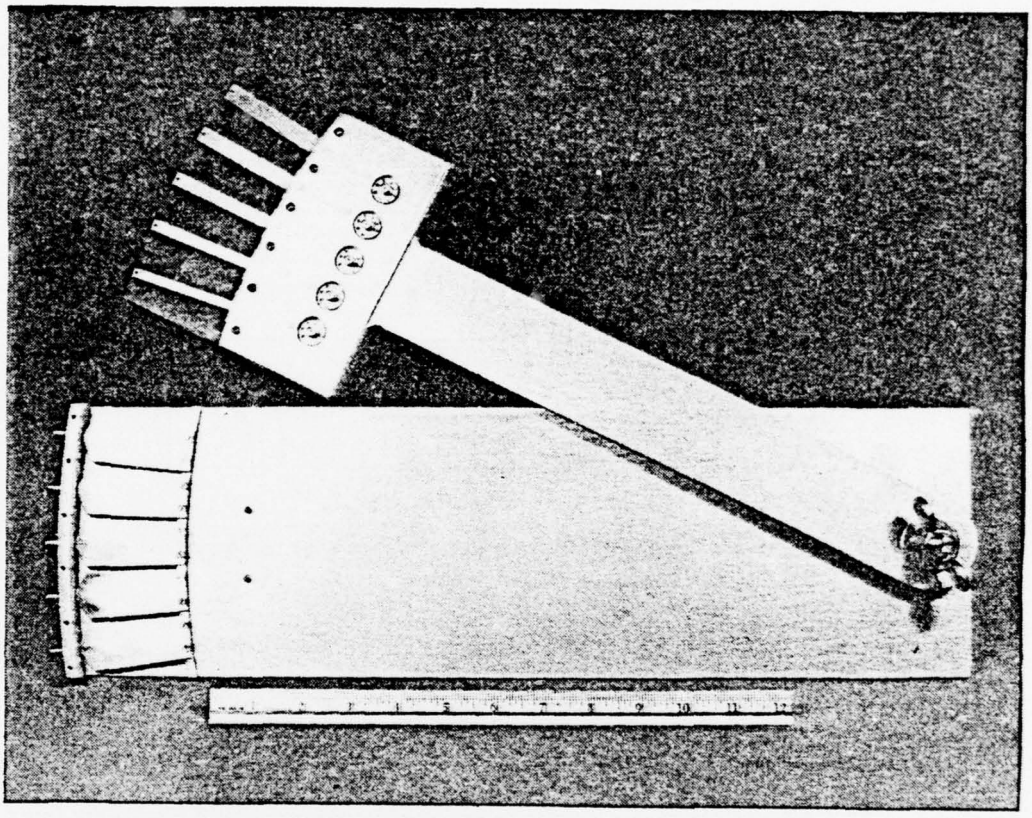

Figure 13. Loop Coupler Test Fixture

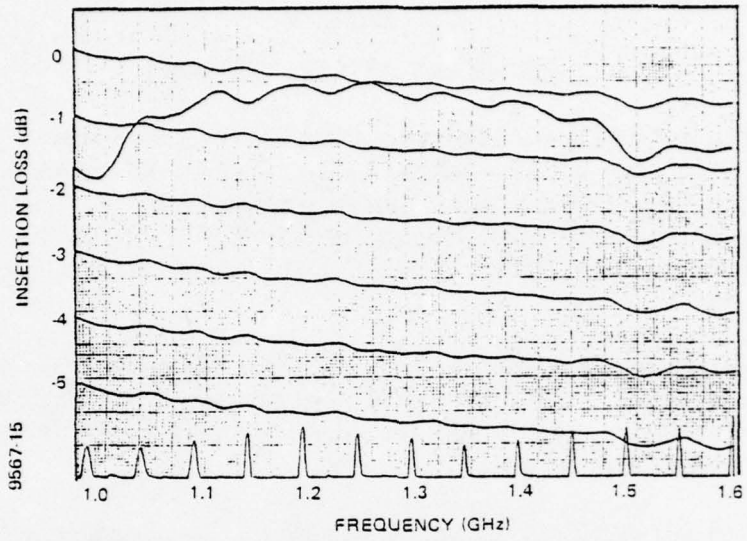

Figure 14. Measured Insertion Loss vs Frequency of Loop Coupler Test Fixture

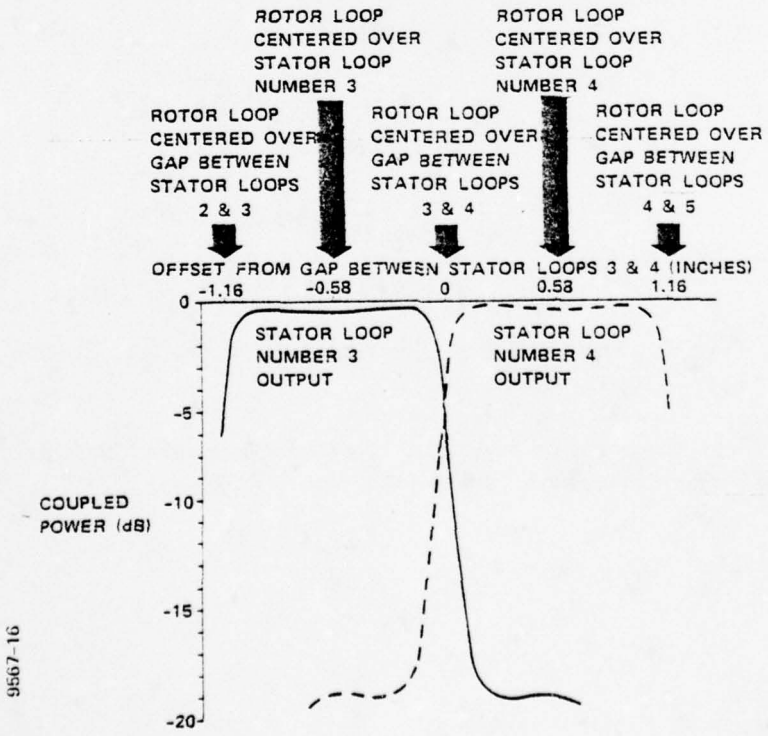

Figure 15. Measured Loop-Coupled Power vs Offset

USE OR DISCLOSURE OF PROPOSAL DATA IS SUBJECT TO THE RESTRICTION ON THE TITLE PAGE OF THIS PROPOSAL

Section V

SUMMARY AND CONCLUSIONS

The development of a low-inertia commutating feed for azimuth steering the beam of a circular array has been described. The stripline feed network has been configured, and the $\lambda/4$ overlap directional couplers, used in the series array feeds, have been built and tested. These couplers are flat within ±0.25 dB, with isolation greater than 18 dB, and VSWR less than 1.07:1 over the operating frequency band of 1.2 to 1.4 GHz.

Noncontacting magnetic loop couplers for low-loss transfer and commutation of RF energy have been built and evaluated. Insertion loss of only 0.2 dB is achieved over the 1.2 to 1.4 GHz frequency band, and less than 0.5 dB over the extended range of 1.1 to 1.5 GHz.

When fabrication and assembly are completed, the commutating feed is expected to offer superior electrical performance over that of electronic scanning systems, as well as to provide significant improvements in reliability and LCC.

Section VI

REFERENCES

1. H. Howe, Jr., *Stripline Circuit Design*, Artech House, Inc., Dedham, Ma., 1974, pp. 126, 132-150, 153-157.

2. S. Cohn, *Characteristic impedance of broad side coupler transmission lines*, IEEE Trans. Microwave Theory Tech, Vol. MTT-8, pp. 633-637, 1960.

September 1979

A HIGHLY THINNED ARRAY USING THE IMAGE ELEMENT ANTENNA

Presented at the Third Annual Antenna Applications Symposium
Robert Allerton Park, Illinois

By

Raymond G. Immell
and
Bill H. Sasser

MOTOROLA
Government Electronics Division
8201 E. McDOWELL ROAD, SCOTTSDALE, ARIZ. 85252

1. INTRODUCTION

This report presents the results of an investigation into the potential for obtaining usable directive gain enhancement from common radiating elements such as slots, dipoles, or spirals. A short article by Giswalt Von Trentini[1] showed that the gain of a simple radiating element could be increased to arbitrarily large values simply by placing the element between two reflecting planes, one of which is a semi-reflector and the other a perfect reflector. The operation of this antenna is based on the theory of images or reflections. Therefore, this type of antenna has been designated the Image Element Antenna. The background and development of the Image Element Antenna and the feasibility of using it as an element in an array is the topic of study in this report.

2. THEORY OF OPERATION

A large conducting screen placed behind an antenna can serve as a shield against backward radiation and also affects, depending on its spacing, the forward pattern.[2] Improved directivity in the normal direction is possible only to a limited degree because the illumination of the reflecting screen is not optimum and the rays reflected from more distant zones produce out-of-phase contributions.

Von Trentini found that improved illumination and increase in directivity, and therefore in gain, could be obtained by adding a partially reflecting sheet in front of the antenna and parallel to the reflecting screen, thereby causing multiple reflections between the sheet and screen. The distance between the sheet and screen must be such that the partial rays transmitted through the sheet into space have equal phases in the desired direction of maximum radiation (usually normal to the sheet).

This section will present a summary of the analysis of the image antenna. The basic image antenna can be most readily analyzed in terms of a ray approach in conjunction with transmission line theory. The transmission line approach was chosen for analysis in order to take advantage of the concise and readily manipulated calculations possible for this type of model.

2.1 ANALYSIS OF BASIC IMAGE ANTENNA

Figure 2-1 shows the physical model of the image antenna, consisting of a radiating aperture located in the plane of an infinite ground plane and a partially reflecting sheet placed above the ground plane which introduces multiple reflections with decreasing amplitudes between the two planes. As can be seen from the figure, the reflections form a series of virtual sources or images behind the initial source, whose spacing is twice the spacing to the partially reflecting sheet and whose amplitudes decline geometrically as the reflection coefficient of the partially reflecting surface.

If the complex reflection coefficient is given as: $\rho e^{j\psi}$

then: ρ^2 is equal to the power reflection coefficient and from conservation of energy $1-\rho^2$ is equal to the amplitude of the power transmission coefficient. Therefore the amplitude of the transmitted ray is $\sqrt{1-\rho^2}$. For the once reflected ray 1 the incident power amplitude is ρ^2. One can see that the amplitude of the electric field of the once reflected ray is $\rho\sqrt{1-\rho^2}$. The electric field intensity in the Fraunhofer zone consists of the vector sum of these partial rays, and for an infinite screen and ground plane we may write

$$E = \sum_{n=0}^{\infty} f(\alpha) E_o \rho^n \sqrt{1-\rho^2} \quad e^{j\theta_n} \qquad (2\text{-}1)$$

AD-A077 167 ILLINOIS UNIV AT URBANA-CHAMPAIGN ELECTROMAGNETICS LAB F/G 17/9
PROCEEDINGS OF THE ANTENNA APPLICATIONS SYMPOSIUM (1979) HELD 2--ETC(U)
SEP 79 F19628-79-M-0015
UNCLASSIFIED NL

3 OF 6
ADA 077167

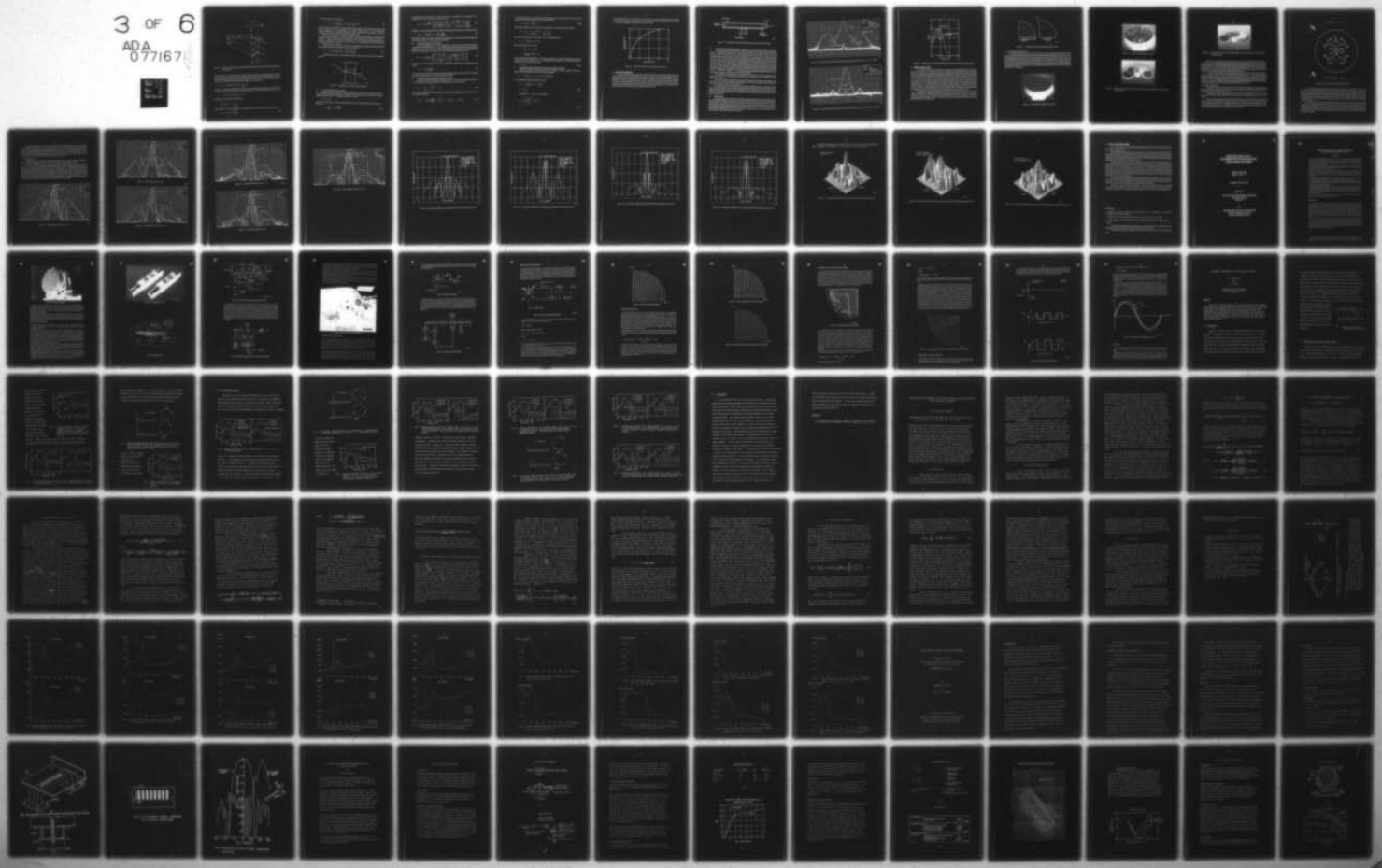

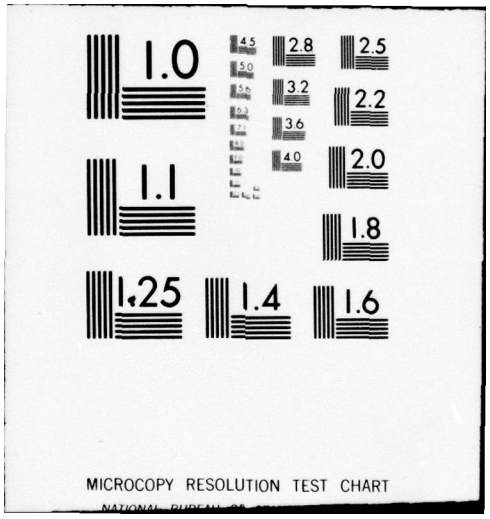
1.0
1.1
1.25
1.4
1.6
1.8
2.0
2.2
2.5
2.8
3.2
3.6
4.0
4.5
5.0
MICROCOPY RESOLUTION TEST CHART

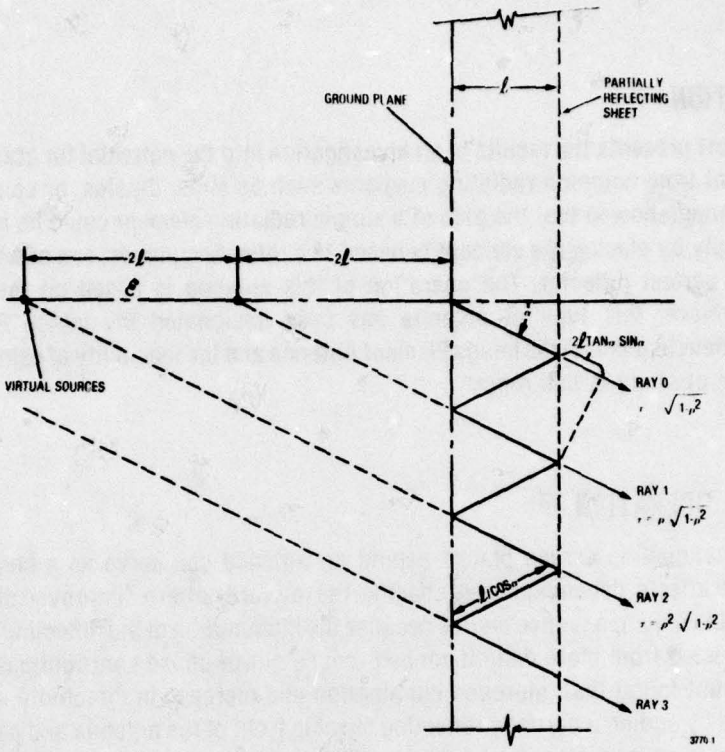

Figure 2-1. Image Array Geometry Showing Multiple Reflections Between Partially Reflecting Sheet and Ground Plane

The phase angle θ_n is composed of the phase delay resulting from the reflections between ground plane and partially reflecting screen, and also the path differences of the partial rays. An additional phase shift occurs when a partial ray passes through the sheet, but because this is the case for all rays it will be ignored. From Figure 2-1 we may derive the phase difference between ray 1 and ray 0 as

$$\theta_1 = \beta(2\ell\tan\alpha\,\sin\alpha) - \beta(2)\,\frac{\ell}{\cos\alpha} - \pi + \psi$$

The term $-\pi$ comes from the phase reversal that occurs at the ground plane. The term ψ is the phase shift that occurs during reflection from the partially reflecting screen. This phase difference has the form of

$$\theta_n = n\phi = n\left[-\frac{4\pi}{\lambda}\ell\cos\alpha - \pi + \psi\right]$$

Because $\rho<1$, we can obtain the following

$$\sum_{n=0}^{\infty}(\rho e^{j\phi})^n = \frac{1}{1-\rho e^{j\phi}}$$

Inserting this term into the expression for the electric field (2-1) and taking the absolute value yields

$$E = f(\alpha)\,E_0\,\frac{\sqrt{1-\rho^2}}{1-\rho e^{j\phi}} \qquad (2\text{-}2)$$

The power pattern therefore becomes

$$S = \frac{1-\rho^2}{1+\rho^2-2\rho\cos\left(\psi-\pi-\frac{4\pi}{\lambda}\ell\cos\alpha\right)} f^2(\alpha) \qquad (2\text{-}3)$$

Equation (2-3) is the expression for the power pattern of an image antenna. This is the expression developed by Von Trentini, where ρ is the magnitude of the complex reflection coefficient, ψ is the phase of the reflection coefficient, ℓ is the distance of the partially reflecting sheet above the ground plane, α is the angle of incidence of radiation, and $f(\alpha)$ is the element voltage pattern.

Because ρ, in general, is a function of angle of incidence and polarization, an expression was developed using the concept of directional impedances.[3] The characteristic impedance of the medium is given by $Z_{/} = \eta\cos\theta$ for parallel or E-plane polarization, where θ is the angle of incidence to normal and η is the intrinsic impedance of the medium which is defined as $\sqrt{\mu/\epsilon}$. For perpendicular or H-plane polarization the expression becomes $Z_{/} = \eta\sec\theta$.

These directional impedances were used in the trasnsmission line equation where the impedances at the interface of Z_1 and Z_2, from the Z_1 direction, are given by

$$Z_{12} = Z_2 \frac{Z_3 \cos k_2\ell + jZ_2 \sin k_2\ell}{Z_2 \cos k_2\ell + jZ_3 \sin k_2\ell} \qquad (2\text{-}4)$$

See Figure 2-2 where Z_1, Z_2, and Z_3 are the directional impedances of the medium and θ is the angle of incidence.

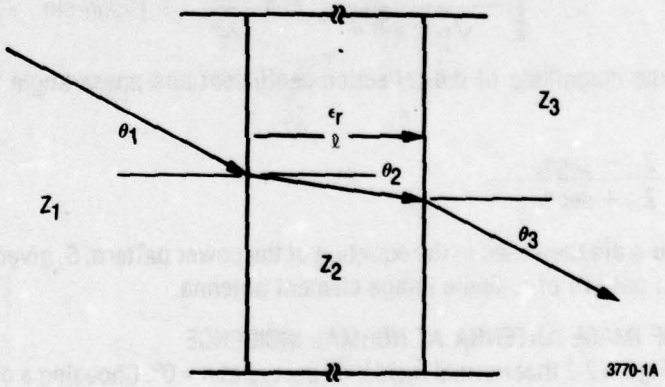

Figure 2-2. Transmission of a Wave Through a Dielectric

2.2 E-PLANE IMPEDANCE CALCULATIONS

Substituting the boundary conditions discussed above for the characteristic impedance for waves polarized parallel to the plane of incidence and assuming mediums one and three are air and medium two is a dielectric sheet of thickness ℓ and dielectric constant ϵ_r, we have

$$Z_1 = Z_3 = \cos\theta_1$$

where the values of Z_1 and Z_3 have been normalized. From Snell's law we can substitute and solve for Z_2 in terms of θ_1

$$Z_2 = \frac{\cos\theta_2}{\sqrt{\epsilon_r}} = \frac{\sqrt{\epsilon_r - \sin^2\theta_1}}{\epsilon_r} \qquad (2\text{-}5)$$

By substituting this expression for Z_2 into the transmission line equation (2-4), the impedance at the boundary of Z_1 and Z_2 for E-plane polarization becomes:

$$Z_{12} = \frac{\sqrt{\epsilon_r - \sin^2\theta_1}}{\epsilon_r} \left[\frac{\cos\theta_1 \cos\frac{2\pi\ell}{\lambda\epsilon} + j\frac{\sqrt{\epsilon_r - \sin^2\theta_1}}{\epsilon_r}\sin\frac{2\pi\ell}{\lambda\epsilon}}{\frac{\sqrt{\epsilon_r - \sin^2\theta_1}}{\epsilon_r}\cos\frac{2\pi\ell}{\lambda\epsilon} + j\cos\theta_1 \sin\frac{2\pi\ell}{\lambda\epsilon}} \right] \tag{2-6}$$

Therefore, ρ and ψ the magnitude of the reflection coefficient and phase angle for the E-plane becomes

$$\rho e^{j\psi} = \frac{Z_{12} - Z_1}{Z_{12} + Z_1} = \frac{Z_{12} - \cos\theta_1}{Z_{12} + \cos\theta_1} \tag{2-7}$$

These values of ρ and ψ are used in the equation of the power pattern, S, given previously to calculate the E-plane radiation pattern of a single image element antenna.

2.3 H-PLANE IMPEDANCE CALCULATIONS

Recall from paragraph 2.1 that for perpendicular or H-plane polarization the characteristic impedance of the medium becomes $Z_z = \eta\sec\theta$. Therefore, substituting the boundary conditions discussed previously we can solve for Z_2 in terms of θ_1. By substituting this expression into the transmission line equation, the impedance of the boundary of Z_1, and Z_2 for H-plane polarization becomes:

$$Z_{12} = \frac{1}{\sqrt{\epsilon_r - \sin^2\theta_1}} \left[\frac{\sec\theta_1 \cos\frac{2\pi\ell}{\lambda\epsilon} + j\frac{1}{\sqrt{\epsilon_r - \sin^2\theta_1}}\sin\frac{2\pi\ell}{\lambda\epsilon}}{\frac{1}{\sqrt{\epsilon_r - \sin^2\theta_1}}\cos\frac{2\pi\ell}{\lambda\theta} + j\sec\theta_1 \sin\frac{2\pi\ell}{\lambda\epsilon}} \right] \tag{2-8}$$

Therefore, ρ and ψ the magnitude of the reflection coefficient and phase angle for H-plane polarization becomes

$$\rho e^{\psi} = \frac{Z_{12} - \sec\theta_1}{Z_{12} + \sec\theta_1} \tag{2-9}$$

These values of ρ and ψ are then used in the equation of the power pattern, S, given previously to calculate the H-plane radiation pattern of a single image element antenna.

2.4 ANALYSIS OF IMAGE ANTENNA AT NORMAL INCIDENCE

Recall from Figure 2-2 that normal incidence occurs at $\theta = 0°$. Choosing a dielectric thickness of $\ell = \lambda/4$ and substituting into equation (2-6) for the impedance at the interface we have

$$Z_{12} = \frac{1}{\sqrt{\epsilon_r}} \frac{j\frac{1}{\sqrt{\epsilon_r}}}{j} = \frac{1}{\epsilon_r} \tag{2-10}$$

This result can be obtained from equation (2-8) in the same manner. Substituting this result into equation (2-7) shown below yields

$$\rho e^{j\psi} = \frac{Z_{12} - \cos\theta_1}{Z_{12} + \cos\theta_1} = \frac{\frac{1}{\epsilon_r} - 1}{\frac{1}{\epsilon_r} + 1} = \frac{1 - \epsilon_r}{\epsilon_r + 1} = -\frac{\epsilon_r - 1}{\epsilon_r + 1} \tag{2-11}$$

Note this important point, for real values of dielectric constant, (i.e., positive real values >1), this term is a negative real reflection coefficient which can be expressed as

$$\rho = \frac{\epsilon_r - 1}{\epsilon_r + 1} \quad \text{where } \psi = \pi \tag{2-12}$$

With this information we must now return to the equation of the power pattern shown below

$$S = \frac{1 - \rho^2}{1 + \rho^2 - 2\rho\cos\left(\psi - \pi - \frac{4\pi}{\lambda}\,\ell\cos\alpha\right)}$$

Note that maximum power in the direction of $\alpha = 0°$ is obtained when

$$\psi - \pi - \frac{4\pi}{\lambda}\,\ell\cos\alpha = 0 + n2\pi$$

Solving this equation for ℓ we have

$$\ell = \frac{\lambda}{4\pi}\,(\psi - \pi - 2n\pi)$$

$$\ell = \frac{\lambda}{2}\left(\frac{\psi}{360} - 0.5\right) + n\,\lambda/2$$

where ψ is expressed in degrees and n = 0,1,2,3, etc. Substituting $\psi = \pi$ or 180° into this equation shows that maximum power in the direction of $\alpha = 0°$ is obtained when the dielectric is $\lambda/4$ thick and is spaced at multiples of $\lambda/2$ above the ground plane.

$$\ell = n\,\lambda/2 \tag{2-13}$$

2.5 GAIN IMPROVEMENT OBTAINED FROM THE IMAGE ELEMENT ANTENNA

Utilizing the boundary conditions discussed in paragraph 2.4 we can substitute directly into equation (2-3) the expression for the power pattern. By letting

$$\rho = \frac{\epsilon_r - 1}{\epsilon_r + 1},\ \psi = \pi,\ \alpha = 0,\ \ell = \lambda/2, \text{ and } f(\alpha) = 1,$$

(i.e., omni-directional radiation patterns) we have

$$S = \frac{1 - \rho^2}{1 - 2\rho + \rho^2} = \frac{1 - \rho^2}{(1 - \rho)^2}$$

$$S = \frac{1 + \rho}{1 - \rho} \tag{2-14}$$

Substituting $\rho = \frac{\epsilon_r - 1}{\epsilon_r + 1}$ we can see that

$$S = \frac{1 + \frac{\epsilon_r - 1}{\epsilon_r + 1}}{1 - \frac{\epsilon_r - 1}{\epsilon_r + 1}} = \frac{2\,\epsilon_r}{2} = \epsilon_r$$

$$S = \epsilon_r \tag{2-15}$$

This expression shows that the gain improvement is directly proportional to the dielectric constant. Figure 2-3 shows a graph of gain improvement versus dielectric constant. Note that for a dielectric constant of $\epsilon = 25$, a gain improvement of approximately 14 dB is realized.

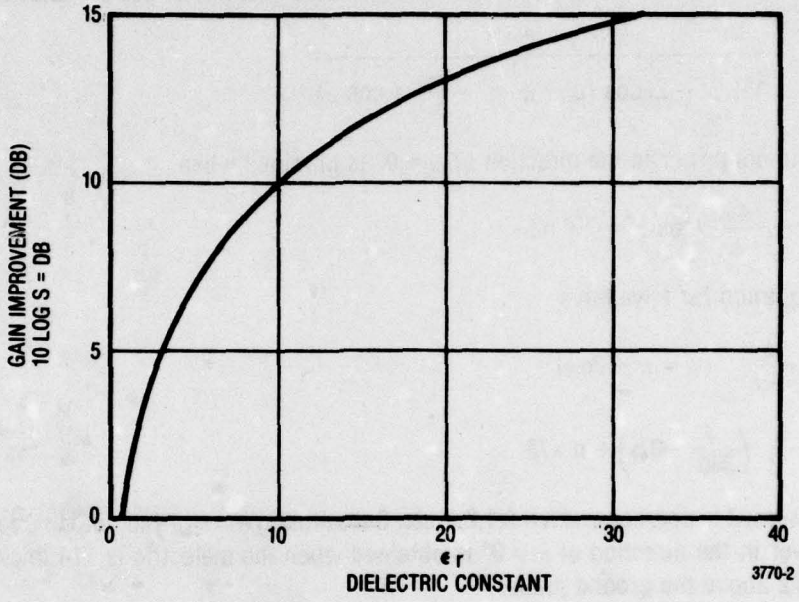

Figure 2-3. Gain Improvement in dB versus Dielectric Constant

3. QUALITATIVE ANALYSIS

A simple form of the image antenna was constructed at 10 GHz using a single waveguide slot as the radiating element. The slot was located in the center of a 12 inch x 12 inch aluminum ground plane. The antenna was constructed sufficiently large to allow the direct measurement of its radiation pattern, aperture distribution, and mutual coupling. Figure 3-1 shows a cross section of the antenna. A dielectric material (Emerson & Cummings STYCAST Hi-Hi-K with ϵ_r=25) one-quarter wavelength thick was located on dielectric spacers one-half wavelength above the ground plane, as determined in paragraph 2-4. The characteristics of the antenna and basic antenna design considerations are presented.

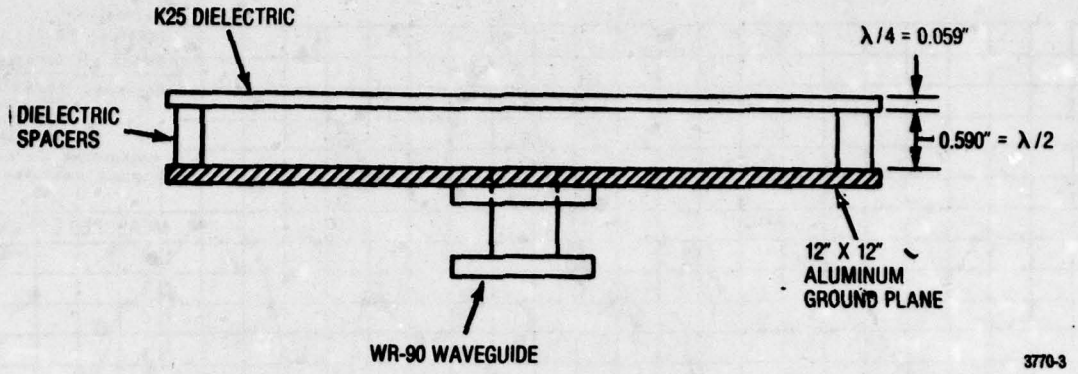

Figure 3-1. Cross-Section of Basic Image Element Antenna Constructed at 10 GHz

3.1 RADIATION PATTERN MEASUREMENTS COMPARED TO CALCULATED MATH MODEL PATTERNS

Radiation patterns were measured in the Anechoic Chamber at Motorola's Government Electronics Division in Scottsdale. Calculated math model patterns compared very favorably with the measured patterns. Figures 3-2 and 3-3 show the E and H-plane patterns at 10 GHz. Note in Figure 3-2 the close correlation between the mainbeam in both the calculated and measured patterns. The calculated pattern falls off sharply at 90° because the math model equations assume an infinite ground plane and infinite dielectric. Because we have a finite ground plane and dielectric the measured pattern shows a large amount of radiation at 90°. This was believed due to a high electric field at the edge of the ground plane. Since the field in the H-plane tapers off more rapidly than the E-plane it was believed that the electric field at the edge of the ground plane was lower, therefore, the pattern correlation in Figure 3-3 is very good. The measured E-plane pattern shows very large sidelobes at 78°. This corresponds to the Brewster angle which is defined as $\theta = \tan^{-1} \sqrt{\epsilon_2/\epsilon_1}$ where $\epsilon_2 = 25$ and $\epsilon_1 = 1$. The Brewster angle corresponds to the angle where there is total transmission through the dielectric covering the image antenna.

Cross polarization measurements are also shown in Figures 3-2 and 3-3. Because the cross polarization is down at least 25 dB the image element antenna could be a good candidate for a dual polarization antenna.

Gain versus frequency calculations were made by integration of the math model equation. This theoretical gain curve was compared to the measured gain over the same frequency range. A graph of the gain versus frequency data is shown in Figure 3-4.

These results compare very favorably, with the deviation between the two curves being only about 0.1 dB. The measured gain curve is lower in frequency than the calculated curve by about 175 MHz. This is apparently caused by the deviation in dielectric spacing above the ground plane. The theoretical spacing should have been 0.590 inches; however, this frequency difference could have been caused by an actual spacing of 0.601 inches.

3.2 CONCLUSIONS

The close comparison between the calculated math model patterns and measured patterns show that the assumptions made in the development of the math model were indeed correct. The element pattern can be ignored in the calculation of the power pattern of an image antenna using high values of dielectric constant. Mutual coupling measurements in both planes proved to be down at least 25.5 dB; this indicates the feasibility of using the Image Element Antenna as an element in an array. The increase in directivity also shows that the image antenna can be used as a technique for "thinning" arrays; i.e., reducing the number of active elements. This will be discussed in Section 4.

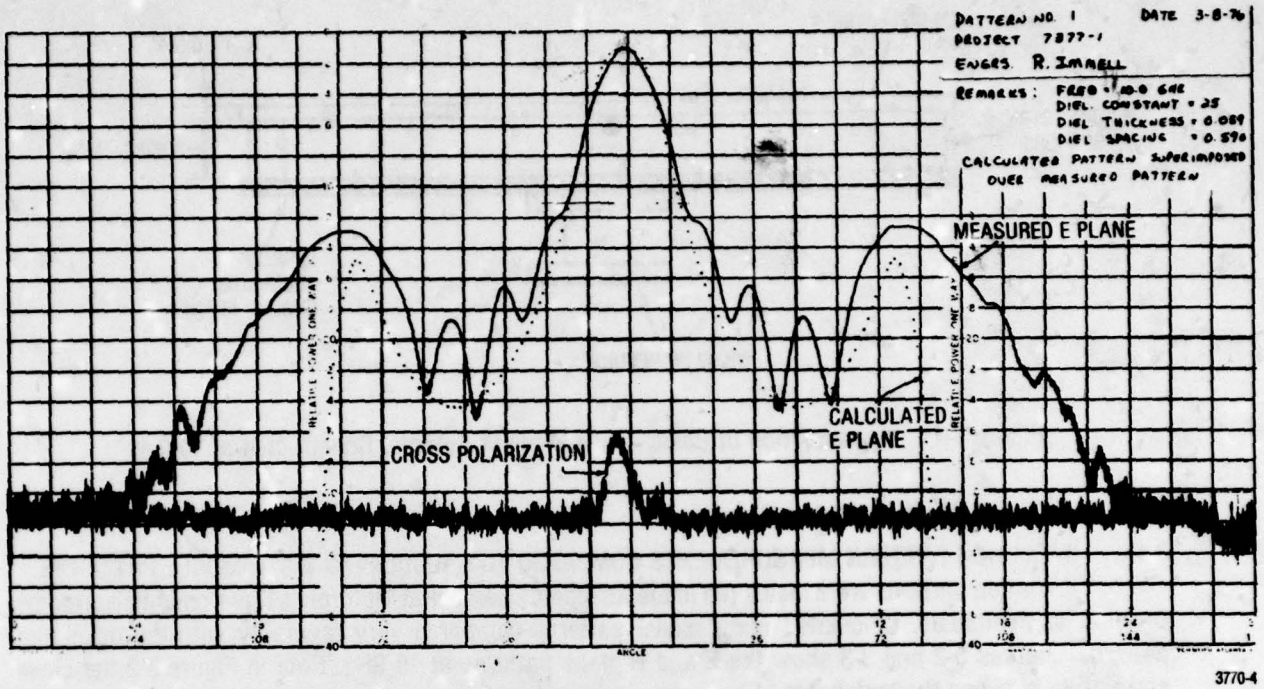

Figure 3-2. Calculated E-Plane Pattern Superimposed Over Measured E-Plane Pattern at Freq = 10.0 GHz

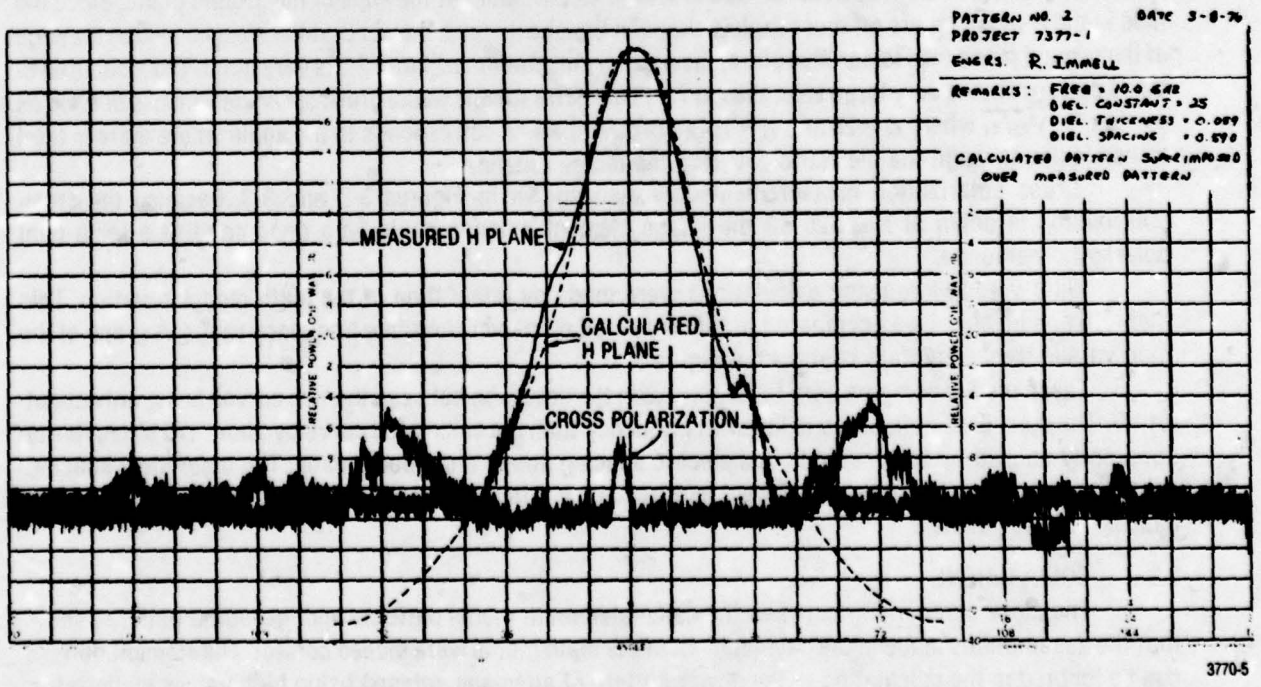

Figure 3-3. Calculated H-Plane Pattern Superimposed Over Measured H-Plane Pattern at Freq = 10.0 GHz

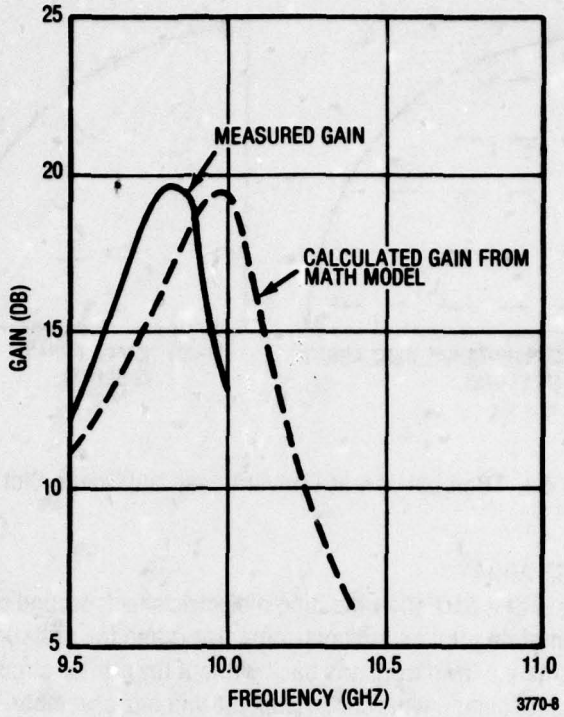

Figure 3-4. Calculated Gain Vs. Measured Gain of Image Element Antenna With K25 Dielectric

4. IMAGE ELEMENT ARRAY

This section will follow the development of utilizing the Image Element Antenna as an element in an array. The antenna array discussed will be a phase monopulse array arranged for two-axis monopulse operation. The image antenna technique has shown to be applicable to missile seekers and fuzing systems where small physical size and low cost are important. Motorola's work with the Image Antenna has resulted in a new class of small, high efficiency monopulse antennas characterized by an aperture thinning of up to 10:1. The resulting low number of elements per antenna contributes to the high antenna efficiency by eliminating much of the conventional antenna distribution network. These arrays, by utilizing a stripline corporate feed, do not suffer degradation due to aperture blockage. Figure 4-1 compares the number of radiating elements of a conventional stripline slot array to an Image Antenna Array of equal performance. This 10:1 reduction in radiating elements reduces distribution network complexity, cost and loss while permitting total integration of receiver and ECCM functions within the same stripline layer.

The following paragraphs compare the predictions of the math model with actual far field antenna pattern measurements. Differences between the measured and predicted patterns are caused by manufacturing tolerances and limitations of the math model because it does not account for the effects of the physical edge of the aperture. Some of these effects continue to be evaluated by Motorola to improve pattern prediction and optimization.

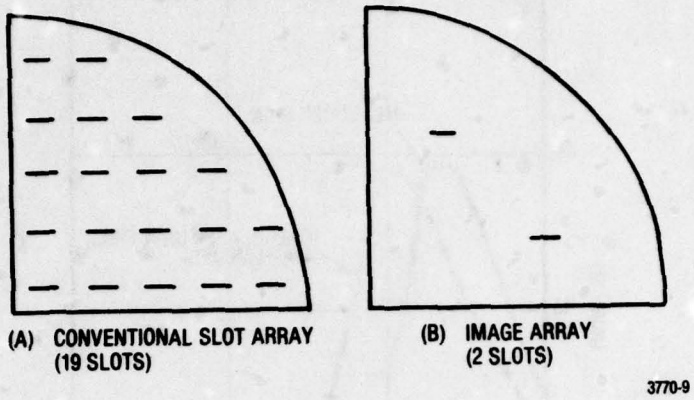

Figure 4-1. Comparison of Conventional and Image Slot Arrays

4.1 EIGHT ELEMENT IMAGE ARRAY

The antenna consists of a partially reflecting dielectric sheet, ground plane and that portion of the antenna/receiver board containing the microwave comparator and the radiating slots. Figures 4-2 and 4-3 show a photograph of the antenna from front and back without the printed circuit board. Figures 4-4 and 4-5 show a photograph of the major components comprising the antenna assembly. The components include the dielectric sheet, the fiberglass wall, the honeycomb spacer, the titanium ground plane without gold-plated foil, the test antenna and the antenna/receiver stripline assembly. The antenna shown in these photographs has a dielectric diameter of 5.3 inches. This size represents the diameter allowed by the interior surface of the radome on a test missile.

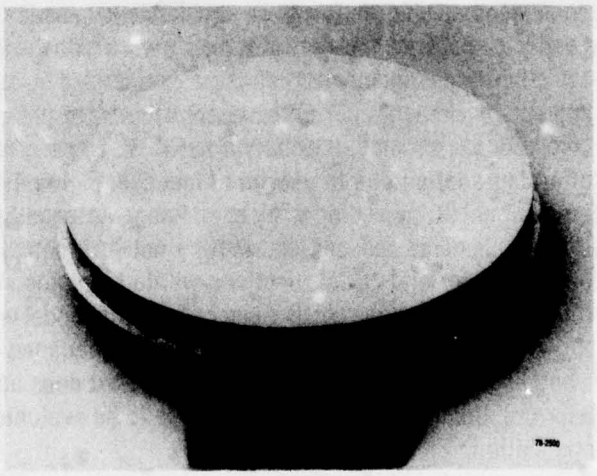

Figure 4-2. Front View of 8 Element Test Antenna

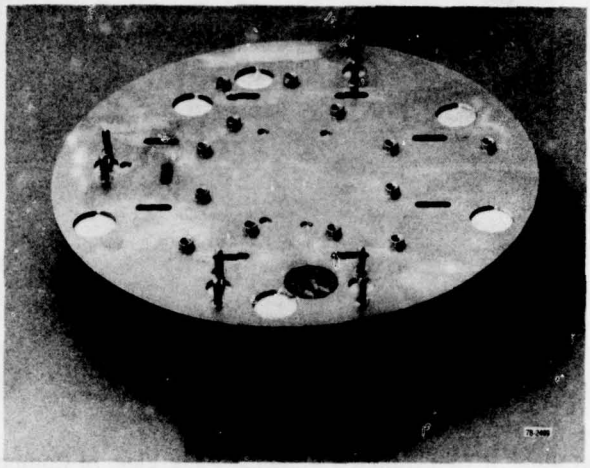

Figure 4-3. Back View of 8 Element Test Antenna

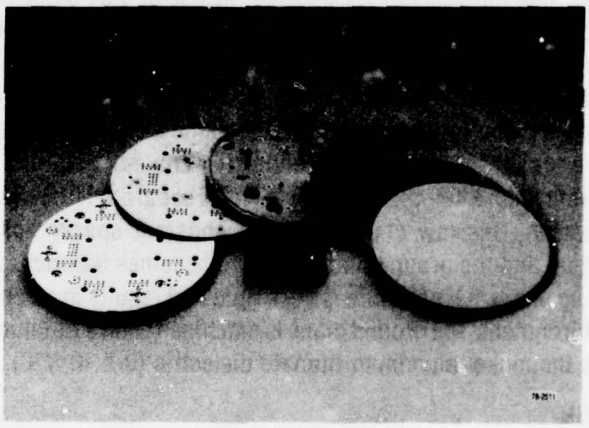

Figure 4-4. Exploded View of Test Antenna Showing Front View of Components, Test Antenna, and Antenna/Receiver

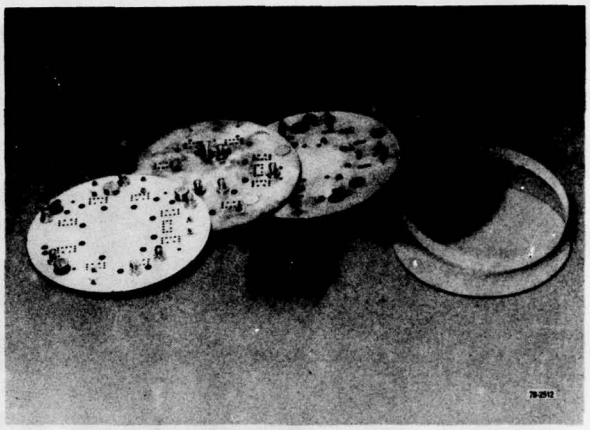

Figure 4-5. Exploded View of Test Antenna Showing Back View of Components, Test Antenna and Antenna/Receiver

Motorola's Image Antenna Technology allowed the use of only eight stripline slot elements in the antenna for a reduction of up to 90 percent in the number of elements normally used in planar arrays of this size and frequency. The reduced size and complexity of the resulting distribution network not only improved antenna efficiency with lower line losses but also released sufficient space so that the microwave receiver and ECCM circuitry could be wholly integrated into the same stripline board, further improving system sensitivity by eliminating the losses of any interconnecting cables.

As can be seen from Figure 4-4, the dielectric sheet is separated from the antenna ground plane by a dielectric honeycomb spacer. This low (1.02) dielectric constant spacer not only controls the spacing between the dielectric sheet and the ground plane but also becomes a structural member when bonded to both of these. The resulting sandwich structure is very rigid and results in a very strong antenna capable of operation in a missile environment. The ground plane is machined from a titanium sheet, which has the same expansion coefficient as the nickel-aluminum titanate dielectric ($9 \times 10^{-6}/°C$).

4.2 DESIGN DESCRIPTION

The dielectric used on this antenna has a dielectric constant of 30. The reflection coefficient is about 0.94 and this yields a gain improvement of 14.75 dB. It is this increase in element gain caused by the end-fire effect which allows the aperture to be thinned.

Arraying of the image antennas is done in the same manner as other end-fire antennas. The final slot locations and element voltages are determined by comparison of calculated patterns for various array layouts.

Figure 4-6 shows the resulting circuit layout of the test antenna. The 5.3-inch antenna has a total of eight slots plus a cross-polarized slot for ECCM. The power divider network uses four 3 dB power dividers. The line lengths are equal to each slot except for the addition or deletion of one-half wavelength to correct the phase of the upside down slots. In addition to being the correct length for phasing purposes, it was also desirable to have the lines as short as possible to minimize losses.

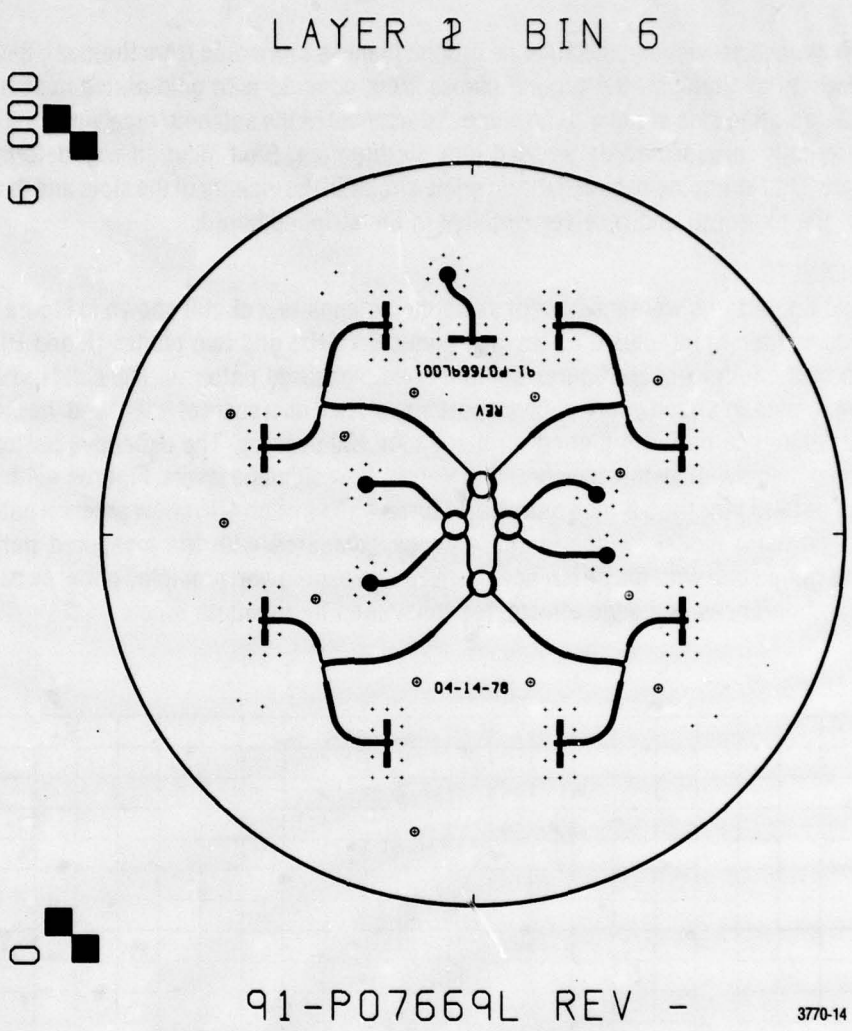

Figure 4-6. Circuit Layout of 8 Element Test Antenna

The phase monopulse radiation patterns are formed by the microwave comparator in the center of the circuit. The principle component of the comparator is the ring hybrid. The ring hybrid provides equal power division and 90-degree phase difference between its two outputs on the opposite side of the ring. To correct the 90-degree phase offset and place the sum pattern peak and difference pattern nulls on the mechanical axis, a one-quarter wavelength length of transmission line was added to each ring hybrid. With this added length of line, the hybrid outputs became the same as the "magic-tee" used in conventional monopulse networks.

The antenna stripline circuitry, including the stripline slots, distribution network, and microwave comparator, was fabricated using standard printed circuit techniques on 3M Corporation's Teflon fiberglass. This material was chosen as a compromise of dielectric loss and mechanical properties such as high temperature capability and resistance to cold flow. In a similar manner, the ground plane spacing of one-sixteenth-inch utilizes standard material thicknesses and is sufficiently small to maintain a TEM wave and prevent "moding".

As explained previously, the antenna ground plane is fabricated from titanium. Because of the high volume resistivity of titanium, the ground planes were covered with gold-plated copper foil which was bonded to the radiating side of the ground plane. Attachment of the antenna/receiver to the platform was by means of internally-threaded studs pressed into the titanium. Stud location was determined to provide approximately 2 PSI clamping between the stripline circuit in the vicinity of the slots and to miss the gyro (in the center of the platform) and receiver circuitry in the stripline board.

4.3 TEST RESULTS

Radiation patterns were measured, using the antenna test circuit shown in Figure 4-6, at three Ku-band frequencies (mid-band, plus 0.1 GHz, and minus 0.1 GHz) and two planes (E and H).

Each of the following six figures contains five measured patterns. The solid curves are the sum, difference and cross-polarized guard channel patterns plotted on a scale of ±180° and the dashed curves are the sum and difference patterns plotted on a scale of ±30 degrees. The expanded patterns allow better determination of beamwidth while the normal patterns show sidelobe levels. Figures 4-7 through 4-12 show the measured patterns for the 5.3-inch antenna. Figures 4-13 through 4-16 show antenna patterns calculated from Motorola's math model for the Image Antenna compared with the measured patterns at F_o. The comparison is quite good with the differences between measured and predicted patterns being attributed to manufacturing tolerances and edge effects not considered by the math model.

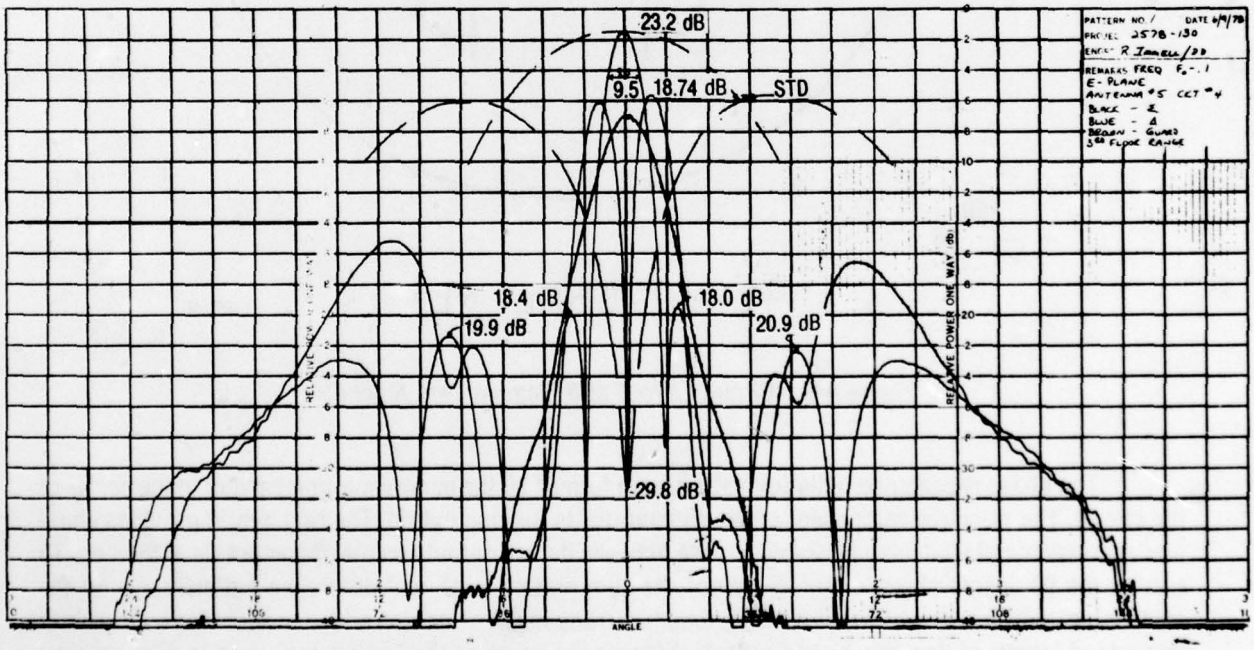

Figure 4-7. E-Plane Radiation Pattern at $F_o - 0.1$

3770-15

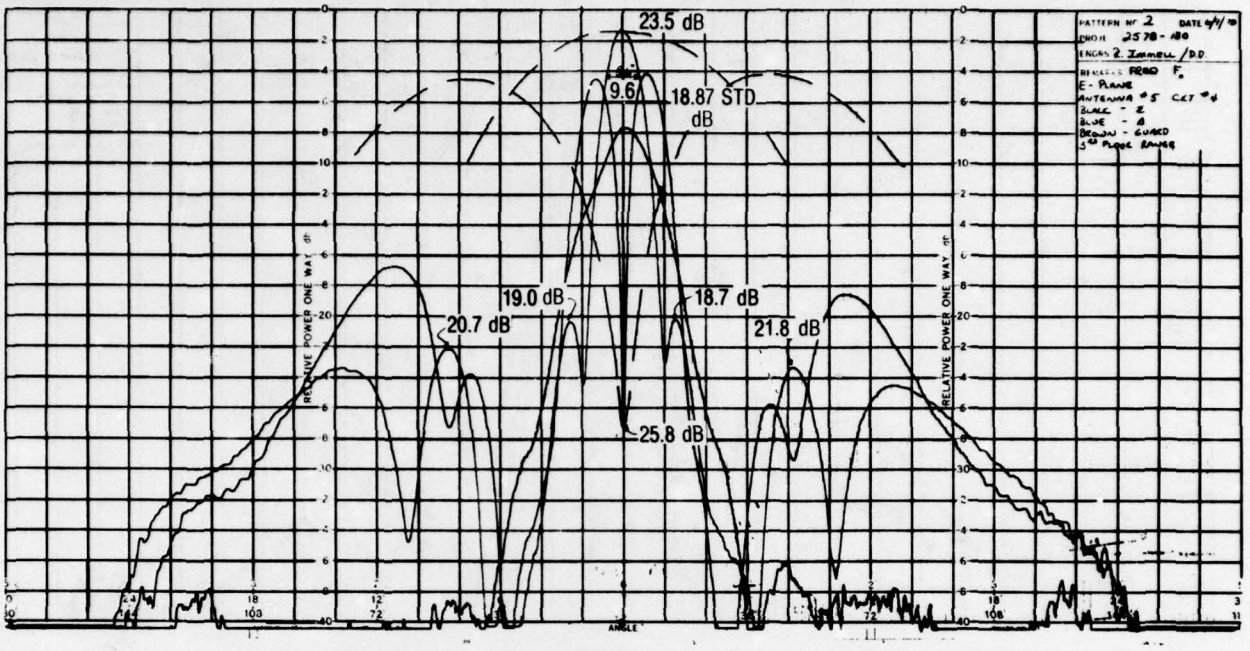

Figure 4-8. E-Plane Radiation Pattern at F_o

3770-16

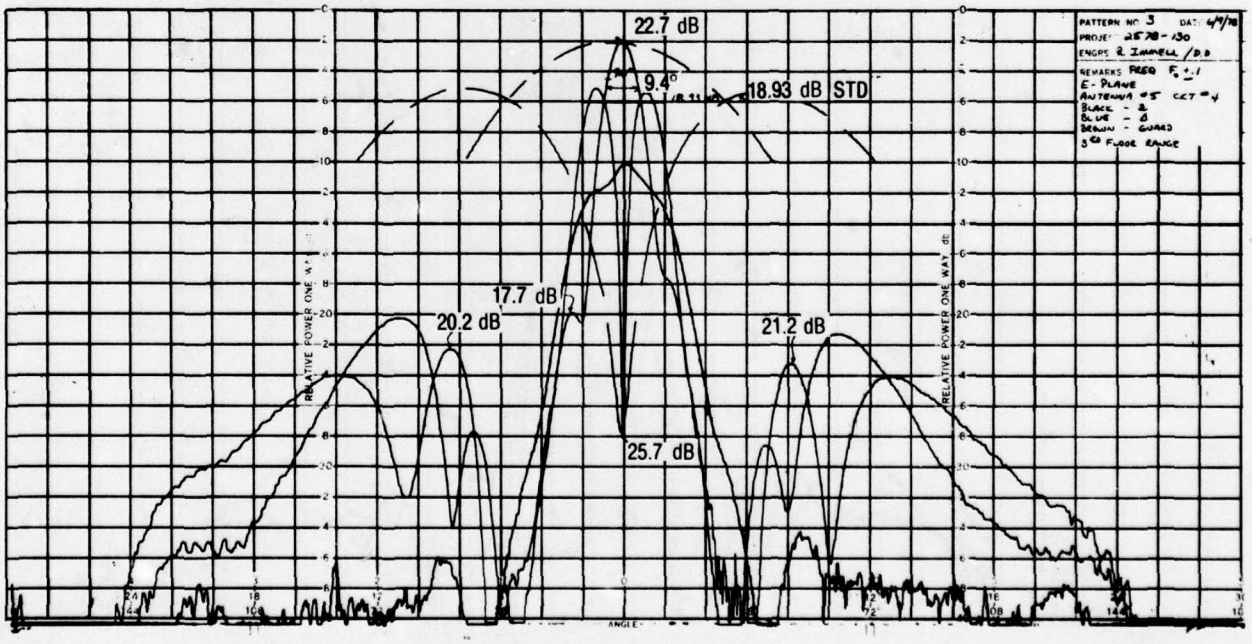

Figure 4-9. E-Plane Radiation Pattern at $F_o + 0.1$

3770-17

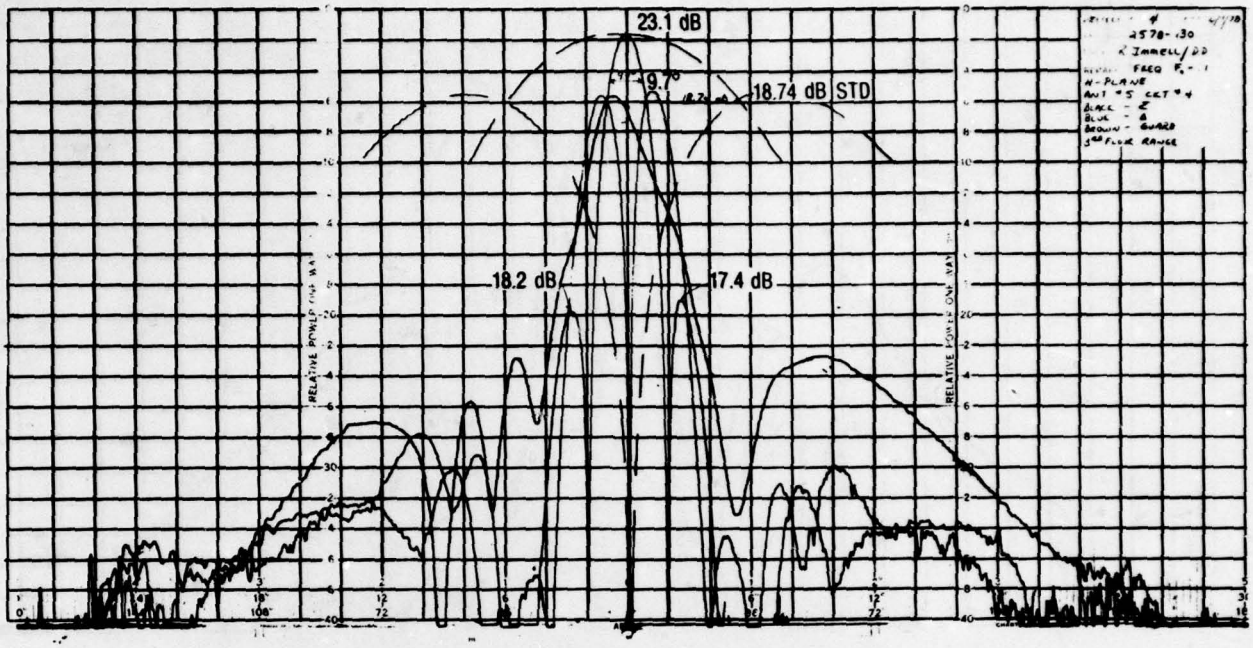

Figure 4-10. H-Plane Radiation Pattern at $F_o - 0.1$

3770-18

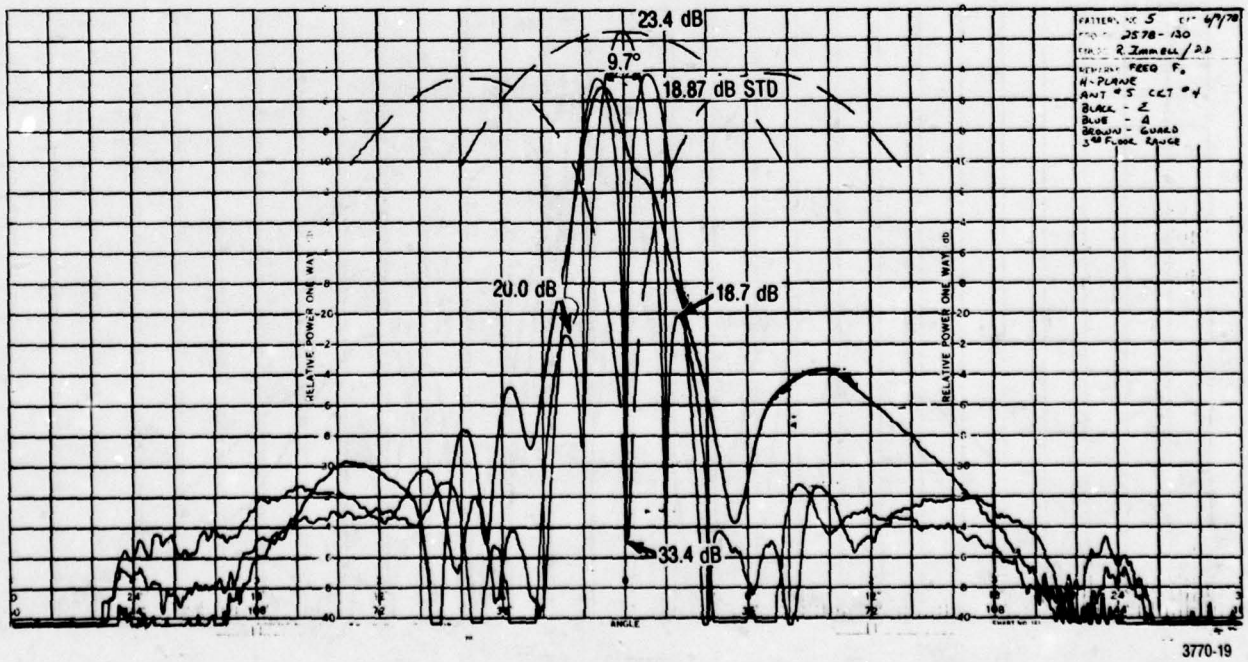

3770-19

Figure 4-11. H-Plane Radiation Pattern at F_o

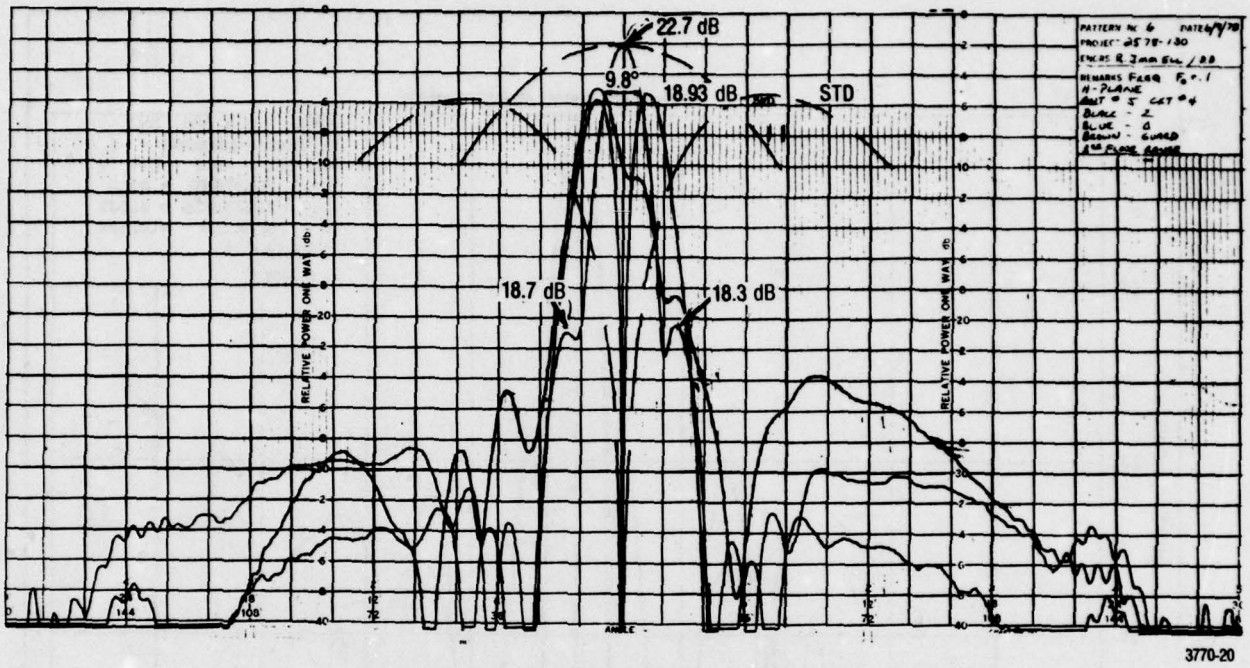

Figure 4-12. H-Plane Radiation Pattern at $F_o + 0.1$

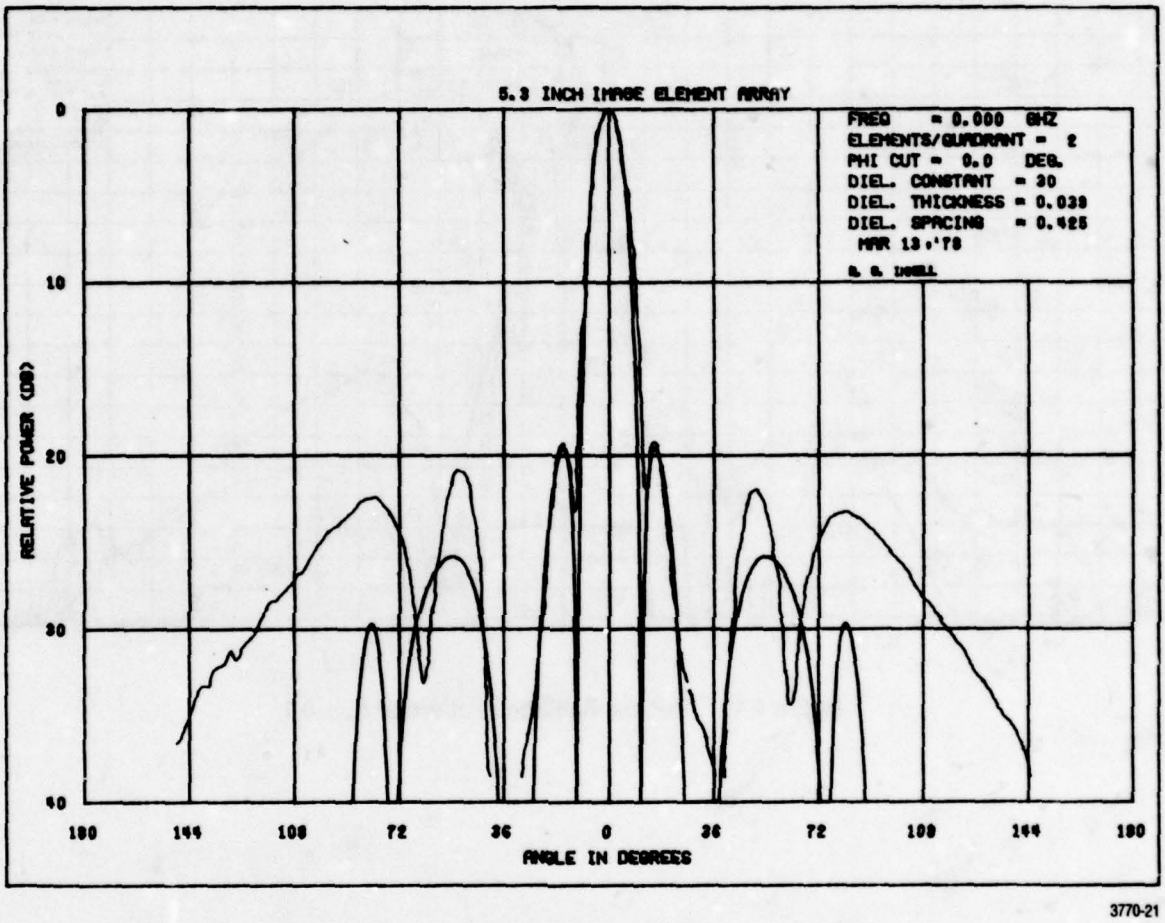

Figure 4-13. Comparison of Measured Vs Calculated E-Plane Sum Radiation Pattern at F_o

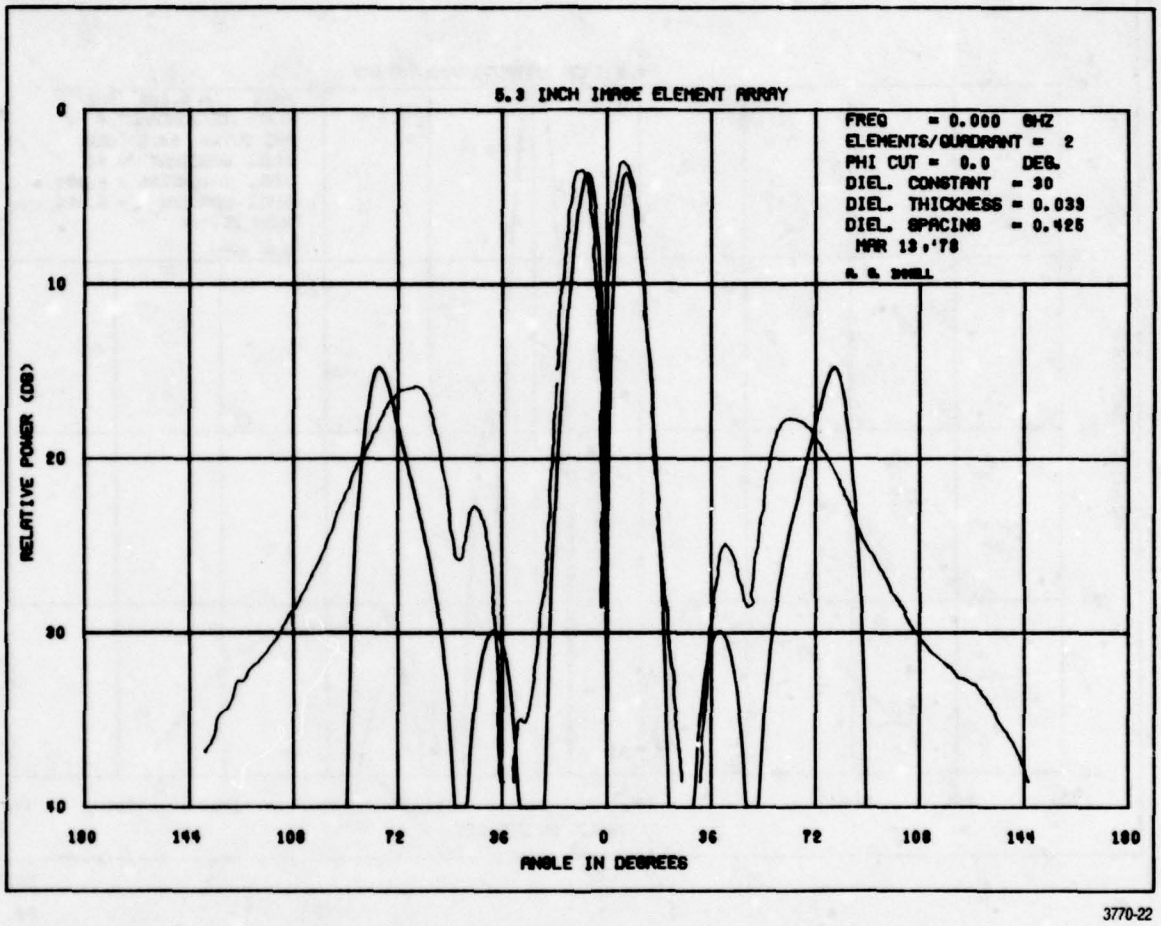

Figure 4-14. Comparison of Measured Vs Calculated E-Plane Difference Radiation Pattern at F_o

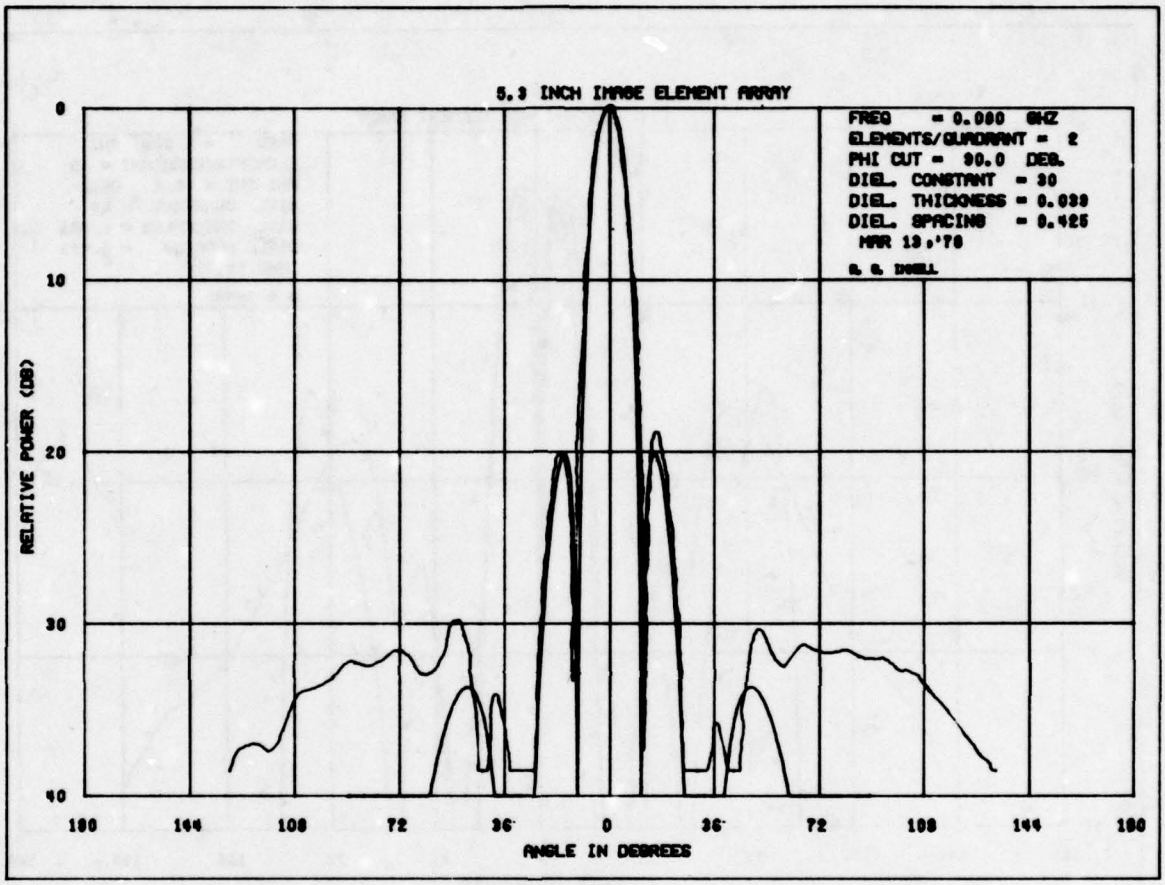

Figure 4-15. Comparison of Measured Vs Calculated H-Plane Sum Radiation Pattern at F_o

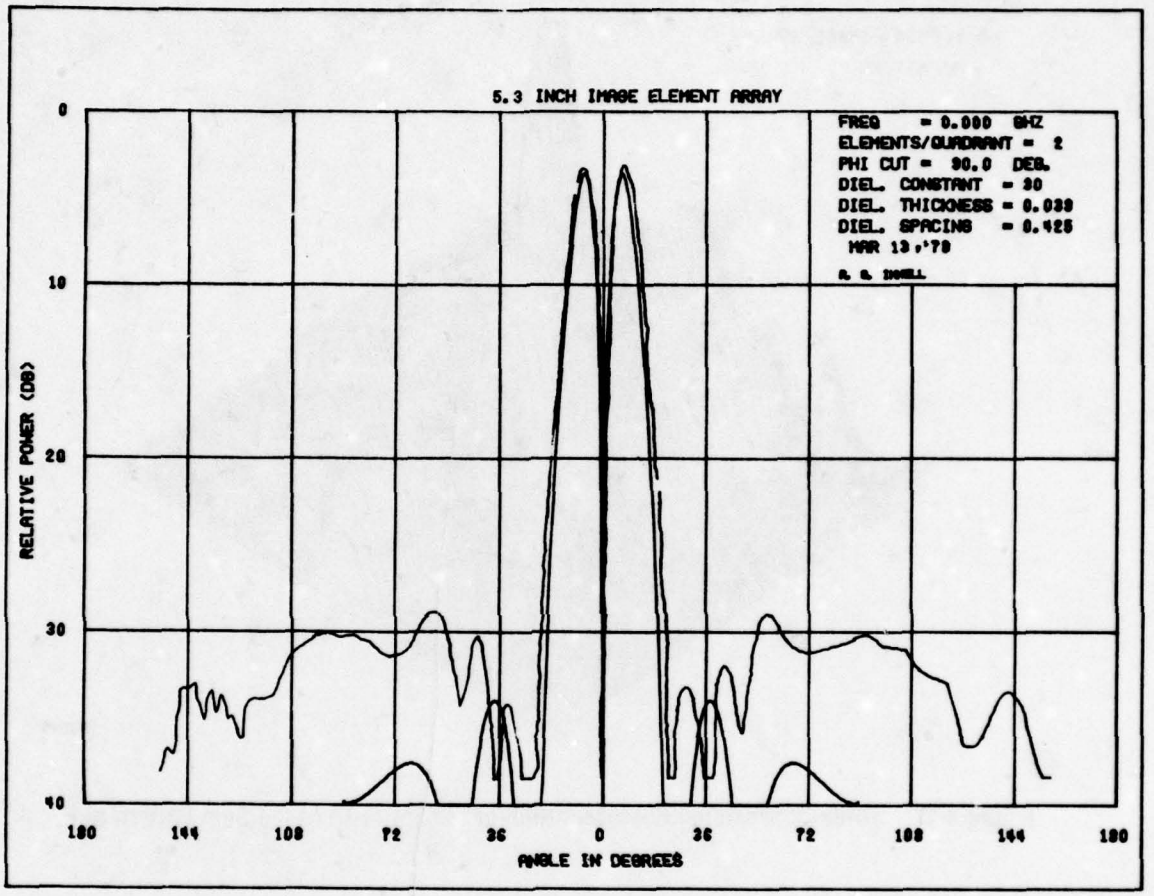

Figure 4-16. Comparison of Measured Vs Calculated H-Plane Difference Radiation Pattern at F_o

The math model was expanded to calculate three-dimensional far field patterns. These patterns for the Sum, E-difference, and H-difference at F_o can be seen in Figures 4-17 through 4-19.

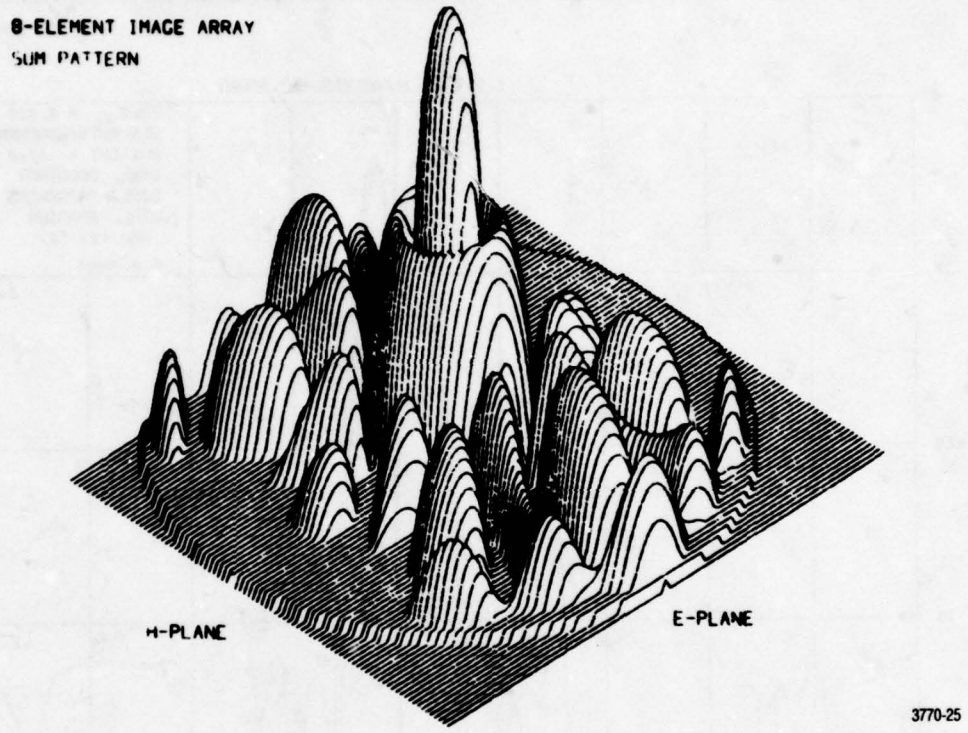

Figure 4-17. Three-Dimensional Representation of the Far Field of the Sum Pattern at F_o

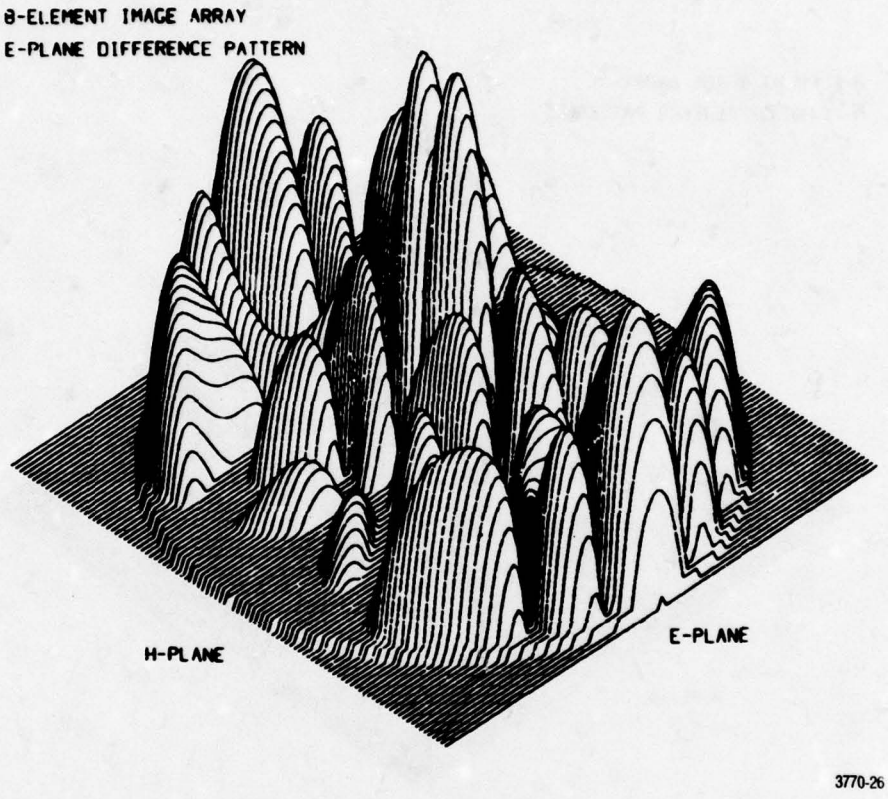

Figure 4-18. Three-Dimensional Representation of the Far Field of the E-Plane Difference Pattern at F_o

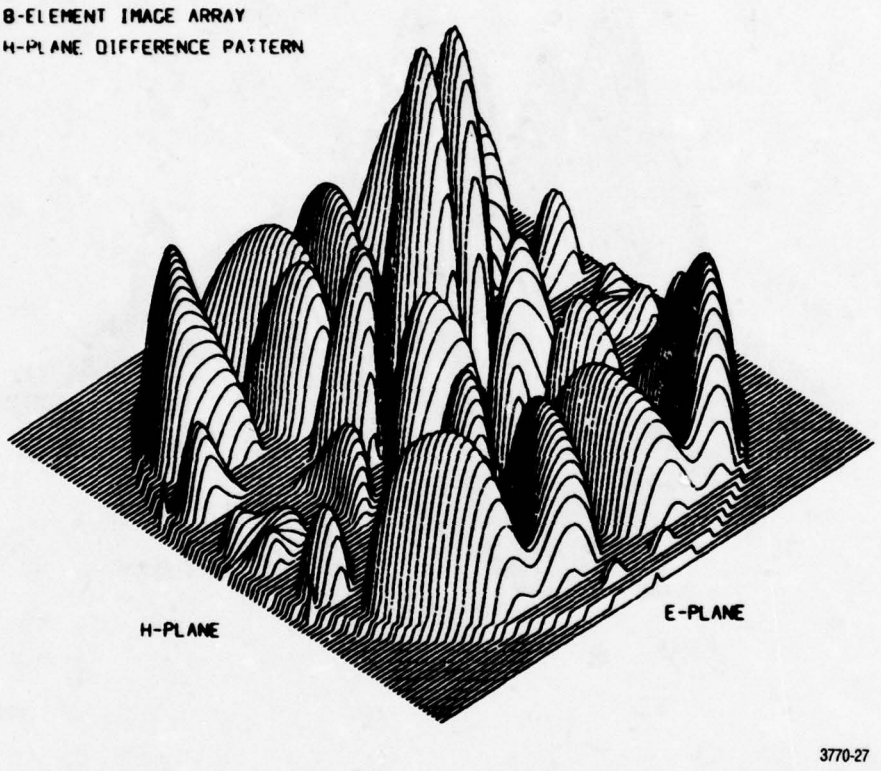

Figure 4-19. Three-Dimensional Representation of the Far Field of the H-Plane Difference Pattern at F_o

5. RESULTS AND CONCLUSIONS

The work described in this report has demonstrated the ability to obtain usable gain enhancement from common radiating elements. The techniques have been demonstrated for a single wave-guide slot and for a stripline monopulse array.

The image antenna was analyzed by a ray approach in conjunction with transmisson line theory. This analysis characterized the image antenna for normal and perpendicular incidence as well as expanding the analysis to all angles of incidence. From this analysis a mathematical model of the image antenna was developed to calculate the radiation pattern and directivity. The analysis indicated that the element pattern could be ignored for high values of dielectric constant.

The most significant result of this study was that the gain improvement of an image antenna is directly proportional to the dielectric constant. For dielectric materials with $\epsilon_r = 30$, a gain improvement of approximately 15 dB could be realized. This increase in directivity is the property which allows the array to be "thinned." This reduction in elements, by as much as 10:1, contributes to the high overall aperture efficiency of the antenna by eliminating much of the conventional antenna distribution network. In the case of the single waveguide slot, because waveguide has essentially zero loss, an overall aperture efficiency of 98 percent was realized. In the case of the eight element array, an overall aperture efficiency of 66 percent was obtained at the comparator outputs.

The comparison of calculated to measured radiation patterns showed good agreement in all cases. This result verified that the math model was accurate, but that it could be improved by analyzing the effect of the aperture edge. The math model developed on this program has become a valuable synthesis technique in the design of various aperture distributions for sidelobe control at Motorola.

This effort is being continued by fabricating a large array incorporating frequency reuse and polarization diversity. Because of its high efficiency, small size and weight, the image array should be considered in preference to conventional slotted waveguide or stripline arrays for many applications.

REFERENCES

1. Giswalt Von Trentini, "Partially Reflecting Sheet Arrays," IRE Transactions on Antennas and Propagation, October 1956; pp. 666-671.

2. John D. Kraus, "Antenna," McGraw-Hill Book Co., Inc. New York, N.Y., Ch. 12-2, 1950.

3. Richard K. Moore, "Traveling-Wave Engineering," McGraw-Hill Book Company, 1960, pp. 301-304.

PATENTS

The Image Antenna described within this report is protected by U.S. Patent No. 3 990 078 (E. Bellee; R. Breithaupt; D. Godwin; & S. Walker), November 1976; Assigned to Motorola.

Two other patents have been applied for by E. Bellee, R. Immell, and B. Sasser and are pending at this time.

COMPUTER-AIDED FAULT DETERMINATION FOR AN ADVANCED PHASED ARRAY ANTENNA

Donald K. Alexander
Roger P. Gray, Jr.

September 26-28, 1979

Prepared for

1979 ANTENNA APPLICATIONS SYMPOSIUM
University of Illinois
Urbana, Ill.

By

WESTINGHOUSE ELECTRIC CORPORATION
Systems Development Division
Baltimore, Maryland 21203

COMPUTER-AIDED FAULT DETERMINATION FOR AN ADVANCED PHASED ARRAY ANTENNA

Abstract

The EAR (Electonically Agile Radar) system was developed by the Westinghouse Systems Development Division under contract to the Air Force Avionics Laboratory. The unique feature of the system is its two-axis phased array antenna. A brief description of the antenna system is presented.

During antenna range testing, a general-purpose minicomputer was used to control the antenna and simulate the commands of the radar system data processor. The method used to initially phase tune the array is described.

During the range evaluation of the EAR antenna, a number of procedures were developed for determining the status of its 1818 phase control modules (PCM) and diagnosing faults. In this paper, the following fault determination procedures will be described.

1. **Element Voltage Determination** - Information gained during the phase-tuning procedure is used to determine the relative voltage for each element in the array.
2. **Failed PCM Determination** - By comparing normalized element voltages with their theoretical values, errors may be computed and expressed as a percentage. A threshold is then applied to determine failed PCM's.
3. **Circular Polarization Status** - A separate phase tune is performed with the array switched to CP. Faulty PCM's and/or circuitry may then be determined and printed out.
4. **PCM Performance Evaluation** - By using the entire array as a phase reference, the phase performance of a single phase shifter, in the presence of its neighbors, may be measured and printed out.

For each of the fault determination procedures, typical examples using computer printout from measured data will be presented.

Introduction

The radiation beam agility and versatility of a two-axis phased array has long been considered desirable for use with multimode airborne radar sets. Inertialess scanning and complete aperture phase control provide system designers wide latitude in the selection and interleaving of modes. In all cases, these advantages must be traded against the considerably higher cost of phased array antennas. Increasingly, in military procurements, emphasis is being placed on life cycle cost, and not just the up-front acquisition cost. This emphasis means that suppliers of systems and subsystems must not only produce their wares at reasonable cost, but must also make them reliable in service and easily maintained.

The Electronically Agile Radar (EAR) System, developed by Westinghouse under contract to the Air Force Avionics Laboratory, was produced under the balanced design concept in which cost, reliability, maintainability, and survivability are considered, along with performance in arriving at a system design. The EAR System features a two axis phased array antenna, (see figure 1), the configuration and performance of which has been described in previous presentations*.

*"High Performance Electronically Scanned Array for Airborne Multimode Radar," M.J. Kiss and B.A. Sichelstiel, 24th Annual Tri-Service Symposium, Monterey, Calif., 1978.

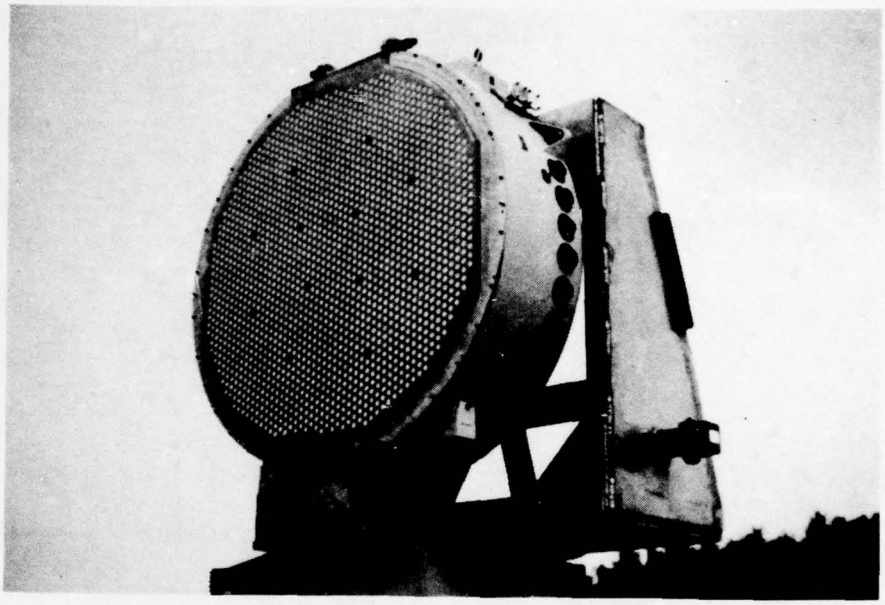

Figure 1. EAR System Antenna

This paper will describe techniques which enhance that antenna's maintainability.... The ability of the array to self-test in operational service, and the ability to define and locate faults when they occur. These concepts are especially appropriate to a phase array antenna which employs a multiplicity of individual devices, each of which may fail or malfunction independently.

In this paper, the configuration of the EAR antenna will be briefly reviewed. Then, the array phase tuning procedure which is basic to subsequent techniques will be described. Finally, several computer-aided procedures will be described which permit rapid detection and location of phase control module (PCM) failures and malfunctions, and other faults.

EAR Antenna Configuration

The major components of the EAR array are the phase control modules (PCM's), feed network or manifold, thermal control system, beam steering controller, and signal distribution network.

The array uses 1818 PCM's which are reciprocal latching ferrite phase shifters incorporating the radiating element and the driver assembly. Polarization is switchable between vertical and one sense circular. The PCM's were identified as critical components, and a parallel effort for their development was maintained throughout the program (see figure 2). The two units developed are mechanically and electrically interchangeable as a set in the array. A set from each manufacturer was used in the two developmental antennas. Considerable attention was given to the manufacturing processes and controls necessary to obtain reasonable production yields.

The feed network is a directional coupler waveguide manifold with quadrant partitioning for two axis monopulse operation. An interleaved quadrant partitioning scheme (see figure 3) was used to decrease azimuth difference pattern sidelobe levels well below those normally associated with a phase monopulse array.

The thermal control system is a closed-loop freon evaporative system with an external liquid heat exchanger (see figure 4). The liquid coolant flow rate to the heat exchanger is controlled to maintain the overall array temperature to within $\pm 5°C$ of the design value. In addition, the thermal stabilizing properties of the freon system maintains the temperature differential between any two elements in the array to less than 3°C.

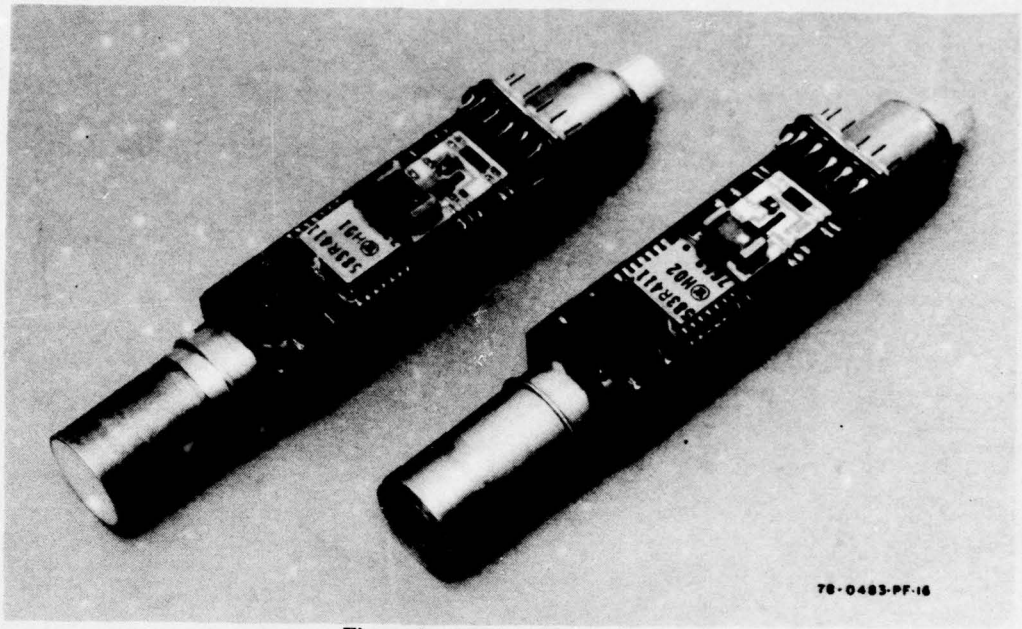

Figure 2. Antenna Front View

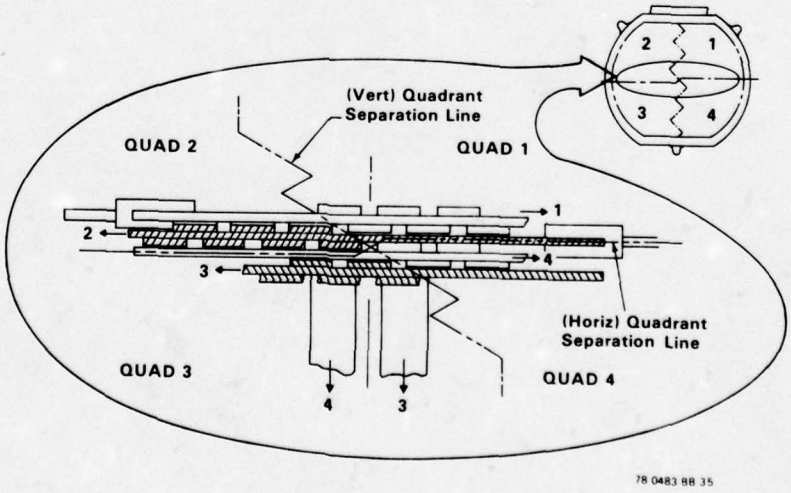

Figure 3. Quadrant Split

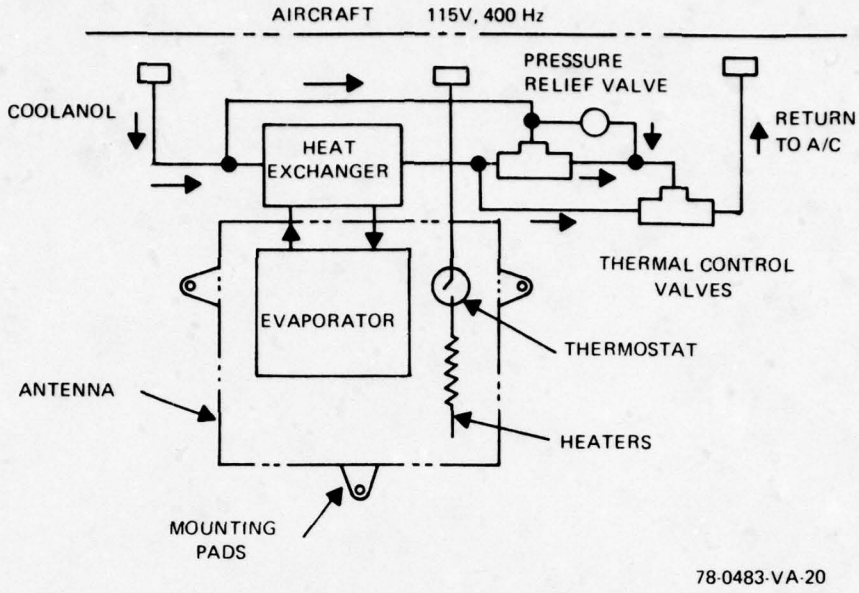

Figure 4. Block Diagram of the Thermal Control System

The beam steering controller is a special purpose computer that calculates the required phase commands for each element in the array given a set of direction cosines, and such additional information as frequency and beam shape. The phase commands are computed serially by column and loaded into the memory elements on the PCM dirvers (see figure 5). The beam shapes available are pencil, cosecant-squared, and azimuth or elevation fan beams. The cosecant-squared beam may also be modified to align the scanned beam with isodop contours on the ground, thus easing the doppler processing required for certain mapping modes. Extensive built-in-test capability, incorporated in the beam steering controller, has proven very effective in detecting and isolating faults in the command circuitry of the array.

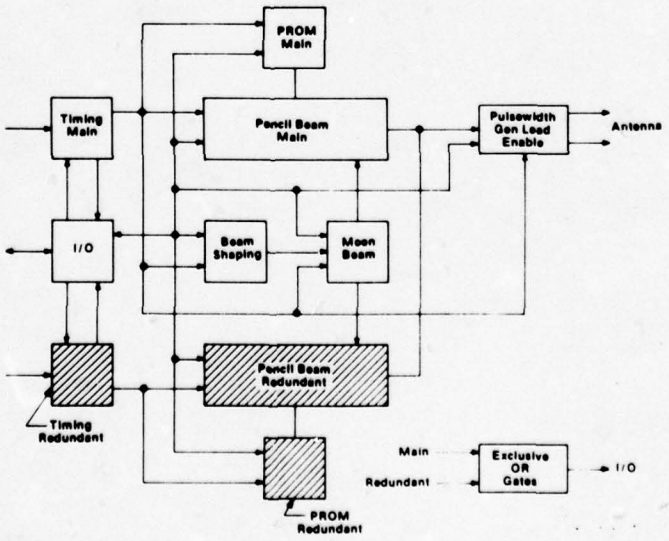

Figure 5. Block Diagram of the Beam Controller Architecture

The power and control signals are fed to each of the phase control modules through a 14-layer printed circuit wiring board. The PCM driver circuit plugs into the circuit board. The board covers the manifold plate with the exception of clearance holes for the body of the phase shifter which permit RF coupling to the manifold.

During extensive range testing, the EAR antennas performed well in all regards. Of particular interest were peak and average sidelobe levels, beam pointing accuracy, and confirmed graceful degradation with its reliability implications. Security limitations preclude the presentation of performance data in this paper.

One of the EAR systems has been installed in a B-52 flight test aircraft (see figure 6) for a program being conducted at Boeing, Witchita. The other system is installed on a test tower site at Westinghouse where it is undergoing extensive system test and evaluation. Both antennas are operating satisfactorily.

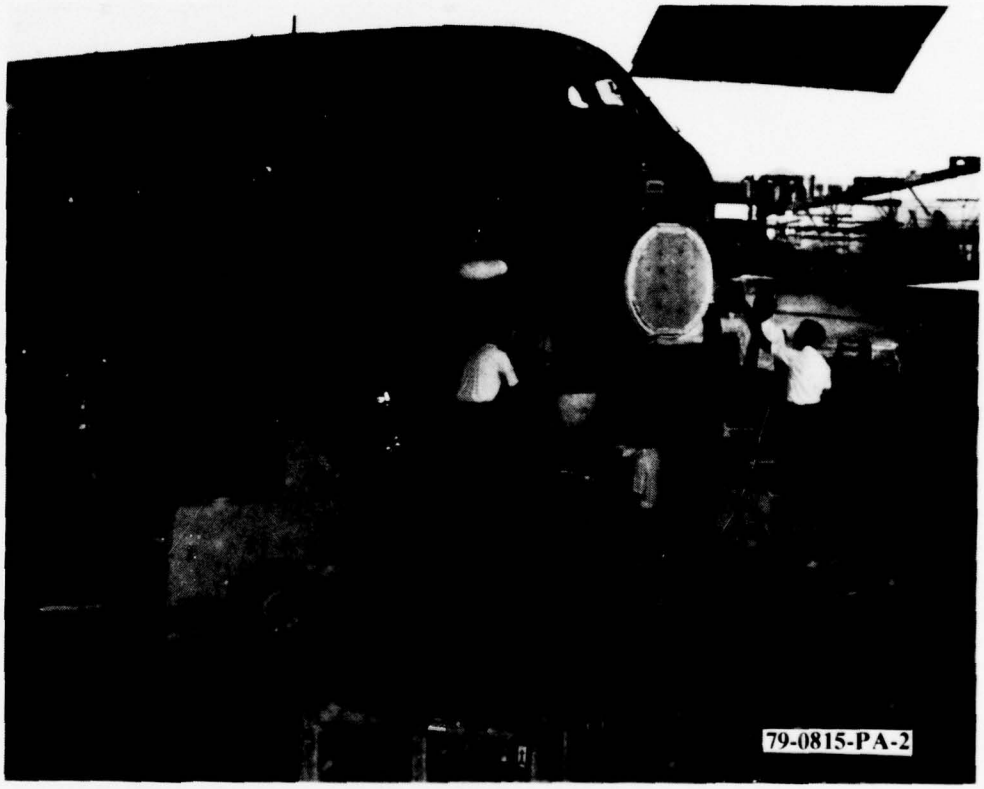

Figure 6. B-52 with EAR System Installed

Antenna Phase Tuning Procedure

The initial phase tuning of the EAR antenna was accomplished using a method which utilizes the phase shifters and controller as part of the test equipment. The tuning operation performs an insertion phase trim for each element to remove phase errors associated with the RF feed network, and variations between PCM's. The result of a tune is a set of reference phase commands which, when applied to the antenna, cause the contribution of each element of the array to be in phase with the sum of the other elements.

The phase tuning is accomplished as follows. Figure 7 shows the vector relationship between the element being tuned, (the small 0° vector) and the sum of all the other elements. If we phase modulate the element thru phase states of 0°, 90°, 180°, and 270°, an envelope detector will produce the waveform shown on the right in figure 7. We may now adjust the initial or 0° state of the element until the 90 and 270 degree states produce equal

levels on the modulation envelope. The initial state so achieved is the tuned state for that element aligning its contribution with the sum of the remaining elements and the phase state value is stored.

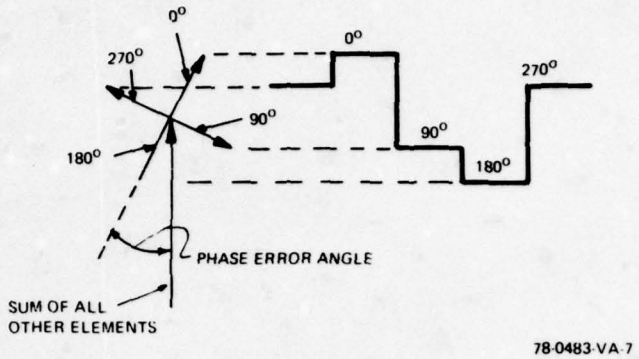

Figure 7. Range Time Operation

During the phase tune, as with all other aspects of range testing, the EAR antenna is under the control of a general-purpose-minicomputer. This permits automated control of the phase tune procedure including sequencing the elements, applying the phase modulation, and determining and storing the tuned states. A block diagram of the test configuration used is shown in figure 8. The procedure was used extensively during range test of the EAR antennas, and serves as a basis for the additional diagnostic procedures which follow.

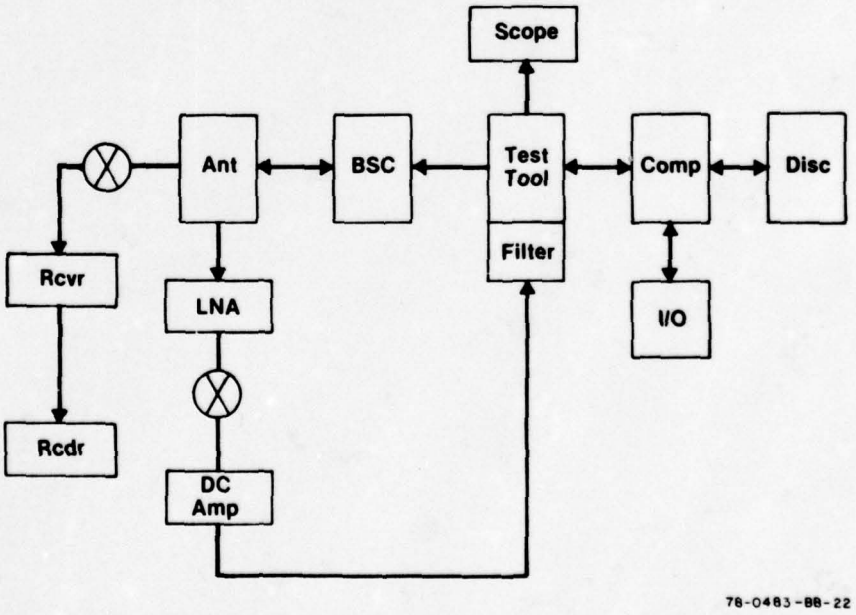

Figure 8. Range Time Block Diagram

Element Excitation Determination

In the phase tuning procedure just described, the addition of one technique will yield significant additional information. The reader is referred to figure 9. Here, the solid lines in the diagram indicate a $\pm 90°$ phase modulation of an arbitrary array element, and its associated modulation envelope as employed in the phase tuning. Suppose now that the initial phase state of the element is changed by 90°, and the $\pm 90°$ phase modulation is again applied. The result is indicated by the dashed lines in figure 9, a second vector relationship and modulation envelope.

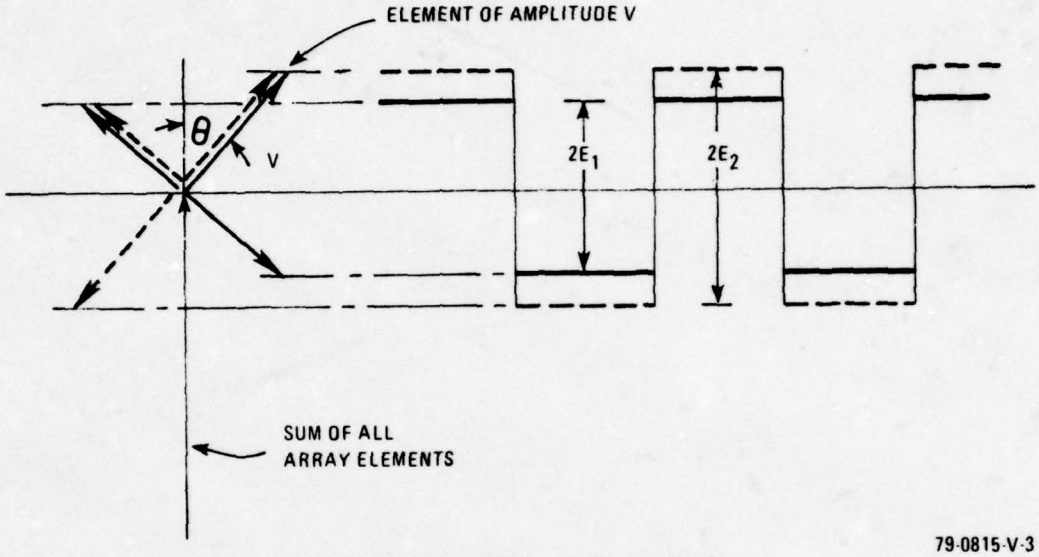

Figure 9. Element Amplitude Determination

The two amplitudes, E_1 and E_2, are easily measured. Using these and the vector diagram, the following relationship may be written.

$$E_1 = V \sin \theta$$
$$E_2 = V \cos \theta$$

Squaring and adding the equalities:

$$E_1^2 + E_2^2 = V^2(\sin^2 \theta + \cos^2 \theta)$$

Finally:

$$V = E_1^2 + E_2^2$$

Thus, we have obtained a simple expression for the unknown element excitation in terms of the mesurable quantities, E_1 and E_2.

This procedure was used extensively during range testing of the EAR antenna to examine element excitations. The general-purpose minicomputer, used to control the antenna, was programmed to implement the phase modulation, read and process measured data, and store voltage excitation values for all the elements. Figure 10 is a printout of the relative voltage excitations for one quadrant of the EAR array. Using this information as a data base, one can tell a great deal about the condition of the antenna.

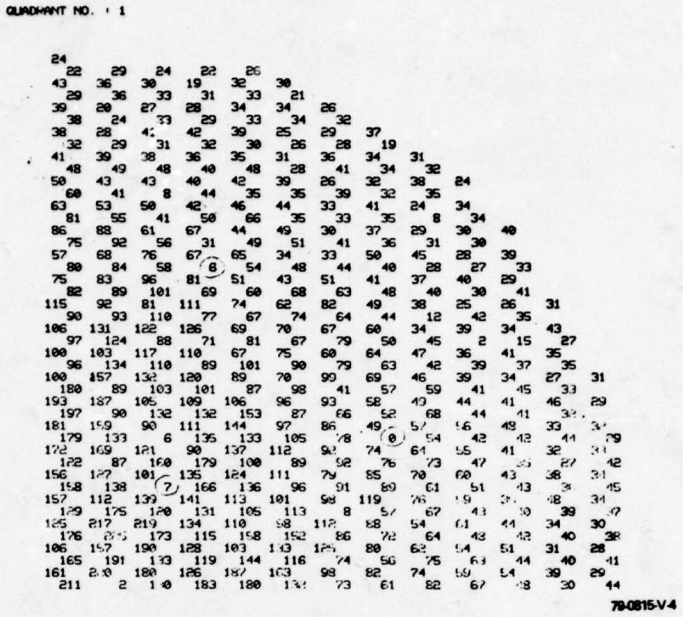

Figure 10. Printout of Element Amplitudes

PCM Failure Determination

The detected signal used to derive the voltage excitation values is an amplitude modulated signal, resulting from the phase modulation of the element in question. If a particular phase shifter is inoperative, no phase modulation occurs ($E_1 = E_2 = O$), and an excitation value of near zero is obtained. (Noise limitations, in general, preclude obtaining precisely zero readings). Thus, the location of phase shifter failures is discernible on the amplitude printout by the appearance of relatively small (but not necessarily, zero) excitation values. The reader may have noted the three small voltage readings circled in figure 10. These correspond to three missing elements in the quadrant to facilitate structural members. They respond the same electrically as an inoperative phase shifter, thus yielding the near-zero voltage readings.

One additional processing step makes it much easier to identify phase control module (PCM) failures. Suppose we compare the measured element voltages with the computed or theoretical value at each location. Specifically, the following computation may be performed.

$$\%\ \text{amplitude error} = \frac{V_{measured} - V_{theoretical}}{V_{theoretical}} \quad X100$$

The results of this computation for the array quadrant excitations in figure 10 are shown in figure 11. Now the impact of the intentional aperture amplitude function is accounted for. The PCM failure situation becomes even clearer when all element locations having an amplitude error below a selected threshold are assigned the value zero. Using the same data base as before, figure 12 presents such a display with all amplitude erros less than 50% set to zero. Experience has shown a 50% threshold to be an appropriate value for designating phase shifter failures.

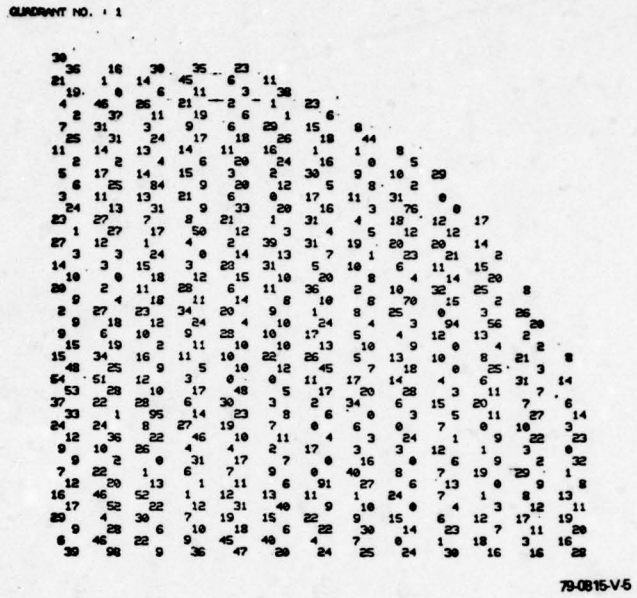

Figure 11. Element Amplitude Errors on in Percentage

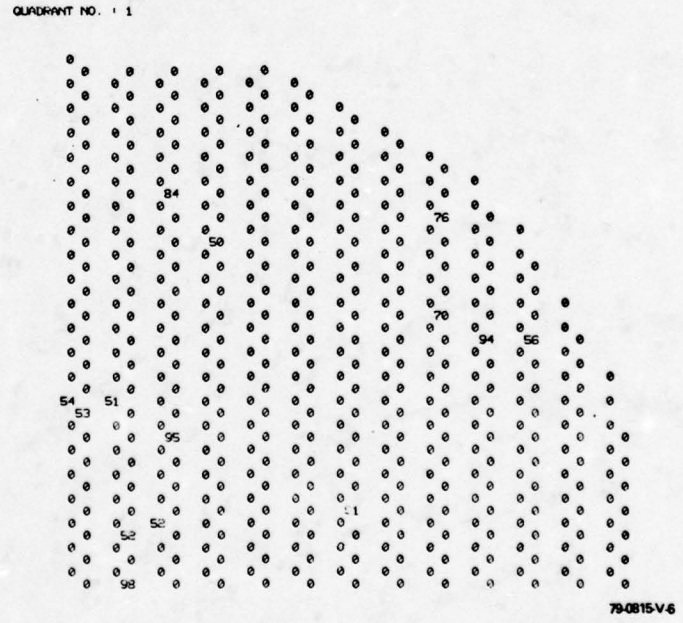

Figure 12. Element Amplitude Errors in Percentage, 50% Threshold

Fault Diagnosis of the Circular Polarization Mode

The performance of certain air-to-ground modes in a modern radar set may be enhanced under adverse weather conditions by the addition of a circular polarization capability to the antenna. The EAR antenna provides this capability by the inclusion of a polarization switch in each PCM. The switch consists of a switchable Faraday rotator section in combination with a ferrite "quad" or quarter wave plate. The switch is operated by exciting the coil of the Faraday rotator. The coils are wired in strings of nine as indicated in figure 13. For purposes of fault detection and isolation, it is essential to check the status of individual switches and the associated wiring. A technique for so doing was conceived and implemented during the developmental testing of the EAR antennas.

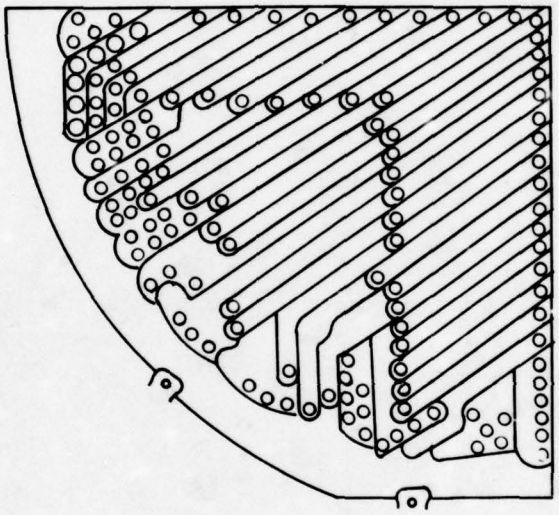

79-0815-V-7

Figure 13. Partitioning of Polarization Wiring

In a preceding section, a procedure was outlined for determining array element amplitudes by processing data obtained during the phase tuning procedure. This procedure may be repeated under slightly different conditions. Suppose the array is switched to circular polarization (by energizing the polarization switch windings in all the PCM's), the range transmitter is retained in linear polarization, and the element amplitudes measured as before. This time, the element amplitudes will measure nominally 0.7 times their former value. However, consider an element whose polarization switch is inoperative. Such an element will remain linearly polarized, and its measured amplitude will be greater, on the average 1.4 times greater, than that of its near neighbors or of its theoretical value. Thus, in a tabulation of array amplitudes, the location of inoperative polarization switches is discernible by the appearance of larger than theoretical amplitudes.

As before, the situation may be more easily evaluated through further processing of the amplitude data. Consider again the expression for percent amplitude error.

$$\%\ \text{amplitude error} = \frac{V_{\text{theoretical}} - V_{\text{measured}}}{V_{\text{theoretical}}} \quad X100$$

For an inoperative polarization switch:

$$V_{measured} = 1.4\, V_{theoretical}$$

Yielding:

$$\%\ \text{amplitude error} = -40\%$$

Such errors may be easily detected and displayed using the element amplitude determination procedure outlined in the previous section. An example will serve to illustrate this point.

During one phase of range testing on the second EAR antenna, the current to the polarization switches was observed to be varying 10 to 20 percent in an erratic fashion. The procedure outlined in this section (antenna switched to circular polarization, range transmitter vertically polarized) was initiated to diagnose the problem. The element amplitude data was obtained and stored as before. Percentage errors were computed, and only those errors exceeding 25% (+ or −) were printed out. The result is shown in figure 14 for the third quadrant of the array. In the figure, there is an obvious "belt" of negative values across the quadrant. Comparing this printout to the wiring partitioning schematic of figure 13 leads to immediate location of probable circuit faults. Because of the aforementioned erratic behavior of the fault, and the fact that the amplitude determination procedure requires a number of minutes to run, some of the elements were probably circularly polarized at the instant they were phase modulated. This accounts for the fact that some elements in the "belt" have amplitude errors within the selected range of ±25%, and thus record a value of zero. Upon subsequent disassembly and repair of the antenna, the circuit faults were easily isolated to the subgroup indicated in the printout.

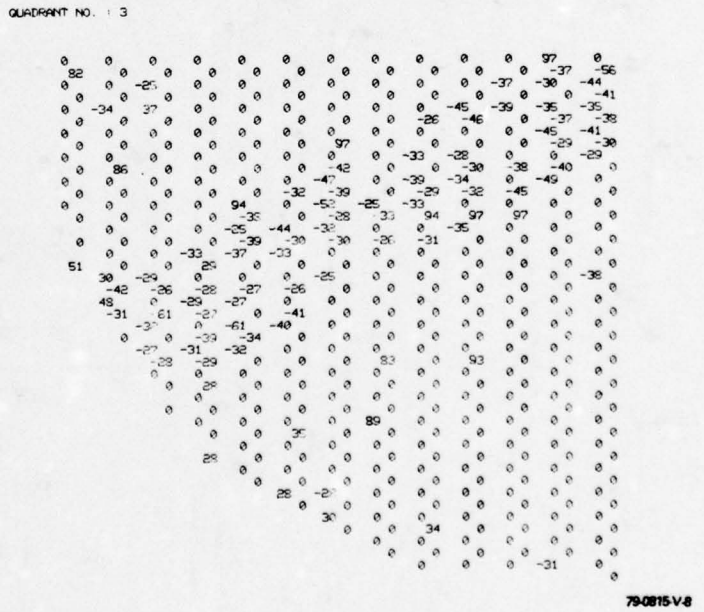

Figure 14. Percentage Amplitude Errors, Circular Polarization, 25% Threshold

Testing Phaser Performance in the Array

This final section describes a technique for determining the phase response of a phase shifter (commanded vs actual phase shift) in the array environment. As before, this technique is based on the basic phase tune procedure described earlier.

Consider again the phase tune vector diagram as shown in figure 15(a). This shows the element under test of voltage V in its tuned state (aligned in phase with the sum of the remaining elements). If we phase modulate the test element $\pm 90°$, the resultant modulation envelope will nominally be the time invariant response indicated in figure 15.

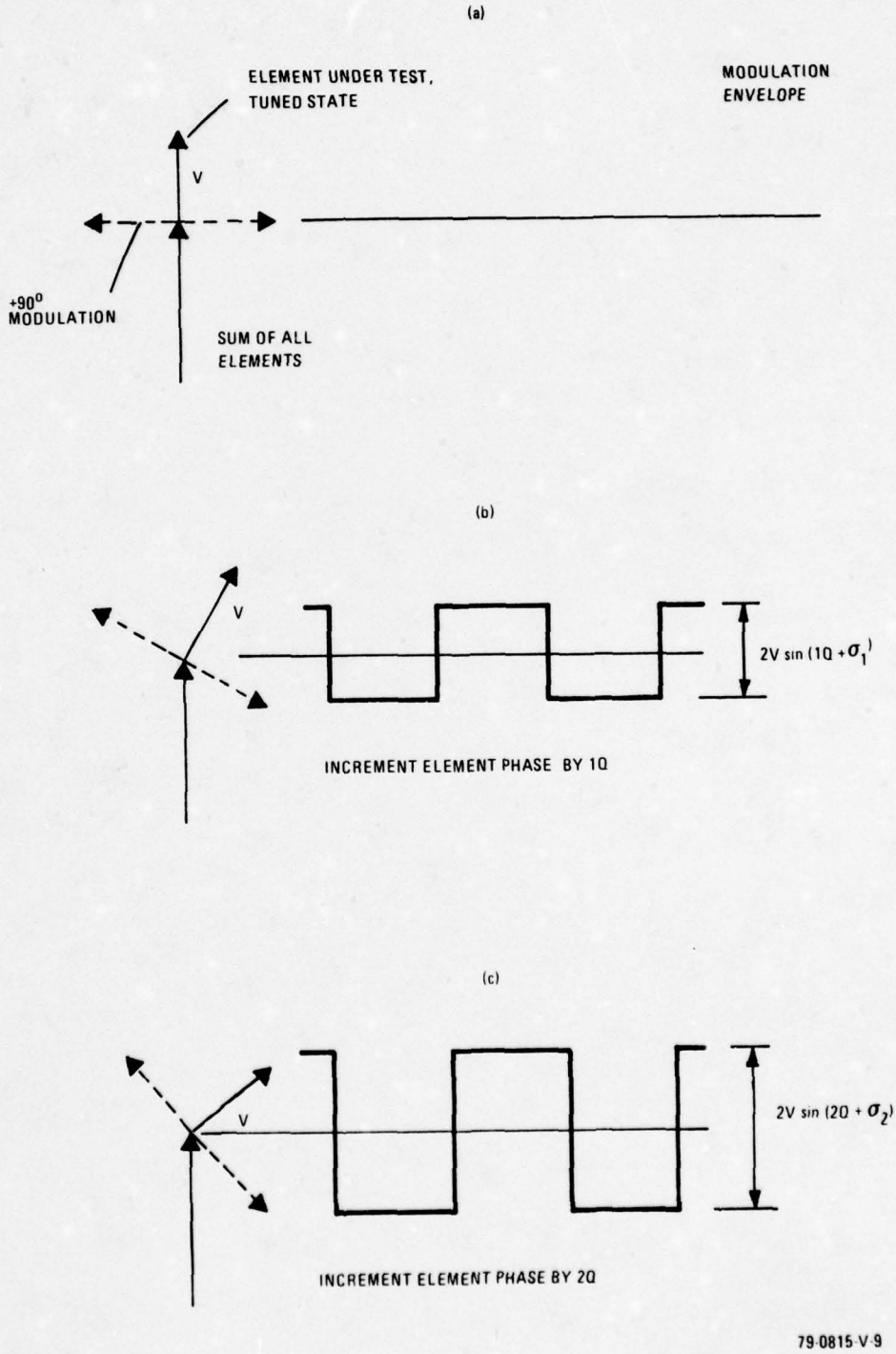

Figure 15. Phase Shifter Error Measurement

Now suppose the element phase in incremented by Q where

$Q = 360/N$ degrees

and N is number of equally phase states to be examined. Applying $\pm 90°$ phase modulation yields the modulation envelope shown in figure 15(b). Though commanded a phase increment of Q, the actual test element will change in phase by $(Q + \sigma_1)$ where σ_1 is the associated phase error. The amplitude of the modulation envelope is thus proportional to $V \sin (Q + \sigma_1)$.

Figure 15(c) is a similar presentation for a phase increment of 2Q, a phase error of σ_2, and detected modulation envelope whose amplitude is proportional to $V \sin (2Q + \sigma_2)$. In the general case, a phase increment of nQ is commanded with the attendant phase error, σ_n (n = 1, 2,.....N). For each value of n, the measured value of the modulation, $V \sin (nQ + \sigma_n)$ may be compared with the expected value, $V \sin nQ$. If we obtain N such pairs of data for a particular phase shifter and draw a smooth curve through the points, command vs measured response curves which might resemble the curves of figure 16 are obtained. This data may be processed to yield a quantitative evaluation of phase shifter response.

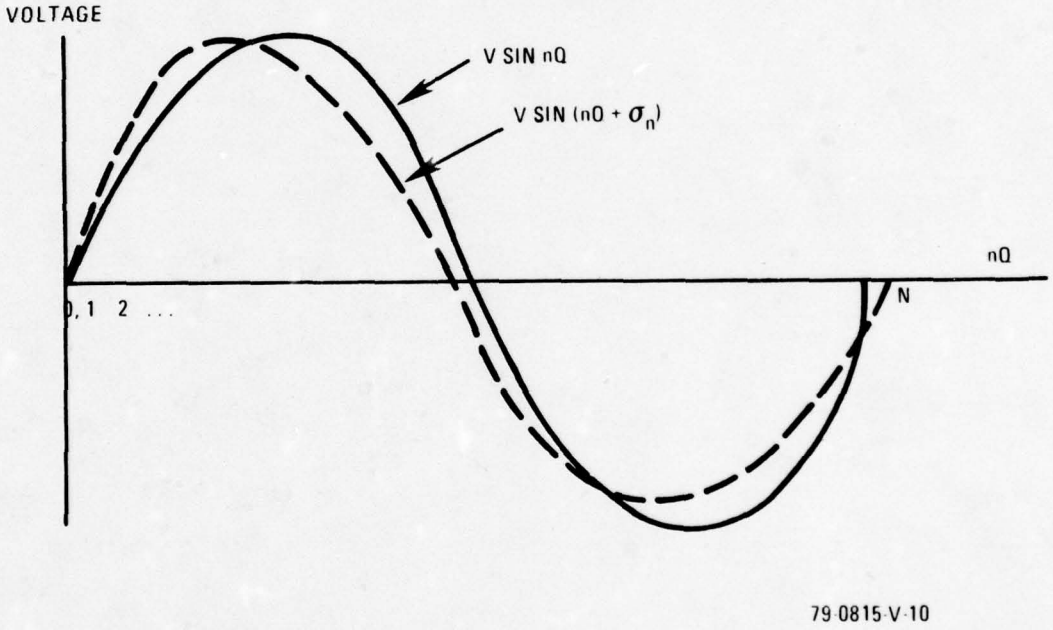

Figure 16. Command vs Measured Response Curve

Conclusion

Several techniques have been described which demonstrate how computer-control of a large phased array permits timely detection and isolation of array faults and malfunctions.

Doubtless, many additional techniques have been or will be conceived and implemented. Though developed using a passive phased array, these procedures may be adapted for use with active aperture arrays as well. Such technology enhances the chances that the high procurement cost of phased arrays will be offset by reduced life-cycle costs.

RESONANCE PHENOMENA ON MULTIPLE-YAGI ARRAYS

J.M. Tranquilla

and

G.B. Graham

University of New Brunswick
Fredericton, New Brunswick
Canada

Abstract

Theoretical and experimental swept-frequency radiation and impedance characteristics of several multiple-Yagi arrays indicate that in addition to the resonance phenomena associated with the dipole cutoff region of the single Yagi, other resonances are also present on the multiple-Yagi configuration and that these resonances are dependent not only upon the individual Yagi parameters but also upon the relative orientation and spacing of the array antennas. Substantial variations are also observed in the array gain, bandwidth, and front-to-back ratio with the antenna spacing and position.

I. Introduction

Study of a certain class of resonance phenomena on the single Yagi antenna[1] has shown that these resonances are associated with a strong reflection of energy from the front end of the antenna or from a stop region which has entered the director segment of the antenna. It has also been shown that a scheme of progressively tapering the director lengths toward the front of the antenna effectively eliminates these resonances by preventing the stop region from entering the antenna and by providing

a smooth transition of phase velocity to near the free space value. The resonances themselves are characterized by narrow-band reductions in directivity and front-to-back ratio and are associated with very large out-of-phase currents on two or more adjacent directors. The frequency of the resonances is determined by the coupling between all the elements in the array and so is dependent upon the antenna geometry (element size, length and spacing). This paper considers the additional effects of placing two seven-element antennas in a "piggy-back" array as shown in Figure 1. The antennas are modelled as in [1] except with the necessary complication of considering coupling effects between individual antennas. The model allows for either or both antennas to be excited at any element location. The element base currents are solved from which the far-field swept-frequency radiation fields are computed.

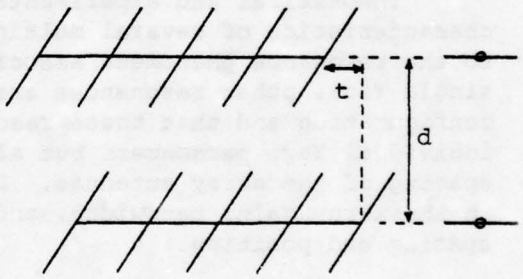

Fig. 1 Geometry of two Yagis in "piggy-back" configuration.

II. Both Antennas Excited, Variable Shift, t

Figure 2 shows the swept-frequency radiation pattern for two identical driven seven-element Yagis in paggy-back configuration with relative shift t = 0. The array separation, d, of 2.0 cm. (.05λ at the half-wavelength frequency of the driven elements) is chosen to emphasize the effects of

close spacing although similar effects are present (to a lesser degree) for spacings up to 0.5λ. Note that the sharp resonance at 735 MHz. is similar to the resonance which occurs on the cutoff edge of the single seven-element Yagi[1] and that this resonance can be eliminated by element tapering as for the single antenna. However, when the antennas are shifted (variable t) several new anomolous responses appear (Figure 3) both within and outside the

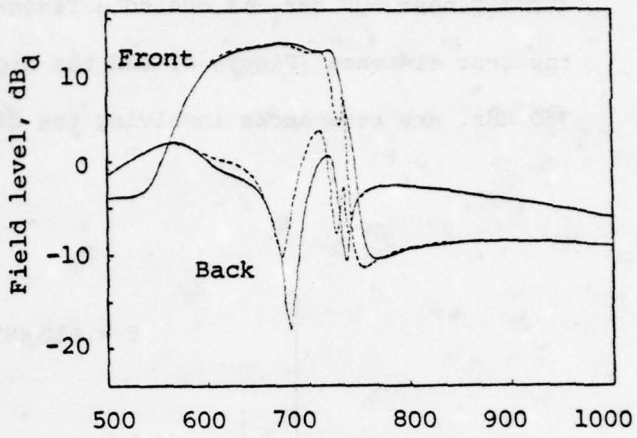

Fig. 2 Calculated radiation pattern for two 7-element Yagis, t = 0, d = 2.0 cm. Dashed lines are for untapered antennas, solid lines are for antennas with two front directors tapered by 0.25 cm.

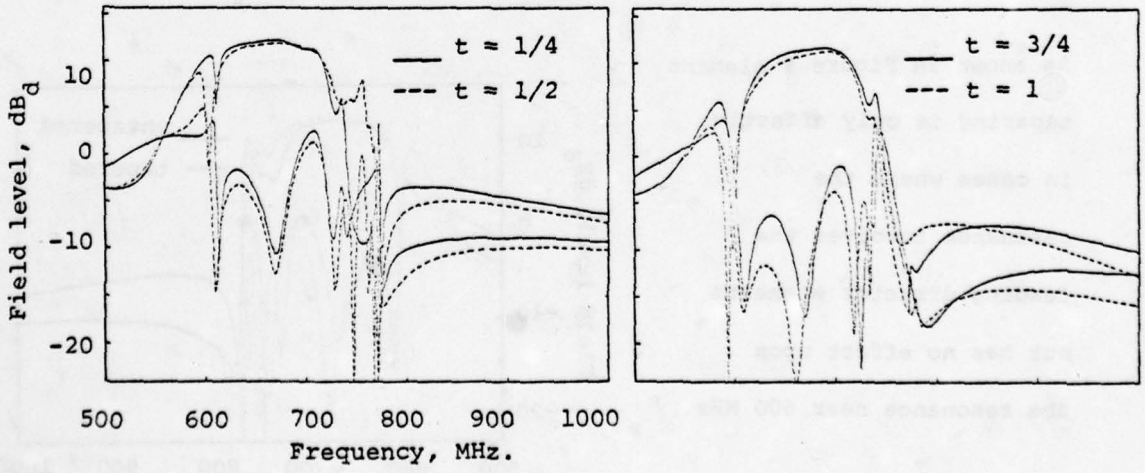

Fig. 3 Calculated radiation patterns for two 7-element Yagis, d = 2.0 cm., with variable shift t = 1/4, 1/2, 3/4, 1 times the director spacing.

antenna passband in addition to the 735 MHz. resonance. The low frequency anomaly near 600 MHz. is due to a resonance between the antennas involving the rear elements (Figure 4) and the higher-frequency anomalies around 750 MHz. are resonances involving the directors on each antenna.

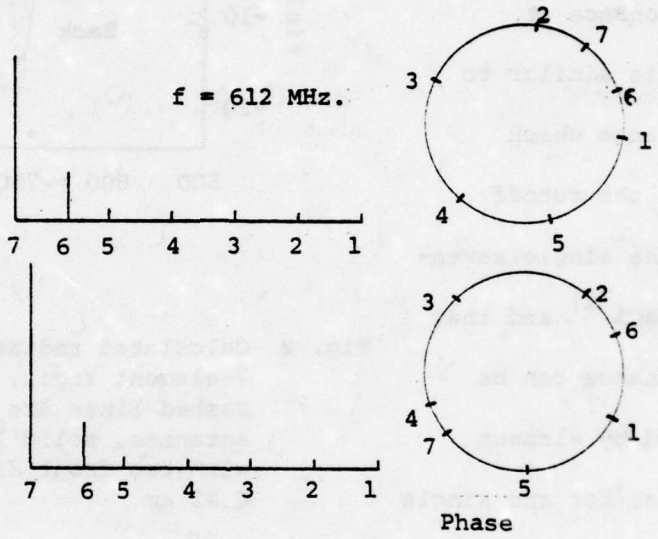

Fig. 4 Normalized computed dipole base current magnitude and phase for two 7-element Yagis at 612 MHz. resonance, d = 2.0 cm., t = 1/4 director spacing. Elements are shown numbered from front end. Elements #6 are excited in phase.

As shown in Figure 5 element tapering is only effective in cases where the resonance involves the leading director elements but has no effect upon the resonance near 600 MHz.

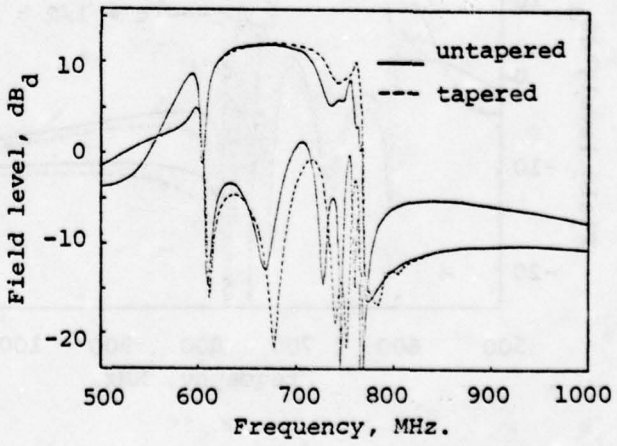

Fig. 5 Radiation patterns for two 7-element Yagis, d = 2.0 cm., t = 1/2 director spacing.

III One Antenna Excited

When only one of the antennas is excited (with the other antenna parasitic and terminated either reactively or resistively) the radiation characteristics of the array may be severely altered. Figure 6 shows the case for the parasitic antenna terminated in both a short circuit and 50 Ω. For the short circuit termination the resonance at 735 MHz. is present

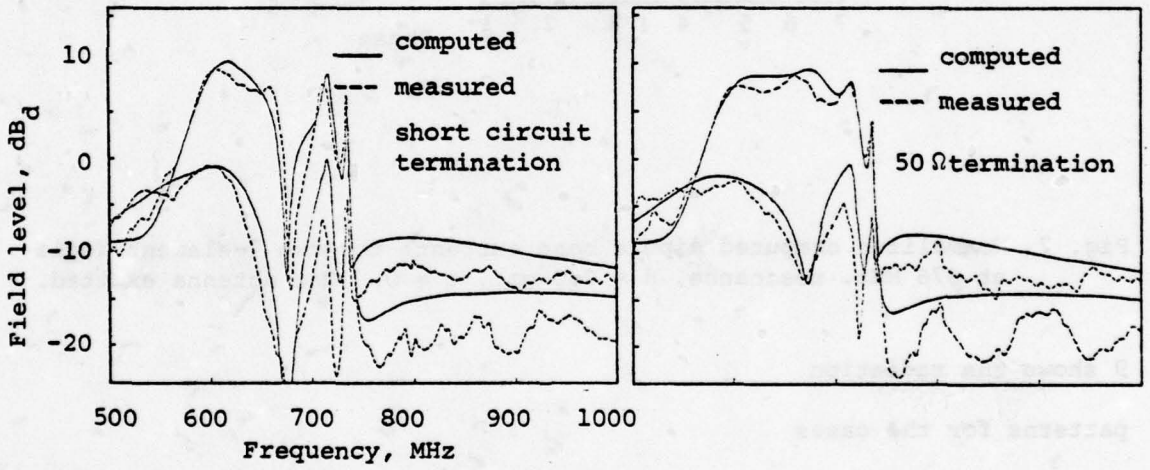

Fig. 6 Radiation patterns for two 7-element Yagis, d = 2.0 cm., t = 0, one antenna excited.

as well as an extremely large resonance in the centre of the passband (676 MHz.). This resonance involves large out-of-phase currents on the two "driven" elements (Figure 7). Terminating the normally-driven element on the parasitic antenna eliminates the 676 MHz. anomaly and the additional effect of element tapering is to eliminate the 735 MHz. resonance as well (Figure 8). When the antennas are shifted with respect to each other the resonance effects become even more pronounced. Figure

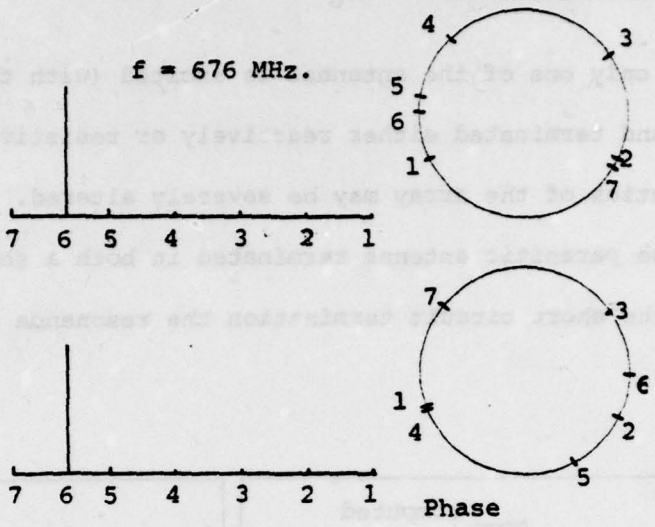

Fig. 7 Normalized computed dipole base currents for two 7-element Yagis at 676 MHz. resonance, d = 2.0 cm., t = 0. One antenna excited.

9 shows the radiation patterns for the cases where the driven antenna is shifted ahead of the parasitic antenna by a distance equal to one-quarter and one-half the director spacing. The result is the occurrence of another low

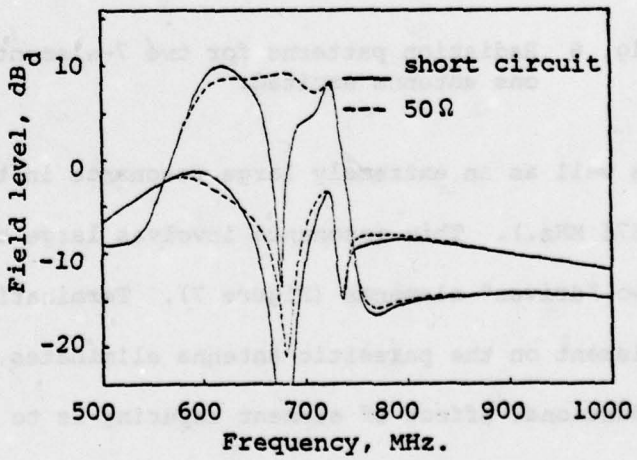

Fig. 8 Computed radiation patterns for two 7-element Yagis, d = 2.0 cm., t = 0, one antenna excited, both antennas tapered 0.25 cm. per element on two front directors.

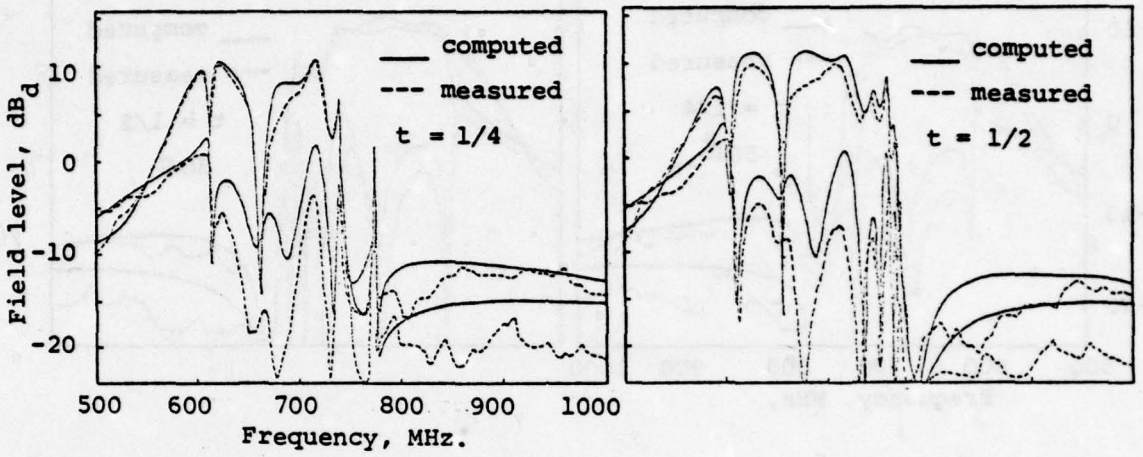

Fig. 9 Radiation patterns for two 7-element Yagis, d = 2.0 cm., t = 1/4, 1/2, director spacing, one antenna excited, second antenna short circuit terminated. Excited antenna is shifted ahead of parasitic antenna.

frequency anomaly at 604 MHz. in addition to several others throughout the passband. Terminating the parasitic antenna affects the 676 MHz. resonance as shown in Figure 10. Since the 604 MHz. anomaly involves large currents on the parasitic antenna reflector element (Figure 11) the termination has no effect upon this resonance. If, instead of shifting the driven antenna ahead, one shifts the driven antenna behind the parasitic antenna one obtains the radiation patterns shown in Figure 12 where several of the resonance frequencies are now different from the previous case. As before, terminating the parasitic antenna affects only the resonance for which large currents flow on the parasitic-antenna "driven" element (Figure 13).

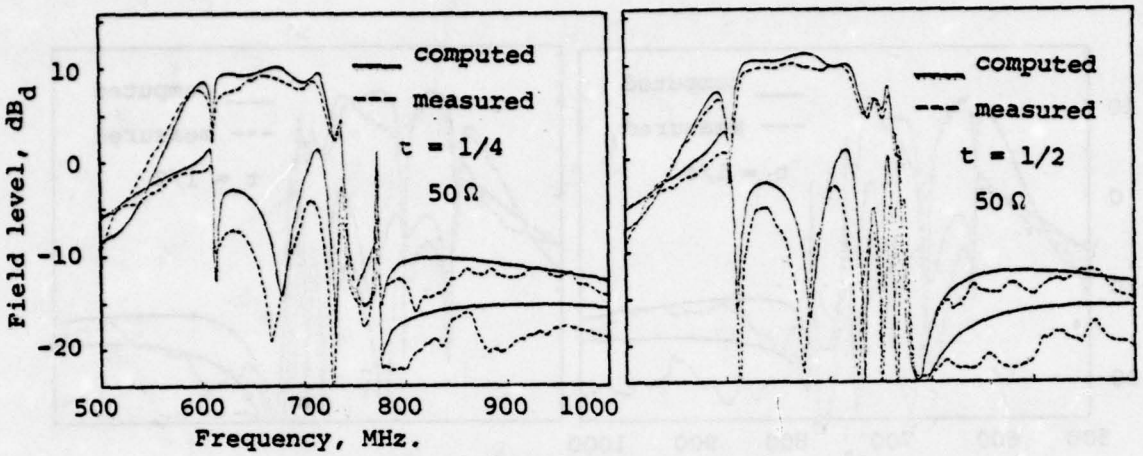

Fig. 10 Radiation patterns for two 7-element Yagis, d = 2.0 cm., t = 1/4, 1/2 director spacing, one antenna excited, second antenna terminated with 50 Ω. Excited antenna is shifted ahead of parasitic antenna.

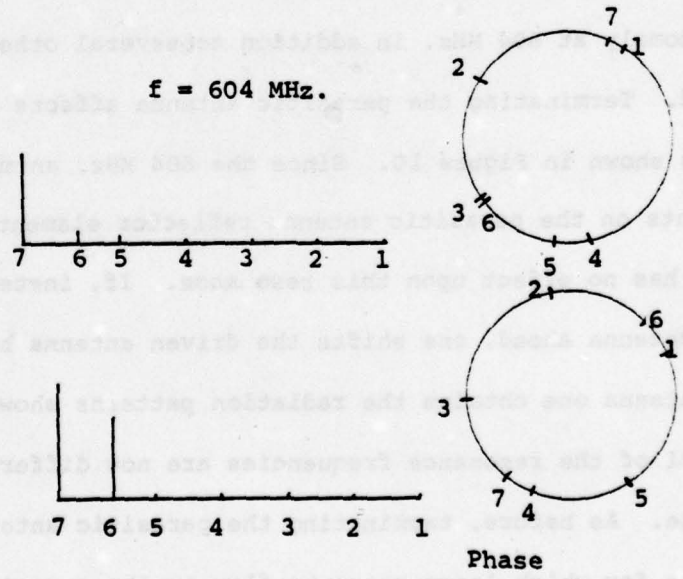

Fig. 11 Normalized computed dipole base current for two 7-element Yagis at 604 MHz. resonance, d = 2.0 cm., t = 1/2 director spacing, one antenna excited, other antenna short-circuit terminated. Excited antenna is shifted ahead of parasitic antenna.

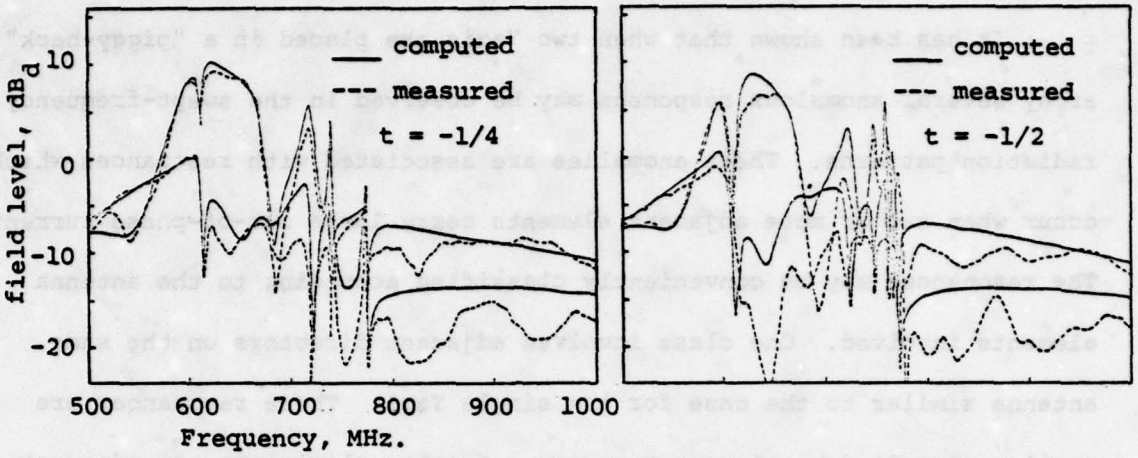

Fig. 12 Radiation patterns for two 7-element Yagis, d = 2.0 cm., t = -1/4, -1/2 director spacing, one antenna excited, other antenna short-circuit terminated. Excited antenna is shifted behind parasitic antenna.

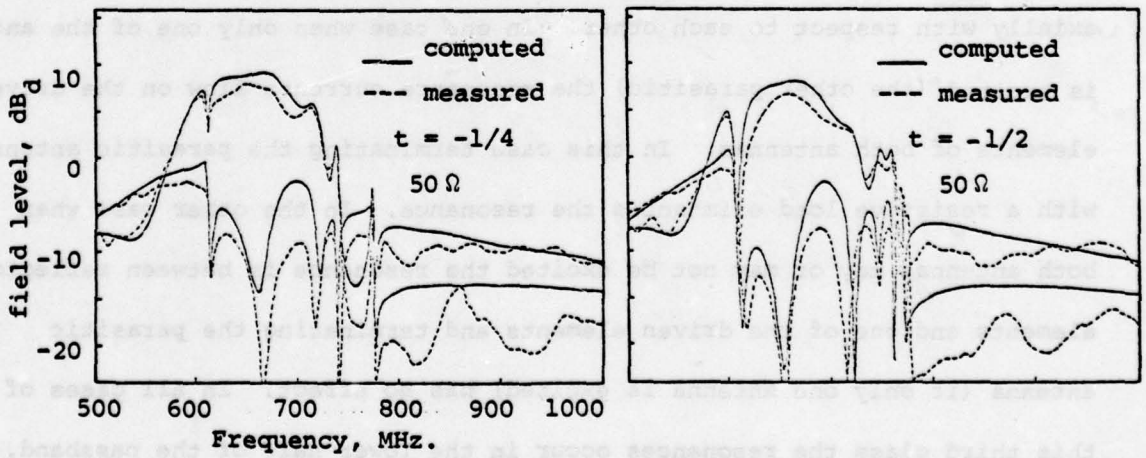

Fig. 13 Radiation patterns for two 7-element Yagis, d = 2.0 cm., t = -1/4, -1/2 director spacing, one antenna excited, other antenna terminated in 50 Ω. Excited antenna is shifted behind parasitic antenna.

IV. Conclusions

It has been shown that when two Yagis are placed in a "piggy-back" array several anomalous responses may be observed in the swept-frequency radiation patterns. These anomalies are associated with resonances which occur when two or more adjacent elements carry large out-of-phase currents. The resonances may be conveniently classified according to the antenna elements involved. One class involves adjacent directors on the same antenna similar to the case for the single Yagi. These resonances are easily controlled by element tapering. Another class involves adjacent directors on opposite antennas when the antennas are shifted axially with respect to each other. These resonances may also be controlled by element tapering. Both of the above classes of resonances involving director elements occur in the upper half of the passband and particularly near the upper bandedge. A third class of resonances involves the driven and reflector elements on opposite antennas when the antennas are shifted axially with respect to each other. In one case when only one of the antennas is excited (the other parasitic) the resonance currents flow on the driven elements of both antennas. In this case terminating the parasitic antenna with a resistive load eliminates the resonance. In the other case when both antennas may or may not be excited the resonance is between reflector elements and one of the driven elements and terminating the parasitic antenna (if only one antenna is excited) has no effect. In all cases of this third class the resonances occur in the lower half of the passband. The practical implication of this work is that when two or more Yagis are stacked in close proximity (within 0.5λ) to each other either to

achieve greater directivity or as a result of multiple usage of a common mast structure great care must be taken to ensure that antenna performance does not become seriously degraded. In many cases element tapering and careful alignment (to avoid axial shift) have proven to be effective in controlling resonant behaviour.

References

1. J.M. Tranquilla, K.G. Balmain, "Resonance Phenomena on Yagi Arrays", Joint IEEE-AP/S-URSI Symposium, Seattle, Washington, USA, June 1979.

RADIATION FROM CONFORMAL DIPOLE ARRAYS MOUNTED ON DIELECTRICALLY-CLAD CONDUCTING CYLINDERS

K.S.Lee and G.Eichmann

Department of Electrical Engineering, The City College of City University of New York, New York, N.Y. 10031

Abstract: An active element pattern for a dipole array mounted at the surface of a dielectric layer clad on a conducting cylinder is derived. Mutual couplings between dipole columns are calculated using a Watson transform method. The poles of this transform are traced from their initial locations with a perturbation technique which varies gradually the dielectric constant of the layer from the free space value to the final value. A mode coupling is resulted in by the emergence of new set of poles(T.E.) in addition to the original poles(T.M.) as the beam of the array is lifted away from the horizontal plane. As an elevation beam angle is increased from zero, a resonance due to an emerging real pole out of the mode coupling takes place inside the dielectric layer. Due to the resonance, the elevation angle cut of the active element pattern undergoes a significant change from the cut on the horizontal plane.

1. Introduction

Planar dipole arrays with or without ground planes have been discussed by several authors (1),(2),(3). Variations of a dipole input impedance in a E- or H-plane scan have been investigated using various approximations for an element dipole

current. These studies show that, due to a steep variation of the dipole input impedance at a H-plane scan grating lobe angle, a wide angle coverage in the H-plane scan is difficult. On the other hand, the change in a dipole input impedance in a E-plane scan is moderate. To investigate the possibility of a wide angle E-plane scan while maintaining a constant beam pattern on a horizontal plane through a full 360 degree azimuthal scanning, a dipole array mounted on a dielectrically-clad conducting cylinder is considered.

The geometry of the array is shown in Fig.(1). The array has a large number of dipole columns mounted circular symmetrically at the surface of a thin dielectric layer clad on a large conducting cylinder. Each dipole column is an infinite collinear array of axial dipole elements, which are excited at their center gaps with feedlines of a given characteristic admittance driven by voltage sources. To study the overall beam scan characteristics of this array, the active element pattern is derived.

In the following section, a numerical formulation of the problem is presented. In section 3, approximation methods for the calculation of Green's functions in a near zone are discussed. In section 4, the active impedance of a dipole element as a function of azimuthal beam scan direction is found. The active element pattern is derived in section 5 and, in the final section, concluding remarks are presented.

2. Numerical formulation.

Due to the periodic nature of this array in the axial direction, the active element pattern can be separated from an array factor in z-direction. By scanning the beam of a single dipole column from a horizontal plane toward the axial direction

and normalizing radiated power both in azimuth and elevation to the horizontal maximum radiation, the active element pattern of the array is derived. Calculating pattern cuts at various elevation angles, the active element pattern can be synthesized.

To find the active element pattern cut at a given elevation angle, dipole currents of all columns must be known when a single dipole column is excited. The phases of the exciting voltage sources are linearly varied in the axial direction to steer the beam to the given elevation angle. Dipole elements are excited at their centers with feedlines of a given characteristic admittance which are matched to the sides of voltage generators. To derive the active element pattern, the voltage sources of all dipole columns except the excited one are short-circuited. To find the dipole currents of all columns in such an array environment, N number of voltage phase sequences, equal to the number of dipole columns, are applied to the dipole columns in a circumferential direction(4). A dipole input admittance, which is a function of an excited phase sequence, is first derived, and the response current for the phase sequence is found. Superposing the response currents for N number of phase sequences, dipole currents of all columns for a single column excitation are known.

For a given phase sequence excitation, dipole currents of all columns are the same except the imposed phase difference. The dipole currents are expanded into a series of five known current terms with the same number of unknown constants. The five unknown constants are determined by imposing a E-field boundary condition at a dipole surface of a reference column. E and H fields can be superposed with TE and TM modes with respect to the axial direction of the cylinder. TE and TM modes are derived respectively from z-component magnetic and electric Hertzian potentials(5). The electric Hertzian potential determines z-component electric field, E_z at a dipole surface of the reference column.

$$E_z = \left(k^2 + \frac{\partial^2}{\partial z^2} \right) \overline{\pi}_z^e \qquad (1)$$

Inside the dielectric layer, the electric Hertzian potential due to a single dipole column at the interface of the dielectric and the free space can be superposed with $\overline{\pi}_i$'s which are defined as

$$\overline{\pi}_i(\rho,\phi,z:b,\phi') = \sum_{n=-\infty}^{\infty} G_n(\rho,\phi:b,\phi') \exp(j\beta_n z) \frac{1}{2d} \int_{-h}^{h} I_i(z') \exp(-j\beta_n z')\, dz'$$
$$(i=1,2,\cdots 5) \qquad (2)$$

$I_i(z')$ is one of the five current terms (3), $\beta_n = k_o \sin\theta + \overline{\pi}\, n/d$, $2h$ is a dipole length and θ is an elevation beam angle measured from the horizontal plane. A dipole center-to-center distance in the axial direction is $2d$ and (b,ϕ') is the coordinates of the source column. $G_n(\rho,\phi:b,\phi')$ is a two dimensional spatial harmonic Green's function.

$$G_n(\rho,\phi:b,\phi') = \frac{j}{\omega\varepsilon\sqrt{k^2-\beta_n^2}\, b} \sum_{m=-\infty}^{\infty} \exp(jm(\phi-\phi'))\, Z(\rho) R / \Big[\Big\{ X(\varepsilon_o/\varepsilon) H_m^1(\sqrt{k^2-\beta_n^2}\, a) -$$
$$T(\varepsilon_o/\varepsilon) H_m^2(\sqrt{k^2-\beta_n^2}\, a) \Big\} R - \left(\frac{m\beta_n}{k\sqrt{k^2-\beta_n^2}\, b} \right)^2 \left(\frac{k^2-k_o^2}{k_o^2-\beta_n^2} \right)^2 Z(b) W \Big] \qquad (3)$$

where
$$X(x) = H_m^{2\prime}(\sqrt{k^2-\beta_n^2}\, b) - x \frac{\sqrt{k^2-\beta_n^2}}{\sqrt{k_o^2-\beta_n^2}} \frac{H_m^{1\prime}(\sqrt{k_o^2-\beta_n^2}\, b)}{H_m^1(\sqrt{k_o^2-\beta_n^2}\, b)} H_m^2(\sqrt{k^2-\beta_n^2}\, b) \qquad (3a)$$

$$T(x) = H_m^{1\prime}(\sqrt{k^2-\beta_n^2}\, b) - x \frac{\sqrt{k^2-\beta_n^2}}{\sqrt{k_o^2-\beta_n^2}} \frac{H_m^{1\prime}(\sqrt{k_o^2-\beta_n^2}\, b)}{H_m^1(\sqrt{k_o^2-\beta_n^2}\, b)} H_m^1(\sqrt{k^2-\beta_n^2}\, b) \qquad (3b)$$

$$Z(x) = H_m^1(\sqrt{k^2-\beta_n^2}\, a) H_m^2(\sqrt{k^2-\beta_n^2}\, x) - H_m^1(\sqrt{k^2-\beta_n^2}\, x) H_m^2(\sqrt{k^2-\beta_n^2}\, a) \qquad (3c)$$

$$W = H_m^{1\prime}(\sqrt{k^2-\beta_n^2}\,a)\,H_m^2(\sqrt{k^2-\beta_n^2}\,b) - H_m^1(\sqrt{k^2-\beta_n^2}\,b)\,H_m^{2\prime}(\sqrt{k^2-\beta_n^2}\,a) \qquad (3d)$$

$$R = X(1)\,H_m^{1\prime}(\sqrt{k^2-\beta_n^2}\,a) - T(1)\,H_m^{2\prime}(\sqrt{k^2-\beta_n^2}\,a) \qquad (3e)$$

ε and ε_o, k and k_o are dielectric constants and wave numbers respectively within the dielectric layer and in the free space. a is the cylinder radius. H_m^1 and H_m^2 are first and second kind Hankel functions of m-th order. $H_m^{1\prime}$ and $H_m^{2\prime}$ are the derivatives of the Hankel functions with respect to their arguments.

The total vector potential π_z^e for p-th phase sequence excitation can be superposed with π_i from each column.

$$\pi_z^e(\rho,\phi,z:p) = \sum_{i=1}^{5} C_i(p) \sum_{\ell=0}^{N-1} \pi_i(\rho,\phi,z:b,\frac{2\pi}{N}\ell)\exp(j\frac{2\pi}{N}\ell p) \qquad (4)$$

C_i's are the unknown five constants to be solved. Also, from the boundary condition on the tangential E-field and Eq.(1), z-dependence of π_z^e at a dipole surface is given as

$$\pi_z^e(z) = \frac{1}{k}\left(A\cos(kz) + B\sin(kz) - \frac{V}{2}\sin|kz|\right) \qquad (5)$$

A and B are unknown constants, and V is a dipole gap voltage (4). Matching Eqs. (4) and (5) at seven sampling points at a dipole surface, the five unknown constants plus A and B are determined as a function of V. This calculation gives dipole input admittance Y(p) for p-th phase sequence excitation. For a given feedline characteristic admittance Y_g, the response dipole current can be derived. Once π_i's due to all columns are found, π_z^e's for $0 \le p \le N-1$ can be found simultaneously with Fast Fourier Transform algorithm (FFT). To find π_i's, both summations in Eqs. (2) and (3) must be carried out. This step will be discussed in the following section.

3. Green's function in a near zone.

The first summation to be considered is the one in Eq.(3). The direct harmonic series summation for G_n in a near zone has a poor convergence when the radius of the cylinder is large. For this reason, alternate approximation schemes are used. When a field point is located outside the immediate neighborhood of the source column, $G_n(\rho,\phi:b,\phi')$ is calculated using a Watson transform method. This method can cover most of the angular region around the cylinder. In the immediate neighborhood of the source column, where $|\phi-\phi'|$ is small, a planar approximation replaces the Watson transform method.

In the Watson transform method, the harmonic series for G_n is transformed to residue series with poles in the upper half of a complex ν-plane. The contour integral at infinite semicircle in the plane goes to zero. Poles in the complex ν-plane can be traced by varying the value of the dielectric constant of the layer from the free space value ε_o to its final value ε. If the order of Hankel function m in Eq.(3) is substituted with ν of the complex plane, the poles of G_n when $\varepsilon=\varepsilon_o(k=k_o)$ are zeroes of $H_\nu^1(\sqrt{k_o^2-\beta_n^2}\,a)$, because, in this case, $T(1)=0$ and $X(1)=-4j/\{\pi\sqrt{k_o^2-\beta_n^2}\,b\cdot H_\nu^1(\sqrt{k_o^2-\beta_n^2}\,b)$ using Wronskian relationship of Hankel functions. The zeroes of $H_\nu^1(\sqrt{k_o^2-\beta_n^2}\,a)$, ν_m's in a complex ν- plane are well known functions of the argument (6). As ε is varied from ε_o, in addition to the shifts of ν_m's from their original locations, a new set of poles are emerging unless $\beta_n=0$, because the cancelation of R in the numerator and the denominator of G_n is not possible any more. This new set of poles ν_m''s can be traced from zeroes of $H_\nu^{1\prime}(\sqrt{k_o^2-\beta_n^2}\,a)$ which also can be found as a function of the argument, $\sqrt{k_c^2-\beta_n^2}\,a$. Due to the presence of R in the numerator, the residues of the new poles are slowly increasing from zero as ε is varied from ε_o. The residue arising from a pole which deviates far from its beginning position has a large value. Except for ν_1' originating from the first zero of $H_\nu^{1\prime}(\sqrt{k_c^2-\beta_n^2}\,a)$,

both sets of poles do not drift away far from their initial positions and can be readily traced. Generally, the imaginary parts of the poles are decreased. When ε is increased from ε_o, ν_1' undergoes a remarkable transition in the ν-plane, dropping down rapidly toward the real axis. When the argument of $H_\nu^{1'}(\sqrt{k_c^2-\beta_n^2}\,a)$ is real, the real part of ν_1' is increased while its imaginary part goes to zero. The residue series for G_n at the surface of a dipole column at (b,ϕ) is given by the following equation.

$$G_n(b,\phi:b,\phi') = \frac{2\pi}{j\omega\varepsilon\sqrt{k^2-\beta_n^2}\,b} \sum_{\nu_m,\nu_m'} \frac{\cos\nu(|\phi-\phi'|-\pi)}{\sin(\nu\pi)}\ \mathrm{Res}(\nu) \qquad (6)$$

where

$$\mathrm{Res}(\nu) = \frac{Z(b)R}{\frac{\partial}{\partial\nu}\left[\left\{X(\varepsilon_o/\varepsilon)H_\nu^1(\sqrt{k^2-\beta_n^2}\,a) - T(\varepsilon_o/\varepsilon)H_\nu^2(\sqrt{k^2-\beta_n^2}\,a)\right\}R - \left(\frac{\nu\beta_n}{k\sqrt{k^2-\beta_n^2}}\right)^2\left(\frac{k^2-k_o^2}{k_o^2-\beta_n^2}\right)Z(b)W\right]}$$

$X(x)$, $Y(x)$, $Z(x)$ and R are the same functions as in Eq.(3) except the order of Hankel functions is a complex value ν instead of a real integer m. ν_m's and ν_m''s as well as various Hankel functions in Eq.(6) are evaluated using Langer's representation for Hankel functions of large and complex orders. Unless $\beta_n=0$, the dominant pole of Eq.(6) is ν_1' of the real axis. Because of the absence of an imaginary part in ν_1', the magnitude of the residue due to ν_1' does not decrease as the angular distance between the source and the field column $|\phi-\phi'|$ is increased. As a result, ν_1' causes a resonance with a standing wave inside the dielectric layer.

In the case of the fundamental(n=0), which is the most important one for $\overline{\pi}_i$ in Eq.(2), if the elevation beam scan direction is to the horizontal, i.e. $\theta = 0$ and $\beta_n = 0$, ν_m's, the first set of poles are the only poles of G_o. As the beam is lifted away from the horizontal plane, ν_m''s are emerging in addition to ν_m's ,because $\beta_n \neq 0$. The resonance due to the real pole ν_1' is

getting stronger as θ is increasing. Because the fundamental Green's function has more importance than other spatial harmonics, the emergence of new poles ν'_m's, especially the resonant one ν'_1 when the beam is scanned away from the horizontal plane has a significant impact on the active element pattern. This will be discussed in detail in section 4.

For all other spatial harmonics except n=-1 when $|\beta_1| < k_o$, the argument of Hankel function $H_\nu^1(\sqrt{k_o^2-\beta_n^2}\,a)$ and its derivative is imaginary (The branch cut of the argument is taken such that the sign of the imaginary value is positive). The initial positions of ν_m's and ν'_m's in such cases are on the imaginary axis. As ε is increased from ε_o, there are no large shifts from the initial positions except ν'_1, which has a significant drift toward the real axis and, when ε is further increased after ν'_1 hits the real axis, the transition of ν'_1 is along the positive real axis. Because ν'_1 has a small imaginary value compared with other poles regardless whether it is on the imaginary or real axis, G_n for harmonics is mainly determined by ν'_1. As the following discussion shows, the approximate location of ν'_1 can be found more easily using a planar approach.

In the immediate neighborhood of the source column where $|\phi-\phi'|$ is small, the residue series of Eq.(6) is not efficient because of a slow convergence. In this region, G_n is calculated using a planar approximation. The cylindrical surface is replaced with a planar one, and $G_{np}(b,\phi:b,\phi')$ which is a planar version for $G_n(b,\phi:b,\phi')$ is given as

$$G_{np}(b,\phi:b,\phi') = -\frac{2}{\omega\varepsilon}\int_0^\infty \left\{\left[1-\exp\left\{j\sqrt{k^2-\beta_n^2-k_y^2}\,2(b-a)\right\}\right] R_p \cos\left\{(\phi-\phi')bk_y\right\} dk_y \Big/ \left\{\left\{U(\varepsilon_o/\varepsilon)\right.\right.\right.$$
$$\left.\left.\left.+\exp\left\{j\sqrt{k^2-\beta_n^2-k_y^2}\,2(b-a)\right\} U(-\varepsilon_o/\varepsilon)\right\} R_p + \left(\frac{k_y\beta_n}{k}\right)^2 \left(\frac{k_o^2-\beta_n^2}{k_o^2-\beta_n^2}\right)^2 \left\{1-\exp\left(j\sqrt{k^2-\beta_n^2-k_y^2}\,4(b-a)\right)\right\}\right] \tag{7}$$

where $$U(x)=\sqrt{k^2-\beta_n^2-k_y^2} + x\frac{k^2-\beta_n^2}{k_o^2-\beta_n^2}\sqrt{k_o^2-\beta_n^2-k_y^2}$$

$$R_p = U(1) - \exp\left\{j\sqrt{k^2-\beta_n^2-k_y^2}\,2(b-a)\right\}U(-1)$$

For the fundamental (n=0) and lower harmonics such that $k^2-\beta_n^2 > 0$, the total integration interval in Eq.(7) is divided into a finite and an infinite one. In the finite interval, the integration is carried out numerically. In the infinite interval where $k_y^2 >> k^2-\beta_n^2$ all exponential terms can be neglected and the integral can be approximated with an asymptotic expansion. For higher harmonics such that $k^2-\beta_n^2 < 0$, the integral in Eq.(7) can be approximated with Kelvin function of zero order.

The numerical integration for G_{np} must be handled with care when $k_o^2 - \beta_n^2 > 0$, because the denominator of the integrand has a pole, k_{yp} on the real axis unless $\beta_n=0$. When $\beta_n=0$, as the case in Eq.(3), R_p both in the numerator and in the denominator can be canceled eliminating the pole. We can reduce the denominator of Eq.(3) to that of Eq.(7) for a real and large ν using the relation between ν and k_y: $\nu = bk_y$. Once the pole of Eq.(7), k_{yp} is known, the approximate location of the real pole in Eq.(3), ν_1' is given by the same relation.

The planar approximation of G_n with G_{np} is not complete unless an additional term is included. This term arises from a wave rotation around the cylinder, which does not exist in a planar case. The effect of rotational waves other than the one arising from the real pole ν_1' can be ignored because of exponential wave decays around the circumference of the cylinder. By investigating the angle dependent part of Eq.(6), the additional term can be found.

$$\frac{\cos\nu(|\phi-\phi'|-\pi)}{\sin(\nu\pi)} = j\left\{\frac{\exp(-j2\pi\nu)}{1-\exp(-j2\pi\nu)} - \frac{\exp(j2\pi\nu)}{1-\exp(j2\pi\nu)}\right\}\cos(\nu|\phi-\phi'|) + \sin(\nu|\phi-\phi'|) \qquad (8)$$

Because of its phase, the first term of Eq.(8) can be identified as a rotational wave around the cylinder. From Eqs.(6),(7) and (8), $G_n(b,\phi:b,\phi')$ for a small $|\phi-\phi'|$ is given by the following equation.

$$G_n(b,\phi:b,\phi') = G_{np}(b,\phi:b,\phi') + \frac{2\pi}{j\omega\varepsilon\sqrt{k^2-\beta_n^2}\,b}\frac{\cos\nu_1'\pi}{\sin\nu_1'\pi}\cos\nu_1'|\phi-\phi'|\cdot\mathrm{Res}(\nu_1') \qquad (9)$$

The additional term is needed only when ν_1' is near or on the real axis of the complex ν-plane. For a smooth transition of the Green's function at the boundary between the two regions, 15 residue terms each for ν_m's and ν_m''s are included for the series in Eq.(6).

4. Dipole input admittance as a function of a phase sequence.

The summation in Eq.(2) is a superposition of various spatial harmonics to find a partial electric Hertzian potential $\pi_i(\rho,\phi,z:\rho',\frac{2\pi}{N}\ell)$ arising from one of five current terms of ℓ-th column at $(\rho',\frac{2\pi}{N}\ell)$. To impose E-field boundary condition at a dipole surface of the reference column at $(b,0)$, $\pi_i(b,0,z:b,\frac{2\pi}{N}\ell)$'s for $0\le\ell\le(N-1)$ must be known. The number of spatial harmonics needed in the summation depends on the angle between the source and the reference column, $\frac{2\pi}{N}\ell$. Unless the reference column is in the immediate vicinity of the source column, two terms, a fundamental(n=0) and a first harmonic(n=-1) can replace the infinite summation in most cases. As we discussed in section 3, for higher harmonics, the arguments of Hankel functions and their derivatives are imaginary with imaginary poles for G_n. Because of the fast decrease of $|G_n|$ due to the imaginary poles along the circumference of the cylinder, the contribution of higher harmonics to π_i is small.

When the angular distance between the reference and a source column is small, more harmonic terms are needed. The harmonic Green's function in this region is given by Eq.(9). Unless ℓ is not equal to zero, four or five harmonics plus the fundamental are needed for $\pi_i(b,0,z:b,\frac{2\pi}{N}\ell)$. When $\ell = 0$, π_i at the dipole surface of the reference column is due to the current of the same column, and many harmonic terms are needed. For this case, $(\phi-\phi')b$ in Eq.(7) is replaced with the radius of a dipole r_o. Since r_o is small, $|G_{np}|$ is a slowly decreasing function as $|n|$ is increased, and many harmonic terms must be included for π_i. The integrals for higher harmonics are approximated with Kelvin functions of zero order as discussed in section 3. For $r = 0.007\lambda_o$ and $\varepsilon = 2.5\varepsilon_o$, π_i is calculated with sixty harmonic terms ($|n| \leq 30$). λ_o is a free space wavelength.

Finally, π_i's are summed to give the total Hertzian potential π_z^e at a dipole surface of the reference column with a weighting phase factor $\exp(j\frac{2\pi}{N}\ell p)$ as shown in Eq.(4). As mentioned earlier, $\pi_i(b,0,z:b,\frac{2\pi}{N}\ell)$ for a large ℓ is mainly determined by the fundamental G_o (and G_{-1} when $k_o^2 - \beta_{-1}^2 > 0$), which, in turn, can be approximated only with the residue arising from the real pole ν_1', because the residues of higher poles have significant decays along the cylinder circumference. From Eqs.(2),(4) and (6), $S(\ell_1, N-\ell_1:p)$, the weighted summation of π_i's from ℓ_1-th dipole column to $(N-\ell_1)$-th dipole column which are located in the shadow of the cylinder with respect to the reference column, is given as

$$S(\ell_1, N-\ell_1:p) = \sum_{\ell=\ell_1}^{N-\ell_1} \pi_i(b,0,z:b,\frac{2\pi}{N}\ell)\exp(j\frac{2\pi}{N}\ell p)$$

$$= \frac{2\pi\exp(j\beta_o z)}{j\omega\varepsilon\sqrt{k^2-k_o^2}\,b}\left(\frac{1}{2d}\int_{-h}^{h} I_i(z')\exp(-j\beta_o z')\,dz'\right)\mathrm{Res}(\nu_1')\sum_{\ell=\ell_1}^{N-\ell_1}\frac{\cos\{\nu_1'(\frac{2\pi\ell}{N}-\pi)\}}{\sin\nu_1'\pi}\exp(j\frac{2\pi\ell}{N}p) \qquad (10)$$

When γ_1' of the first harmonic Green's function G_{-1} is also real, another summation due to the residue from this pole also must be included in Eq.(10). Since the summation in Eq.(10) has a closed form expression, Eq.(4) is summed only for those dipole columns which are not included in the summation of Eq. (10).

As discussed in section 2, by matching π_z^e's of Eqs. (4)and (5), the active dipole input admittance Y(p) is derived. Y(p) is a widely varying function of the imposed phase sequence p. Since the phase sequence determines an azimuthal beam scan angle ϕ, which is the angle of outgoing beams from the normals of the cylinder surface, the active dipole input admittance can be considered as a function of ϕ. Using a planar approximation locally along the circumference of a large cylinder, ϕ is given from the excited phase sequence p by the following equation.

$$\phi = \sin^{-1}\left(\frac{p}{d_c N\sqrt{1-\sin^2\theta}}\right) \qquad (11)$$

where d_c is the distance between dipole columns. In the following discussion, the number of dipole columns N is fixed as 200. Also, the thickness of the dielectric layer (b-a) and a dipole length 2h are constants, respectively $0.1768\lambda_o$ and $0.5\lambda_o$ where λ_o is a free space wavelength. The elevation beam angle from the horizontal plane θ, the dielectric constant ε of the layer, the distance between dipole columns d_c and a z-direction dipole center-to-center space 2d are variables. When both d_c and 2d are $0.7\lambda_o$ and $\theta = 0$, the active dipole input impedances for different values of the dielectric constant are plotted as a function of ϕ in Fig.(2). In the figure, as ε is increased, the discontinuity of a slope is more pronounced and the angle where it occurs is shifting toward the broadside direction. In Fig.(3)

with $\varepsilon = 2.5\varepsilon_0$, $2d = 0.7\lambda_0$ and $\theta = 0^\circ$, the distance between dipole columns d_c is varied. Fig.(3) shows that the angle of slope discontinuity, which roughly determines the beam width of an elementary pattern, is mainly dependent on d_c.

As the elevation scan angle θ is increased from zero, Y(p) has remarkable changes because of the emergence of new poles, especially the resonant pole ν_1' of the fundamental Green's function. The active dipole input impedance curve has more slope discontinuities besides the one which is caused by the same effect as a grating lobe discontinuity in a planar array. For a given value of ν_1', $S(\ell_1, N-\ell_1 : p)$ of Eq.(10) is a rapidly varying function of p. Its magnitude has a large value when $\nu_1' \approx p$, or $\nu_1' + p \approx N$, because the summation in Eq.(10) is in phase for such a value of p. The slope discontinuity of the active impedance curve occurs around a corresponding azimuthal beam scan angle ϕ determined by the phase sequence p from Eq. (11). With $\varepsilon = 2\varepsilon_0$, $d_c = 0.7\lambda_0$ and $2d = 0.55\lambda_0$, the active impedance curves when $\theta = 0^\circ$, 15°, 30° are plotted in Fig.(4). For these elevation angles, there is only one resonant pole which is from G_0. ν_1' from the first harmonic G_{-1} is still on the imaginary axis way up from the origin and does not have much influence on the active impedance curves. When the z-direction dipole center-to-center distance 2d is varied from $0.55\lambda_0$ to $0.7\lambda_0$, ν_1' from G_{-1} has a large downward shift on the imaginary axis as θ is changed from 0° to 15°. When θ is further increased to 30°, there exist two resonant poles on the real axis, since ν_1' from G_{-1} is also a real pole resulting in multiple resonances inside the dielectric layer. The active impedance curve for this case is shown in Fig.(5). In the above examples, by reducing the distance between dipole elements in the z-direction, the downward shift of ν_1' from G_{-1} is suppressed. When ε is varied to $2.5\,\varepsilon_0$ with $2d = 0.55\lambda_0$ and $d_c = 0.7\lambda_0$, similar impedance curves are obtained in Fig.(6). For these elevation angles, we have a single resonant pole from G_0.

5. Active element patterns.

In the following derivation of active element patterns, it is assumed that the characteristic admittance Y_g is matched to the real part of $Y(p)$ when both the elevation and the azimuthal beam scan angle θ and ϕ are equal to zero and the imaginary part of $Y(p)$ for these directions is eliminated with a compensation network to result in a maximum power radiation to broadside.

Superposing the response currents for N number of phase sequence excitations, the dipole currents of all columns for a single reference column excitation can be found. When the dipoles of the reference column are excited through feedlines driven by unit amplitude voltage sources while those for other columns are short-circuited, the dipole current of ℓ-th column $I^{\ell}(z)$ is given as

$$I^{\ell}(z) = \frac{Y_g}{N} \sum_{p=0}^{N} \exp\left(j\frac{2\pi}{N}\ell p\right) \frac{Y(p)}{Y_g + Y(p) - jB_o} \frac{\sum_{i=1}^{5} C_i(p) I_i(z)}{\sum_{i=1}^{5} C_i(p) I_i(0)} \qquad (12)$$

where $z=0$ is taken as a dipole center and B_o is the susceptance of $Y(p)$ when both p and θ are zero. To derive a far field radiation pattern from these dipole currents, $I^{\ell}(z)$'s are first Fourier integrated as the near field calculation in Eq.(2).

$$\mathcal{F}\left[I^{\ell}(z)\right] = \int_{-h}^{h} I^{\ell}(z) \exp(-jk_o z \sin\theta_1)\, dz \qquad (13)$$

θ_1 is the elevation beam angle which is determined by the element-to-element voltage phase shift of the reference

dipole column. Using a FFT algorithm, N number of $\mathcal{F}\{I^{\ell}(z)\}$'s for $0 \leq \ell \leq (N-1)$ can be found simultaneously. Linearly superposing $\mathcal{F}\{I^{\ell}(z)\}$'s from all dipole columns with a far field pattern $g(\phi:\theta_1)$ of an isolated dipole column located at (b,0) and scanned to an elevation angle θ_1, the active element pattern cut at θ_1 is derived.

$$f(\phi:\theta_1) = \sum_{\ell=0}^{N-1} g(\phi - \frac{2\pi}{N}\ell : \theta_1)\, \mathcal{F}\{I^{\ell}(z)\} \qquad (14)$$

$g(\phi:\theta_1)$ is a far field version of $G_n(\rho,\phi:b,\phi')$ in Eq.(3) when $n=0$, $\phi'=0$ and $\beta_o = k_o \sin\theta_1$. Since the direct harmonic series summation for $g(\phi:\theta_1)$ has the same convergence problem as in a near field calculation for a large radius cylinder, $g(\phi:\theta_1)$ is approximated using an alternate scheme. For a planar case where a dipole column is placed on the surface of a thin dielectric slab with a conducting ground plane, the far field is found in a closed form expression using a stationary phase integration. Alternatively, it can also be superposed with a direct ray from the dipole column and various transmitted rays from the surface of the dielectric after singly or multiply reflected from the ground plane. The later approach is adopted to calculate $g(\phi:\theta_1)$ with a modification which takes account of the fact that, in the cylindrical case, the transmitted rays radiating to a given azimuthal angle ϕ have different ray-paths inside the dielectric. $g(\phi:\theta_1)$ in the shadow region can be found with a Watson transform method for a far field.

Active element pattern cuts on the horizontal plane whose dipole input impedance curves are shown in Fig.(2) are plotted in Figs.(7),(8) and (9), where the only variable is the dielectric constant ε which is $2\varepsilon_o$, $2.5\varepsilon_o$ and $3\varepsilon_o$ respectively. Ripples at broadside and narrow beamwidths characterize

the pattern cuts. A reduction in beamwidth as well as a clear beam cutoff off broadside are anticipated from Fig.(2) where the slope discontinuity of an impedance curve is more pronounced and the azimuthal angle it occurs is shifting towards a broadside direction as ε is increased. The relation between a dipole column-to-column distance d_c and the beamwidth of an active element pattern cut on the horizontal plane can be noticed by comparing Figs.(8),(10) and (11) where d_c is $0.7\lambda_o$, $0.6\lambda_o$ and $0.8\lambda_o$ respectively with a fixed value of ε as $2.5\varepsilon_o$. The corresponding impedance curves have been shown in Fig.(3) where the angle of a slope discontinuity is moving towards broadside for an increased d_c. The above comparisons between active dipole input impedance curves and elementary pattern cuts on the horizontal plane show that the azimuthal beamwidth of an active element pattern is approximately determined by the angle of a slope discontinuity and, after this angle, the power radiation of an array is negligible.

Because of the resonance inside the dielectric layer, an active element pattern cut has a remarkable change as θ is increased from zero. Figs.(12) and (13) show the active element pattern cuts at $\theta = 0°$, $15°$ and $30°$ for those arrays whose dipole input impedance curves were presented in Figs.(4) and (5) respectively. In these figures, $\varepsilon = 2\varepsilon_o$ and $d_c = 0.7\lambda_o$, but 2d is $0.55\lambda_o$ in Figs.(4) and (12) and $0.7\lambda_o$ in Figs.(5) and (13). The major difference between Figs.(12) and (13) can be found at broadside when $\theta = 15°$. Fig.(13) has more power reduction at broadside than Fig.(12) as θ is varied from zero to $15°$. This is due to an impedance mismatch at broadside caused by the large shifts of impedance curves as in Fig.(5). The rapid downward shift of ν_1' from G_{-1} when $2d = 0.7\lambda_o$ results in the large variation in the active dipole input impedance. The ν_1' transition is suppressed for $2d = 0.55\lambda_o$. When θ is further increased to $30°$, the resonance inside the dielectric is stronger than

at $\theta=15^{\circ}$ and, as a result, both Figs.(12) and (13) show excessive pattern oscillations. When $\varepsilon = 2.5\varepsilon_0$ with $d_c=0.7\lambda_0$ and $2d=0.55\lambda_0$, the active element pattern cuts at various elevation angles are plotted in Fig.(14). Corresponding dipole input impedance curves have been shown in Fig.(6). Fig.(14) shows similar pattern oscillations as Figs.(12) and (13).

5. Conclusion

Mutual couplings between dipole columns are evaluated effectively using a Watson transform technique for a spatial harmonic Green's function. The poles of the Green's function are traced in the complex plane from their initial locations using a perturbation technique, which varies gradually the dielectric constant of the layer from the free space value to its final value. A mode coupling inside the dielectric layer is caused by the emergence of new set of poles(T.E.) in addition to the original poles(T.M.) of the Green's function when the beam of the array is lifted away from the horizontal plane.

The active element pattern of the array on the horizontal plane is characterized by the ripples at broadside and a narrow beamwidth. The beamwidth can be adjusted by the distance between dipole columns. As the dielectric constant of the layer is increased, the beamwidth is narrowed, while the pattern has a strong ripple effect at broadside and a clear beam cutoff off broadside.

When the elevation angle from the horizontal plane is increased from zero, the active element pattern undergoes a significant change. A resonance due to an emerging real pole from the mode coupling takes place inside the dielectric. As the elevation angle is increased, the resonance is getting stronger causing large oscillations in the active element pattern cut. From this reason, a pattern deterioration for a syn-

thesized beam of this array is expected when the beam is scanned away from the horizontal plane.

References.

1. L.Stark,"Radiation impedance of a dipole in an infinite planar phased array," Radio Sci., vol.1, pp.361-376, Mar. 1966.
2. A.L.VanKoughnett and J.L.Yen,"Properties of a cylindrical antenna in an infinite planar or collinear array," IEEE Trans. Antennas Propagat. vol. AP-14, pp.750-757,Nov.1967.
3. V.W.H.Chang,"Infinite phased dipole array," Proc. IEEE, vol.56, pp.1892-1900, Nov. 1968.
4. R.W.P.King,"Cylindrical antennas and arrays," Chapter 9, Antenna theory, pp.384-392, edited by R.E.Collin and F.J. Zucker, McGraw-Hill, 1969.
5. G.Tyras, Radiation and propagation of electromagnetic waves, Chapter 9, Academic Press, 1969.
6. L.L.Bailin and R.J.Spellmire,"Convergent representation for the radiation fields from slots in large circular cylinders," IRE Trans. Antennas Propagat. vol. AP-5, pp.374-383, Oct. 1957.

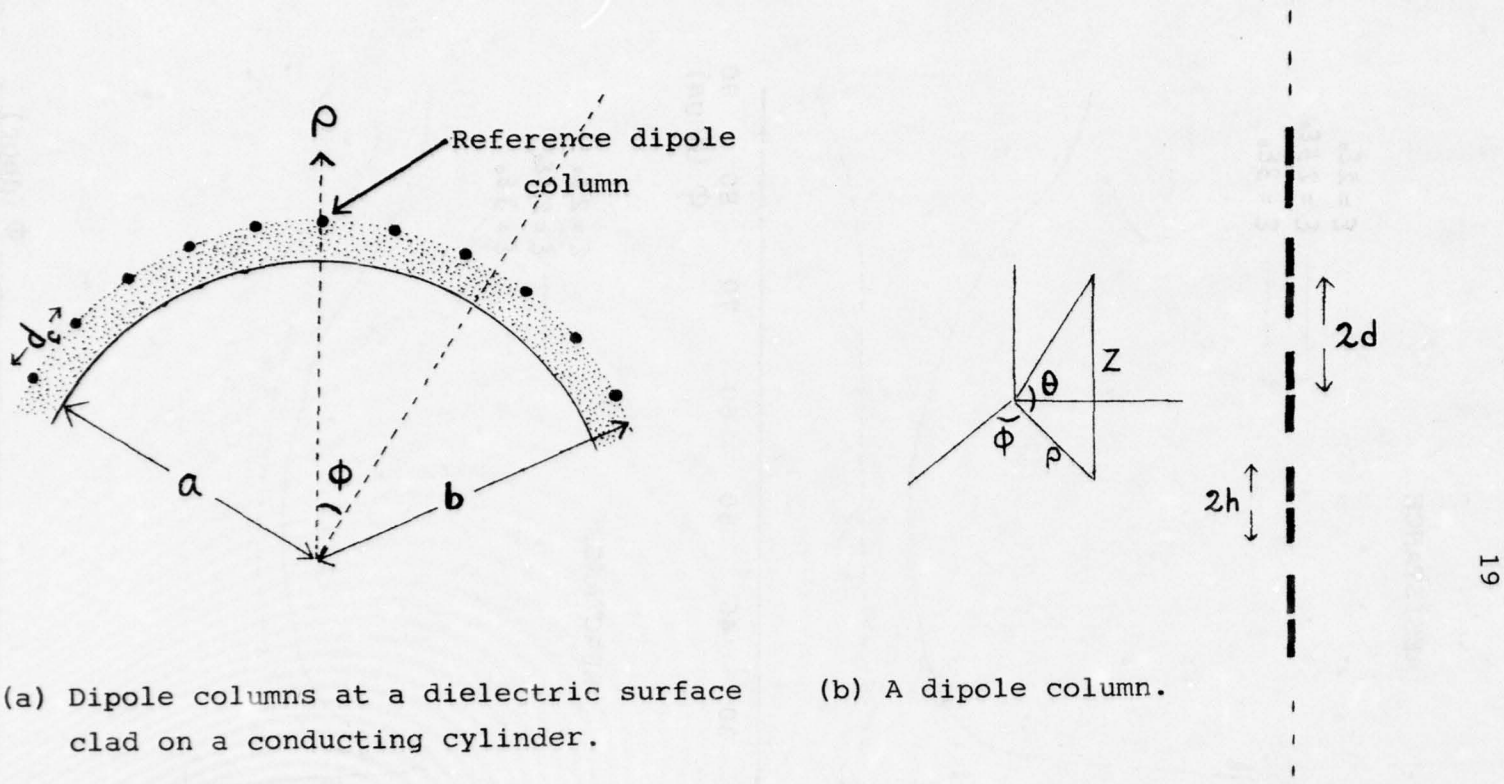

(a) Dipole columns at a dielectric surface clad on a conducting cylinder.

(b) A dipole column.

Fig.1 Geometry of an array

(Number of total dipole columns N=200, thickness of a dielectric layer $b-a=0.1768\lambda_o$, the length of a dipole $2h=0.5\lambda_o$ and the radius of a dipole $r_o=0.007\lambda_o$. N, b-a, 2h and r_o are constants. A distance between dipole columns d_c, a z-direction dipole center-to-center distance 2d, elevation beam scan angle θ and the dielectric constant of the layer ε are variables. λ_o is a free space wavelength.)

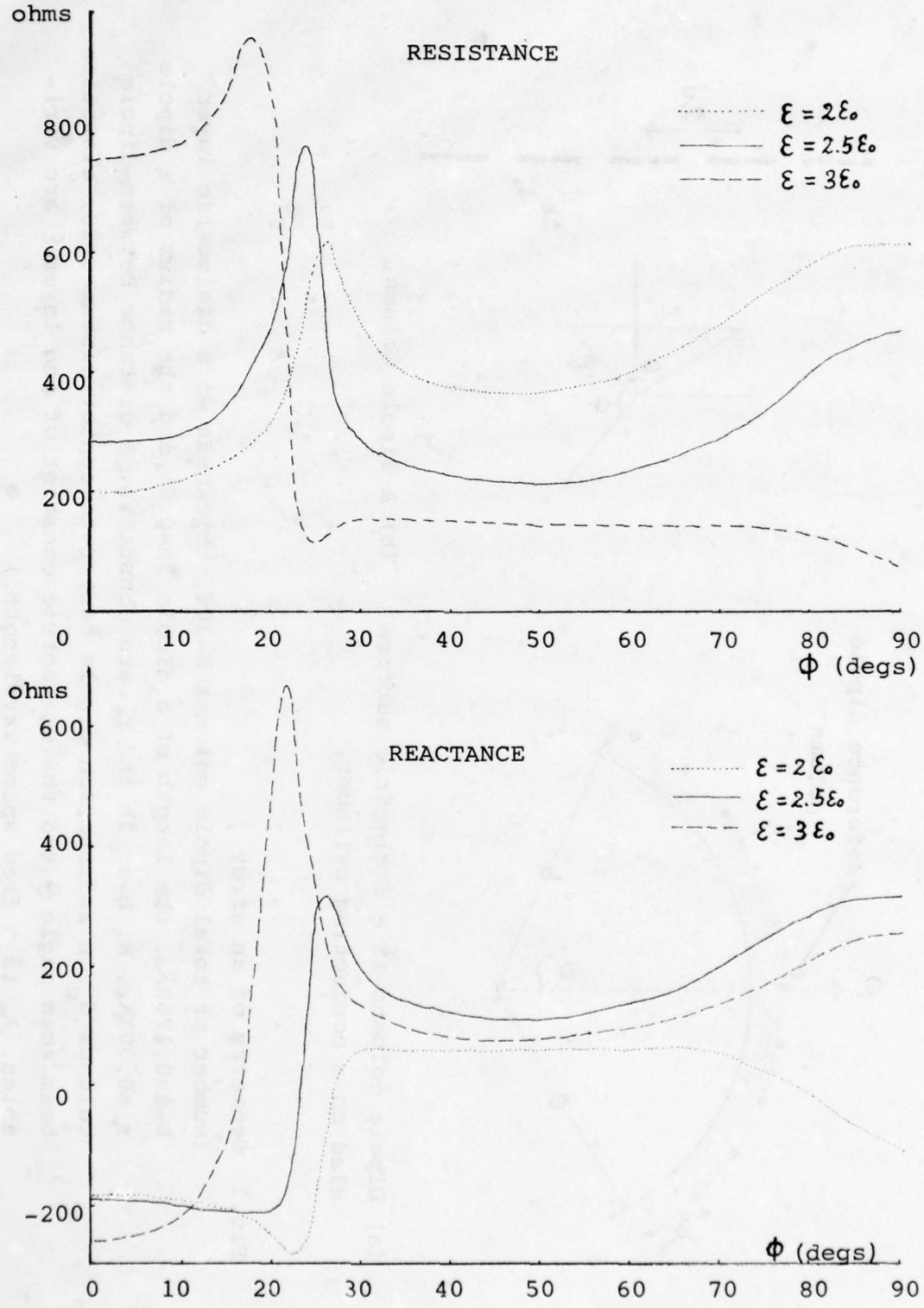

Fig.2. Active dipole input impedance versus azimuthal beam scan directions ($\theta = 0°$, $d_c = 2d = 0.7\lambda_o$).

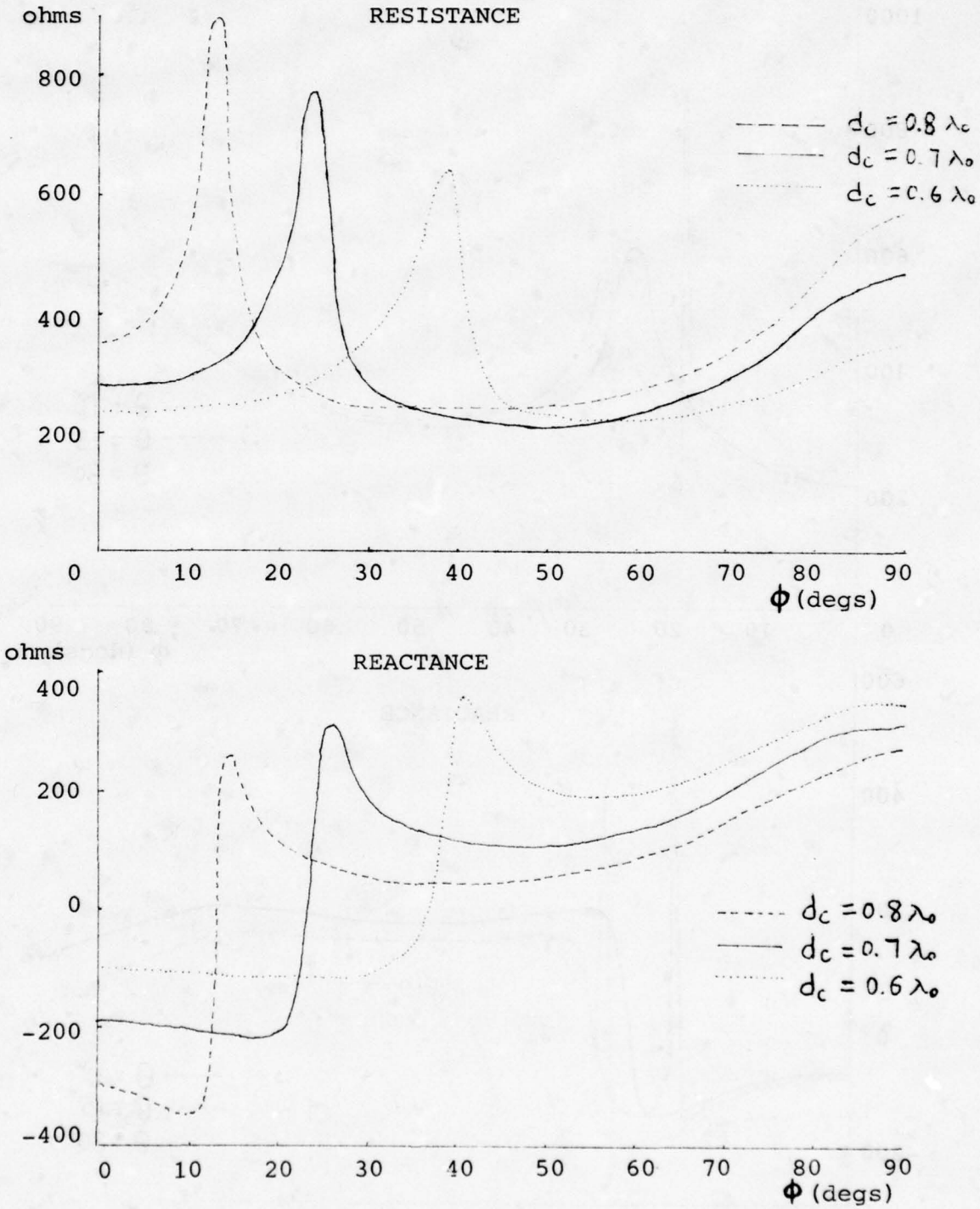

Fig.3. Active dipole input impedance versus azimuthal beam scan directions($\theta = 0^\circ$, $\varepsilon = 2.5\varepsilon_o$, $2d = 0.7\lambda_o$)

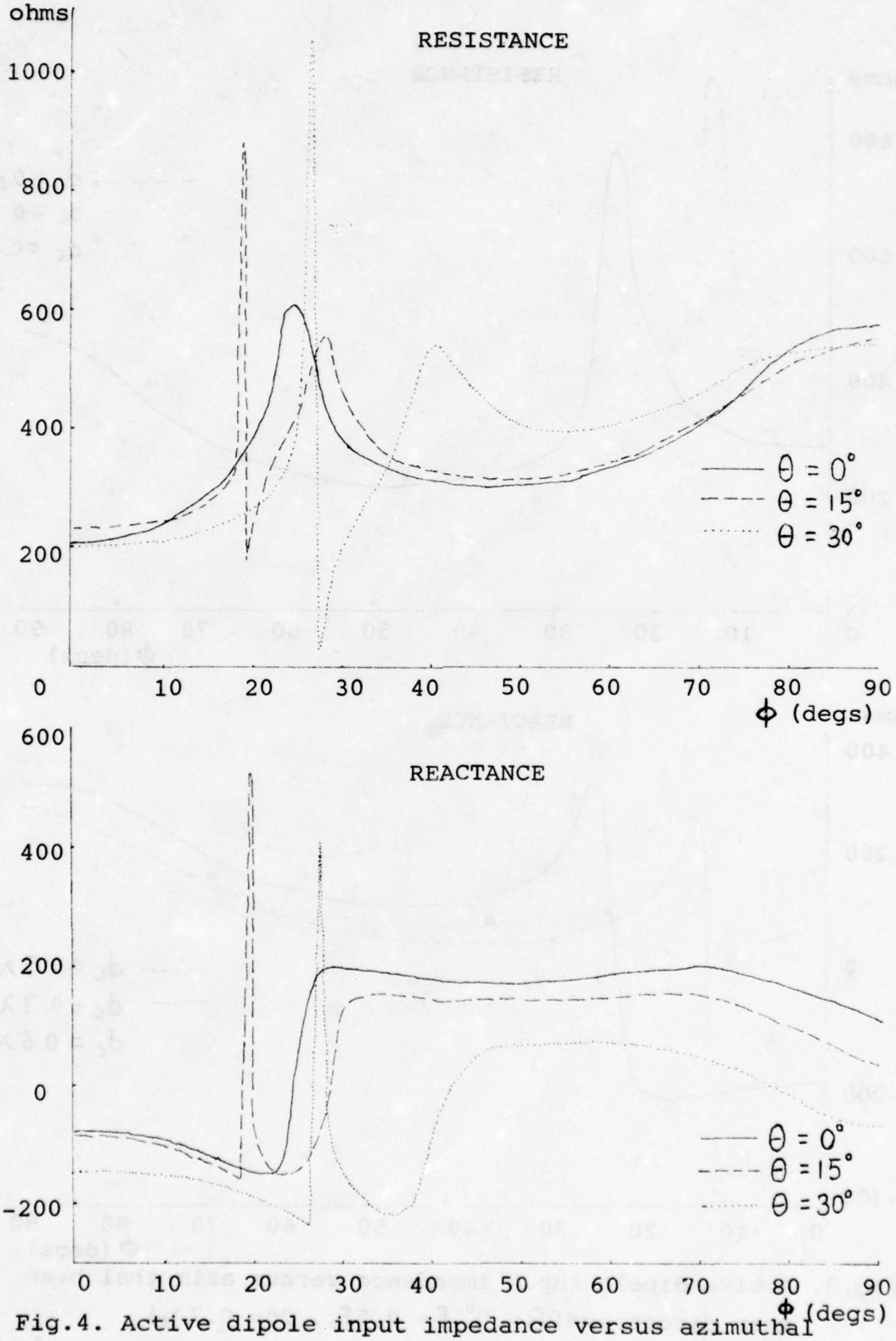

Fig.4. Active dipole input impedance versus azimuthal beam scan directions ($\varepsilon = 2\varepsilon_o$, $2d = 0.55\lambda_o$, $d_c = 0.7\lambda_o$)

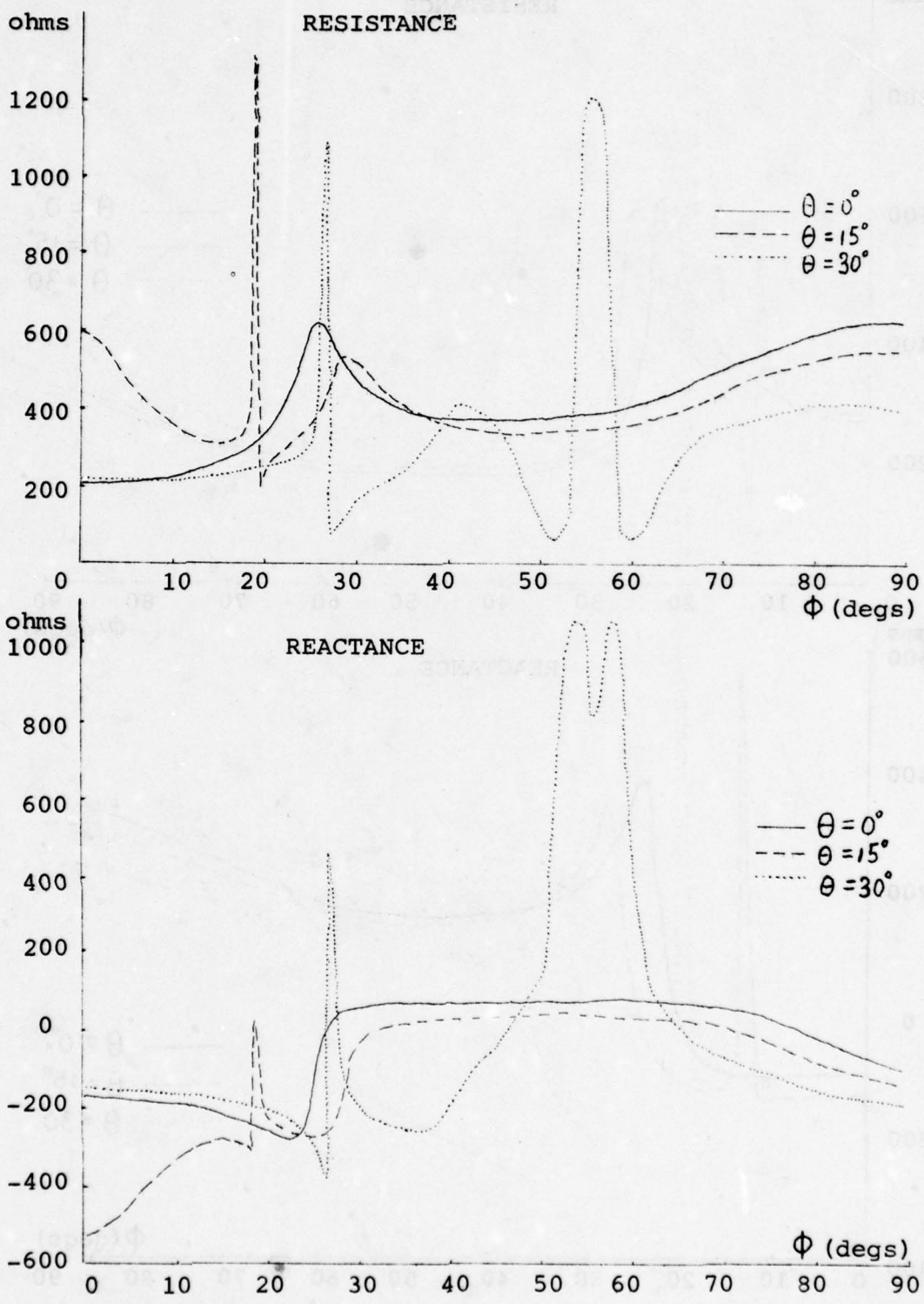

Fig.5. Active dipole input impedance versus azimuthal beam scan directions ($\varepsilon = 2\varepsilon_o$, $2d = d_c = 0.7\lambda_o$)

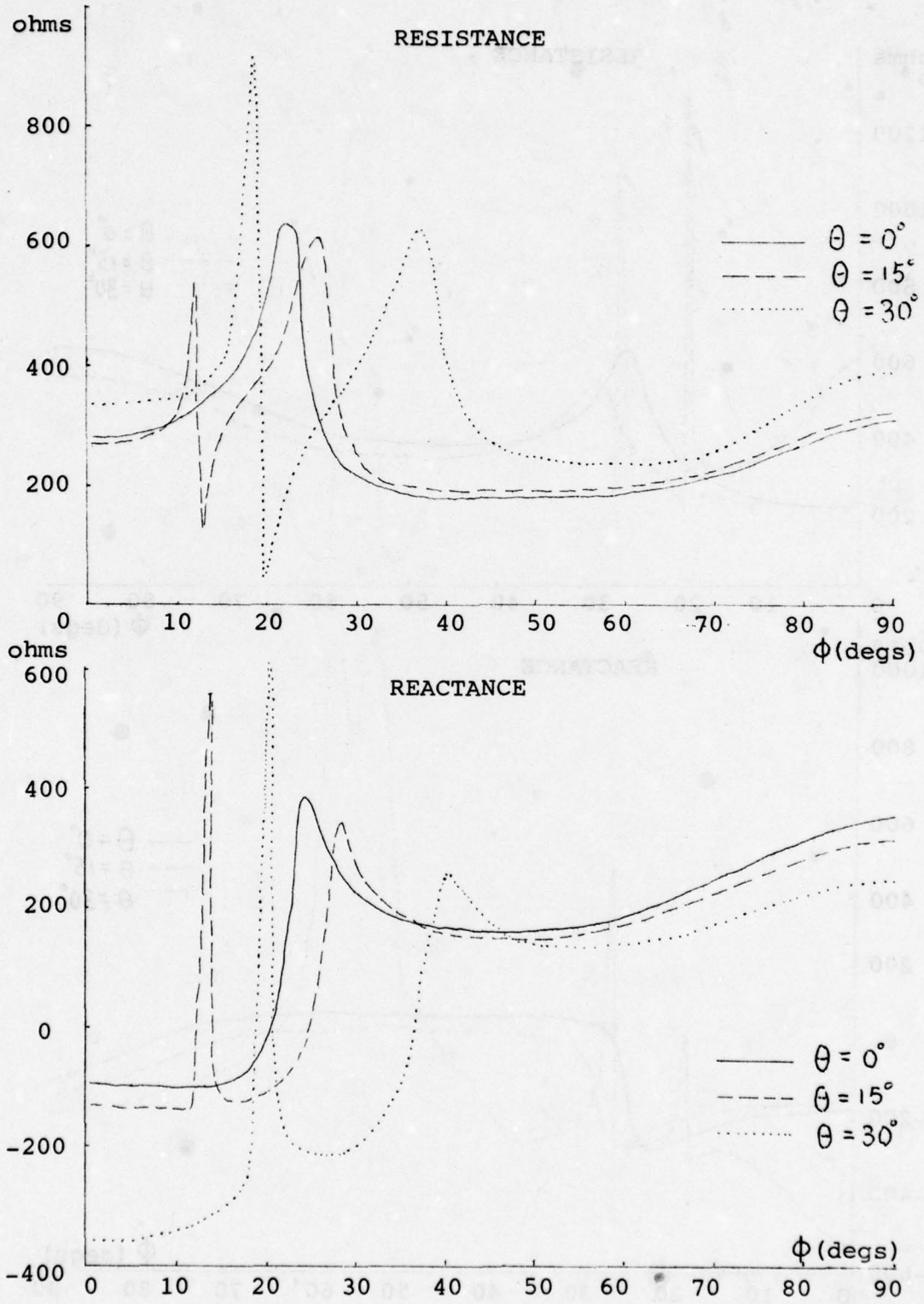

Fig.6 Active dipole input impedance versus azimuthal beam scan directions($\varepsilon=2.5\varepsilon_o$, $d_c=0.7\lambda_o$, $2d=0.55\lambda_o$).

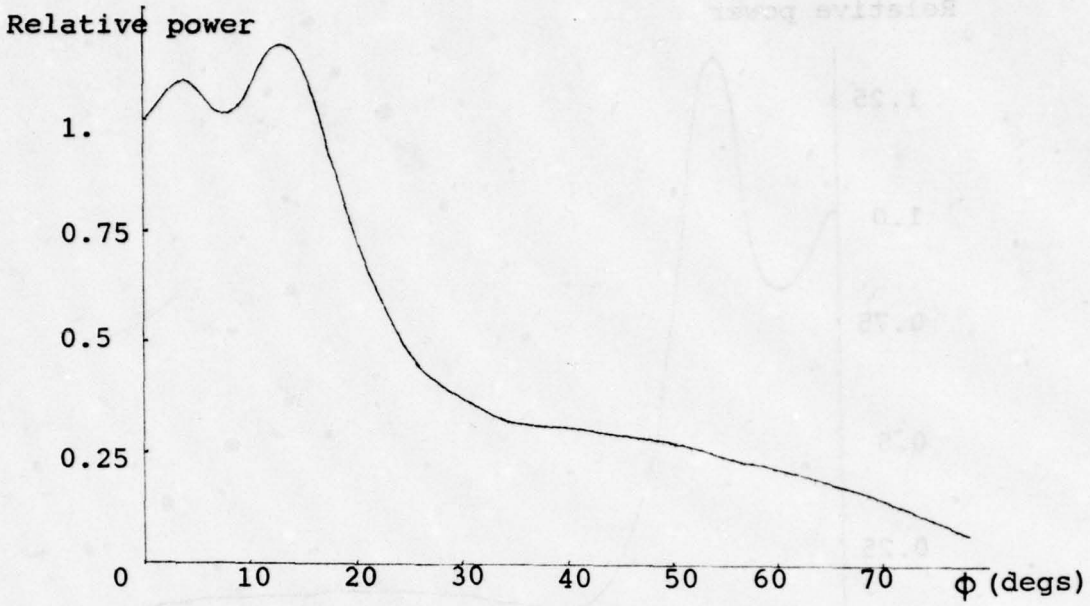

Fig.7 Active element pattern on the horizontal plane.
($\varepsilon = 2\varepsilon_o$, $d_c = 2d = 0.7\lambda_o$)

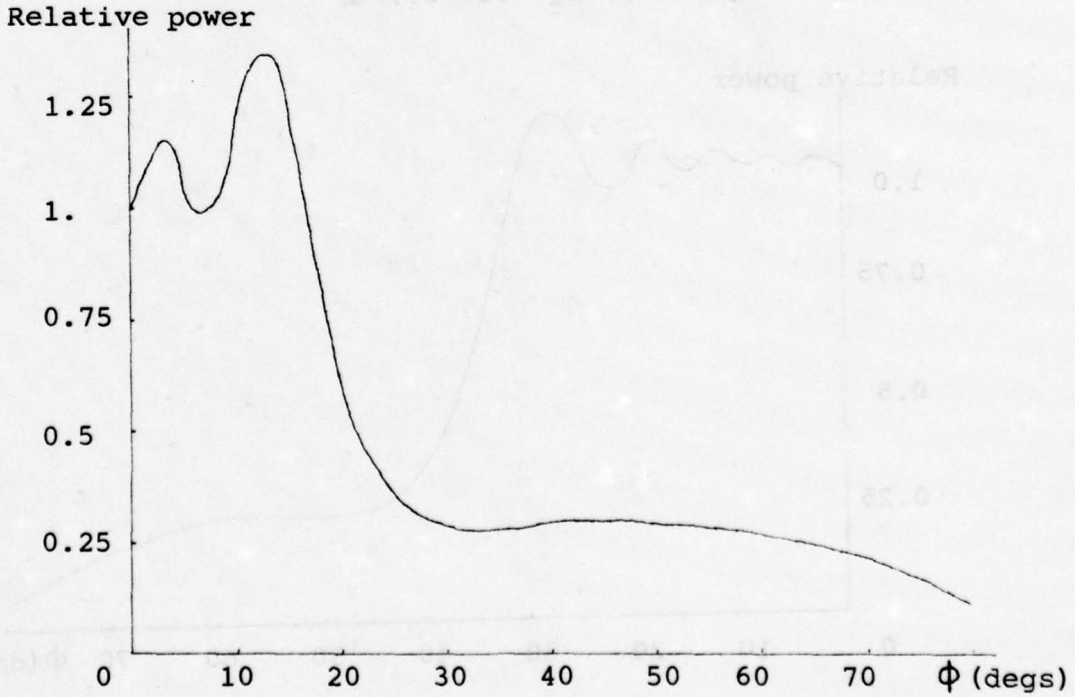

Fig.8 Active element pattern on the horizontal plane.
($\varepsilon = 2.5\varepsilon_o$, $d_c = 2d = 0.7\lambda_o$)

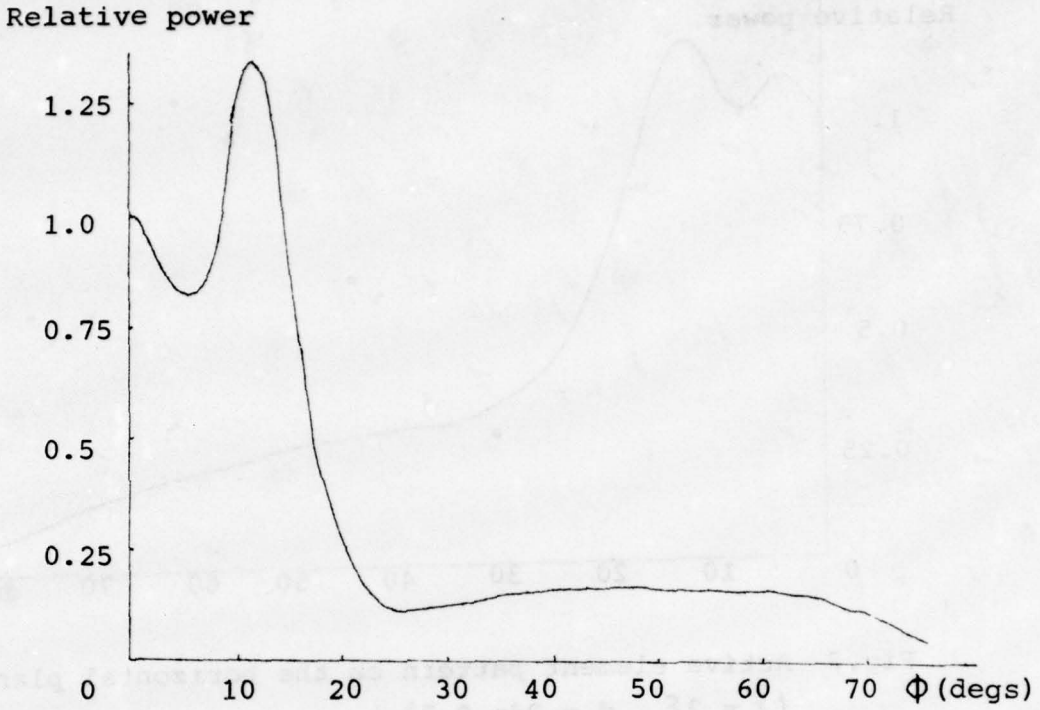

Fig.9 Active element pattern on the horizontal plane.
($\varepsilon = 3\varepsilon_o$, $d_c = 2d = 0.7\lambda_o$)

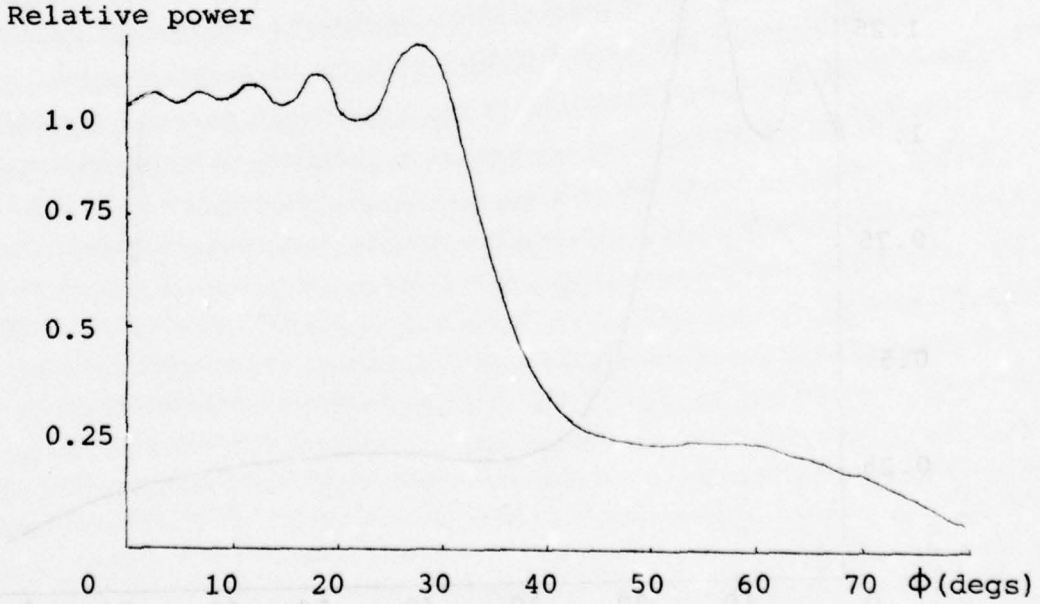

Fig.10 Active element pattern on the horizontal plane.
($\varepsilon = 2.5\varepsilon_o$, $d_c = 0.6\lambda_o$, $2d = 0.7\lambda_o$)

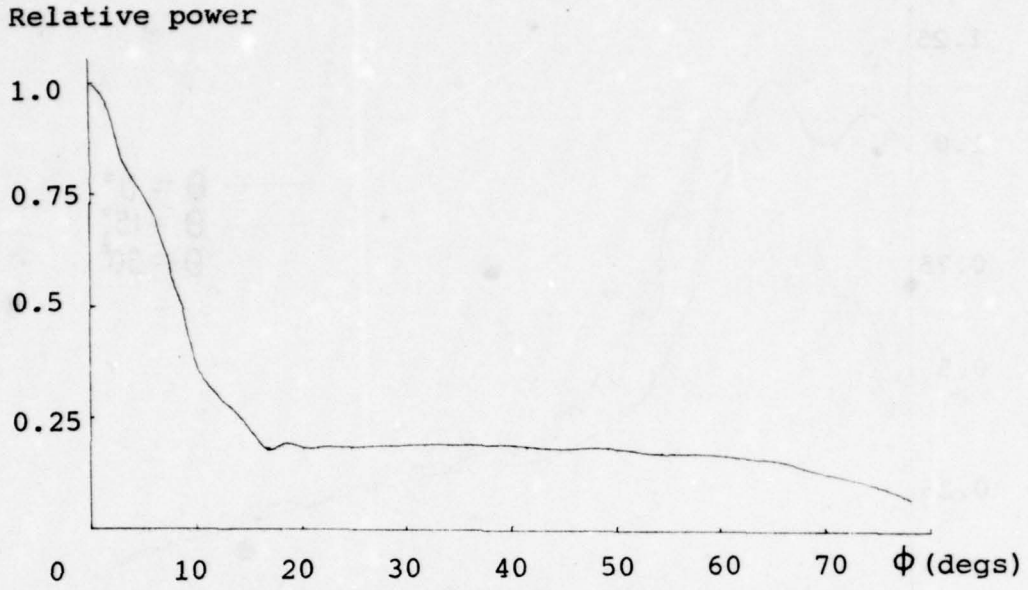

Fig. 11 Active element pattern on the horizontal plane.
($\varepsilon = 2.5\varepsilon_o$, $d_c = 0.8\lambda_o$, $2d = 0.7\lambda_o$)

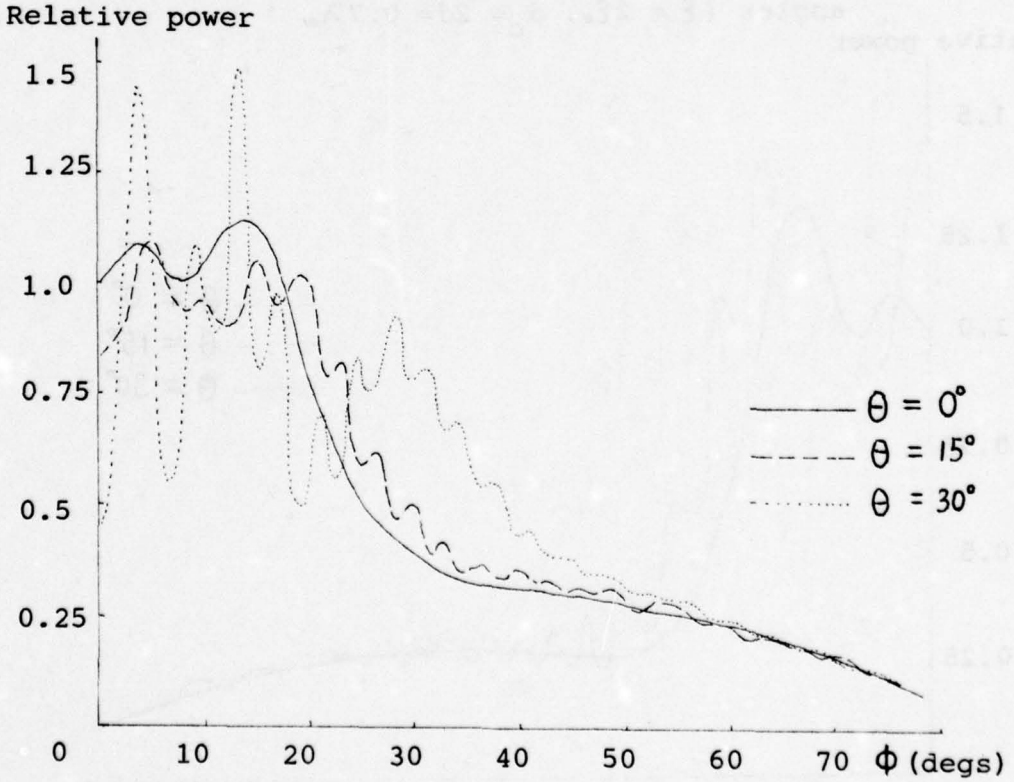

Fig.12 Active element pattern cuts at various elevation angles ($\varepsilon = 2\varepsilon_o$, $d_c = 0.7\lambda_o$, $2d = 0.55\lambda_o$)

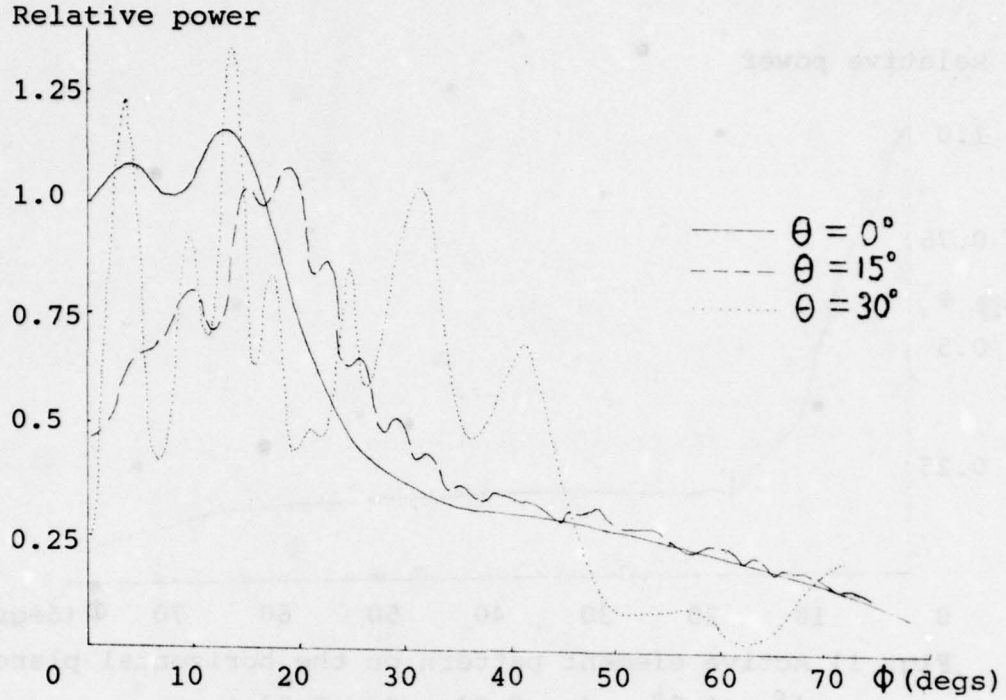

Fig.13 Active element pattern cuts at various elevation angles ($\varepsilon = 2\varepsilon_o$, $d_c = 2d = 0.7\lambda_o$)

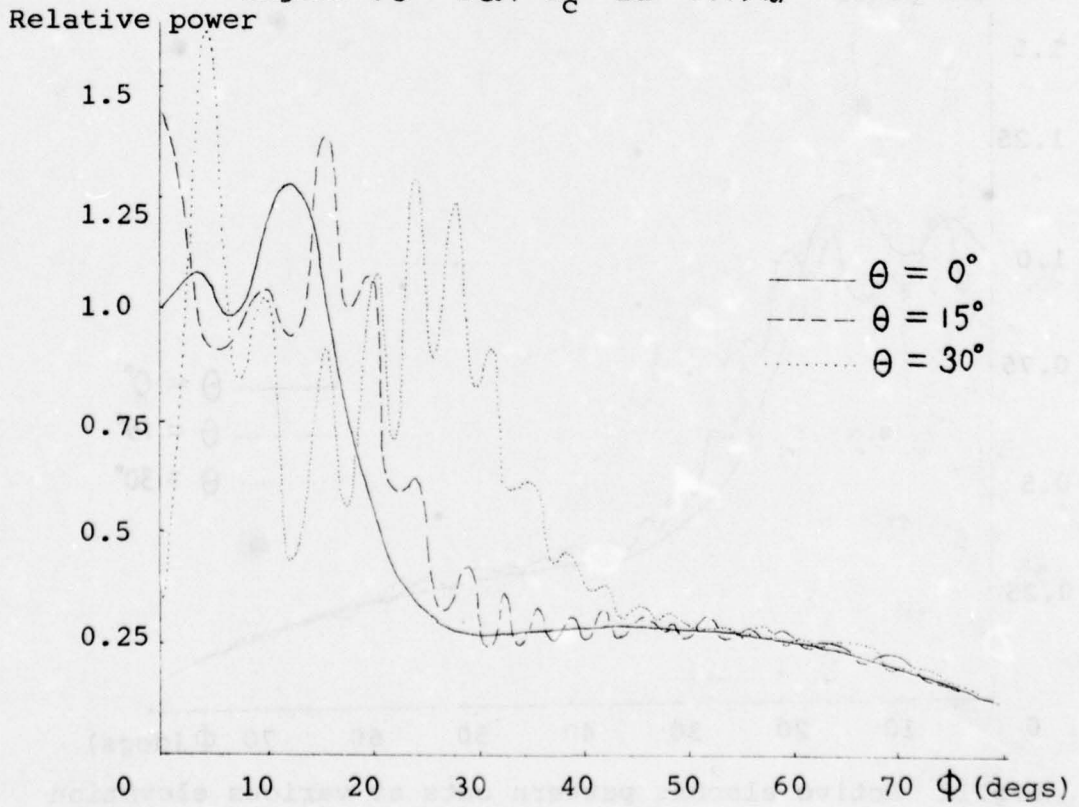

Fig.14 Active element pattern cuts at various elevation angles ($\varepsilon = 2.5\varepsilon_o$, $d_c = 0.7\lambda_o$, $2d = 0.55\lambda_o$)

EIGHT ELEMENT PRINTED PROBE ARRAY ANTENNA

Presented at the
THIRD ANNUAL ANTENNA APPLICATION SYMPOSIUM
Allenton Park, Monticello, Illinois

SEPTEMBER 26-28, 1979

By

RAINEE N. SIMONS

&

DILIP T. SHAHANI

The authors are with the

Centre for Applied Research in Electronics
Indian Institute of Technology Delhi
Hauz Khas, New Delhi-110029 (India)

INTRODUCTION

In recent times, a new class of millimeter-wave integrated circuits using quasi-planar techniques has been introduced. This new class includes the planar circuit mounted in waveguide (PCMW) proposed by Konshi et al [1], the integrated fin-line (IFL) and the printed-probe circuit (PPC) both proposed by Meier [2].

Conventional millimeter-wave antenna are of the parabolic dish type [3], The design of transmitter and receiver units using quasi-planar circuits requires special antenna design compatible with the technology. Integrating an antenna with a receiver can provide advantages in terms of size, weight, and production cost. Such an integration is especially desirable when a large number of antena/receiver modules are required, as in a phased array or multichannel direction-finding system [2].

In this paper a new antenna structure has been proposed viz., an eight element array using the printed-probe circuit technology. It consists of a linear array of probes printed on a dielectric board and supported in the E-plane of a rectangular housing. This structure possess the features of light weight, compactness, reproducibility and ease of integration with other E-plane circuits, thereby fulfilling the needs for an antenna which is compatible with the new integrated circuit technology.

The antenna has been experimentally optimised to yield the maximum gain.

ANTENNA CONSTRUCTION AND DESIGN

The printed probe array antenna and the cross-section of the housing, are fully illustrated in Fig.1. Figure 2 shows the polystyrene board B carrying the printed array of probes P.

The feed for the printed probe array consists of a rectangular metal waveguide (WR-90) fabricated in two parts with E-plane symmetry and incorporating waveguide bends with UG-39/U flanges for compatibility with WR-90 instrumentation. Further, the top and bottom broadwalls W1 and W2 are slotted along the E-plane to accept a pair of dielectric boards.

The array consists of printed probes which are printed on one of the polystyrene boards B of size 125 x 40 x 0.5 mm. When the board is placed in the rectangular housing, the probes protrude by a height H equal to $\lambda/8$ from the ground plane G of size 300 x 200 x 1.5 mm, which also forms the top wall of the housing. A second polystyrene board of the same size inserted in the E-plane helps to centre the probes in the slot and insulate them from the housing. Radiation from the lower broadwall W2 is negligible because the slot is centred, and the wall thickness is chosen to be a quarter wavelength in the dielectric medium just as in the case of a fin-line. Nylon screws exterior to the broadwalls hold the two halves of the housing together and align the boards.

A number of eight element printed probe arrays are fabricated on polystyrene boards having different probe depth D, height above the ground plane H, width W and the separation S (Fig.2). The gain of the antenna is measured for each of these arrays. Based on this data a probe depth of $\lambda/8$, height of $\lambda/8$, width of $\lambda/15$ and separation of $(\lambda/2) - 2\Delta$, (where $\Delta = \lambda/30$ and λ is the free space wavelength) gave a maximum gain of 11.5 dB at 10.0 GHz.

The edge of the dielectric sheet contains a quarter wavelength notch N to provide an impedance match between the air-filled and slab-loaded waveguides.

RESULTS

The experimental antenna provides a bidirectional end-fire radiation pattern with a major and minor lobe. By placing a metal reflector R of size 200 x 150 mm perpendicular to the ground plane at approximately λ from the end element on the minor lobe side the two beams add in phase to provide a unidirectional end-fire radiation pattern. The measured E-and H-plane radiation patterns with the metal reflector are shown in Fig. 3.

The measured beam widths in the E-and H-planes are 15° and 34° respectively. The gain at 10 GHz is 11.5 dB and the cross-polarization is less than 24 dB. The E-and H-plane side lobe levels is less than 8 dB and 20 dB, respectively. The VSWR at the feeding end is less than 2.0 over 10% bandwidth.

CONCLUSION

Special antennas compatible with the quasi-planar technology are required. In this paper a new type of antenna structure compatible with the quasi planar technology has been reported viz., an eight element array using the printed-probe circuit technology. This antenna is very simple in construction and does not require any special power division or impedance matching network. The antenna provides an end-fire radiation pattern. The various parameters of the antenna has been experimentally optimized for maximum gain in terms of the free space wavelength. This antenna can find extensive applications at millimeter wave frequencies.

ACKNOWLEDGEMENT

The authors wish to thank Prof. (Miss) Bharathi Bhat for her valuable comments and discussions.

REFERENCES

1. Konishi, Y.: "Planar Circuit Mounted in Waveguide used as a Down Converter", IEEE Trans., 1978, MTT-26, pp. 716-719.

2. Meier, P.J.: "Millimeter Integrated Circuits Suspended in the E-plane of Rectangular Waveguide", IEEE Trans., 1978, MTT-26, pp. 726-733.

3. Kay, A.F.: "Millimeter-wave Antennas", Proc. IEEE, 1966, 54, pp. 641-647.

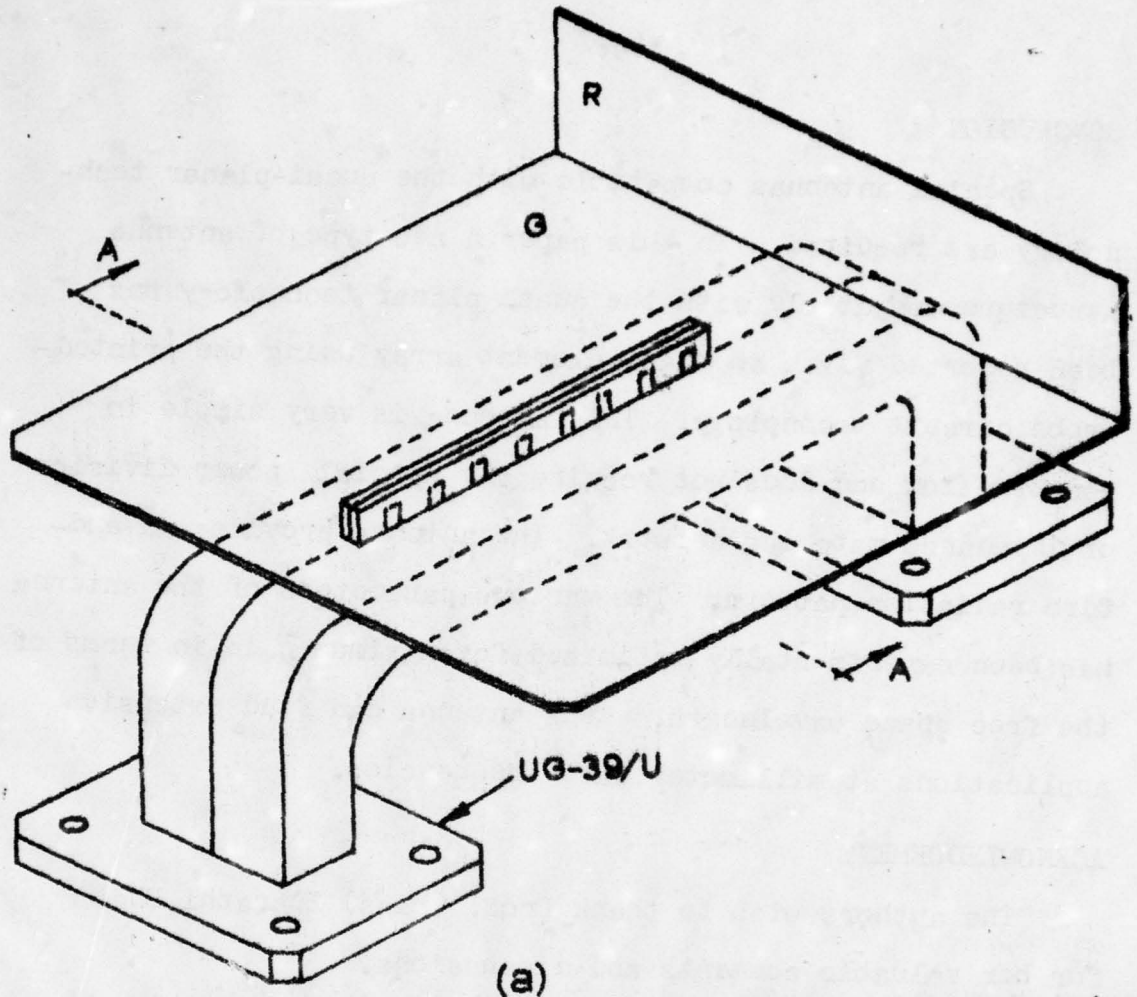

(a)

Fig.1 (a) Schematic of the eight element printed-probe array antenna

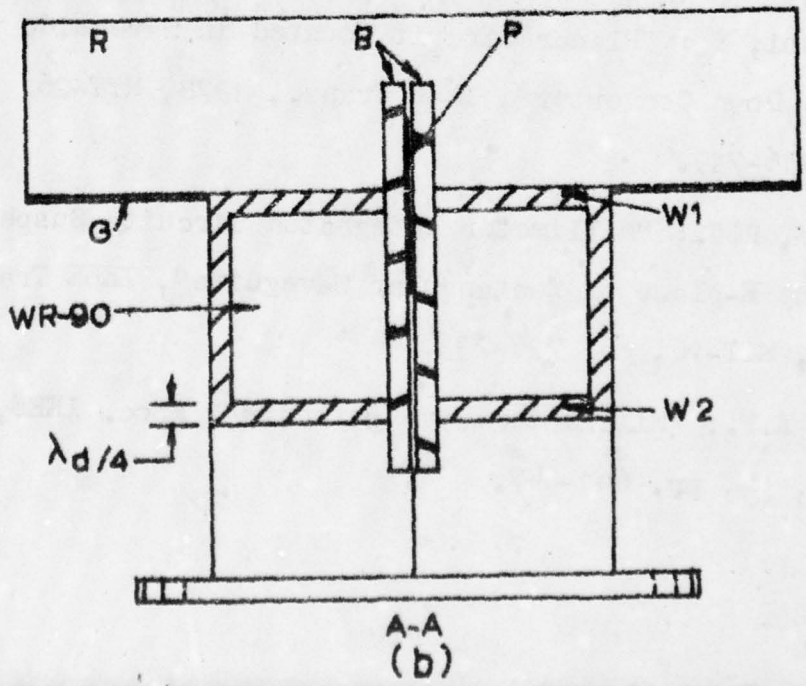

(b)

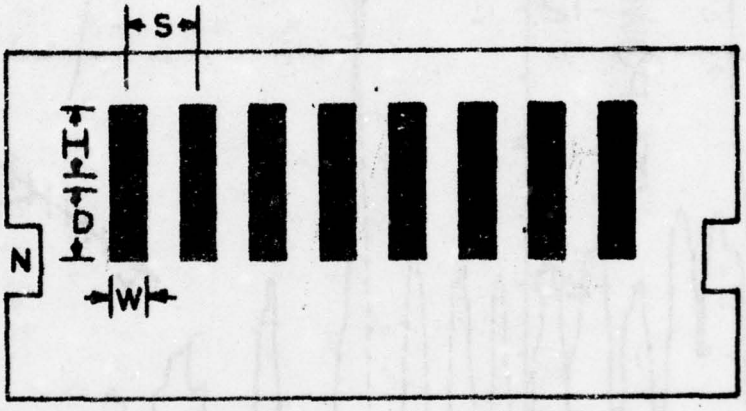

FIG.2. POLYSTYRENE BOARD CARRYING THE PRINTED RADIATORS

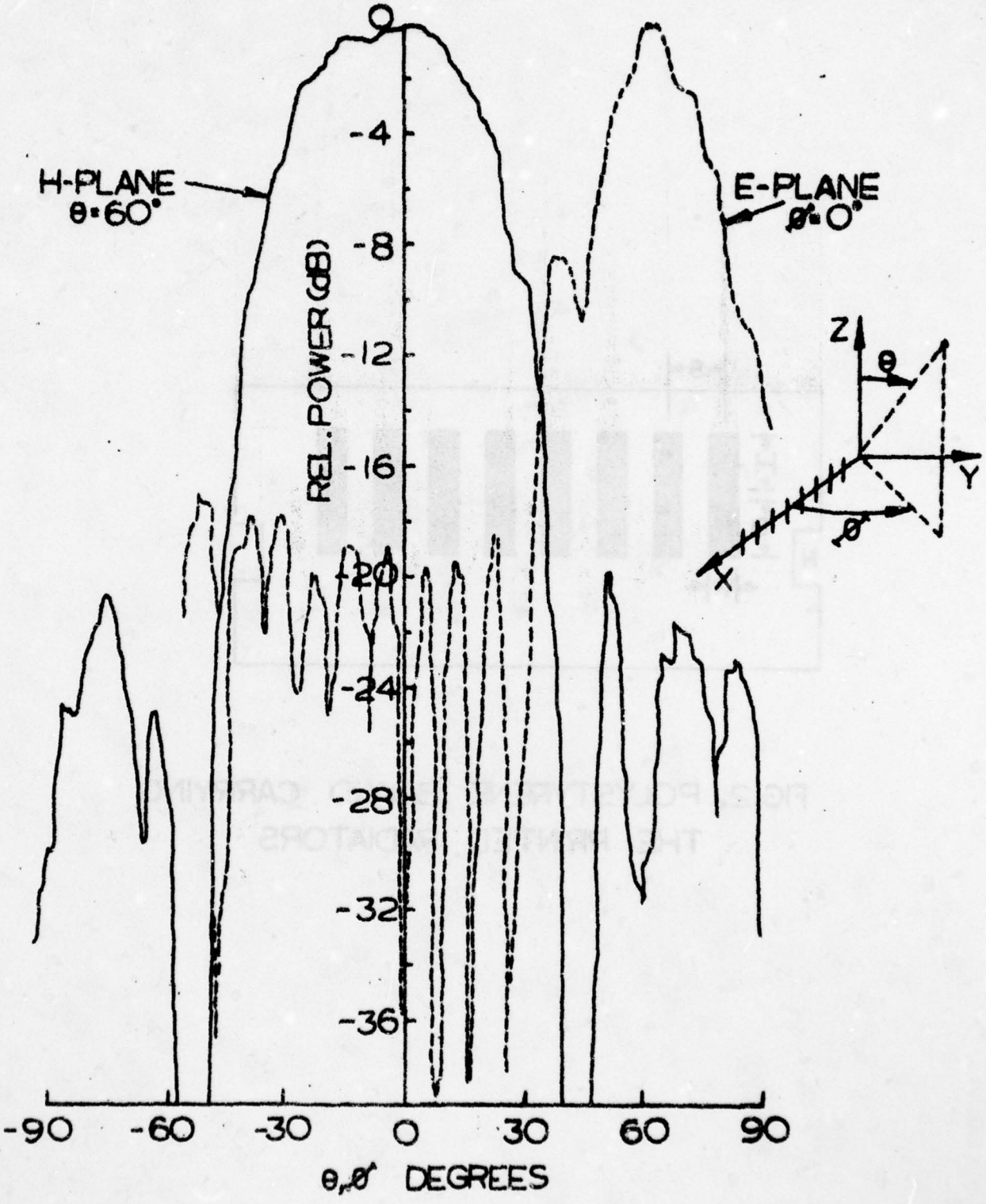

FIG.3. MEASURED E-AND H-PLANE RADIATION PATTERNS

A MICROWAVE POWER TRANSMISSION ANTENNA SYSTEM FOR THE SOLAR POWER SATELLITE

By

WALTER W. LUND JR.*

Large geosynchronous satellites are being proposed that will collect solar energy, convert it to microwaves and deliver it, in a beam, to Earth. The antenna technology involved in forming and receiving the microwave beam is the subject of this paper.

Starting with the large scale picture, the key parameters in a power transmission system are developed and related in graphic form. These parameters include the system power, transmitting array power density, ionospheric and Earth power density, and size of transmitting and receiving apertures. Array power density is related to thermal problems. Receiving power densities are related to bio-standards and ionospheric heating. Trades between illumination taper and beam efficiency are discussed. Cost trades between transmitting and receiving aperture sizes are covered.

Small scale considerations include taper implementation and the design and layout of the space array. The importance of the retro directive phase control system for the modular elements of the array is emphasized. The elements of this phase control subsystem discussed include power amplifier loop, receiver, pilot receive antenna, phase reference distribution network, phase conjugating circuitry and pilot signal spectral characteristics. Finally, antenna designs being considered for the power beam reception are discussed.

*The Author is with the Boeing Aerospace Company, Seattle, WA. The work reported in this paper was supported in part by Contract NAS 9-15196 with the NASA Johnson Space Center.

PART I THE LARGE SCALE PICTURE

Introduction

The concept of beaming microwave energy to Earth from synchronous orbit has been the subject of a number of recent studies. What has evolved as a preliminary baseline is a relatively high power (5 GIGAWATT) system that utilizes an approximate 1 KM diameter transmitting antenna and 10 KM diameter receiving aperture. In this section the rationale behind the configuration and the performance to be expected will be discussed.

System Power

The economics of manufacturing and space transportation have led to a delivered power unit cost that is competitive at the high power levels mentioned. This in turn has led to the mandatory consideration of tolerable power densities in the system.

System Power Density Constraints

The power density on the space transmitting antenna (locally referred to as the Spacetenna) is thermally constrained. The need to radiate waste heat with reasonable temperature rises places an upper limit at around 22 KW/M^2 on the spacetenna RF power density. The transmit antenna power density can of course be reduced by increasing the antenna size for a given power. This results in an increase in the power density incident on the ionosphere and the Earth. Early studies of the microwave heating of the ionosphere Reference (1) have indicated the possibility of thermal runaway. Current thinking is that power density levels of 23 milliwatts/cm^2 are tolerable, but the plasma stability issue is less clear. Figure 1 shows the aperture distribution with peak power density P_1 and the incident radiation on the rectenna with peak power density P_2.

POWER DENSITY CONSTRAINTS

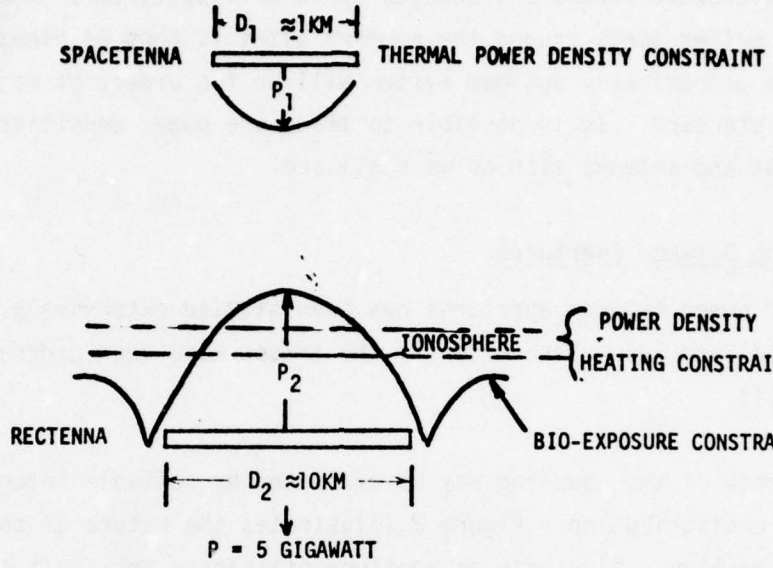

FIG. 1

BEAM EFFICIENCY

CIRCULARLY SYMMETRIC

APERTURE DISTRIBUTION

$$\eta_B = \underbrace{\left[\frac{1}{2\,\epsilon^2_{MAX}(\theta)} \int_0^{\theta_0} \epsilon^2(\theta)\ \mathrm{SIN}\ \theta\ d\theta\right]}_{\text{SPATIAL EFFICIENCY}} \left[\frac{4\pi}{\lambda^2}\right] \underbrace{\pi a^2}_{\text{PHYSICAL APERTURE}} \underbrace{\left[\frac{\left[2\int_0^1 f(\rho)\,\rho\,d\rho\right]^2}{2\int_0^1 [f(\rho)]^2\,\rho\,d\rho}\right]}_{\text{APERTURE EFFICIENCY}}$$

EFFECTIVE APERTURE

GAIN

FIG. 2

In addition it is economically desirable that the beam near sidelobes be below the microwave exposure standards of 10 milliwatts/cm^2. The need for protective buffer zones around the receive sites is thus eliminated. Sidelobes in an economically optimum system will be two orders of magnitude below this standard. It is possible to trade the power densities with power output and antenna size as we shall see.

The Coupling Between Apertures

Coupling of power between apertures has been studied extensively. See Reference (2) and (3). More recently the trades have been generalized Reference (4).

The efficiency of the coupling may be evaluated by suitable integration of the aperture distribution. Figure 2 illustrates the nature of the beam efficiency problem. High gain or aperture efficiency in itself is not important as long as the beamwidth compensates for any loss of gain by appropriately broadening, to cover a larger percentage of the sphere. The peak normalized integral of the power density over the sphere is referred to as the spatial efficiency. In general those illumination functions which have the least aperture efficiency and hence lowest sidelobes will exhibit the greatest beam efficiency as one might expect. Figure 3 shows some of the distributions investigated. At the current time the 10 DB Gaussian is considered a reasonable cost trade subject to further more accurate studies.

The efficiency of coupling between apertures is succinctly expressed as a function of the aperture diameter product (D_1D_2) Figure 4 shows the relationship for a uniform and a 10 DB Gaussian illumination function. The superiority of the tapered illumination is clear and the tentative choice of a 10 square kilometer product is indicated.

The Power Beaming Equations

It is possible to write two equations relating the spacetenna peak power density and diameter. The equations are shown in Figure 5. One involves

APERTURE DISTRIBUTIONS

Distribution	S. L. level	D/Du	Beam Eff.
Uniform	17.	1.0	84.0
10 DB Gaussian	25	1.20	96.5
15 DB "	31	1.35	98.8
20 DB "	37	1.56	99.8

FIG. 3

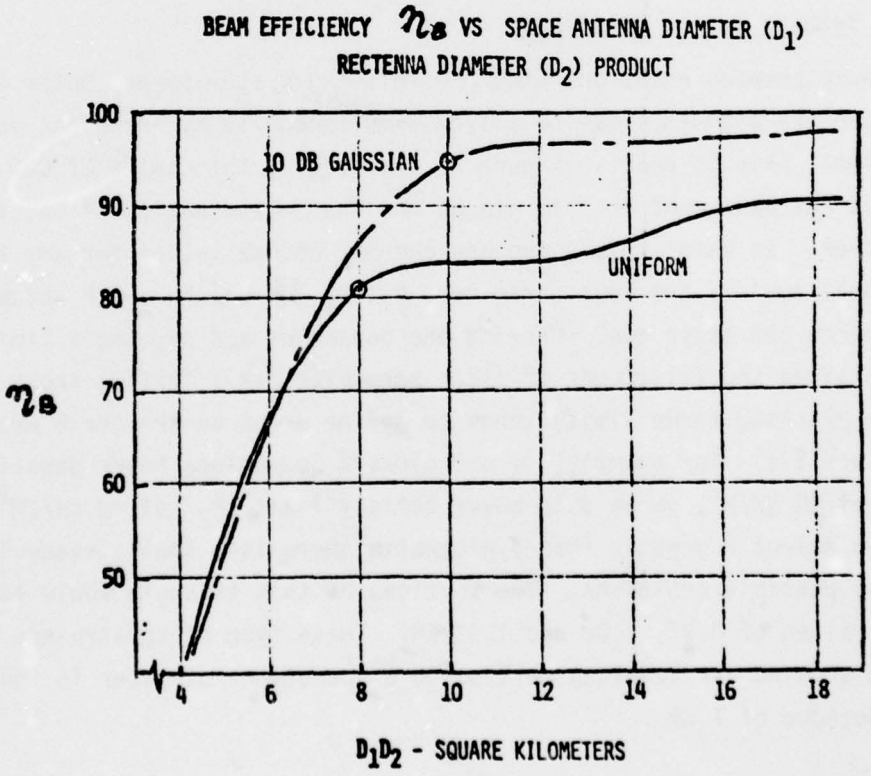

FIG. 4

the rectenna power output (P) and the other the peak power density (P_2) incident upon the ionosphere and the rectenna. The constants in these equations are discussed in Reference (4). They are derived from the illumination function selected, involve the pattern beam efficiency and choice of aperture diameter produce (D_1D_2).

Loss Estimates

To determine the equation constants it is also necessary to evaluate the losses of the system. The estimates that have been arrived at in preliminary studies are shown in Figure 6. The subarray errors will be discussed in a later section. The rectenna RF-DC conversion efficiency is based largely on the work of W. C. Brown of the Raytheon Company Reference (5).

Power Beaming Design Solutions

The power beaming equations Figure 5 relating system power, power densities, and aperture diameters may be solved simultaneously by graphical superposition. This is done in Figure 7. Obviously, the choice of D_1D_2 product has been made in this graph, and the determination of one fixes the other. In using this nomograph one may choose values for any two (and only two) of the four parameters P_1, D_1 or D_2, P_2 and P which then determines the other two. Picking one parameter and setting a limit on a second gives the full range of other parameters that fulfill those conditions. Picking three limits tends to define areas on the graph where solutions lie. For example, if one picks a Spacetenna power density (P_1) limit of 40 KW/M^2, on an axis power denisty limit (P_2) of 40 mW/CM^2 and a power output P greater than 5 gigawatts there is a small triangular area of possible soultions. The vertices of this triangle would lie at D_1 values of 0.77, 1.02 and 1.33 KM. These type of constraints which were discussed earlier tend to lead to a spacetenna diameter in the neighborhood of 1 KM.

POWER BEAMING EQUATIONS

$$P_1 = \frac{k_1 P}{(D_1)^2}$$

$$P_1 = \frac{k_2 P_2}{(D_1)^4}$$

P_1 = Peak Power Density on Spacetenna

P = Power Output of Rectenna

D_1 = Diameter of Spacetenna

P_2 = Peak Power Density on Rectenna

K_1, K_2 Computed From Choices of:

- Illumination Function
- D_1 D_2 Product
- Rectenna Conversion Efficiency

FIG. 5

LOSS ESTIMATES

RF GENERATION η_G		
• DC-RF CONVERSION EFFICIENCY	0.85	
• WAVEGUIDE I^2R	0.985	
		.837
INCIDENT EFFICIENCY η_i		
• IDEAL BEAM (14.2 db BELOW PEAK)	0.946	
• INTER-SUBARRAY ERRORS	0.956	
• INTRA-SUBARRAY ERRORS	0.981	
• ATMOSPHERIC ABSORPTION	0.98	
		.869
RECTENNA CONVERSION EFFICIENCY η_R		
• INTERCEPTION EFFICIENCY (POLARIZATION AND SCATTERING)	0.97	
• RECTENNA RF-DC CONVERSION	0.890	
• GRID INTERFACING	0.97	
		.837

FIG. 6

SPS-2672

Solar Power Satellite Beaming Nomograph

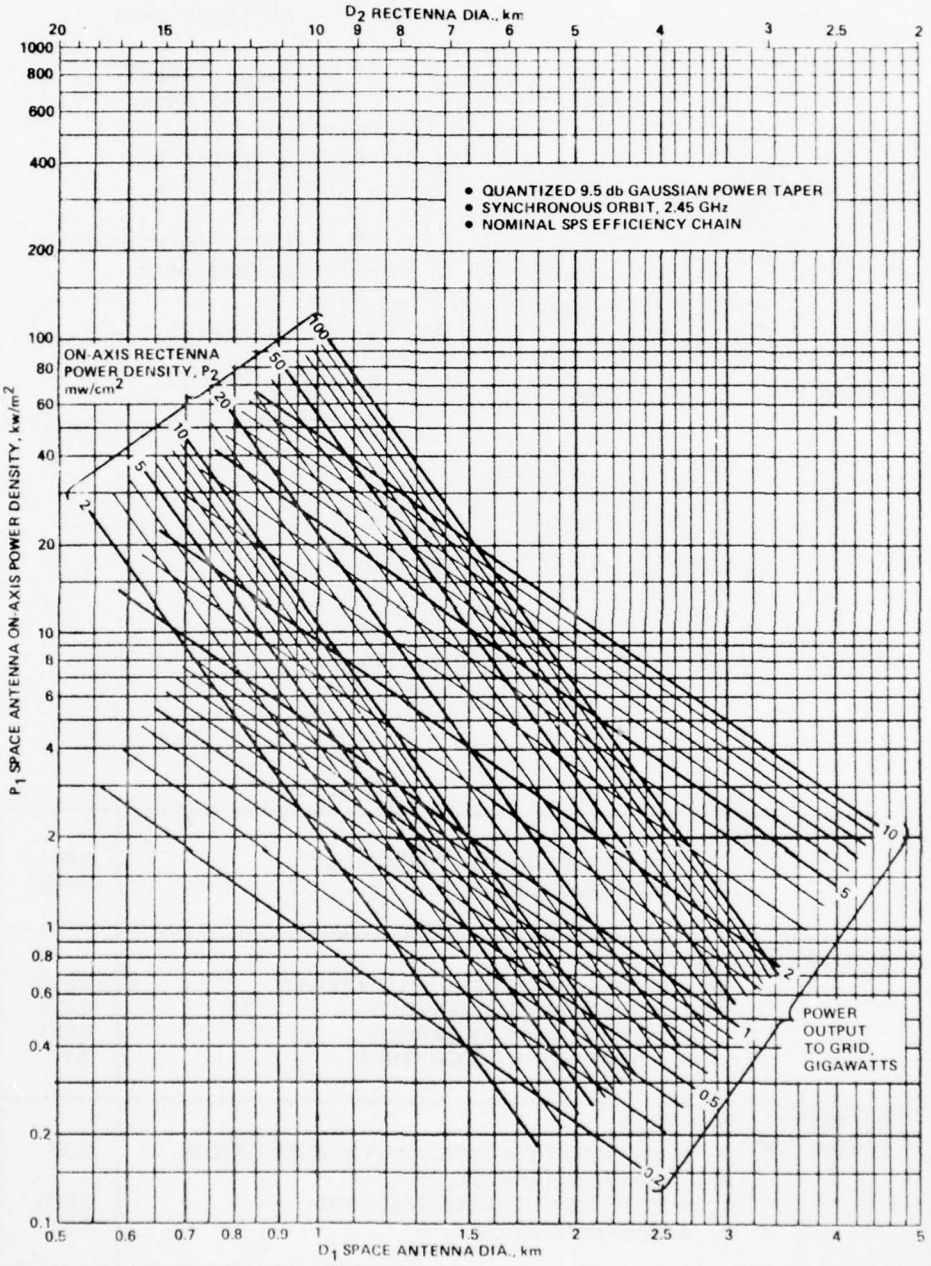

FIG. 7

Total Antenna System Cost

The question arises as to the cost reasonableness of an antenna system with a collecting aperture diameter ten times that of the transmitting aperture. It turns out to be rather reasonable if consideration is given to the relative difficulty of construction an extremely large completely coherent, high powered array, that must be transported into and maintained in synchronous orbit, as compared to an incoherent, low power, ground based array. A simple linear analysis Fig. 8 shows total system cost to be minimum with a spacetenna diameter in the vicinity of 1 KM for the unit area costs that are in the ratio of approximately 100/1. Cost studies have been documented in References (6) and (7).

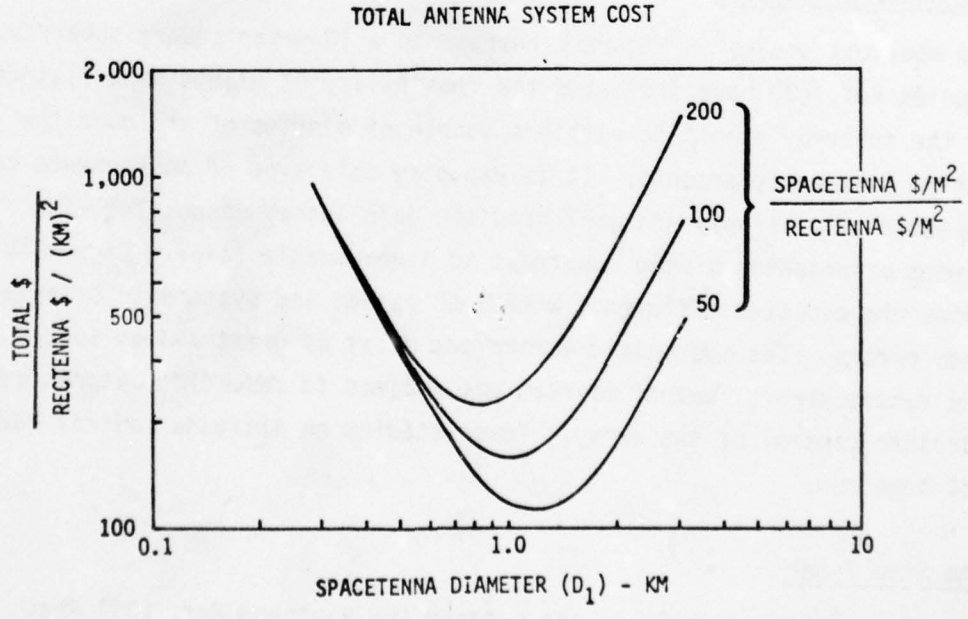

FIG. 8

Part II The Small Scale Picture

Introduction

Having established the general outward characteristics of the antenna system desired for high power microwave transmission of energy we turn our attention to the detailed mechanization of the antenna system. The general approach is an array of uniformly excited subarray elements that are actively controlled to form a retro directive array.

The Mechanical Configuration

The structural approach to the array design is shown in Figure 9 . This is a 1 km diameter antenna fed D.C. power through rotary azimuth and elevation joints. The entire antenna is attached to the end of the solar collecting structure that is 2 orders of magnitude larger area wise than the microwave antenna. A deep rigid body type of antenna structure is planned.

The Subarray Concept

The smallest square in Figure 9 represents a 10 meter square subarray. Studies Ref. (8) have indicated the feasibility of maintaining flatness of the subarray panels to within a couple of minutes of arc over the entire 1 km array antenna. It is expected this type of performance can be achieved passively and will keep the gain losses associated with random orientation of the subarrays to a reasonable level. Figure 10 shows the expected efficiency with both random and systematic orientation errors. The systematic errors are about as great a loss source as the random errors, but of course, are subject to reduction by precision attitude control of the array. Trade studies on attitude control have not been run.

The Step Taper

It was established early in the program (by Raytheon Ref. (3)) that a ten step taper approximation to the truncated Gaussian power density

MECHANICAL CONFIGURATION

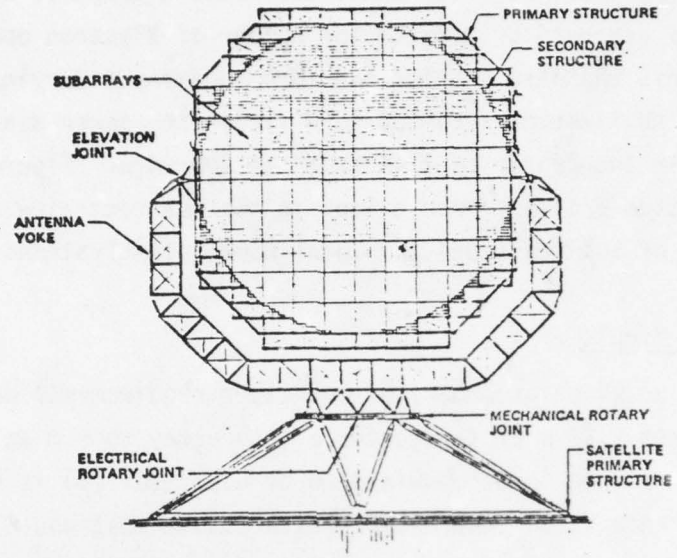

FIG. 9

TILT LOSSES

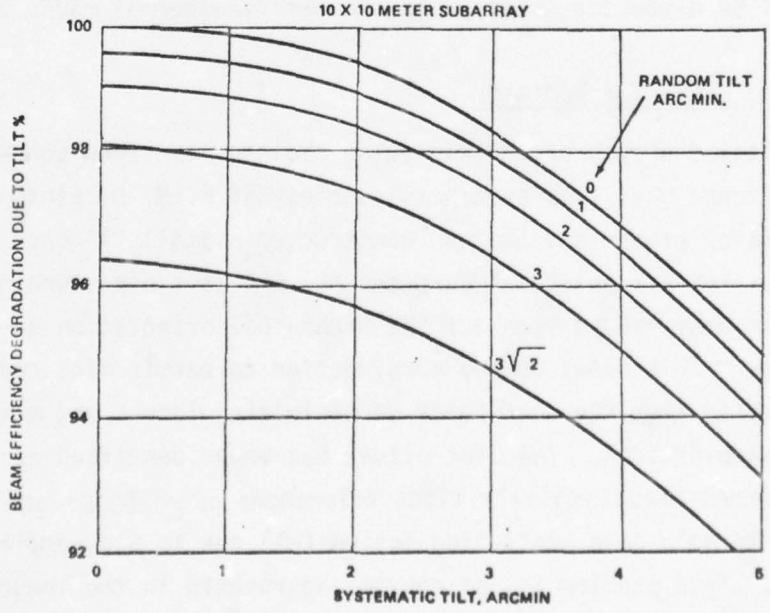

FIG. 10

AD-A077 167 ILLINOIS UNIV AT URBANA-CHAMPAIGN ELECTROMAGNETICS LAB F/G 17/9
PROCEEDINGS OF THE ANTENNA APPLICATIONS SYMPOSIUM (1979) HELD 2--ETC(U)
SEP 79 F19628-79-M-0015
UNCLASSIFIED NL

4 OF 6
ADA 077167

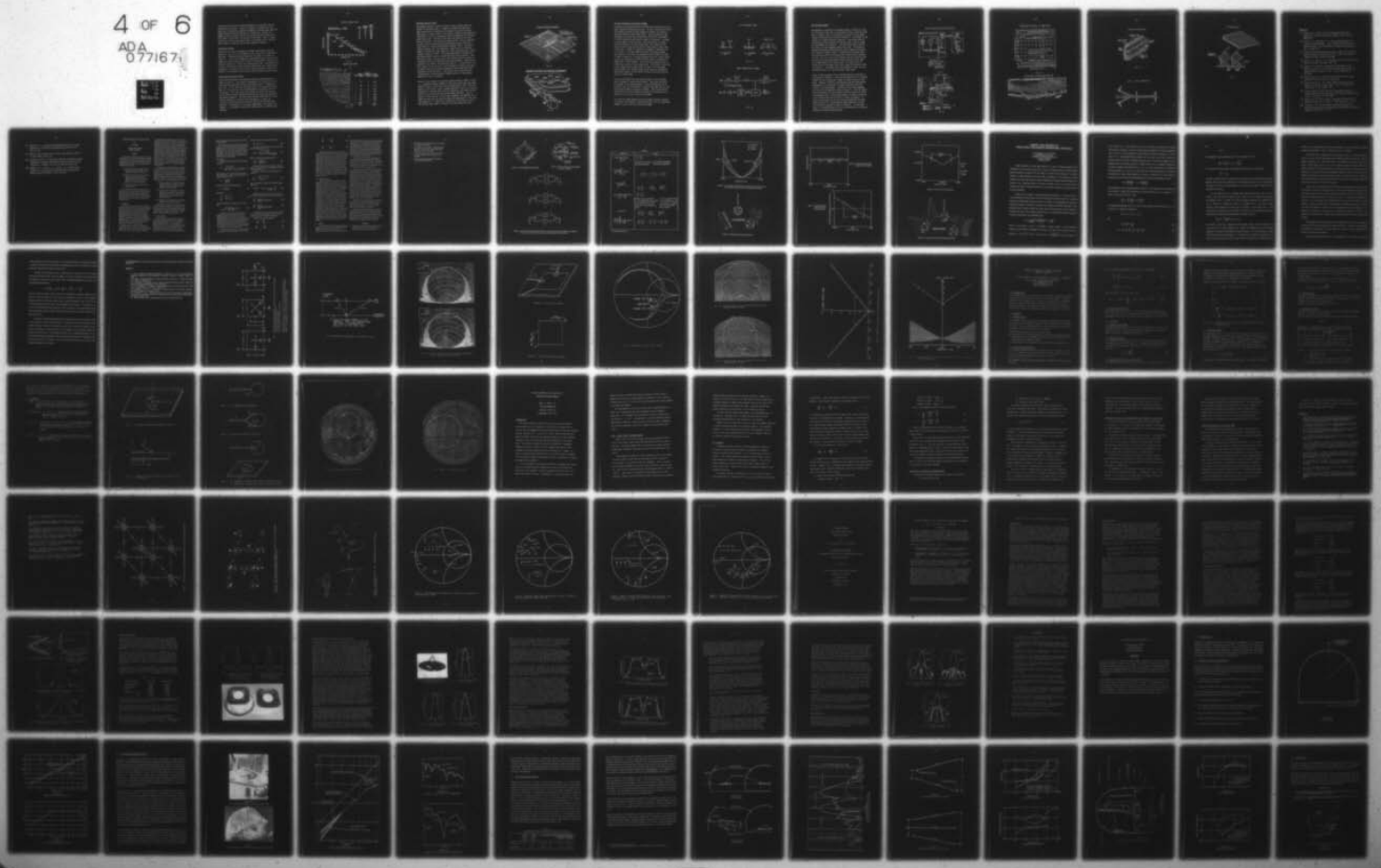

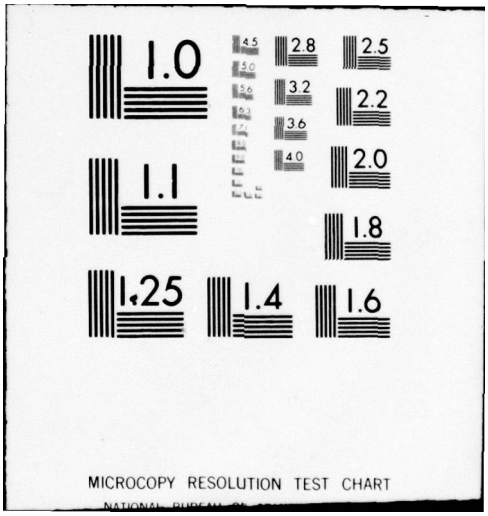
1.0
1.1
1.25
1.4
1.6
1.8
2.0
2.2
2.5
2.8
3.2
3.6
4.0
4.5
5.0
5.6
6.3
7.1
8.0
9.0
MICROCOPY RESOLUTION TEST CHART

distribution was virtually indistinguishable in performance from the continuous distribution. Figure 11 illustrates a proposed ten step taper that is achieved by varying the number of klystron power amplifier module elements that are feeding one 10 m subarray. Varying this number of 70 KW klystrons from 36 to 4 varies the power density from 22.14 KW/M^2 in the center to 2.46 KW/M^2 at the edge. Figure 12 shows how this 10 step 9/1 taper would look in the quadrant view. Note the total number of subarrays and the total number of klystrons.

The Klystron Module

The module size which accommodates the taper requirements described above vary from 1.67 m at the center of the array to 5 m at the edge of the array. A module layout envisioned by G.E. (Ref. 9) is shown in Figure 13 . This is an intermediary size module that would be utilized toward the edge of the array at a radius of around 380 m. Shown here is the basic concept of a shunt slot standing wave array. The module array is fed in two halves from dual klystron output ports by a standing wave feedguide. Also shown in this Figure is the phase control electronics which will be discussed shortly and the passive thermal radiator system.

The Slotted Waveguide Radiator

A more detailed sketch of the waveguide radiator and feed concept is shown in Figure 14 . This sketch is courtesy of R. M. Dickinson of the Jet Propulsion Laboratory who has constructed a small 'X' Band array Ref. (10). For all practical purposes the SPS is a non-scanning array, that is, it only has to scan out the mechanical orientation error of 2 arc minutes. This opens up the array design to permit slot spacings to be selected from the standpoint of minimizing losses and maximizing the thermal bandwidth. The slot offset has been identified as the most critical dimension. Typically tight tolerances of $\pm$ .0005" are required to hold down scattering losses (½%) due to slot amplitude variation. This problem is, of course, aggravated in the longer stick lengths. It is planned to trade stick length against a corporate feed structure.

QUANTIZED POWER TAPER

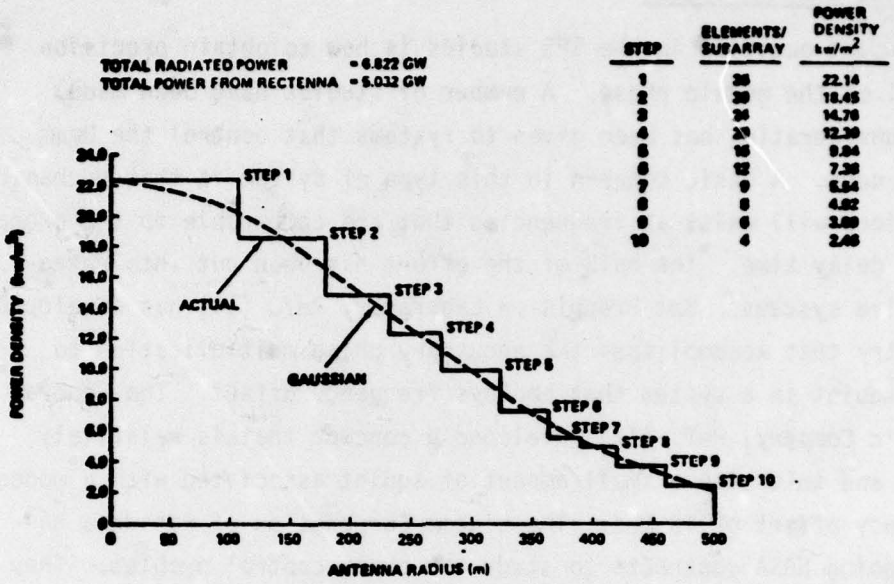

FIG. 11

TRANSMITTING ARRAY

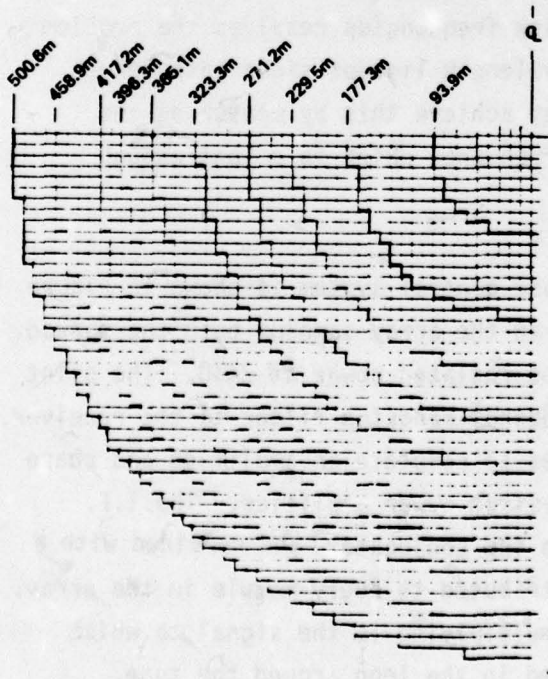

STEP	NUMBER SUBARRAYS	NUMBER KLYSTRONS/ SUBARRAYS	NUMBER KLYSTRONS
1	276	36	9,936
2	632	30	18,960
3	644	24	15,456
4	628	20	12,560
5	784	16	12,544
6	900	12	10,800
7	664	9	5,976
8	612	8	4,896
9	1,052	6	6,312
10	1,028	4	4,112
Totals	7,220		101,552

FIG. 12

The Phase Control System

A paramount question in the SPS studies is how to obtain precision control of the module phase. A number of studies have been made. Some consideration has been given to systems that control the beam from ground. A basic concern in this type of system is that mechanical vibrations will exist at frequencies that are comparable to the propagation delay time. The bulk of the effort has been put into retrodirective systems. Jet Propulsion Laboratory Ref. (11) has developed circuitry that accomplishes the necessary phase multiplication to avoid squint in a system that employs frequency offset. The General Electric Company, Ref. (12) developed a concept that is relatively simple and tolerated a small amount of squint associated with a modest frequency offset of 10 MHz. The Lincom Corporation of Pasadena has had ongoing NASA contracts to study the phase control problem. They have come up with a system, which is the current baseline concept, of a spread spectrum pilot about the power beam frequency. These various approaches are roughly illustrated by Figure 15 . In both the JPL and G.E. schemes the use of dual up link frequencies resolves the problem of ambiguities due to multiple wavelength line-of-sight path length differences across the array. They achieve this by measuring the received phase of the difference frequency which is a long enough wavelength to have no ambiguity.

The basic block diagram of the phase control system is shown in Figure 16 . A separate antenna imbedded in the array samples both the spread spectrum signal from ground and the radiated power at 2450. The pilot signal is fed through a power frequency bandstop filter to the receiver. The sample of radiated power serves to complete an amplitude and phase control loop placed around the klystron power amplifier. The I.F. tone out of the receiver is fed to the conjugator and combined with a phase reference that has been distributed to every module in the array. The conjugated I.F. signal after multiplying is the signal to which the radiated power sample is locked in the loop around the tube.

Typical Klystron Module

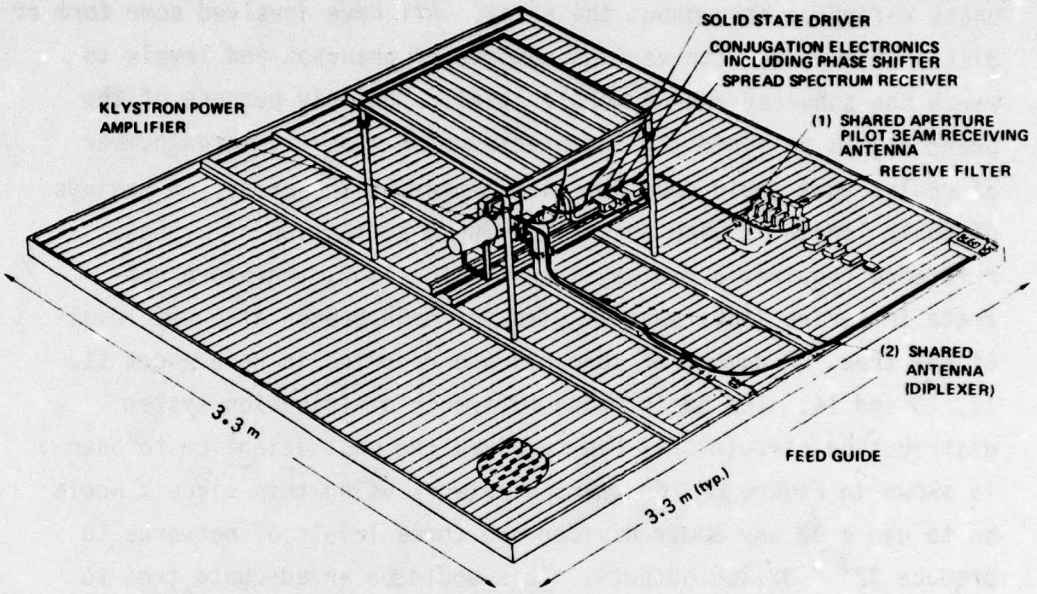

FIG. 13

S-BAND SLOTTED WAVEGUIDE SUBARRAY

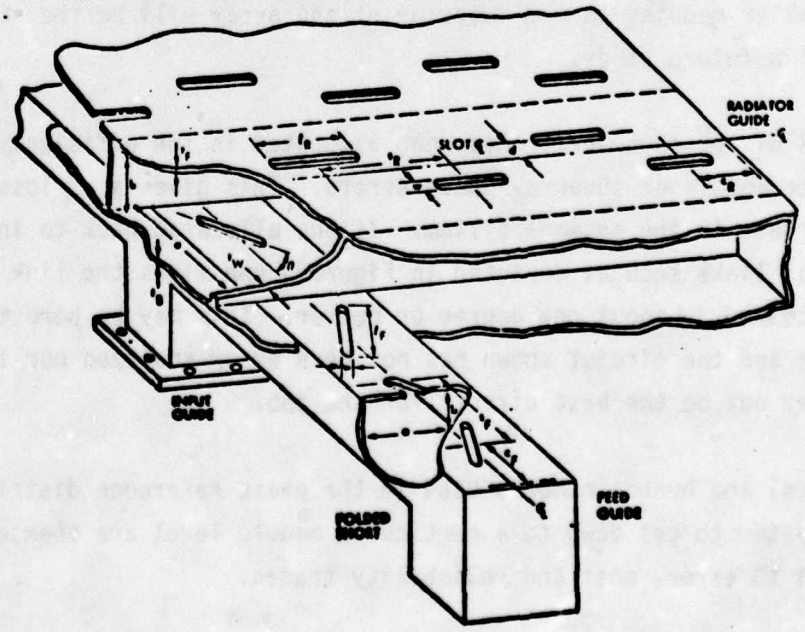

FIG. 14

The Phase Reference Distribution System

A number of approaches have been considered for distribution of the phase reference throughout the array. All have involved some form of distribution tree with various numbers of branches and levels to reach the subarray and/or module level. The only purpose of the branching is to avoid the inconvenience of the very large number of cables that would come into the center of the array. A savings of cable length is also possible. The distribution of a phase reference requires a two way transmission link, therefore separate in series links must be used for each branch at every level of the tree. A number of concepts are reported in References 11, 12, 13 and 14. The basic phase reference distribution system distribution circuit that has received the most attention to date is shown in Figure 17. An example network using this circuit would be to use a 32 way power divider and three levels of networks to produce 32^3 = 32,768 outputs. This would be an adequate tree to extent phase control to the 5 meter level. Five meters is the size of the largest antenna module which is used in the outer power density taper ring. Whether phase control should be extended to the smaller modules in the interior of the array will be the subject of a future study.

A total of 10° phase error has been allocated in the efficiency buget to module or subarray phase errors. This gives a 3% loss, the largest in the antenna system. If one allocated back to individual links such as depicted in Figure 17 one finds the link performance must be about one degree or better. This may be hard to achieve and the circiut shown has not been error analyzed nor indeed may not be the best circuit for the job.

The level and branch numbers used in the phase reference distribution system to get down to a particular module level are themselves subject to error, cost and reliability trades.

PILOT FREQUENCY PLANS

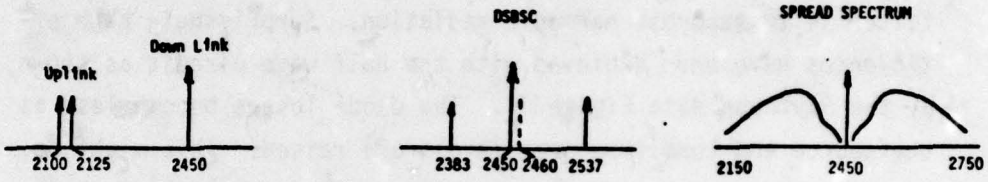

JPL Frequency Plan

G.E. Frequency Plan

LinCom Frequency Plan

FIG. 15

PHASE CONTROL BLOCK DIAGRAM

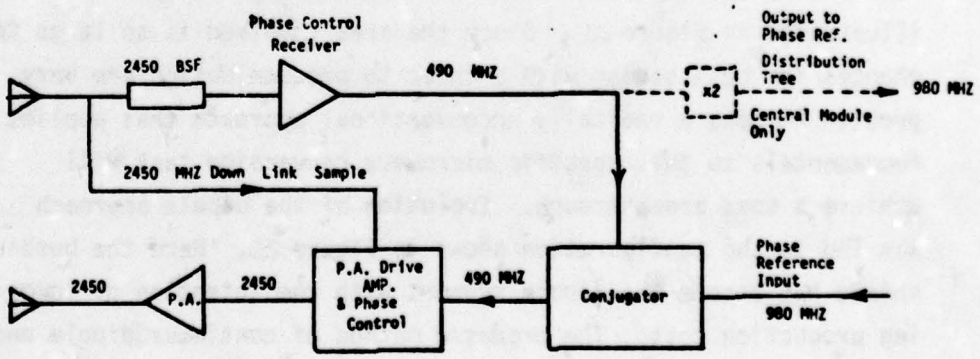

FIG. 16

The Rectenna Concept

The approach to receiving the microwave energy is basically a simple individual dipole over a ground plane driving a diode rectifier and D.C. busbar. This is the same basic concept that was demonstrated at Goldstone and is shown in Figure 18. The purpose of the filter is to suppress harmonic radiation. Surprisingly high efficiences have been achieved with the half wave circuit as shown by the Raytheon data Figure 19 . The diode losses become less as the source and load impedance levels are raised. This might be accomplished through transforming the dipole impedance and hence be a trade with network losses. Alternatively the dipole resistance may be raised to 153 ohms by using minimum dipole spacings of 0.5λ. This is a cell size 25% smaller than has typically been used in the rectenna experiments reported and 44% smaller than an isolated dipole over a ground plane. The smaller cell of course collects less power which itself lowers efficiency as seen in Figure 19 . The smaller cell also produces a higher cost rectenna which calls for a cost/efficiency trade study.

Panels of these dipoles will be oriented toward the satellite as illustrated in Figure 20 . Since the area involved is so large the chances for cost saving with a cheap to produce design are very great. Perhaps a radically unconventional approach that applies fundamentals to this specific microwave conversion task will achieve a cost breakthrough. Evolution of the dipole approach has led to the configuration shown in Figure 21. Here the busbar shield has become the dipole support with the intention of lowering production cost. The proposed method of continous dipole and circuit fabrication from wire rolls is shown in Figure 22. To maintain diode power at efficient levels consideration has been given to the use of a concentrating scheme combining line horn and cylindrical parabola as shown in Figure 23. In the larger sizes it is estimated that an f/d = .25 configuration will have an aperture efficiency approaching 97%.

PHASE REFERENCE DISTRIBUTION CIRCUIT

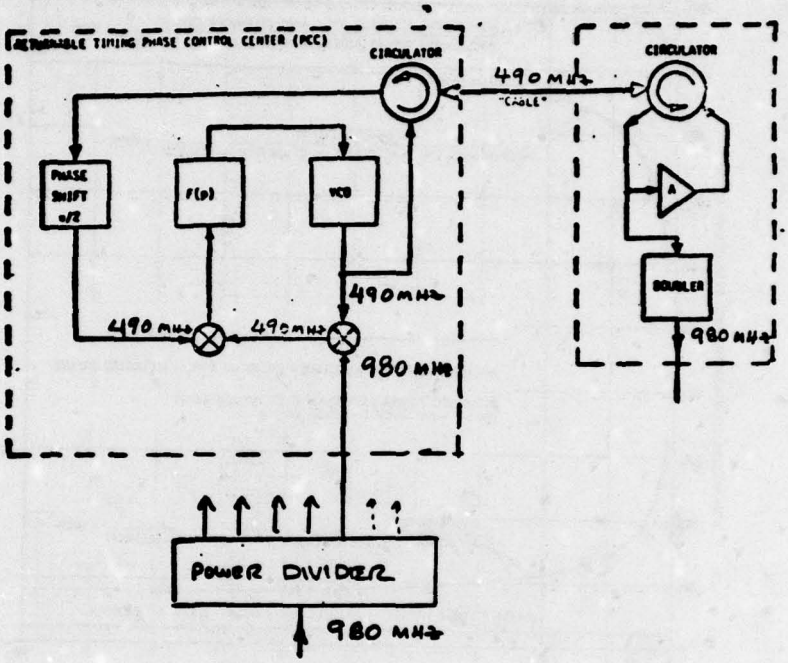

FIG. 17

RECTENNA ELEMENT

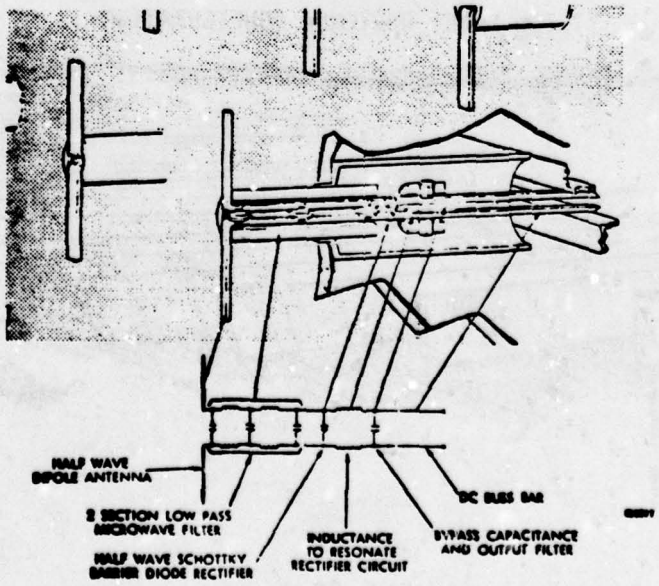

FIG. 18

CONVERSION EFFICIENCY vs. POWER INPUT

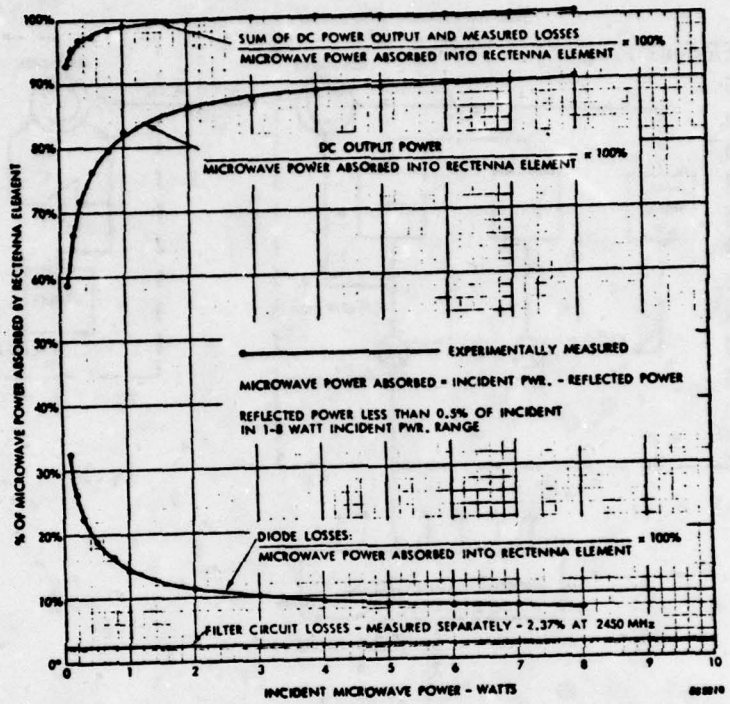

FIG. 19

TILTED PANEL RECTENNA CONFIGURATION

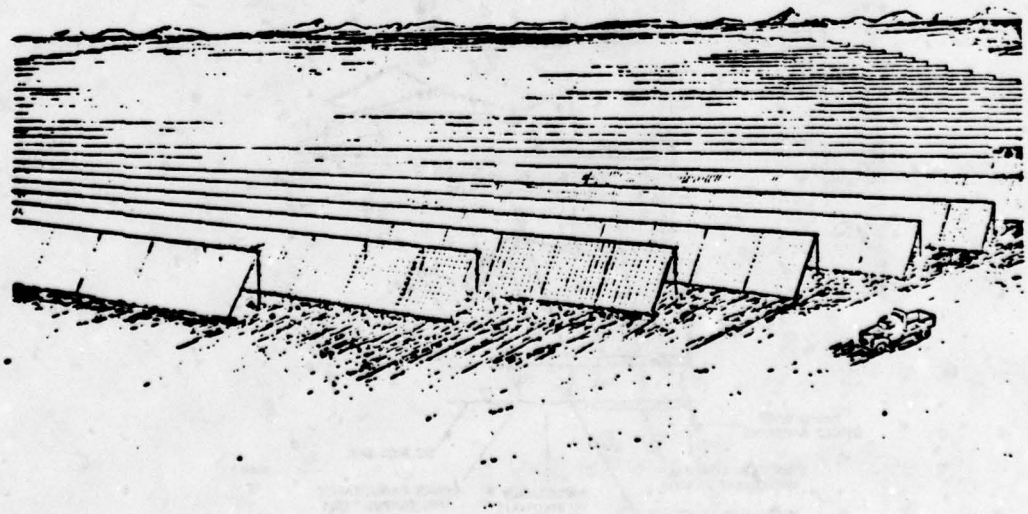

FIG. 20

RECTENNA CONFIGURATION

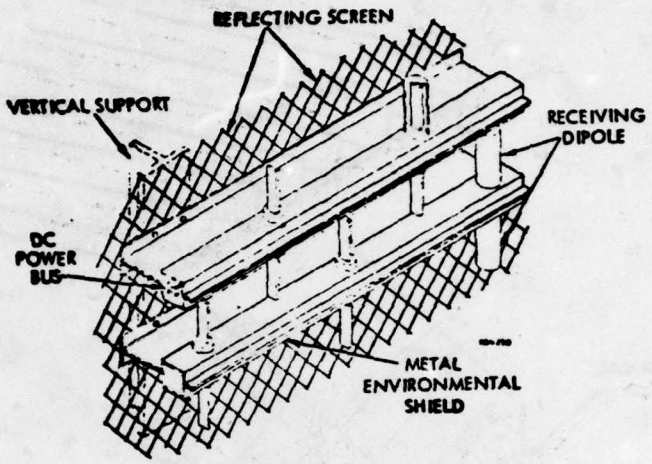

FIG. 21

DIPOLE - CIRCUIT FABRICATION

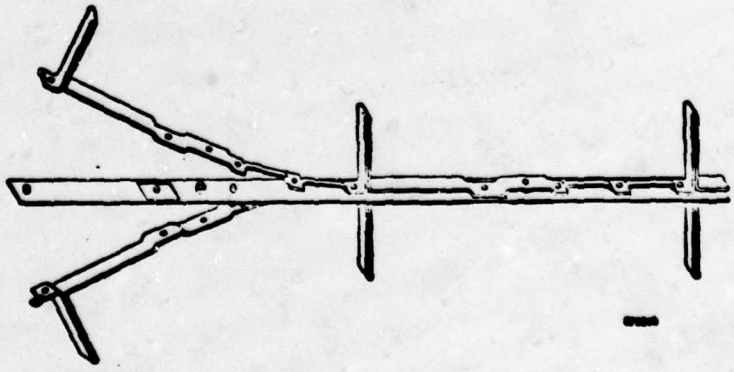

FIG. 22

RECTENNA CONCEPT

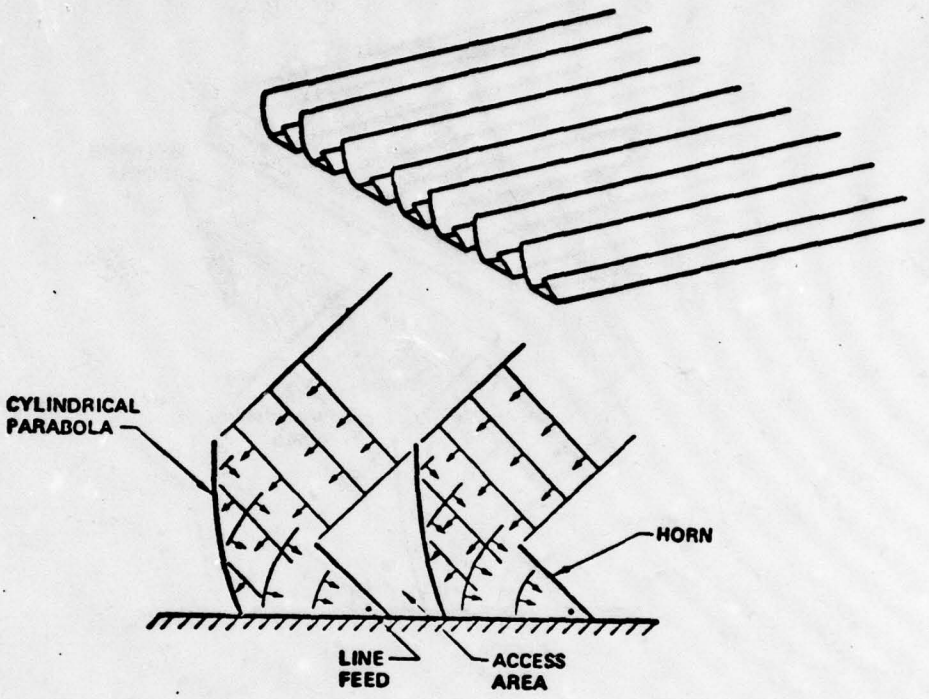

FIG. 23

References

(1) Gordon, Wm. E., Duncan Lewis M, Ionosphere/Microwave Beam Interaction Study, Rice University, Houston, Texas, July '78, NAS9-15212.

(2) Primich, R. I., Northover, F. H., Use of Focused Antenna for Ionized Trail Measurements: Part I, Power Transfer Between Two Focused Antennas, IEEE Transactions on Antennas and Propagation, Vol. II, March '63.

(3) Raytheon Advanced Development Laboratory, Sudbury, MA, Microwave Power Transmission System Studies, Vol, II, Dec. '75, NASA CR-134886, ER75-4368, Contract NAS3-17835.

(4) Nalos, E. J., Lund Jr., W. W., Nomograph Aids Solar Power Satellite Design, Microwave System News, Dec. '78.

(5) Brown, W. C., Electronic and Mechanical Improvement of the Receiving Terminal of a Free-Space Microwave Power Transmission System PT-4964, Raytheon Co., Aug. 1, 1977, NASA Report No. CR-135194.

(6) Boeing Aerospace Co., Solar Power Satellite Preferred Concept System Definition D-180-24071-1, March 1978.

(7) Boeing Aerospace Co., Solar Power Satellite System Definition Study, Sixth Monthly Progress Report, June '77, Contract NAS 9-15196, DRL T-1346, DRD MA - 179T.

(8) General Dynamics, Convair Division, Achievable Flatness in a Large Microwave Power Antenna Study, Final Report, CASD-NAS-78-011, 18 Aug. '78, Contract No. NAS9-15423.

(9) General Electric Space Division, Solar Power Satellite System Definition Study, Part 4, Phase 1 - Final Report, Dec. 14, '78.

(10) Dickinson, R. M., Microwave Power Transmitting Phased Array Antenna Research Project Summary Report, Jet Propulsion Laboratory, Publication 78-28, Dec. 15, '78.

(11) Chernoff, R. C., Large Active Retrodirective Arrays for Space Applications, Jet Propulsion Laboratory Publication 78-20, Jan. 15, '78.

(12) General Electric Space Division, Solar Power Satellite, Phase 3, Final Report, March '78.

(13) Lindsey, William C., A Solar Power Satellite Transmission System Incorporating Automatic Beamforming Steering and Phase Control. Lincom Corp., Pasadena, CA, June '78, Contract NAS 9-15237.

(14) Thompson, M. Y., Taylor, T. H., Lund Jr., W. W., Phase Control Concepts for Large Space-Borne Retrodirective Antenna Arrays, Boeing Document D180-24970-1, April 18, 1979.

A VARIABLE IMPEDANCE RATIO PRINTED CIRCUIT BALUN

by

R. Y. Shimoda

BOEING AEROSPACE COMPANY
SEATTLE, WASHINGTON

ABSTRACT

A unique printed circuit (stripline) balun has been developed for use with conical spiral antennas. Essentially, it is a coupled line one wavelength ring hybrid whose interconnecting line impedances are varied to accommodate different antenna impedances. This balun possesses the following desirable features:

(a) The balun internally transforms the output to any value of antenna impedance in addition to the conventional 2:1 and 1/2:1.

(b) The balun does not extend within the spiral antenna and thus does not perturb the antenna performance and is entirely contained within the spiral base due to its small size and circular shape factor.

(c) The balun is completely shielded from the radiating element.

The circuit was realized and incorporated into the base of two types of log conical spiral antenna which are to be used on the IUS (Inertial Upper Stage)vehicle. This balun transforms a 140 ohm antenna impedance to 50 ohms over a 27% bandwidth at S Band. The design philosophy, construction and the performance characteristics will be described.

I. INTRODUCTION

This report describes a printed circuit (stripline) balun that transforms the 140 ohm impedance of a balanced conical spiral antenna to an input unbalanced impedance of 50 ohms. Many antenna subassemblies consist of a radiating element and a balun which transforms the balanced radiating element impedance to an unbalanced impedance of the circuitry to which the subassembly is connected. Generally in a 50 ohm system, the impedance transformation ratio is fixed to either one-half or twice this value. Other transformation ratios are usually achieved using additional $\lambda/4$ transformers.

Numerous coaxial realizations of baluns exist. However, the number of printed circuit realizations are rather limited. Bawer and Wolfe[1] described a microstrip realization of a coaxial balun proposed by Roberts[2]. In order to obtain an impedance match for a 2:1 ratio, the input transmission line's impedance was tapered. The physical size of the balun was 3/4" x 1" for an octave band centered about 3 GHz. Another microstrip realization of a coaxial balun was presented by Laughlin[3]. His version was a two level microstrip circuit with three conductor planes. The balanced to unbalanced impedance ratio was matched by mutually considering the effects of the cavity, open-circuited stub, and quarter wave transformer. The quarter wave transformers were inserted on the output arms for an impedance ratio of 2:1. The physical size of an octave S band balun centered at 3 GHz was approximately .6" x 2.5" with the outputs approximately $\lambda/2$ apart. Its shape factor may be altered by folding the transmission lines so that the outputs are closer together.

A printed circuit (stripline) balun described here has been developed for use with conical spiral antennas. Essentially, it is modification of a coupled line one wavelength ring hybrid previously proposed by March[4]. The novel feature introduced here was to modify the hybrid interconnect impedance levels to achieve a balun which will accommodate different antenna impedance levels. This balun possesses the following desirable features:

(a) The balun internally transforms to any value of antenna impedance in addition to the conventional 2:1 and 1/2:1 without the use of external transforming sections.

(b) The balun does not extend within the spiral antenna and thus does not perturb the antenna performance and is entirely contained within the spiral base due to its small size and circular shape factor.

(c) The balun is self shielded from the radiating element by the stripline ground planes.

The circuit was realized and incorporated into the base of two types of log conical spiral antenna which are to be used on the IUS (Inertial Upper Stage) vehicle. The balun developed, which will be described, transforms a 140 ohm antenna impedance to 50 ohms over a 27% bandwidth at S Band with a VSWR less than 1.35:1.

II. BALUN DESCRIPTION

March proposed the one wavelength ring hybrid to increase the frequency performance of the conventional one and one-half wavelength rat race. The circuit is shown schematically in Fig. 1. A signal entering entering port (1) splits into two equal amplitude signals: one traveling to output port (2) experiences a delay equivalent to 90° and the other traveling to port (3) experiences an advance equivalent to 90° thereby result-

ing in a 180° phase difference between ports (2) and (3) at center frequency.

The stripline version of this component is depicted in Fig. 2. The even mode impedance of the phase reversing coupled section is such that the lines are overlapped. Although the rest of the circuitry is standard stripline, the circuit has to be made using three layers of dielectric material. The short circuits to ground are 3 mil x 15 mil copper wire ribbons soldered to the metalization pattern and to both ground planes.

III. ANALYSIS

The characteristic impedance of the coupled section is given by

$$Z_c = \frac{2 Z_{oo} - Z_{oe} \sin\theta}{\left[(Z_{oe} - Z_{oo})^2 - (Z_{oe} + Z_{oo})^2 \cos^2\theta\right]^{1/2}} \quad (1)$$

where Z_{oe} and Z_{oo} are the even and odd mode impedances and θ is the electrical length of the coupled region. At center frequency, $\theta = 90^\circ$ and

$$Z_c = \frac{2 Z_{oe} Z_{oo}}{Z_{oe} - Z_{oo}} \quad (2)$$

Z_c must also satisfy the following condition

$$Z_c = \sqrt{Z_{oo} Z_{oe}} \quad (3)$$

which leads to

$$\begin{aligned} Z_{oe} &= (\sqrt{2} + 1) Z_c \\ Z_{oo} &= (\sqrt{2} - 1) Z_c \end{aligned} \quad (4)$$

The phase shift through the coupled line arm is given by:

$$\phi = \cos^{-1}\left[\frac{(Z_{oe} + Z_{oo})}{(Z_{oe} - Z_{oo})} \cos\theta\right] \quad (5)$$

In order to derive the equations describing the impedance transformation properties of the hybrid, a more general analysis will be used. The equivalent circuit shown in Fig. 3(a) will be referred to in arriving at the expression for input reflection coefficient while that of Fib. 3(b) and Fig. 3(c) will be referred to in arriving at the expressions for the amplitudes and phases of the signals at the output ports. The matrix elements for the various networks are listed in Table I.

The voltages and currents of the primed and unprimed arms are related by the ABCD parameters of their respective paths together with the additional condition.

$$(I_4 + I_4') Z_1 = V_4 \quad (6)$$

Using these known relationships, it can be shown that the input impedance at port 1 is

$$Z_{in}(1) = \frac{A B' + B A' + \frac{B B'}{Z_1}}{-2 + BC' + DA' - D'A + \frac{BD' + DB'}{Z_1}} \quad (7)$$

and the corresponding reflection coefficient,

$$\Gamma_{in}(1) = \frac{Z_{in}(1) - Z_1}{Z_{in}(1) + Z_1} \quad (8)$$

The input impedance at port 4 when port 1 is terminated is obtained by replacing the A parameters with their respective D parameters.

When port 1 is terminated, the ratio V_1/V_4 can be shown to be

$$\frac{V_1}{V_4} = \frac{\frac{B B'}{Z_1} + A B' + B A'}{B + B'} \quad (9)$$

and the corresponding insertion loss (isolation) between ports 1 and 4

$$\text{LOSS (dB)} = 20 \log \frac{1}{1 + \Gamma_{in}(1)} \frac{V_1}{V_4} \quad (10)$$

Then with the aid of Fig. 3(b) and 3(c), one can also show that the voltage ratios of the output ports are,

$$\frac{V_3}{V_1} = \frac{B''' + B''}{\frac{B'' B'''}{Z_2} + A''' B'' + A'' B'''} \quad (11)$$

$$\frac{V_2}{V_1} = \frac{B^{iv} + B^{v}}{\frac{B^{iv} B^{v}}{Z_2} + A^{iv} B^{v} + A^{v} B^{iv}} \quad (12)$$

The expression for the voltage transfer ratio between ports 2 and 3 and input impedances of the rest of the ports may be derived using the same techniques.

At mid band, the equations reduced to

$$Z_{in}(1) = \frac{Z_c^2}{2 Z_2} \quad (13)$$

$$\frac{V_3}{V_1} = j \frac{Z_2}{Z_c} \quad (14)$$

$$\frac{V_2}{V_1} = -j\frac{Z_2}{Z_c} \quad (15)$$

$$\frac{V_1}{V_4} = \frac{V_3}{V_2} = \infty \quad (16)$$

Equation (14) predicts that the voltage at port 3 leads the input voltage by 90° while equation (15) predicts that the voltage at port 2 lags the input voltage by the same amount at center frequency. In order that the input be matched at midband, equation (13) requires that the characteristic impedance of the interconnecting transmission lines be the geometric mean of twice the product of Z_1 and Z_2. Hence, to transform an unbalanced impedance of 50 ohms to a balanced impedance of 140 ohms Z_c must equal 83.67 ohms. For this example, the amplitude imbalance is 0.24 dB and predicted phase deviation from 180° is 5.7° in an octave band. The frequency dependence of the VSWR's of the input and output ports are shown in Fig. 4. At the band edges, the maximum VSWR is 1.80:1 occurring at port 4.

IV. CIRCUIT REALIZATION

The above analysis was used to develop a hybrid functioning as a balun which was suitable for use with conical spiral antennas. The balun had to be less than two inches in diameter and permit satisfactory antenna performance from 1.75 to 2.3 GHz. Fig. 5 is a photograph of the balun assembly which transforms a balanced 140 ohm antenna impedance to an unbalanced 50 ohms. The unbalanced 50 ohm input is connected perpendicular to the circuit with an SMA connector and the balanced outputs are connected to the circuit with .086 inch semi-rigid coaxial lines. A 50 ohm pill termination is connected to the isolated port. The stripline ground plane spacing is .130 inch with a center board thickness of .005 inch on which the circuit is etched. Grounding interconnections from one side of the outer board to the other is accomplished with .0005 inch thick x .040 inch wide copper ribbons. Ribbons .015 inch wide x .003 inch thick are used to connect the coupled-line short-circuited ends to both ground planes. The width of the lines in the coupled section is .0135 inch with an overlap of .0066 inch for Z_{oe} = 202 ohms and ϵ_r = 2.22. The length of the coupled section was shortened to allow for the inductance of the shorting ribbons which were assumed to be 0.6 nanohenry.

V. RESULTS

The characteristics of the transforming hybrid were measured in a 50 ohm system using the HP 8542B Automatic Network Analyzer (ANA). Two 2-section 50-70 ohm Chebychev impedance transformers were used to substitute for the antenna and transform the hybrid output impedance to 50 ohms. Since the transformers were not identical, characteristics were measured with the transformers in one configuration and then measurements were repeated with the transformers switched. The insertion characteristics of the path with the lower VSWR transformer were taken as the characteristics of the hybrid while the second transformer was used to terminate the other port. The VSWR of the better transformer was less than 1.15:1 over the frequency range of interest.

The initial hybrid had an amplitude imbalance of one dB at the lower band edge and the phase deviation from 180° was 2.3° at the center frequency. The amplitude imbalance is due to the difference in loss between the two paths and the inequality of the impedances of the two paths caused by variations in etch undercut.

From the loss values provided by stripline material manufacturers and Reference (5), it was estimated that the additional losses of the high even mode impedance coupled line section was .23 dB more than an equivalent transmission line with the same characteristic impedance. The characteristic impedance of the coupled line section was lowered to 77.7 ohms in order that the two insertion losses overlap 0.12 dB. The length of the through arm was lengthened to assure that the phase deviation between outputs be 180° at center frequency. The performance of the hybrid which had these corrections incorporated are shown in Fig. 6 through 8. The amplitude balance is less than .15 dB and the 180° phase deviation is $\pm$ 3.5° in the 27% band. The maximum insertion loss is .25 dB. The input return loss exhibited a value of 18 dB at the band edges with the 50-70 ohm transformers connected to the output ports. Hence, the measurement of Fig. 8 includes the effects of the transformers.

The circuit has been incorporated into the base of two types of log conical spiral antennas which are to be used for tracking, telemetry, and command on the IUS (Inertial Upper Stage) vehicle. Figure 9 shows the medium gain antenna and balun subassembly.

With the same ground plane spacing and centerboard thickness used for the I.U.S. balun, balanced impedance values (antenna impedance) up to 170 ohms may be transformed to 50 ohms. The lower bound of balanced impedance will be determined most likely by practical values of the radiating element. The hybrid itself is capable of transforming antenna impedances less than 50 ohms.

REFERENCES

1. R. Bawer and J.J. Wolfe, "A printed circuit balun for use with spiral antennas," IRE Trans. Microwave Theory Tech., MTT-8, p. 319-325, May 1960.

2. W.K. Roberts, "A new wide-band balun," Proc. IRE, 45, pp. 1628-1631, December 1957.

3. G.J. Laughlin, "A new impedance - matched wide-balun and magic Tee," IEEE Trans. Microwave Theory Tech., MTT - 24, pp. 135-141, March 1976.

4. S. March, "A wideband stripline hybrid ring," IEEE Trans. Microwave Theory Tech., MTT - 16, p. 361, June 1968.

5. H. Howe, Stripline Circuit Design, Massachusetts: Horizon House--Microwave, 1974.

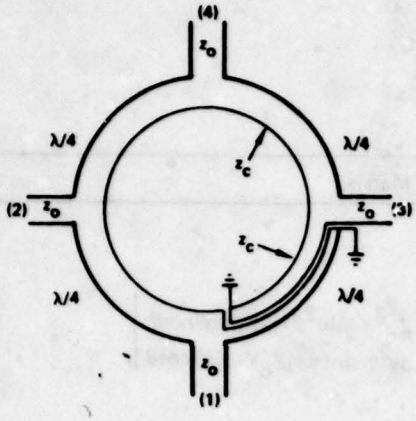

Figure 1. One Wavelength Ring Hybrid

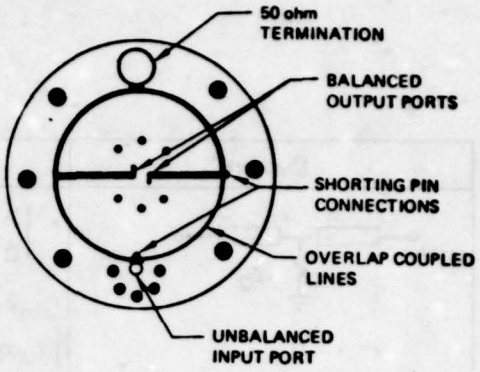

Figure 2. Stripline Version of Ring Hybrid (Conductor Pattern)

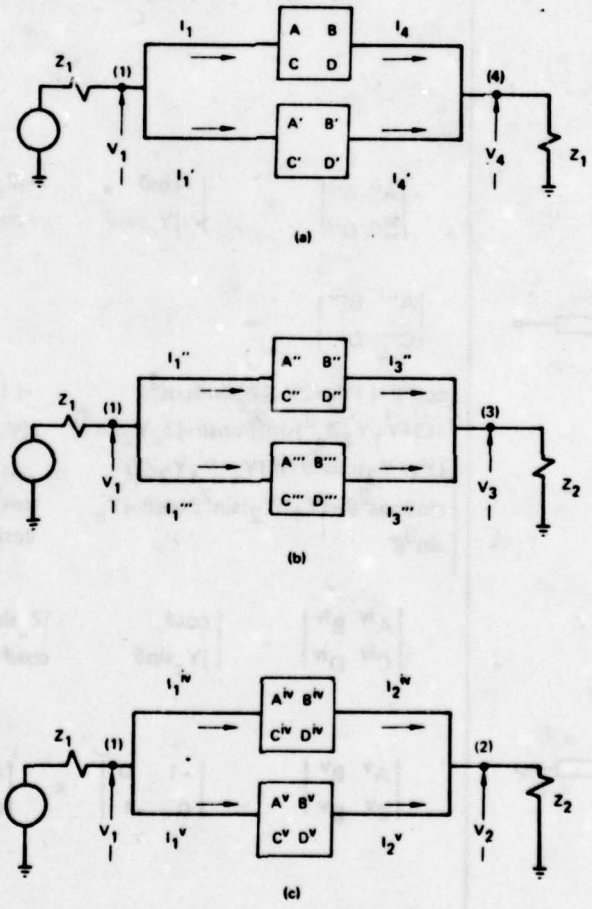

Figure 3. Schematic of Circuit Used to Derive: (a) Isolation and Input Reflection Coefficient, (b) and (c) Insertion Amplitude and Phase of Signals at Ports 2 and 3

Table 1.

Network*	Matrix
	$\begin{vmatrix} A & B \\ C & D \end{vmatrix} =$ $\begin{vmatrix} \cos^2\theta - \sin^2\theta + jY_2Z_c\sin\theta\cos\theta & -Z_c^2Y_2\sin^2\theta + j2Z_c\sin\theta\cos\theta \\ Y_2\cos^2\theta + j2Y_c\sin\theta\cos\theta & \cos^2\theta - \sin^2\theta + jZ_cY_2\sin\theta\cos\theta \end{vmatrix}$
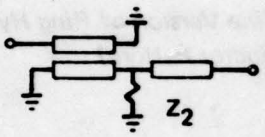	$\begin{vmatrix} A' & B' \\ C' & D' \end{vmatrix} = \begin{vmatrix} -1 & 0 \\ 0 & -1 \end{vmatrix} \times \begin{vmatrix} A & B \\ C & D \end{vmatrix}$
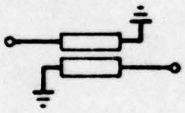	$\begin{vmatrix} A'' & B'' \\ C'' & D'' \end{vmatrix} = \begin{vmatrix} -\cos\theta & -jZ_c\sin\theta \\ -jY_c\sin\theta & -\cos\theta \end{vmatrix}$
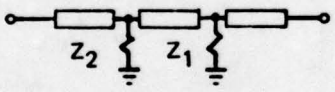	$\begin{vmatrix} A''' & B''' \\ C''' & D''' \end{vmatrix} =$ $\begin{vmatrix} \cos^3\theta + j(Y_2+2Y_1)Z_c\sin\theta\cos^2\theta & -j(Z_c+Y_1Y_2Z_c^3)\sin^3\theta - 2Z_c^2 \\ -(3+Y_1Y_2Z_c^2)\sin^2\theta\cos\theta - jZ_cY_2\sin^3\theta & (Y_1+Y_2)\sin^2\theta\cos\theta + j3Z_c\sin\theta \\ (Y_1+Y_2)\cos^3\theta + j(3Y_c+Y_1Y_2Z_c) & \cos^2\theta\cos^3\theta + j(Y_1+2Y_2)\sin\theta \\ \sin\theta\cos^2\theta - (Y_1+Y_2)\sin^2\theta\cos\theta - jY_c & \cos^2\theta - (3+Z_c^2Y_1Y_2)\sin^2\theta \\ \sin^3\theta & \cos\theta - jY_1Z_c\sin^3\theta \end{vmatrix}$
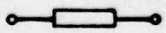	$\begin{vmatrix} A^{iv} & B^{iv} \\ C^{iv} & D^{iv} \end{vmatrix} = \begin{vmatrix} \cos\theta & jZ_c\sin\theta \\ jY_c\sin\theta & \cos\theta \end{vmatrix}$
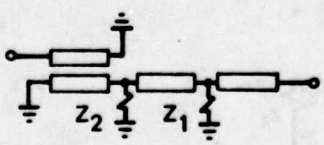	$\begin{vmatrix} A^{v} & B^{v} \\ C^{v} & D^{v} \end{vmatrix} = \begin{vmatrix} -1 & 0 \\ 0 & -1 \end{vmatrix} \times \begin{vmatrix} A''' & B''' \\ C''' & D''' \end{vmatrix}$

*All transmission lines = Z_c

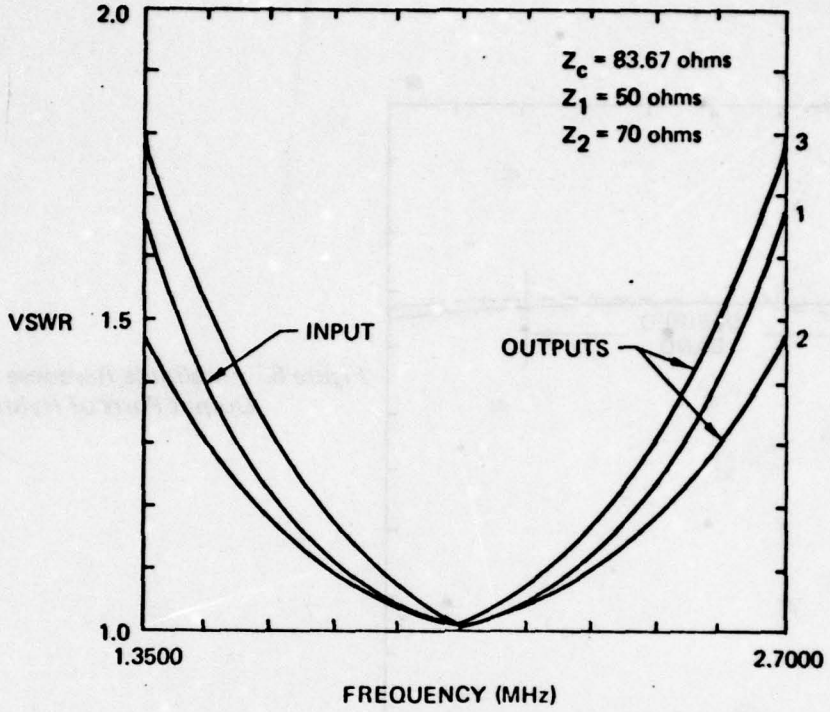

Figure 4. Octave Band VSWR Responses of the Input and Output Ports of the Hybrid (Isolated Port Terminated With 50 ohms)

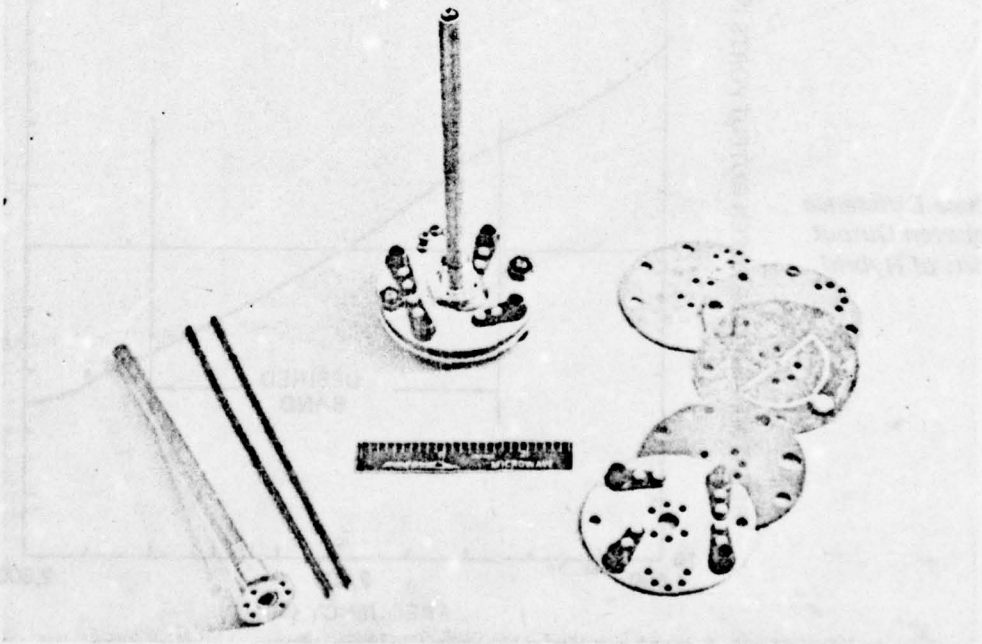

Figure 5. Photograph of Balun Subassembly

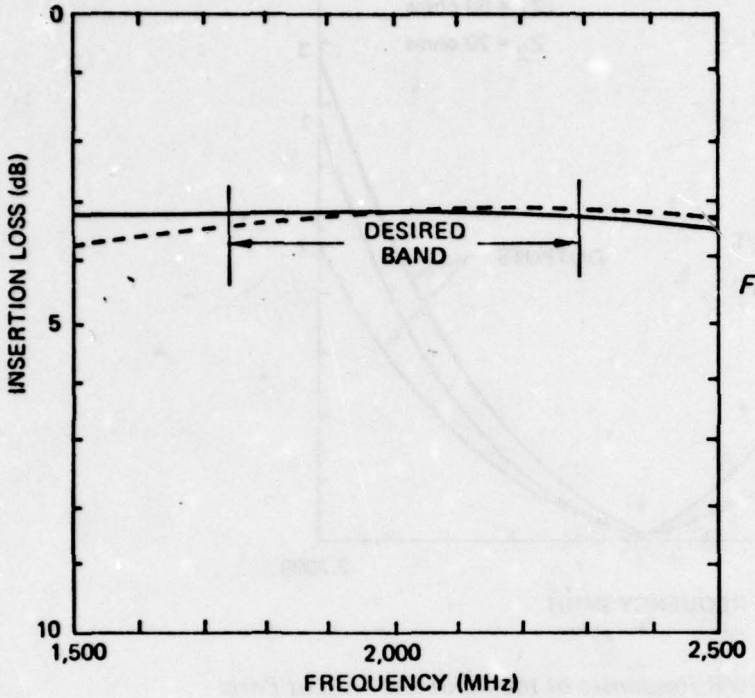

Figure 6. Amplitude Response of Output Ports of Hybrid

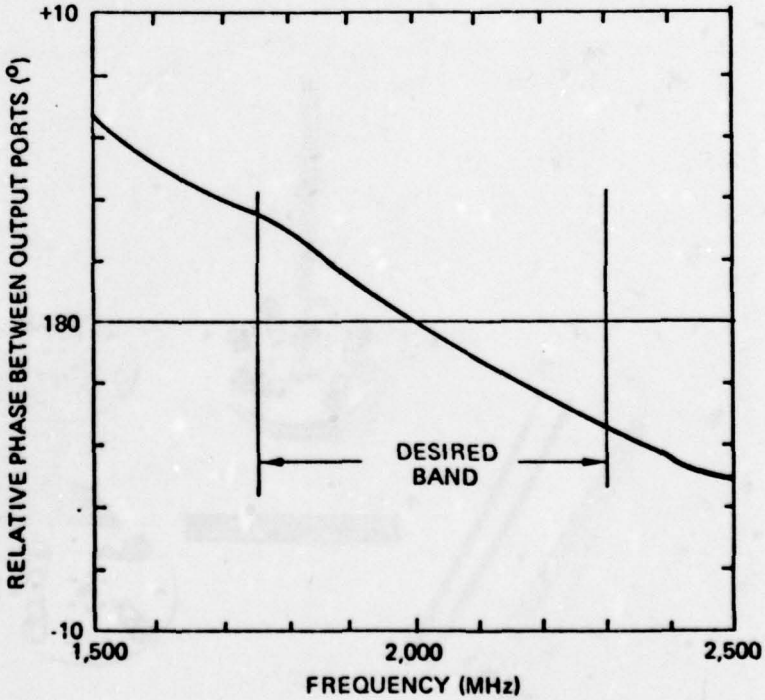

Figure 7. Phase Difference Between Output Ports of Hybrid

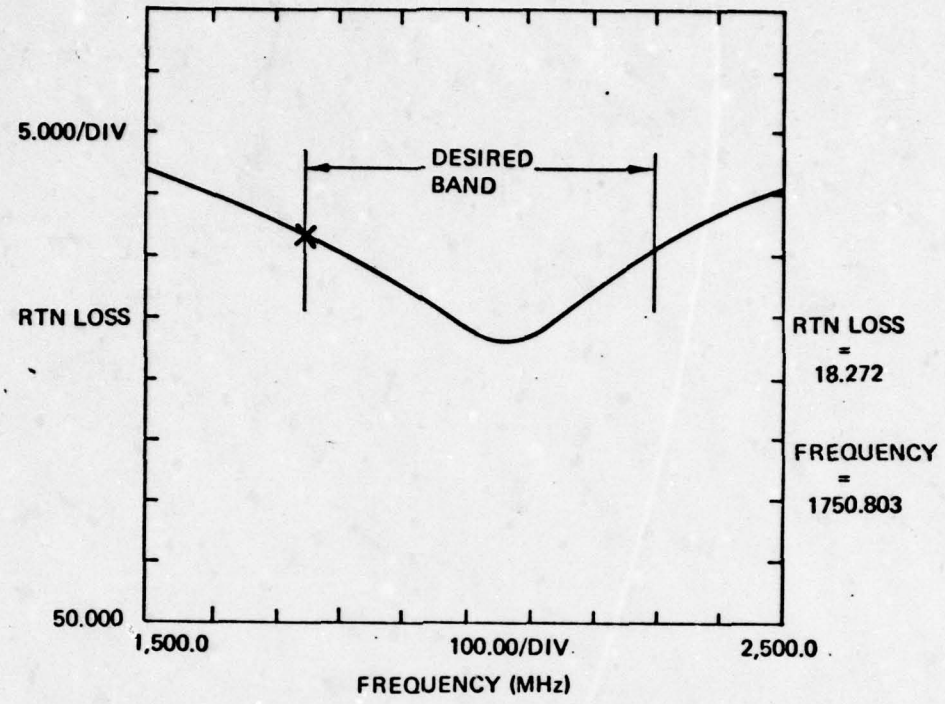

Figure 8. Input Return Loss of Hybrid

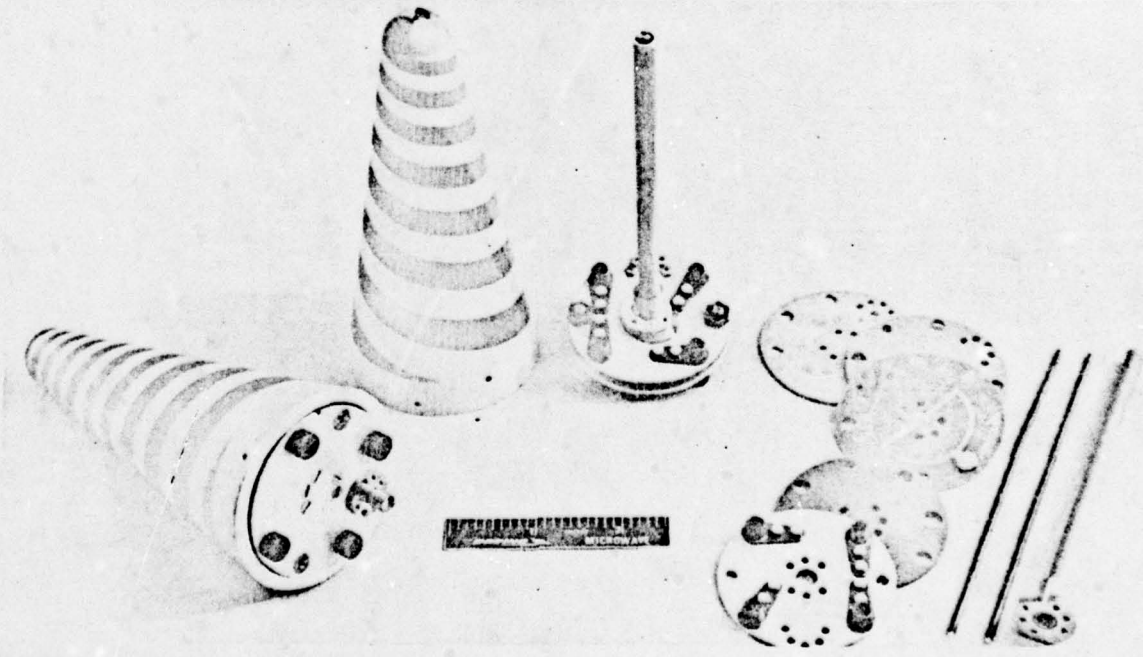

Figure 9. Integration of Balun With Radiating Element

DESIGN AND THEORY OF CIRCULARLY POLARIZED MICROSTRIP ANTENNAS

W. F. Richards, Y. T. Lo, P. Simon
Electromagnetics Laboratory
Department of Electrical Engineering
University of Illinois
Urbana, IL 61801

Circular Polarization (CP) has been reported in a variety of microstrip antennas [1]-[3]. Experimental work was recently reported [3] on a class of CP antennas derived from disk and square microstrip antennas by cutting slots in their interiors or corners off their perimeters. For all these antennas, the theory presented in this note provides an explanation for the mechanism of antenna operation, and in some cases, provides a means for predicting the necessary dimension needed for CP operation. This is important because CP operation is possible only for a very narrow band of frequency, and without a theoretical prediction, it would take many painstaking cut-and-trials to reach the correct dimensions.

Consider, as a first example, a *nearly square* microstrip of dimension $a \times b$ as shown in Fig. 1a. It was demonstrated in previous papers [4]-[6] that the electric field within the interior of a microstrip antenna can be approximated with good accuracy by the fields in the corresponding cavity formed by enclosing the boundary of the patch by a magnetic wall, provided that an effective loss tangent, which includes the effect of radiative, surface wave, copper, and actual dielectric losses, is used to characterize the losses in the cavity. Thus, the fields within the interior of a rectangular patch antenna are given by a sum over all the modes of the corresponding cavity:

$$E = jk_0\eta_0 \sum_{m=0}^{\infty}\sum_{n=0}^{\infty} \frac{\phi_{mn}(x,y)\phi_{mn}(x',y')}{k^2-k_{mn}^2}\, j_0\left(\frac{m\pi d}{2a}\right)$$

where $k^2 = \epsilon_r(1-j\delta_{eff})k_0^2$, $k_0 = 2\pi f/v$, f = frequency, v = speed of light, ϵ_r = relative dielectric constant, δ_{eff} = the "effective loss tangent" of the cavity = $1/Q$, where Q is the quality factor of the antenna, $\eta_0 = 377\Omega$, $k_{mn}^2 = (m\pi/a)^2 + (n\pi/b)^2$, $\phi_{mn}(x,y) = \left[\frac{\epsilon_{0m}\epsilon_{0n}}{ab}\right]^{1/2} \cos(m\pi x/a)\cos(m\pi y/b)$,

$j_0(x) = \sin(x)/x$, $\epsilon_{0m} =$ 1 for $m=0$ and 2 for $m\neq 0$, d is the width of a uniform strip of z directed source current of one amp, a, b, and t are the width, length, and thickness of the antenna, respectively, and (x,y) and (x',y') are the coordinates of the observation and feed points, respectively. If $b+c=a$ where $c/b \ll 1$, then the resonant wave numbers of the (0,1) mode, k_{01}, and of the (1,0) mode, k_{10}, will be very close to one another. Feeding the antenna at point 1 will excite the ϕ_{10} mode but not ϕ_{01}. Feeding at point 3 will excite ϕ_{01} but not ϕ_{10}. Feeding at point 2 or on the diagonal through point 2 will excite a dominant field proportional to $\psi_+ = \phi_{01} + \phi_{10}$. With a feed at point 4, the excited field will be proportional to $\psi_- = \phi_{01} - \phi_{10}$. In the far field, in the direction perpendicular to the plane of the microstrip, the electric fields produced by ϕ_{01} and ϕ_{10} are polarized in the x and y directions, respectively, and can be written for the appropriate choice of input current magnitude and phase as

$$E_x \approx \frac{\cos(\pi x'/a)}{k^2 - k_{10}^2}, \quad E_y \approx \frac{\cos(\pi y'/b)}{k^2 - k_{01}^2} \quad . \tag{1}$$

The contributions of the non-resonant modes are ignored in (1) for frequencies near the resonances of the two modes. To obtain CP in the direction of the zenith, the ratio of E_y to E_x should be $e^{\pm j\pi/2}$. Define $A = \cos(\pi y'/b)/\cos(\pi x'/a)$. Then,

$$\frac{E_y}{E_x} \approx A\,\frac{k^2 - k_{10}^2}{k^2 - k_{01}^2} \approx A\,\frac{k - k_{10}}{k - k_{01}} \quad . \tag{2}$$

It is particularly illuminating to plot k, k_{01}, and k_{10} in the complex k plane as was done in Fig. 2. For E_y/E_x to be $e^{j\pi/2}$, equation (2) requires that

$$\Delta k = k_{01} - k_{10} = L\left(A + \frac{1}{A}\right). \tag{3}$$

But

$$\frac{L}{k} \approx \frac{1}{2}\delta_{\text{eff}} = \frac{1}{2Q}\,, \tag{4a}$$

$$k_{01} - k_{10} = \frac{\pi}{b} - \frac{\pi}{a} = \frac{\pi}{b} - \frac{\pi}{b+c} \approx \frac{\pi c}{b^2}\,. \tag{4b}$$

and

$$\bar{k}b \approx \pi \ . \tag{4c}$$

(The parameters $\bar{k}$ and L are defined in Fig. 2.) Thus, combining (3) with (4),

$$\frac{\Delta k}{\bar{k}} = \frac{k_{01} - k_{10}}{\bar{k}} \approx \frac{c}{b} \approx \frac{A + \frac{1}{A}}{2Q} \ .$$

For the case of the feed point taken on the diagonal of the microstrip, $A=1$ and, therefore,

$$\frac{a}{b} = 1 + \frac{1}{Q} \ .$$

The sense of rotation of the CP wave produced by the antenna fed at point 2 will be left hand circularly polarized. Figure 3 shows the far-field pattern of the nearly square antenna taken with a rotating dipole. The quality of the CP is very good broadside to the antenna and, as expected, degrades to linear polarization on the horizon.

For the antenna of Fig. 1b, the analysis follows along the same lines as that for Fig. 1a. However, in this case, rather than using ϕ_{10} and ϕ_{01} modes, ψ_+ and ψ_- are used with corresponding wave numbers k_+ and k_-. Of course, if the corners of the square microstrip are not trimmed off, then $k_+ = k_-$. However, by trimming the corners, k_- is increased while k_+ stays nearly constant. Obviously, if the opposite pair of corners were to be trimmed, k_+ would increase and k_- would remain constant, reversing the sense of polarization. The amount of shift in resonant frequency due to truncation of the corners has been estimated using a perturbation formula [7]:

$$\frac{k_- - k_+}{\bar{k}} \approx \frac{2(a-a')}{\pi a} \sin[\pi (a-a')/a] \ .$$

This formula is based on the assumption that the boundary condition along the perimeter of the microstrip is that of a perfect magnetic wall. Although this assumption has proven reasonably applicable to the analysis of most aspects of microstrip antennas, it is not entirely adequate to predict the shift in poles in this critical application. It is believed that the complicated fringing fields at the corners where the perturbation formula is applied make the approximation of insufficient accuracy.

However, one can *experimentally* refine the proper dimensions by simply measuring the resonant frequencies corresponding to k_+ and k_- by feeding at ports 2 and 4, respectively.

The antenna in Fig. 1c operates by the same mechanism as that in 1a. In this case, however, the pole k_{10} can be varied by simply adjusting the capacitance attached to the antenna. (Since the capacitor is located at $y=b/2$, a null of the ϕ_{01} mode, k_{01} is unaffected by the capacitor.) If the range of capacity is large enough, and $a<b$, one is able to adjust the antenna to produce fields of any polarization and sense. Thus the antenna can be at one moment left hand CP, linear at the next, and right hand CP at some other time by simply changing the capacitance. However, since only one pole is affected by the capacitor, the frequency of operation shifts as the capacitance is varied. It should be noted that the capacitor could just as well have been located in the corner of the antenna in which case one would feed at points 1 or 3 to achieve CP operation.

Figure 4 shows a square microstrip antenna loaded by two independently biased varactor diodes. The varactors are located on the nodal lines of the ϕ_{10} and ϕ_{01} modes. The biasing arrangement shown in the figure ensures RF and DC isolation between bias supplies and antenna. The location of the varactors allows independent adjustment of the poles k_{01} and k_{10}. By this scheme, the difference in the poles $k_{01}-k_{10}$ can be adjusted while keeping their mean, $\bar{k}$, fixed. Thus for operation at a fixed frequency, virtually any polarization can be achieved simply by adjusting the varactor biases. Figures 5 and 6 show the impedance and radiation patterns of this antenna for the various polarizations. The asymmetry in the patterns is probably due to the asymmetrical placement of the diodes. It is conjectured that using two pairs of matched diodes on opposite sides of the antenna would minimize this effect.

Other single-feed CP microstrip antennas can be explained in the same way as the rectangular. A disk microstrip antenna was designed on the basis of this theory. A capacitor to the ground plane was attached to the circumference of the disk. When fed at an angle of forty-five degrees from the capacitor, CP operation was also obtained.

Using the double-tuned antenna of Fig. 4, it is also possible to vary the frequency of operation

without interfering with the state of polarization. The double-tuned antenna constructed by the authors is tunable from 800 MHz to 840 MHz while still maintaining quite good CP. Obviously, the tuning bandwidth is dependent on the quality of varactors used.

Although all these antennas are able to produce good CP without the need of an external phase-shifter and power divider, a distinct advantage, it is clear from the theory given above that their CP operation is *extremely narrow band.* Figure 7 shows the predicted degradation in axial ratio with normalized frequency defined as

$$\xi = \frac{f - \bar{f}}{f_{01} - f_{10}} \quad \text{where } \bar{f} = \frac{v\bar{k}}{2\pi},\ f_{01} = \frac{v\epsilon_r^{-1/2}}{2b},\ f_{10} = \frac{v\epsilon_r^{-1/2}}{2a}.$$

Thus, for an axial ratio within 3 dB (at zenith) which would produce a polarization mismatch loss of less than 1/4 dB with respect to CP, one is limited to a bandwidth of about 35% of the frequency difference between the two dominant poles or about $35/Q$ percent bandwidth. Figure 7 applies to any CP microstrip whose feed excites both of the near degenerate modes equally. A more general set of curves for less symmetrically located feeds can easily be constructed. The close agreement between theory and experiment is shown in Fig. 8 where axial ratio as a function of frequency is plotted for the nearly square antenna.

In conclusion, the mechanism characterizing the operation of singly fed CP microstrip antennas has been described in a simple and useful manner. For geometries for which the difference in the resonant frequencies of the two nearly degenerate modes can be computed with sufficient accuracy (such as the rectangular or elliptical patches), the exact dimensions can be successfully calculated by knowing the Q of the antenna. For perturbed patches that lead to nonseparable geometries, one can fairly quickly determine the dimensions without making pattern measurements by adjusting the pole location such that $\Delta k/\bar{k} = 1/Q$. Finally, a curve has been plotted which allows one to quickly predict the pattern bandwidth of the CP antenna.

Acknowledgement: This work is supported by Rome Air Development Center, Deputy for Electronic Technology.

References

1 J. L. Kerr, "Microstrip polarization techniques," *Proceedings of the 1978 Antenna Applications Symposium* (Sponsored by Electromagnetics Laboratory, University of Illinois, Urbana, IL 61801)

2 C. M. Kaloi, "Notched/Diagonally Fed Electric Microstrip Antenna," U.S. Patent Application No. 740,696, November 1976.

3 H. D. Weinschel, "A cylindrical array of circularly polarized microstrip antennas," *IEEE AP-S International Symposium Digest,* pp. 175-180, June 1975.

4 Y. T. Lo, D. Solomon, W. F. Richards, "Theory and Experiment on Microstrip Antennas," *IEEE Trans. Antennas Propagat.,* vol. 27, no. 3, March 1979.

5 W. F. Richards, Y. T. Lo, D. D. Harrison, "An Improved Theory of Microstrip Antennas," accepted for publication in *Electronics Letters.*

6 W. F. Richards, Y. T. Lo, "An Improved Theory for Microstrip Antennas and Applications," Technical report submitted to Rome Air Development Center under contract number F19628-78-C-0025, December 1978.

7 C. C. Johnson, *Field and Wave Electrodynamics,* pp. 229-232, McGraw Hill, 1965.

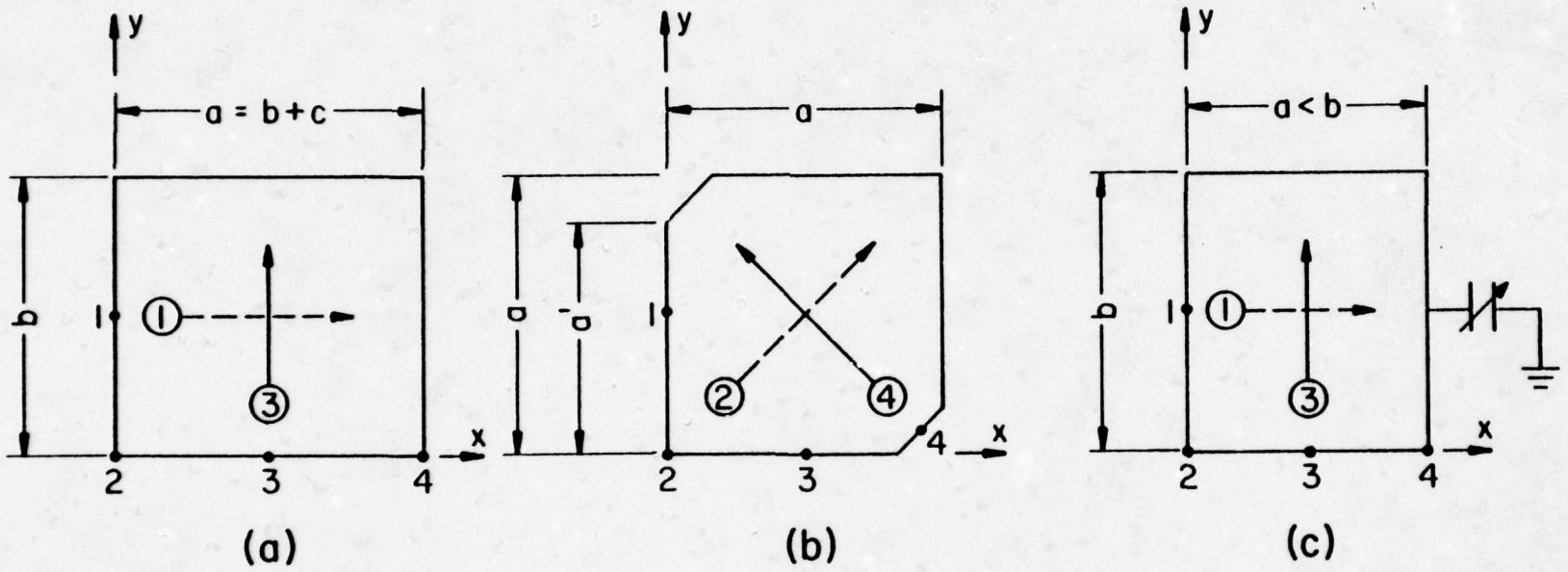

Fig. 1. Microstrip antennas capable of producing circular polarization
(a) Nearly square microstrip.
(b) Truncated microstrip.
(c) Capacitively loaded microstrip.

Polarization of the far field in the z-direction (zenith) is indicated by either a solid or a dashed arrow with a circled number corresponding to the feed location number.

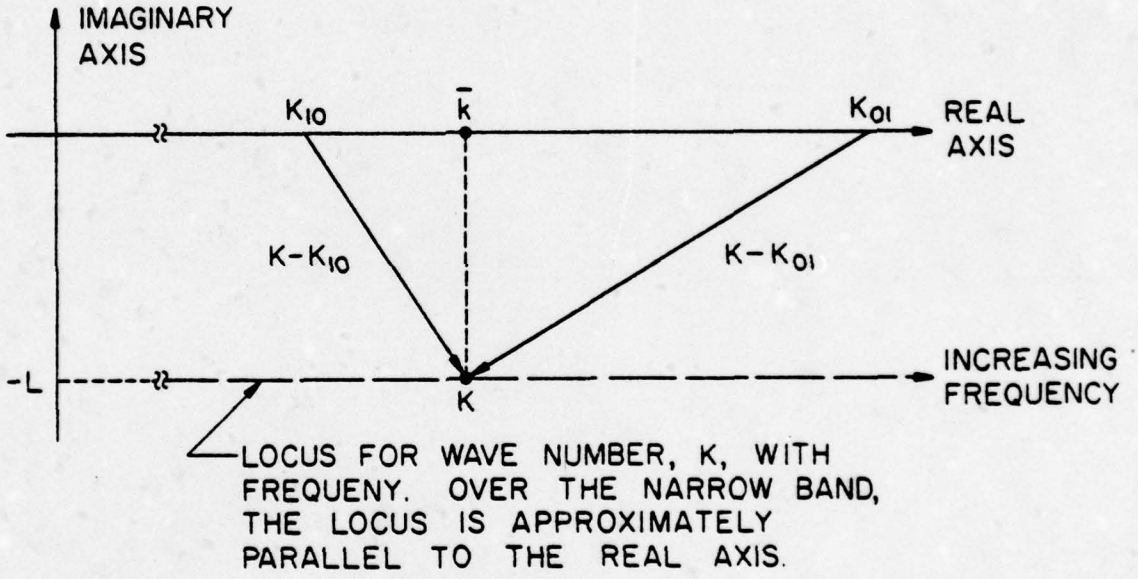

Fig. 2. Relative pole positions in the complex K plane.

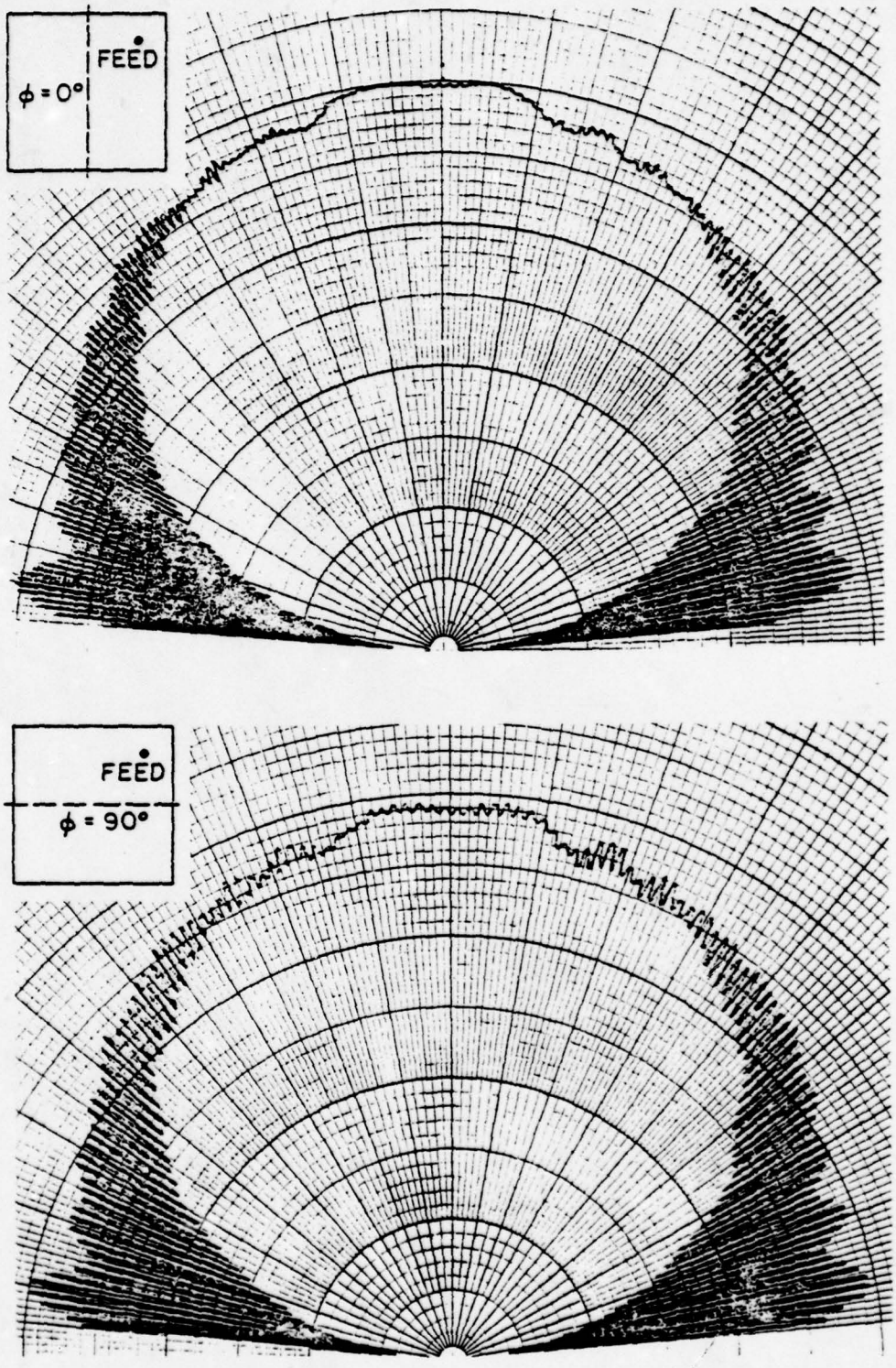

Fig. 3. Elevation patterns taken with rotating dipoles for nearly square microstrip antenna

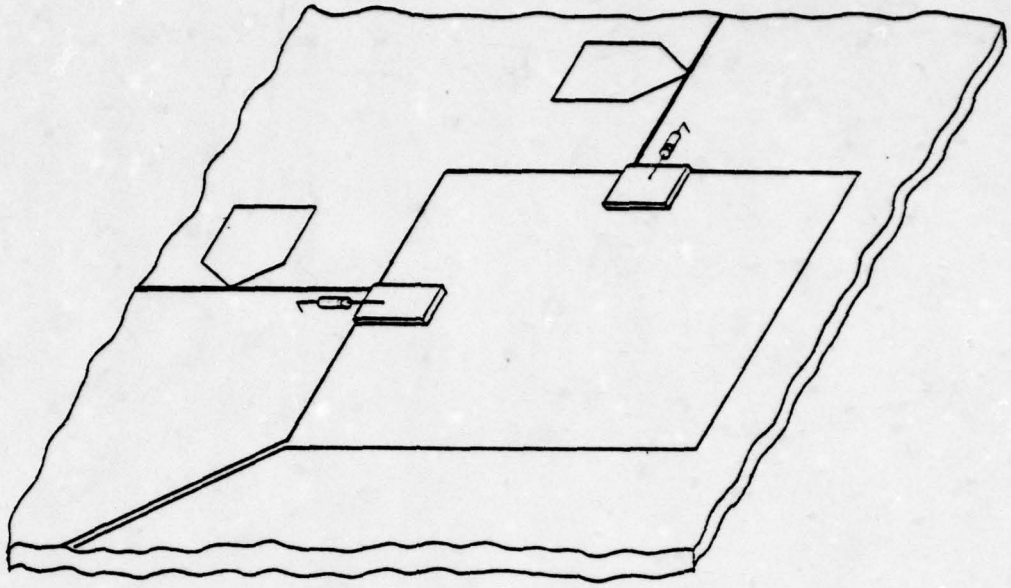

Figure 4a. Double tuned antenna.

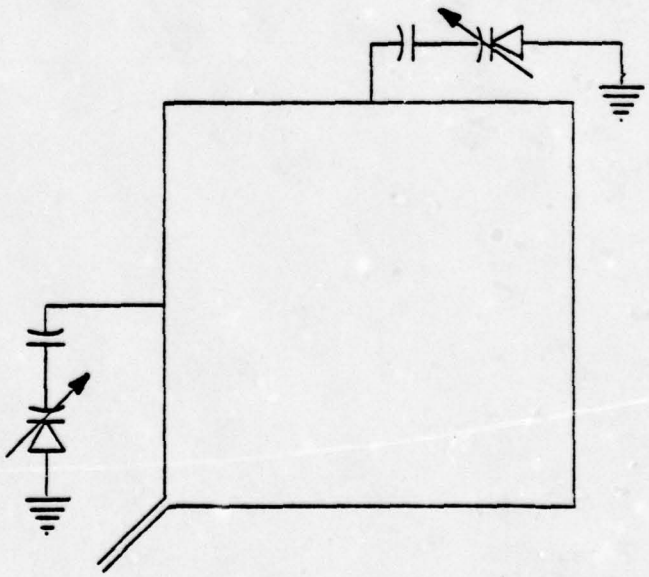

Figure 4b. Double tuned antenna schematic.

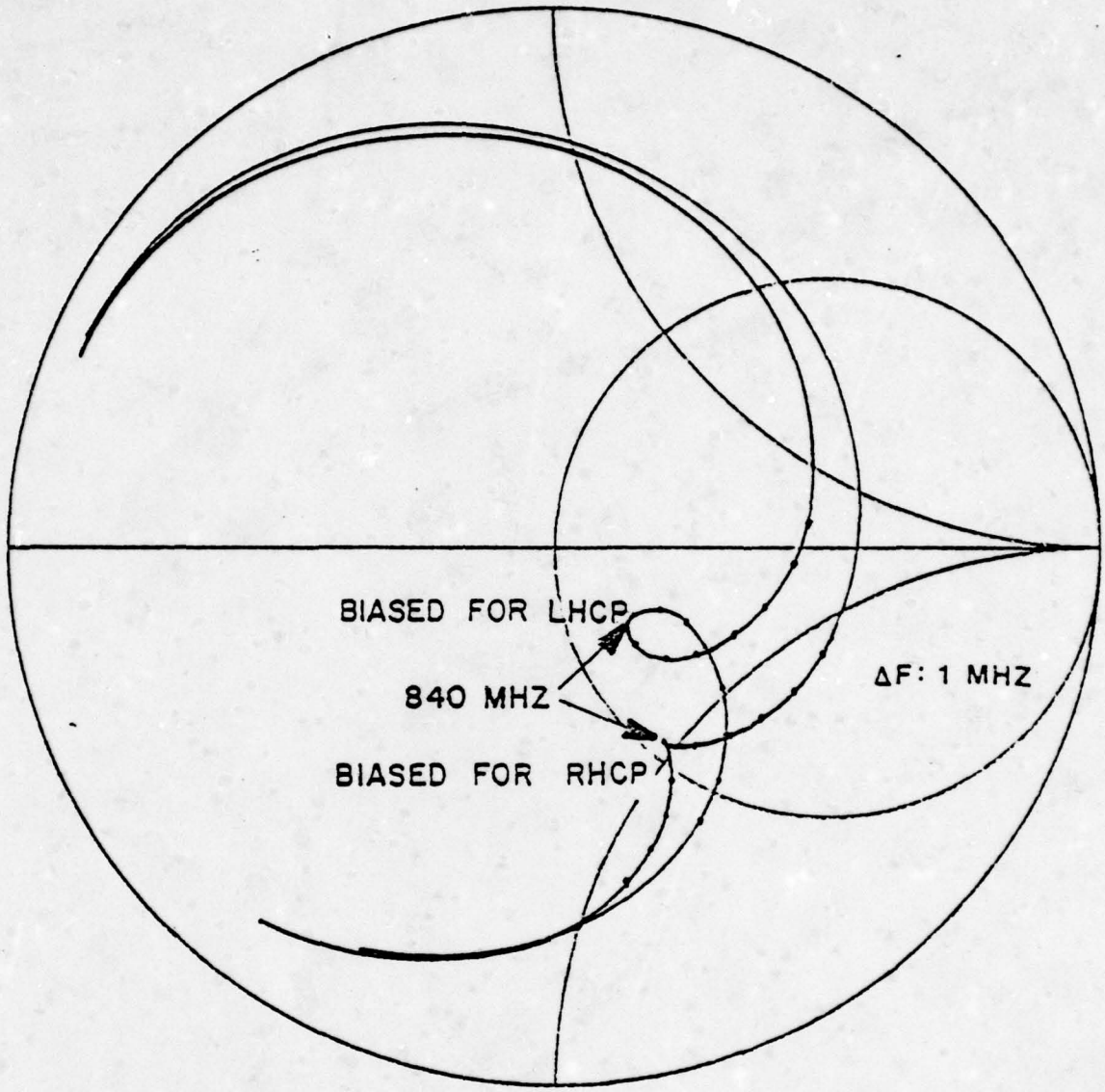

Fig. 5. Impedance of double tuned antenna.

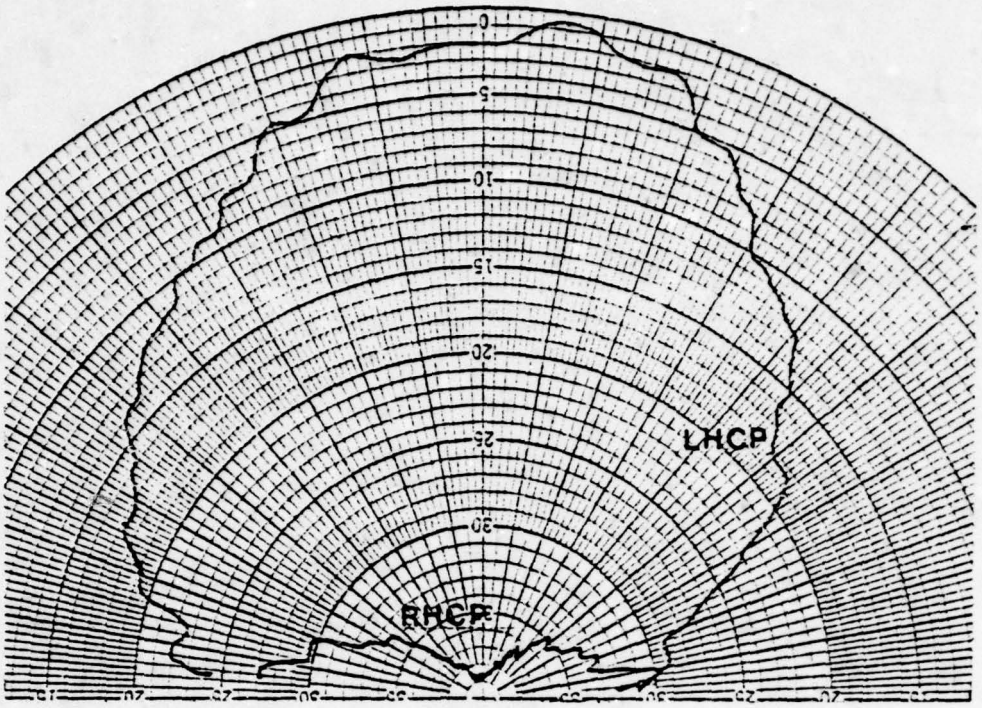

Fig. 6a. Left and right hand CP patterns of double tuned antenna biased for LHCP.

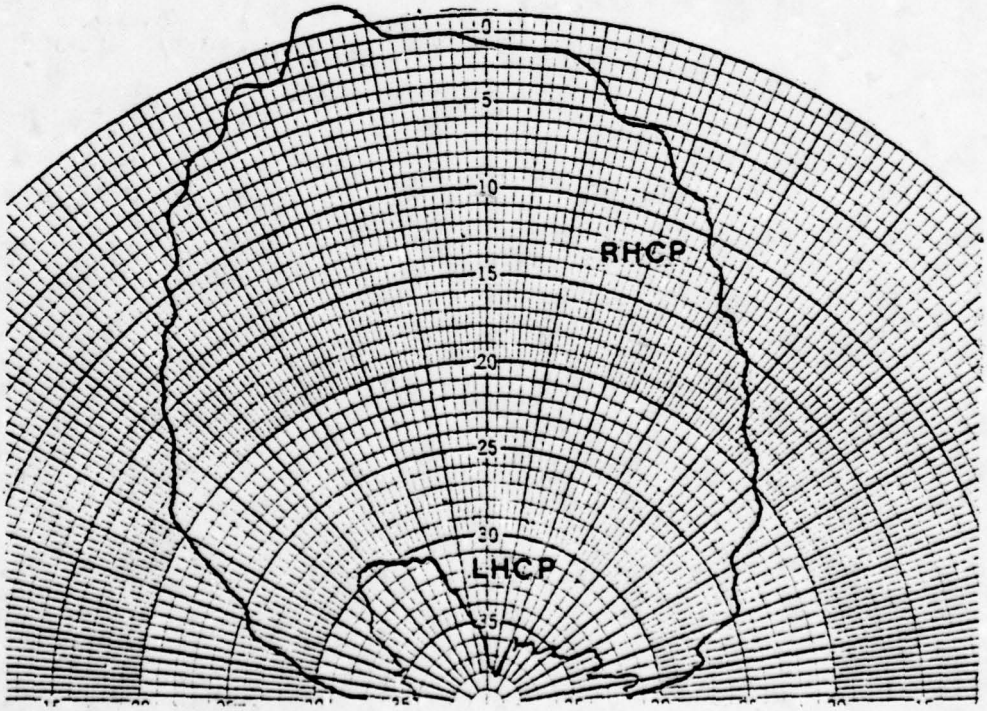

Fig. 6b. Left and right hand CP patterns of double tuned antenna biased for RHCP.

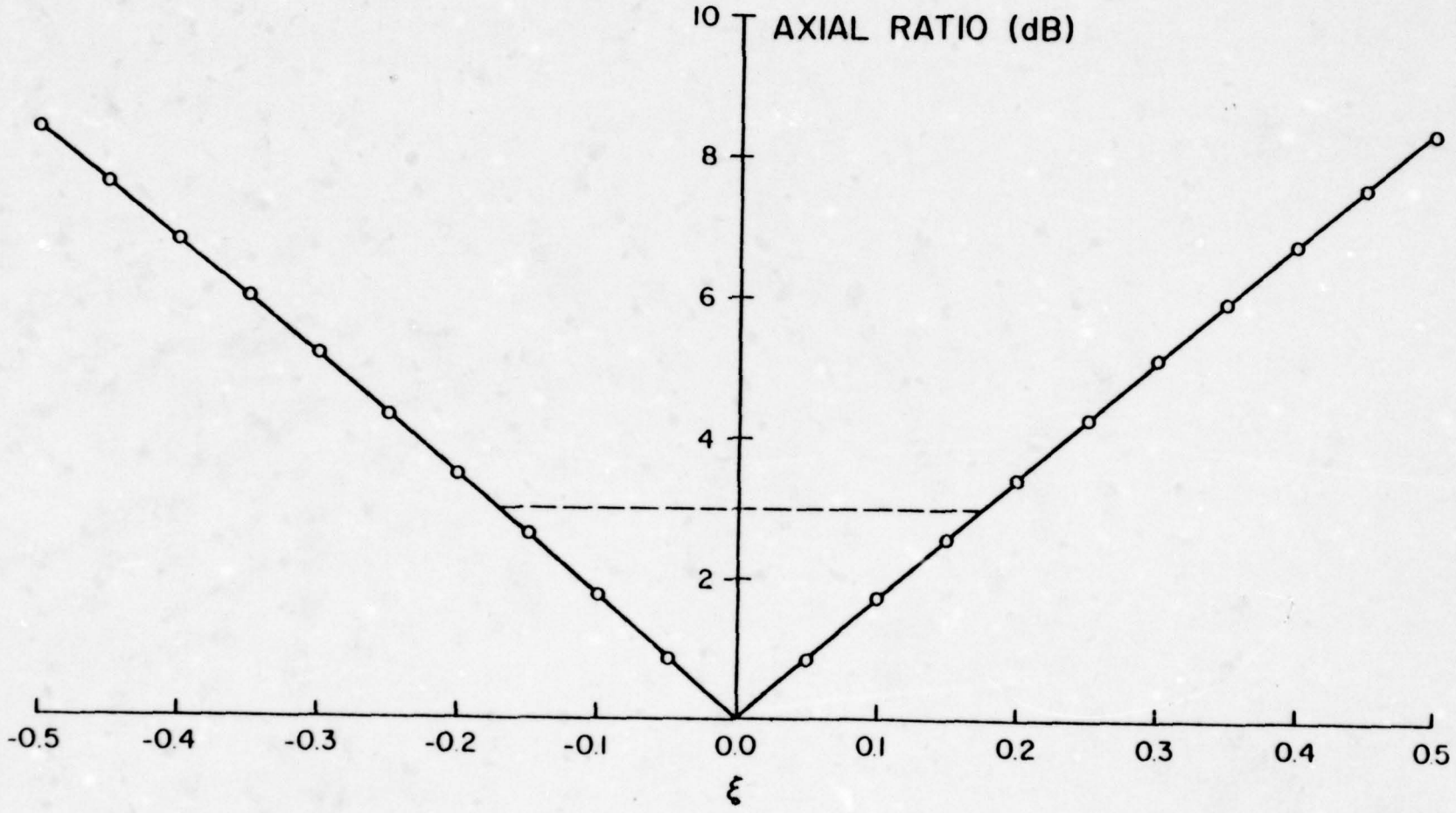

Fig. 7. Degradation of axial ratio with normalized frequency.

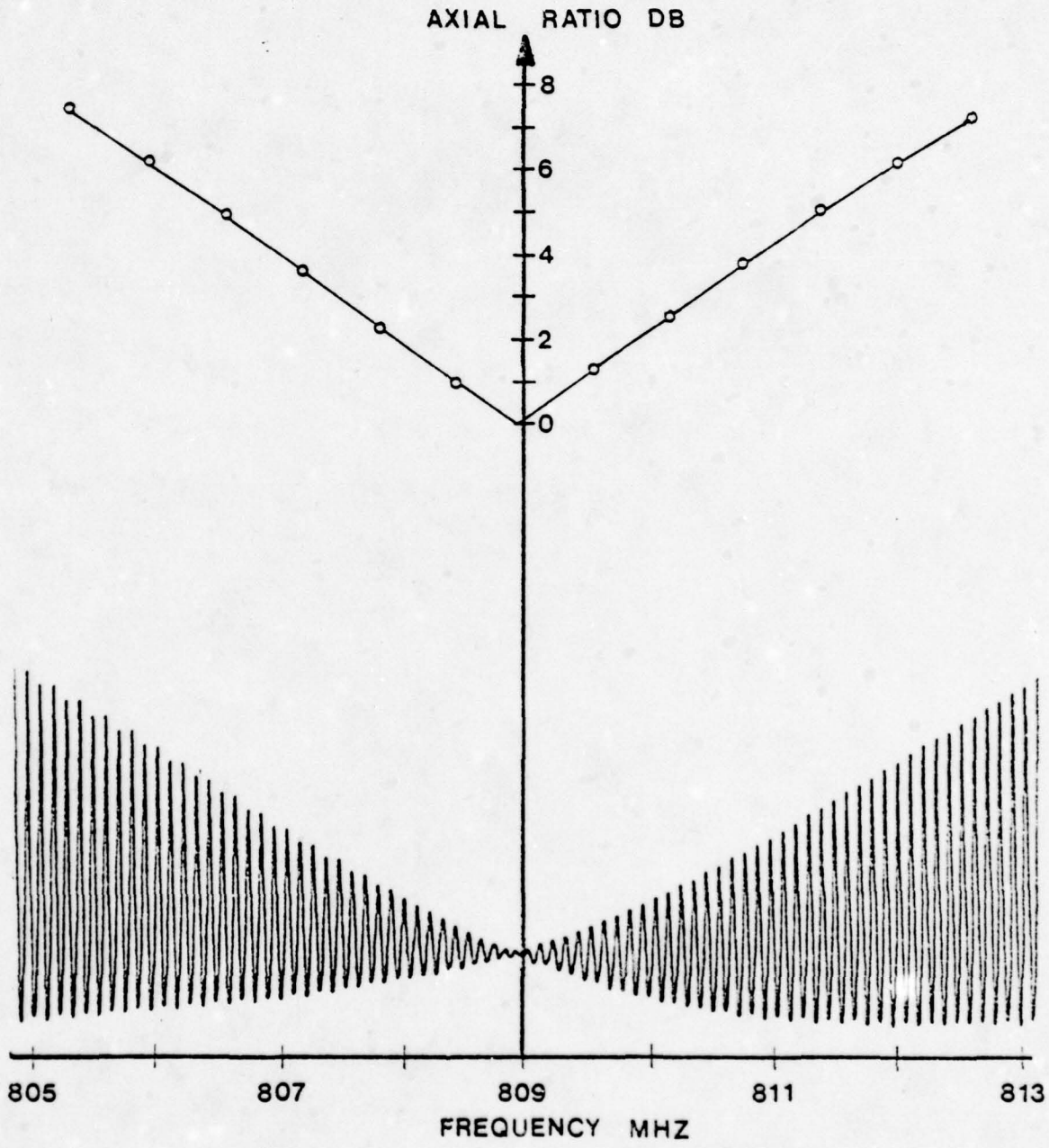

Fig. 8. Measured response of rotating dipole and plot of axial ratio for nearly square antenna.

ANALYSIS AND DESIGN OF CIRCULAR MICROSTRIP RESONATOR ANTENNAS

A. VAN DE CAPELLE, B. VAN DEN MOOTER, H. VERBIEST, J. VANDENSANDE

K.U.L., DEPT. OF ELECTRICAL ENGINEERING
DIV. MICROWAVES & LASERS
KARD. MERCIERLAAN 94
B-3030 HEVERLEE, BELGIUM

1.0. INTRODUCTION

The analysis model [1] developed for the rectangular microstrip resonator antenna has also been applied to the circular one [2] . Radiation pattern, input impedance, quality factor and directivity of fundamental as well as higher order modes are easy to calculate with this model. Very much attention has been paid to match the high input impedance of the circular microstrip resonator antenna to a microstrip line of 50 Ω.

2.0. ANALYSIS

2.1. APERTURE MODEL

The radiation field of a microstrip resonator antenna can be explained as produced by the tangential electric field in the plane of the resonator patch. Only the outside region in the neighbourhood of the edge of the patch contains an important field component.

Problem solving consists of the following steps :

a.- calculation of the electromagnetic fields inside a closed resonator
b.- determination of the tangential electric field in the plane z = o in function of the resonator fields
c.- calculation of the radiated field and the antenna characteristics.

2.2. CLOSED CIRCULAR RESONATOR

In the closed resonator model the circular microstrip resonator antenna (Fig. 1) is examined as a closed cavity with electric conducting upper and bottom surface and magnetic conducting side walls.

This research program has been supported by the Belgian National Science Foundation.

over the dielectric substrate at the edge of the resonator.

$$V_{\rho_1}^{\rho_2} = \int_{\rho_1}^{\rho_2} \bar{E} \cdot d\bar{l} = E_1 \cdot \rho_1 \ln \frac{\rho_2}{\rho_1} \tag{8}$$

$$V_0^h = \int_0^h E_z \cdot dz = E_z \cdot h \tag{9}$$

Using expression (1) for E_z, one finds :

$$E_t = E \cdot J_n(k_o \rho_1) \frac{h}{\ln \frac{\rho_1}{\rho_2}} \cdot \frac{1}{\rho} (A \cdot e^{jn\phi} + B \cdot e^{-jn\phi}) \tag{10}$$

2.4. ANTENNA CHARACTERISTICS

Knowing the aperture field $\bar{E}_t$ in a circular ring slot around the edge of the resonator patch, the calculation of the radiation field, radiation resistance, directivity and quality factor is tedious but straightforward.

3.0. EXCITATION

3.1. IMPEDANCE TRANSFORMER

Impedance matching between a 50 Ω microstrip feedline and the input resistance of the circular resonator antenna can be performed by means of a quarter wavelength impedance transformer (Fig. 3).

3.2. SPLITTED FEEDLINE

If the radiation resistance R is higher than the feedline impedance Z_o, the feedline can be splitted (Fig. 4). The angle ϕ_i between the axis of the feedline and the point of excitation at the edge of the patch is given by :

$$\cos \phi_i = \sqrt{\frac{Z_o}{R}} \tag{11}$$

3.3. DIRECT EXCITATION AT ONE INSIDE POINT

This method consists of exciting the resonator by a microstrip line in a

The fields inside the resonator are obtained from the Helmholtz-equation together with the appropriate boundary conditions. The fact that the thickness of the substrate is much smaller then the wavelength enables to simplify the results; only TM-modes are of interest.

Taking this simplification into account, the cavity fields are given by :

$$E_z = E \cdot J_n(k_o r) \cdot (C \sin n\phi + D \cos n\phi) \tag{1}$$

$$E_r = 0 \tag{2}$$

$$E_\phi = 0 \tag{3}$$

$$H_z = 0 \tag{4}$$

$$H_r = \frac{j\omega\varepsilon}{k_o^2} \cdot \frac{E}{r} \cdot J_n(k_o r) \cdot (C\, n \cos n\phi - D\, n \sin n\phi) \tag{5}$$

$$H_\phi = -\frac{j\omega\varepsilon}{k_o} : E \cdot J_n'(k_o r) \cdot (C \sin n\phi + D \cos n\phi) \tag{6}$$

with J_n, J_n' : the Bessel function and its first derivative of the first kind and order n.

2.3. APERTURE FIELD $\bar{E}_a$

The tangential electric field is zero on the surface of the circular patch. At great distances from the patch the tangential electric field can be neglected. The region where this field is of importance is very narrow due to the small thickness of the substrate. Therefore it is not necessary to know exactly how the electric field varies in the radial direction. We have assumed the tangential electric field to vary inversely proportional to the radius (Fig. 2) :

$$E_t = \frac{C}{\rho} = \frac{E_1 \cdot \rho_1}{\rho} \tag{7}$$

The potential difference over the aperture equals the potential difference

point inside the circle of the patch (Fig. 5). This method is similar to excitation, by means of a coaxial cable, in a point of the patch where the radiation resistance is equal to the characteristic impedance of the coaxial cable.

In case the radiation resistance at a point on the edge $r = a, \phi = o$ was R, one finds the inside point $r = r_o, \phi = o$ from the next equation

$$J_n^2 (k_o r_o) = J_n^2 (k_o a) \frac{R_e(Z_o)}{R} \qquad (12)$$

4.0. ANTENNA DESIGN

To design the dimensions of the antenna configuration or to calculate the resonant frequencies an algorithm has been written based on the microstrip resonator theory of Wolf and Knoppik [4] .

Also the wall impedance method [3] can be used.

5.0. EXPERIMENTAL RESULTS

Matching the antenna to the feedline with a quarter wavelengthtransformer and with a splitted line are compared.

Table I shows the substrate characteristics and the antenna dimensions.

TABLE I

Antenna	ε_r	h[mm]	a[mm]	f_{rc} [GHz]	f_{rm} [GHz]	excitation method
1	2.24	0.51	18.6	3.	3.15	splitted line
2	2.6	1.05	15.4	3.368	3.47	$\lambda/4$ transfo

with : ε_r : relative permittivity of the dielectric substrate

h : substrate thickness

a : patch radius

f_{rc} : calculated resonant frequency for the TM_{110} modus

f_{rm} : measured resonant frequency for the TM_{110} modus

Fig. 6 and Fig. 7 show the input reflection coëfficient for both antennas. Feeding with a splitted line assures a better matching than feeding with a quarter-wavelength transformer due to the fact that, because of the small line width, the quarter wavelength line was etched with less accuracy.

6.0. REFERENCES

1. Hammer, P., Van Bouchaute, D., Verschraeven, D., Van de Capelle, A., A Model for Calculating the Radiation Field of Microstrip Antennas, I.E.E.E. Trans. on A.&P., March £979, pp. 267-270.

2. Van den Mooter, B., Verbiest, H., Studie van de Circulaire Microstrip Resonator Antenna, Master Thesis, (in Dutch), Cath. Univ. of Louvain, June 1977.

3. Van Lil, E., Van Loock, R., Van de Capelle, A., Design Models for Rectangular Microstrip Resonator Antennas, Proc. of the I.E.E.E. Int. Symp. on Ant. & Prop., Washington, D.C., 1978, pp. 264-267.

4. Wolff, I., Knoppik, N., Rectangular and Circular Microstrip Disc Capacitors and Resonators, I.E.E.E. Trans. on M.T.T., Vol. M.T.T.-22, October 1974, pp. 857-864.

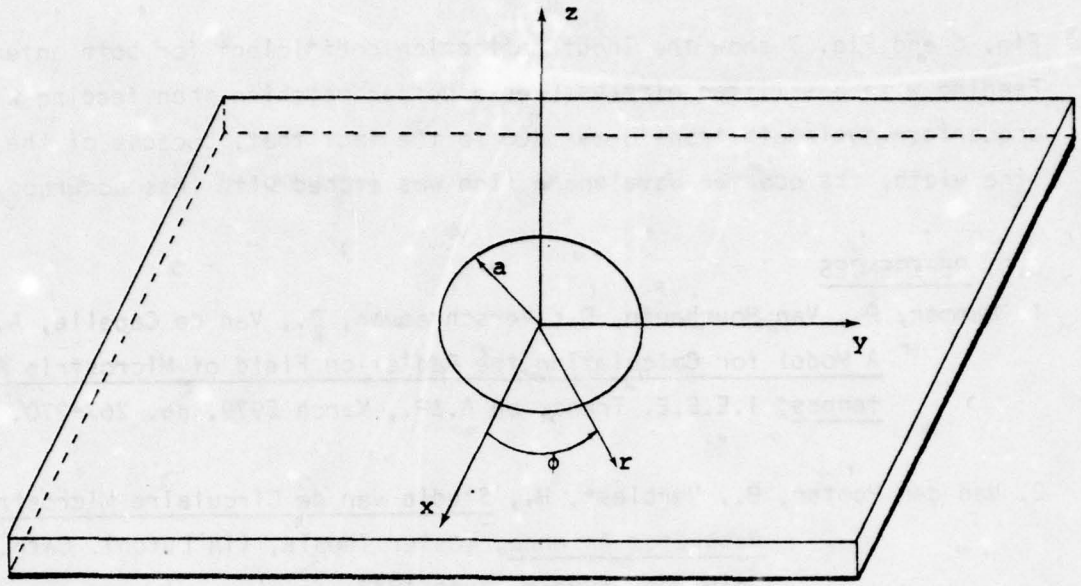

Fig. 1 : Circular microstrip resonator antenna.

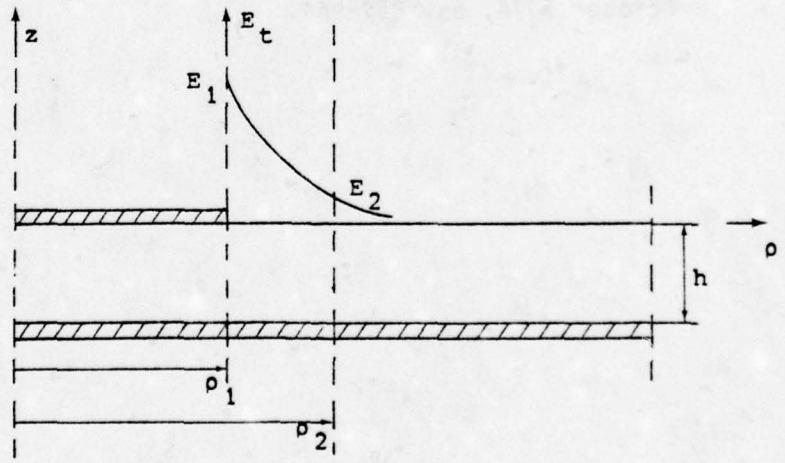

Fig. 2 : Tangential field component E_t near the edge of the patch.

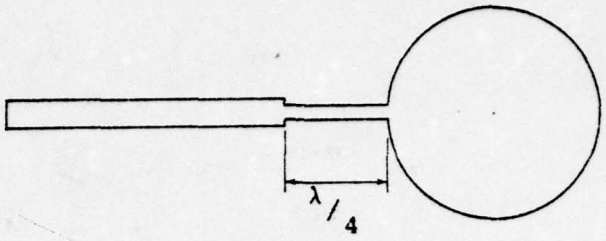

Fig. 3 : λ/4 impedance transformer.

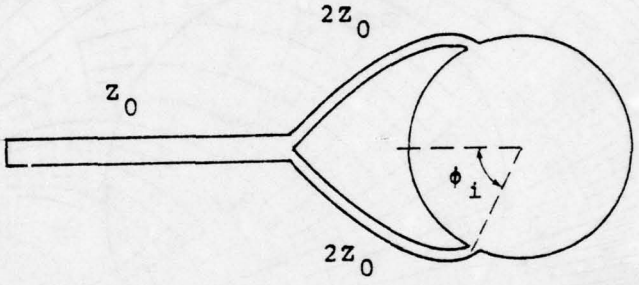

Fig. 4 : Splitted misrostrip feedline.

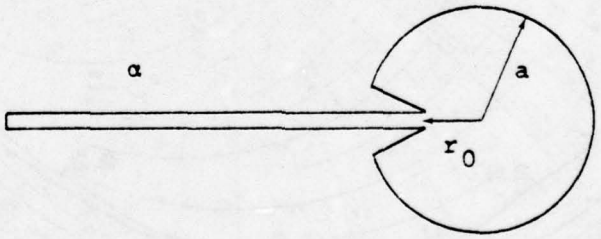

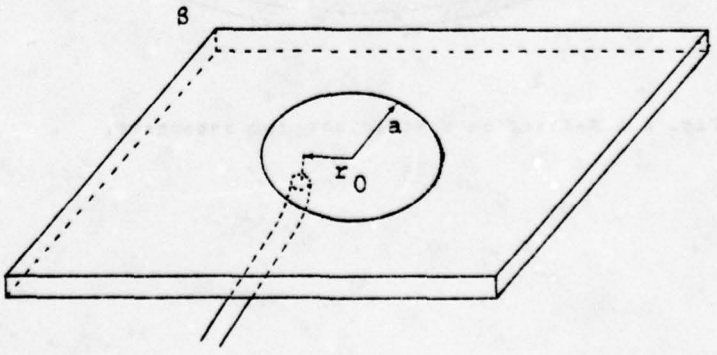

Fig. 5 : α. Feeding an inside point with a microstrip line.
β. Feeding an inside point with a coaxial cable.

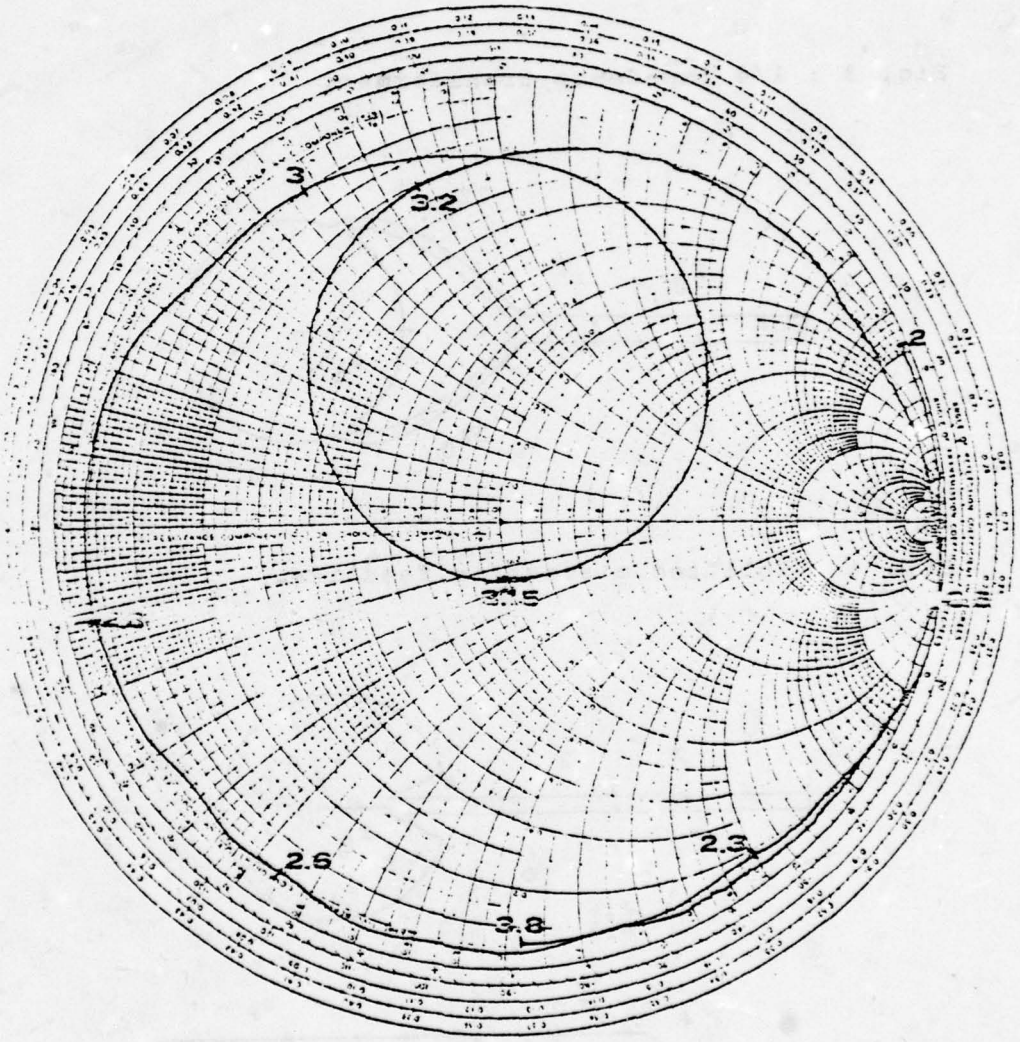

Fig. 6 : Reflection coefficient for antenna 1.

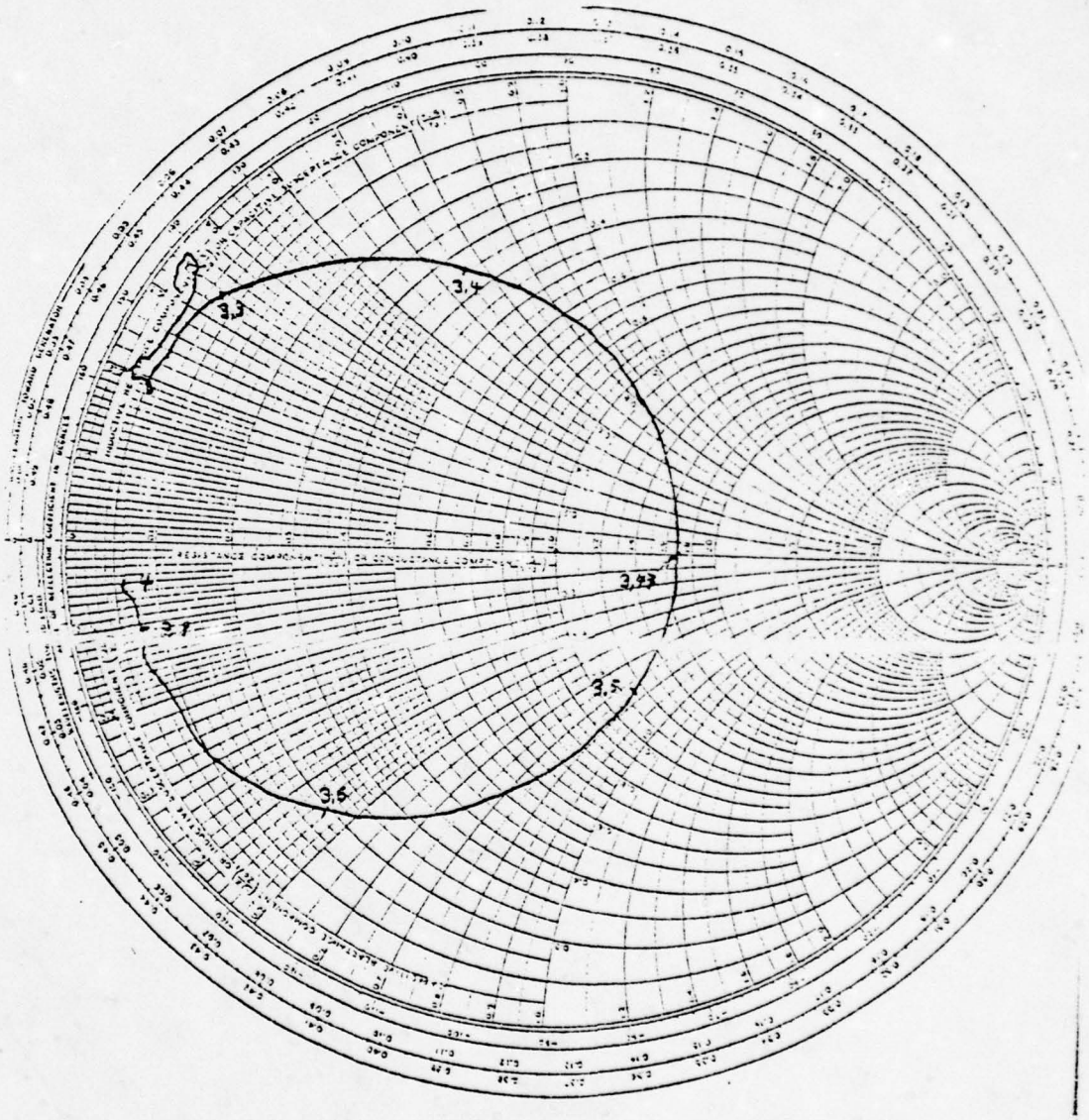

Fig. 7 : Reflection coefficient for antenna 2.

A UNIFIED APPROACH TO THE SOLUTION OF MICROSTRIP ANTENNA PROBLEMS

EDGAR L. COFFEY, III
THE BDM CORPORATION
2600 YALE BLVD S.E.
ALBUQUERQUE, NM 87106

INTRODUCTION

Microstrip radiators rank high on the list of possible design choices when low cost, lightweight, and low profile antennas are required. Much development work and performance data on microstrip antennas has been reported [1, 2, 3, 4], but it is only recently that work has begun in earnest to explain the theoretical behavior of these antennas. Rectangular and circular patches have been modeled by Lo and others [5,6]. In addition, numerical solutions for Weinschel's pentagonal element [7] as well as models for wall impedance and coaxial probe attachment have been obtained by Carver and Coffey [6]. However, to date, no method has been reported that can be used to model all aspects of the microstrip problem simultaneously, which is theoretically rigorous and numerically tractable.

It is the purpose of this paper to describe an approach that can be used to incorporate the work accomplished to date in the modeling of feed point, wall impedance, arbitrarily-shaped microstrip cavity, and copper and dielectric losses. Furthermore, it is possible with this

method actually to connect the microstrip antenna to other electromagnetic and electronic system elements (transmission lines, varactors, RF amplifiers, etc.) or to analyze the coupling among two or more elements or multiply-fed elements.

This new method is called the "Direct Form of Network Analogs," or DFNA, and is grounded solidly upon fundamental physics (Maxwell's Equations). All parameters and variables are directly traceable to E- and $\vec{H}$-fields, ε, μ, and σ. Because DFNA is a network modeling approach (not network synthesis), feed corrections and wall boundary impedances are trivially connected to the circuit model of the microstrip patch itself.

DFNA: DIRECT FORM OF NETWORK ANALOGS

DFNA is one of two circuit analog techniques developed by BDM in early 1979 to model source-region EMP coupling and MX missile external coupling. (The other method, IFNA, is derived from integral equation formulations of Maxwell's equations and will not be discussed in this paper.)

Electromagnetic modeling by circuit analogs was first investigated in the mid 1940's by Kron [8], who published a series of papers on circuit models for a variety of physical phenomena. Kron, of course, had no digital computer, and his work could not be put to any practical use. One of Kron's three-dimensional electromagnetic models is shown in Figure 1. Later Branin [9] attacked the same problem from a graph theoretic viewpoint and pointed the way toward understanding how network

analogs could be derived for many physical processes. However, he offered no circuits of his own. In 1958, Karplus [10] discussed finite difference analogs on squares and triangles, but like the later finite element techniques of the 1960's and 1970's, these derivations were based on numerical considerations, not the underlying physics.

The most familiar network analog model is the one-dimensional L-C transmission line model, which is usually derived from the finite difference approximations of the transmission line equations.

However, this is a very special case of a much more general technique. It should be noted that DFNA is not network synthesis. While network synthesis is a viable modeling tool for many electromagnetic problems [11,12], it has the disadvantage that the circuit component values are not directly related to any physical process.

THE TECHNIQUE

Following the method of Branin, the electromagnetics problem is divided into topology operators (Maxwell's equations) and algebraic relations (constituitive relations). This is represented pictorally in Figure 2. The circuit elements are derived from the algebra, and the interconnection of elements is determined by topology. This division allows the physics to be described within a small region, which is called a "unit cell." Then all unit cells are connected together by the topological operators.

For example, consider a triangular unit cell as shown in Figure 3. A two-dimensional TM_z transmission line (E_z, H_x, H_y) has been superimposed

on the drawing. Notice that there are intra-cell elements and inter-cell elements. The intra-cell connections can be deduced from

$$\oint \bar{H} \cdot d\bar{\ell} = \iint \dot{\bar{D}} \cdot d\bar{S} \qquad (1)$$

If ℓ describes the perimeter of the triangle, then S must indicate the triangular area bounded by the perimeter. Equation (1) states that the line integral of $\bar{H}$ around the perimeter (represented by the currents in the three inductors) equals the time derivative of the electric flux (displacement current) through the triangular area. In terms of the circuit analog, the capacitor current is equal to the sum of the three inductor currents. Hence, from Kirchoff's current law, we deduce that the intra-cell connection is at a node. We also see that the current in each inductor is $H_\ell d\ell$ and that the capacitor current is $\varepsilon \dot{E}_z dA_z$.

The inter-cell connection is derived from

$$\oint \bar{E} \cdot d\bar{\ell} = -\iint \dot{\bar{B}} \cdot d\bar{S} \qquad (2)$$

The magnetic flux in equation (2) must be that flux which passes through the area which is bounded by the two capacitors and interconnecting inductor. Equation (2) is a network loop equation since $d\bar{\ell}$ must traverse the boundary of $d\bar{S}$. Hence the difference in capacitor voltages ($E_z dz$) equals the inductor voltage ($\mu \dot{H}_\ell dA_\ell$).

In summary, we now know the following quantities:

Inductor current: $H_\ell d\ell = I_\ell$

Capacitor current: $\varepsilon \dot{E}_z dA_z = I_c$

Capacitor voltage: $E_z dz = V_c$

Inductor voltage: $\mu \dot{H}_\ell dA_\ell = V_\ell$

The circuit component values may now be calculated:

$$C = \frac{I_c}{\frac{dV_c}{dt}} = \frac{\varepsilon \dot{E}_z dA_z}{\dot{E}_z dz} = \frac{\varepsilon dA_z}{dz} \tag{3}$$

$$L = \frac{V_\ell}{\frac{dI_\ell}{dt}} = \frac{\mu \dot{H}_\ell dA_\ell}{\dot{H}_\ell d\ell} = \frac{\mu dA_\ell}{d\ell} \tag{4}$$

Similar relationships can be derived for $TE_z(E_x, E_y, H_z)$ modes. Higher order TM and TE modes may be simulated by "stacking" the circuits already derived.

Notice that this two-dimensional analog requires a three-dimensional circuit just as a one-dimensional transmission line requires a two-dimensional circuit. It can be shown that a three-dimensional analog requires a "four-dimensional" circuit. This can be visualized by interlaced three-dimensional cubes of capacitors (E-field) and inductors ($\bar{H}$-field) with dependent sources coupling the two problems together.

No assumptions concerning linearity or time-independence have been made. In fact, one of the most powerful applications of the method is to time-varying, non-linear problems.

APPLICATION TO MICROSTRIP ANTENNA MODELING

The microstrip antenna problem may be divided into three parts:

(1) Modeling of the feed

(2) Modeling of the cavity wall impedance

(3) Modeling of the cavity itself

A microstrip antenna may have either a coaxial probe feed or a microstrip transmission line feed. The microstrip transmission line may be modeled as a Thevenin equivalent impedance and voltage source. The coaxial probe requires the addition of a series inductance [6] where

$$\chi_L = \frac{Z_o}{\varepsilon_r} \tan \frac{2\pi t}{\lambda_o} \quad (\Omega) \tag{5}$$

t is the dielectric thickness and ε_r is the relative permittivity of the dielectric. In either instance the feed circuit model is connected directly to the cavity circuit model at the point in the analog that represents the physical connection point.

Each cavity wall impedance can be modeled as a parallel RC circuit [6]. This model is valid as long as the field along a wall is constant. For higher order modes or for non-separable geometries, the field may not be constant and a more complicated model is needed. One model which allows mutual coupling between wall nodes can be derived from slot antenna mutual impedance considerations [13] or the application of method of moments to a magnetic line source. In either case the appropriate circuit elements are connected directly to the patch model.

The cavity itself is modeled exactly as described in the preceding section using unit cells of appropriate geometry (triangles, rectangles, etc.). The complete antenna circuit is then solved using a large-scale network analysis code (such as NET-2 or SCEPTRE). The computer code

prints out input impedance and cavity wall electric field. The input impedance can be used directly. The cavity wall electric field is transformed into an equivalent magnetic current backed by a perfect conductor. The far field pattern can then be found using the standard diffraction integral [6].

COMPARISON OF RESULTS WITH MEASURED DATA AND THEORETICAL CALCULATIONS

Three patch geometries have been modeled using the DFNA method: (1) rectangular, (2) circular, and (3) Weinschel pentagon. Both theoretical and experimental data are available for (1) and (2) while measured data is available for (3).

An edge-fed rectangular patch is shown in Figure 4. The DFNA method agrees almost exactly with the theoretical work of Carver and Coffey [6]. This is to be expected, since for the dominant mode, the DFNA two-dimensional model reduces to a one-dimensional transmission line. The wall impedance is the same and thus the only discrepancy in the results would be due to numerical error in the DFNA method.

The effect of the coaxial probe inductance is seen in Figure 5, where the feed point has been moved in toward the center of the patch. Again, DFNA agrees well with previous theoretical results because of the same reasons as stated above.

The impedance of a circular patch is shown in Figure 6. In this case the small discrepancy between DFNA and theoretical results is more apparent. This is because in the DFNA model, no a priori assumptions are made regarding the dominant mode structure.

The previous three examples illustrate the integrity of the DFNA method compared to theoretical and experimental data. The fourth example is the Weinschel pentagon, and no theoretical data exists. However, it can be seen that the DFNA and experimental curves do agree closely, though perhaps not as much as one might desire. Preliminary far-field pattern results do agree much closer, and the single-feed circular polarization of the pentagon is predicted with an axial ratio of 2.5dB.

SUMMARY AND SUGGESTIONS FOR FURTHER WORK

The DFNA method has been shown to be a viable technique for the analysis of arbitrarily-shaped microstrip antennas. Because DFNA models the antenna as a circuit, it is quite easy to include boundary conditions, probe corrections, etc., into the techniques.

Two major extensions to the technique hold promise. First, if DFNA can be extended to three dimensions, then mutual coupling between stacked antennas or widely spaced patches may be simulated. There are two problems that need to be overcome--one computational, the other software development. Computational problems arise in any large three-dimensional model just because of the sheer magnitude of computer resources required. This can be alleviated to a large degree by judicious use of Unimoment [15] or Monte Carlo techniques [16] so that large volumes of space may be modeled as an "equivalent impedance matrix." The software development problem can be solved by the extension of present circuit analysis codes to true three-dimensional systems codes in which, not only points and branches have significance, but also areas and volumes.

Second, it is possible to combine DFNA with integral equation techniques (IFNA or method of moments) in order to study mutual coupling and interaction with nearby metallic bodies.

REFERENCES

1. C. W. Garvin et al., "Low Profile Electrically Small Missile Base Mounted Microstrip Antennas," IEEE International Symposium on Antennas and Propagation Digest, pp. 244-247, June 1975.

2. J. Q. Howell, "Microstrip Antennas," IEEE International Symposium on Antennas and Propagation, p. 177, December 1972.

3. R. E. Munson, "Conformal Microstrip Antennas and Microstrip Phased Arrays," IEEE Trans. on Antennas and Propagation, Vol. AP-22, pp. 74-78, January 1974.

4. G. G. Sanford, "Conformal Microstrip Phased Array For Aircraft Tests with ATS-6," National Electronics Conf., Vol. 29, pp. 252-257, October 1974.

5. Y. T. Lo, D. Soloman, F. R. Ore, D. D. Harrison, and G. A. Deschamps, "Study of Microstrip Antennas, Microstrip Phased Arrays, and Microstrip Feed Networks," Dept. of Electrical Engineering, Univ. of Illinois, Urbana; Rome Air Development Center report RADC-TR-77-406, 21 October 1977.

6. K. R. Carver and E. L. Coffey, "Theoretical Investigation of the Microstrip Antenna" (Semi-Annual Progress Report), Physical Science Laboratory, New Mexico State University, Las Cruces; PSL Technical Report PT-00929, January 23, 1979.

7. H. D. Weinschel, "A Cylindrical Array of Circularly Polarized Microstrip Antennas," 1975 AP-S International Symposium, p. 177 of digest.

8. G. Kron, "Equivalent Circuit of the Field Equations of Maxwell," Proc. IRE, pp. 289-299, May 1944.

9. F. H. Branin, Jr., "The Algebraic-Topological Basis For Network Analogies and the Vector Calculus," Proc. Symposium on Generalized Networks, Polytechnic Institute of Brooklyn, pp. 453-491, April 1966.

10. W. J. Karplus, Analog Simulation, McGraw-Hill Book Co. (New York: 1958).

11. M. A. Messier, Coupling to Antennas (DNA Handbook Revision, Ch. 10) prepared for Harry Diamond Laboratories, Contract DAAG39-73-C-0010, Appendix 10.B.

12. D. H. Schaubert, "Application of Prony's Method to Time-Domain Reflectometer Data and Equivalent Circuit Synthesis," IEEE Trans. on Antennas and Propagation, Vol. AP-27, pp. 180-184, March 1979.

13. A. G. Derneryd, "Mutual Coupling in Array Antennas," School of Electrical Engineering, Chalmers University of Technology, Göteborg, Sweden, Technical Report 60, 1976.

14. G. A. Dunn, "Design and Construction of a 3-element Microstrip Antenna Array," Dept. of Electrical and Computer Engineering, New Mexico State University, December 1978.

15. K. K. Mei, "Unimoment Method of Solving Antenna and Scattering Problems," IEEE Trans. on Antennas and Propagation, Vol. AP-22, pp. 750-766, November 1974.

16. E. L. Coffey, "An Analog/Hybrid Computer Solution of Electromagnetic Scattering Problems," (Ph.D. dissertation, Virginia Polytechnic Institute and State University, Blacksburg), June 1976.

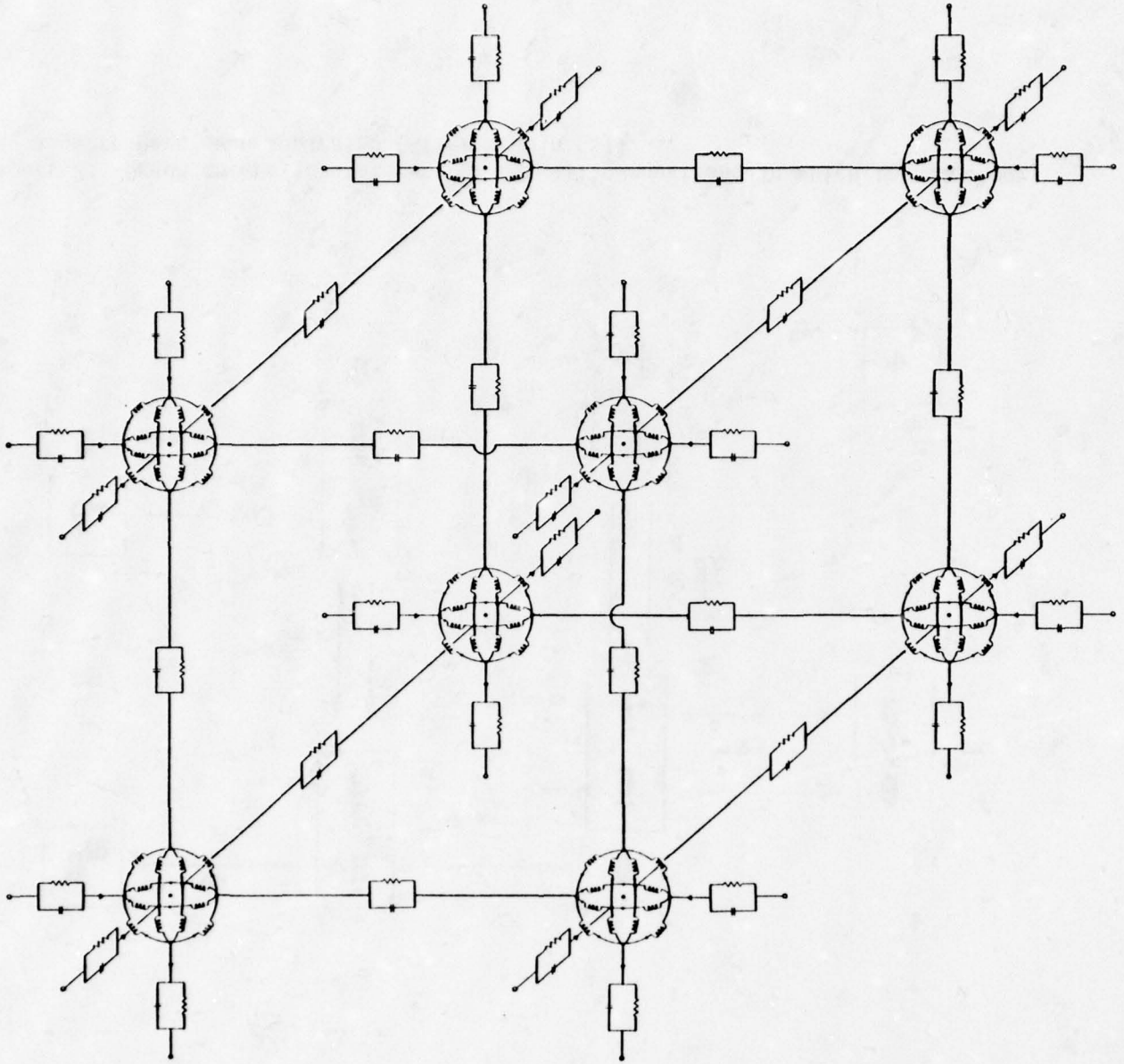

Figure 1. Interconnection of eight three-dimensional unit cells (After Kron [8]).

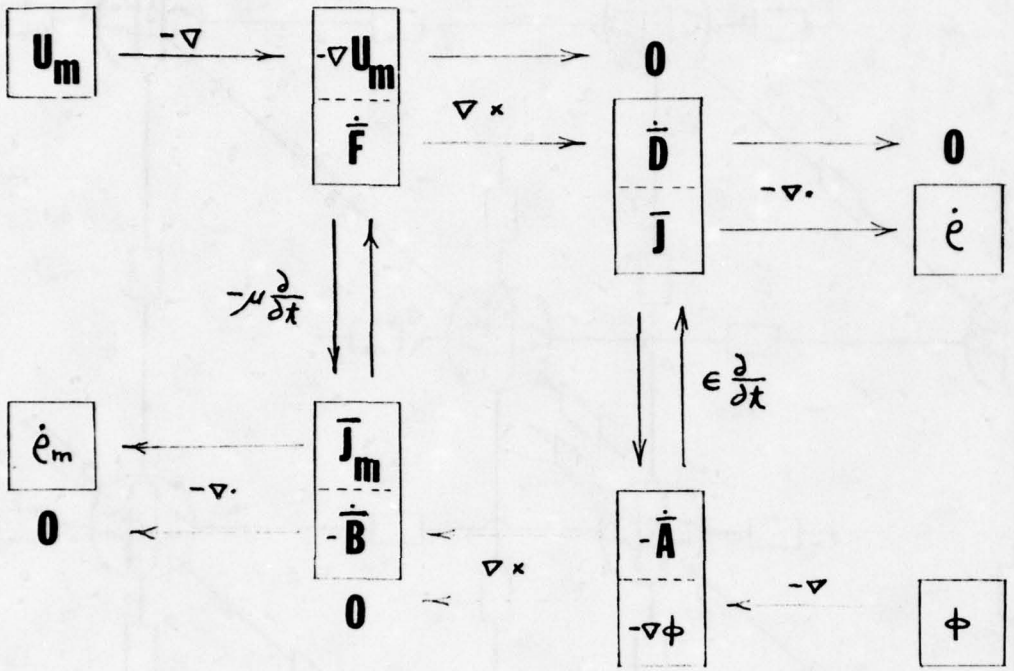

Figure 2. Graph theoretic statement of Maxwell's equations in which the topology and algebra have been separated (After Branin [9]).

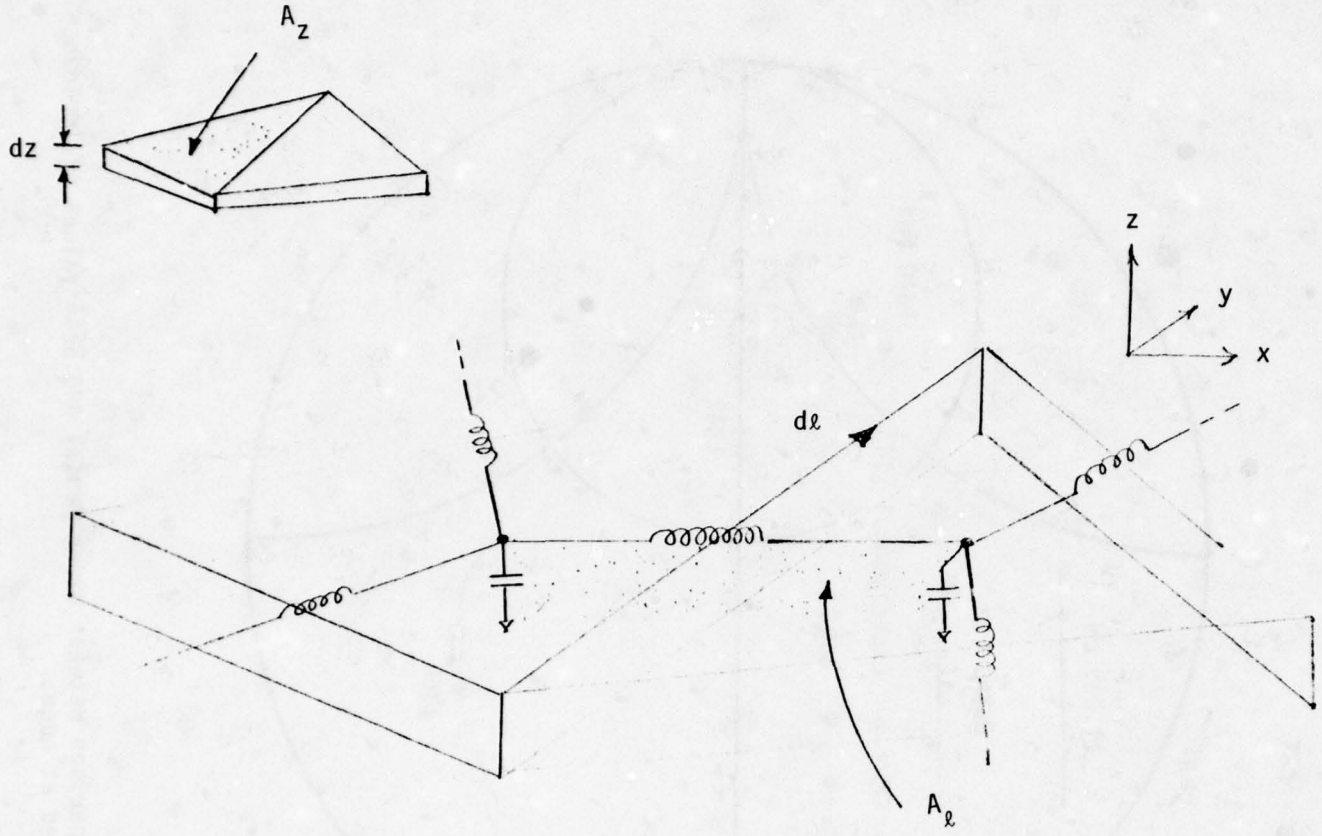

Figure 3. Two triangular unit cells. The dimensions dz, A_z, dℓ, and A_ℓ are discussed in the text.

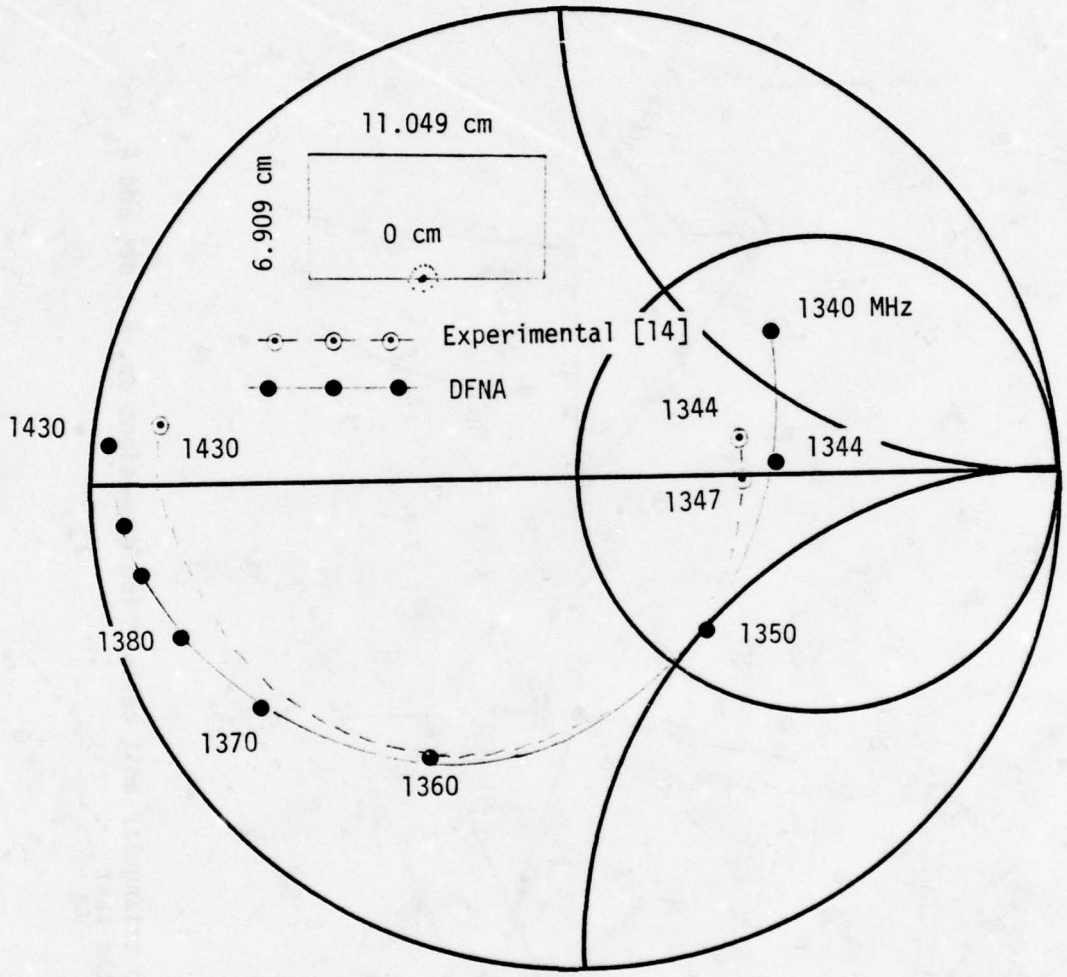

Figure 4. Comparison between experimental and DFNA values of impedance for L-band patch fed at edge.

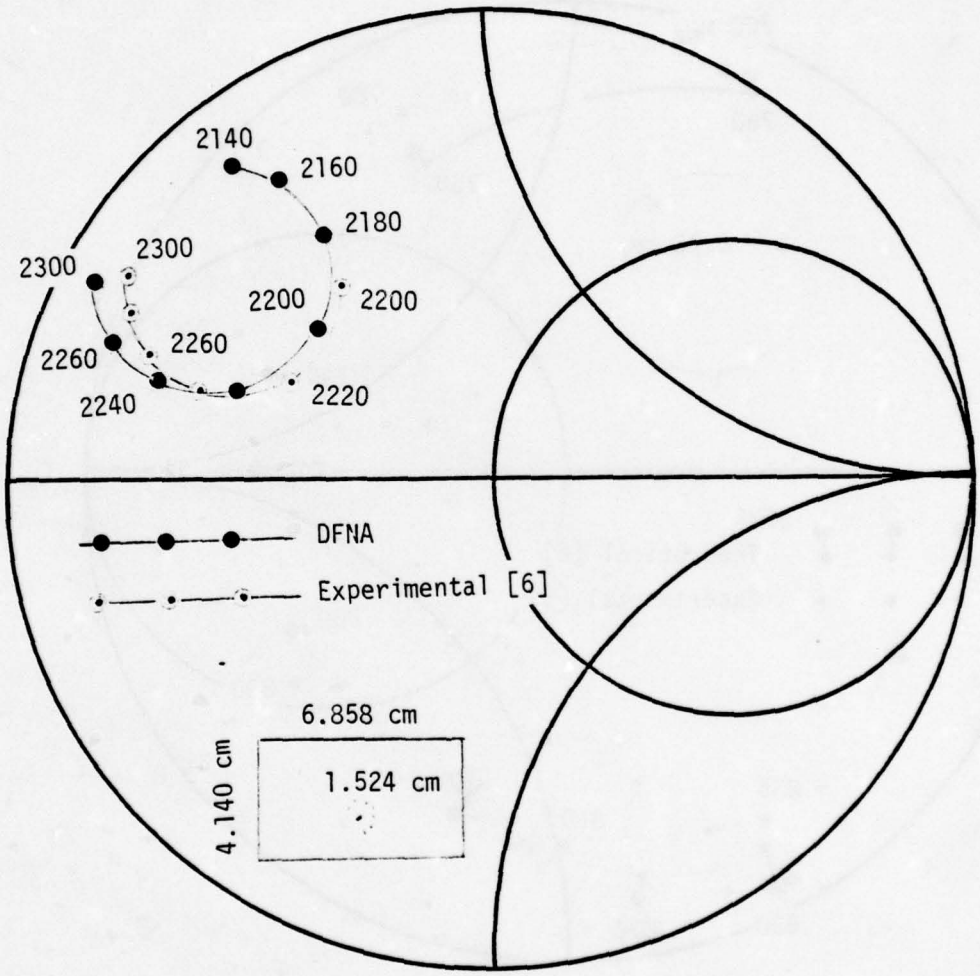

Figure 5. Comparison between DFNA and experimental values of impedance for S-band patch fed 1.524 cm from edge.

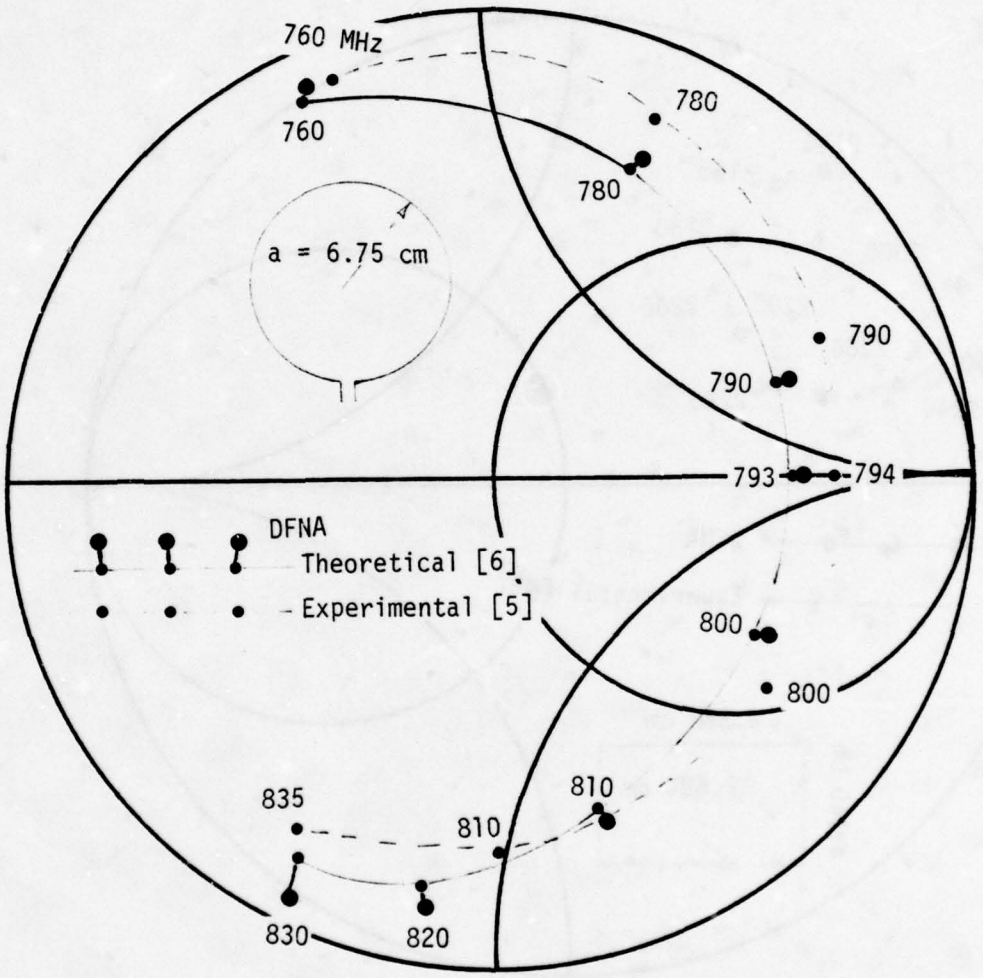

Figure 6. Comparison between DFNA, theoretical, and experimental input impedance values of a circular microstrip patch with a = 6.75 cm, t = 0.1588 cm, and ε_r = 2.65.

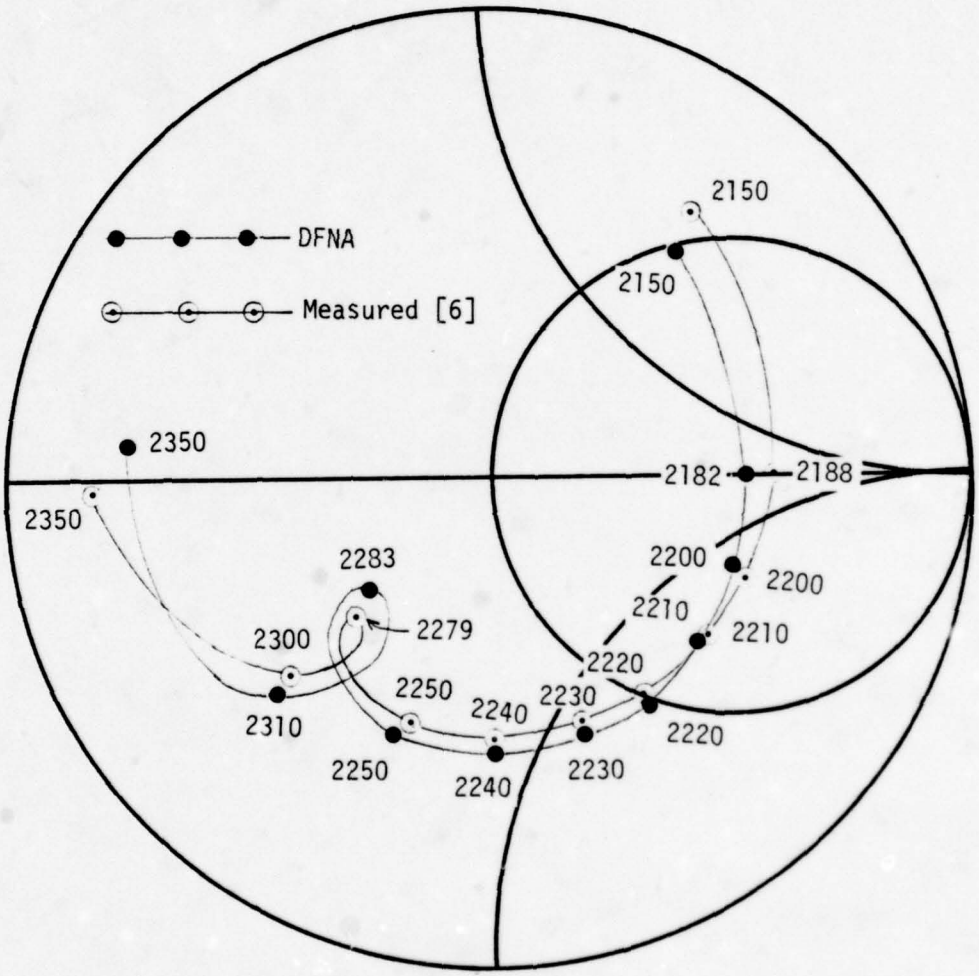

Figure 7. Comparison of measured and DFNA input impedance for an S-band pentagon patch [7]. Impedance includes effect of quarter-wave matching transformer.

A COMMON APERTURE S- AND X-BAND FEED FOR THE DEEP SPACE NETWORK

BY

W. F. Williams and J. R. Withington

JET PROPULSION LABORATORY

TELECOMMUNICATION SCIENCE AND ENGINEERING DIVISION

PASADENA, CALIFORNIA

Presented at

THE 1979 ANTENNA APPLICATIONS SYMPOSIUM

UNIVERSITY OF ILLINOIS

ALLERTON PARK

MONTICELLO, ILLINOIS

SEPTEMBER, 1979

A COMMON APERTURE S- AND X-BAND FEED FOR THE DEEP SPACE NETWORK

W. F. Williams and J. R. Withington

(ABSTRACT)

This article discusses a new prototype X/S-band horn feed for future use in the NASA/JPL Deep Space Network of large reflector antennas. The present system is a reflex-dichroic asymmetric (two horn) feed which optimizes S-band performance with a penalty of about 0.5 dB G/T at X-band. Since the use of X-band telemetry is to be emphasized in the future, a symmetric system (with one horn handling both frequency bands) is being developed.

Two major research areas were considered:

1. The Horn Itself: Development of a technique that would result in acceptable illumination functions at both frequencies.

2. The Combiner - or Diplexer: Development of a two band combiner that does not contribute significantly to small dissipative losses.

The first requirement was met by using a very deeply grooved corrugated horn operating in a so-called "beamwidth saturation" mode. A sufficiently large flare angle is used to bring the structure of the two radiated patterns into coincidence at the 10 dB points.

The diplexer design called for the horn to be fitted with a radial waveguide structure for the low frequency excitation. The X-band signal is then conventionally fed at the vertex of the horn. Certain moding and bandwidth problems occurred in the first models. However, after substantial work, the original concept was realized and all design criterion satisfied. The first generation system is now in operation at Deep Space Station (DSS) 13 at Goldstone. Results of a performance evaluation of the entire antenna system show total operating system noise levels in the 25 kelvin class at both frequency bands, as well as aperture efficiencies consistent with predictions.

The research described in this publication was carried out by the Jet Propulsion Laboratory/Caltech under NASA contract No. NAS7-100.

A COMMON APERTURE S- AND X-BAND HORN FOR THE DEEP SPACE NETWORK

INTRODUCTION

Nearly seven years ago the JPL 64 meter antenna at the Goldstone Deep Space Net (DSN) was modified for X-band usage and, shortly thereafter, the other two 64 meter antennas in Spain and Australia were similarly modified. A reflex cassegrain system (ref. 1) was used wherein, using separated single band feedhorns, the X-band was passed through a high pass low loss dichroic plate to the cassegrain hyperboloid and the S-band was reflected from this plate to the hyperboloid. In each case the apparent phase center was near the aperture of the X-band horn. This feed system was recently selected for further implementation in a 34 meter upgrade project.

The reflex feed permits full high performance for telemetry within S-band while at the same time allowing for operation in the new telemetry frequencies within X-band. Although the X-band corrugated horn used with this reflex feed is very good, it is also true that the use of the dichroic plate in the system and the large asymmetric feed structure results in about 0.5 dB G/T compromise of X-band performance. This is because of some small loss in the dichroic plate and some backscatter at X-band resulting primarily in an increase (2-3 Kelvins) in the X-band antenna noise temperature. When applied to a very low noise system (25 Kelvins) this small noise increase becomes serious.

In the future, the use of X-band telemetry is to be emphasized, at the expense of S-band if necessary. It was decided to develop an alternate feeding technique that would more nearly optimize X-band performance, perhaps with some degradation of S-band performance. Also any new and improved X/S band feed unit could then be used in future DSN stations, such as a proposed array of 40 meter class antennas. It is evident that if the dichroic plate is to be removed, then the two bands must operate concentrically or coaxially from the same or coaxial apertures. Some obvious approaches to accomplish this are: (1) an X-band horn within (coaxial with) the S-band horn, (2) an X-band end fire element (disc-on-rod or helix) within the S-band horn, and (3) an array of four or more S-band horns surrounding the X-band radiator, much like a monopulse system. These approaches all would result in a considerable S-band performance compromise (say 2 dB) and the use of anything but a very good horn for X-band might well have as much loss (0.03 dB) as the dichroic plate. The only obvious approach available is to actually use the same horn with both bands and develop a technique that will result in acceptable illumination functions in both of these widely separated frequencies.

The technique chosen to accomplish this is a very deeply grooved large corrugated horn that will radiate both frequency bands and operate at gain limit to achieve approximate pattern equivalence. A unique characteristic of such a horn is that the phase center has moved back, from near horn aperture, nearly to the throat of the horn in both bands.

The Horn Concept

Jeuken (Ref. 2) suggested this technique of operation in different frequency bands. The corrugated horn derives its operating characteristics from the fast wave structure of the horn walls and this characteristic is obtained by grooving the walls perpendicular to power flow so that the surface impedance becomes capacitive. For this to occur, the input grooves must be between $\lambda/4$ and $\lambda/2$ deep (λ =wavelength within a groove) at the operating frequency, or in the range $\lambda\,[(2N-1)/4]$ to $\lambda[2N/4]$, where N may assume any integer value. Once this fast wave is established, the grooves may gradually become shallow and inductive and the fast wave will still exist and propagate.

There are two basic degrees of freedom or choices in the design of such a horn. These are:

1. The groove structure used to create a condition to support multiband operation, and

2. The flare angle and final aperture size to obtain a desired pattern beamwidth.

The technique used to generate and support two widely separated frequency bands in the same horn is to use a deeply grooved corrugated horn surface. Because of the periodic behavior of the corrugation impedance in the frequency spectrum, there will be a multiplicity of frequency bands for which any corrugated horn will support the proper fast waves. For instance, a groove depth can be found that is a multiple for the two frequency bands, (N = 1, 3 at S- and X-band), which presents the correct boundary conditions to support the corrugated hybrid mode (fast wave).

Now to consider the second degree of freedom, the flare angle. As a horn with fixed flare angle becomes longer, the aperture becomes larger and radiation patterns become narrower. A point is reached however when additional size does not make the pattern narrower nor the horn to develop higher gain, generally because of total phase error in the aperture. For this discussion we may call this "gain limit" or "saturated operation." As size is further increased, some change in pattern texture may be detected; however, the pattern remains essentially unchanged. Therefore, flare angle alone determines the final pattern "saturated" beamwidth.

One now sees the possibilities. A groove depth can be chosen which satisfies the depth requirement above within two (or more) frequency bands for proper corrugated horn operation, and sufficiently large to just be "saturated" in the lowest band so that the higher bands would be operating well above this point for nearly equal pattern characteristics. The beam width for these "saturated" conditions is a function only of the horn flare angle, and <u>not</u> the aperture size. Narrower flares result in narrower saturated beamwidths, with consequent longer horn lengths.

In this saturated operation, the pattern phase center for all frequencies has moved back into the throat of the horn, near the horn vertex, instead of its usual position near the aperture face. This will give a somewhat unusual appearance to a retrofitted Cassegrain system because the horn aperture will now extend a larger distance away from the feedcone-centered hyperboloid focal point, towards the hyperboloid.

Thomas (Ref. 3) has suggested a region where this saturation may be considered to start. Figure 1 depicts this condition, i.e., when $\Delta = (R/\lambda_o)(\text{Sin } \theta_o)(\tan \theta_o/2) > 0.75 \lambda_o$. The hybrid modes that can exist in the corrugated cylindrical waveguide or conical horn have been discussed by various authors (Ref. 4, 5, 6, 7, 8). These modes have been designated $HE_{n,m}$, and $EH_{n,m}$,. Almost all discussion has centered on the n=1 modes, and particularly m=1, where the HE_{11} mode results in the usual symmetrical E and H plane radiation pattern with a maximum on boresight. The EH_{11} mode develops a minimum on boresight.

A recent paper by Thomas (Ref. 9) was particularly useful in understanding these hybrid modes as applied to the design of this horn system. It emphasizes some interesting facts to be remembered in developing a multi band corrugated horn, e.g., (1) the EH_{11} mode will be supported in a smaller waveguide than the HE_{11} modes if the groove impedance is inductive ($d < \lambda/4$), (2) above cutoff, the inductive groove will support both an HE_{11} mode and an EH_{11} mode, (3) only the HE_{11} mode will be supported if the groove is capacitive ($d > \lambda/4$).

Theoretical Calculations

A paper by Clarricoats (Ref. 10) developed a characteristic equation that is very useful for predicting mode behavior and radiation patterns from corrugated horns. A computer program was prepared (Ref. 11) for calculating this performance, using the characteristic equation. This program was used at length in calculations of horn patterns for various flare angles from 20 to 40 degrees. Figure 2 represents a compilation of the calculations for a horn of 36 degree flare angle (18° half flare). This figure depicts the 10dB beamwidth as the horn is made larger (longer with larger aperture) through the gain saturation point. A 10dB beamwidth is chosen since it represents in general the taper level in illuminating the hyperboloid subreflector. It is noted that the 10 dB beamwidth reduces to about 27 degrees and holds this level for much larger horns. This "saturation" aperture size is about 7.5 wavelengths, or 98 cm (38.6 inches) for 2.3 GHz. At 8.4 GHz, the aperture is 27.8 wavelengths, and still in the same beamwidth range. Figures 3 and 4 show the calculated patterns for a horn of 34.2° flare angle and 106.7 cm (42 inch) aperture, using 5.093 cm (2.005 inch) deep grooves. This horn has been fabricated for tests and possible use at DSS-13, a 26 meter station at the DSN. The aperture is 8.16 wavelengths at S-Band and 30.0 wavelengths at X-band. The 5.093 cm grooves represent depths of 0.34λ to 0.403λ from 2.0 GHz to 2.4 GHz and 1.21λ to

1.44λ from 7.1 GHz to 8.5 GHz. These are the dual bands over which this horn is intended to operate.

The 10 dB beamwidths are nearly the same for the two bands. However, there is an obvious difference in the structure of these two patterns. The S-band pattern flares out much more resulting in more spillover energy beyond the normal illumination point of -10 dB taper. Calculated efficiencies of the horn as an equivalent paraboloid prime focus illuminator are as follows, at the polar angle of 13.4°, and 8.150 GHz.

$$\eta_s(\text{spillover}) = 0.9474$$

$$\eta_i(\text{illumination}) = 0.8874$$

$$\eta_p(\text{phase}) = \underline{0.9987}$$

$$\eta_t(\text{total}) = 0.8397$$

The X-band phase center is about 67-1/2 inches behind the aperture. When the S-band patterns is calculated about this same point, the following calculated efficiencies result at the polar angle of 13.4° and 2.295 GHz,

$$\eta_s(\text{spillover}) = 0.8632$$

$$\eta_i(\text{illumination}) = 0.8857$$

$$\eta_p(\text{phase}) = \underline{0.9865}$$

$$\eta_t(\text{total}) = 0.7543$$

indicating that X-band is being optimized at some expense to S-band performance. For reference, the same calculations can be made using the present DSN corrugated horn as used in an equivalent paraboloid system. Those results are:

$$\eta_s(\text{spillover}) = 0.9145$$

$$\eta_i(\text{illumination}) = 0.8911$$

$$\eta_p(\text{phase}) = \underline{0.9983}$$

$$\eta_t(\text{total}) = 0.8136$$

This shows the new feed, as applied in a conventional paraboloid system gains 2.6% at X-band and loses 5.9% at S-band, as a direct substitute.

Probably one of the most valuable results from this type of horn is the complete lack of any sort of sidelobe. Note that at X-band the main lobe reduces to -60 dB and does not reappear. This makes the horn very attractive for dual reflector antenna shaping applications since it will improve spillover efficiency even more and aid in further reduction of total antenna noise.

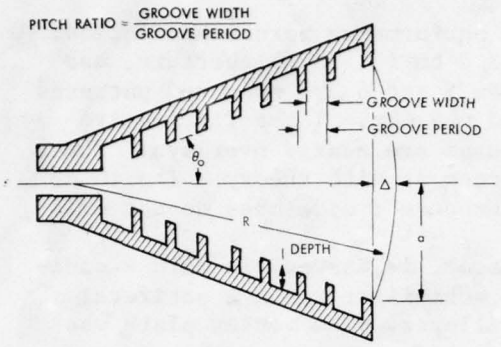

Fig. 1. Corrugated Horn Parameters

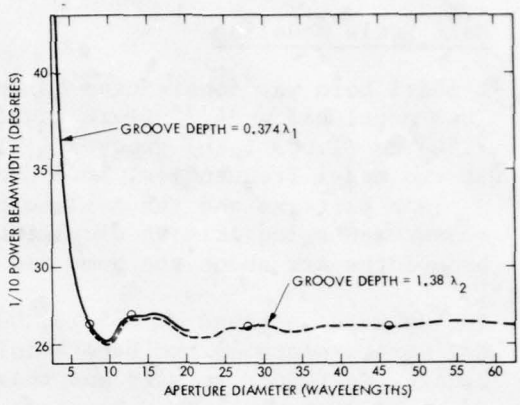

Fig. 2. The "Saturated" 36° Corrugated Horn - Variable Size and Two Wavelengths

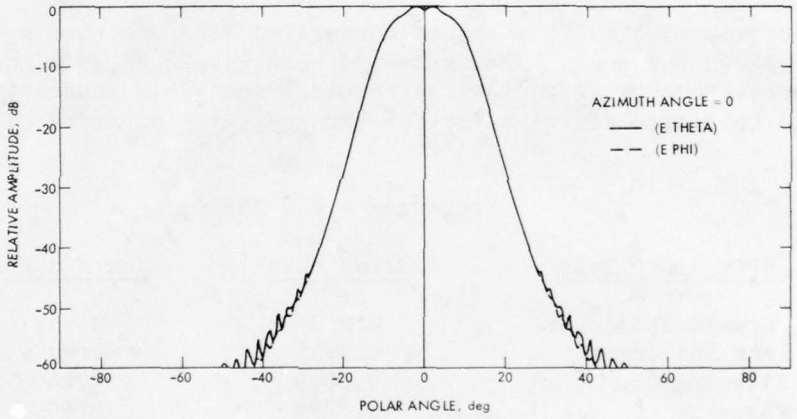

Fig. 3. Amplitude Pattern for the 17.1 deg Horn, 42 inch Aperture, 2.005 inch Grooves, freq = 8.150 GHz

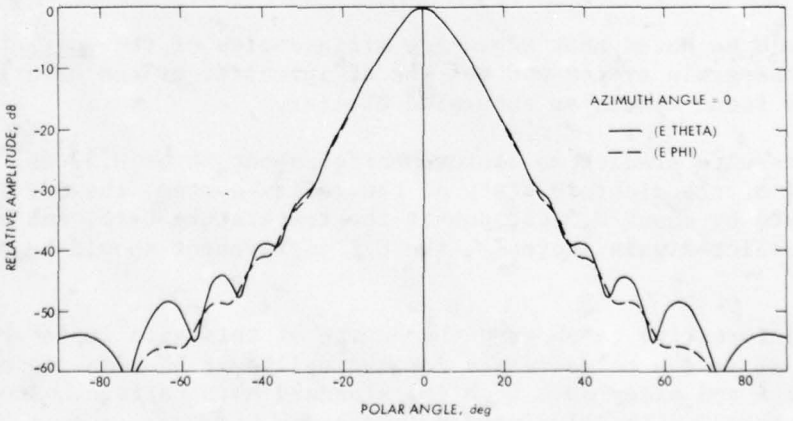

Fig. 4. Amplitude Pattern for the 17.1 deg Horn, 42 inch Aperture, 2.005 inch Grooves, freq = 2.200 GHz

Half Scale Modeling

A model horn was constructed to check performance versus prediction. This model had a 34.2° flare angle, 53.3 cm (21 inch) aperture, and 2.548 cm (1.003 inch) grooves. Figures 5 and 6 are measured patterns at two model frequencies, 16.3 GHz and 4.4 GHz. These figures are H-plane patterns and the E-plane patterns are nearly overlays. These measurements indicate an excellent agreement with theory. The 10 dB beamwidths are about the same and as expected; sidelobes do not exist.

The 26 meter antenna at DSS-13, Goldstone, is Cassegrain with a conical vertex plate on the hyperboloidal subreflector and a periferal flange, to reduce forward and rear spillover. The vertex plate was developed for previous S-band only operation. However, the measured half scale model pattern, figure 5, was scattered (theoretical calculation using a computer program to calculate scattering) from this subreflector, at X-band, to determine the exact improvement over the present horn.

A comparison with a JPL standard corrugated 4.7λ aperture non gain-limited horn was done. That standard horn has 22 dB gain and very low sidelobes, however some sidelobe shoulder energy is apparent. Below are the tabulated efficiencies for the scattered patterns of these two horns.

Frequency = 8.5 GHz

Efficiency Type	22 dB Horn	New X/S Horn
Forward Spillover	0.9707	0.9897
Rear Spillover	0.9968	0.9956
Illumination	0.8019	0.8480
Phase	0.8894	0.9005
Blockage	1.000	1.000
Cross Polarization	0.9990	0.9990
Total	0.6894	0.7515

It should be noted that these are efficiencies of the scattered pattern in a Cassegrain system and not the efficiencies of the horn itself in a prime focus system as tabulated earlier.

These results predict an improvement of about 6% or 0.37 dB. With the removal of the dichroic plate of the reflex system, the G/T is increased by about 0.5 dB, due to the temperature term, and so with this predicted gain increase, the G/T improvement should be nearly 0.9 dB.

It is informative to observe the source of this gain improvement. Nearly 2% is due to decreased forward spillover by removing all shoulders and side lobes from the standard horn pattern. The remaining 4% is picked up in illumination, which can be observed as an unusual squareness in this X-band pattern.

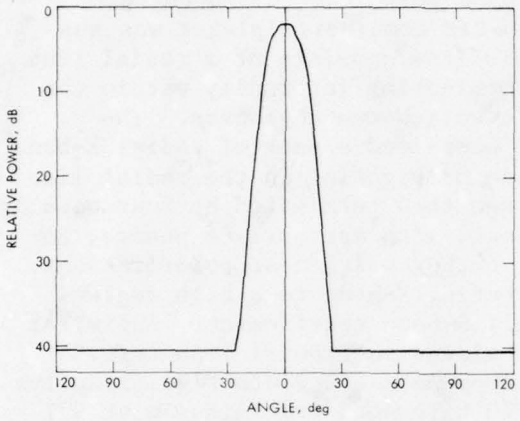

Fig. 5. Measured Pattern of a 17.1 deg Horn, 21 inch Aperture, 1.003 inch Grooves, freq = 16.3 GHz, H-Plane

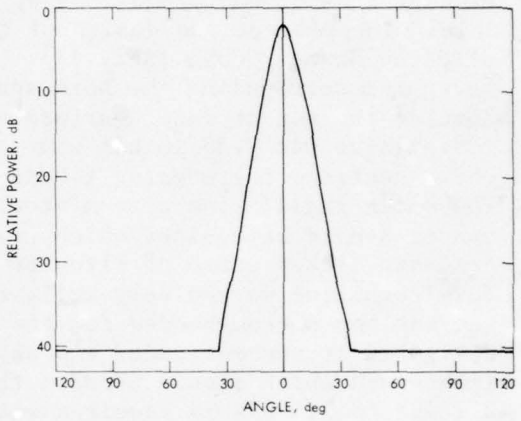

Fig. 6. Measured Pattern of a 17.1 deg Horn, 21 inch Aperture, 1.003 inch Grooves, freq = 4.4 GHz, H-Plane

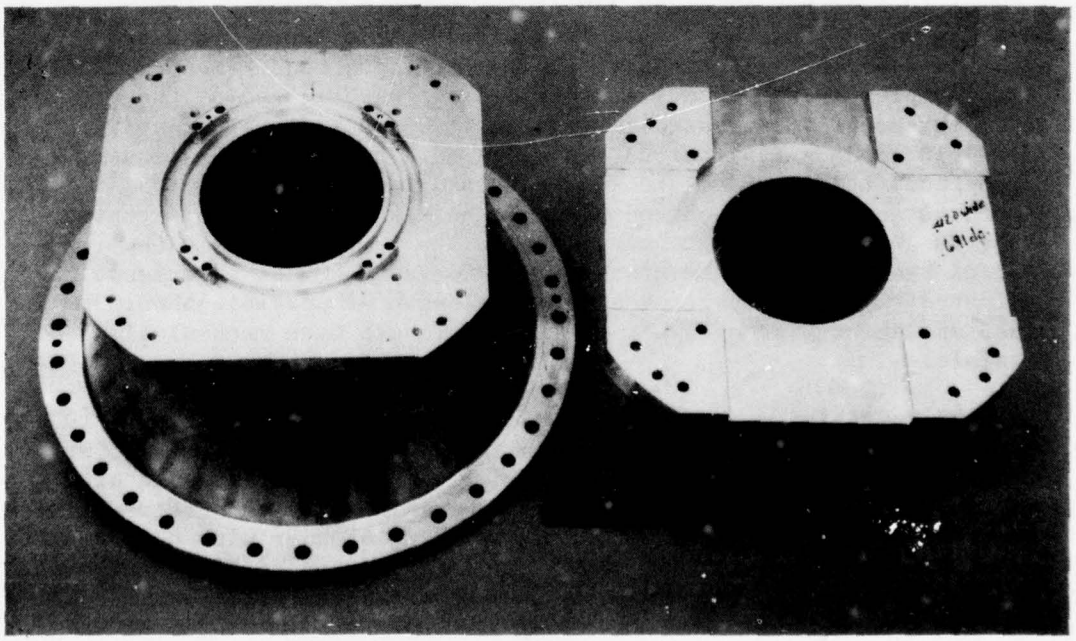

Fig. 7. The Diplexer

Engineering Design of the Full Scale Horn for DSN

In designing a full scale prototype multi-band horn for experiment, a technique must be devised for injecting the lower frequency band. In the JPL system, S-band must be applied with a nearly zero sacrifice at X-band, < 0.02 dB loss at X-band being considered acceptable. The concept and design of this S/X combiner/diplexer was supplied by Seymour Cohn (Ref. 12). This item consists of a radial line waveguide surrounding the horn and terminating internally within the horn at the top or inner surface of a wall between grooves. The radial line was 0.35 inches wide and contained a pair of radial X-band choke sections for keeping X-band from propagating in the radial line. The outer radial line circumference was then terminated by four equally spaced S-band waveguides which are used, with appropriate phases, to generate either sense of circular or orthogonal linear polarizations. This technique worked very well, rejecting X-band to a high degree, but was too narrow banded for the full S-band requirement. A similar design is at present under way which widens the radial line to 0.5 inches and which should broaden the impedance bandwidth significantly. 2.1 GHz to 2.4 GHz is required with 20 kilowatts transmission at 2.1 GHz. A photo of this diplexer is shown in figure 7. It has been separated in the picture to show the X-band radial rejection chokes.

The first prototype model of a full scale horn, pictured installed in a 26 meter antenna in figure 8, had a 106.7 cm (42 inch) aperture and was 172.7 cm (68 inches) long from aperture to throat vertex. The grooves in the small conical input section used only for X-band, were 1.02 cm (0.434 inches) deep, satisfying the groove depth requirement that $\lambda/4 < d_\lambda < \lambda/2$ across the required band. This section had a half flare angle of 14° to suit a diameter input requirement for the S-band diplexer injection. At this S-band injection point the groove depth is abruptly increased to 4.98 cm (1.96 inches) resulting in $d_\lambda = 1.18$ to $d_\lambda = 1.41$ across the required X-band; the $5\lambda/4$ mode. For S-band, this 4.98 cm groove depth results in $d_\lambda = 0.35$ to $d_\lambda = 0.40$ across the required S-band, the $\lambda/4$ mode. In this region also, the half flare angle was increased to 17.1° to obtain the desired beamwidth in saturated gain performance. Past experience had indicated that as many grooves per wavelength as possible should be used, and about 5 grooves per X-band wavelength were mechanically feasible.

Measured radiation patterns of this horn are shown in figures 9, 10 and 11. Although these patterns were acceptable, there are some differences from the measured half scale model at frequencies in the high end of the X-band region (Figure 5). There is a marked difference in the E and H plane patterns, the E plane being broader with a 1 dB null (or dip) on axis. This will result in more forward spillover from this broader E-plane pattern and a somewhat reduced efficiency.

The E and H plane patterns (Figure 10) at 7.175 GHz overlay much better although there is evidence of some difference near boresight where slight dips occur. Figure 11 indicates a slight difference in the E and H plane patterns at 2.295 GHz, but so minor as to be ignored.

Fig. 8. The First Model Horn on DSS13 of the DSN

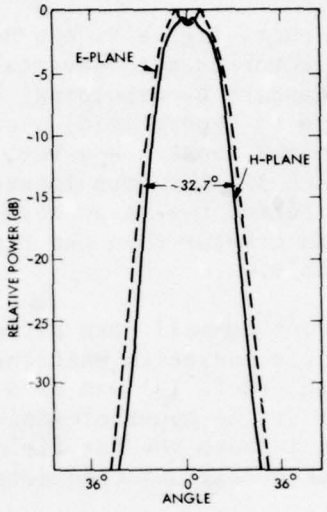

Fig. 9. Final X/S Horn Pattern, freq = 8.425 GHz

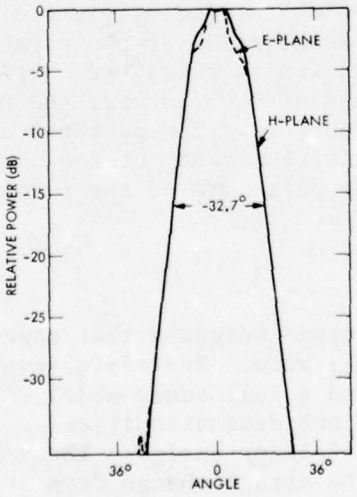

Fig. 10. Final X/S Horn Pattern, freq = 7.175 GHz

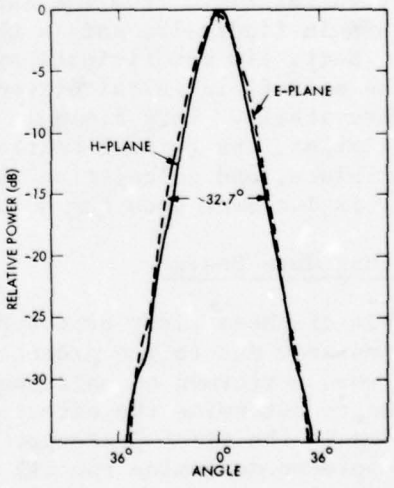

Fig. 11. Final X/S Horn Pattern, freq = 2.295 GHz

When this final high frequency pattern is scattered from the 26m system subreflector, as was the half scale model pattern, an efficiency of just under 74% was calculated, or about 1.5% less. (See above section on half scale modeling.) This was mostly due to increased spillover although some increase in illumination efficiency was noted.

In the photo figure 8, the horn aperture appears closer to the subreflector than is acceptable for the far field pattern assumption of a standard hyperboloidal cassegrain system. The distance from horn aperture to hyperboloid is only about 3.35 meters and this is less than the Fresnel range. However, the radiation pattern does resemble that of a much smaller horn located near the hyperbola focus, some 1.7 meters behind the large horn aperture. For this smaller horn, the range is greater than the Fresnel range and far field assumptions are acceptable.

However, the small horn pattern differences did cause some concern about near field radiation patterns. Therefore a spherical wave expansion technique (Ref. 13) was used to ascertain very accurately the horn pattern at the hyperboloidal reflecting surface. The resulting scatter pattern in both the far field and at the very short range of the horn aperture itself was then determined.

A spherical wave expansion in the coordinates of a spherical system (r, θ, ϕ) is much like a regular Fourier expansion in the single frequency coordinate ω. Coefficient magnitudes for the spherical harmonics are found much as the Fourier coefficients are calculated for the frequency harmonics. In the case under discussion, 58 coefficients of the measured far field horn pattern are calculated and shown to contain more than 99.9% of the energy. These are then used to calculate the field at the range of the subreflector and thence the scattered far field from the subreflector is calculated. This field is shown in figure 12, and is the assumed illumination of the paraboloid. Next, 110 coefficients are determined for this scatter pattern and the near field is calculated at the range of 4.09 meters, the horn aperture itself. This field is shown in figure 13. The patterns are very similar, the reduced central blockage is the result of the conical vertex plate, and calculation indicates that only .08% of the total energy is incident upon the horn aperture.

The Final Horn Design

Analysis of these first prototype horn patterns indicated that some problems were due to the presence of the EH_{11} mode. Therefore several tests were performed on half scale models and a full scale model section to determine the effects of the various discontinuities included in the first prototype because of diplexer design. These tests were to determine the (1) effect of the abrupt change from cylindrical waveguide to a 14° flare, (2) effect of the large (2.54 cm) ungrooved region where the diplexer was located, (3) effect of flare angle change from 14° to 17° (4) effect of the abrupt change of groove depth from 1.1 cm to 4.98 cm (5) effect of groove width, or ratio of groove width to groove period.

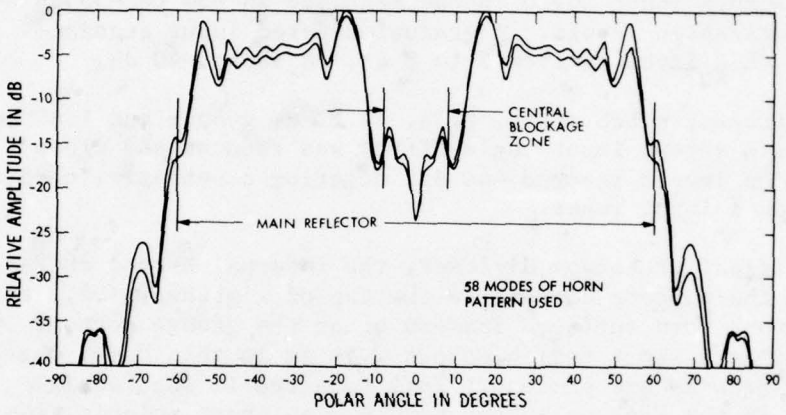

Fig. 12. Calculated Far-Field Scattering from the DSS-13 Subreflector When Fed with the Measured Horn Pattern

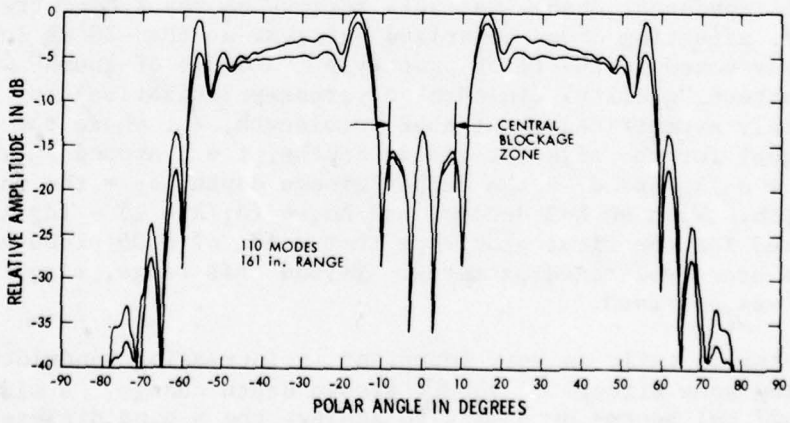

Fig. 13. Calculated Near-Field Scattering (4.09 cm) from the DSS-13 Subreflector When Fed with the Measured Horn Pattern

The presence of the EH_{mn} mode is indicated in cross polarized patterns in the 45° plane. This is normally zero for the pure HE_{11} mode. Using Potter's (Ref. 11) hybrid horn program, it was determined that phasing between EH_{11} and HE_{11} had no effect on this cross polarization level and that if their relative amplitudes were held constant, the cross polarized component remained constant. Hence, one has a method of determining effects of mode generation due to the above mentioned discontinuities. The following results were observed:

1. With the original pitch ratio (groove width/groove period) of 0.5, the abrupt input angle change resulted in -30 to -35 dB cross polarization levels. A gradual tapered input section decreased this level by from 5 to 8 dB, to about -40 dB.

   With a different pitch ratio, 0.78, (1.27 cm groove and 1.63 cm period) this abrupt input angle effect was reduced and cross polarization levels reached -40 dB, negating a potential need to use a gradual input taper.

2. In the original prototype diplexer, the internal X-band chokes reflected their short circuit to the top of a groove, i.e., to the innermost horn surface, instead of at the groove bottom. The result is a short region, about 2.54 cm in this case, where no X-band grooves are present. This resulted in substantial shoulders in the E-plane pattern and a high cross polarization level. This is being corrected by reflecting this short to the bottom of a groove; hence, there is no interruption of the groove pattern for X-band.

3. The flare angle change has no noticeable effect, even from an 11° to 18° change.

4. With the original pitch ratio of 0.5, the abrupt groove depth (therefore impedance) change was very serious at the X-band frequency band edges, affecting cross polarized patterns at the -20 dB level, those levels noted in the first prototype. A "rule of thumb" was noted. Pattern "quality" (in teams of cross-polarization) is approximately symmetrical about that wavelength, λ_o, where the impedance is equal for the adjacent groove depths, i.e., around λ_o when $d_1/\lambda_o = 1 + d_2/\lambda_o$ and d_1 = the deeper groove depth, d_2 = the shallow groove depth. With an N=3 design, and $\Delta d_\lambda = (d_1/\lambda - 1) - (d_2/\lambda)$, it was noted for the first prototype that a Δd_λ of 0.05 produced acceptable cross polarized patterns. Beyond this range, significant EH moding was observed.

5. The groove pitch ratio is very important in increasing bandwidth and negating some effects of abrupt groove depth change. A wider groove (1.27 cm) became necessary to achieve the S-band diplexer bandwidth in the second prototype. Therefore the resulting increase in X-band horn pattern bandwidth was serendipitous. With a second prototype pitch ratio of 0.78, the range of Δd_λ became 0.1 (from 0.05) for acceptably low level cross polarized patterns.

It should be noted that the abrupt groove depth change does not appear necessary; the deeper grooves could extend down into the horn throat. In this design, however, this would require the virtual short (due to the radial line X-band reject filter) at a point deep in the S-band diplexer with a resulting larger radial line diameter. This would negate attempts to achieve S-band bandwidth which is already restricted. Hence the need for a shallow groove at diplexer input and the good fortune in discovering that the wider groove would help solve the bandwidth problem generated by the abrupt change in groove depth.

New horn sections have now been fabricated incorporating the above knowledge. Although the abrupt groove depth change is retained, the groove width is increased to 1.27 cm with a thin wall and a pitch ratio of 0.78. The diplexer input is altered so that the X-band short (from the radial line reject filter) is reflected to the base or bottom of a shallow groove resulting in no groove interruption in this region.

Figures 14, 15 and 16 present the result of pattern measurements on a partial section of this final horn design. Figure 14 is the result at the low end of the high frequency band. The groove depth at input is 0.271 wavelengths ($>\lambda/4$) and for the deeper groove it is 1.18λ. This difference ($0.271-0.18=0.091$) is representative of the groove impedance mismatch at this abrupt change. Figure 15 presents the center band where input groove depth is 0.297λ and output is 1.29λ for no impedance change. Figure 16 is the band top where input groove depth is 0.324λ and output is 2.41λ for a change of 0.086λ.

Conclusion

A dual band (X/S) horn has been designed for the NASA/JPL Deep Space Network. It is expected that this horn will provide a 0.9 dB improvement over the present G/T at the various DSN antennas. The horn is corrugated with input grooves operating in the $\lambda/4$ mode and output grooves operating in both a $\lambda/4$ and $5\lambda/4$ mode.

This horn has extremely low (nearly non-existent) sidelobes and hence is an excellent candidate for shaped antenna systems where advantage is taken of this fact by achieving extremely high spillover efficiencies.

Acknowledgements

The authors would like to thank Harry Reilly for invaluable help in part fabrication and measurements and Dan Bathker, Dave Nixon and Art Freiley for their aid in developing the total system. The continued understanding and support of the JPL Telecommunication Division, the JPL Tracking and Data Acquisition Office, as well as the NASA Office of Space Tracking Data Systems is acknowledged.

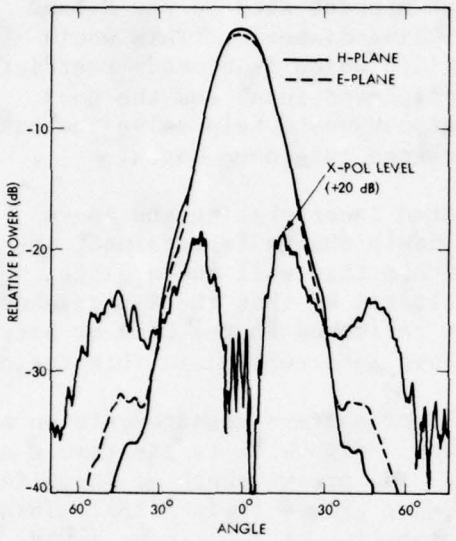

Fig. 14. Pattern of "Partial" New Design at 7.1 GHz

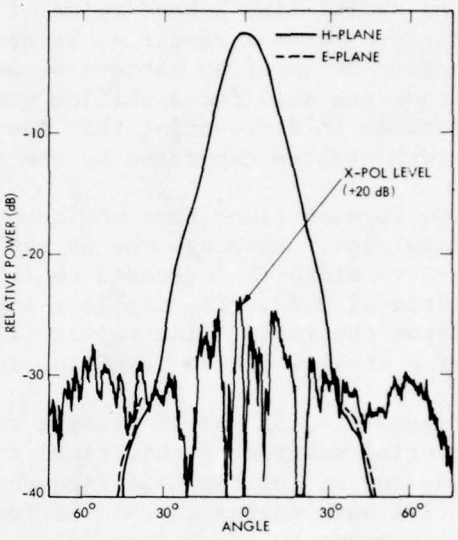

Fig. 15. Pattern of "Partial" New Design at 7.8 GHz

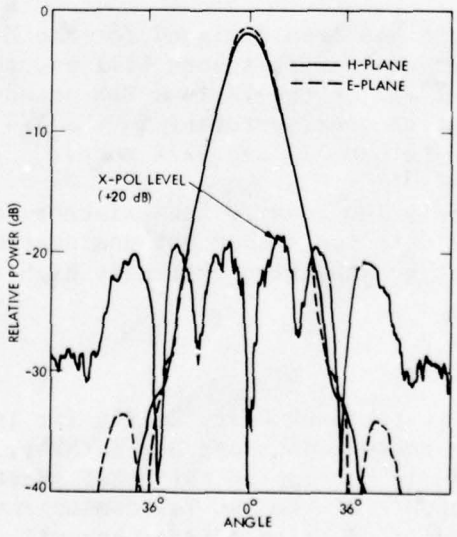

Fig. 16. Pattern of "Partial" New Design at 8.5 GHz

References

1. P. D. Potter "S- and X-Band Feed System", JPL Technical Report 32-1526, Vol. XV, pp. 54-58.

2. E. J. Jeuken and V. J. Vokurka, "Multi-Frequency Band Corrugated Conical Horn Antenna," 1973 European Microwave Conference Proceedings, Vol. 2, Sept. 4-7, 1973, Brussels University, Brussels, Belgium.

3. B. MacA. Thomas "Design of Corrugated Horns" IEEE Trans. on Ant. and Prop., Vol. AP-26, No. 2, March 1978.

4. H. C. Minnett, B. MacA. Thomas "A Method of Synthesizing Radiation Patterns with Axial Symmetry" IEEE Trans. on Antennas and Propagation; Vol. AP-14, pp. 654-656, Sept. 1966.

5. P. Clarricoats, P. Saha "Theoretical Analysis of Cylindrical Hybrid Modes in a Corrugated Horn" Electron, Lett. Vol. 5, pp. 187-179, May 1, 1969.

6. P. Clarricoats "Analysis of Spherical Hybrid Modes in a Corrugated Conical Horn" Electron. Lett. Vol. 5, pp. 189-190 May 1, 1969.

7. B. MacA. Thomas "Bandwidth Properties of Corrugated Conical Horns". Electron Lett. Vol. 5, pp. 561-563, Oct. 30, 1969.

8. B. MacA. Thomas "Mode Conversion Using Circumferentially Corrugated Cylindrical Waveguide" Electron. Lett., Vol. 8, pp. 394-396, July 27, 1972.

9. B. MacA. Thomas, H. C. Minnett "Propagation in Cylindrical Waveguides with Anisotropic Walls", Radiophysics Publication RPP 1346, CSIRO, Sydney, Australia, Jan 1977. (Short version was published in the Proc. Inst. Elec. Eng.)

10. P. Clarricoats, P. Saha "Propagation and Radiation Behavior of Corrugated Feeds-Part 1, Corrugated Waveguide Feed", Proc. Inst. Elec. Eng. Vol. 118, pp. 1167-1176, Sept. 1971.

11. P. D. Potter, "Efficient Antenna Systems: A New Computer Program for the Design and Analysis of High Performance Conical Feedhorns," JPL Technical Report 32-1526, Vol. XIII.

12. Seymour Cohn Associates, Encino, California.

13. Arthur C. Ludwig "Near-Field Far-Field Transformations Using Spherical Wave Expansions," IEEE Trans. on Ant. and Prop., Vol. AP-19, March 1971, pp. 214-220.

THE LOOK THROUGH ANTENNA

D. Killion and W. McNaul
Cubic Corporation
San Diego, California

ABSTRACT

A dual band, high gain, steerable antenna design is presented. The concept realizes optimum utilization of limited swept volume to provide high directivity and reduced sidelobes across the band from 0.5 to 18 GHz. The two bands are overlapping, and both are linearly and orthogonally polarized. Aperture efficiencies in excess of 30 percent are demonstrated for frequencies below 1 GHz and physical aperture dimensions less than two wavelengths.

A three-phase R & D effort evaluating predefined design parameters and their effects on antenna performance characteristics is summarized. Phase I is an investigation of a high band, parabolic reflector antenna design that is transparent to radiation from the low band subassembly. Phase II leads to the development of a low band, vertically polarized antenna subassembly. Phase III is a study of possible pattern degradation resulting from merging the antenna subassemblies of Phases I and II in a common swept volume.

1.0 INTRODUCTION

Engineering constraints prescribed by modern electronic intelligence systems continually necessitate innovative antenna design compromises. The objective of this paper is to present the details of a unique solution to a customer requirement for a broadband, steerable, narrow beam antenna configuration. Electrical and mechanical requirements are presented. Design considerations and tradeoffs are investigated with the ultimate goal being the fabrication and testing of working hardware.

2.0 GENERAL ANTENNA REQUIREMENTS

An antenna system was required to meet certain electrical and mechanical constraints. Limited physical size and stringent gain and sidelobe specifications ruled out standard narrowband antenna techniques. Simply stated, the proposed antenna configuration was to conform to these specified mechanical limits:

(1) The antenna must be steerable through 360 degrees and must be contained within a swept volume (see Figure 2-1).

(2) Mechanical integrity must be maintainable in an airborne environment.

Most of the antenna's electrical parameters were customer specified. The only specifications to present significant obstacles to our R & D effort were:

(1) DF antenna shall operate from 0.5 to 18 GHz.

(2) RF frequency coverage shall be in two orthogonally polarized overlapping bands (0.5 to 2.0 GHz vertically polarized, and 1 to 18 GHz horizontally polarized).

(3) Gain requirements across the band are plotted in Figure 2-2a.

(4) Azimuth sidelobe level requirements across the band are plotted in Figure 2-2b.

(5) Low band and high band main beams shall be codirectional.

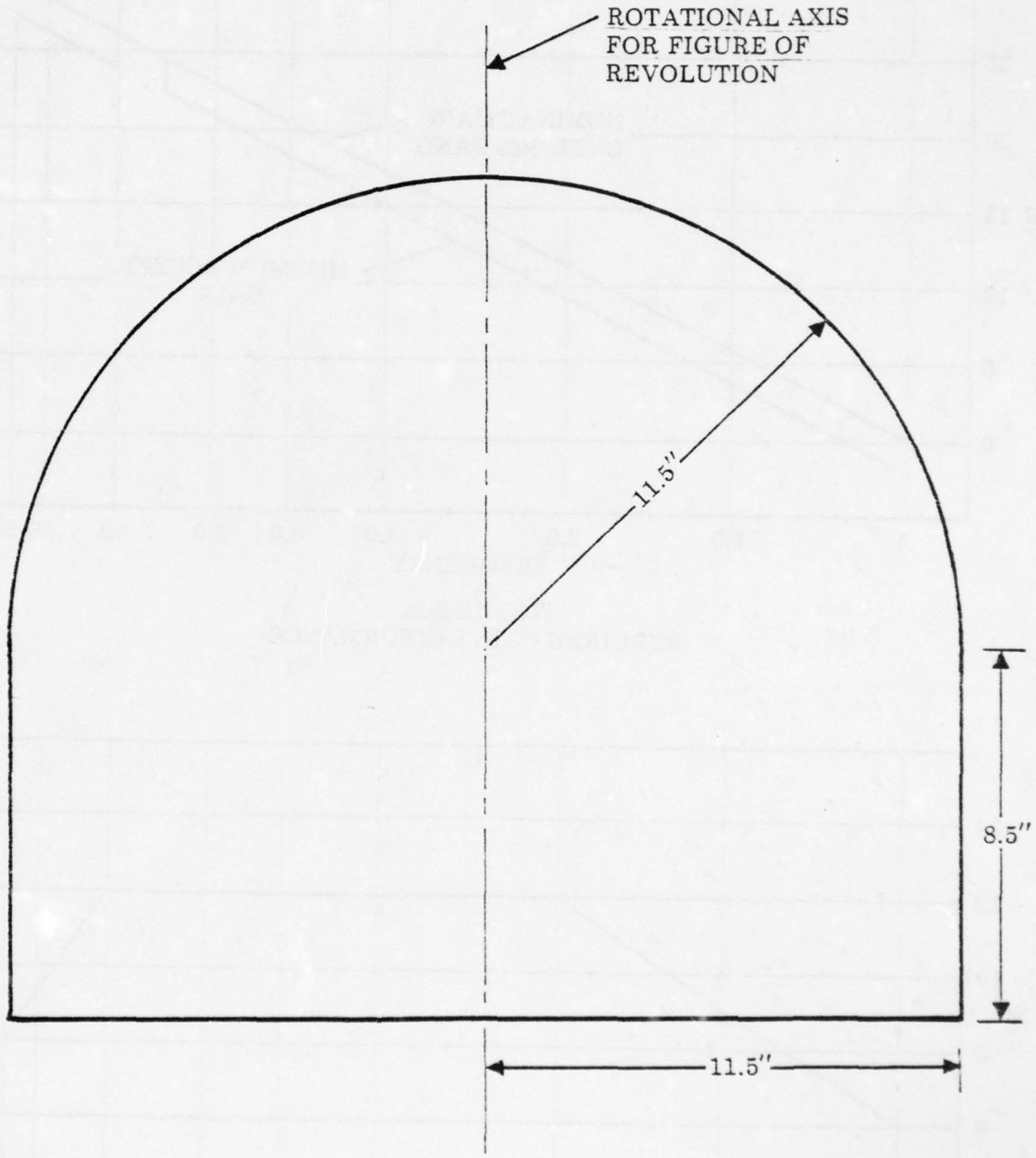

FIGURE 2-1
SWEPT VOLUME

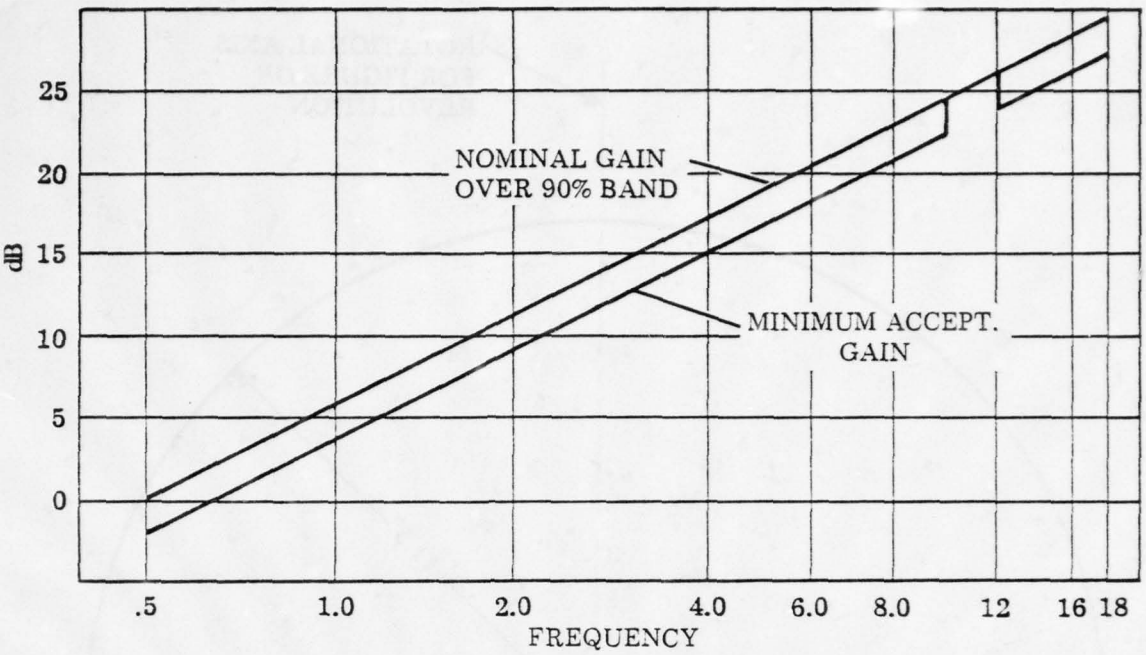

FIGURE 2-2a
REQUIRED GAIN PERFORMANCE

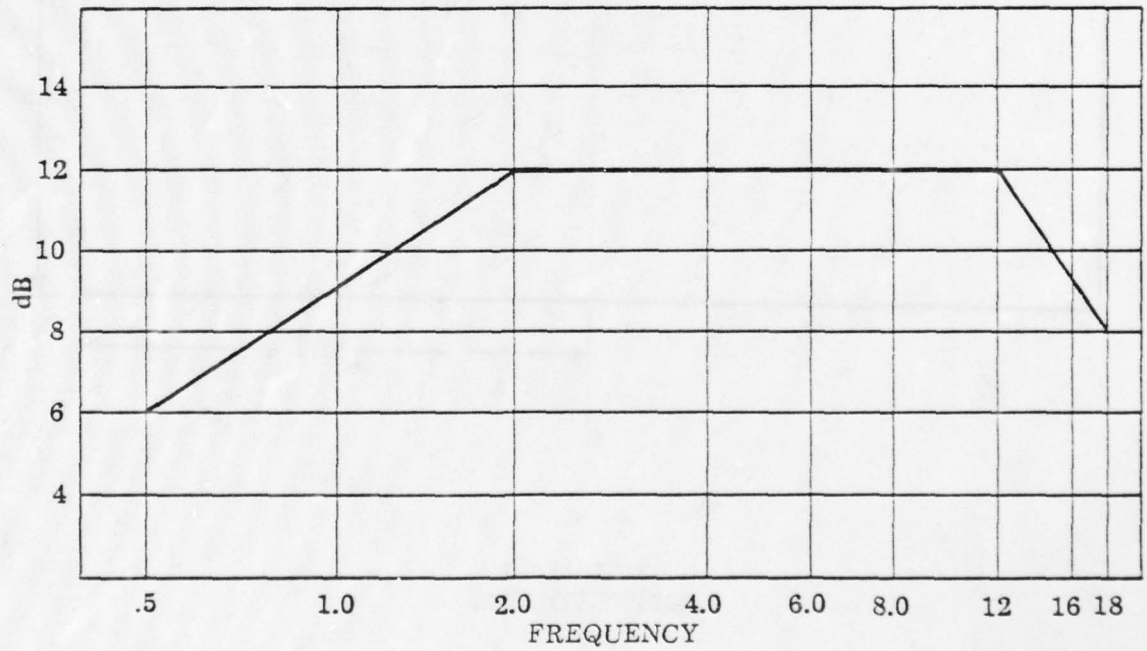

FIGURE 2-2b
REQUIRED SIDELOBE LEVEL LIMIT

3.0 ENGINEERING CONSIDERATIONS

Individually, the requirements outlined in Section 2.0 present no major technical obstacles. A parabolic reflector fed by a pair of orthogonally polarized broadband feeds is one viable approach to achieving the specified electrical limits. Figure 3-1 illustrates one specific system that has been used with considerable success. On the other hand, swept volume constraints as outlined in Section 2.0 cause severe reduction in the size of the reflector. This size reduction, in turn, results in degradation of gain and sidelobe performance. "Small reflector" effects such as feed backlobe interference, feed defocusing (as in the case of log periodic dipole feed), aperture blockage, and small geometry have been discussed in the literature[1]. Figure 3-2 is presented as a summary of these effects on a perfectly efficient reflecting antenna falling within the constraints of the swept volume under consideration.

Another approach to providing low band capability in the physical environment of the parabolic reflecting antenna is shown in Figure 3-3. Here the low band coverage is facilitated by arraying two log periodic dipoles (LPDs) in front of the parabolic reflector. This approach must use LPDs having an α angle on the order of 15 degrees to ensure adequate front-to-back ratio to reduce destructive phasing of the array main beam with the array backlobe radiation focused by the parabolic reflector. Figures 3-4a and -4b illustrate the dramatic effect of using high α angles in order to fit a single LPD in front of a parabolic reflector (7-inch focal length). The swept gain data shown in Figure 3-4a is for an α angle of 15 degrees and an LPD as close as possible to the reflector surface and coaxial to the parabolic axis. Figure 3-4b is for the same test conditions, but with an LPD having an α of 30 degrees. Special note should be made of the "holes" in the swept gain as the LPD is made shorter (i.e., α is made larger). In order for the technique shown in Figure 3-3 to be usable, sufficient room must be available between the reflector and volume limit to accommodate "long" LPD's.

The swept volume of Figure 2-1 presents a mechanical constraint that does not allow the use of a low band array in front of the reflecting surface. Further study of the electrical constraints, however, reveals one specification that can be used to advantage--namely, the required orthogonality of the low and high bands. The theory of polarizing gratings and striped reflectors has been discussed in the literature[1]. It is known that an obstacle made of horizontally placed conducors, given certain physical constraints, represents a

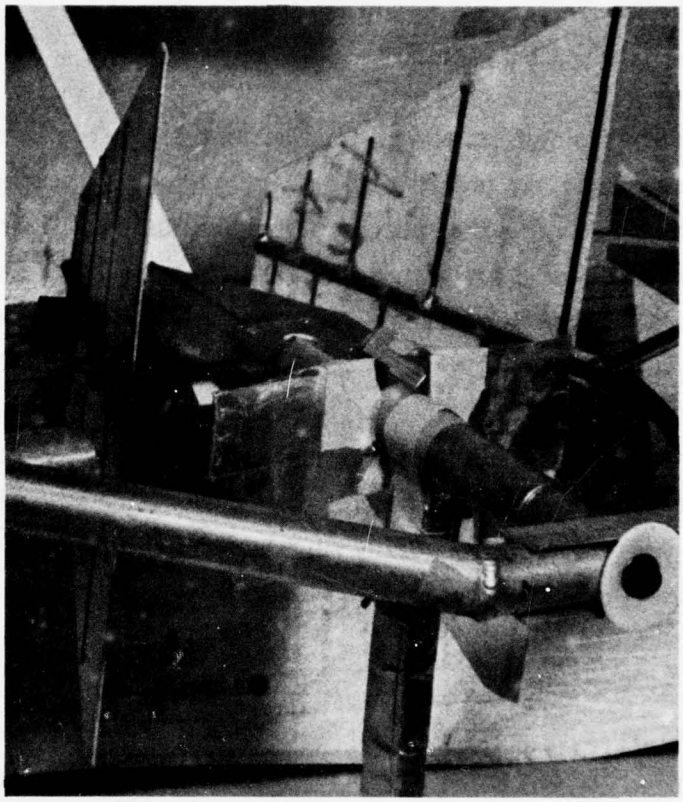

FIGURE 3-1
DUAL BAND, ORTHOGONALLY POLARIZED FEED

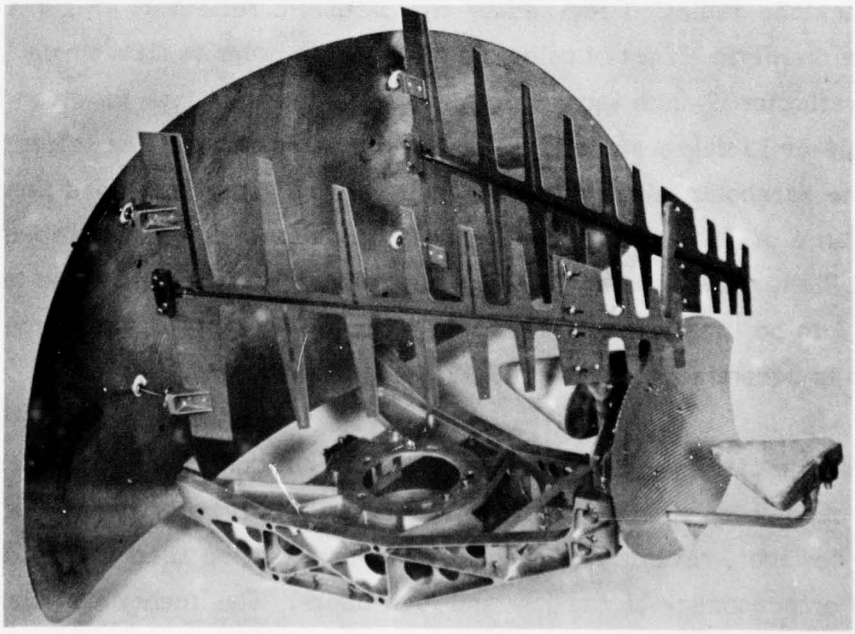

FIGURE 3-3
LOW BAND ARRAY IN FRONT OF HIGH BAND REFLECTOR

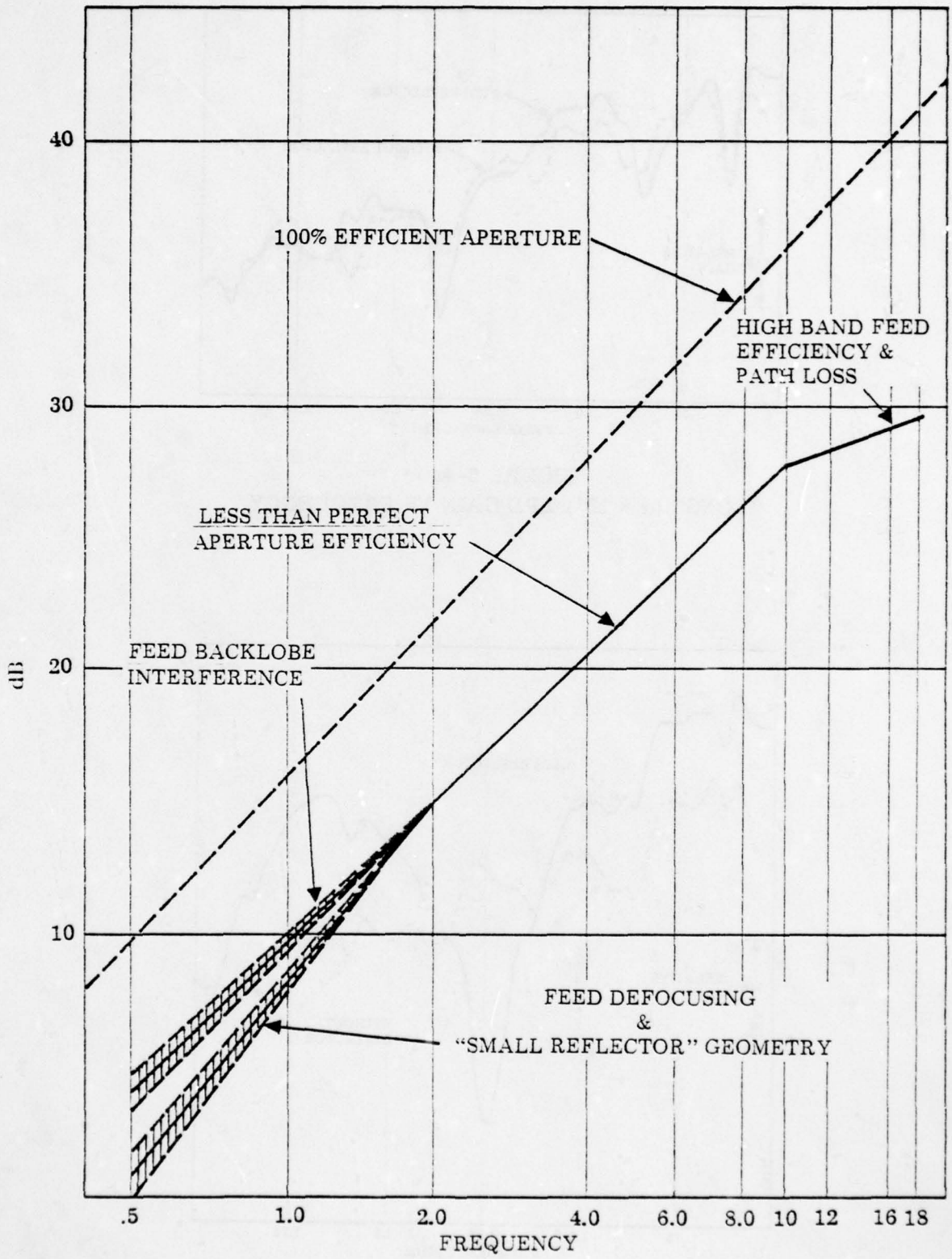

FIGURE 3-2
"SMALL REFLECTOR" GAIN DEGRADATION

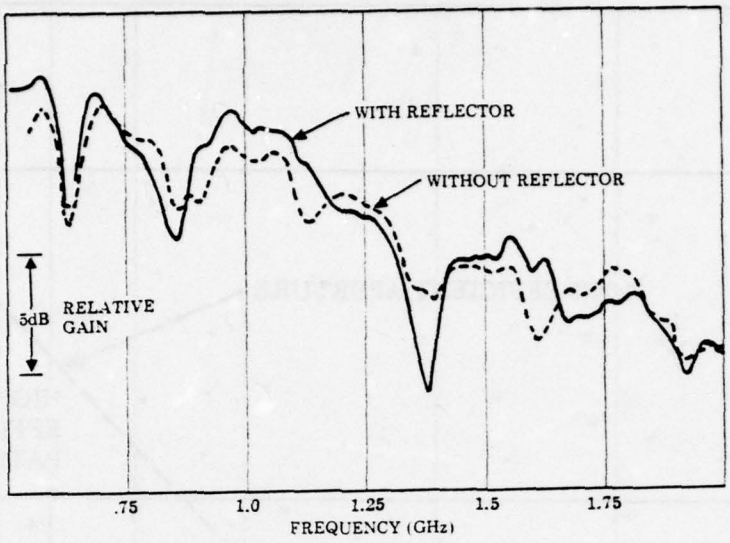

FIGURE 3-4a
"LONG" (α = 15°) LPD GAIN VS FREQUENCY

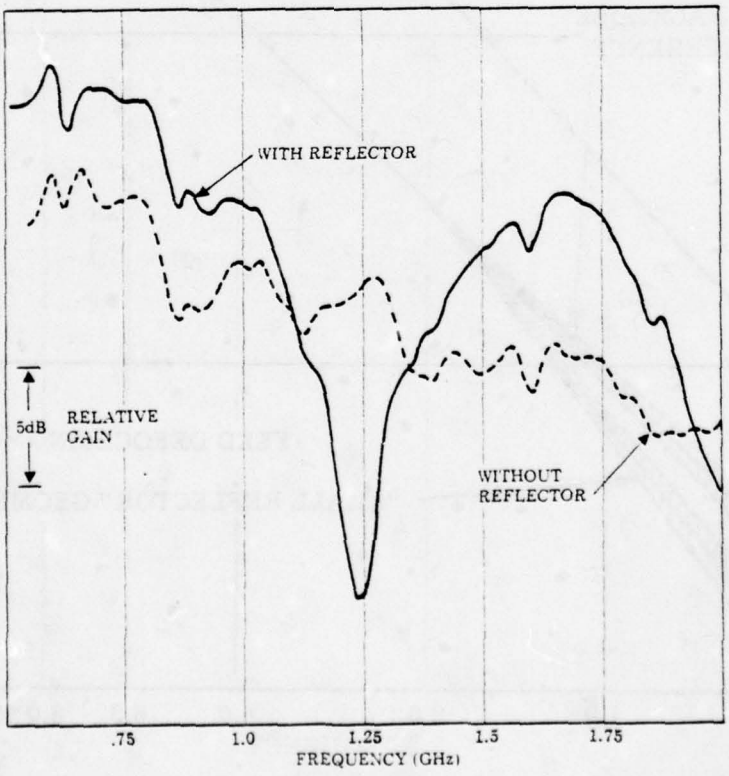

FIGURE 3-4b
"SHORT" (α = 30°) LPD GAIN VS FREQUENCY

nearly perfect reflecting surface to horizontally polarized radiation and approaches transparency for vertically polarized radiation. With this in mind, it is conceivable that a vertically polarized LPD array and a horizontally polarized reflector assembly with a horizontally striped reflector would physically occupy the same space, each being "blind" to the other. Based on the preceding analysis, the concept of a "look-through" antenna technique was established.

4.0 PROTOTYPE DEVELOPMENT

Extensive tests were run in order to evaluate the practicality of the "look-through" approach to limited volume, broadband, high gain antenna systems design. The prototype consisted of an array of LPD antennas for the low band and a parabolic reflector fed by a log periodic dipole feed for the high band. Current LPD design techniques[2] allow for inexpensive construction of broadband antennas exhibiting nearly frequency-insensitive characteristics. LPD design parameters for the two bands are summarized in Table 4-1. Phase I of our prototype development dealt with the optimization of the parabolic reflector antenna that was both mechanically and electrically transparent to a 0.5 to 2.0 GHz radiator (i.e., an LPD array). This consisted of establishing reflector stripe width and spacing (both ¼ inch) and an offset feeding arrangement to move the feed out of the way of the low band array. The reflector was made of thin fiberglass constructed on a 7-inch focal length parabolic mold. Stripes were then painted on with silver paint. Slots were cut to pass the low band array through the reflector, and fiberglass support structures were designed. Results of initial tests from the high band alone showed that only minor degradation in pattern shape and gain resulted from striping. Most gain loss occurred at the high end of the band and was approximately 1 dB.

TABLE 4-1
LOG PERIODIC DIPOLE ANTENNA DESIGN PARAMETERS

	LOWER BAND LIMIT (GHz)	UPPER BAND LIMIT (GHz)	LOG PERIODIC DIPOLE PARAMETERS			
					ELEMENT LENGTH	
			α	τ	Longest	Shortest
Low Band	0.5	2.0	15 deg.	0.85	10.5 in.	2.13 in.
High Band	1.0	18.0	30 deg.	0.80	7.45 in.	0.248 in.

Initial measurements on the striped reflector were with the on-axis feed arrangement shown in Figure 4-1a. In order to allow space for the low band array, the feed was eventually moved off-axis as shown in Figure 4-1b. The off-axis feed arrangement is not an offset feed in the true sense of the word; the LPD feed was moved off axis in such a manner that the axis of the LPD was in line with the vertex of the parabolic reflector. This resulted in a slight elevation boresight shift with frequency. More significant was the sidelobe level change evidenced in the elevation patterns shown in Figure 4-2.

Phase II resulted in the development of a low band array that met the requirements of gain and sidelobe levels specified earlier. In the initial stages of the design, a two-element array was investigated. An overall low-frequency element spacing of the array was set at 12 inches and the tip spacing S was adjusted to achieve optimum results (see Figure 4-3a). Gain and sidelobe specifications were easily met at all but the high end of the band. The data (Figures 4-4a and -4b) shows that a two-element array at 2 GHz will not meet the requirements for gain and sidelobe levels.*

Further refinement was accomplished by adding a third element (see Figure 4-3b). This allowed for the gain improvement without the increase in sidelobes (dashed curves, Figures 4-4a and -4b). However, tapering of the feed to the three elements was necessary to lower the sidelobe levels to usable values (solid curves, Figures 4-4a and -4b).

Phase III resulted in the integration of the two subsystems. Figure 4-5 shows the final dimensional relationships of the various components. Free space low band performance was altered through greatly increased sidelobe levels across the band and slight gain change at the high end of the band (see Figures 4-6a and -6b). High band performance suffered most at the low end of the band, where gain loss of 1 to 4 dB was evidenced.

---

* Allowing for possible degradation in the final assembly with the high band.

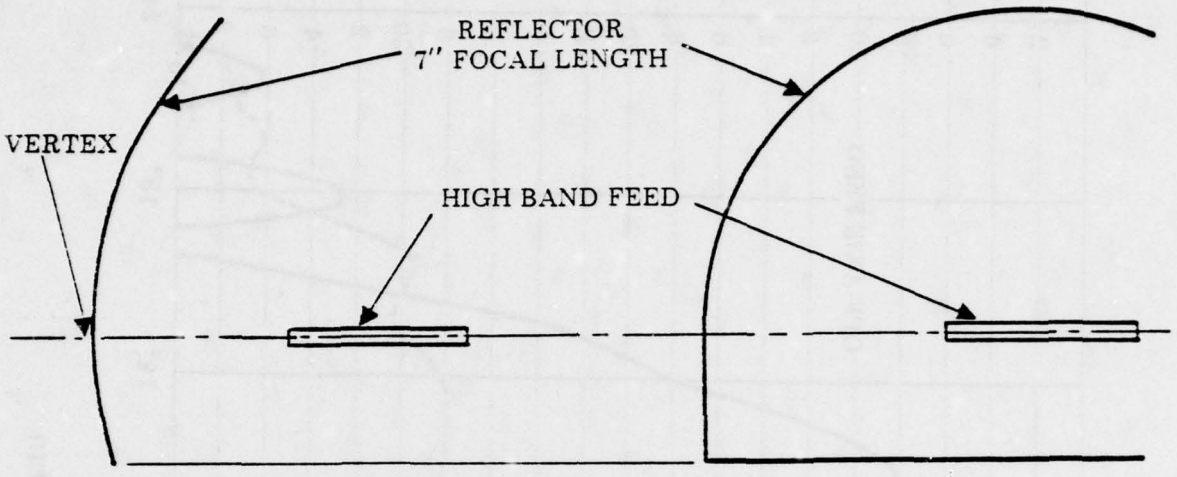

FIGURE 4-1a
ON AXIS FEED

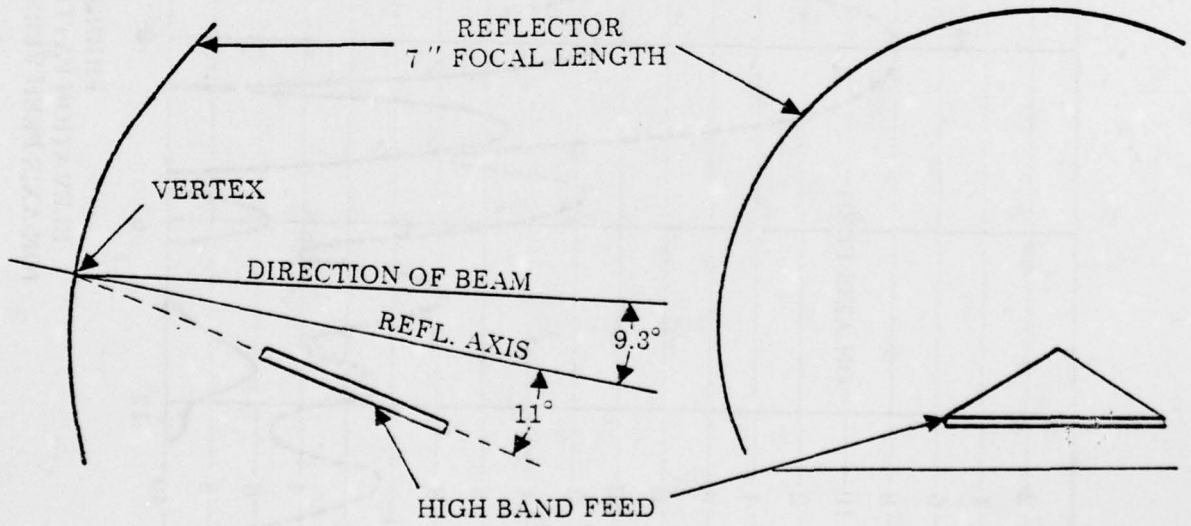

FIGURE 4-1b
OFF AXIS FEED

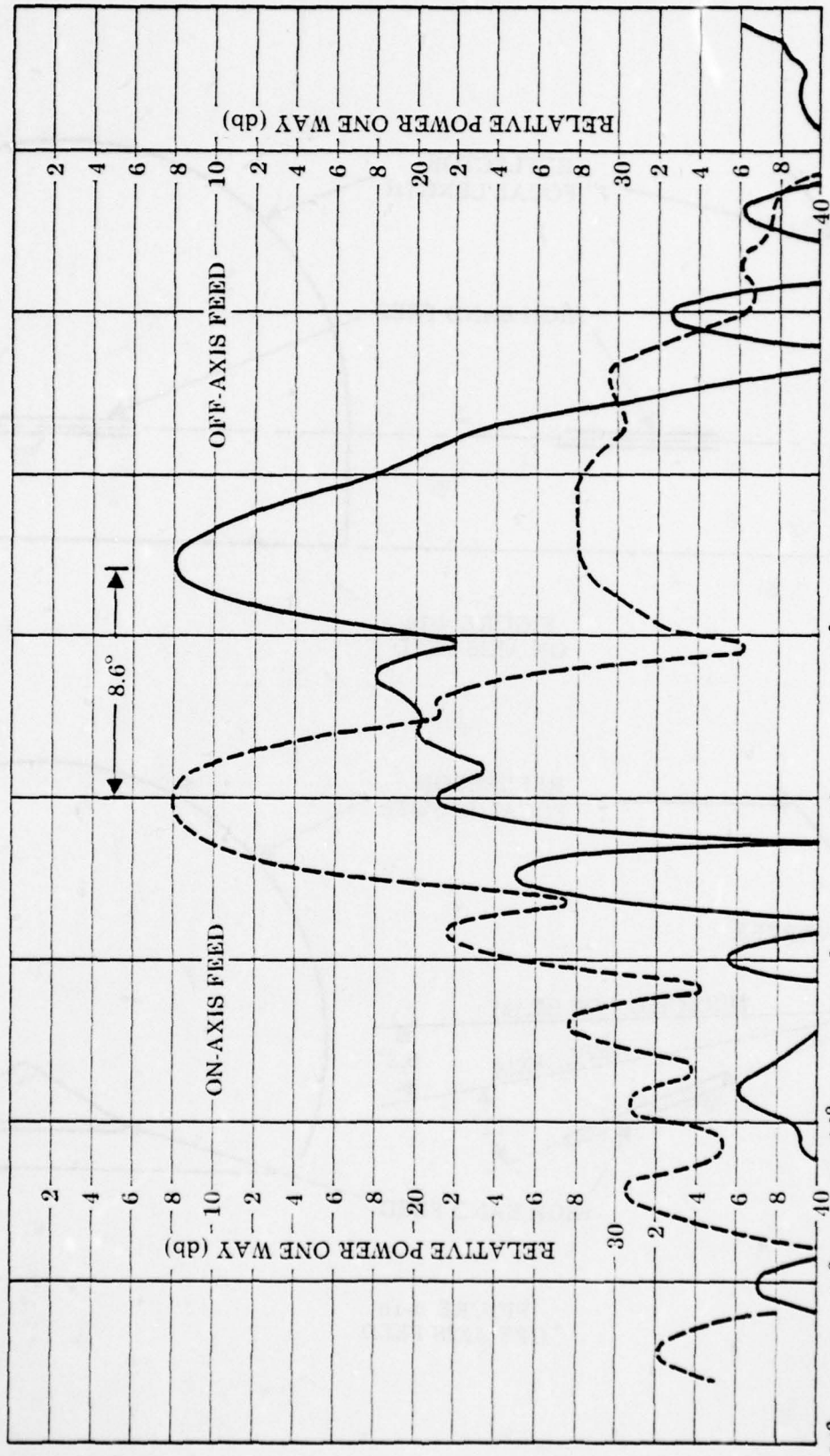

FIGURE 4-2
ELEVATION PATTERNS AT 14 Ghz.
(ON-AXIS FEED VERSUS OFF-AXIS FEED)

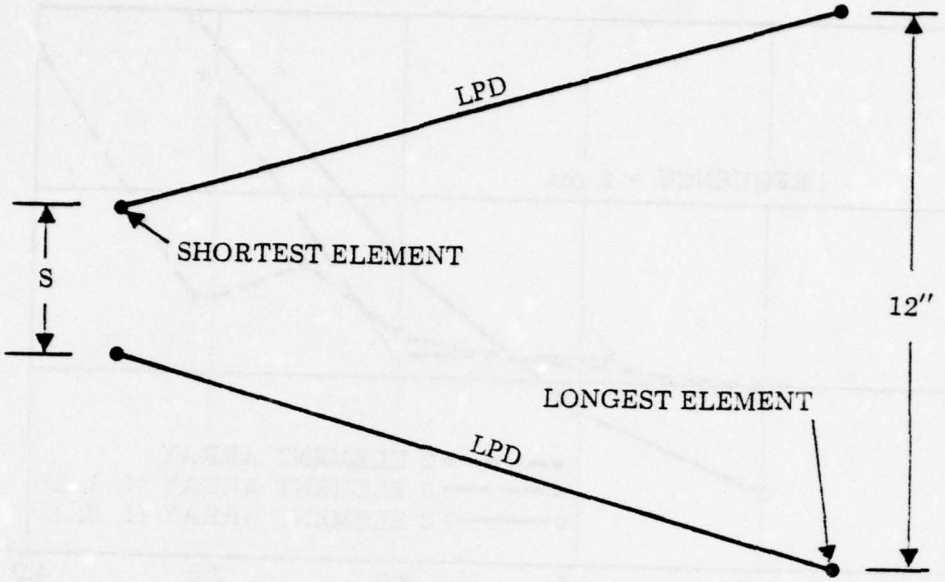

FIGURE 4-3a
TWO-ELEMENT ARRAY GEOMETRY

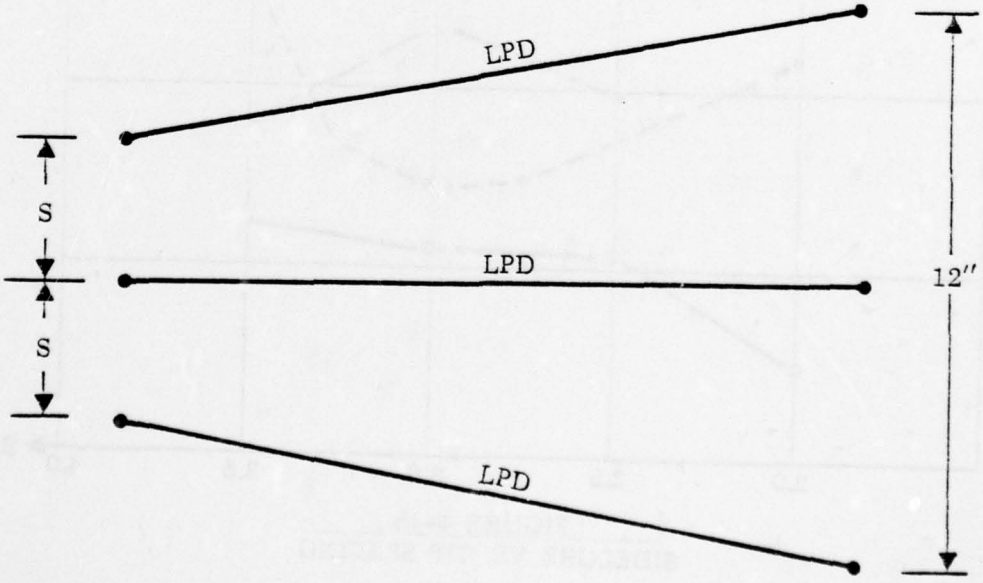

FIGURE 4-3b
THREE-ELEMENT ARRAY GEOMETRY

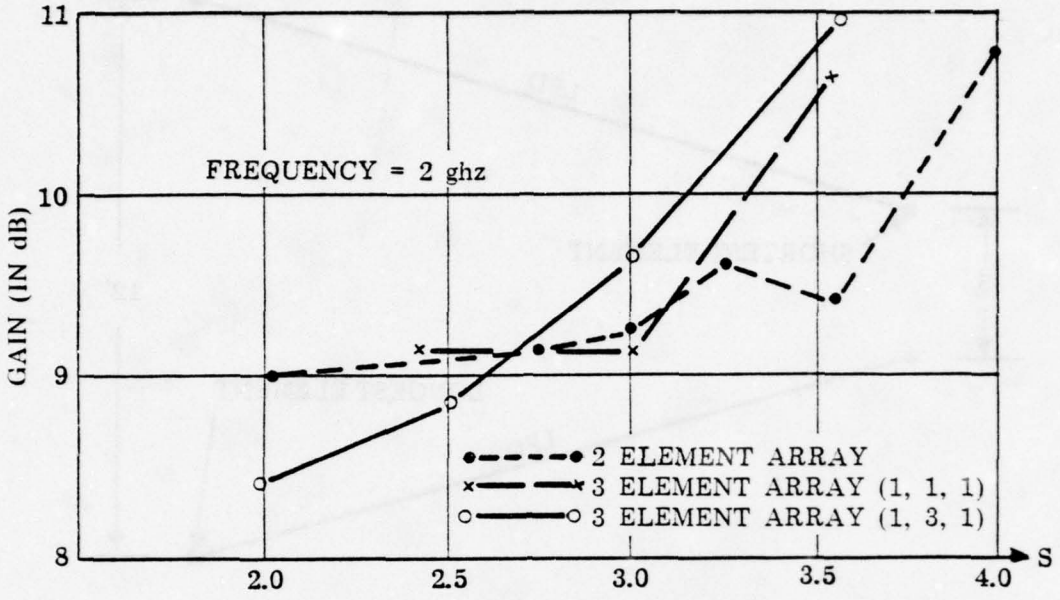

FIGURE 4-4a
GAIN VS. TIP SPACING

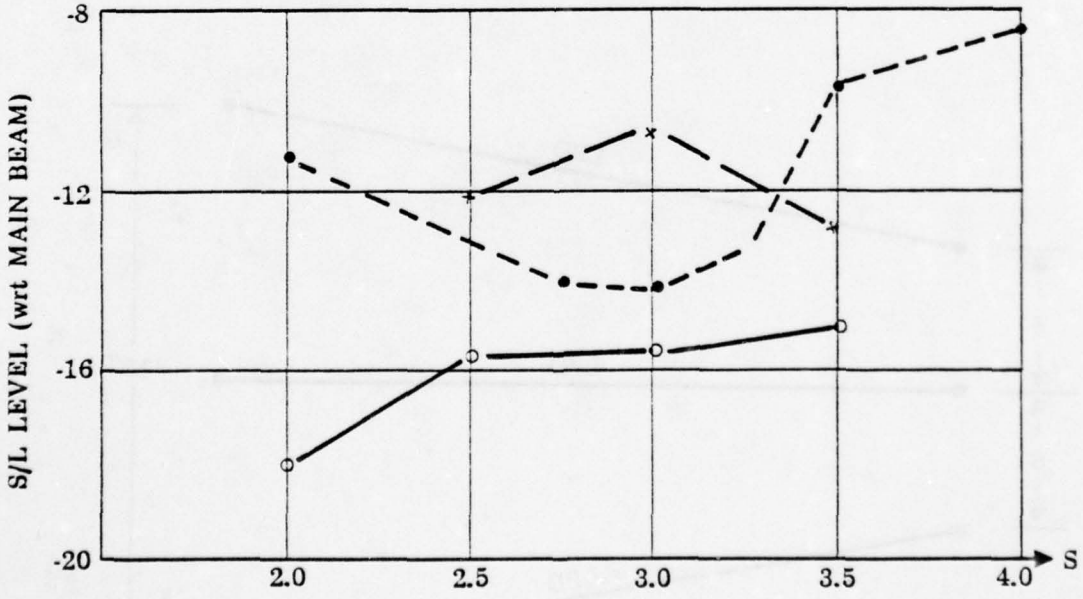

FIGURE 4-4b
SIDELOBE VS. TIP SPACING

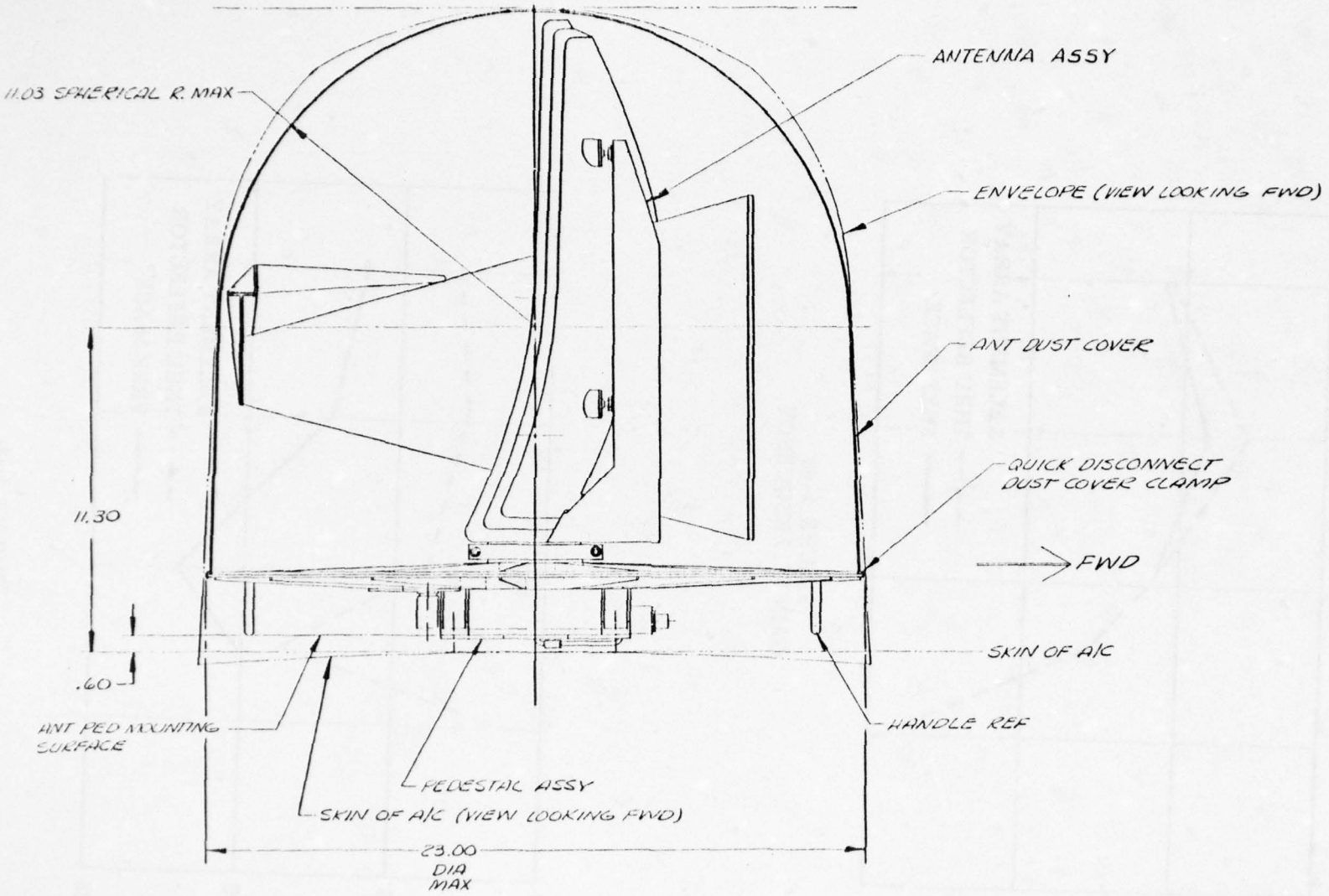

FIGURE 4-5
TOTAL SYSTEM ASSEMBLY

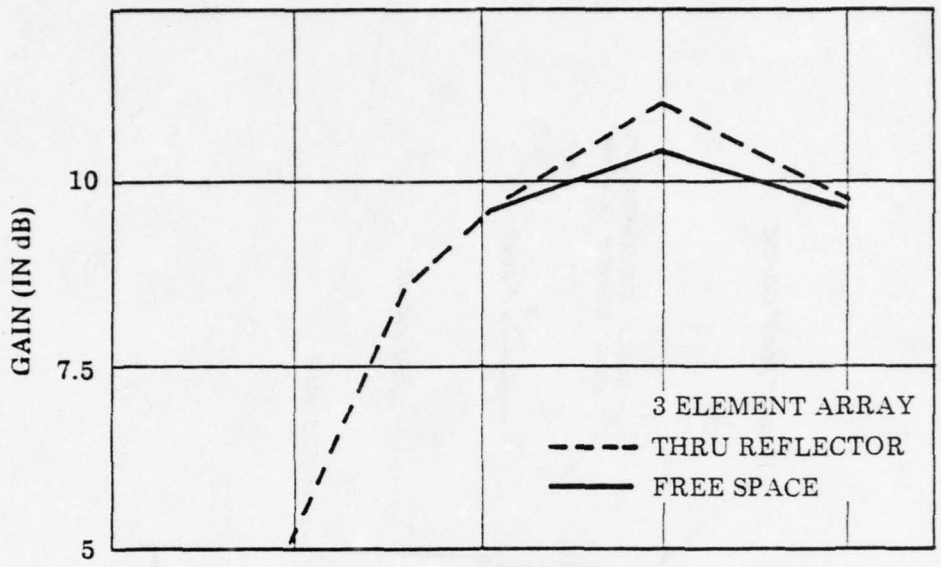

FIGURE 4-6a
GAIN VS. FREQUENCY

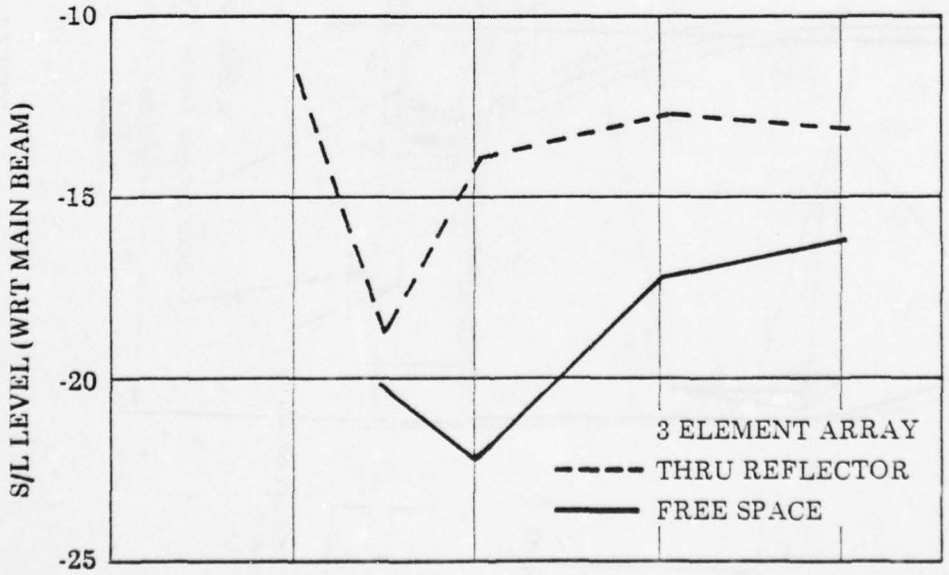

FIGURE 4-6b
SIDELOBE VS. FREQUENCY

5.0 CONCLUSION

In Figure 3-2, gain for a parabolic reflector of reduced size was modelled. Figure 5-1 shows the measured gain curves for the "look-through" antenna. Of particular significance is the marked improvement in efficiency at the low end of the low band.

Ultimately, a dual-channel rotary joint would be utilized to allow simultaneous low and high band monitoring. This and the fact that the low and high band main beams are codirectional realizes significant improvement over current back-to-back dual band steerable systems. It is possible that this "look-through" scheme may provide solutions to many of today's airborne, limited volume, high gain antenna dilemmas.

REFERENCES

1. Silver, S., Microwave Antenna Theory and Design, Radiation Laboratory Series, Vol. 12. New York: McGraw-Hill Book Co., Inc., 1950.

2. Smith, Carl E., Log Periodic Antenna Design Handbook, Cleveland, Ohio: Smith Electronics, Inc., 1966.

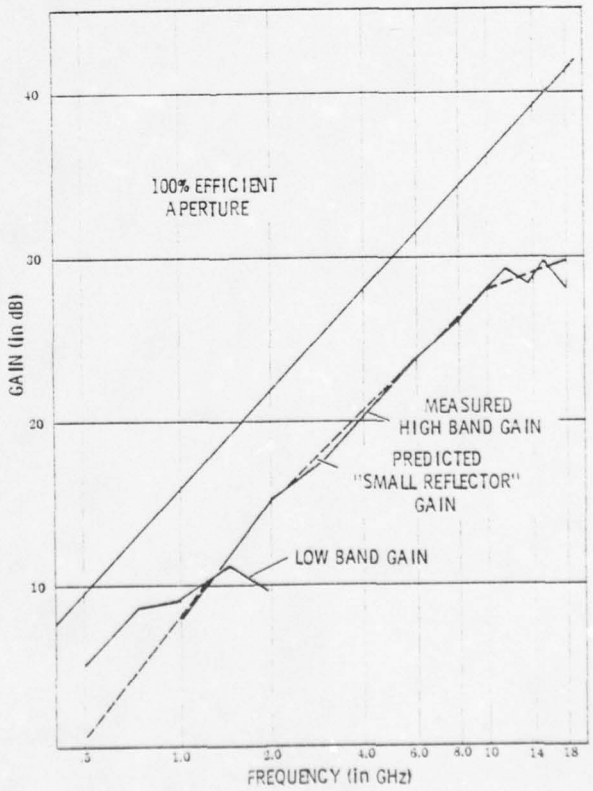

FIGURE 5-1
FREQUENCY FOR TOTAL SYSTEM

AD-A077 167 ILLINOIS UNIV AT URBANA-CHAMPAIGN ELECTROMAGNETICS LAB F/G 17/9
PROCEEDINGS OF THE ANTENNA APPLICATIONS SYMPOSIUM (1979) HELD 2--ETC(U)
SEP 79 F19628-79-M-0015
UNCLASSIFIED NL

5 OF 6
ADA 077167

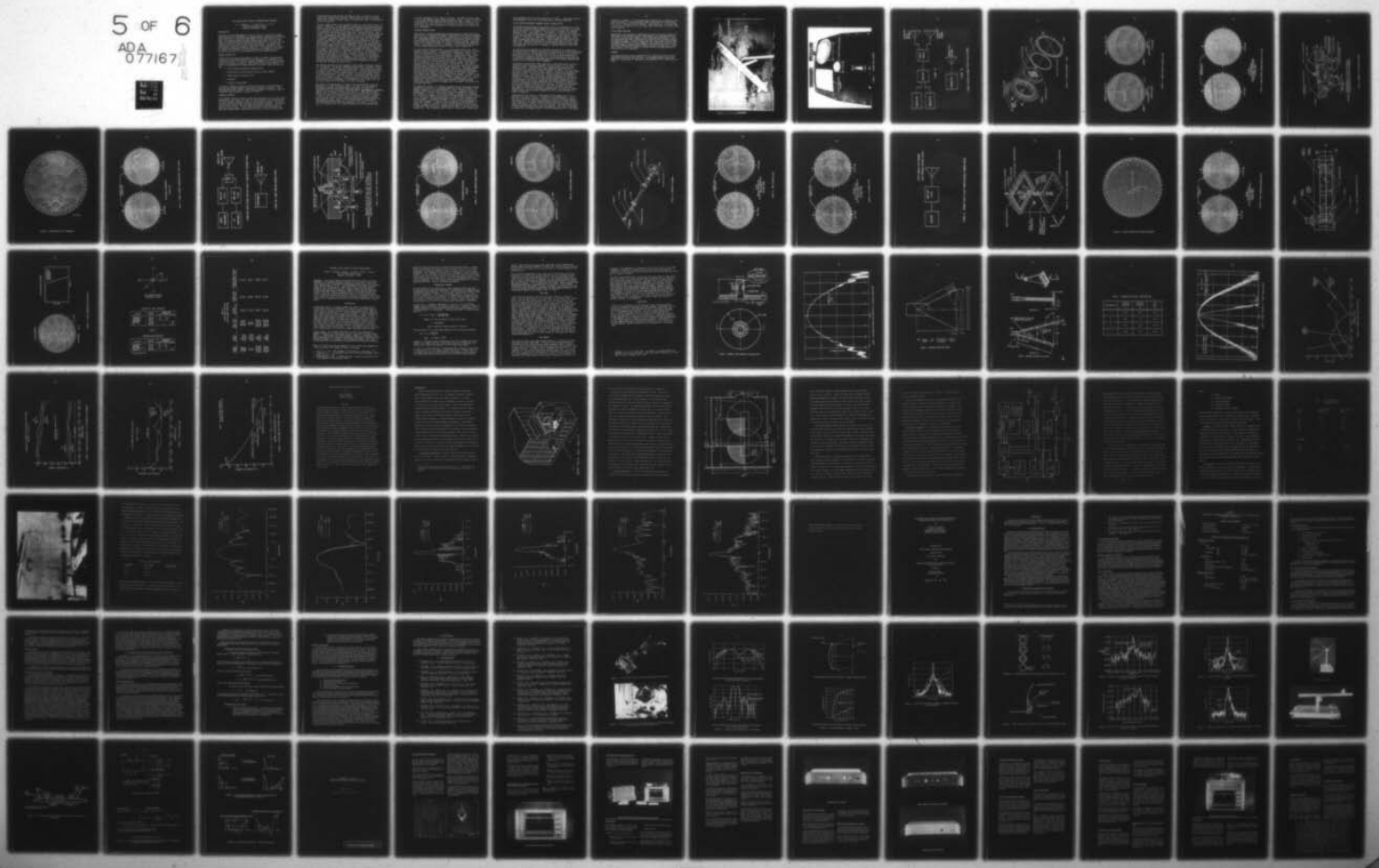

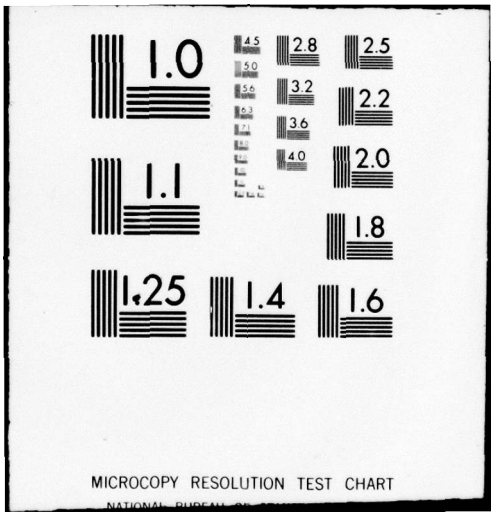
1.0
1.1
1.25
1.4
1.6
1.8
2.0
2.2
2.5
2.8
3.2
3.6
4.0
4.5
5.0
5.6
6.3
MICROCOPY RESOLUTION TEST CHART

AIR LAUNCH CRUISE MISSILE INSTRUMENTATION ANTENNAS

R. E. Lantagne, J. P. Grady and G. E. Miller
The Boeing Aerospace Company
Seattle, Washington 98124

INTRODUCTION

Concurrent with the development of the Air Launch Cruise Missile (ALCM), specifications for instrumentation antennas/antenna systems were established which would fulfill the unique requirements of the ALCM flight test program. The antennas/antenna systems developed were required to be small, efficient radiators which exhibited high reproducability, low cost, and low impact upon the air frame of the flight test vehicle. In addition the antennas were required to operate without performance degradation over a wide range of severe environmental conditions. The mechanical and electrical design and performance of the antennas/antenna systems which fulfill the ALCM flight test R.F. performance criteria are presented herein.

GENERAL DESCRIPTION

Flight line installation requirements, as well as thermal considerations, dictated that the antennas/antenna system components be configured on the flight test vehicle in a tightly grouped arrangement and yet simultaneously satisfy the pattern coverage and inter-system isolation requirements. The specific instrumentation systems employed on the ALCM flight test vehicle are:

* Flight Termination/Remote Command Control
* High Accuracy Multiple Object Tracking System (HAMOTS)
* Identification Friend/Foe (IFF)
* Telemetry
* Tracking (C-Band Radar)

The specific antenna locations on ALCM are exhibited in the photograph of the full-scale antenna pattern range model displayed in Figure 1. The instrumentation door assembly, which may be uploaded into ALCM for specific flight test configurations, is shown in Figure 2.

TELEMETRY ANTENNAS

Two different telemetry antenna systems were developed for use on the instrumented ALCM's (See Figure 3): one is a single annular slot system and one is a dual antenna system consisting of two microstrip patches. The single antenna system was designed to provide omni-azimuth coverage in the horizon sector of the vehicle. The dual antenna system was designed to provide good spherical coverage. This second system was a later requirement to meet the expanded need to transmit data not only to ground stations (best

accomplished with good horizon coverage) but also to transmit to chase planes and airborne relay stations. These latter two types of stations could have a variety of aspect angles to the vehicle; thus a more spherical pattern was desired.

The dual system, which is the one used on most all of the test flights, is shown in Figure 3A. The two antennas are the same design except for window contours and thicknesses and minor related impedance matching differences. One is located on the top centerline of the vehicle at Station 53 and one is located near the bottom on the right side at about Station 46. See Figure 1 for a view of the antenna locations. The lower antenna is mounted in the instrumentation door (See Figure 2) and as such can be installed with the door from under the ALCM on the flight line. The upper antenna is normally attached to a adapter ring which also permits it to be installed from under the vehicle through the access provided by the instrumentation door. This flight line installation capability is a feature which permits rapid change from an operational to an instrumentated flight. Each antenna element is a linearly polarized, rectangular microstrip patch on a 0.3 inch thick Teflon-Fiberglass circuit board as shown in Figure 4. The element is contained in a housing and covered with a Teflon-Fiberglass window whose outer contour is flush with the vehicle. The antenna is compact and was designed to fit within the cutout in the door originally provided for the annular slot design. The two antennas are oriented so that their polarizations are orthogonal. The top unit is longitudinally polarized; the bottom unit is circumferentially polarized. This relationship was chosen to provide the best pattern coverage with minimum overlap and the fewest aft sector nulls.

The antennas operate over the standard S-band telemetry frequency range of 2.2 to 2.29 GHz. The typical impedances of both units are shown in Figure 5. The VSWR's are well under 2:1 over the band. Each antenna can handle 3 kW peak at altitudes up to 98,000 feet (MSL). Typical transmitter powers are under 5 watts. Figure 6 shows vehicle roll and pitch plane patterns of the antenna system. As shown in Table I, the system provides a directivity of at least -13.4 dBI for RHCP and -13.8 dBI for LHCP over 95 percent of the radiation sphere. Over 95 percent of the horizon sector for θ angles from 30 to -60 degrees, a RHC directivity of at least -14.8 dBI and a LHC directivity of at least -14.9 dBI is provided.

The annular slot design shown in Figure 7 and described herein was not employed in its final form on the ALCM. This was due to the change to the broader coverage requirements mentioned before. A previously developed version of the annular slot with similar performance was employed, however, on nine special Jettision Test Vehicles. These vehicles were used to test the separation characteristics of the ALCM from its carrier. The earlier version of the annular slot differed from the one in Figure 7 in that it had a molded silicon rubber window which covered a separate metal aperture plate. The new design was developed and tested during the instrumentation design phase. It is a larger version of the C-band tracking antenna design described elsewhere in this paper. It has the same unique feature that its window and aperture are an integrated part.

A typical impedance plot is shown in Figure 8. The VSWR's are well under 2:1 over the standard S-band telemetry frequency range. The roll and pitch plane patterns of the antenna on the vehicle are shown in Figure 9. The system provides a RHC directivity of at least -12.4 and a LHC directivity of at least -12.5 over 95 percent of the horizon sector for θ angles from 30 to -60 degrees.

TRACKING ANTENNA SYSTEM

Three distinct tracking systems may be employed on any given ALCM flight test mission. The 908-928 MHz HAMOTS, 1030-1090 MHz IFF, and the 5400-5900 MHz C-band radar antennas provide for transmission and reception of coded R.F. transponder signals for the purpose of yielding real time air vehicle position data for range safety and flight evaluation purposes. Block diagrams of the systems are shown in Figure 10. Diplexing of the HAMOTS/IFF signals is provided by the pair of bandpass filters connected to the coaxial tee through appropriate lengths of coaxial cable (Figure 10A).

The ALCM C-band tracking antenna is a cavity-backed annular slot, flush mounted on the air vehicle. Its approximate location is Station 39 on the vehicle bottom centerline. Polarization is predominately linear. The cavity is excited by a conical feed element. Capacitive tuning is accomplished by connection of an annular plate to the feed cone. Inductive tuning results from attaching tuning pins to the capacitive plate and by employing inductive tuning straps in the aperture. The radiating annular slot is etched on a 1/8" thick Teflon-Fiberglass radome. The radome is shaped to fit the local vehicle contour. The cavity is filled with a uniformly dense foam which maintains a moisture free interior and provides added structural rigidity to the interior components. The design concept provides for making the cavity an integral part of the instrumentation door and ensures consistently good electrical and mechanical performance. Connection to the antenna is provided through an SMA female connector (MIL-C-39012 type) purchased to a commercial part number. A sketch of the construction of the C-band tracking antenna is shown in Figure 11. Typical antenna patterns appear in Figure 12. Input impedance data is given in Figure 13A. Table I displays the antenna pattern coverage provided. Power handling was tested to be greater than 3.3 kW peak (.001 duty cycle) at 65,000 feet (MSL).

The HAMOTS/IFF antenna is a linearly polarized quarter wavelength monopole mounted at Station 20, on the bottom centerline of the air vehicle. The monopole element is a rod, approximately .2 inch in diameter, which is perpendicular to the air vehicle skin surface and extends to a height of approximately 2.5 inches. The antenna element is mechanically attached to a cylindrical aluminum cavity, which is flange mounted to the air vehicle skin. The cavity contains an epoxy glass dielectric that surrounds the element assembly. The monopole element is fed via coaxial transmission line, down the center of the rod, which is attached to an SMA female connector (MIL-C-39012). A sketch of the construction of the HAMOTS/IFF antenna is shown in Figure 14. Typical antenna patterns for the antenna, at both the HAMOTS and the IFF frequencies are shown in Figures 15 and 16, respectively. Input impedance data is given in Figure 13B. Antenna pat-

tern coverage is given for both frequencies in Table I. Peak power handling was determined to be 1.5 kW (.001 duty cycle) at 50,000 feet (MSL).

FLIGHT TERMINATION/REMOTE COMMAND CONTROL ANTENNA SYSTEM

The antenna system employed on the ALCM to provide a communication link for the flight termination/remote command control functions consists of a single UHF cavity backed C-slot antenna with an integral low pass and a separate bandpass filter. (See Figure 17). The antenna is located on the bottom left side of the ALCM at approximately Station 45. The cavity of the antenna is cast and machined into the basic instrumentation door assembly. (See Figure 2). The cavity is fed with an inductive loop and tuned with a concentric sleeve-type capacitive tuner. These assemblies along with the low pass filter assembly are mounted in the cavity and foamed in place. (See Figure 18). One end of the low pass filter provides the output feed from the antenna and the other end is adapted to connect directly to the inductive feed loop.

The radiating C-slot aperture is fabricated by etching it on copper clad (one side) Teflon Fiberglass sheet which is machined to fit flush with the local air vehicle contour. The aperture plate (radome) is bolted to the instrumentation door structure and capacitive tuner and uniformly compresses an O-ring gasket to provide a moisture seal. Screws attached to the tuner are wet sealed on installation and areas around the filter output connector are potted to form a "moisture tight" assembly.

The antenna is electrically small because of volume restrictions and has a relatively narrow frequency bandwidth, 1.8% for a VSWR of 2:1 or less, based on 50 ohms. The capacitive tuner compensates for manufacturing tolerances and is capable of tuning the antenna to VSWR's of 1:5 to 1 or less over a frequency range of 480 to 496 MHz. Typically, the antenna VSWR was found to be 1:5 to 1 or less when tuned to an operating frequency of 487 MHz $\pm$ 0.7 MHz. (See Figure 19). The polarization of the antenna is predominately linear with its E-Plane oriented orthogonal to the vehicle roll-axis. This orientation provides maximum energy radiation around the circumference of the vehicle, increasing the pattern coverage over the radiation sphere and allowing compliance with the spherical coverage directivity requirements using the single antenna. The antenna, when mounted on the ALCM, provides directivities of -16.5 dBI or better over 95% of the radiation sphere when viewed with left hand circular polarization. (See Table I). It has an efficiency exceeding 63%. Pitch and roll plane patterns taken with the antenna mounted on a full scale ALCM model are shown in Figure 20.

The low pass filter, which is integrated into the antenna cavity, is a maximally flat coaxial filter. It consists of seven elements, 3 capacitors and 4 inductors, developed coaxially on the filter center conductor. (See Figure 21). The filter center conductor assembly is fitted inside a Teflon tube which is loaded into the cylindrically bored housing and captivated using Teflon end plugs. The filter housing is moisture sealed using silicone rubber and epoxy based potting compounds. The filter is designed to operate over a frequency range of 175 MHz to 6000 MHz with a 3 dB cutoff

frequency of 936 MHz. In its passband the insertion loss is typically less than 0.2 dB while in the reject band (2200 to 6000 MHz) the filter insertion loss is typically 50 dB or greater. (See Figure 22). The input VSWR of the filter is typically 1.2:1 or less, based on 50 ohms, in the pass band (See Figure 22).

INTER-SYSTEM ISOLATION

Measurements were conducted to determine the level of coupling present between each of the antenna systems. Measurements were performed with the air vehicle pattern model placed inside a simulated B-52 bomb-bay since it was determined that this configuration resulted in the most severe antenna coupling environment. Table II summarizes the inter-system isolation data. The HAMOTS and IFF signal levels present at the output port of the Flight Termination/Remote Command Control antenna required the addition of a band pass filter, as shown in Figure 17, which provides a minimum attenuation of 55 dB from 918 to 5900 MHz.

SUMMARY

The antennas/antenna systems described in this paper are currently being flown upon ALCM flight test vehicles. The antennas/antenna systems are meeting, or exceeding, all performance requirements of the flight test program.

BEST AVAILABLE COPY
FROM COPY FURNISHED TO DDC

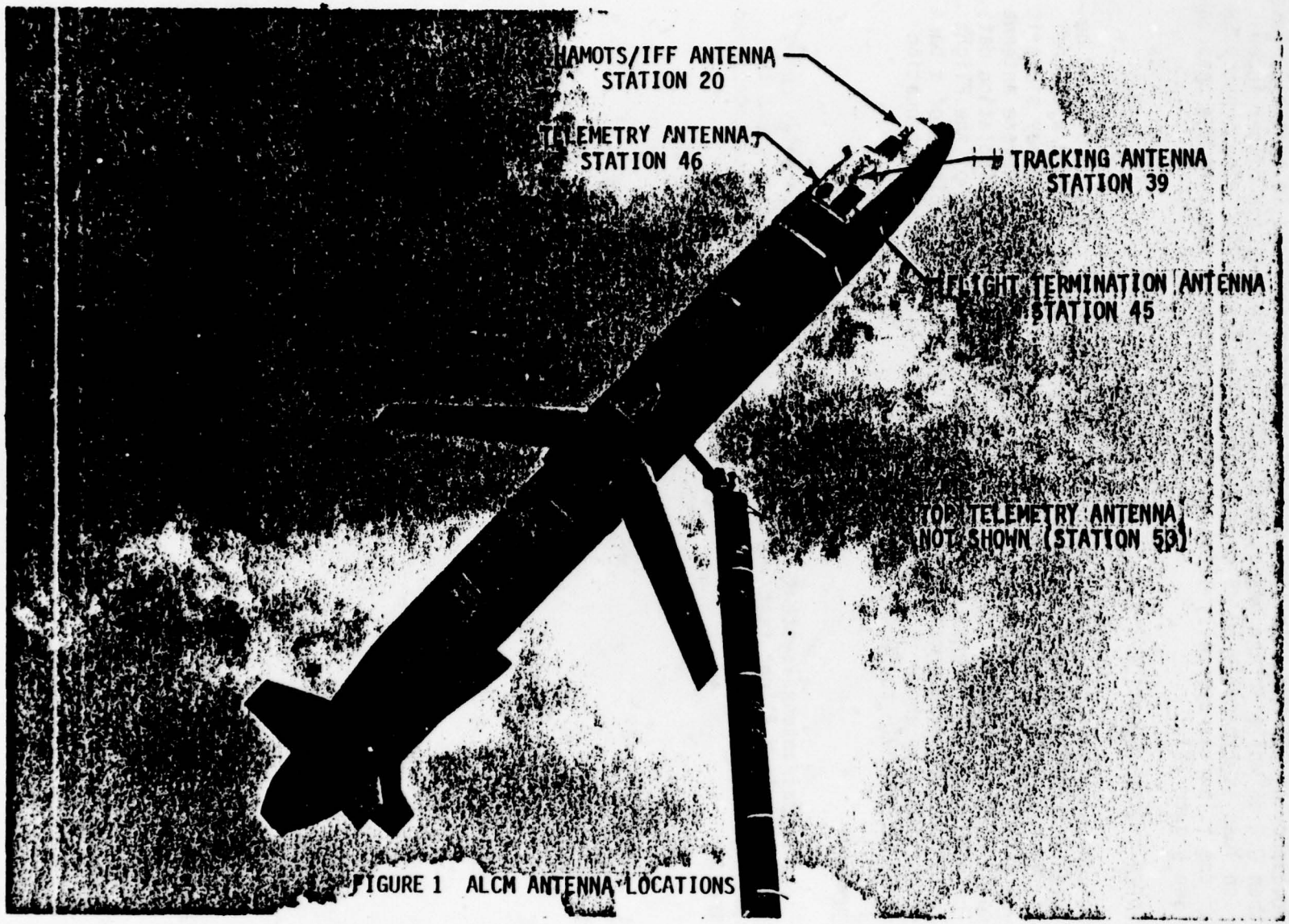

FIGURE 1 ALCM ANTENNA LOCATIONS

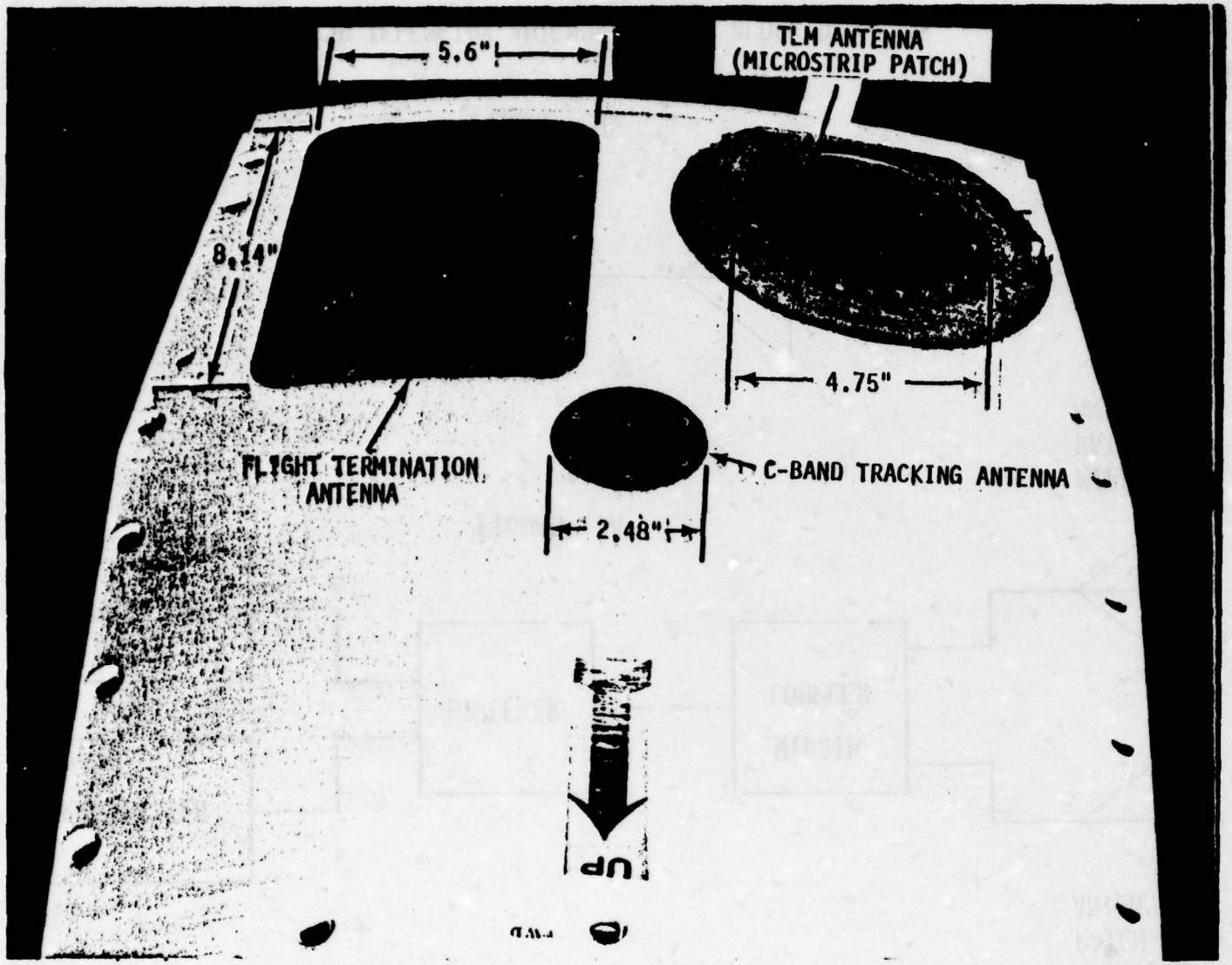

FIGURE 2 ANTENNA DOOR ASSEMBLY

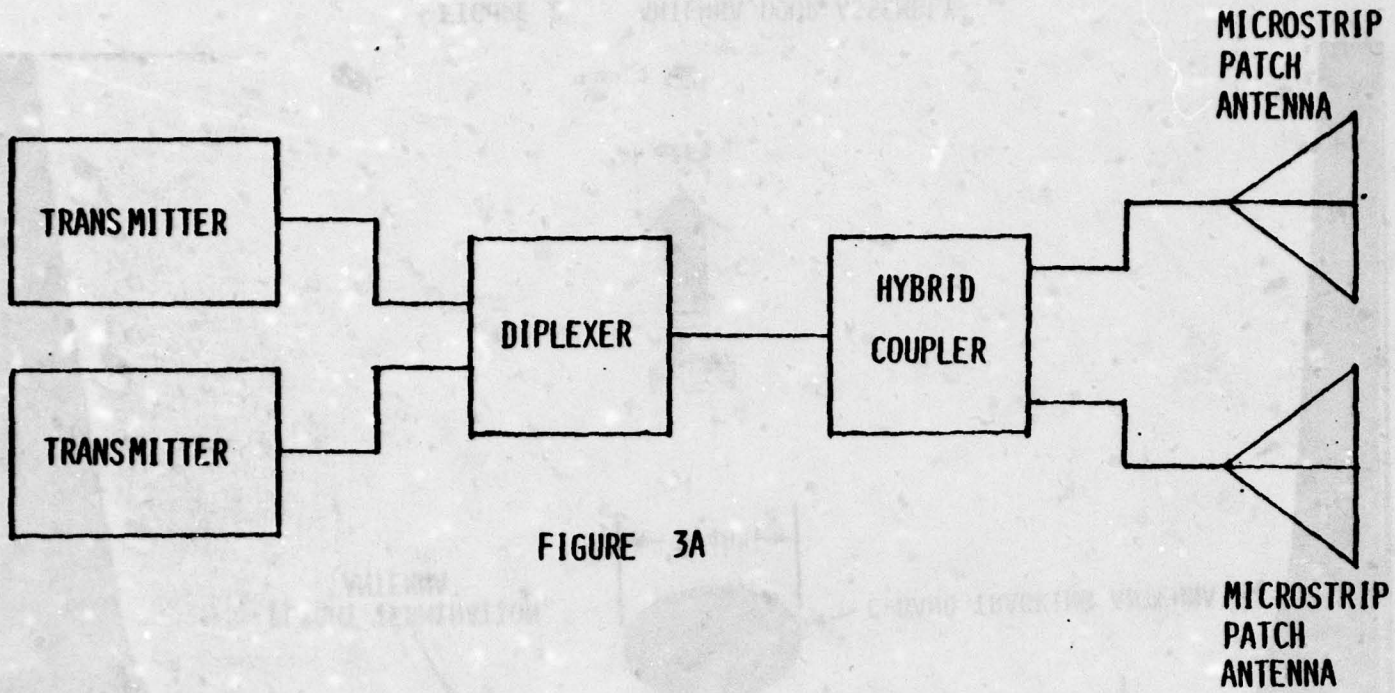

FIGURE 3A

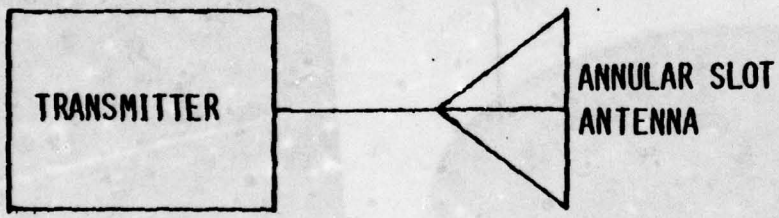

FIGURE 3B

S-BAND TELEMETRY ANTENNA SYSTEM BLOCK DIAGRAMS

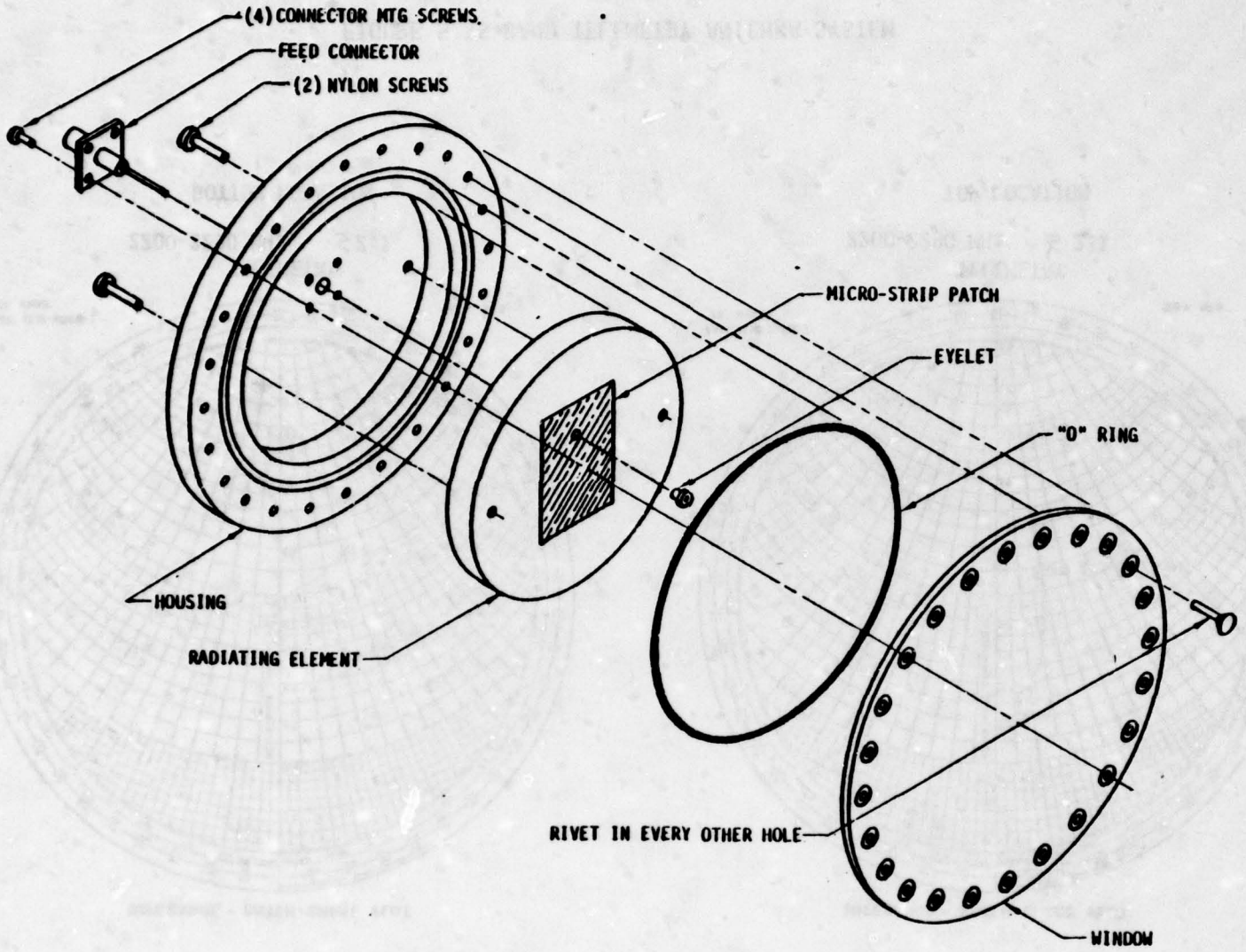

FIGURE 4 TELEMETRY ANTENNA - S-BAND

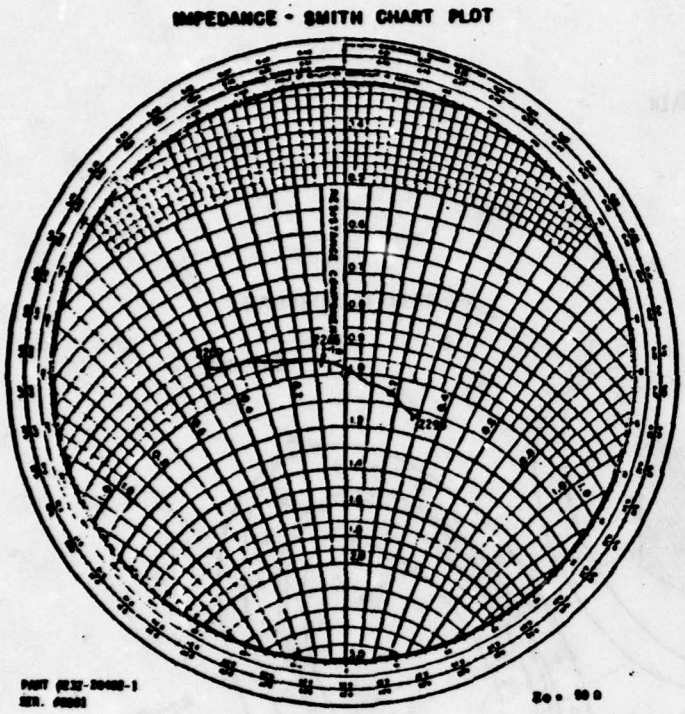

TELEMETRY
2200-2290 MHz ≤2:1

BOTTOM LOCATION

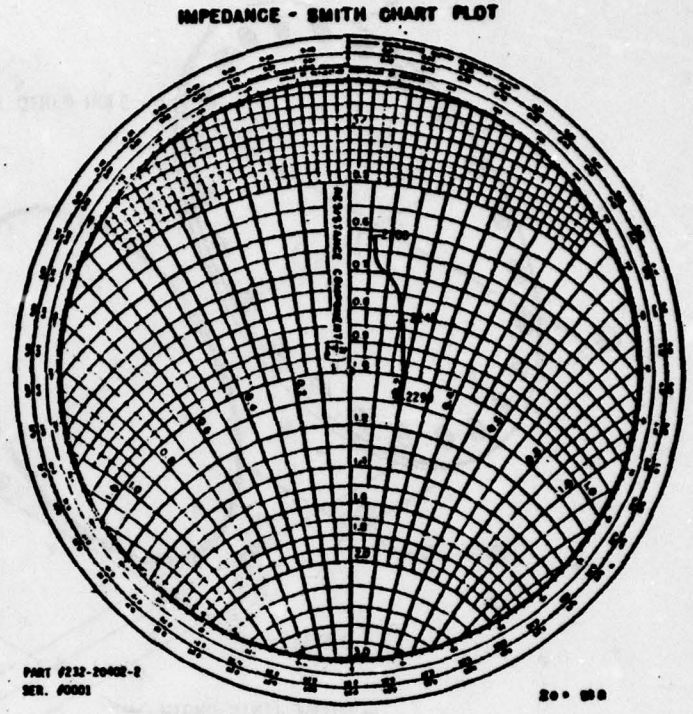

TELEMETRY
2200-2290 MHz ≤ 2:1

TOP LOCATION

FIGURE 5 S-BAND TELEMETRY ANTENNA SYSTEM

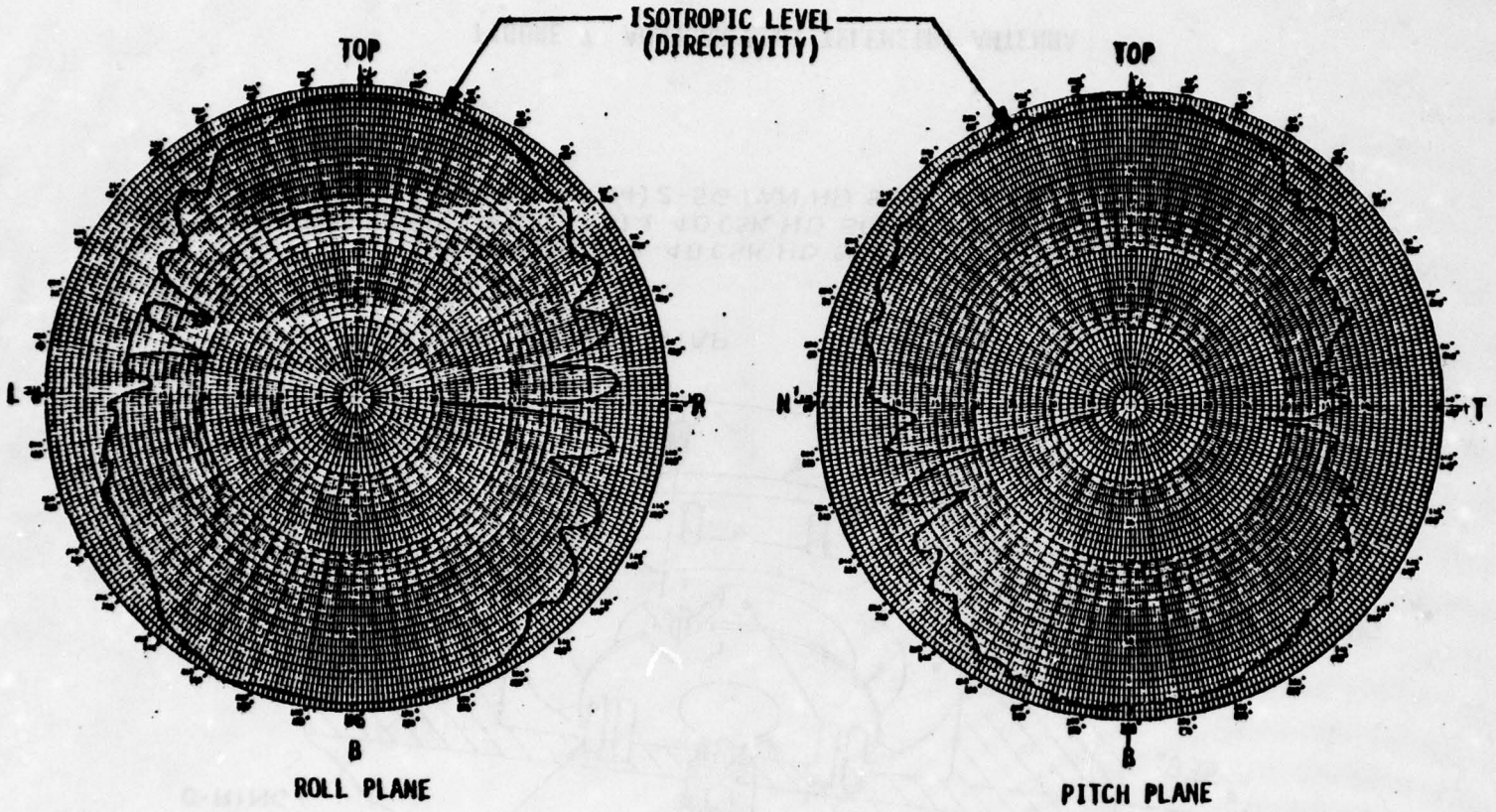

2215 MHz
RHC POLARIZATION
642-004 VEHICLE CONFIGURATION
STA 46 BOTTOM & STA 53 TOP
TOP MODEL MOUNT

FIGURE 6 S-BAND TELEMETRY ANTENNA SYSTEM DUAL ANTENNAS

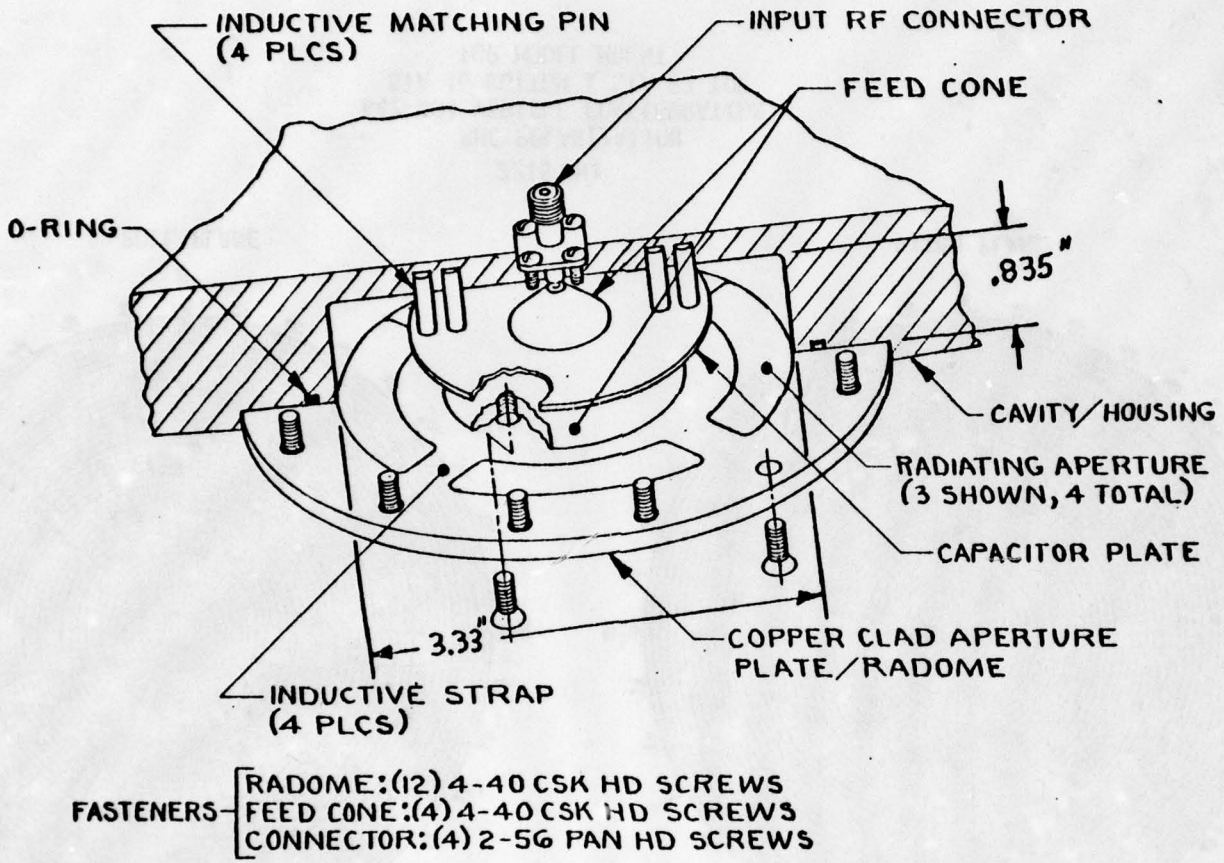

FIGURE 7 ANNULAR SLOT TELEMETRY ANTENNA

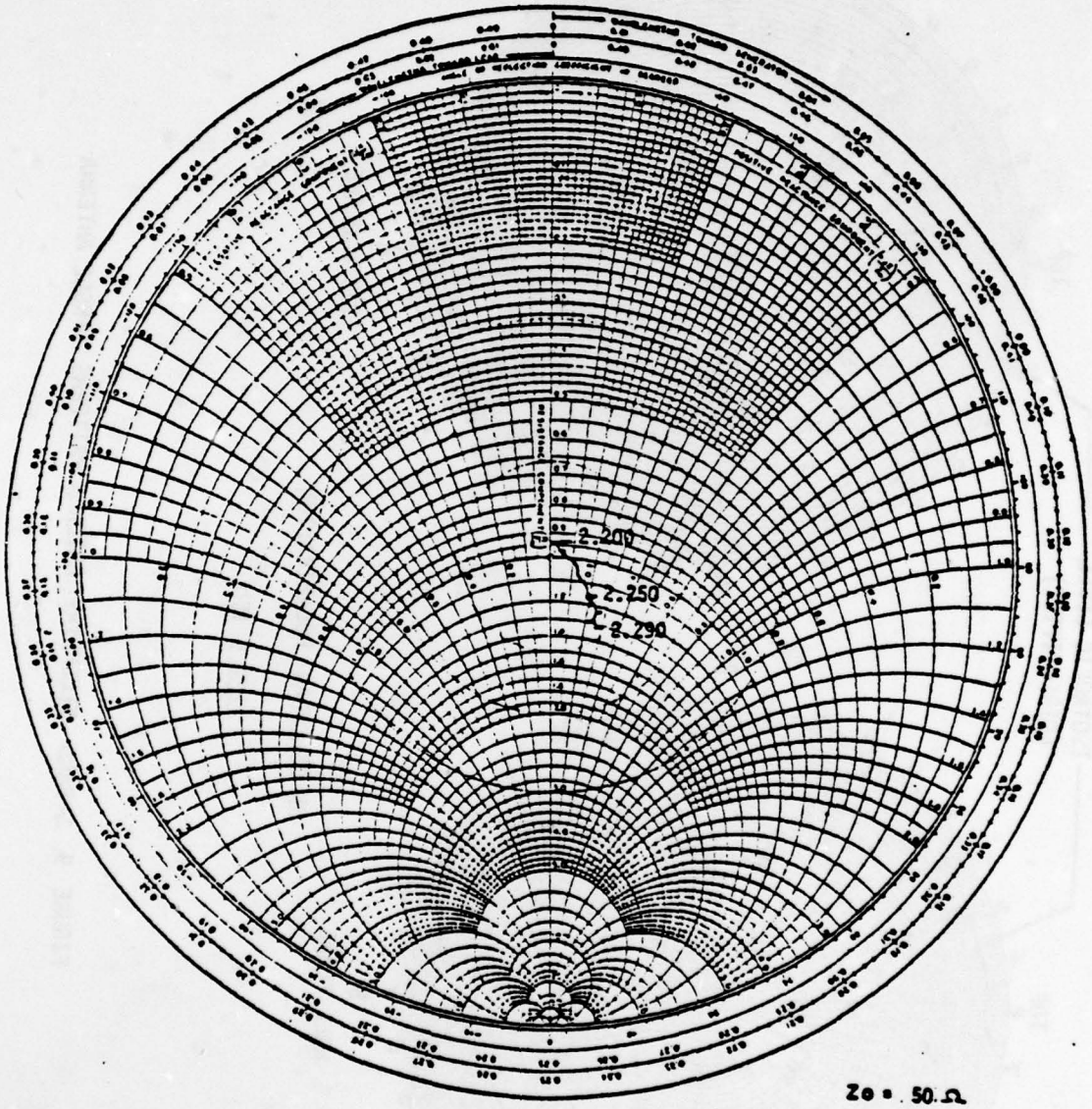

FIGURE 8 S-BAND ANNULAR SLOT IMPEDANCE

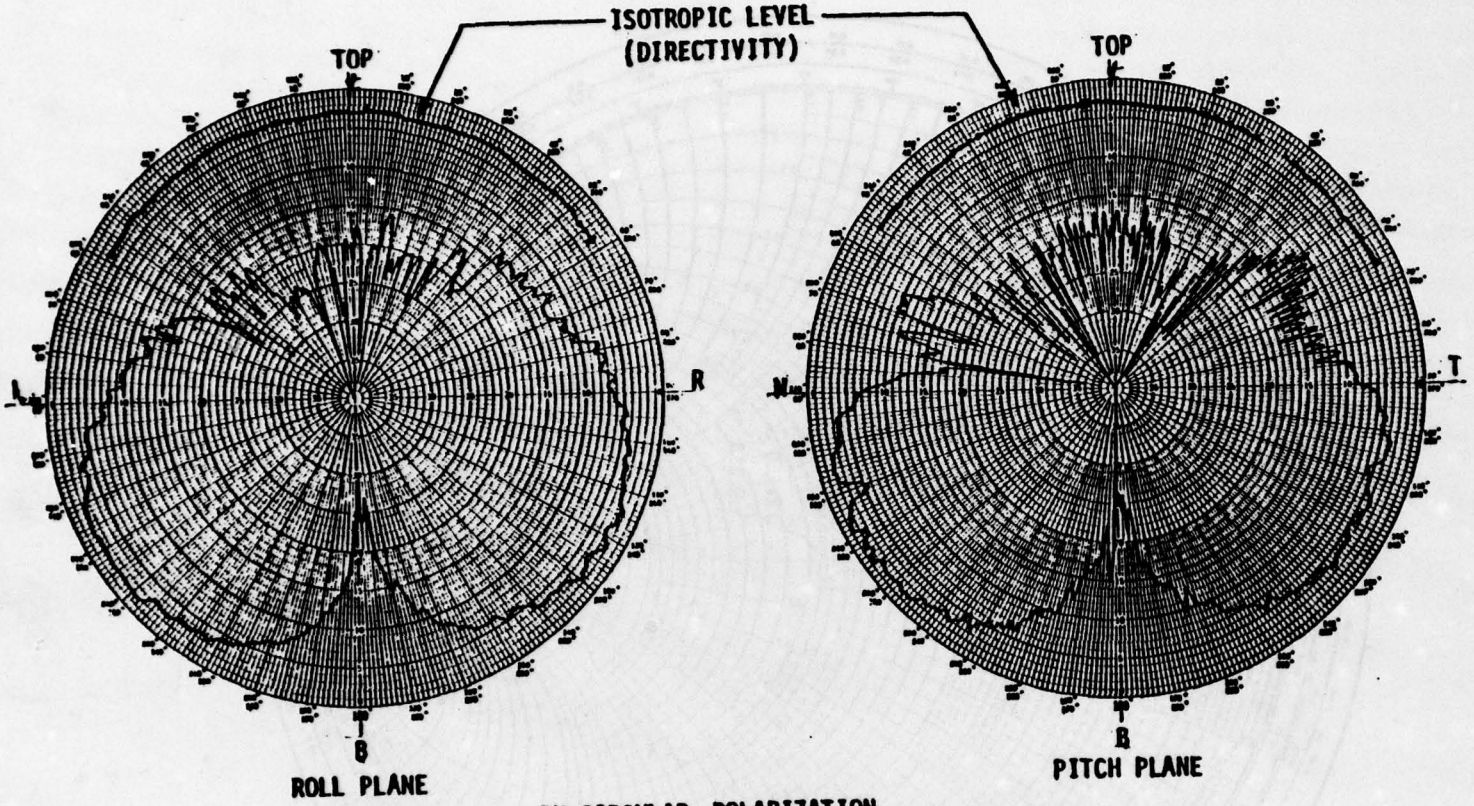

RH CIRCULAR POLARIZATION

2223.5 MHz

FIGURE 9 S-BAND TELEMETRY ANTENNA PATTERNS SINGLE ANTENNA

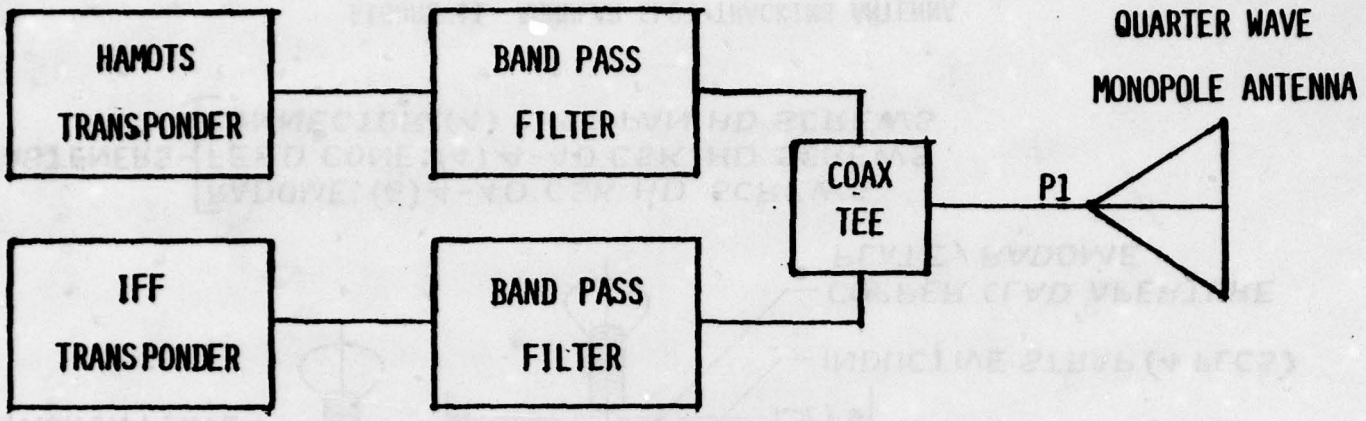

FIGURE 10A HIGH ACCURACY MULTIPLE OBJECT TRACKING/IFF ANTENNA SYSTEM

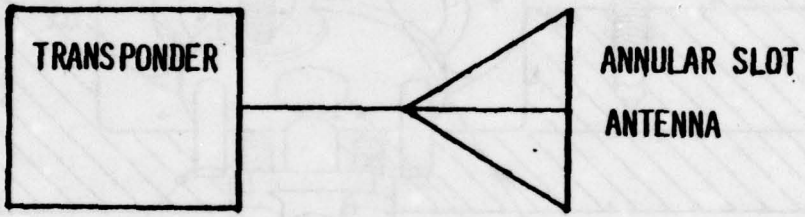

FIGURE 10B C-BAND TRACKING ANTENNA SYSTEM

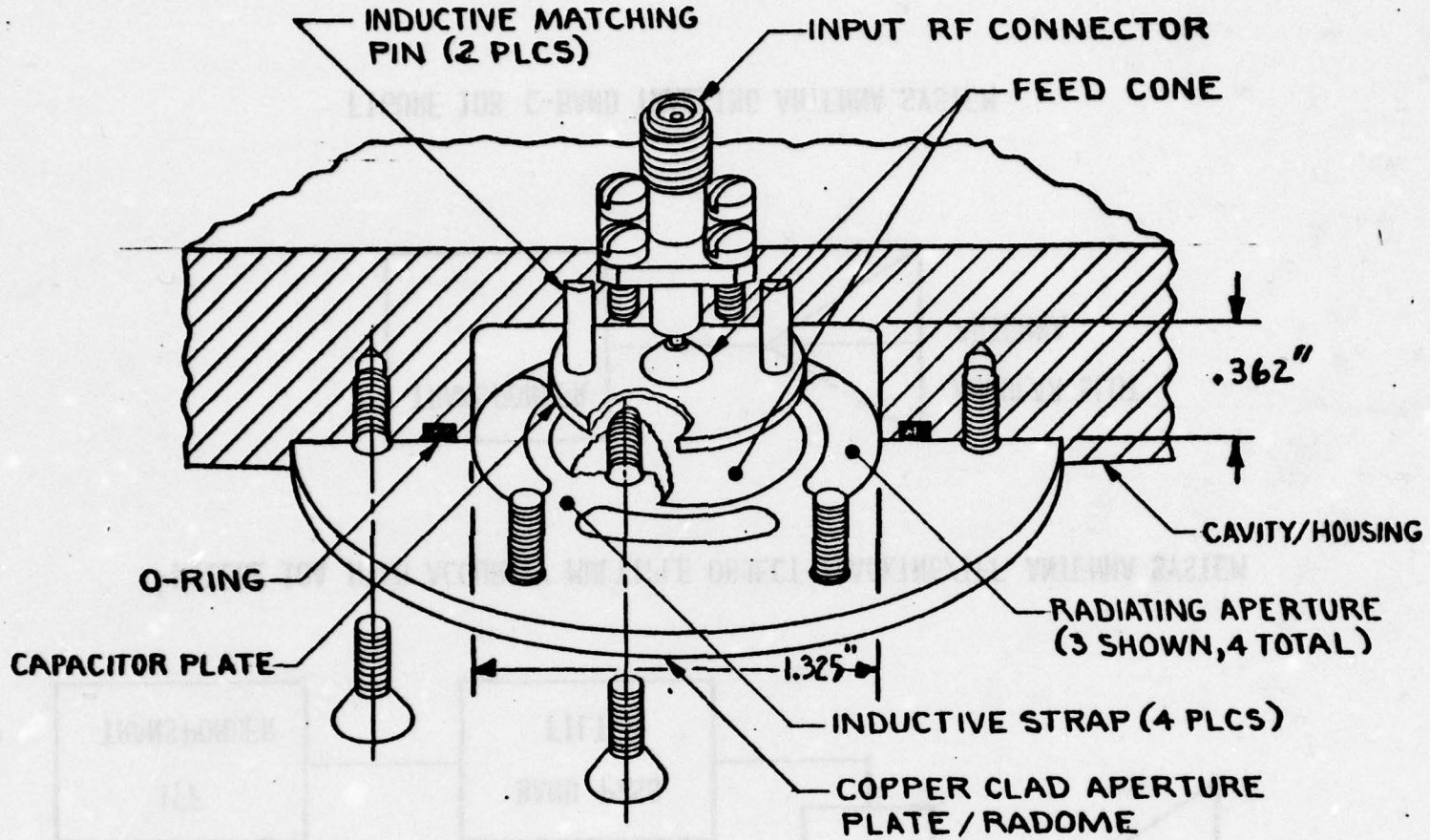

FASTENERS
- RADOME: (6) 4-40 CSK HD SCREWS
- FEED CONE: (4) 4-40 CSK HD SCREWS
- CONNECTOR: (4) 2-56 PAN HD SCREWS

FIGURE 11 ANNULAR SLOT TRACKING ANTENNA

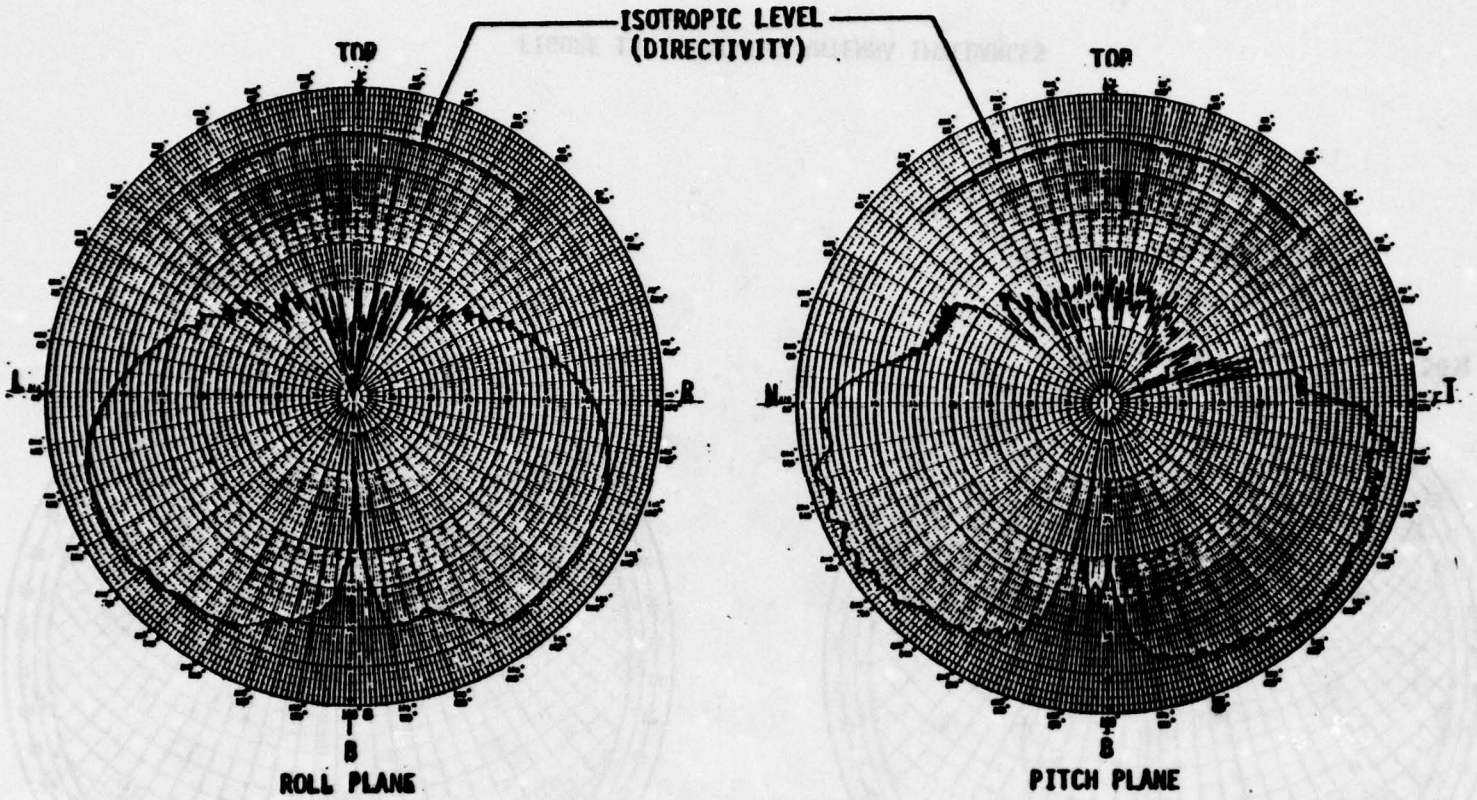

FIGURE 12 C-BAND TRACKING ANTENNA PATTERNS

C-BAND

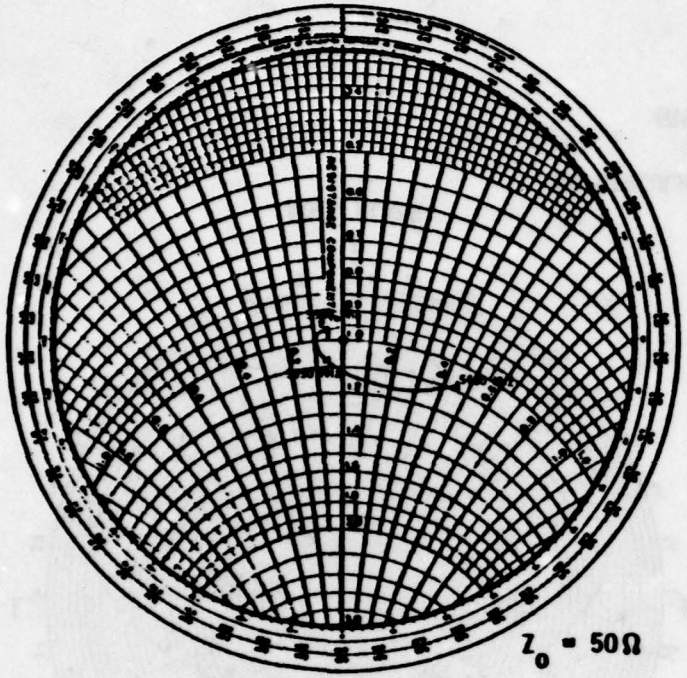

$Z_0 = 50\Omega$

5400-5900 MHz $\leq 1.5:1$

HAMOTS/IFF

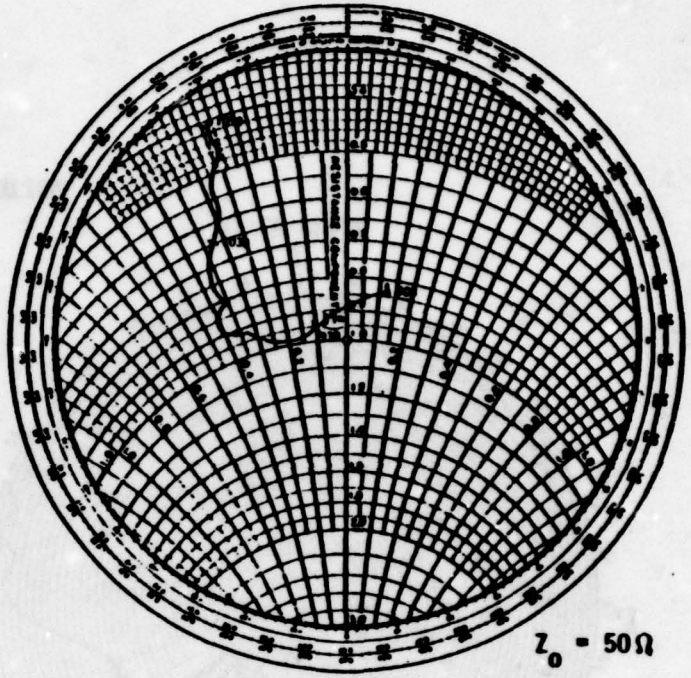

$Z_0 = 50\Omega$

908-928 MHz $\leq 2:1$

1030-1090 MHz $\leq 2.7:1$

FIGURE 13 TRACKING ANTENNA IMPEDANCES

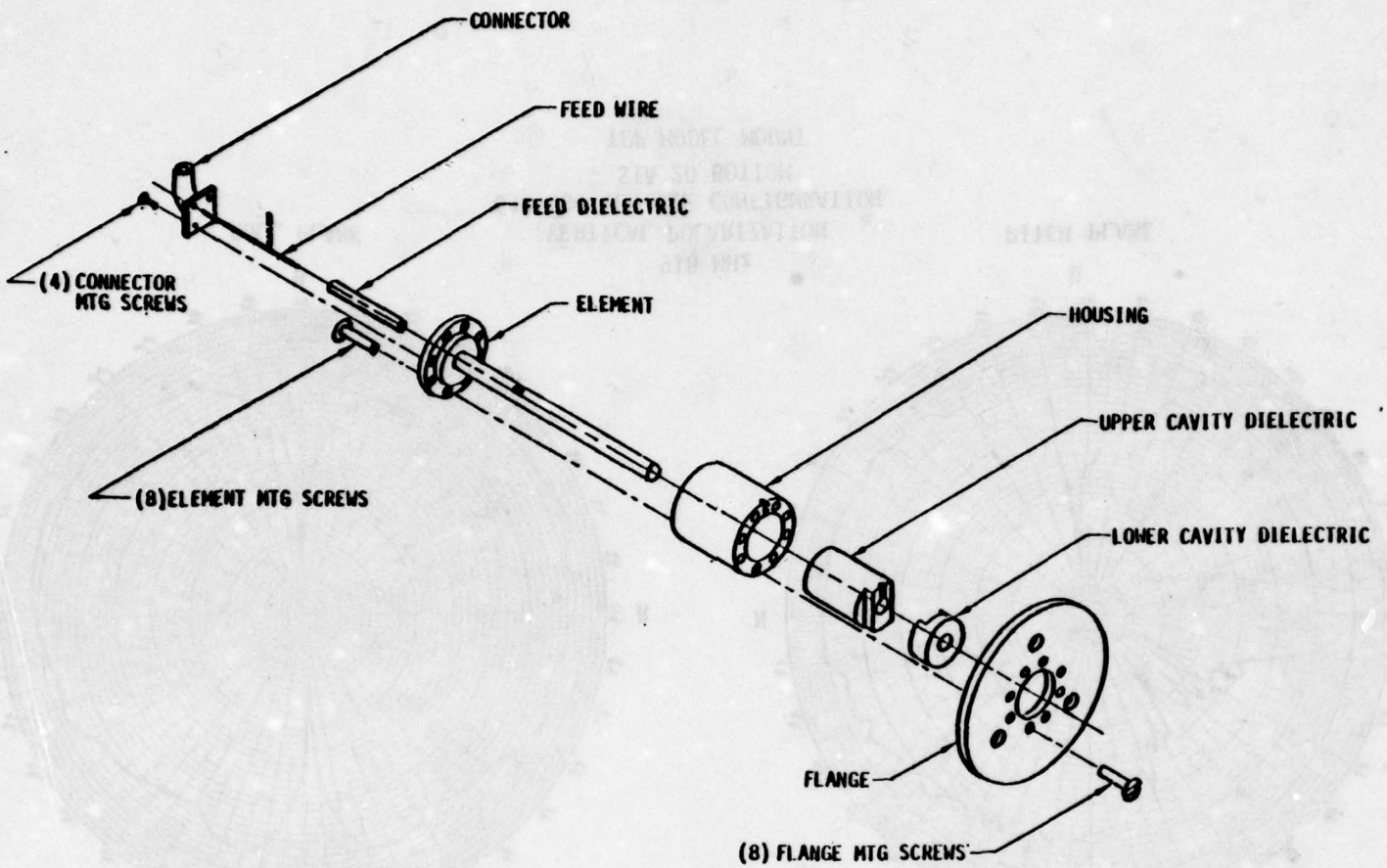

FIGURE 14 HAMOTS/IFF ANTENNA

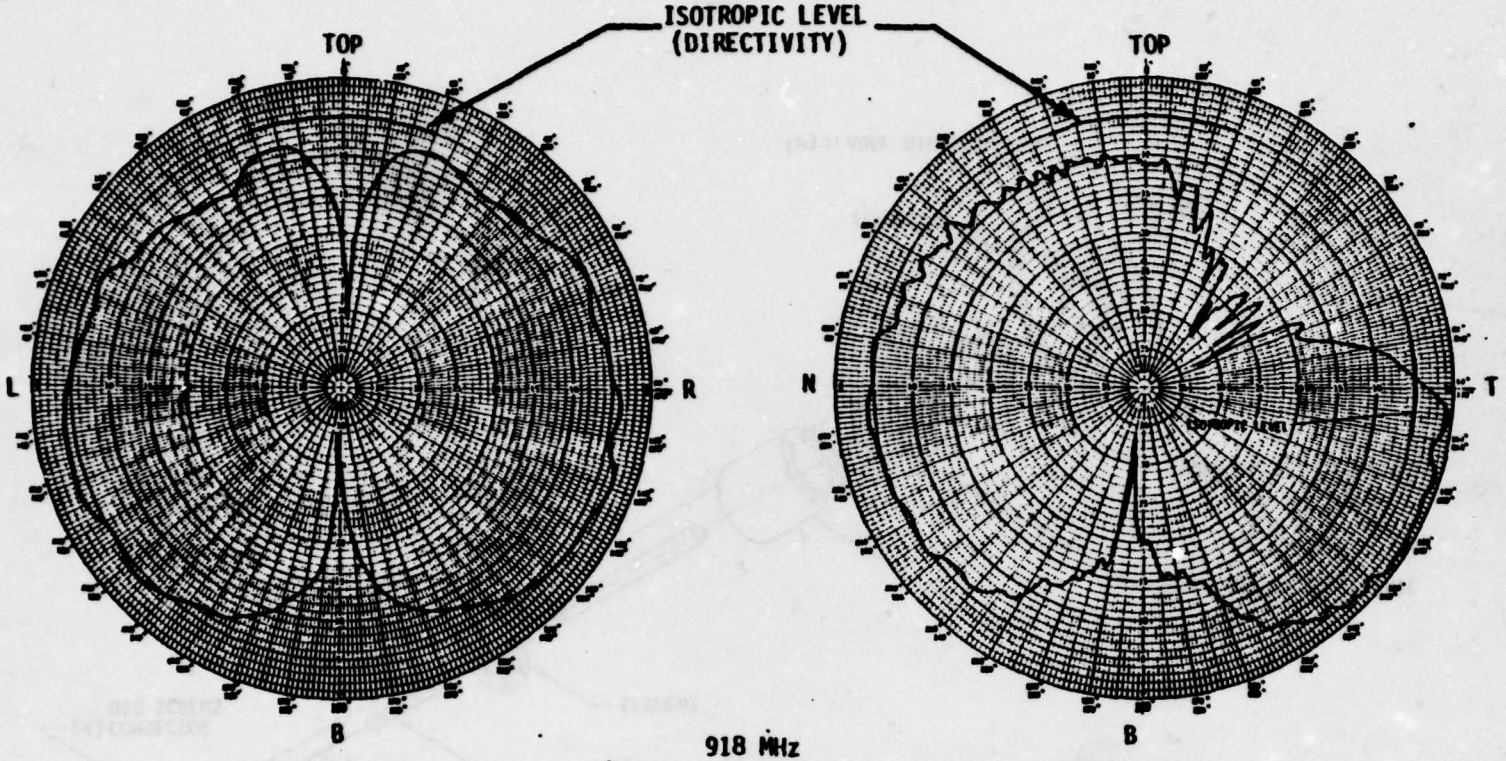

918 MHz
VERTICAL POLARIZAITON
642-004 VEHICLE CONFIGURATION
STA 20 BOTTOM
TOP MODEL MOUNT

FIGURE 15 HAMOTS ANTENNA SYSTEM

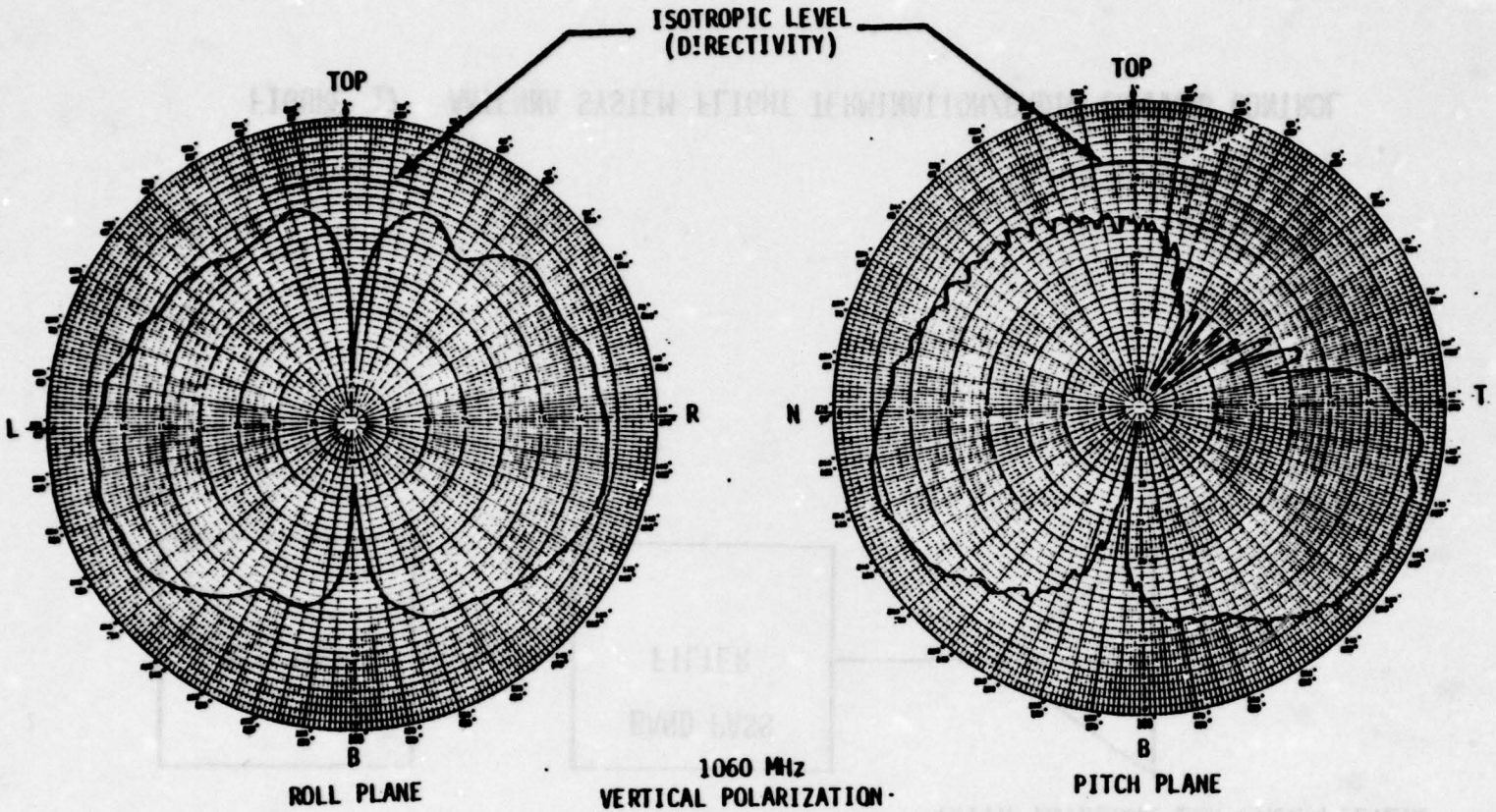

FIGURE 16 IFF ANTENNA SYSTEM

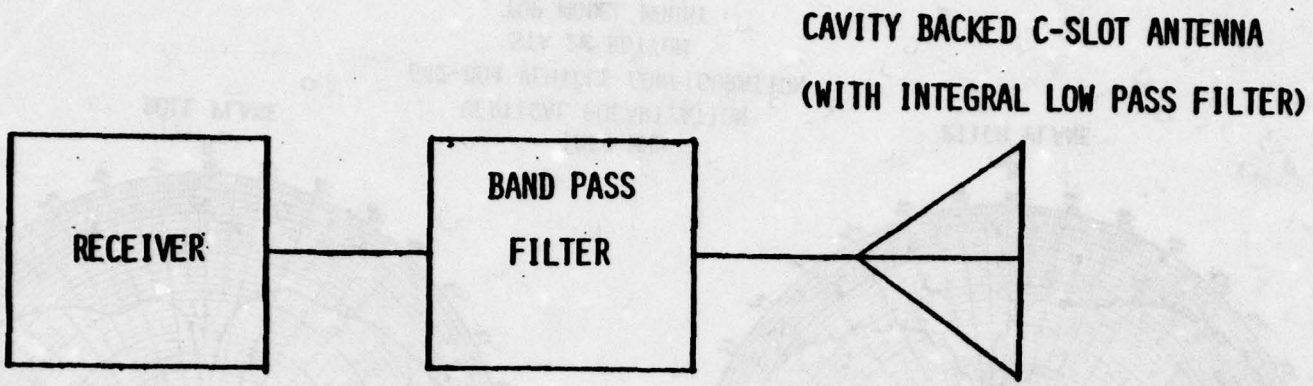

FIGURE 17 ANTENNA SYSTEM FLIGHT TERMINATION/RADIO COMMAND CONTROL

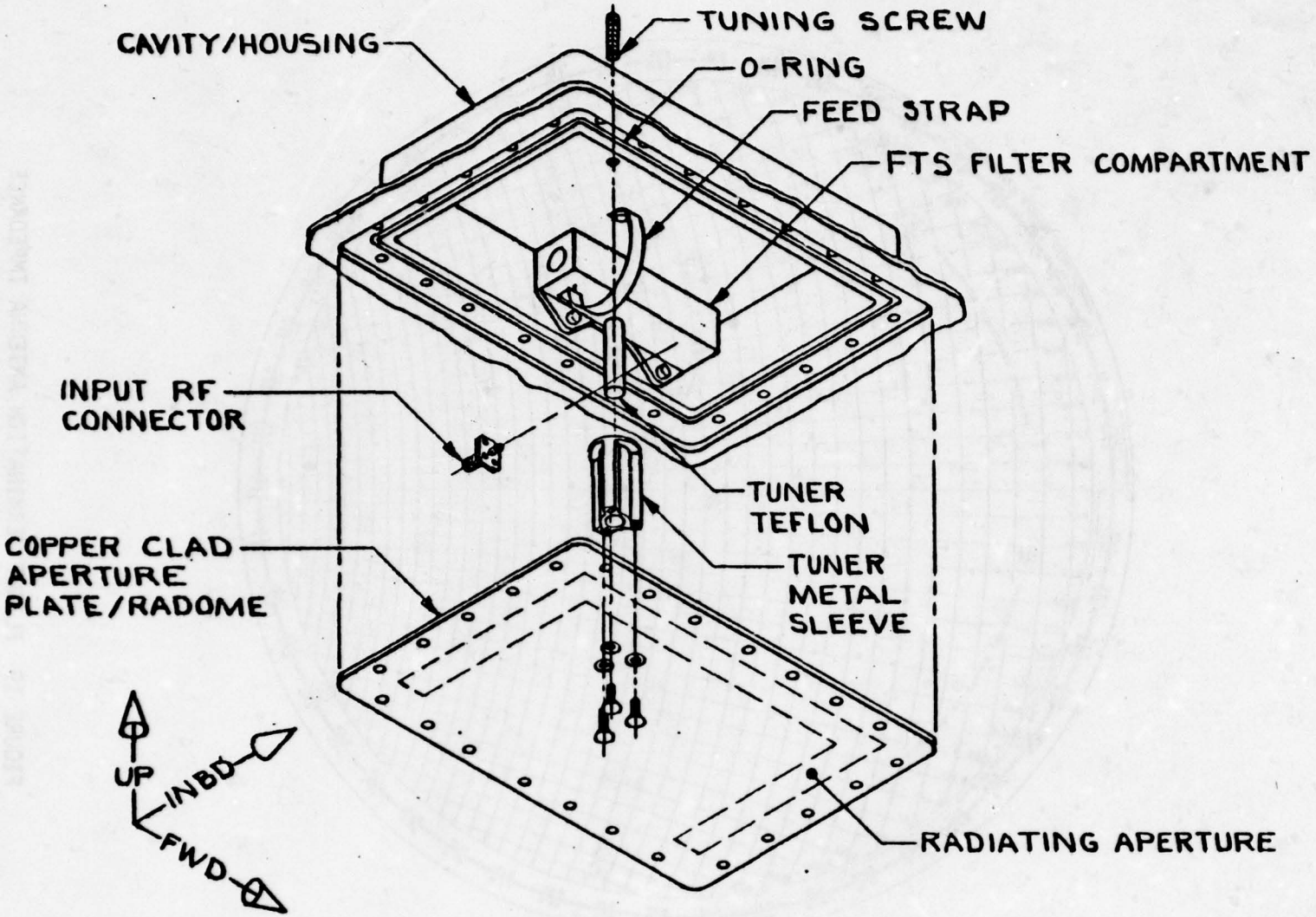

FIGURE 18 C-SLOT FLIGHT TERMINATION ANTENNA

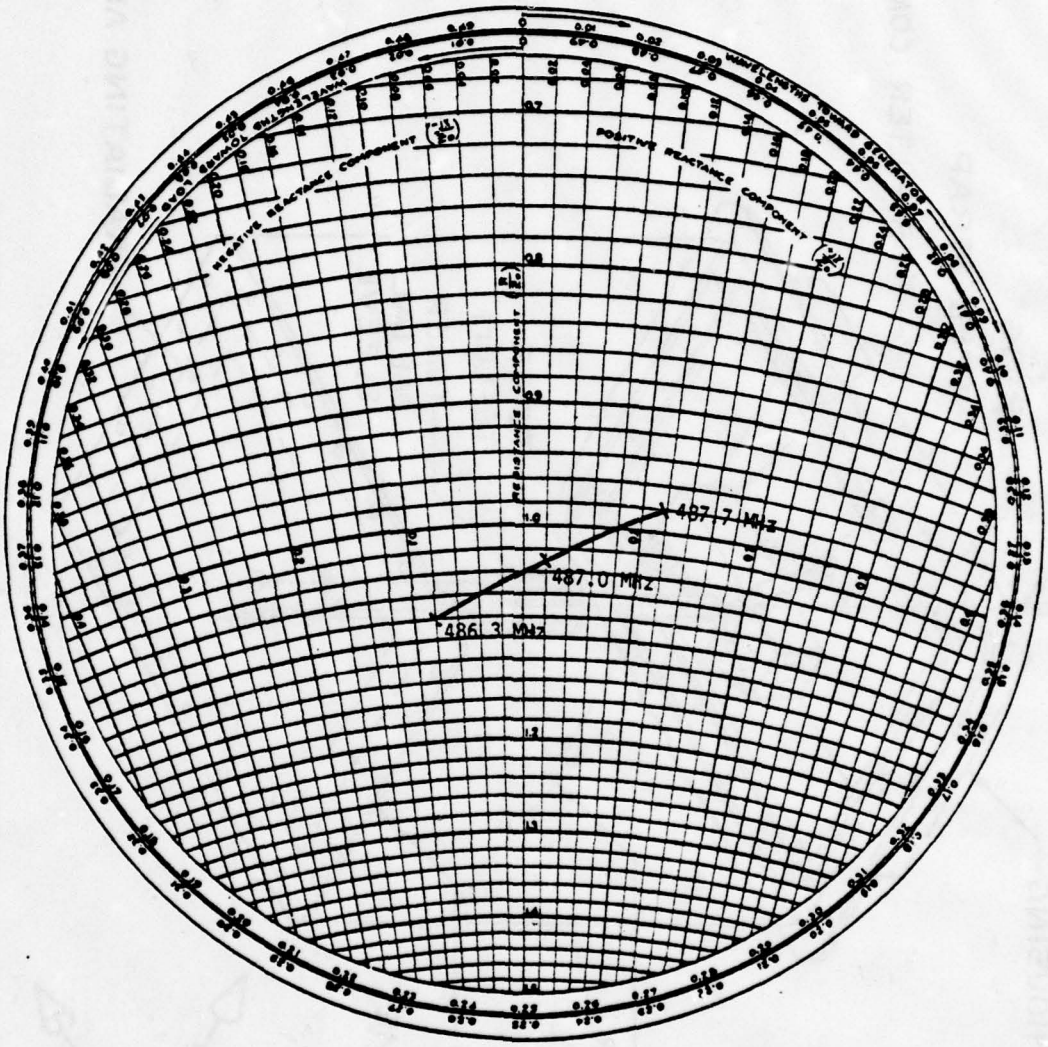

FIGURE 19 FLIGHT TERMINATION ANTENNA IMPEDANCE

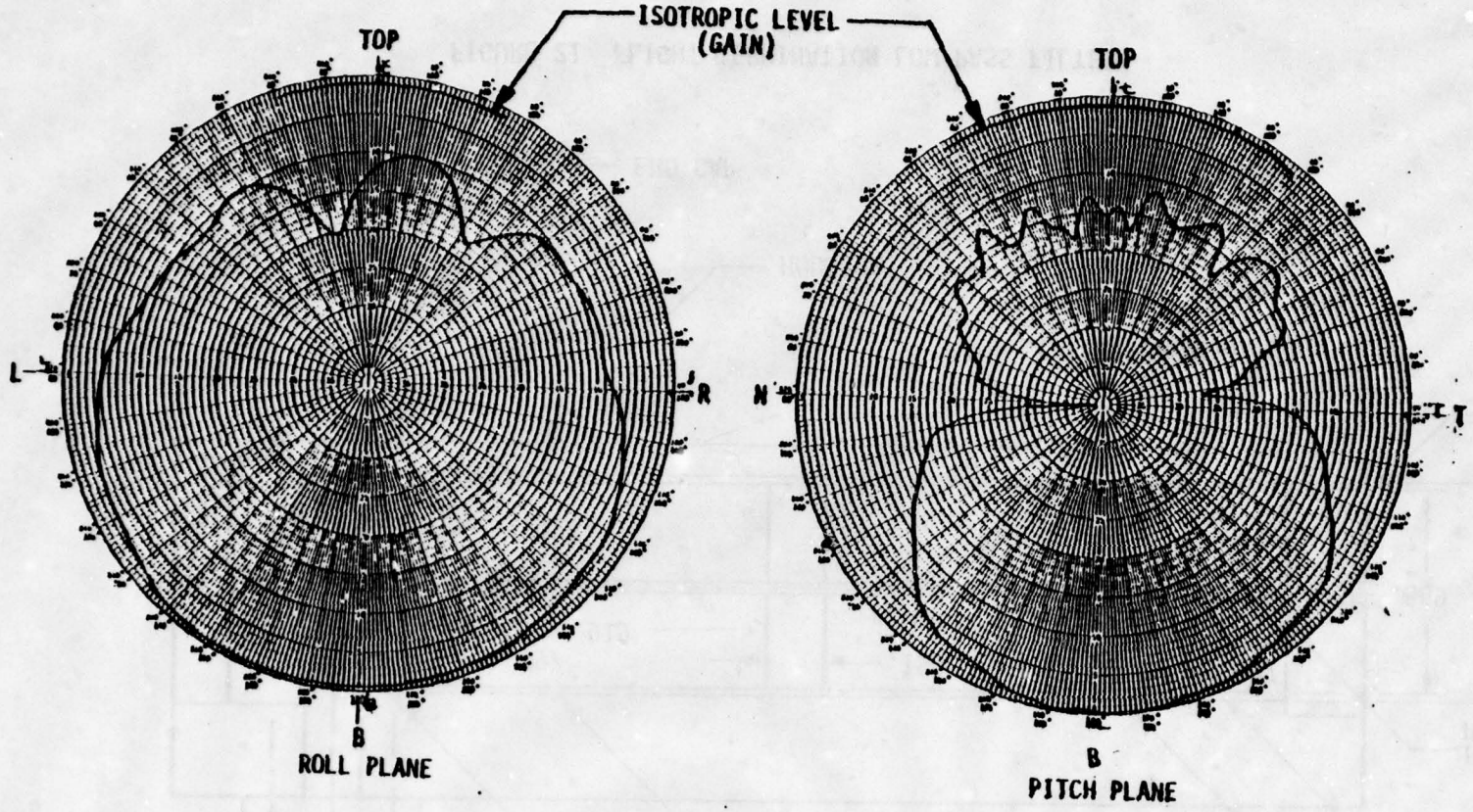

487 MHz
LHC POLARIZATION
642-004 VEHICLE CONFIGURATION
STA 45 BOTTOM
TOP MODEL MOUNT

FIGURE 20 FLIGHT TERMINATION ANTENNA SYSTEM

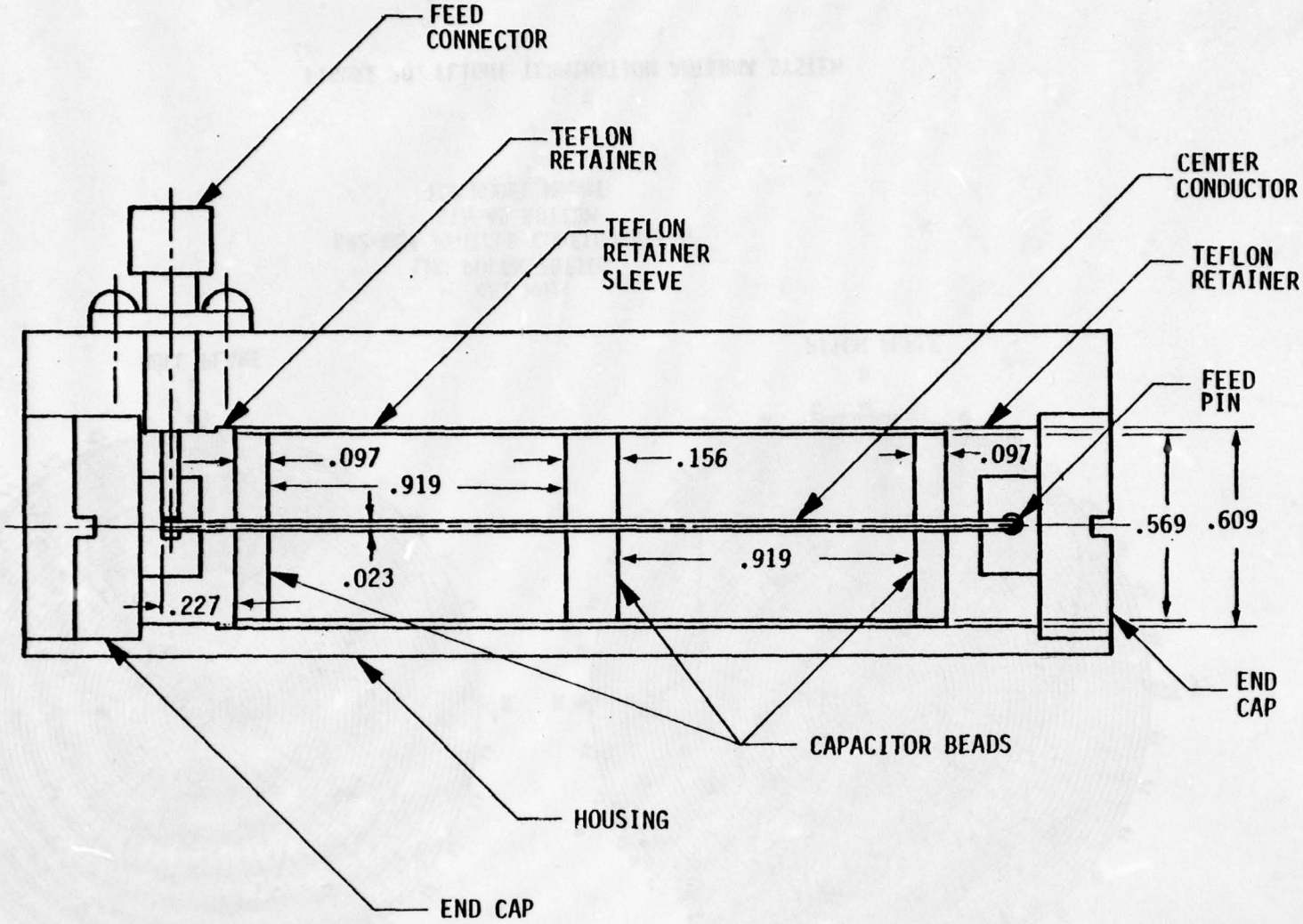

FIGURE 21 FLIGHT TERMINATION LOW PASS FILTER

FILTER IMPEDANCE

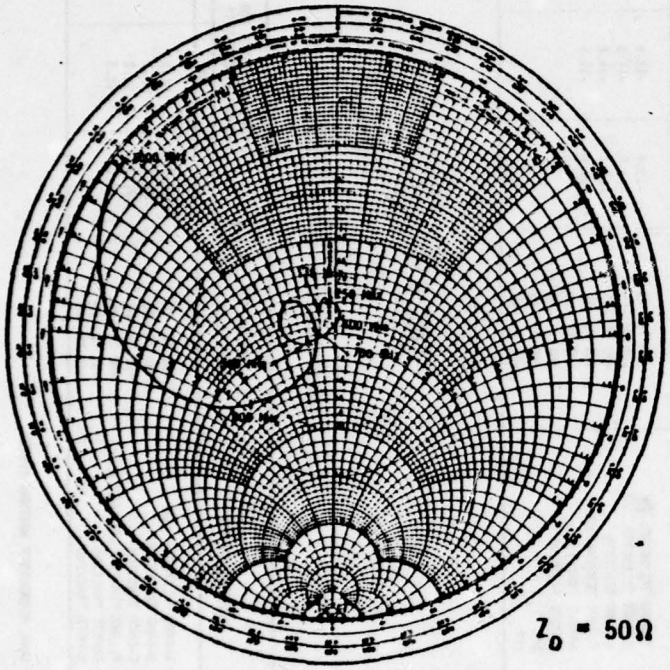

$Z_0 = 50\Omega$

400-500 MHz $\leq 1.5:1$

FILTER FREQUENCY RESPONSE

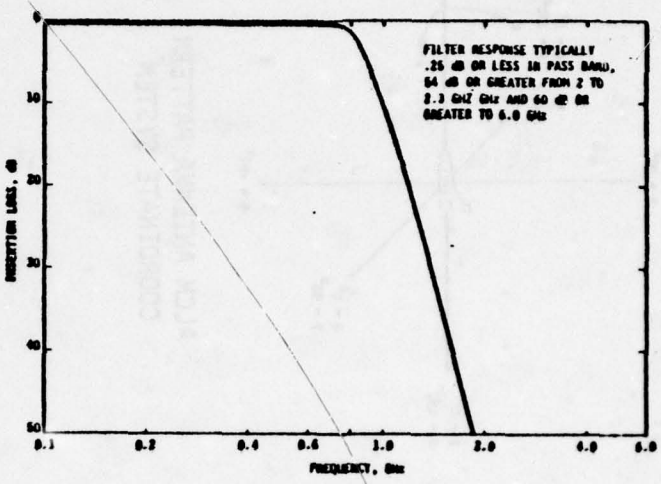

FIGURE 22 FLIGHT TERMINATION LOW PASS FILTER

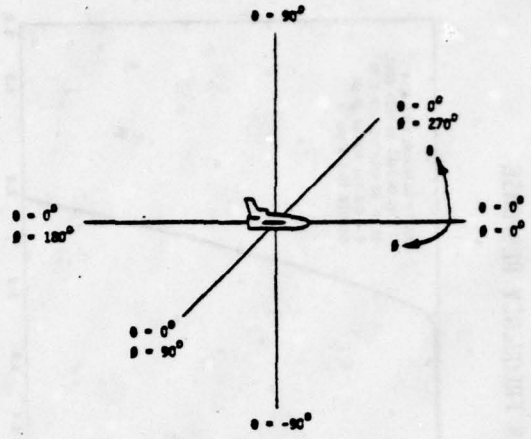

ALCM ANTENNA PATTERN
COORDINATE SYSTEM

DIRECTIVITY LEVEL PROVIDED

ANTENNA SYSTEM	θ - SECTOR (°) (360° IN φ)	DIRECTIVITY FOR 95% COVERAGE LEVEL (dBI)		
		RHC	LHC	LINEAR
S-BAND TELEMETRY ▶	+90 TO -90	-13.4	-13.8	
S-BAND TELEMETRY	+30 TO -60	-14.8	-14.9	
C-BAND TRACKING	+30 TO -60	-17.1	-16.8	
FLIGHT TERMINATION	+90 TO -90	-16.6	-16.5	
HAROTS TRACKING	+90 TO -90			-13.4
HAROTS TRACKING	+48 TO -48			-12.5
IFF	+90 TO -90			-14.9
IFF	+48 TO -48			-12.7

TABLE I

COVERAGE LEVEL PROVIDED

ANTENNA SYSTEM	θ - SECTOR (°) (360° IN φ)	% COVERAGE LEVEL FOR -15 dBI DIRECTIVITY		
		RHC	LHC	LINEAR
S-BAND TELEMETRY ▶	+90 TO -90	96.7	96.3	
S-BAND TELEMETRY	+30 TO -60	96.3	96.1	
C-BAND TRACKING	+30 TO -60	91.3	92.2	
FLIGHT TERMINATION (467 MHz)	+90 TO -90	92.0	91.5	
HAROTS TRACKING	+90 TO -90			96.5
HAROTS TRACKING	+48 TO -48			97.0

▶ DUAL MICROSTRIP ANTENNA SYSTEM

TABLE II

INTER-SYSTEM ISOLATION

ALCM IN BOMBAY DOOR MOCKUP

TRANSMIT ANTENNA	RECEIVE ANTENNA	TRANS. FREQ. RANGE (MHz)	MINIMUM ISOLATION (dB)	MAXIMUM TRANS. POWER (dBm)	MAXIMUM SIGNAL AT RECEIVE ANTENNA OUTPUT (dBm)
HAMOTS	FTS	908-928	59	44	-15
HAMOTS	TELEMETRY	908-928	45	44	-1
HAMOTS	TRACKING	908-928	64	44	-20
IFF	FTS	1090	70	60	-10
IFF	TELEMETRY	1090	50	60	+10
IFF	TRACKING	1090	62	60	-2
TELEMETRY	FTS	2200-2290	90	40	-50
TELEMETRY	HAMOTS	2200-2290	60	40	-20
TELEMETRY	TRACKING	2200-2290	75	40	-35
TRACKING	FTS	5400-5900	90	50	-40
TRACKING	HAMOTS	5400-5900	46	50	+4
TRACKING	TELEMETRY	5400-5900	49	50	+1

SECTORAL SCALAR HORNS FOR PRECISE BEAM CONTROL

Wayne A. Schneider, Thomas L. Blakney, Vincent J. Zanella
The Boeing Aerospace Company
Seattle, Washington 98124

Abstract - A new design method for developing either linear or circular polarized, low sidelobe corrugated sectoral horn antennas is described. These antennas may be designed to provide beam aspect ratios for cross sections ranging from 2:1 to 5:1. Such performance is achieved over bandwidths of up to 20 percent for dual-linear or circular polarization. Potential applications include use in communication satellite reflector systems where beam shaping, frequency reuse, or high adjacent beam isolation is required. Selecting aperture phase distribution rather than simply minimizing aperture phase error is the key to obtaining these results. Mechanical designs and performance data are presented to facilitate fabrication of antennas which satisfy a wide range of performance requirements.

INTRODUCTION

During recent years, an increasing need has arisen for antennas which illuminate elliptically-shaped areas by controlling beam cross section. Typical uses of antennas providing precise beam aspect ratios* (BARs) or cross sections ranging up to 5:1, include radiometry, mapping, communications surveillance and power transmission systems. In some instances the scalar horn serves alone as the beam forming antenna system. In many other cases these beams are formed, with a horn as primary radiator for a reflector antenna system. For reflector type antenna systems, a highly-efficient circular or dual-linearly polarized beam is usually desired. This has posed a problem since illumination efficiency and circular or dual-linear polarization cannot be obtained simultaneously with conventional sectoral horn antenna feeds. Also, such antennas exhibit relatively high sidelobe levels (> -10 dB) which impair secondary beam efficiency.

Several papers, which address the design of scalar horn antennas for symmetric beam and low sidelobe applications, have been published (Reference 1). A beam aspect ratio (BAR) control concept is introduced in this paper which applies the findings of Buchmeyer (Reference 2) and Narashimhan and Rao (Reference 3) to develop a new corrugated sectoral scalar horn. Various BAR levels are achieved with the scalar horn antenna by selecting

*Ratio of widest plane pattern beamwidth to most narrow plane beamwidth at minus 10 dB level with respect to peak on main beam.

1. Love, A. W., ed., "Electromagnetic Horn Antennas", IEEE Press, 1976.
2. Buchmeyer, S. K., "Corrugations Lock Horns with Poor Beamshapes", Microwaves, January, 1973.
3. Narasimham, M. S. and V. Venkateswara Rao, "Radiation Characteristics of Corrugated E-Plane Sectoral Horns".

phase distribution rather than minimizing aperture phase error. A design method is presented for developing either linear or circularly-polarized corrugated horn antennas capable of achieving BARs up to 5:1 over large bandwidths. Low sidelobes, characteristic of symmetrical beam corrugated antennas, are not affected in achieving the high BAR values with these new scalar sector horns in either circular or linear polarization modes. Dimensional design data and tests results, verifying performance predictions, are also presented. The test results verify that maintenance of a specific aperture phase error results in optimum performance.

THEORETICAL APPROACH

Since the advent of the scalar horn in 1967, numerous papers have been written about analytical and experimental investigations of symmetric-beam corrugated (scalar) antennas. One such circularly-polarized symmetric beam antenna is sketched in Figure 1. This antenna consists of a 1.1 inch (2.8 CM) section of circular waveguide, a perpendicular corrugated ground plane, and an internal pin polarizer. A typical rotating-linear polarization pattern for this antenna is shown in Figure 2. Many of the papers written about this family of horn antennas are documented in Reference 1.

A paper by S. K. Buchmeyer (Reference 2) reveals a close relationship between optimum performance and aperture phase error. Buchmeyer found that symmetric-beam scalar horns performed best when the aperture phase error was approximately 0.5 wavelengths. The exact expression for aperture phase error is:

$$(1)\quad P.E. = \frac{r - \ell}{\lambda} = \frac{a(1-\cos\ \alpha_o)}{2\lambda\ \sin\ \alpha_o}$$

Where α_o = the included half angle of the horn

λ = wavelength

and a = aperture length as shown in Figure 3.

The phase error (P.E.) may be approximated by the following expression:

$$(2)\quad P.E. = \frac{a\ \sin\ \alpha_o}{4\lambda}$$

When α_o is small ($< 30^o$)

Equation (1) should be used in designing horns with included half flare angles (α_o) greater than 30°, since phase error calculations may be in error by 7% or more using equation (2) for larger flare angles.

In 1973, M. S. Narasimhan and V. Venkateswara Rao (Reference 3) described an investigation of a corrugated sectoral-beam horn. Although the half wavelength phase error criteria identified by Buchmeyer was not applied, this antenna did perform satisfactorily and exhibited -26 dB sidelobe

levels. More recent test results have shown that such performance was achieved because design parameters are much less critical when the relative phase error is less than 0.5 λ as was the case for the Narashimhan and Rao antenna design.

The results from References 2 and 3 were used in developing a new corrugated sectoral scalar horn concept featuring very low sidelobes and dual-linear or circularly-polarized BAR control. The half-wavelength phase error criteria, identified by Buchmeyer, and the narrow-corrugated flared walls as used by Narishiman and Rao were applied simultaneously to develop the new horn design. A third feature was also added: scalar surfaces were mounted perpendicular to the broad walls of the horn. These surfaces functioned in the same manner to reduce sidelobes in the narrow wall plane as the corrugated surfaces mounted around the open-ended waveguide of the conventional symmetric beam antenna shown in Figure 1.

TEST MODEL

A dual-polarized sectoral scalar horn was fabricated for a series of tests. The horn was flared in only one plane. In the other plane, there was no flare and the radiator was simply an extension of the 0.9 inch (2.29 CM) square feeding waveguide. Figure 4 is a sketch of the test antenna configuration showing the critical dimensions. The narrow corrugated walls were hinged in order to permit variation of the horn flare angle. The corrugated sides of the horns were made up of a number of "add-on" sections with joints as shown in Figure 4. The hinged walls and "add-on" sections facilitated simulation of a number of horn configurations with different flare angles and lengths from the single test antenna model. Changes were accomplished by rotating the narrow walls to accommodate different antenna half angles. The length of the horn was varied by adding 3.0 inch (7.62 CM) increments of corrugated sections. The walls of the non-flared plane of the antenna consisted of properly-dimensioned aluminum plates bolted to the narrow corrugated walls. Smooth, rather than corrugated surfaces were used, since no corrugations are needed when the E-field is polarized parallel to the surface. For perpendicular polarization, the corrugations at the radiating aperture accomplish the desired effect. Dimensions of the four horn configurations selected for verification tests are shown in Table 1. In each case, the half angle (α_0) and the aperture width (a) were related by the phase error approximation from equation (2).

TEST RESULTS

Four sectoral scalar horns were tested extensively in both the circular-polarized and dual-linear modes. Circular polarization performance is typified by the two rotating-linear antenna patterns shown in Figure 5. An axial ratio of less than 0.5 dB was obtained over a 2% bandwidth using a throat polarizer. The BAR at the 10 dB beamwidth points is -5:1. The bandwidth for the circularly-polarized sectoral scalar horn with throat polarizer is relatively narrow because of differences in position of the $E_\perp$ (fields perpendicular to the broad wall) and $E_{//}$ (fields parallel to the broad wall) phase centers within the horn structure as a function of

frequency. The bandwidth was increased to $\approx$ 17% (axial ratio < 3 dB) when a meanderline polarizer (Reference 4) was placed at the horn aperture. A comparison of test results using the throat polarizer and meanderline polarizer is shown in Figure 6.

For dual linear polarization, typical measured data (Figure 7) show that a beam aspect ratio of 5:1 was achieved over a bandwidth of $\approx$ 20 percent at the 10 dB pattern beamwidth points. Sidelobe levels for these antennas were typically more than 35 dB below beam peak. For example, Figure 8 shows sidelobe levels of -35 dB as measured through the plane of the narrow beam of the largest sectoral horn evaluated. Extensive testing over relatively large bandwidths showed well-behaved BAR and sidelobe characteristics and verified that the design concept is both predictable and broadband. A design curve, which shows measured BAR values at the -10 dB beamwidth points as a function of aperture size in the narrow beam plane, is shown on Figure 9. This figure may be used to select the largest dimension of the aperture of a sectoral beam horn required to provide a desired -10 dB beamwidth.

CONCLUSIONS

A family of low sidelobe, circular and dual-linear polarized sectoral horns with rectangular apertures has been developed. Beam aspect ratios ranging from 2:1 to 5:1 and sidelobes typically 35 dB below beam peak over a 20% bandwidth were attained. The key to these designs consists of: 1) controlling phase error to a value of one-half wavelength across the large dimension of the horn aperture, 2) employing a scalar surface perpendicular to the walls on each side of the narrow dimensions of the aperture and 3) introducing scalar surfaces oriented perpendicular to the longest dimension sides of the horn aperture. Additionally, it has been demonstrated that a meanderline polarizer may be effectively used to generate isolated circularly-polarized beams over a large bandwidth.

4. Blakney, T. L., S. B. Cohn, and J. R. Burnett, "A Design Methof for Meanderline Circular Polarizers", 22nd USAF Antenna Symposium, Allerton Park, Illinois, October 11-13, 1972.

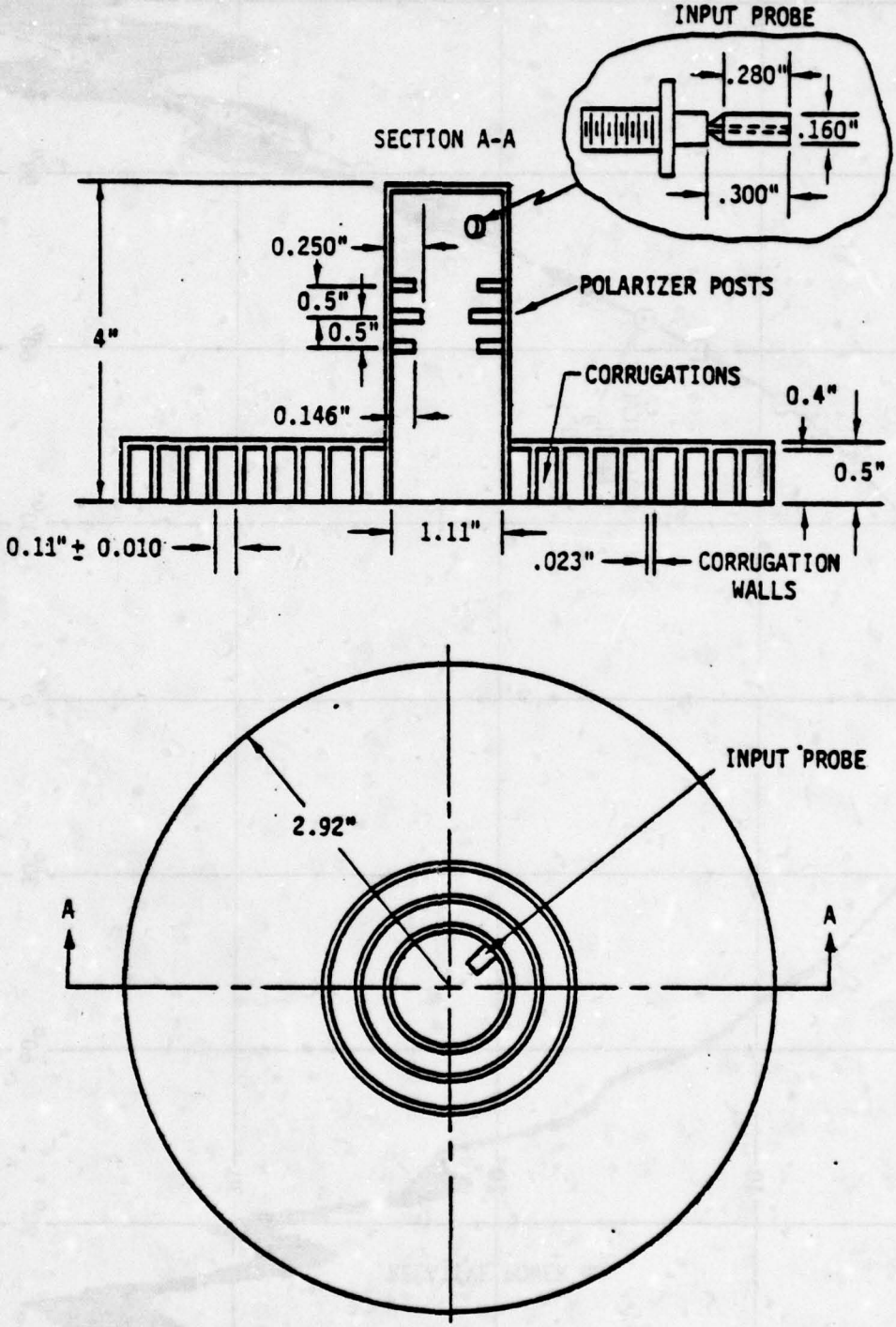

FIGURE 1 SYMMETRIC BEAM CORRUGATED WAVEGUIDE FEED

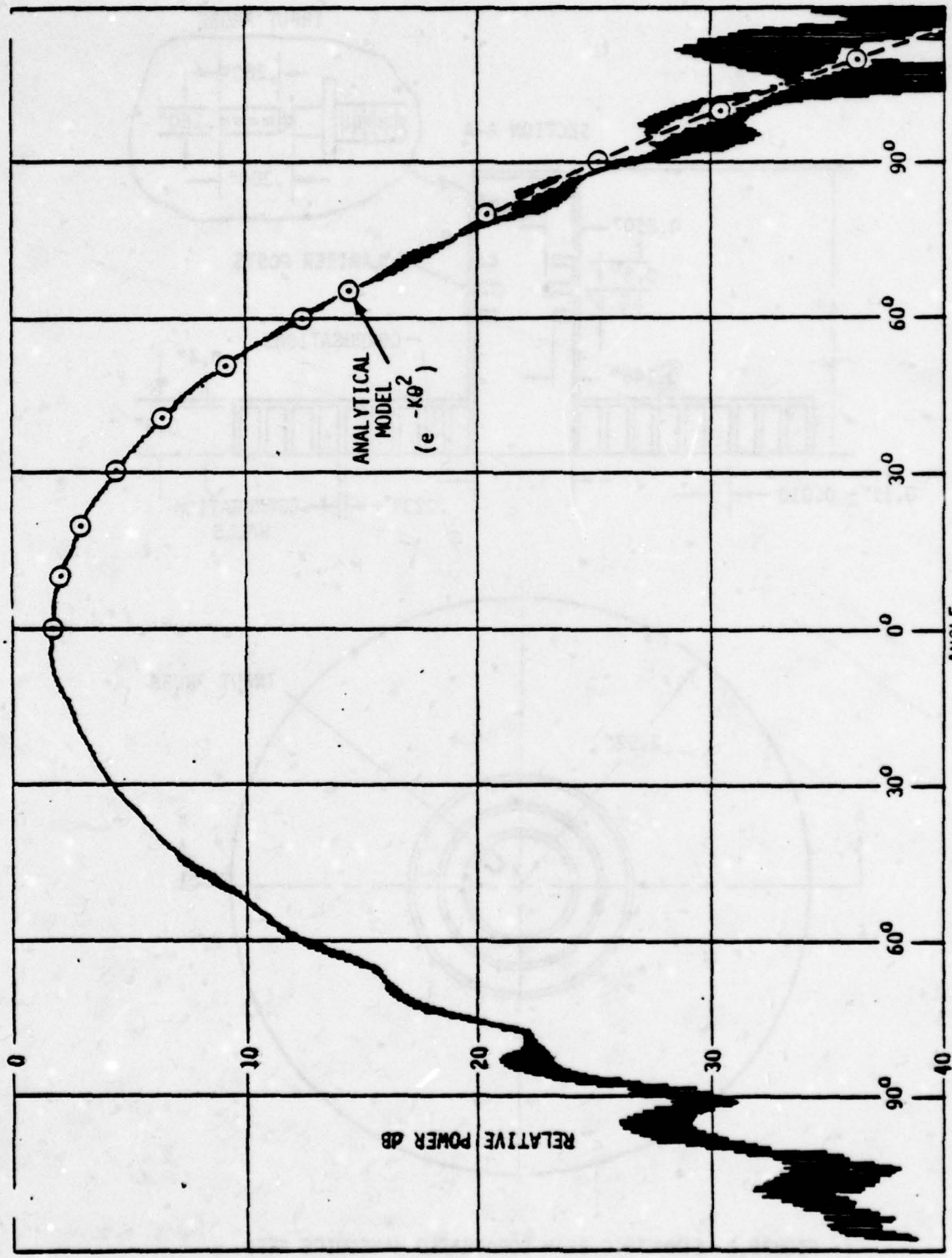

FIGURE 2 OPEN ENDED WAVEGUIDE AFTER ADDITION OF A CORRUGATED GROUND PLANE

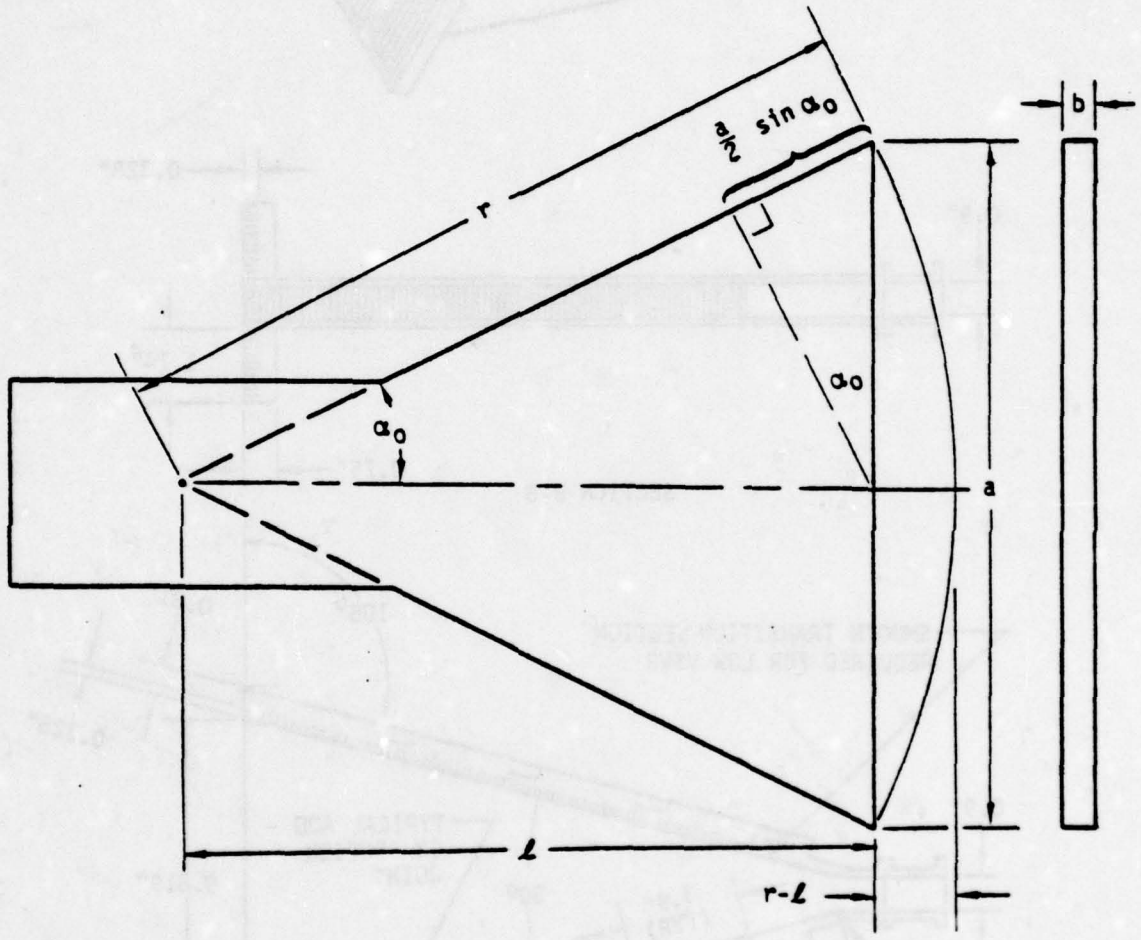

NOTE: PHASE ERROR $= \frac{r-\ell}{\lambda} = \frac{a(1-\cos\alpha_o)}{2\lambda\ \mathrm{SIN}\alpha_o} \cong \frac{a\ \mathrm{SIN}\alpha_o}{4\lambda}$

FIGURE 3 CORRUGATED HORN PHASE ERROR

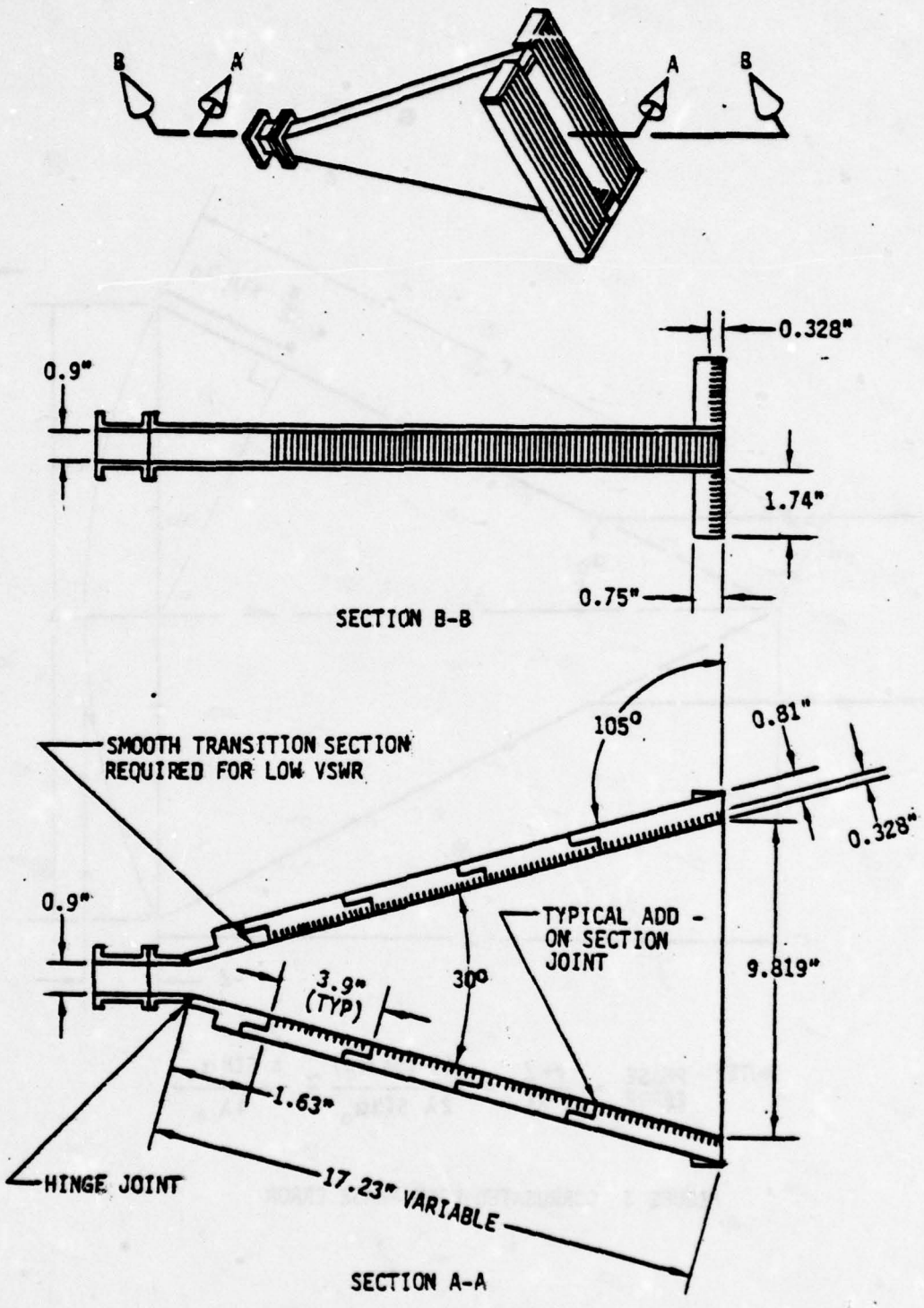

FIGURE 4 VARIABLE APERTURE SCALAR HORN

TABLE 1 CORRUGATED HORN TEST CONFIGURATIONS

CONFIGURATION	APERTURE DIMENSION a	APERTURE DIMENSION b	HALF ANGLE α_o
1	10.0"	0.9"	13.8^o
2	8.8"	0.9"	15.0^o
3	7.2"	0.9"	21.0^o
4	5.49"	0.9"	24.5^o

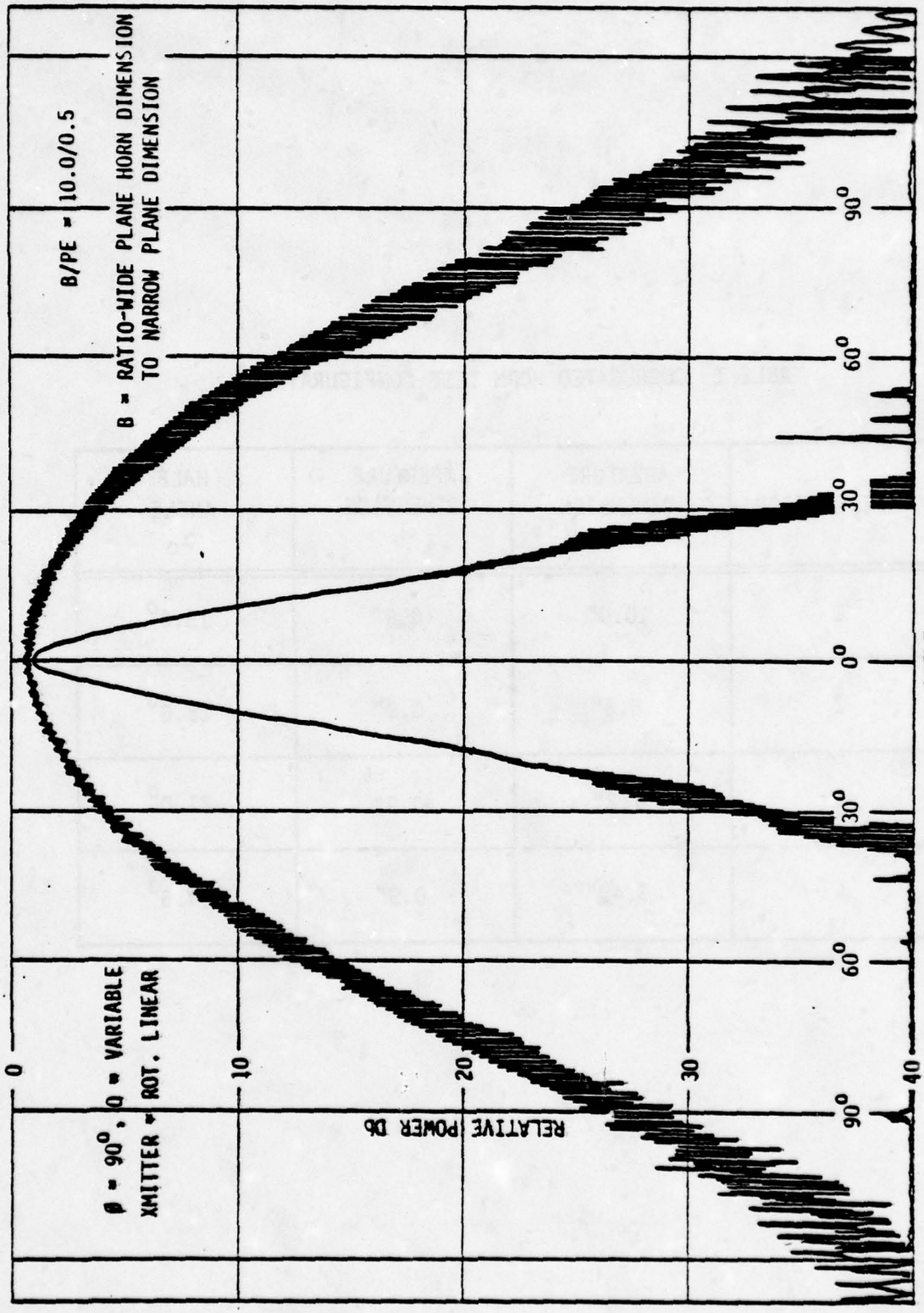

FIGURE 5 SECTORAL SCALAR HORN - SPINNING LINEAR PATTERNS

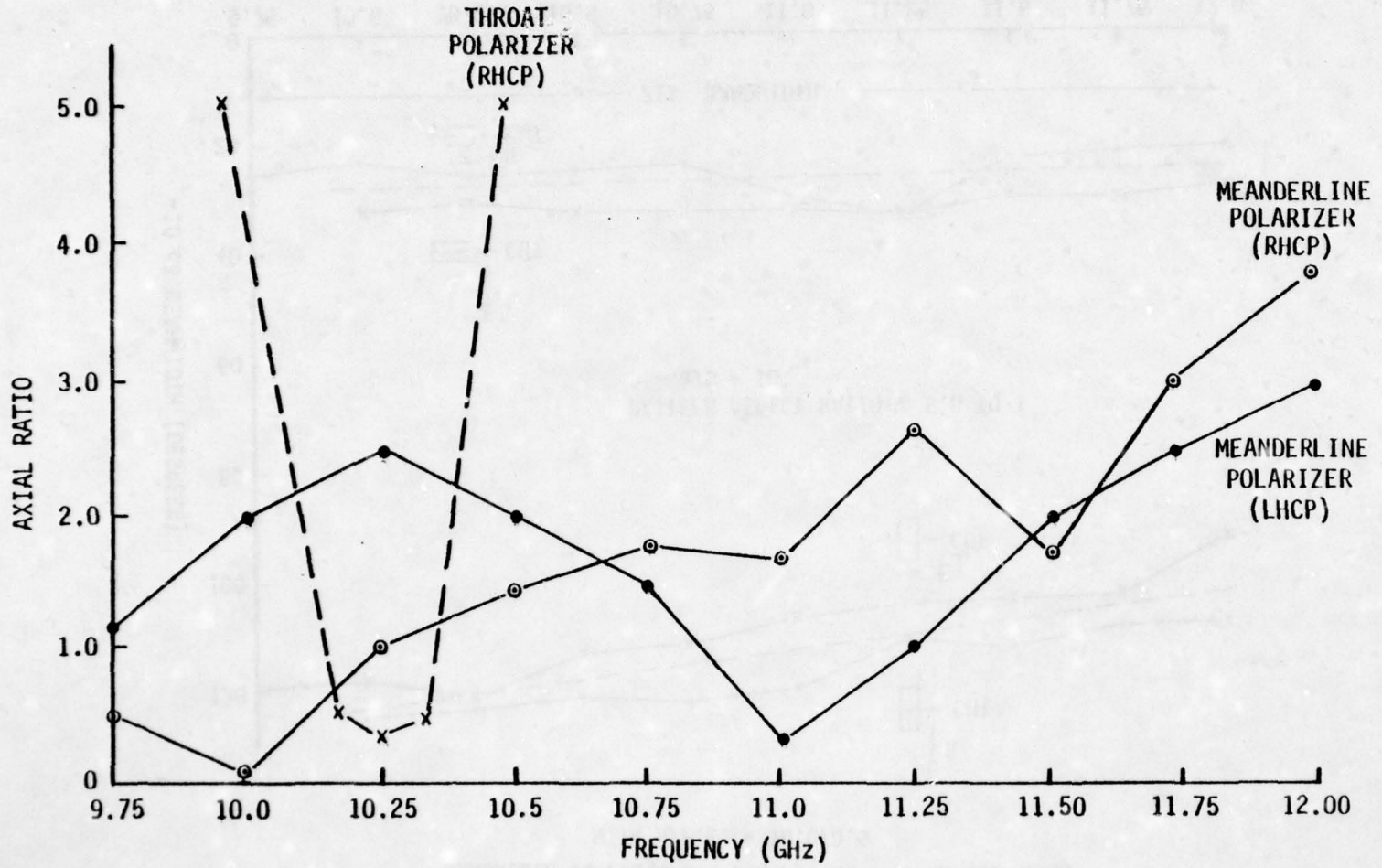

FIGURE 6 SECTORAL SCALAR HORN AXIAL RATIO

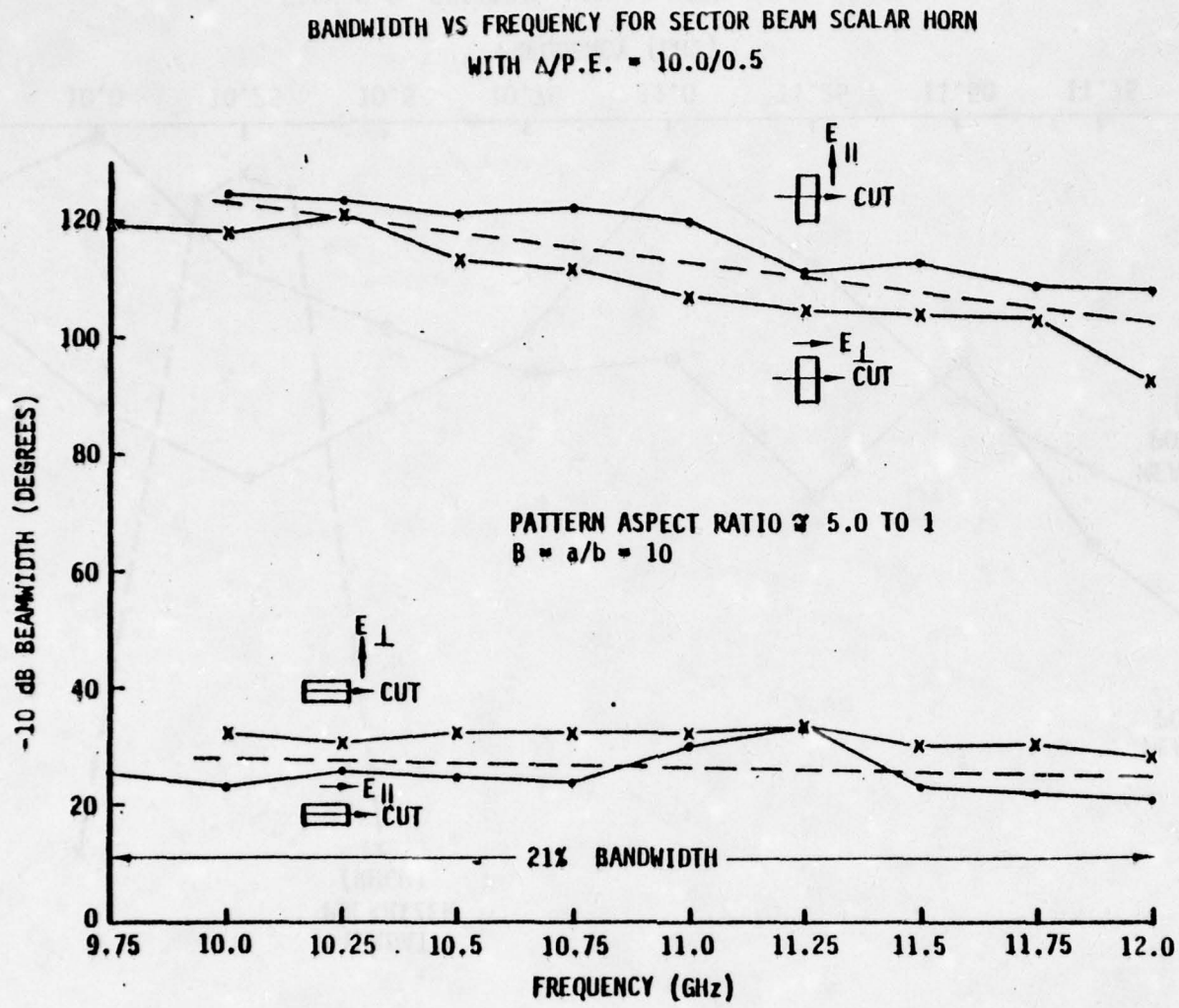

FIGURE 7 SECTORAL BEAM SCALAR HORN, -10 dB BEAMWIDTHS VS FREQUENCY

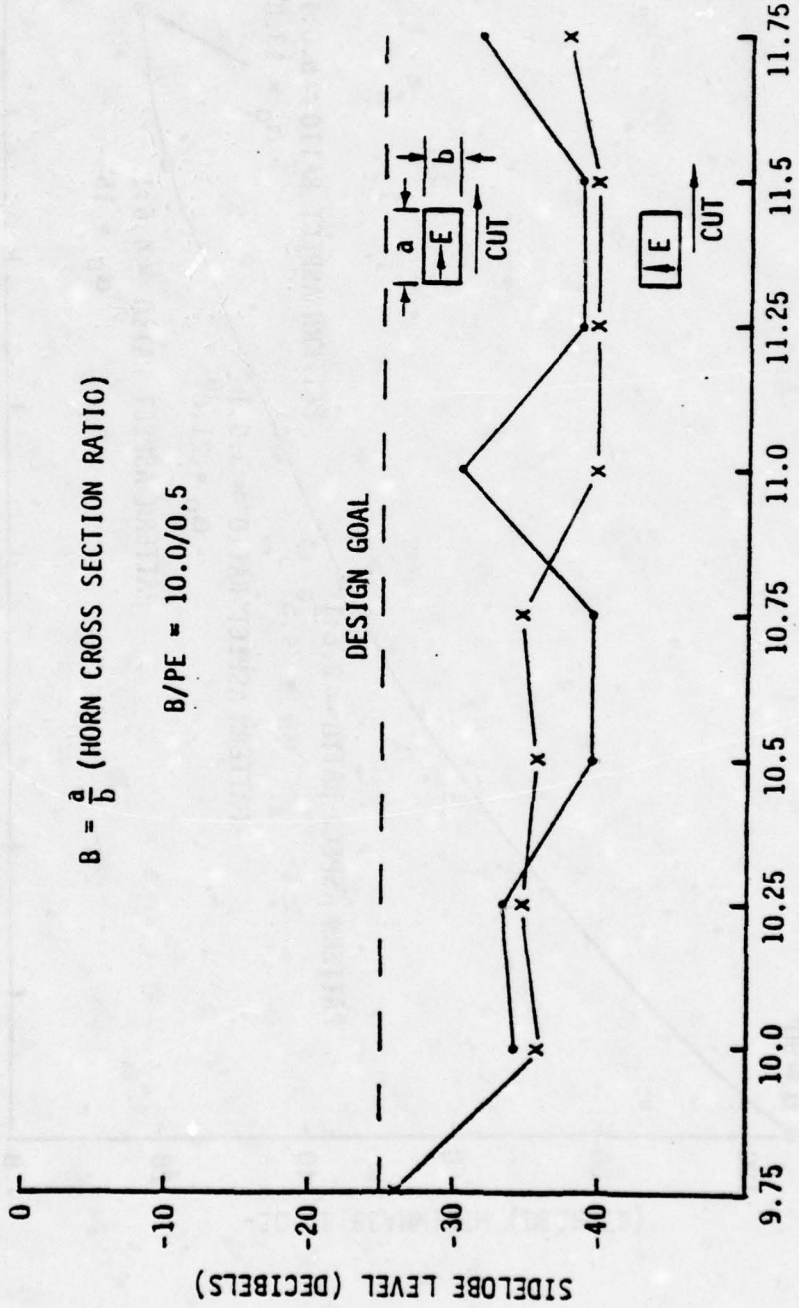

FIGURE 8 SECTORAL SCALAR HORN

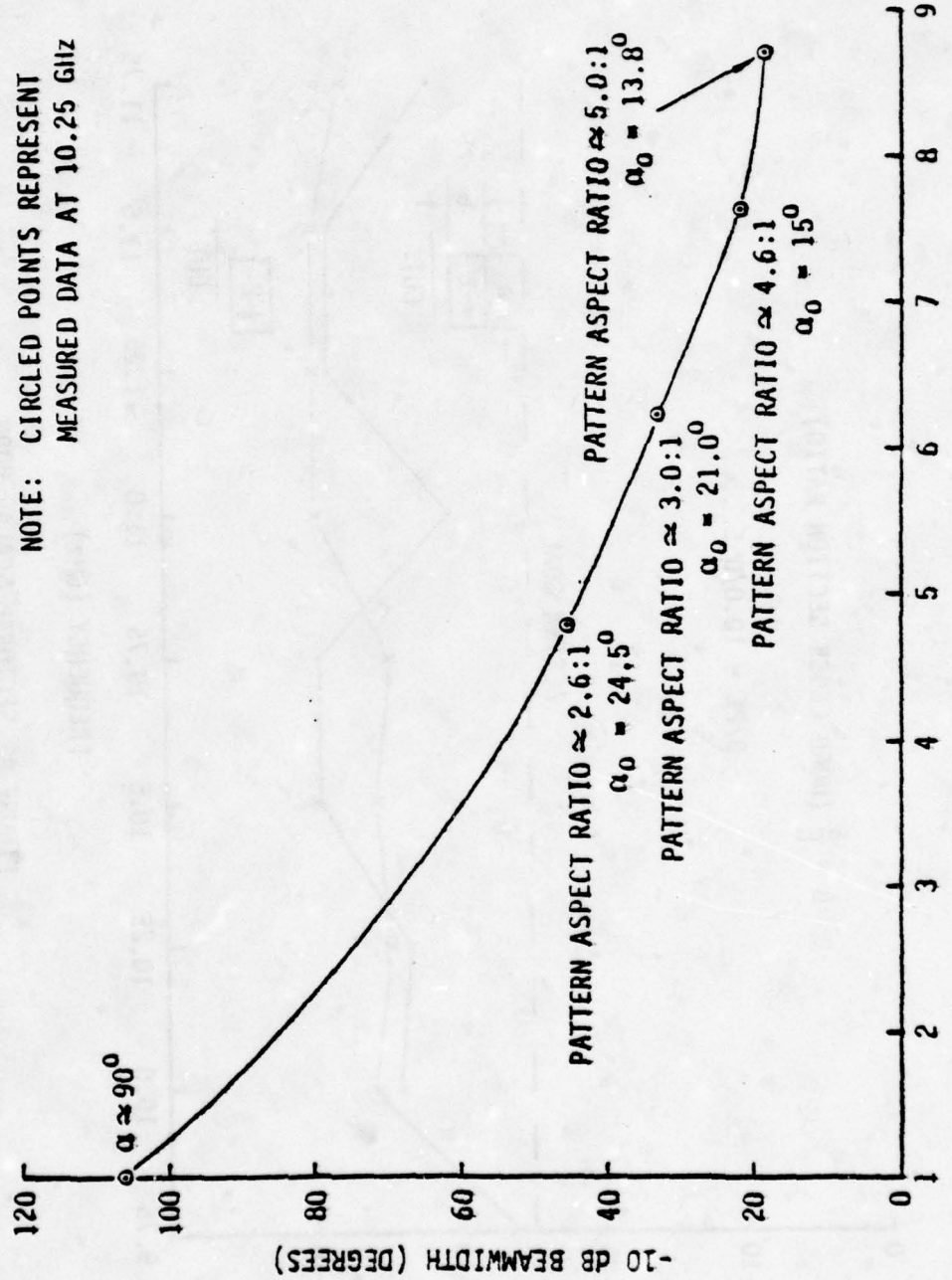

FIGURE 9 DESIGN CURVE FOR SECTORAL SCALAR

Near Field Pattern Measurement Facility

by

C. E. Kirchhoff
Martin Marietta
Denver, Colorado

Abstract

This paper describes an operational facility which has been built by Martin Marietta Aerospace to measure antenna patterns of large aperture (50 foot diameter) antennas. The pattern data is obtained by first measuring the antenna near field phase and amplitude and then using a Fast Fourier Transform (FFT) to transform the phase and amplitude to the far field antenna pattern. The system design will be described together with the subsystem (hardware) requirements derived therefrom. The electronics hardware (receiver, digital interfaces, motor controllers, laser measurement system, transmitter) which was built to satisfy these requirements will be detailed together with the associated operating parameters. The mechanical equipment (translation ways and probe carriage) will be briefly described together with the associated installed tolerances. The actual measured electrical parameters (such as phase measurement accuracy and transmitter stability) together with the actual measured mechanical tolerances have been used to calculate the facility measurement accuracies. The results of pattern and gain measurements on a 10 foot dish will be presented together with a comparison of these results with National Bureau of Standards measurements on the same dish. The measurement accuracies demonstrated by the facility will be correllated with the calculated accuracies above to demonstrate actual facility performance. The computer hardware configuration, which includes an array processor, will be described along with data measurement and data processing times for the 10' dish. Projected run times for larger dishes will also be given.

Introduction

Martin Marietta Aerospace has recently completed a nearfield pattern measurement facility for the testing of antennas of greater than 50 foot diameter which can be flown on Shuttle. A previous paper[1] described the designs for the measurement facility: this paper will describe the as-built facility and will detail the measurement accuracies which are being obtained. The facility utilizes a complement of equipment consisting of: two-channel receiver; synthesizer signal source; probe positioning mechanism; control system; minicomputer; array processor. A planar-rectangular scan grid is utilized to measure the nearfield data (phase and amplitude) of the antenna under test: this data is then transformed via a Fast Fourier Transform (FFT) to obtain the farfield pattern of the antenna. The probe positioning mechanism has been constructed to extremely tight mechanical tolerances in order to minimize the measurement errors. Likewise, the receiver phase measurement capability is very accurate in order to provide accurate farfield patterns. A description of the system and its components is given below and this is followed by the results obtained on a 10 foot diameter dish which has been tested in the facility.

Measurement Methodology A isometric view of the facility containing a test antenna is shown in Figure 1. The test antenna is translated parallel to the long dimensions of the building (x axis) and the measure-

---

1 "Large Aperture Pattern Measurement Facility", C. E. Kirchhoff, Proceedings of the 1978 Antenna Application symposium, University of Illinois

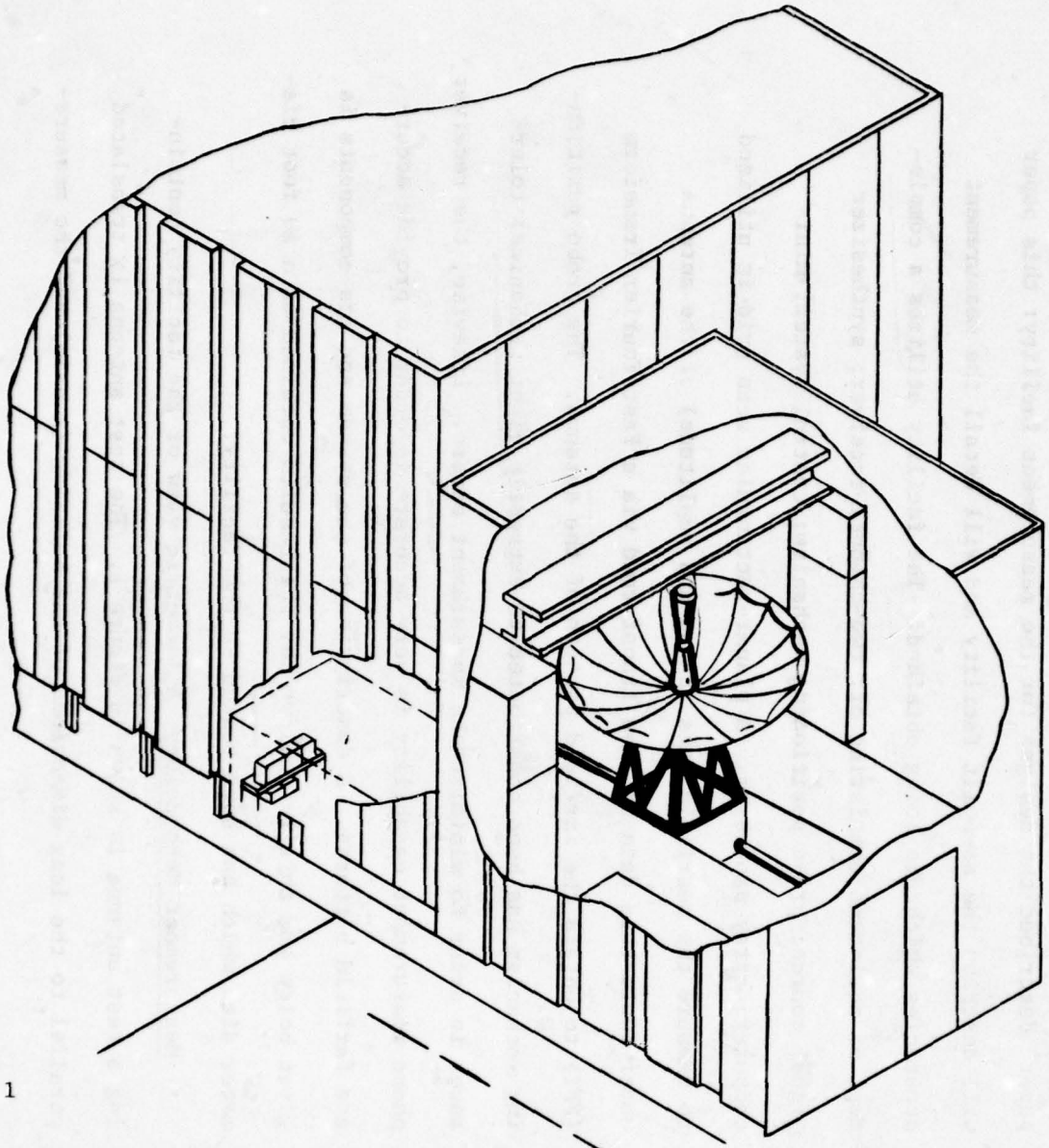

Figure 1

NEAR FIELD TEST FACILITY

ment probe train is translated on the beam above the antenna and perpendicular to the direction of dish motion (y axis). Thus, the x-y data grid of nearfield data is obtained by moving the antenna in x and the measurement probes in y. Small antennas ($\sim$10' diameter) can be measured directly by this method: larger antennas, however, are measured one quadrant at a time. The quadrant measurement system was devised and implemented in order to maximize the antenna size that could be tested while at the same time keeping the building dimensions as small as possible. The quadrant data collection matrix is shown in Figure 2. The quadrant to be measured is shown in the dotted line area of this plan view. The initial position of the dish will be to the right side of the figure; the probe train (data collection) is moved along the probe mechanism box beam support (left dotted line) for 40 feet to gather data (y axis). Since the probe train is comprised of 4 probes spaced 10 feet apart, only 10 feet of probe train movement is required in order to obtain 40 feet of data. After the first line of data is obtained, the antenna is indexed to the left in the figure (x axis) and the probe train is moved to collect 40 feet of data; this procedure is repeated until the antenna has been indexed forty feet to the far left position at which time one quadrant of data will have been obtained. The antenna will then be rotated about its axis 90° and returned to the far right position (Figure 2) in order to repeat the process for the second quadrant. After four quadrants have been measured in this manner, a data rearrange must be performed to yield a matrix of data 80 feet by 80 feet centered on the antenna under test.

Mechanical Complement The antenna translation system consists of a pair of hardened and ground ways (utilizing Tychoway roller bearings)

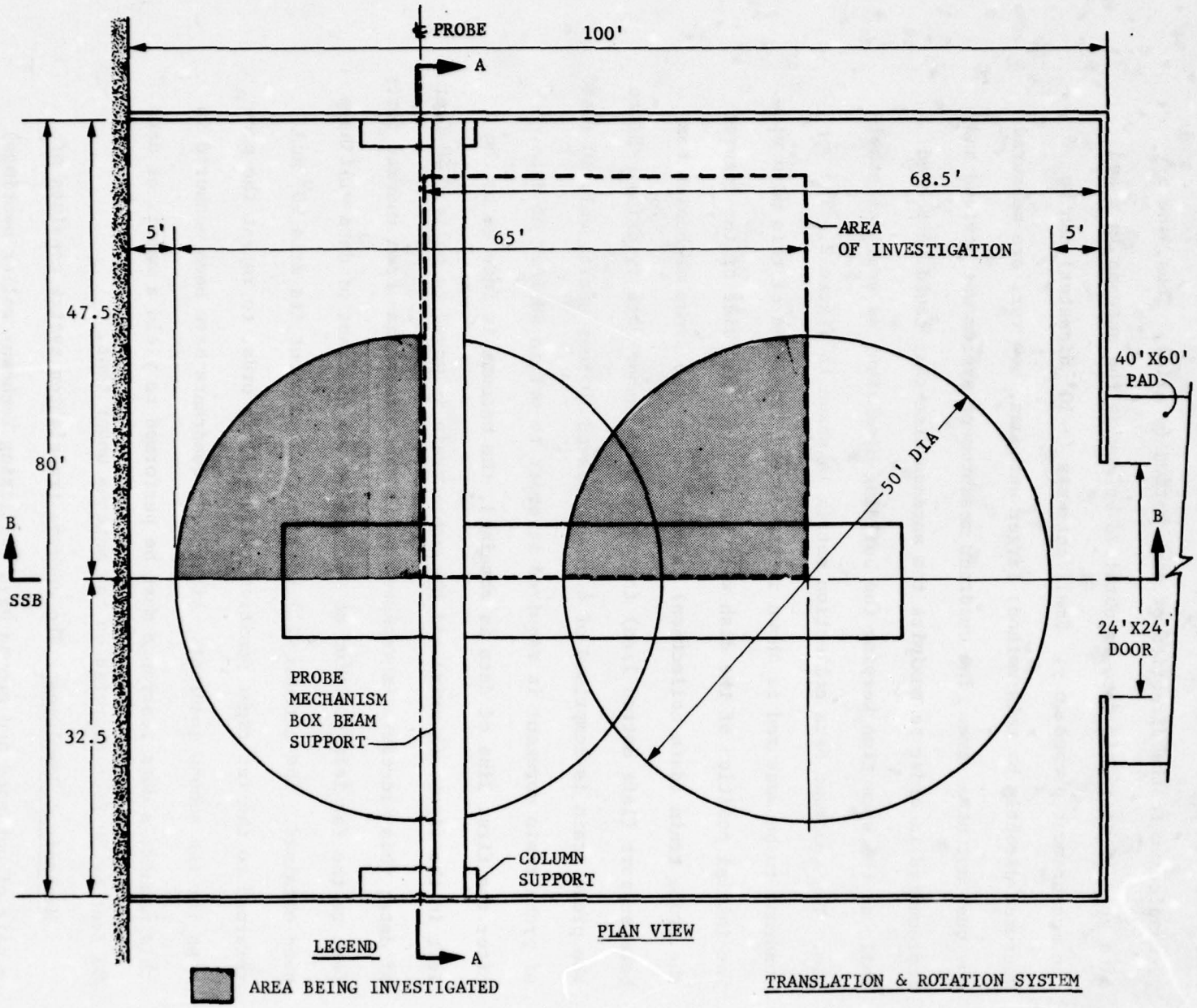

Figure 2 SCAN AREA

and of sufficient length to provide greater than 40 feet of antenna travel in the x direction. These tracks have been installed to a measured straightness and flatness of ± 0.0025" over their length; this is the tolerance which was allocated to these tracks in the system design. The probe translation system consists of a pair of precision Thompson roundways (one foot center-to-center) covering 72 feet in the y axis. The probe train can be positioned so that it will travel any place on this axis. These tracks have been installed to a measured straightness and flatness of ± 0.0025" over their length; again, this is the tolerance which was allocated for these tracks in the system design.

The perpendicularity between the sets of tracks is ± 0.004" on a 50 foot arm: this ± 0.004" is an effective x position error in one case and a skew error to the x-y grid in the other case. For the x position error, the ± 0.004 is additive to ± 0.0025" straightness of the probe train tracks and still falls (± 0.0065") well within the ± 0.015" of x position error allocated in the system design. The skew error effect essentially causes an error in y of ± 0.0065" total worst case per quadrant: this error over two quadrants (± 0.013") is still within the ± 0.015" of y position error allocated.

The rotating table is positioned by means of an Inductosyn which has an angular read-out capability of 1 arc second. At a forty foot radius this uncertainty in angle amounts to a .002" x or y error which must be added to the above x or y errors, but the total x or y error is still within the ± 0.015" allowed. The table runout (wobble) has also been measured and is + 0.001" at a distance of eight feet. This run out will, therefore, yield an error of ± 0.0025" at 40 feet which must be added to the track

error of $\pm$ 0.0025" (2 axes) to yield a z error of $\pm$ 0.0075" which is within the $\pm$ 0.008" allowed.

Some careful design was applied to the temperature control of the building in order to control the thermal expansion of the probe train support columns (and thus, to maintain the desired z tolerance). The temperature environment as measured over extended time periods is 78°F $\pm$ 1°F at the floor and 80° $\pm$ 1°F at the probe train. Since these temperatures track each other (i.e. both plus or both minus), the total temperature difference is 2°F but the variation is so small that we haven't been able to measure a z error due to temperature.

Electrical Complement The electronics system for the facility is shown in Figure 3 which is a block diagram detailing the parts: two channel receiver, synthesizer, TWT, displays, probe selection switches, motors, controllers, digital interface, and laser measurement system (L.M.S.). In operation, the measurement parameters are input via a C.R.T. terminal to control the data gathering. Desired positions of probes and the test antenna are controlled via the motor controllers and the L.M.S. Positioning accuracy is on the order of $\pm$ 0.001" non cumulative (i.e. each individual point along a step axis can be obtained to this tolerance). Since the data is gathered on the fly, the positioning inaccuracy does not apply to the scan axis. The data points are triggered via the L.M.S. in the scan axis and, therefore, are not degraded. This is due to the fact that the LMS accuracy is 10^{-6} inches which is three orders of magnitude better than the 10^{-3} inches read out accuracy required.

The digital interface provides a means of allowing the computer to

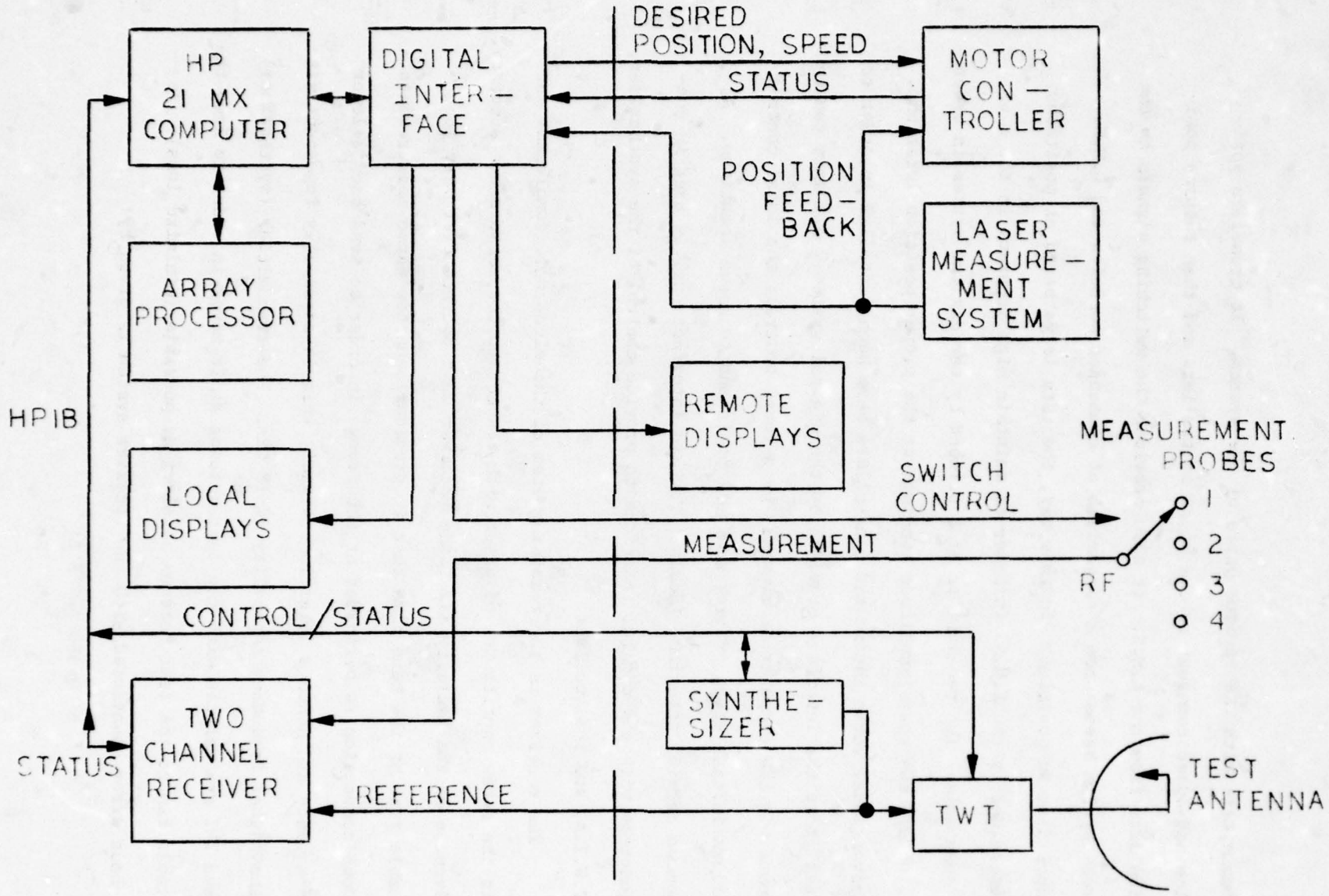

SYSTEM BLOCK DIAGRAM

Figure 3

communicate with the various parts of the system. It transfers position and speed commands to the motor controllers and then returns position data from the L.M.S. It also provides the switching signals to the probe system based upon a comparison of commanded position and L.M.S. input data on position. In this way, the data is gathered at positions determined by the L.M.S. in order to maintain high accuracy in the x or y scan axis. The receiver is also strobed by the digital system in order to obtain the phase/amplitude readings at the proper position locations. Conventional servo motors and controllers have been installed in order to facilitate the interface provided by the digital system. All axes can be moved via the computer or manually by a local control: the local control allows initial setup of peak and null positions to known locations. A common carrier interface (Hewlett Packard Interface Bus) is used in conjunction with the digital interface to provide control of the synthesizer, T.W.T.s, and the receiver.

The receiver is the remaining item of the electronic complement and is the other contributor of error with respect to the measurement accuracy. Because of the facility size, the receiver must operate over very long cable runs at the same time that it provides accurate phase measurements. Down conversion is performed at the probes in order to send back a lower frequency and hence a lower loss signal; this is especially important with the higher frequency capability of 18 GHz. The transmitter (synthesizer) and TWT are carried with the test antenna as it moves in order to keep the cable run to the test antenna as short as possible (minimize loss). The phase error associated with the receiver system is given by:

$$\Delta\phi = 360 \frac{\Delta L}{L_o} \times \frac{\Delta f}{f_o}$$

Where:

$\Delta\phi$ = phase

ΔL = cable length change

L_o = base cable length

Δf = transmitter drift

f_o = transmitter center frequency

With the stable temperatures of the facility and the stable synthesizer it has been determined that the phase error is rather small. The phase error at 10 GHz over a time period of 4 hours is only 1.5^o which is much less than the 5° allocated in the original system design.

Computer The system presently on line consists of a Hewellett Packard 21MX minicomputer using RTE IV in conjunction with a Floating Point Systems array processor model AP120-B. Fifty megabytes of storage is available in a disc peripheral; a magnetic tape unit is also included together with C.R.T/keyboard and a plotter. This configuration was chosen after trade-off studies involving off-line processing on a CDC machine and the use of a programmable disc in conjunction with the minicomputer. The FFT is processed using a standard FOR2D algorithm and a Table I below shows the total processing time for various sizes of square data arrays. The table also includes the data measurement times associated with each matrix.

Test Results A ten foot diameter solid dish has been tested in the facility (Figure 4) to verify the facility performance. Pattern and gain data was obtained on this dish at the National Bureau of Standards before the dish was installed in the facility. Data was obtained at frequencies of 1, 6 & 10 GHz in the facility and principal plane patterns are shown in

TABLE I DATA GATHERING AND PROCESSING TIMES

MATRIX SIZE	DATA GATHERING TIME	DATA PROCESSING TIME
64^2	0.5 hr.	1 min.
128^2	1 hr.	3 min.
256^2	2 hr.	7 min.
512^2	4 hr.	21 min.
Estimated		
1024^2	8 hr.	1 hr. 10 min.
2048^2	16 hr.	3 hr. 20 min.

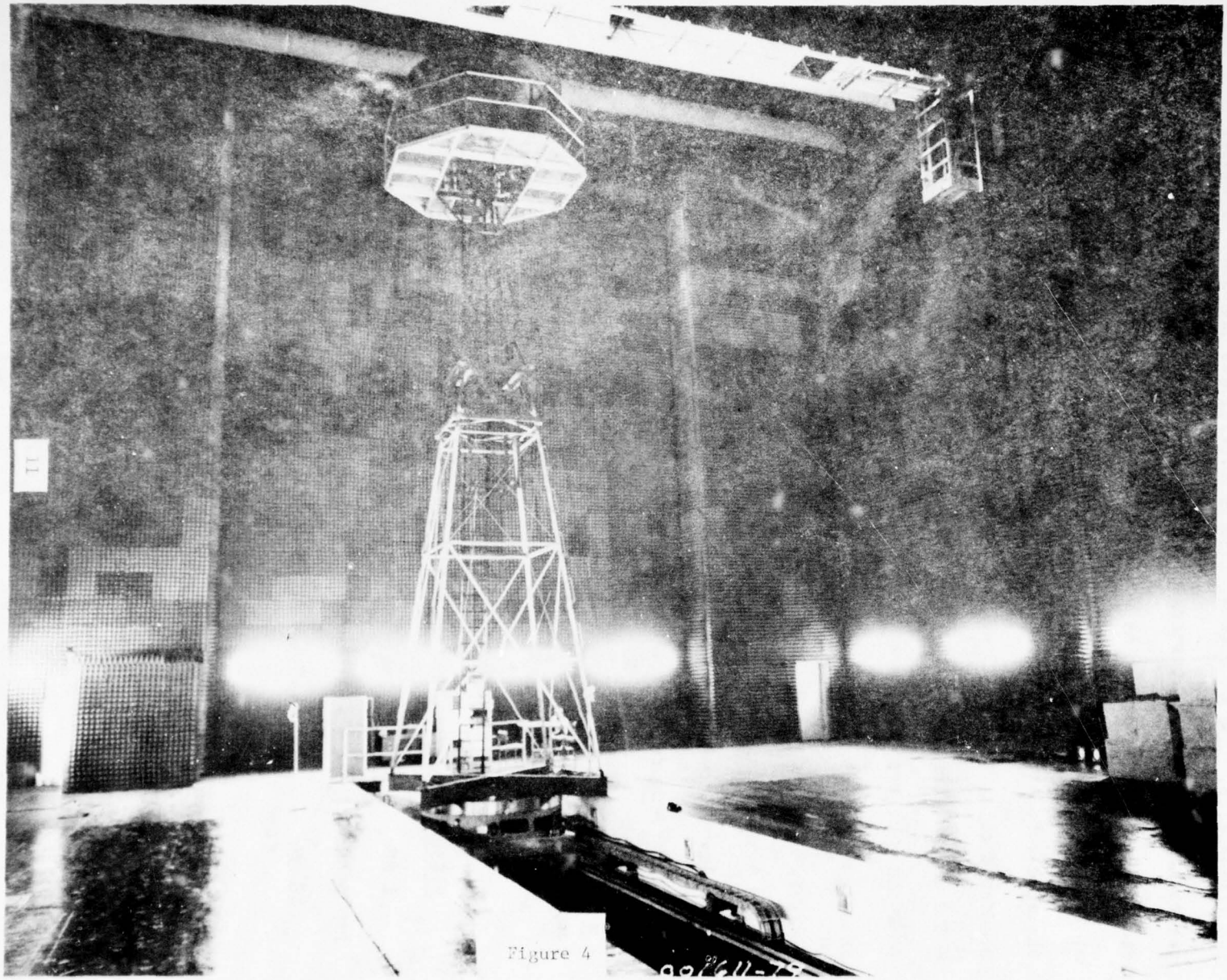

Figure 4

the following figures (Figures 5 through 10) for E&H plane at each of the frequencies. The data is plotted in overlay fashion with the dots representing the data obtained in the facility and the solid lines indicating the N.B.S. data. As would be expected, the comparison is better at 1 GHz than it is at 10 GHz because the error analysis indicated that the side lobe errors would become greater with increasing frequency. The predicted error in the -25 db relative sidelobes is $\pm$ 0.8 db at 1 GHz, $\pm$ 0.9 db at 6 GHz and $\pm$ 1.5 db at 10 GHz. As can be seen in Figure 5 and 6 (1 GHz patterns), the error in the close in ($\sim$ -25db) side lobes is about 1 to 1.5 db. From Figure 7 and 8 (6 GHz patterns), it is seen that the error at -25db is about 2 to 2.5 db. 10 GHz patterns are shown in Figure 9 and 10 and again the error is about 2 to 2.5 db at -25db. The main beams all overlay to the tolerance of the plots and the farther out sidelobe structure follows the general shape of the N.B.S. patterns very well. Gain measurements were also made for the three frequencies and a comparison is shown below in Table 2.

TABLE 2 GAIN COMPARISON

Frequency	N.B.S. Gain	Facility Gain
1 GHz	26.61 db	
6 GHz	41.17 db	
10 GHz	47.02 db	

These gain measurements compare quite well to the data supplied by N.B.S. and they fall within the $\pm$ 0.2 db predicted by the error analysis. The facility designs and hardware/software implementations have provided the

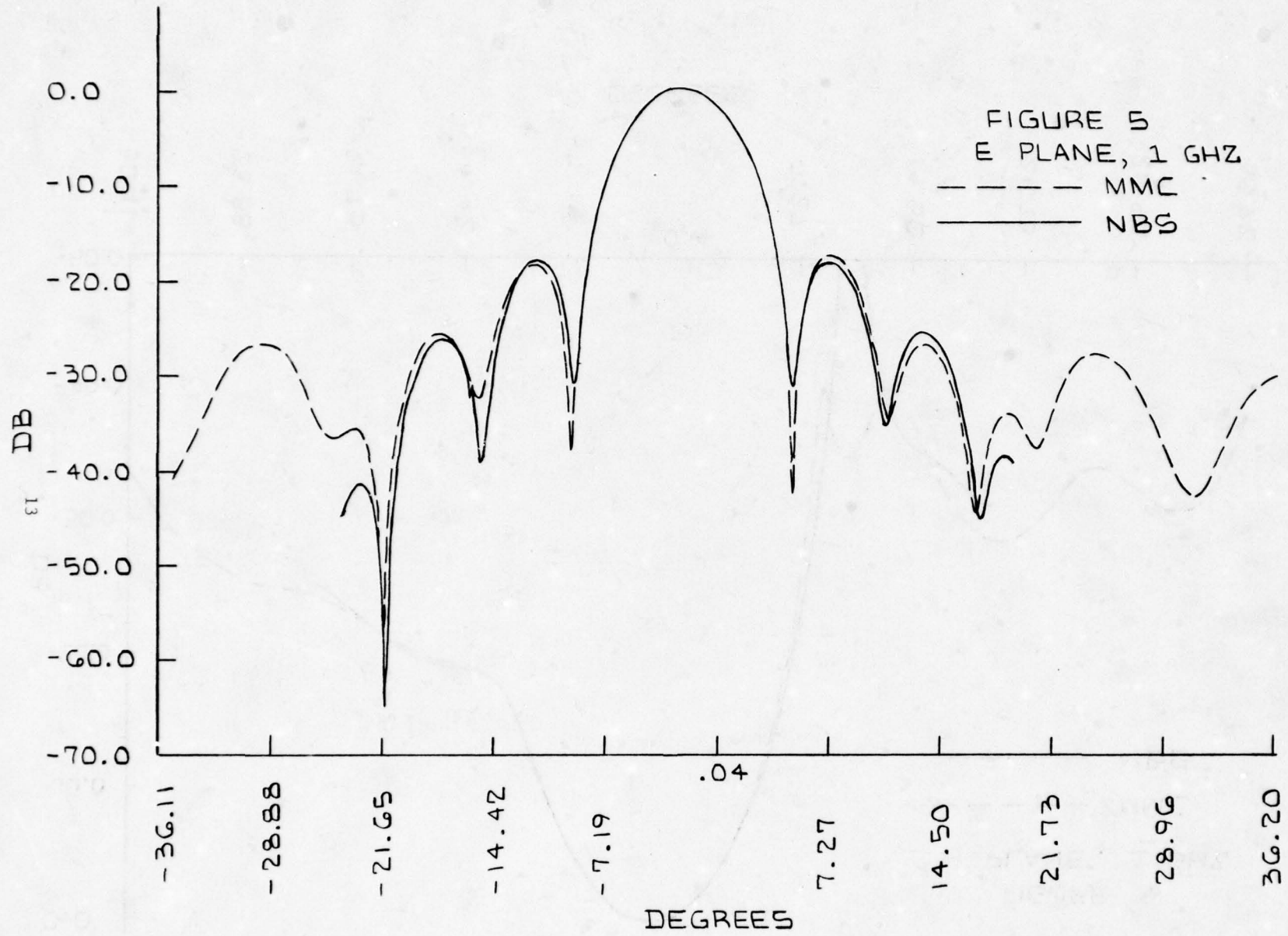
FIGURE 5
E PLANE, 1 GHZ
MMC
NBS
0.0
-10.0
-20.0
-30.0
-40.0
-50.0
-60.0
-70.0
DB
-36.11
-28.88
-21.65
-14.42
-7.19
.04
7.27
14.50
21.73
28.96
36.20
DEGREES

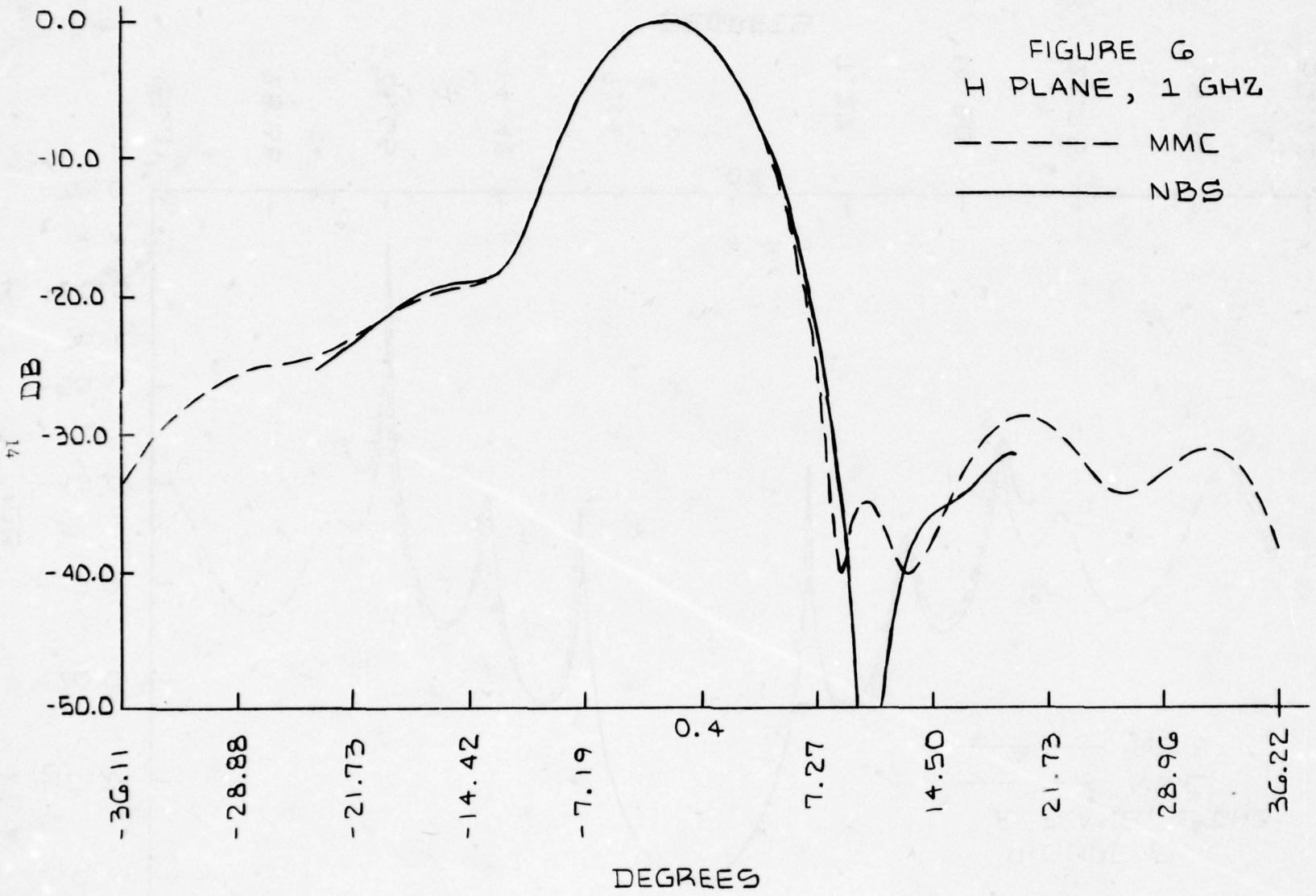

FIGURE 6
H PLANE, 1 GHZ

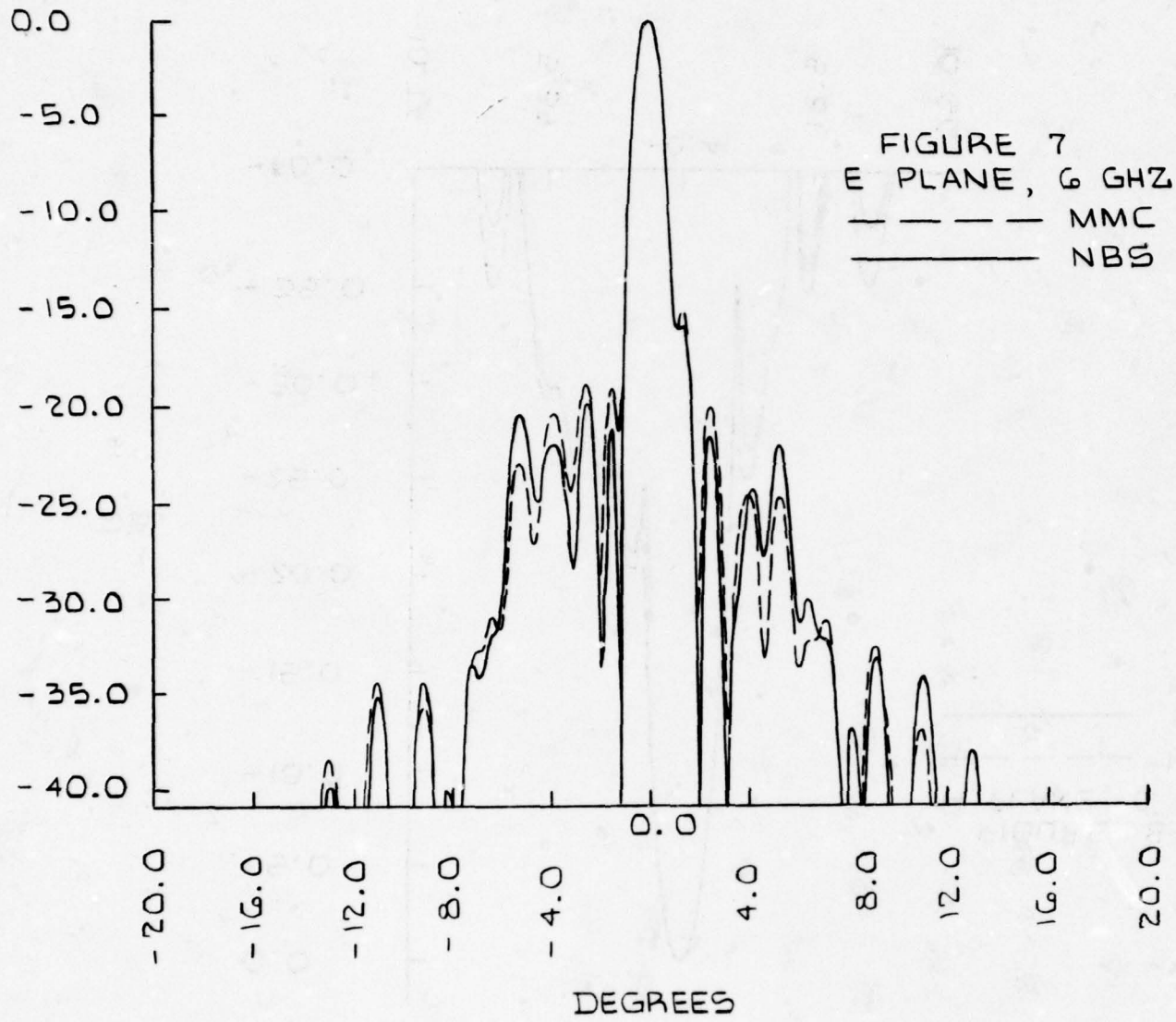

FIGURE 7
E PLANE, 6 GHZ
— — — — MMC
——————— NBS

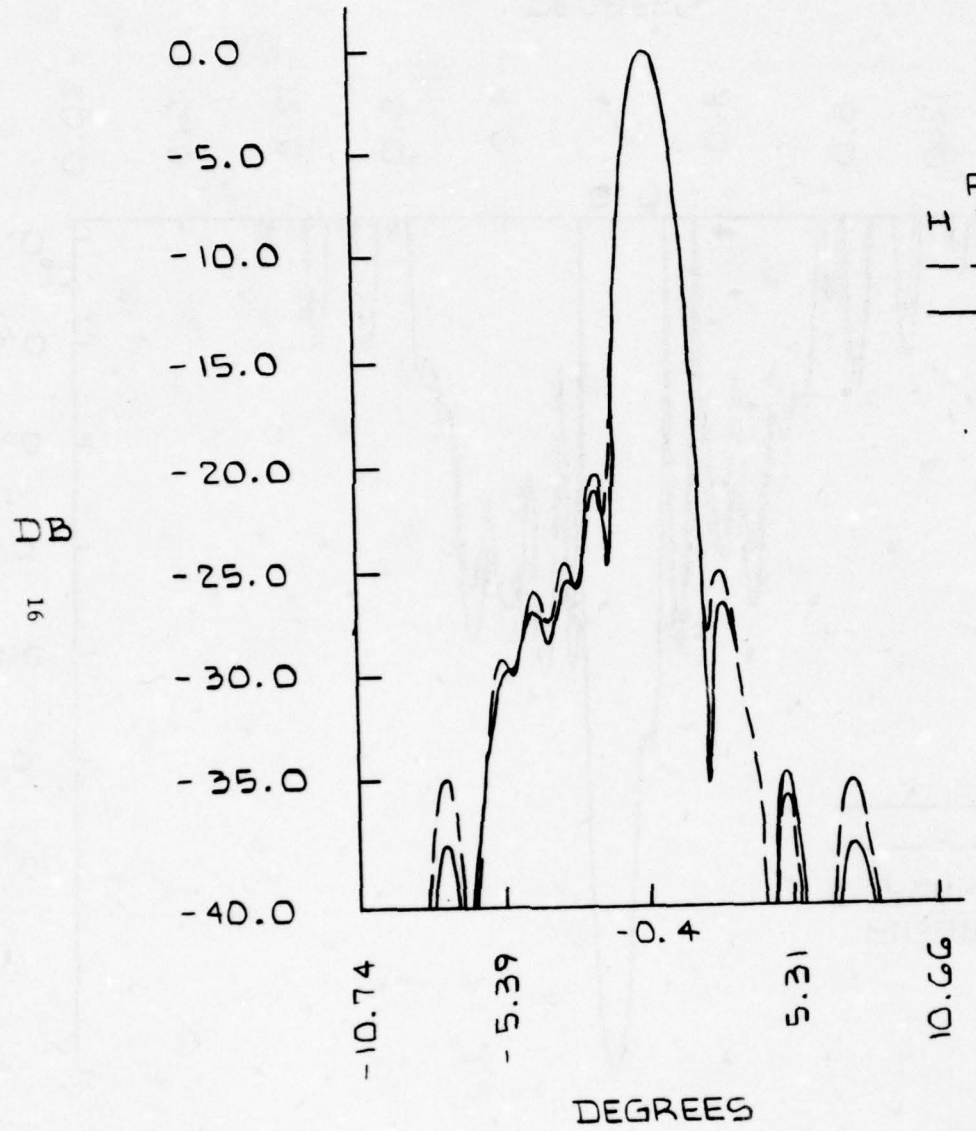

FIGURE 8
H PLANE, 6 GHZ
– – – – – MMC
——— NBS

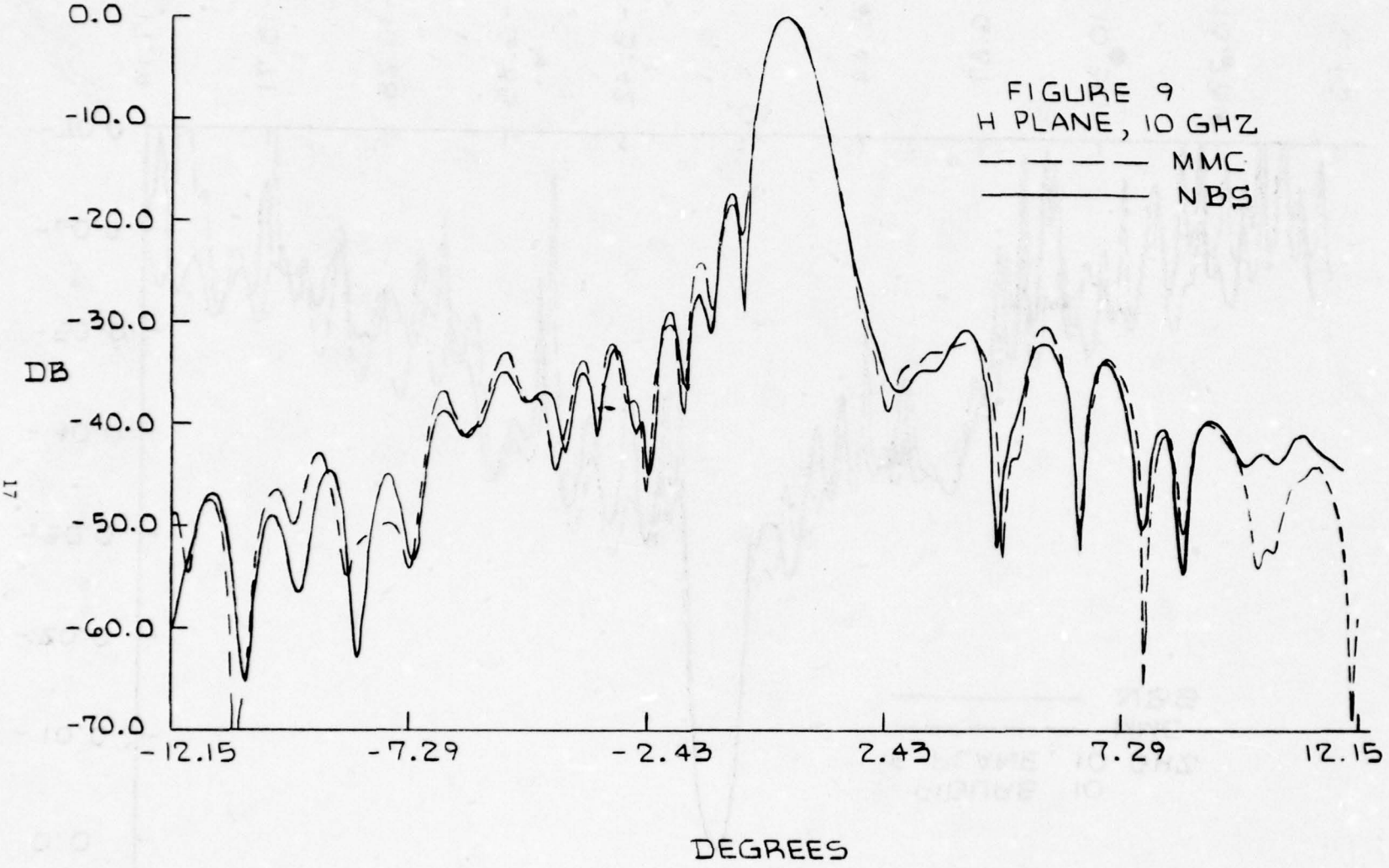

FIGURE 9
H PLANE, 10 GHZ

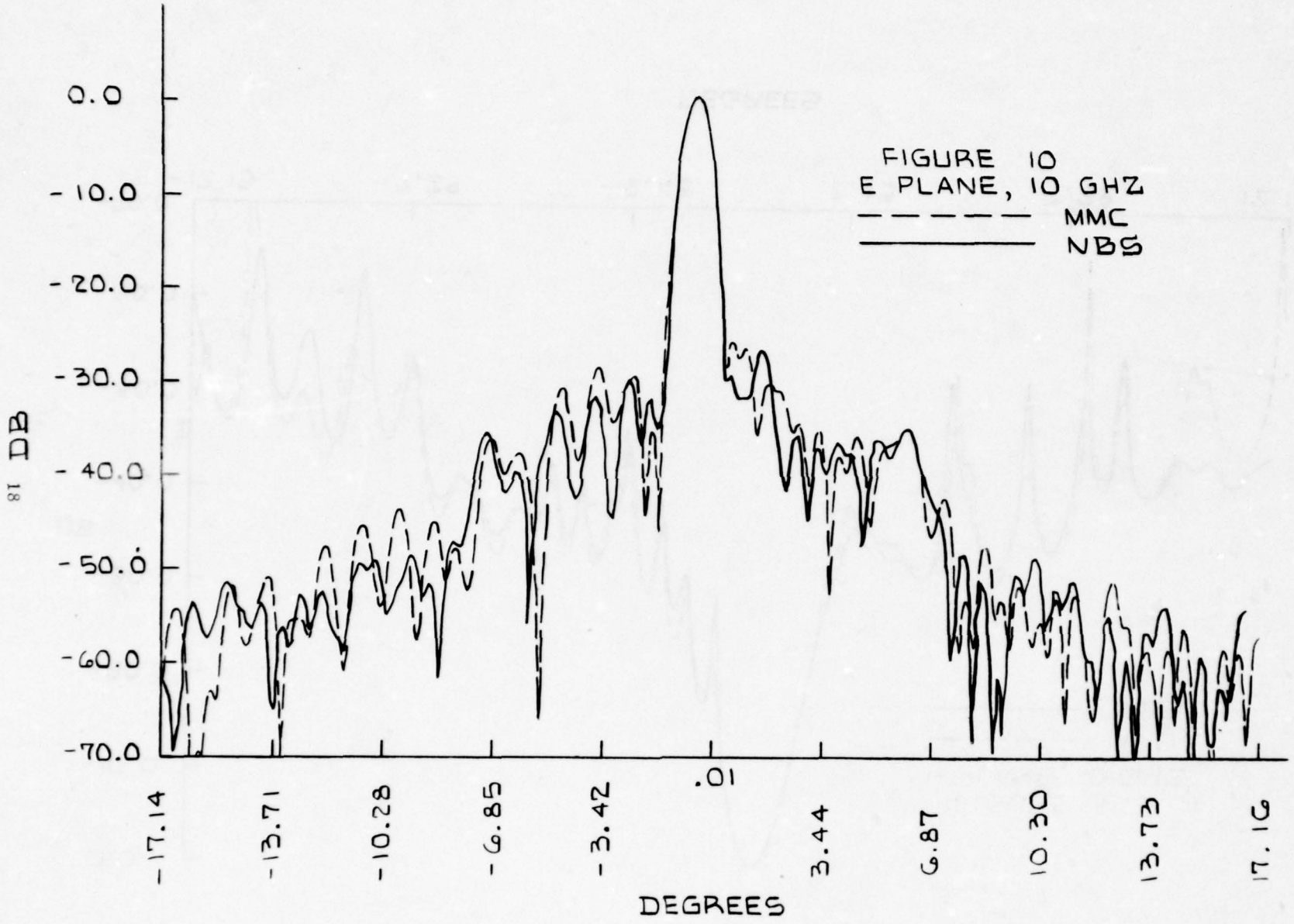
FIGURE 10
E PLANE, 10 GHZ
MMC
NBS
0.0
-10.0
-20.0
-30.0
-40.0
-50.0
-60.0
-70.0
DB
-17.14
-13.71
-10.28
-6.85
-3.42
.01
3.44
6.87
10.30
13.73
17.16
DEGREES

predicted measurement capabilities and accuracies for the 10 foot diameter antenna and we will now continue facility checkout with larger aperture antennas.

PLANAR NEAR FIELD MEASUREMENTS FOR AIRCRAFT ANTENNA APPLICATIONS

by

Jerome D. Hanfling
Raytheon Company
Missile Systems Division
Bedford, Massachusetts

Prepared for

1979 Antenna Applications Symposium

Sponsored by

University of Illinois

and

Electromagnetic Sciences Division of RADC
Hanscom, AFB

Held at

Allerton Park
Monticello, Illinois

on

September 26 - 28, 1979

ABSTRACT

This paper attempts to put into perspective past and current work dealing with planar near field measurements for nose-mounted and fuselage-mounted aircraft antenna applications. Also some recent results and progress are described.

I. INTRODUCTION

Programs have been sponsored by the Air Force Avionics Laboratory (AFAL) and the Aeronautical Systems Division (ASD) of WPAFB for the purpose of developing Planar Near Field Measurement Techniques and Equipment for aircraft antenna applications (12, 16, 21). These efforts have been applied to both nose-mounted directive antennas and to fuselage-mounted broadbeam antennas. Recent endeavors* have been associated with the testing of on-aircraft antennas using a portable near field test system (Portable Pattern Analyzer), as shown in Figure 1 (13). The ultimate objective was the development of a portable near field test system for the flight line. This makes possible far field pattern predictions of operationally-installed directive airborne-antennas by accurately measuring and processing near field data.

Although flight-line near field testing envisions nose-mounted procedures, a major requirement exists for the operational evaluation of low directivity antennas mounted on fuselage locations. The patterns of these antennas are affected by diffraction, reflection and blockage of the air-frame itself. Proven numerical techniques such as the electromagnetic GTD computer model for large aircraft are available and have been used as design aids (8)(5). However, these models depend upon assumptions that the fields from the driven element are known a' priori (theoretically). A method has been explored that would eliminate the a' priori assumptions by incorporating near field measured data from actual antennas processed by a "Backward Fourier Transform" (BXFORM) algorithm in order to synthesize the antenna under test, this is followed by numerical pattern evaluation(20). This will make possible radiation pattern validation and certification of low-profile fuselage-mounted high-frequency (≥ 100 MHz) antennas.

An alternate method for predicting the far field patterns of broadbeam fuselage or wing-mounted antennas incorporates Radar Cross Section data describing the scattering properties of the aircraft, together with near field (NF) antenna plane wave spectrum (PWS) data. This is particularly applicable to tactically configured fighter aircraft, where complex launcher, pylon and stores arrangements occur(6).

II. DIRECTIVE AIRCRAFT ANTENNAS

The portable near field test system has been used to check out several nose mounted on-aircraft directive antennas. These have included the following:

---

*Contract No. F33657-78-C-0679 between the Raytheon Company and the U.S. Air Force Aeronautical Systems Division, Wright-Patterson AFB.

1) The S-band 7' parabolic reflector antenna and the X-band APN-59 search radar on the EC-135N Apollo Range Instrumentation Aircraft A/RIA[17].

2) The APQ-113 Ku-Band attack radar antenna on the FB111A aircraft[13].

3) The APQ-128 Ku-Band terrain following radar antenna on the FB111A aircraft [21]. (See Figure 2.)

4) The APQ-130 Ku-Band attack radar antenna on the F111D aircraft [21]. (See Figure 2.)

Basic Pattern Properties

The fundamental pattern properties such as gain, beamwidths, and sidelobes were measured on all these antennas so that the antenna performance could be compared to a specification. Typical performance specifications for the attack radars are listed in Table I. Also an important capability of the near field test system was to measure the antenna boresight. This is done in conjunction with difference pattern null depth and location measurements and scanner alignment procedures.

Scanner Alignment Technique

A collimating telescope on the scanner probe support together with a mirror bracketed to the aircraft permits alignment of the scanner data sampling plane with a reference plane on the aircraft such as the bulkhead. The determination of the far field difference pattern from near field measurements gives the null direction. Null region blow-ups, as part of the test system software, provide accurate boresight measurements. To achieve more precision, alternate alignment techniques using lasers have been applied.

Scan Limitations

In case 1) listed above, the telemetry antenna aperture was larger than the scanner traverse capability thereby resulting in scan limited near field data. As a result of test techniques and computer software developed previously, the merging of two sets of planar near field data was demonstrated with good results[17]. Also synthetic data extrapolation techniques were investigated. Such techniques create artificial extensions of the scan-limited NF amplitude and phase data to simulate an adequate, but physically unachievable scan length. Figure 3a shows NF amplitude extrapolation using exponentially decaying estimates (exponent NPR = 1.5, 3). Also shown are end point, constraint extrapolations over the unmeasured region found by fitting the measured scan-limited data plus two additional end point samples with an interpolating polynominal. The solid line shows the adequate NF data acquired by merging two measurement rasters. The far field patterns corresponding to these NF data extrapolations have been compared with good results, as shown in Figure 3b [15]. Extrapolation methods have also been used to find accurate far field gain from scan limited NF data [11].

The size of the scanner and the distance from the antenna determine the angular extent over which useful pattern data can be obtained, as shown in Figure 4a and 4b [7]. This is evident in the attack radar tests, as shown in Figure 5. Here with the radome open, the probe was set at 1/2' and 9' distance from the antenna focal region. The pattern characteristics evident at

TABLE 1

ANTENNA PATTERN PARAMETERS OF F111-D ATTACK RADAR ANTENNA (AN/APQ-130)

Typical Test Conditions

Test Frequencies	16, 16.2, 16.4 GHz
Test Direction	Broadside
Test Polarization	Linear
Antenna Polarization	VP, HP, CP

Typical Test Parameters and Requirements

Pencil Beam Mode		
Sum		
Gain		35.7 dBi
Beamwidth	EL	2.6 deg
	AZ	1.7 deg
Sidelobes	EL	-17 dB
	AZ	-17 dB, 16 dB (HP)
Difference		
Gain		33 dBI
Beamwidth (Outer 3 dB)		5 deg
Sidelobes		-15 dB
Null Direction versus Frequency		±0.5 deg
Null Depth		-30 dB (Minimum)
Shaped Beam Mode		
Gain		32 dBI
Beam Shape		$\csc^2 \theta \cos \theta$ within ±2.5 dB from -5 deg to -40 deg
Beamwidth (AZ at toe)		1.7 deg
Sidelobes	AZ	-19 dB
	AZ at toe	-18 dB

the closer distance were cutoff at the longer distance. This spatial filtering effect can also be produced by using directive probes at closer separation distances.

Measurement Errors

A summary of some of the near field measurement and data processing errors is listed below:

1) Probe Position - ΔX, ΔY, ΔZ.
2) Scan-limited Sampling
3) Thinned Data Sets
4) Alignment of Scanner to Antenna Under Test (AUT)
   - Pitch, Yaw, Roll
   - Translation
5) Probe Compensation
6) Multiple Reflections
7) Computation/Processing
8) Instrumentation-Amplitude, Phase
9) RF Leakage

The most critical specification affecting the scanner construction is the distributuion of the probe-positioning errors. Among these errors, planarity (or $\Delta Z(X, Y)$) is the most critical[10].

Data Recording and Processing

A major advance affecting the portable near field concept has been the development of much improved data processing algorithms. Fast executing, minicomputer programs have replaced Fourier processing and are capable of both far field (FF) pattern and gain computations from typical NF data sets in less than 45 seconds after the measurement is complete.

This simplification takes advantage of antenna pattern symmetries so that reduced NF data sets can be recorded. Also, the thinned NF data is collapsed to an equivalent line source so that a particular pattern cut can be determined over an arbitrary angular extent to an arbitrary angular resolution (14), (11), (18).

The collapse technique is illustrated in Figure 6 by sampling the fields of a uniformly illuminated circular aperture. Here step-wise thinning of the data decreases data recording time. Subsequently this thinned data is collapsed to an equivalent line source, and then transformed to obtain the far field for a single pattern cut.

Fault Detection and Diagnosis

Much effort was dedicated to the quick detection and location of antenna faults in a flight test environment. The emphasis here was to minimize the data gathering and data processing tasks so that go/no-go antenna verification could be accomplished. Algorithms were developed that provided useful

NF data with a minimum number of scans and then this data was "collapsed" on a line in order to quickly compute the antenna patterns along a single far field cut [19].

Examples of faults that could be detected were the failure of the vacuum systems used to shape the reflector of the APQ-113 and 130 antennas as shown in Figure 7. The patterns for both the pencil and shaped beam modes are compared, as shown in Figures 8 and 9. Also misalignment of the feed for reflector antennas like the APQ-130 and the ARIA can be detected by observation of difference pattern null shift and null fill [17].

Radome Effects

The effect of the radome is evident by comparing the FF patterns shown with and without the radome in Figures 10 and 11 on the F-111 aircraft. For the sum mode pencil beam, the radome does scatter energy in the sidelobes especially in the E-plane. Even though the data field scan is limited, the pitot tube region of the radome acts as a secondary radiation source enabling a wider field of view of useful pattern information. Further evidence of this occurs for the difference mode where the center of the radome is not illuminated, therefore, the patterns are similar with and without the radome.

The effects of simulated radome damage also were investigated and were easily detected by near field measurements and far field data processing [13].

Portable Near Field Test System

For the flight line application a mock-up of a portable near field test system has been developed as shown in Figure 12. This represents a future generation antenna near field test set and is an alternative to the usual X, Y scanner. It is composed of three separate units of which two are essential for test operations. They are: the scanner, the computerized operator's console, and the peripheral equipment console [21].

The scanner is designed as a rotating arm type with its constantly polarized probe head moving along its length. This type of mechanism can be used to develop polar or cartesian near field data samples on a plane. The maximum scan area is formed by a circle whose radius is equal to the scan length of the scanner arm. There is no restriction on minimum scan area. The scanner can be placed in any attitude of scan plane from horizontal (parallel to the ground) to vertical (perpendicular to the ground); therefore it can be aligned to test nose-mounted or fuselage-mounted antennas. The height is adjustable and can be adapted to different height ranges by changing the length of the post that supports the scanner arm. Stability and adjustments for roll, pitch, and yaw are provided by the screw jacks in the base. Weight is such that all configurations and adjustments can be performed by one person. Test probe motion is provided by three separate axis control mechanisms, with commands coming from a computer controlled processor. Control of scanner positioning is such that position feedback prevents "hunting" by the mechanical systems. Since scanner movement is computer controlled, scanning can be in the conventional rectangular mode or in a circular mode. Positioning of the probe is determined by commanding it to required X, Y or ρ, θ coordinate positions. All data can be expressed with respect to these positions.

In order to control the scanner, process data, etc., the following equipments are employed: the computerized operators console contains the operator's interface, data display, and all other electronics essential to perform near field analysis of antenna systems. It has two modes of operation: antenna test and analysis mode and system programming and diagnostic mode. The system programming and diagnostic mode uses the existing test and analysis operating system for test program development, test generation, program and test editing, and test system diagnosis. Access to this mode is via the console keyboard. Thus, this test system is self supporting. The peripheral equipment console contains a hard copy unit, a paper tape reader, and a paper tape punch.

III. FUSELAGE MOUNTED BROADBEAM ANTENNAS

The patterns of broadbeam antennae on-aircraft can be measured in the far field by full scale aircraft tests or by scale model testing. Both are expensive, time consumming, inconvenient techniques with inaccuracies and approximations depending on the particular situation and facility. Cases occur where modifications to existing antennas or their location or changes to the aircraft stores are made. It becomes particularly inconvenient and costly to perform full scale far field pattern testing.

The approaches being investigated here are to determine the pattern of the antenna by near field measurements and compute its interaction with the aircraft using existing or future Geometrical Theory of Diffraction (GTD) scattering programs for the aircraft [16]. Earlier broadbeam studies developed useful sampling criteria when the antenna was sufficiently decoupled from the air frame [9].

Backward Transform

An approach that includes air frame effects involves measurement of the fields close to the antenna and then fourier transforming the fields back to the aperture plane (backward transform) in order to reconstruct the primary illuminating currents. These currents then become the new sources for GTD programs which model the air frame. This is illustrated for the KC-135 aircraft, as shown in Figure 13.

As with other near field analysis the electromagnetic field is represented by a plane wave spectrum (PWS) on the measurement plane. This representation separates the active part of the field carrying energy away from the aperture from the reactive part stored near the aperture, as formulated in Figure 14a. Whereas in determining the far field the reactive fields are attenuated away from the measurement plane here in the backward transform these fields must be preserved and are amplified, as is formulated in Figure 14b and illustrated in Figure 15. The amplification also increases the effects of computation and measurement noise, see Figure 15. Another source of error is "aliasing" (replicas of the PWS that overlap the desired PWS) which occur as a result of the chosen sample spacing, as shown in Figure 16. These errors in conjunction with the backward transform amplification factor represent fundamental limitations to the accuracy that can be attained in the reconstruction of the aperture fields.

A study was carried out in which the Backward Fourier Transform algorithms were developed and measurement criteria determined. These were applied to data from two planar antenna cases, one a single aperture and the other four apertures both on conducting ground planes; in the former the fields were determined numerically and in the latter from actual near field measurements [4], [20].

The conclusions of the Backward Transform investigation were the establishment of algorithm design and near field measurement criteria as listed below:

Backward Transform Algorithm Design:

In reconstructing the aperature fields use only the incident plane waves u, v that are within a radial distance D,

$$1) \quad \sqrt{u^2 + v^2} \leq D$$

such that in the translation of the fields from the measurement plane to the aperture plane the amplification is less than some prescribed magnitude M,

$$2) \quad e^{|w|d} \leq M \quad \text{(See Figure 14b)}$$

where w is the Z directed wave number

$$w = \sqrt{k^2 - u^2 - v^2} \qquad \text{(in the visible space)}$$

$$w = j|\sqrt{k^2 - u^2 - v^2} \qquad \text{(in the invisible space)}$$

and d is the separation between planes.

In order to avoid "aliasing", choose near field sample spacing(s),

$$3) \quad s \leq \frac{\pi}{D} \quad \text{(see Figure 16)}$$

This means that the invisible region of the PWS on the u, v plane that is used in the backward transform will be limited to the range

$$4) \quad \frac{2\pi}{\lambda} \leq \sqrt{u^2 + v^2} \leq \frac{\pi}{s} \quad \text{(see Figure 16)}$$

Measurement Conclusion:

1) If data are taken at several λ' s from the antenna aperture only the PWS within the visible space should be used in performing the Backward Transform. The reconstructed aperture distribution is then a smoothed version of the true distribution, the fine details are filtered out.

2) If a more accurate reconstruction of the antenna current distribution is sought, the measurements must be taken on a plane as close as possible to the antenna. Only a limited region of the invisible space has to be used and sample spacing must be chosen to avoid aliasing.

Spectral Scattering

Another approach to the inclusion of air frame effects is by near field measurement of the fields scattered from the aircraft. Here a model of the aircraft is illuminated and the fields are measured on a plane. The PWS with and without the aircraft is determined from the near field data and subtracted. The result is the plane wave scattering spectrum of the aircraft. Investigations are proceeding whereby the interaction between the PWS of a free space broadbeam antenna and the PWS from the complex scattering air frame can be used to find the total field of the antenna radiating on the air frame. Earlier studies have confirmed this approach for near zone interactions in shipboard radar applications [23].

IV. PHASED ARRAYS

Measurement of nose mounted phased array antennas will provide a new challenge and important application for the planar near field technique. Near field test data from phased array measurements can be used to derive the usual antenna pattern performance data and in addition, to determine pattern parameters that are characteristic of phased arrays as follows:

1) Individual element failures
2) Element group failures
3) Subarray phase and amplitude alignment
4) Element patterns
5) Pattern characteristics of scanned beams
6) Time multiplexed measurements

Individual and group element failures can be detected and located directly from the near field data. Alignment of the phase and amplitude radiated from subarrays of elements is a natural for the near field technique by either direct or transforming to far field output.

The measurement of the broadbeam element pattern of the array can be done on a deliverable array by connecting to the input of an individual element in the array and measuring the near fields. This avoids the problems inherent in far field pattern measurements of the nondirective radiators. The electronic scanning of the phased array requires either repositioning the scanner to avoid cutting off useful pattern data or data merging. In addition any wide angle measurements requires careful probe calibration. Also electronic scanning together with multiple ports will increase the need for dynamic near field measurements where multiple beams or ports can be measured in a single traverse of the probe by switching. This will have a significant impact on the receiver test equipment to achieve a wider signal-bandwidth capability. Production Phased Array Antennas near field test facilities are already developed for major Navy and Army applications [22]. Advanced airborne phased arrays like the Electronically Agile Radar (EAR) can utilize near field measurements with similar benefits.

V. CONCLUSION

Excellent progress has been made in applying planar near field measurements to aircraft antenna applications. Effort should continue on near field test systems, to support the maintenance of nose-mounted directive antennae, expecially with the emergence of phased array radar antennas. This could be done on the flight line, in the shops or at the depot facilities.

Also, further effort is needed to apply the near field measurements to broadbeam on-aircraft antennae, where electromagnetic interaction with the air-frame and stores is present. Here both the backward transform and spectral scattering approaches appear promising.

VI. REFERENCES

1) Borgiotti, G.V., "A General Way of Representing the Electromagnetic Field," ALTA Frequenza No. 5 Vol. 31, March 1962.

2) Borgiotti, G.V., "Fourier Transform Method in Aperture Antenna Problems," ALTA Frequenza No. 11, Vol. 32, November 1963.

3) Borgiotti, G.V., "A Novel Expression for the Mutual Admittance of Planar Radiating Elements," Vol. AP-16, May 1968.

4) Donn, C. and Thiele, G.A., "Memorandom on the Radiation Pattern of a Slot Asymmetrically Located on a Square Plate," Ohio State University, Technical Report 3468-1, June 1973.

5) Burnside, W.D., Marhefka, R.J., and Yu, C.L., "Roll-Plane Analysis of On-Aircraft Antennas," IEEE Transactions, AP, November 1973.

6) Edwards, J.L., Ryan, C.E., Jr., Storey, W.J., "Measurement of Bistatic Near-Zone Radar Cross Section," 1974 International IEEE AP-S Symposium Program and Digest, Georgia Institute of Technology, pp. 174-177, June 1974.

7) Newell, A.C., and Crawford, M.L., "Planar Near Field Measurements on High Performance Arrays", National Bureau of Standards, NBSIR 74-380, July 1974.

8) Burnside, W.D., Gilreath, M.C., Marhefka, R.J., and Yu, C.L., "A Study of KC-135 Aircraft Antenna Patterns," IEEE Transactions, AP, May 1975.

9) Crawford, M.L., Newel, A.C., Greene, J.W., and Yaghjian, A.D., "Experimental Design Study for a Near Field Broad Beam Antenna Pattern Calibration," National Bureau of Standards AFAL-TR-75-179, February 1976.

10) Grimm, K.R., "Antenna Analysis by Near Field Measurements," Microwave Journal, April 1976.

11) Kaplan, L. J., Dowling, T., Hanfling, J. D., Grimm, K. R., "Rapid Measurement and Determination of Antenna Patterns Using 'Collapsed' Near Field Data," 1977 IEEE Antenna and Propagation Society International Symposium, Palo Alto, California, June 1977.

12) Hanfling, J. D., and Kaplan, L. J., "Near Field Diagnostics Study," Raytheon Company, MSD BR-9754, AFAL-TR-77-141, July 1977.

13) Kirchhoff, G. E., Osborn, J. D., McKeever, B. A., "Flight Line Antenna Pattern Measurements," Symposium on Antenna Applications, (Allerton), 1977.

14) Dowling, T., Kaplan, L. J., Hanfling, J. D., Grimm, K. R., "Small Computer Interactive Near Field Measurements for Directive Antennas," Symposium on Antenna Applications, (Allerton), 1977.

15) Grimm, K. R., and Schmidt, "Scan-Limited Near Field Testing for Directive Airborne Antennas, NAECON, May 1978.

16) Hanfling, J. D., and Kaplan, L. J., "Hybrid On-Aircraft Pattern Evaluation," MSD BR-10541, AFAL-TE-78-142, September 1978.

17) Osborn, J. D., "Aircraft Antenna Pattern Measurements Using Near Field Techniques," Symposium on Antenna Applications, (Allerton), 1978.

18) Kaplan, L. J., Hanfling, J. D., Dowling, T., "Determination of Antenna Gain from Limited Near Field Data Measurements" to be presented at 1978 IEEE Antenna and Propagation Society International Symposium, College Park, Maryland, 1978.

19) Kaplan, L. J., Dowling, T. B., Hanfling, J. D., Grimm, K. R., "Rapid Planar Near Field Measurements," Microwave Journal, January 1979.

20) Hanfling, J. D., Borgiotti, G. V., and Kaplan, L. J., "The Backward Transform of the Near Field for Reconstruction of Aperture Fields," IEEE Antenna and Propagation Society International Symposium, Seattle, Washington, June 1979.

21) Hanfling, J. D., and Trotter, J. D., "Evaluation of the Portable Pattern Analyzer," Final Report to be issued.

22) Staiman, D., "Automated Near Field Antenna Test Set for Phased Array Antenna Production", RCA Moorestown, N. J. (Presented during this conference), September 1979.

23) Ryan, C. E. et al, "Main Beam Distortion Effects of Ships Superstructures on Radar Antenna Performance", Final Report A-1715, GA Tech, January 31, 1976, prepared under Navy Contract N00024-75-C-5099.

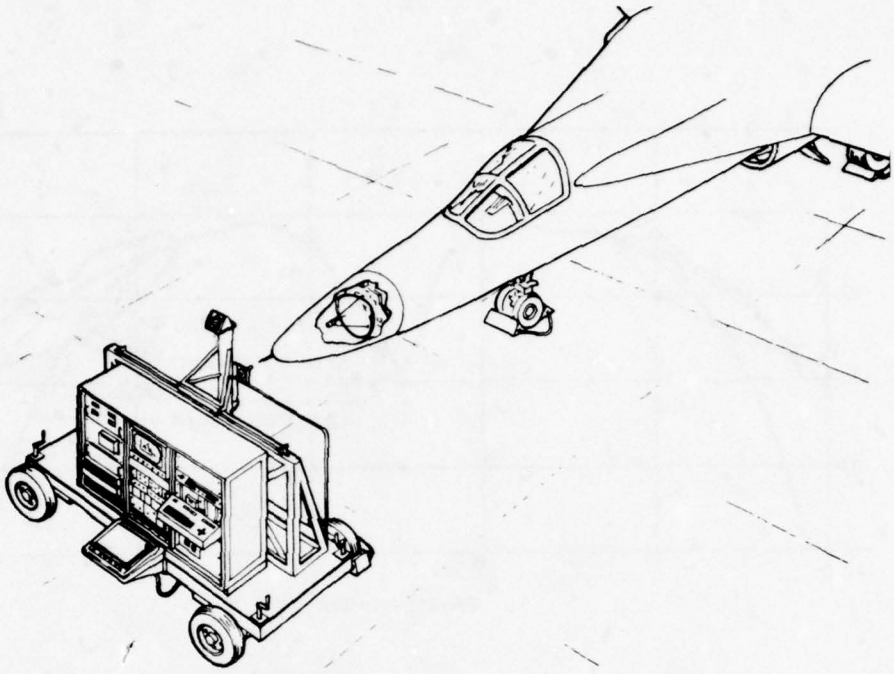

Figure 1 - Near Field Testing of Nose-Mounted Directive Antennas

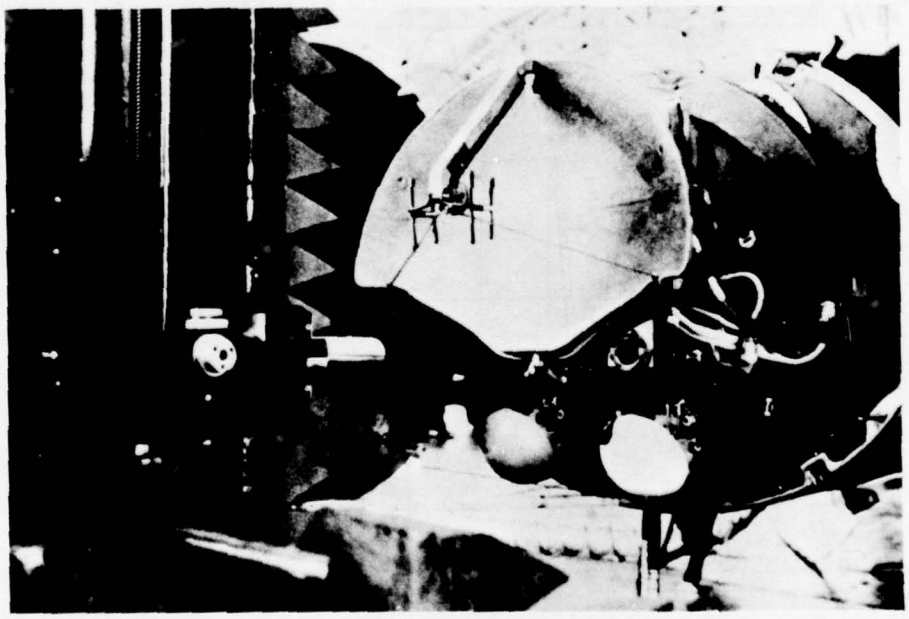

Figure 2 - APQ-130 and APQ-128 Ku-Band Attack and Terrain Following Radar Antennas on F-111D Aircraft

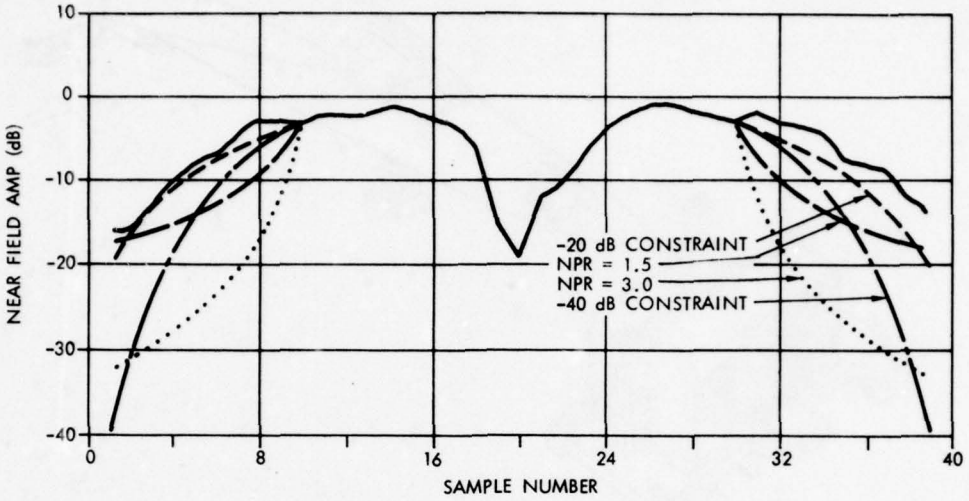

(a) Near Field Amplitude Extension by Power Extrapolation and by End Point Constraint

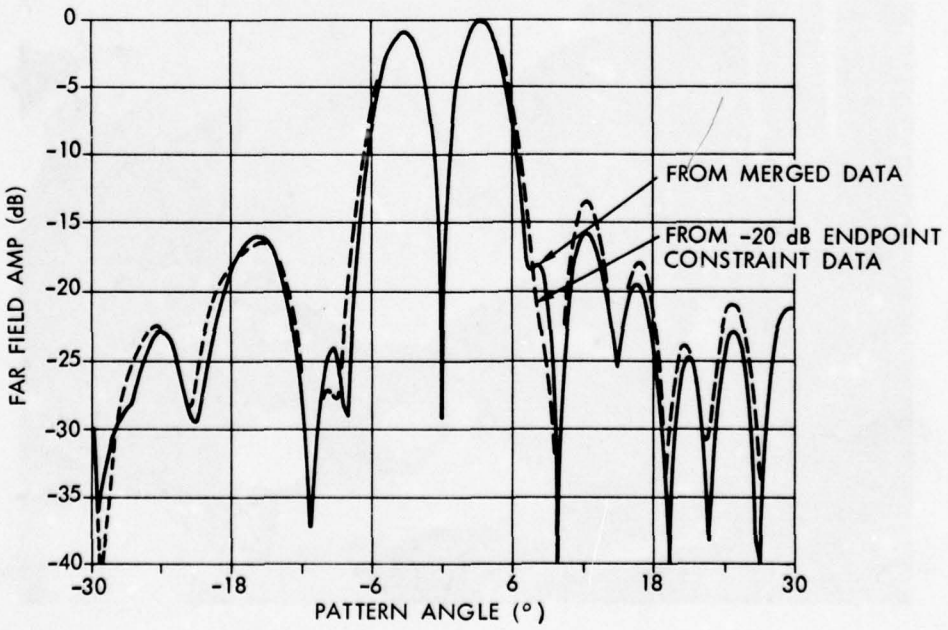

(b) Far Field Pattern from -20 dB End Point Constraint Near Field Extrapolation

Figure 3 - Synthetic Data Extrapolation Techniques

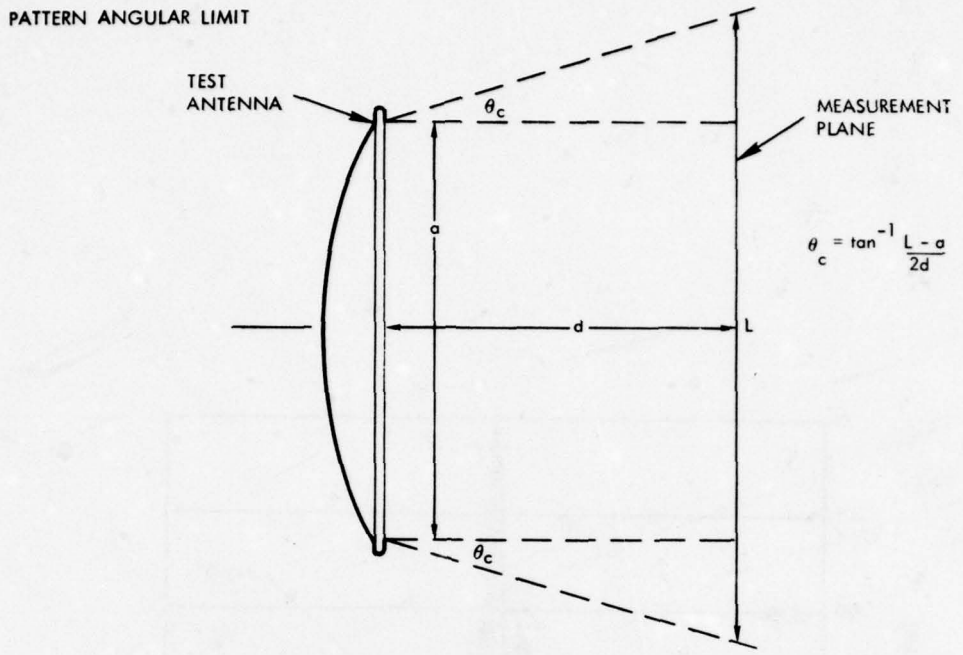

(a) Geometrical Optics Derivation of Angular Limit Formula

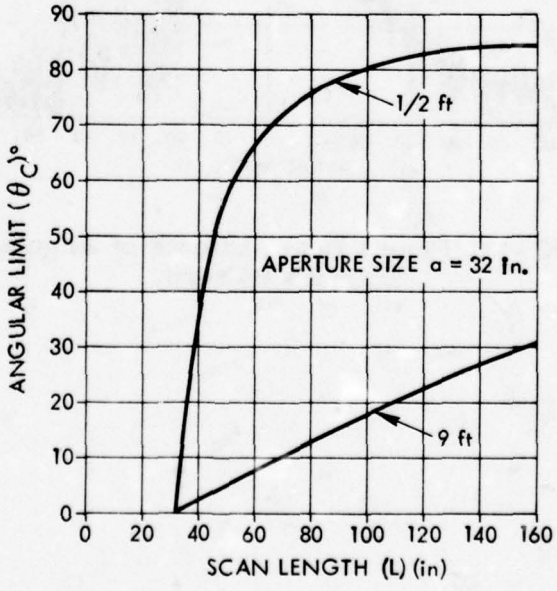

(b) Pattern Angular Limit for APQ-130 Antenna Test Distances

Figure 4 - Far Field Pattern Angular Limits

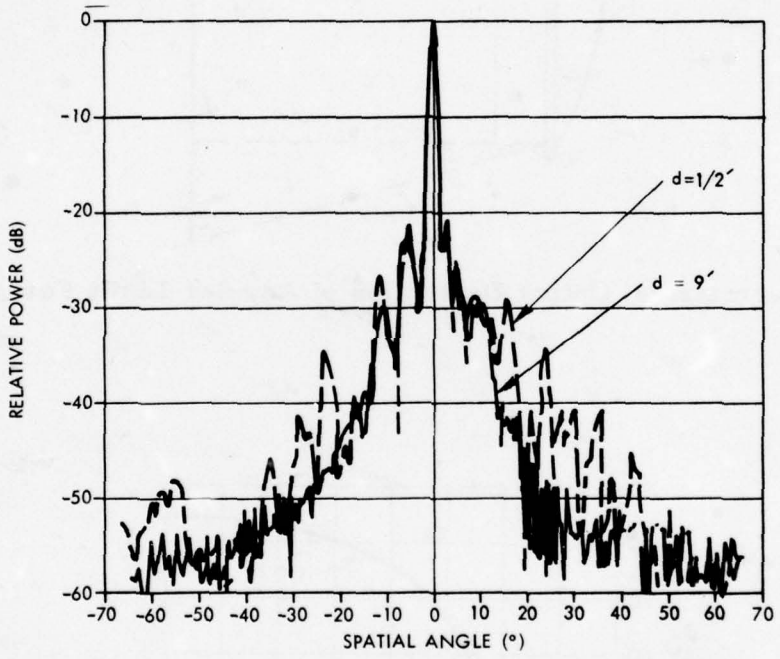

Figure 5 - APQ-130 Pencil Beam Effects of Angular Limits on Azimuth Pattern

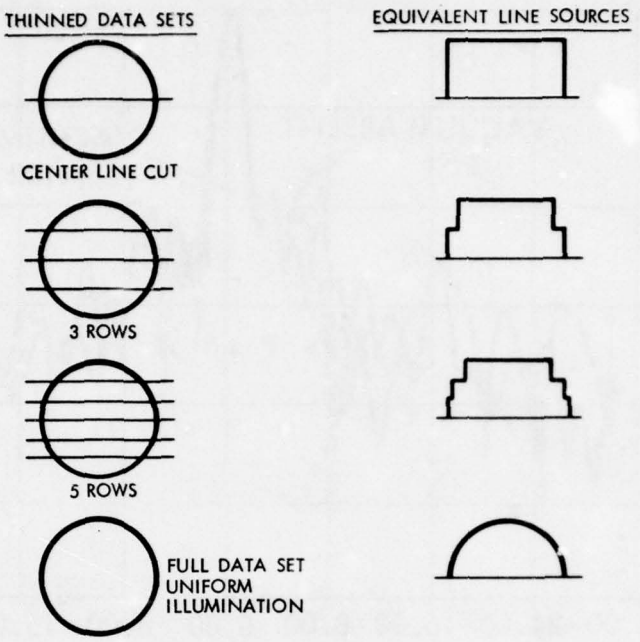

Figure 6 - "Collapsed" Equivalent Line Sources from Thinned Data Sets

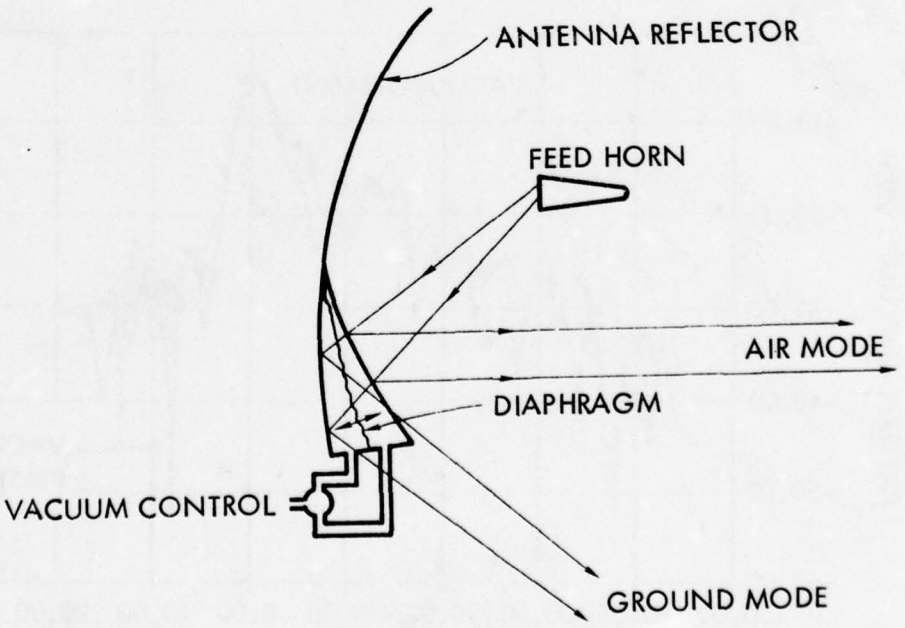

Figure 7 - APQ-130 Antenna Reflector Vacuum Pump Modification System

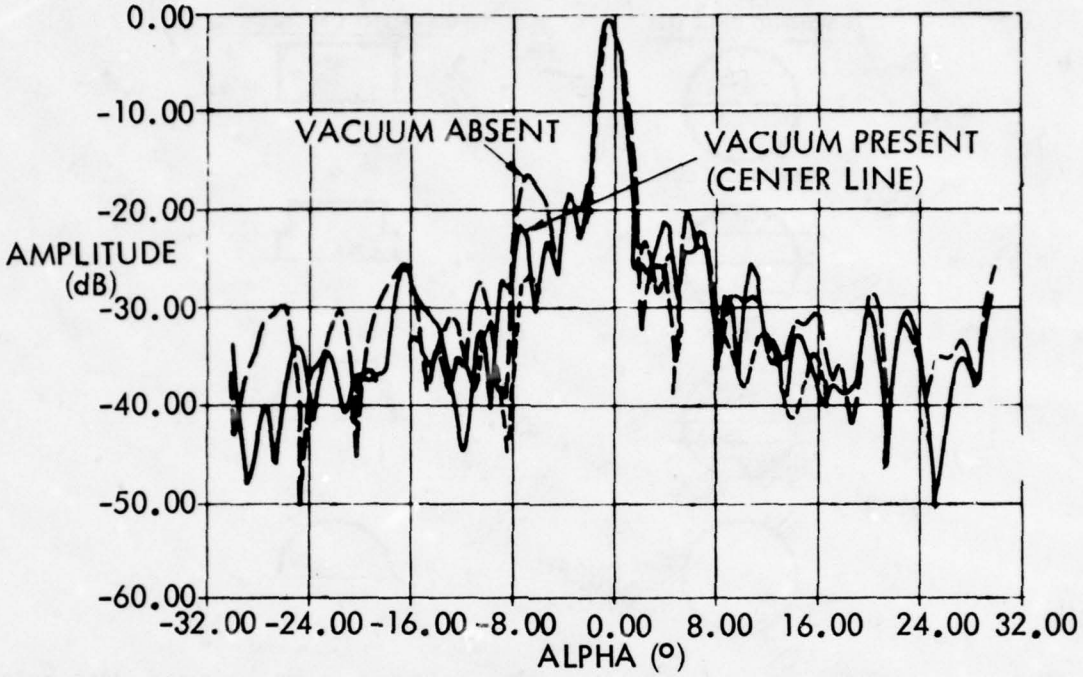

Figure 8 - Effect of Vacuum System Failure on Pencil Beam Patterns of APQ-113 Antenna

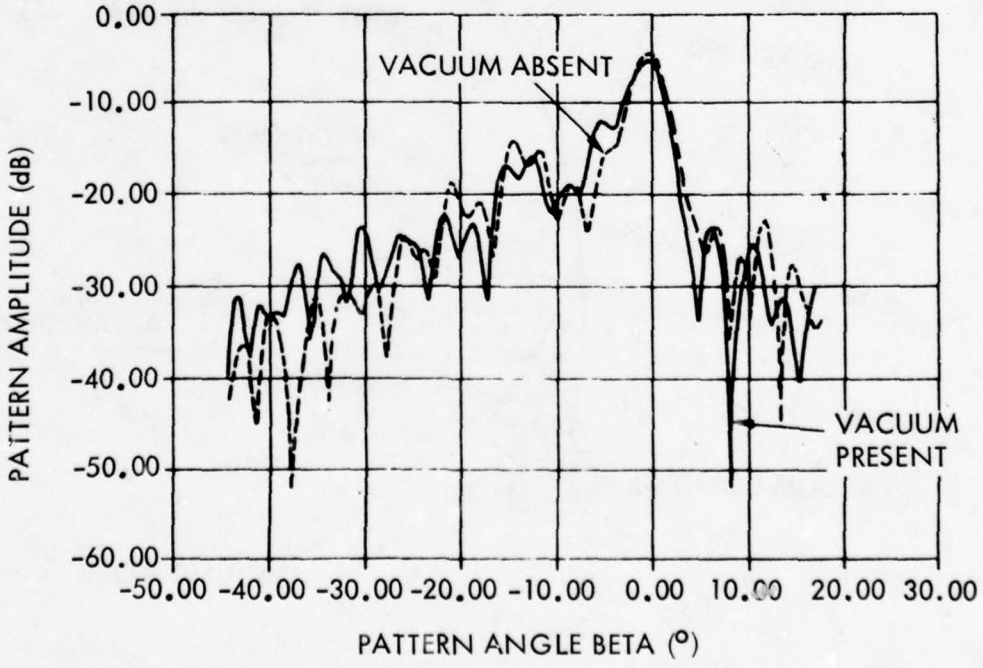

Figure 9 - Effect of Vacuum System Failure on Shaped Beam Patterns of APQ-113 Antenna

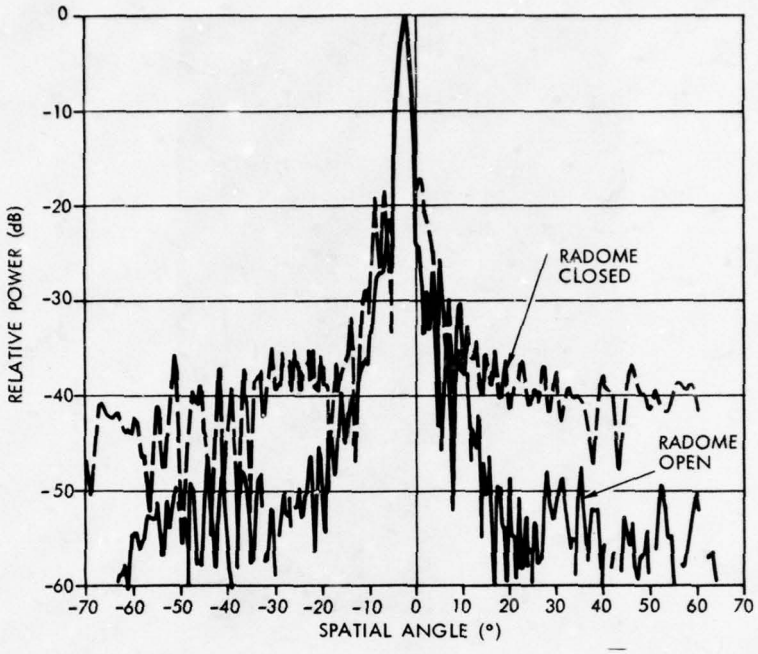

Figure 10 - Effect of Radome on APQ-130 Pencil Beam Sum Pattern, E-Plane

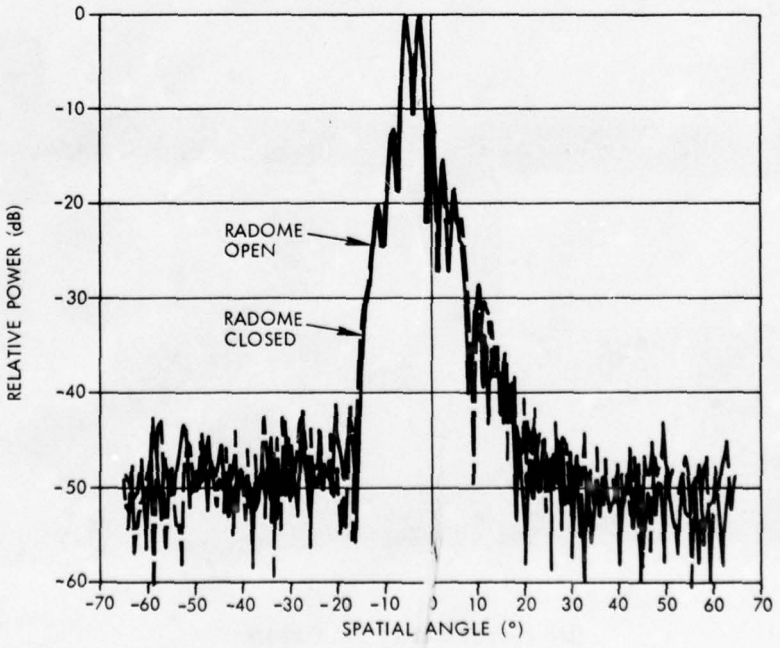

Figure 11 - Effect of Radome on Pencil Beam Difference Pattern, E-Plane

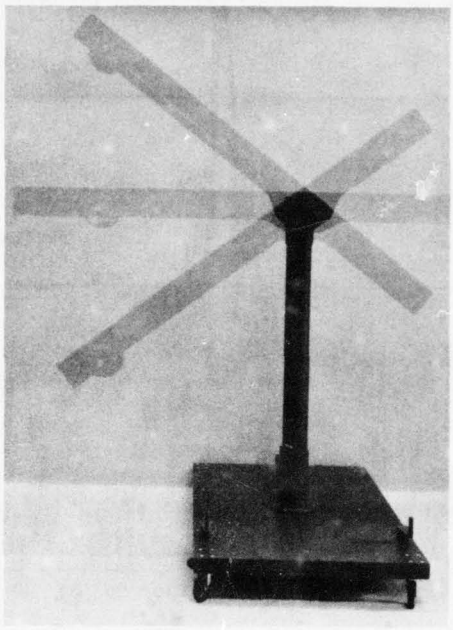

(a) Vertical Position

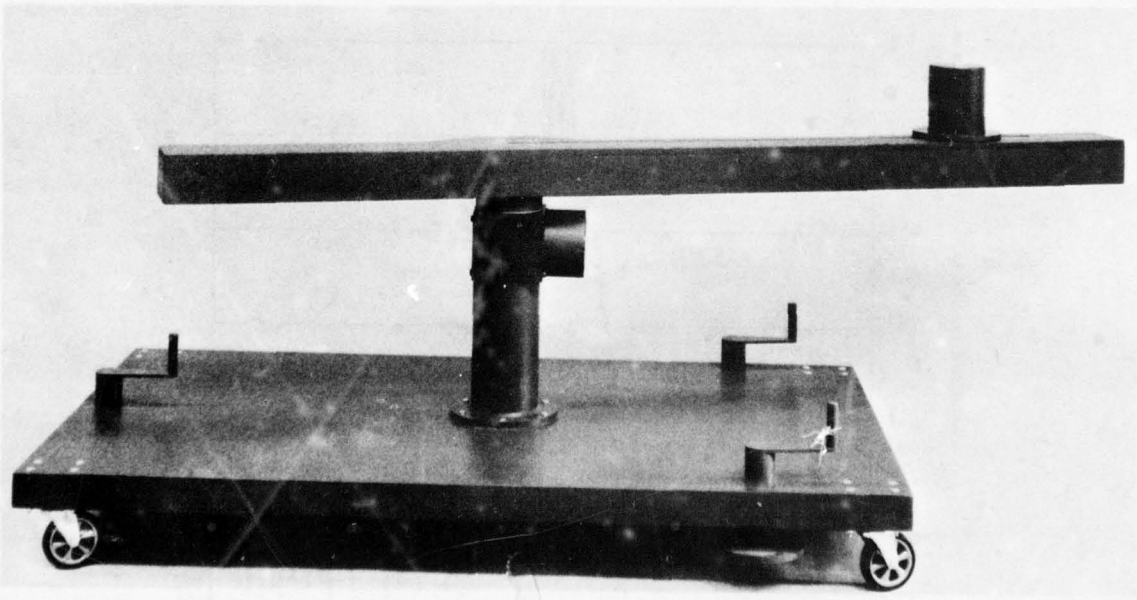

(b) Horizontal Position

Figure 12 - Rotating Arm Portable Near Field Test System

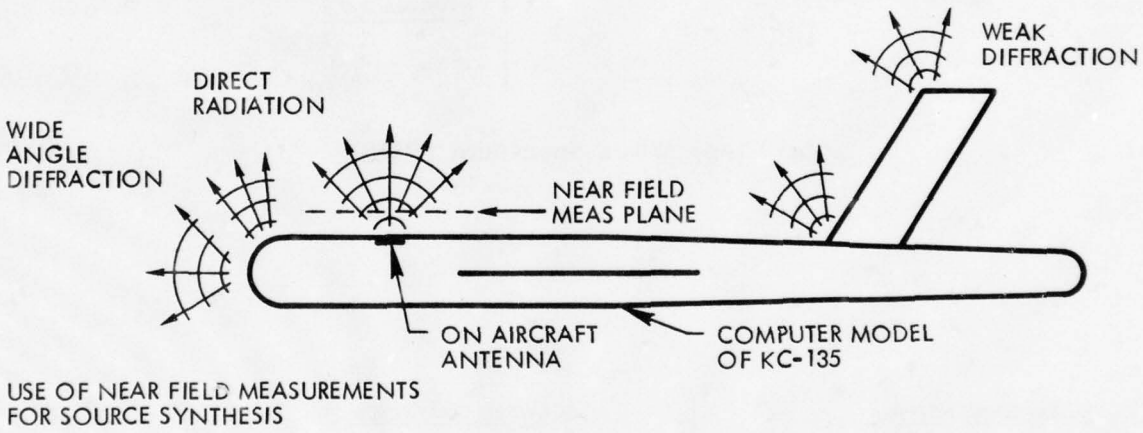

Figure 13 - Electromagnetic GTD Model of Airframe Scattering and Diffraction

GEOMETRY

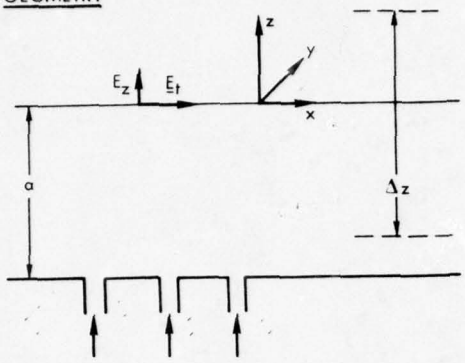

* U, V PROPORTIONAL TO THE DIRECTION COSINES WITH RESPECT TO X, Y AND THE PROPORTIONALITY CONSTANT IS $2\pi/\lambda$

NEAR FIELD:

$$\underline{E}(x,y) = \frac{1}{2\pi}\int_{-\infty}^{+\infty}\int_{-\infty}^{+\infty}\underline{\mathcal{E}}_t(u,v)\, e^{-j(ux+vy)}\, du\, dv$$

*
$$u = \frac{2\pi}{\lambda}\cos(90-\alpha) = \frac{2\pi}{\lambda}\sin\alpha$$
$$v = \frac{2\pi}{\lambda}\cos(90-\beta) = \frac{2\pi}{\lambda}\sin\beta$$

PLANE WAVE SPECTRUM:

$$\underline{\mathcal{E}}_t(u,v) = \frac{1}{2\pi}\int_{-\infty}^{+\infty}\int_{-\infty}^{+\infty}\underline{E}(x,y)\, e^{j(ux+vy)}\, dx\, dy$$

VISIBLE SPACE:

$$u^2 + v^2 < \left(\frac{2\pi}{\lambda}\right)^2$$

INVISIBLE SPACE:

$$u^2 + v^2 > \left(\frac{2\pi}{\lambda}\right)^2$$

(a) Plane Wave Spectrum (PWS)

FORWARD TRANSFORM

$$\underline{\mathcal{E}}_t(u,v,|\Delta z|) = \underline{\mathcal{E}}_t(u,v)\, e^{-jw|\Delta z|}$$

BACKWARD TRANSFORM

$$\underline{\mathcal{E}}_t(u,v,|\Delta z|) = \underline{\mathcal{E}}_t(u,v)\, e^{jw|\Delta z|} \quad \circ\circ$$

$$\underline{E}_t(x,y,|\Delta z|) = \frac{1}{2\pi}\int_{-\infty}^{+\infty}\int_{-\infty}^{+\infty}\left[\underline{\mathcal{E}}_t(u,v)\, e^{jw|\Delta z|}\right] e^{-j(ux+vy)}\, du\, dv$$

WHERE THE z - DIRECTED WAVE NUMBER (W) IS

$$w = \left|\sqrt{k^2 - u^2 - v^2}\right| \text{ (IN THE VISIBLE SPACE)} \quad w = -j\left|\sqrt{k^2 - u^2 - v^2}\right| \text{ (IN THE INVISIBLE SPACE)}$$

& $|\Delta z|$ IS THE DISTANCE FROM THE MEASUREMENT PLANE TO THE PLANE WHERE THE FORWARD OR BACKWARD TRANSFORM IS TAKEN

(b) Backward Fourier Transform

Figure 14 - Mathematical Formulation for the Reconstruction of Aperture Fields From NF Measurements

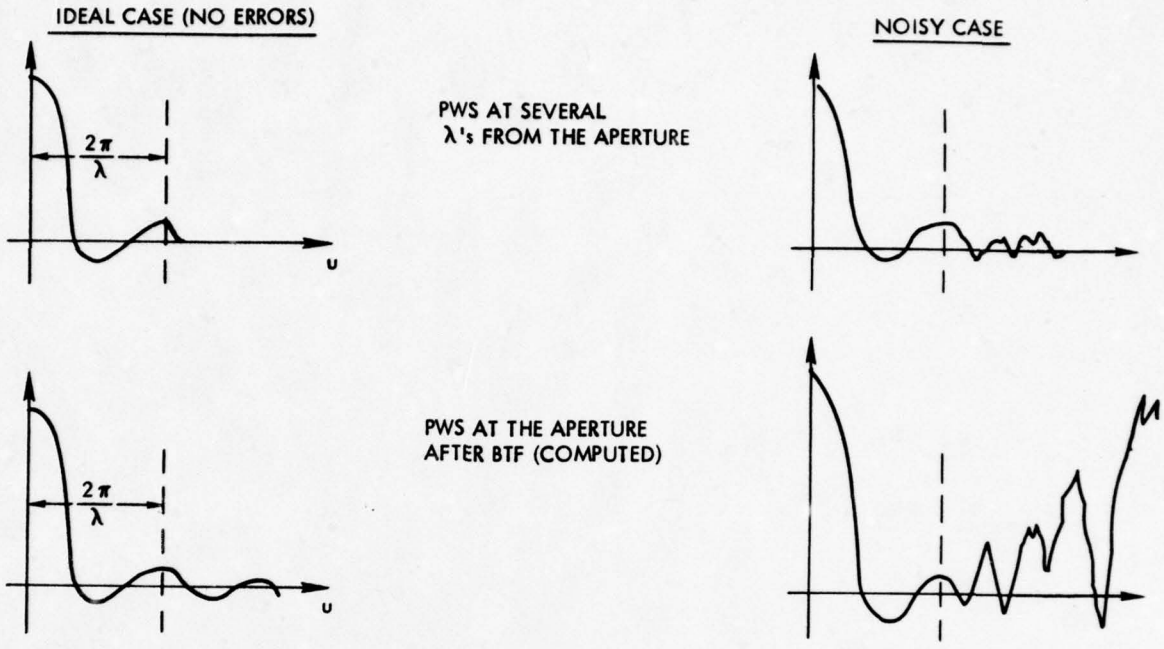

Figure 15 - Backward Transform - Effect of Measurement and Computation Round-Off Errors

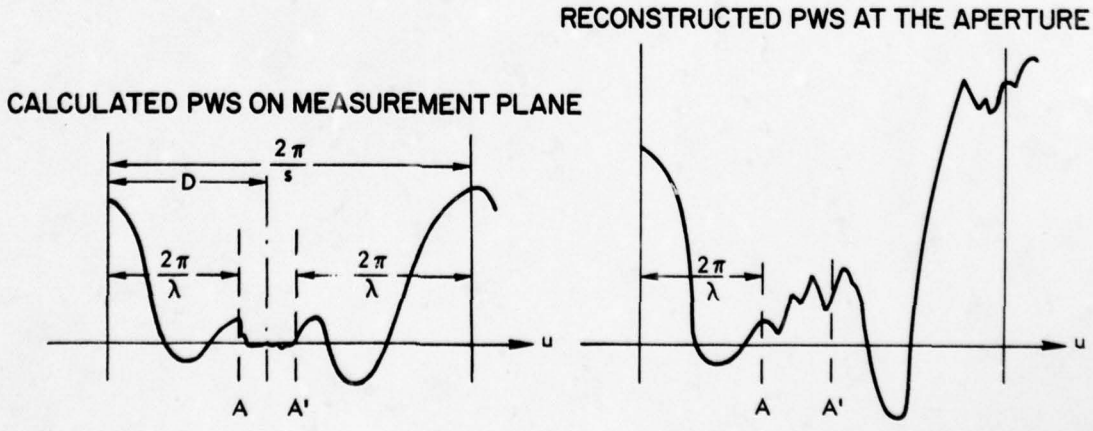

Figure 16 - Backward Transform - Effect of Sampling

SCIENTIFIC-ATLANTA
SERIES 1580 ANTENNA PATTERN RECORDER

by

Joseph H. Pape

Scientific-Atlanta, Atlanta GA

PRECEDING PAGE BLANK-NOT FILMED

PURPOSE AND APPLICATION

Antenna pattern recorders are used to plot the relative signal strength of an antenna under test as a function of the angular position of the antenna.

The signal plotted is obtained from the output of a receiver or directly from a microwave detector.

The position information is normally obtained from synchro transmitters geared to the test positioner axis.

Typical antenna pattern recorders are electromechanical devices which employ servo systems to drive the recorder axis. A chart drive servo system positions the recording paper as a function of the angular position of the antenna. A pen servo system positions a recording pen in response to the amplitude of the input signal.

Usually, provisions are made for a selection of amplitude functions. The pen deflection may be directly proportional to the amplitude of the input signal to the recorder, or the response may be proportional to the square, square-root or logarithm of the input. If the proper pen function is selected for the particular type detector used, either a linear or square law detector, the recording may be proportional to the RF Voltage, power or relative signal level in decibels.

When the receiving system provides a dc signal whose amplitude is proportional to the relative RF phase angle between two signals, the linear pen function may also be used to plot phase angle.

The pen function has typically been accomplished by precision potentiometer physically attached to the pen input servo system. Changing pen functions requires removal and installation of the potentiometer assembly.

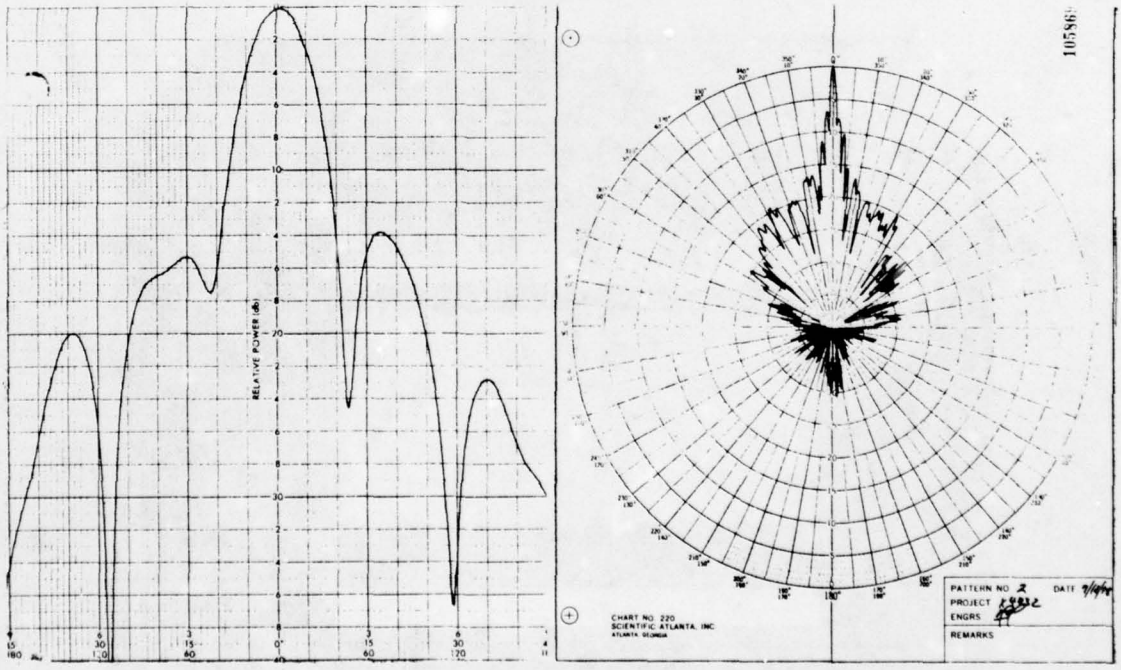

Antenna patterns may be recorded in either polar or rectangular coordinates. Polar coordinates are often preferred for plotting patterns of antennas that are not highly directional.

Generally, polar pattern recorders employ a turntable which rotates as the positioner moves, while rectangular recorders move the chart paper linearly. This mechanical difference requires separate recorder assemblies for generation of polar and rectangular plots.

OVERVIEW OF AN ADVANCED ANTENNA PATTERN RECORDER

With the advent of the microprocessor and other advanced digital devices, many improvements to the Antenna Pattern Recorder design are possible.

- The pattern recorder becomes a digital instrument operating under control of firmware stored in read only memory.
- Pen functions are performed by firmware and are selected by front panel controls.
- Analog or digital inputs are possible in both the chart and pen axis.
- Polar and rectangular plots may be generated on a single recorder.
- Digital interfaces also permit control by calculator or computer outputs.

Such a recorder now exists as the Scientific-Atlanta Series 1580 Antenna Pattern Recorder.

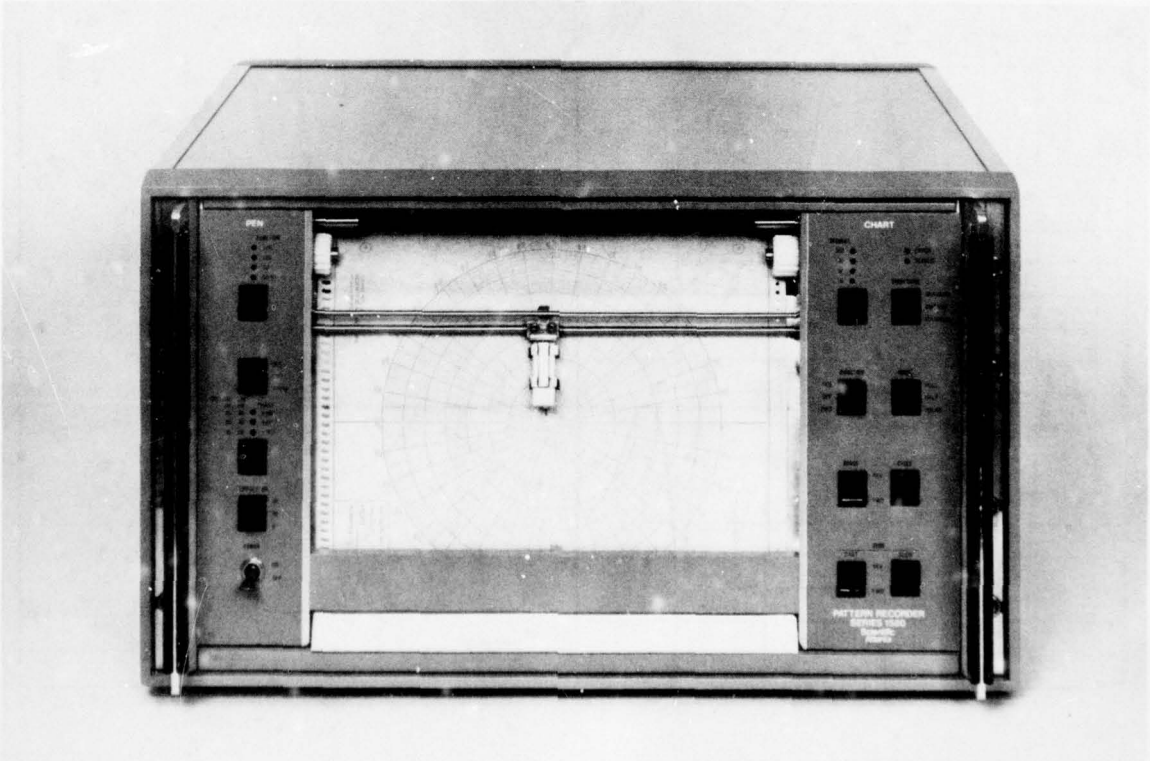

Series 1580 Antenna Pattern Recorder

SERIES 1580 PATTERN RECORDER

The 1580 Pattern Recorder consists of a basic mainframe and a number of optional modules. Some options are installed directly into the mainframe and others are external units.

The following paragraphs will discuss the mainframe, internal options, and then the external options. Later paragraphs will discuss recorder features implemented by firmware.

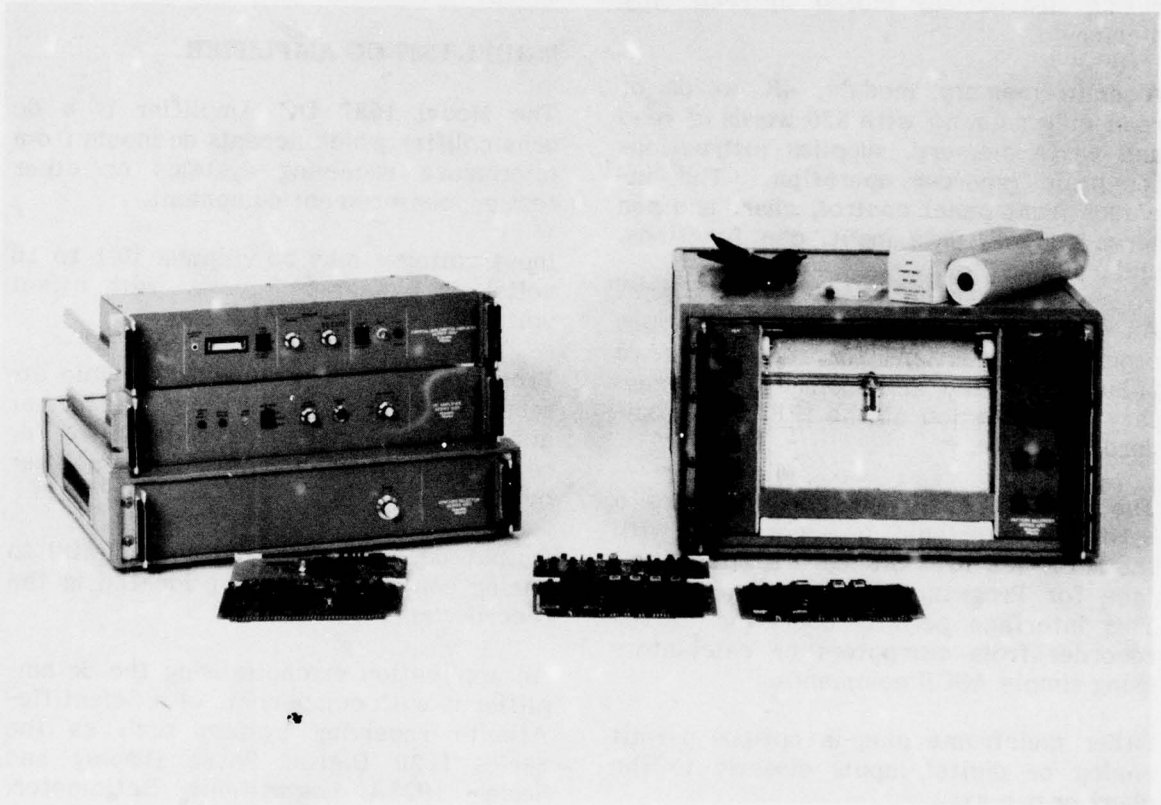

Series 1580 Antenna Pattern Recorder and accessories

MAINFRAME

The recorder mainframe includes the head assembly, control panel, digital card assembly, and power supplies for the mainframe and all optional units.

Contained in the head assembly are:

- Chart and pen drive motors and optical encoder
- Chart drum, paper supply holder, and paper idler arm
- Pen drive pulleys and cable system
- Paper sensors

The head assembly tilts forward and out of the recorder for paper installation. Chart paper is supplied in preprinted rolls with either rectangular or polar format.

The digital card assembly contains the microprocessor and memory circuit boards, front panel interface, chart and

pen servo interface, and slots for optional plug-in cards.

The microprocessor is a Texas Instrument TMS 9900. This is 16-bit general purpose device which internal hardware multiply and divide. Control is provided by executing instructions stored in read only memory.

A main memory module, 4K words of read-only memory with 526 words of read and write memory, supplies instructions for basic recorder operation. This includes front panel control, chart and pen servo control, data input, pen functions, and chart scaling.

An optional 2K memory module supplies program instructions for rectangular to polar conversion and instructions necessary for operation of the IEEE-488 standard interface.

The optional IEEE-488 card provides a hardware interface in accordance with the IEEE-488 1975 Standard Digital Interface for Programmable Instrumentation. This interface permits operation of the recorder from computers or calculators using simple ASCII commands.

Other mainframe plug-in options permit analog or digital inputs directly to the chart or pen axis.

Pen axis input option may be either digital for accepting parallel or byte input from digital devices; or analog to digital converter for interfacing to external AC or DC Preamplifier units.

The chart axis input may also be digital (parallel or byte); or an analog synchro input. Synchro inputs of 1:1 or 36:1 ratio will be accepted and processed by the recorder.

MODEL 1587 DC AMPLIFIER

The Model 1587 DC Amplifier is a dc preamplifier which accepts dc inputs from microwave receiving systems or other test or measurement equipment.

Input voltages may be unipolar (0.1 to 10 volts) or bipolar (±5 volts) with offset voltages up to 100 volts.

Front panel controls include variable attenuation over a 20 dB range and offset adjustments. Indication is provided for reverse polarity inputs and amplifier overload.

Output dc voltage is sent to a digital to analog converter interface located in the recorder mainframe.

An application example using the dc amplifier is with components of a Scientific-Atlanta receiving system such as the Series 1820 Digital Phase Display and Series 1833A Logarithmic Ratiometer. From these units, dc signals are available which permit recording of relative phase or signal level respectively.

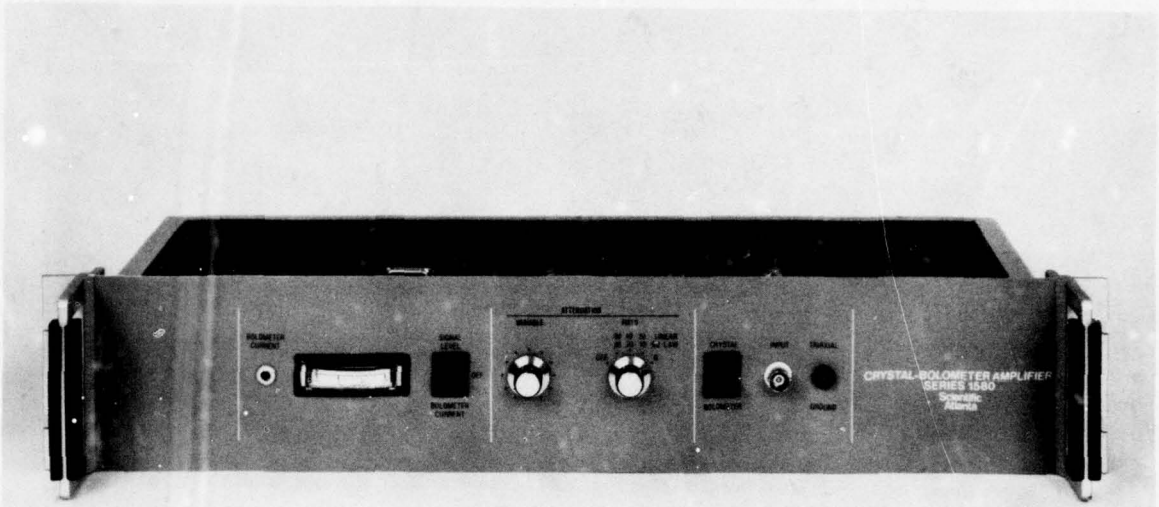

Model 1587 DC Amplifier

MODEL 1586 AC AMPLIFIER

The Model 1586 AC Amplifier is a high gain, low noise, narrow band preamplifier for low level inputs such as generated by bolometer or crystal detectors, or the 1 kHz output of a microwave receiver.

Signal inputs may range from 1 microvolt to 1V RMS for full scale pen deflection. Dynamic operating range is 80 dB.

To reject harmonics of the ac power line, standard filter center frequencies are 1000 Hz for 60 Hz line operation and 1025 Hz for 50 Hz operation. Typical filter bandwidth is 25 Hz. Analog signals processed by the preamplifier are sent to a digital to analog converter interface located in the recorder mainframe.

Front panel controls include bolometer bias adjustments, detector selection, and attenuation controls. Bolometer burnout protection is provided.

MODEL 1588 SYNCHRO SELECTOR

The Model 1588 Synchro Selector permits one of four possible synchro inputs to be switched into the synchro-to-digital converter located in the recorder mainframe.

Synchro input may be 1:1 ratio or 36:1 ratio. The ratio selected is transmitted to the recorder microprocessor and appropriate scaling is performed.

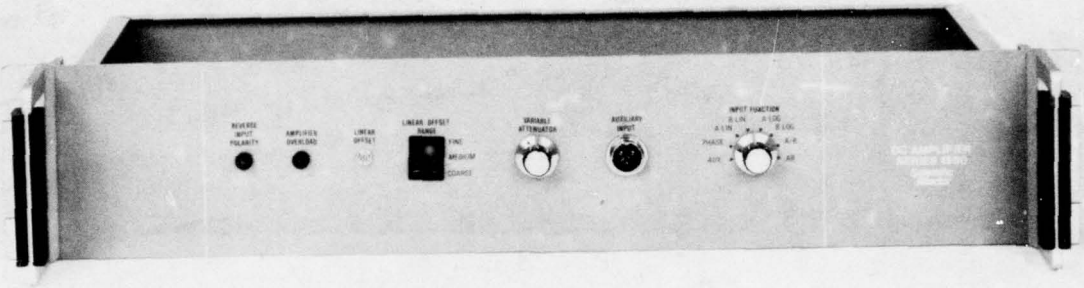

Model 1586 Crystal-Bolometer Amplifier

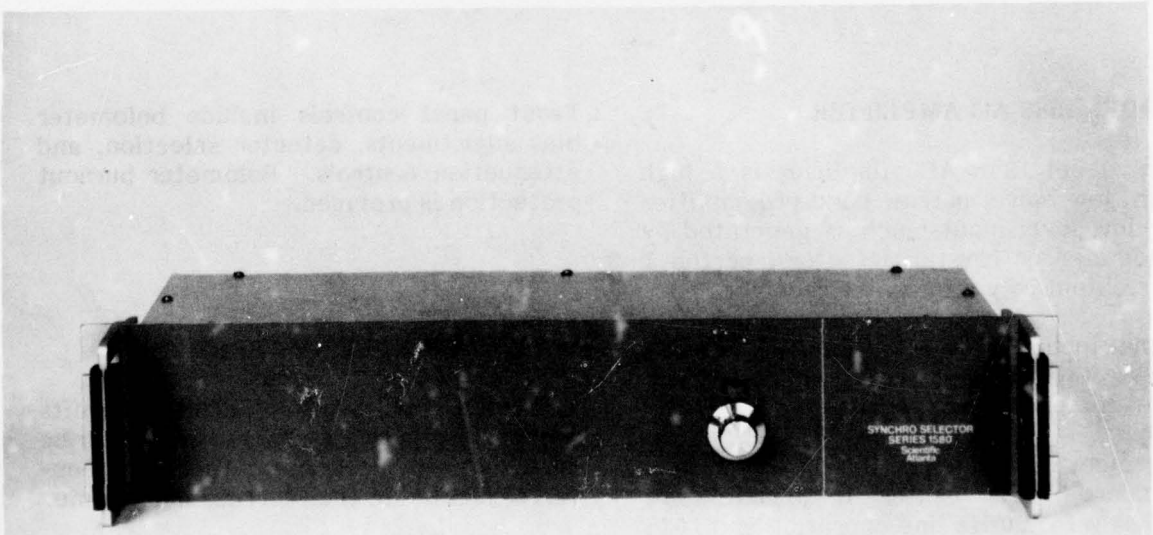

Model 1588 Synchro Selector

OTHER RECORDER FEATURES

Firmware, or microprocessor programs stored in read only memory, provide many features which were not practical to implement in earlier antenna pattern recorders. Firmware instructions can replace functions and operations that previously were implemented in hardware.

Basically, firmware instructions are executed in a continuous "loop" to read input data, perform pen function and chart scaling, and position the chart and pen servo system. Loop time is approximately five (5) milliseconds and varies slightly with the functions selected and options installed.

CHART AND PEN SERVO SYSTEM

Direct current motors provide drive to the chart and pen system. Optical encoders attached to each motor shaft provide position error feedback to the microprocessor. An external rate loop is provided for both chart and pen drive systems.

The encoder provides clockwise and counterclockwise pulses which drive up- down counters. On each program loop the counters are read and reset by the microprocessor. The counter value represents the position error.

Position commands, feedback error, plus any position changes caused by input data (from the receiver or positioner system) are output to digital to analog converters. Power drivers provide amplification for driving the chart and pen torque motor.

Pen position is absolute with 4100 discrete addressable positions over 250mm of pen travel. Maximum pen writing speed is 1500mm per second. Typical position accuracies are ±0.15 dB over a 40 dB dynamic range (pen function).

Chart position is relative with 9600 discrete positions over a full scale chart cycle of 540mm. Maximum chart speed is 750mm per second. At chart speeds of 100mm per second, with a 36:1 synchro input, dynamic position error is 0.127cm. Static position error is 0.038cm.

PEN CALIBRATION

On power up, the microprocessor drives the pen to the top of the chart to establish a physical reference point. From this position all pen movements are referenced.

To eliminate paper expansion error caused by humidity, a pen correction factor is applied to each pen position command. Digital adjustments are provided for the operator to enter the pen correction factor.

When a calibration switch is activated, the pen is driven exactly 4100 counts from the power up reference point. By adjusting the digital pen correction switches until the pen lies on top of the bottom printed line on the chart paper, any dimensional error in the pen axis are effectively removed. When the calibration switch is returned to "operate", all pen positions will be corrected by the microprocessor.

PEN FUNCTION

Pen function calculations involve processing the input pen data in a manner to permit a logarithmic, linear, square or square-root display. All pen functions are performed by microprocessor operations and are selectable by front panel switches.

Analog pen data from the AC or DC Preamplifier units is received in the mainframe through an analog to digital converter. Data includes a 10-bit binary value representing a 22 dB range, and range signals indicating one of four 20 dB ranges. A 2 dB overlap is provided for range switching hysteresis.

Analog signals are processed to permit log, linear, square or square-root displays. Log and antilog conversions are performed by a 22 dB lookup table. Table entries are spaced at 1 dB intervals. Linear interpolation is used for factional dB values. The A/D range bits determine if 20, 40, or 60 dB offset is to be added.

Square-root pen function is performed by accessing the lookup table to determine the log and performing a division by 2.

Digital pen data is displayed using a linear pen function. This permits plotting the data directly as received, since normally digital pen data arrives at the recorder in a directly usable format.

FILTER DELAY CORRECTIONS

Overlayed antenna patterns produced with alternate scan directions with constant frequency and signal level, often show an apparent angular displacement of the plotted pattern. This occurs due to delays of the incoming signal as it passes through analog filters in audio frequency IF amplifiers.

To eliminate this problem, the microprocessor delays the incoming chart command for a time delay equivalent to the analog filter delay.

The delay is accomplished by storing incoming chart commands in a rotating buffer. Buffer rotation time is equivalent to the measured filter delay (17msec) of the AC and DC Preamplifier units.

PEN SMOOTHING

Pen smoothing, a form of digital filtering, is selectable for analog inputs. It is performed by firmware averaging pen data over a number of samples. Chart position commands are delayed (stored by the microprocessor) to permit the average pen positions to be determined by a number of samples before and after the current value. In effect, a "look ahead" is performed since the chart command is delayed.

The degree of smoothing is determined by the number of samples in the average. This feature is selected only when "real time" analog data is being input to the recorder.

RECTANGULAR TO POLAR CONVERSION

For generation of polar plots, the optional memory module contains firmware which converts rectangular pen and chart positions into polar coordinates. Selection of this mode is by front panel switch.

This feature is possible due to the dynamic response of the chart system. At many angular positions of the incoming angular information, the chart will be required to respond to the input signal, including noisy signals.

Coordinate conversion is performed by trigonometric lookup tables. A 90^{0} sine table, at one degree intervals, is used forsine and cosine lookup. Cosines are obtained by accessing the sine table in reverse. All angles are reduced to the table range before lookup. Offsets are then added to restore the original quadrant.

Since the chart axis resolution differs from the pen axis, chart commands are scaled to permit "perfect" circles to be drawn.

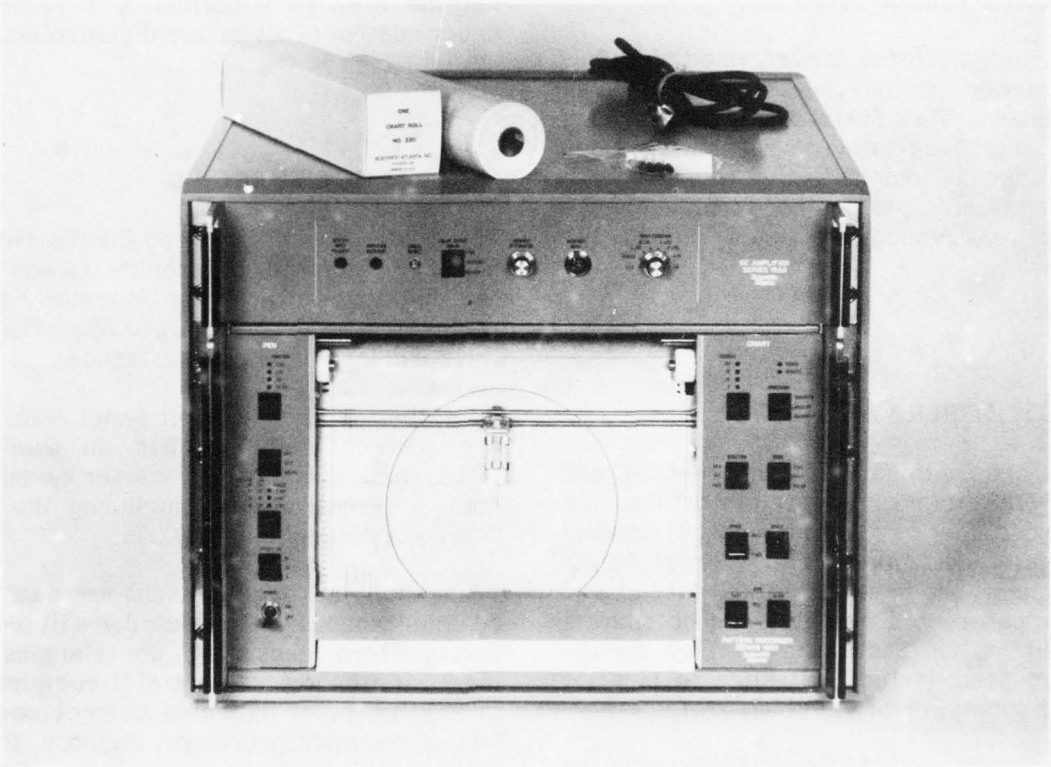

Series 1580 Recorder with polar option

VECTORING

Vectoring is performed by firmware intercepting large chart and/or pen positioning commands and dividing the movement into segments of shorter lengths. Vectoring permits straight lines to be drawn for positioning steps which exceed the capability of the chart and pen servo system.

Straight lines, other than vertical or horizontal lines, require both chart and pen axes to be driven simultaneously. When vectoring is performed, the chart and pen commands are divided into separate vectors and output to the servo system. When the error feedback diminishes to near zero, the next segment is output. This process continues until the end point is reached.

Vectoring does require longer plotting time and is used primarily for computer or caliculator inputs. Normal "real time" data recording, where inputs from a receiver and positioner are monitored continuously, does not use vectoring and pen response is not slowed by the vectoring process.

PAPER SENSE

Paper supply is sensed by a mechanical switch in contact with the roll paper supply. When the paper supply diminishes beyond a certain limit, a signal is sent to the miroprocessor. This feature is primarily for remote operation.

Paper edge sensing is performed by infrared sensor located in the front of the recorder. This feature prevents driving the paper back into the recorder. When the edge is reached, the recorder will automatically perform a format change cycle to advance the paper out of the recorder.

REMOTE OPERATION

With the optional memory module and IEEE-488 standard digital interface, the recorder may be programmed by external computers or calculators. Programming commands are in simple ASCII format and permit all recorder controls to be operated remotely. Status supplied by the recorder permits the controller to monitor paper supply, error, and busy status.

Data inputs may be amplitude or phase angle, and angular position in degrees. With these data formats, the recorder performs processing just as if the data had been received directly from a receiver and positioner.

An alternate data format permits specifying absolute chart and pen position. With the absolute data format, the recorder may be used as a normal X-Y recorder under control of an external controller.

CONFIDENCE EXERCISE

For a microprocessor based instrument, it is often desirable to provide means for the operator to invoke an automatic procedure that will demonstrate operation of the basic instrument performance.

By actuating certain front panel controls, the recorder will perform an exercise which indicates correct performance of many internal circuits, including the microprocessor and memory.

When the front panel buttons are depressed simultaneously, the recorder will plot a test pattern consisting of triangles of increasing height. Successful completion of this exercise indicates correct operation of the microprocessor, memory, front panel interface, and servo system. Other modules, such as input cards, may be exercised by normal recorder operation.

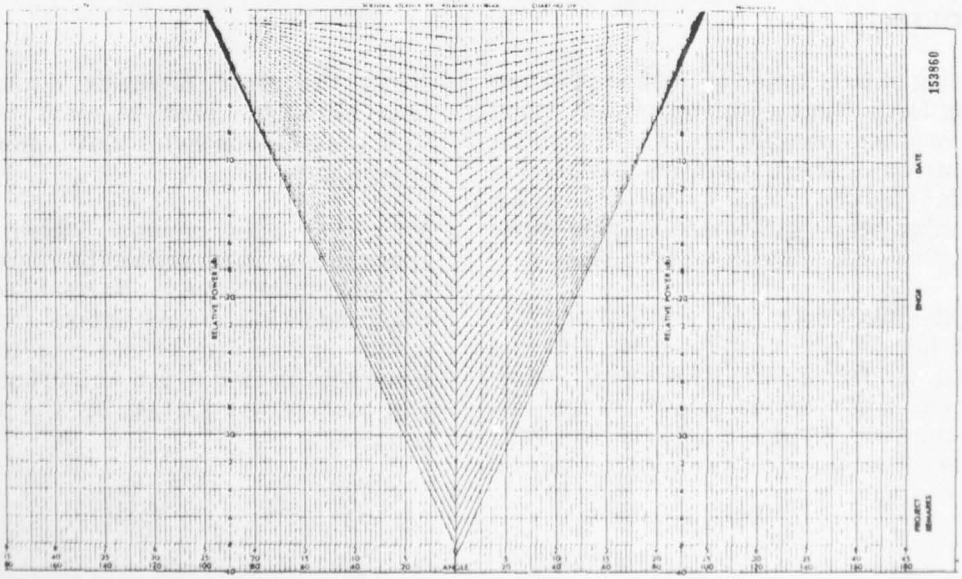

AD-A077 167 ILLINOIS UNIV AT URBANA-CHAMPAIGN ELECTROMAGNETICS LAB F/G 17/9
PROCEEDINGS OF THE ANTENNA APPLICATIONS SYMPOSIUM (1979) HELD 2--ETC(U)
SEP 79 F19628-79-M-0015
UNCLASSIFIED NL

6 OF 6
ADA 077167

END
DATE FILMED
12-79
DDC

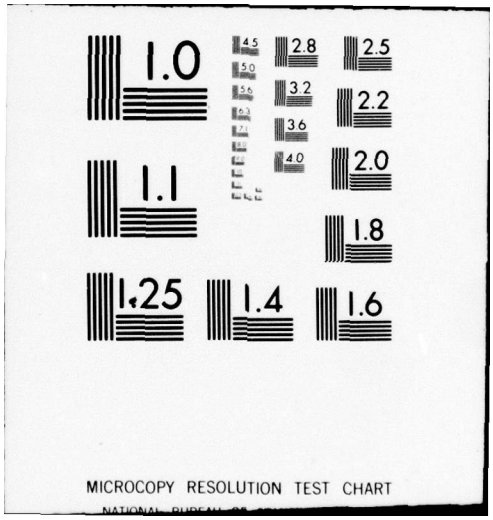
1.0
1.1
1.25
1.4
1.6
1.8
2.0
2.2
2.5
2.8
3.2
3.6
4.0
4.5
5.0
MICROCOPY RESOLUTION TEST CHART

CONCEPTUAL ANALYSIS OF MEASUREMENT ON COMPACT RANGES

by

Richard C. Johnson
Engineering Experiment Station
Georgia Institute of Technology
Atlanta, GA 30332

Doren W. Hess
Scientific-Atlanta, Inc.
3845 Pleasantdale Rd.
Atlanta, GA 30340

Presented at

1979 Antenna Applications Symposium

University of Illinois
Allerton Park
Monticello, Illinois

26-28 September 1979

I. INTRODUCTION

The testing of microwave antennas or the measurement of radar backscatter usually requires that the antenna or target under test be illuminated by a uniform plane electromagnetic wave; however, the creation of such a wave is difficult. In practice, a uniform plane wave is approximated.

The conventional procedure for approximating a uniform plane wave is to locate a transmitting source antenna at such a distance that the incident wave can be considered to be planar. When the source antenna is located $2D^2/\lambda$ away from the test antenna (where D is the largest dimension of the test antenna aperture and λ is the wavelength), the spherical wavefront emitted from the source will produce a maximum phase taper of $\pi/8$ at the edge of the test antenna aperture. For most applications, such a phase taper is acceptable.

In a compact range [1-5], on the other hand, the incident plane wave is created by a range reflector and feed in the immediate vicinity of the test antenna. The basic principle of operation is illustrated in Figure 1. The diverging rays from the point-source feed are collimated by the range reflector, and a plane wave is incident on the test antenna or target. The incident wave has a very flat phase front but the feed-reflector combination introduces a small (but acceptable) amplitude taper across the test zone.

The principal advantage of a compact range is its small size; this allows it to be indoors and free from adverse weather effects. In research and development laboratories, a compact range can be located convenient to the design engineers. In manufacturing or rework facilities, a compact range can be located near an assembly line for use in final testing and adjustment. By placing the range in a shielded room, one can eliminate interference from external sources and provide a test site that is secured against monitoring by outside parties.

II. THE COUPLING BETWEEN THE COMPACT RANGE AND AN ANTENNA UNDER TEST

In this section a simple mathematical description of the coupling between a compact range and an antenna under test will be give from two separate points of view. The case in which the test antenna is receiving electomagnetic energy will be considered first, following the conventional picture usually referred to in explaining the operation of a compact range. Second, the case in which the test antenna is transmitting and the compact range is receiving electromagnetic energy will be considered. It will be seen that the same transmission equation results, from both derivations, as one expects for two reciprocal antennas. The importance of the idea of the operation of the compact range as an angle filter for the wave spectrum results from these considerations.

Compact Range Transmitting and the Test Antenna Receiving

The operational picture of the compact range given in introductory descriptions shows the compact range transmitting an electromagnetic field whose local form in the test zone region is a uniform plane wave field. From this picture one may easily develop a coupling or transmission equation that describes the passage of electromagnetic energy from the port of the compact range feed horn to the port of the antenna under test.

The development of the transmission equation is done in two steps. First, an equation for the power density in the planar wave illuminating field in terms of the power accepted by the feed horn is derived. Then the well known relationship between the effective area and gain of a reciprocal antenna is used to get an expression of the power received by the antenna under test. The details of this approach are given in the following paragraphs.

Consider the feed horn illuminating the compact range reflector; let the feed horn be characterized by its gain G_f and assume that G_f is the peak gain of the horn along the principal ray that passes through the center of the test zone. The compact range reflector is in the far field of the feed horn so that the power density in the wave that illuminates the reflector can be readily calculated from the geometry of the configuration. Let the point Q_o be that point on the reflector where the principal ray intersects the surface; and, let the point Q be the point in the center of the test zone

illuminated by the principal ray in the absence of the test antenna. Let F denote the focal point of the paraboloidal surface and V denote the vertex of the paraboloid, as in the Figure of Appendix II. Then, the distance between the focal point and the principal ray intersection point can be denoted R_o which is the length of the line FQ_o.

The radiation power density S_f in the wave from the feed horn as it strikes the surface of the reflector at Q_o is given simply by the equation

$$S_f(Q_o) = G_f \cdot \frac{P_o}{4\pi R_o^2} \tag{1}$$

where P_o is the power accepted by the feed horn and G_f is the gain of the feed. The effect of the reflector upon the wave from the feed horn is to change the curvature of the phase front from spherical to planar and to reverse its direction of propagation. The amplitude of the field along any particular ray is unaltered by the reflector, assuming a perfectly conducting surface. The propagation of the reflected field leaving the reflector is such that the power density at point Q in the test zone is the same as the power density at point Q_o on the reflector. This is due to the fact that the reflected wave is collimated; hence, there is no curvature to the reflected wave front and no dispersal of rays to give a loss of power density. One may write, therefore, that the power density in the field of the compact range at Q equals that at Q_o:

$$S_{cr}(Q) = S_f(Q_o) \tag{2}$$

When an antenna to be tested is placed in the test zone of the compact range it is illuminated by a planar wave front having power density S_{cr}. One can readily say what the power will be at the port of the test antenna by utilizing the definition of the effective area of the test antenna:

$$P_{rvc}^{aut} = S_{cr} \cdot A_{eff}^{aut} \tag{3}$$

Here, P_{rcv} is the power received and A_{eff}^{aut} is the effective area of the test antenna. This may be expressed in time of the gain G_{aut} of the test antenna by making use of the well known relationship between the gain and effective area of a reciprocal antenna:

$$G_{aut} = \left(\frac{4\pi}{\lambda^2}\right) A_{eff}^{aut} \tag{4}$$

Combining the first two equations gives an expression for the power density of the field in the test zone of a compact range:

$$S_{cr} = G_f \frac{P_o}{4\pi R_o^2} \tag{5}$$

Combining the second two equations gives an expression for the power received by an antenna in terms of its gain and the power density in the field illuminating it:

$$P_{rcv}^{aut} = S_{cr} \frac{\lambda^2}{4\pi} G_{aut} \tag{6}$$

When these are combined, one gets the simple result that:

$$\frac{P_{rcv}^{aut}}{P_o} = \left(\frac{\lambda}{4\pi R_o}\right)^2 G_{aut} G_f \tag{7}$$

This result is strongly reminescent of the Friis' transmission equation which applies to the coupling of two antennas in each other's far field. It is as if one is coupling the test antenna to the feed horn at a distance of R_o. This equation is often used to estimate the port-to-port loss of a compact range-test antenna comfiguration.

Compact Range Receiving with the Test Antenna Transmitting

In order to understand the operation of the compact range when the test antenna is transmitting and the compact range is receiving energy, one can make use of the concept of a plane wave spectrum, taking the point of view that the compact range acts as an "angle filter" for the plane waves emitted by the test antenna.

It is known from the theory of the plane wave analysis that the far field pattern of an antenna is identical to the plane wave spectrum of the field emitted by that antenna. This can be treated as an assumption for the heuristic development given here. One thinks of the field of an antenna as composed of plane waves travelling outward in all directions. In the far field of the antenna one observes the various plane waves one at a time and he may therefore directly measure the plane wave spectrum. The near field, on the other hand, is made up of the entire set of plane waves. In order to get the plane wave spectrum from the near field, one must utilize one of two methods. Either he must perform a Fourier analysis, as is done with data acquired from planar scanning, or he must employ an angle filter such as a compact range to pick out a specific component of the spectrum. One can think of the compact range as an analog device for performing a two-dimensional Fourier transform.

The plane wave spectrum differs in one essential aspect from the conventional idea of a frequency spectrum. The plane wave spectrum is two-dimensional whereas the conventional frequency spectrum is one dimensional.

Another difference is in the matter of units; conventionally one thinks of the various components of a frequency spectrum as being labelled by their respective frequencies. In dealing with the plane wave spectrum, one thinks of the various components as being labelled by their directions of propagation in space, as specified by angles. Because it takes two angles to specify a direction, one readily sees that the plane wave spectrum must be two-dimensional. Just as the spectral density function of a frequency filter might carry the units of $(\text{Hz})^{-1}$, the spectral density function of an angle filter for plane waves would carry the units of inverse solid angle or $(\text{steradian})^{-1}$.

One way of estimating the "angular width" of the plane wave spectrum that is accepted in the pass band of the compact range when it is receiving, is to examine the family of rays associated with plane waves that impinge onto a compact range under axial illumination. The plane wave associated with the principal ray will be focussed at the focal point of the paraboloid where the center of the feed horn is located. The plane waves impinging from directions that are slightly off axis will be focussed just off the center of the feed horn but will also cause a response provided they are focussed within a radius of the focal point equal to the radius of the feed horn's aperture.

From the geometry of the configuration one can see that these plane waves whose angle off axis is less than $\frac{1}{2}(\Delta\Theta)$ will be accepted by the feed providing

$$\tan \tfrac{1}{2}\Delta\Theta \lesssim \frac{a/2}{R_o} \tag{8}$$

Therefore, the angular extent of the pass band of the compact range is

$$\Delta\Omega \simeq (\Delta\Theta)^2 = (a/R_o)^2 \tag{9}$$

where a is the physical radius of the feed horn aperture and R_o is the distance from the focus to the reflector along the principal ray.

There is another way of estimating the spectral width of the compact range pass band which gives the same result and serves as a verification of this first method. Consider the feed plus reflector as an antenna whose pattern one wishes to consider. The aperture size of the antenna is D; its beam width is, therefore, roughly λ/D radian in each plane. Since the far field of this antenna is just its plane wave spectrum, one then knows that the spectrum is appreciable over an extent of solid angle equal to

$$\Delta\Omega = (\lambda/D)^2 \tag{10}$$

Now utilize the requirement imposed upon the feed by asking that it give nearly uniform illumination of the test zone; to accomplish this the angle subtended by the aperture of the reflector at the focus must equal the beamwidth of the feed horn; thus, the beamwidth $\Delta\Theta$ of the feed

$$\Delta\Theta \simeq \lambda/a \tag{11}$$

must be such that

$$\Delta\Theta \simeq D/R_o \tag{12}$$

where D/R_o is the angle subtended by the reflector. Combining these gives $\Delta\Theta$ expressed in terms of a and R_o as was done before:

$$\Delta\Omega = \left(\frac{\lambda}{R_o \lambda/a}\right)^2 = (a/R_o)^2 \tag{13}$$

Therefore, by two separate lines of though it has been shown that the passband of the angle filter represented by a compact range is

$$\Delta\Omega = (a/R_o)^2 \tag{14}$$

This expression for the width of the passband of the compact range angle filter can be utilized to estimate the power level of the signal received by the range, provided one knows the power spectral density in the wave impinging onto the compact range. One gets this as follows:

When the antenna under test is transmitting, denote the radiation intensity in the field by $dP^{aut}/d\Omega$. This quantity is the power per unit solid angle emitted in the radiated field. Considering that the radiated field is made up of a spectrum of plane waves, it is instinctively clear that the power spectral density of the plane wave spectrum must be given by the same quantity. The radiation intensity is related to the gain of the antenna under test by the well known relation

$$\Phi^{aut} \equiv \frac{dP^{aut}}{d\Omega} = G_{aut} \frac{P_o}{4\pi} \tag{15}$$

The compact range will accept only that portion of the plane wave spectrum that is within its passband. The passband of the compact range will be much narrower than the plane wave spectrum of the test antenna, and therefore, one may write that the power received by the compact range will be given by

$$P_{rcv}^{cr} = \left(\frac{dP^{aut}}{d\Omega}\right) \cdot \left(\Delta\Omega\right) \tag{16}$$

Therefore, in view of these last two equation one has

$$P_{rcv}^{cr} = G_{aut} \frac{\Delta\Omega}{4\pi} P_o \tag{17}$$

The previous expression for $\Delta\Omega$ contains a dependence on the dimension of the feed; this can be converted to a dependence on the gain of the feed by

utilizing the relation derived in Appendix I;

$$G_f = \frac{4\pi}{\lambda^2} a^2 \tag{18}$$

Thus,

$$\Delta\Omega = (a/R_o)^2 = \frac{1}{4\pi} (\lambda/R_o)^2 G_f \tag{19}$$

is an alternative expression for the passband of the compact range angle filter. Using this equation and the equation above for the power received by the compact range one gets the desired result that

$$\frac{P^{cr}_{rcv}}{P_o} = \left(\frac{\lambda}{4\pi R_o}\right)^2 G_{aut} G_f \tag{20}$$

which has been derived by assuming that the test antenna is transmitting and the compact range is receiving. Compare this to the previous equation (7).

The fact that this result is exactly the same as one got in the case when the test antenna receives gives one confidence in the correctness of the basic concepts employed.

III. THE COUPLING BETWEEN THE COMPACT RANGE AND A RADAR TARGET

One of the most important applications of the compact range is its use as a tool in measuring radar cross sections. The concepts developed in the previous section can be applied to the case of cross section measurements to get a coupling equation in terms of the parameter of the range and the radar cross section of the target.

Power Loss from a Radar Cross Section Target

For the purpose of this discussion, we take as the definition of mono static radar cross section the following quantity

$$\sigma = 4\pi \frac{dP_{sc}/d\Omega}{dP_{in}/dA} \tag{21}$$

where dP_{in}/dA is the radiation density, or power per unit area, of the plane wave energy incident on the target and $dP_{sc}/d\Omega$ is the radiation intensity, or power per unit solid angle, of the electromagnetic energy scattered from the target, in the direction of the incoming wave. The quantity σ is dependent upon the direction of the monostatic angle relative to the target.

Imagine that a radar target is set in the test zone of the compact range and that it is illuminated by a planar wavefront transmitted by the range. Then the range can also be used to receive the scattered energy and hence to give a measure of the cross section of the target. To do this, a circulator can be used at the port of the feed horn to route the out-going and in-coming signals. The compact range is used as an angle filter to pick out only that small piece of the plane wave spectrum scattered by the target which corresponds to the wave coming directly back along the line of incidence. Let us now examine the process by writing equations that correspond to the successive steps.

When the target is illuminated with energy from the compact range, the power density of the incident plane wave is given by the expression previously derived:

$$dP_{in}/dA = S_{cr}(Q) = G_f \frac{P_o}{4\pi R_o^2} \tag{22}$$

The scattering process is represented by the definition of the radar cross section; the radiation intensity in the scattered wave is given by

$$dP_{sc}/d\Omega = \left(\frac{\sigma}{4\pi}\right)\left(dP_{in}/dA\right) \tag{23}$$

From the spectrum of plane waves scattered by the target the compact range accepts only those members of the spectrum that are within its passband; the power received by the range that is scattered from the target is

$$P_{rcv}^{sc} = (dP_{sc}/d\Omega)\ \Delta\Omega \tag{24}$$

where $\Delta\Omega$ is the width of the passband and is given by

$$\Delta\Omega = \frac{1}{4\pi}\left(\frac{\lambda}{R_o}\right)^2 G_f \tag{25}$$

Combining these last four equations gives

$$\frac{P_{rcv}^{sc}}{P_o} = \frac{\sigma}{\lambda^2}\ \frac{1}{(4\pi)^3}\ \left(\frac{\lambda}{R_o}\right)^4 G_f^{\,2} \tag{26}$$

This equation is the same as the usual radar equation for an antenna whose gain is G_f and for a target placed a distance R_o away. This equation gives a means of estimating the signal level of a target return and is the basis for designing a measurement system for radar cross sections based on a compact range.

In order to illustrate the use of this equation, an example follows in which the case of a target with σ = 0dBsm is worked out. The compact range radar equation alone is first put into logarithmic form

$$10 \log \frac{P_{rcv}^{sc}}{P_o} = 10 \log \left(\frac{4\pi\sigma}{\lambda^2}\right) + 10 \log \left(\frac{\lambda}{4\pi R_o}\right)^4 + 10 \log G_f^{\,2} \tag{27}$$

Taking the following values, which are typical in cases of practical interest,

$$\lambda = 3 \text{ cm} = 1.18 \text{ in}\ ,\ G_f = 8 \text{ dB}\ ,\ R_o = 152 \text{ in} \tag{28}$$

permits one to get a definite appreciation of the practical aspect of the problem.

The first term can be broken up as follows

$$10 \log \left(\frac{4\pi\sigma}{\lambda^2}\right) - 10 \log \left(\frac{\sigma}{1m^2}\right) + 10 \log \left(\frac{4\pi\ m^2}{\lambda^2}\right) \tag{29}$$

to permit an estimate to be adjusted for targets having cross sections of other than $1m^2$ or 0dBsm. In this case, then the loss equation for a 0dBsm target has terms with the following values

$$\begin{aligned} 10 \log \frac{4\pi\ m^2}{\lambda^2} &= +\ 41.5\ dB \\ 10 \log \left(\frac{\lambda}{4\pi R_o}\right)^4 &= -128\ dB \\ 10 \log (G_f)^2 &= +16\ dB \end{aligned} \tag{30}$$

and the loss between the transmitted signal at the port of the compact range and the received signal for the scattered energy is

$$10 \log P_{rcv}^{sc}/P_o = -71\ dB. \tag{31}$$

The peak radar cross section for a square plate is given by the expression

$$\sigma_{sq\ plt} = 4\pi \frac{A^2}{\lambda^2} \tag{32}$$

where A is the physical area of the plate. If the plate is 1 meter on a side, then

$$10 \log \frac{\sigma}{1m^2} = 41.5\ dB_{sm} \tag{33}$$

The loss for a square plate, $1m^2$ in physical area, is then

$$10 \log P_{rcv}^{sc}/P_o = -71\ dB + 41.5\ dB = -29.4\ dB \tag{34}$$

It is worthwhile to keep in mind that the far field distance of $2D^2/\lambda$ for such a plate is equal to 67m, or 214 ft.

IV. CW REFLECTIVITY RANGE

When making measurements on a CW reflectivity range, the procedure generally is (1) to null out the returned signal in the absence of a target, (2) to place the target in the incident field, and (3) to measure the returned signal with the target in place. The signal measured in Step 3 is assumed to be target return since the return from other objects was nulled out in Step 1. (There are some inherent errors due to shadowing of the background by the target and due to multipath return, but these errors generally are small and will not be discussed here.) One easily can see that the sensitivity of the range depends upon the depth and stability of the null which is achieved in Step 1. In other words, if one wishes to measure backscatter from a target with a cross section of -30 dBsm, then the null signal in Step 1 must be well below the signal returned from such a target. The conditions which produced the null in Step 1 must be maintained during the entire measurement procedure, and it usually is considered good practice to remove the target after the measurements in Step 3 and check the null to be sure it has not degraded too much since Step 1.

In a CW compact reflectivity range, there are three main signals that must be nulled out before placing a target on the support structure. They are (1) leakage from the transmitter to the receiver at the circulator (or hybrid), (2) reflections within the transmission lines, and (3) reflections from the room and surrounding equipment. The resultant of the three signals is nulled out by a fourth signal which can be coupled directly from the transmitter line as indicated in Figure 9.

It is convenient to reference the depth of the null to the signal that would be returned by a target having a cross section of one square meter, but let's first estimate the depth of the null which can be achieved.

The four signals indicated in Figure 19 are illustrated as phasors in Figure 10. Signals 1 and 2 are confined to the waveguide (or coax) plumbing. Their phases at the receiver can vary with frequency and temperature changes, but they will be insensitive to movements of range components. Signal 3, on the other hand, radiates into the test chamber, is scattered, and then is received again by the feed. The phase of Phasor 3 can be changed by small movements of the feed, of the range reflector, or of surfaces of the test chamber.

In a compact range within an anechoic chamber about 65 percent of the radiated energy strikes the reflector, is collimated, and then strikes the back wall. About 10 to 12 percent of the energy strikes the ceiling, and the remaininder is essentially divided equally among the two side walls and the floor.

In an absorber-lined chamber, for all practical purposes, one can consider that all energy leaving the feed eventually strikes absorber, so the magnitude of Phasor 3 essentially depends on back-scatter reflections from the absorber and upon the chamber size. In this respect, the signal represented by Phasor 3 can be called "room return" in a manner similar to the custom of using "target return" to refer to the signal returned from a target. Thus, in a well-designed chamber, the room-return power probably would be very low relative to the transmitter power.

One must keep in mind that Phasor 3 is actually the resultant of several phasors, each of which represents a contribution from a particular part of the chamber. For example, if the back wall moves while the rest of the chamber is stationary, then only the components representing reflections from the back wall will be changing phase.

Now the various parts of a compact reflectivity range will be considered to estimate the null-depth sensitivity to movements. The most sensitive part probably is the feed because all energy radiated and received passes through this device. The second most sensitive part is the range reflector because the largest portion of radiated energy strikes the reflector and because rays are reflected from it twice--once on transmission and once on reception. The third most sensitive part is the back wall because essentially all of the energy reflected off of the reflector strikes the back wall. Of lesser sensitivities will be the side walls and the floor.

Since the feed appears to be the most sensitive part, consider it first. The feed actually radiates energy in many directions, so when it moves in a particular direction, all reflected rays are not changing phase at the same rate. Most of the energy is radiated along the feed axis, however, so axial movements should cause the largest phase changes in Phasor 3.

To simplify the problem, consider that the feed is vibrating (moving) axially and that all energy within 45° of the axis is radiated and received axially. In typical compact-range feed horns, about 80% of the energy is radiated and received within a $\pm$ 45° cone; this represents a level only 1

dB below the total radiated power, so simply assume in this discussion that all energy is radiated and received axially.

Next, assume that the feed moves axially a distance $\Delta\ell$. Then the total round-trip (transmission and reception) path length change is $2\Delta\ell$, and the phase change of Phasor 3 is

$$\Delta\xi = \frac{2\pi}{\lambda}(2\Delta\ell) = 4\pi\frac{\Delta\ell}{\lambda} \quad . \tag{35}$$

Let E_3 be the field magnitude of Phasor 3. If under stationary conditions, the received signals have been nulled out, and then Phasor 3 changes phase by $\Delta\xi$, the null will be replaced by a signal of field magnitude ΔE as illustrated in Figure 11. The value of ΔE is

$$\Delta E = E_3\ \Delta\xi$$

or

$$\Delta E = 4\pi\frac{\Delta\ell}{\lambda}\ E_3 \quad . \tag{36}$$

This is the field magnitude of the disturbing signal for axial vibrations of the feed having peak-to-peak excursions of $2\Delta\ell$. The power level in the disturbing signal is related to the power level in the room return by

$$\Delta P = (4\pi)^2\left(\frac{\Delta\ell}{\lambda}\right)^2 P_3 \quad , \tag{37}$$

where P_3 is the power represented by Phasor 3. This signal should be referenced to the signal returned from a target having a radar cross section of one square meter; the latter can be calculated from Equation 26.

It is instructive to perform some simple calculations. Assume that the compact range has about a 12-foot range reflector (height and width) and a 12-foot focal length, then the following values would be typical for X-band operation:

$$\begin{aligned} G &= 8 \\ \lambda &= 3\ \text{cm} \\ R &= 4\text{m} \quad , \end{aligned} \tag{38}$$

then from Equation 26, for a 1 m^2 target,

$$P_r = \frac{(8)^2(3 \times 10^{-2})^2}{(4\pi)^3(4)^4} P_t$$

or

$$P_r = 1.1 \times 10^{-7} P_t \quad . \tag{39}$$

This is the reference signal, that is, the power returned from a target having a radar cross section of one square meter.

Now refer to Equation 37, and assume the room-return power is -60 dB relative to P_t. Also, assume that the peak-to-peak axial vibration of the feed is only 0.002 inch. Then

$$\Delta P = (4\pi)^2 \left(\frac{10^{-3}}{1.18}\right)^2 10^{-6} P_t$$

or

$$\Delta P = 1.1 \times 10^{-10} P_t \quad . \tag{40}$$

From 39 and 40, it can be seen that the disturbing signal is about -30 dBsm for the assumed conditions, and this would be the limit of the achievable null depth. Similar calculations were made for other vibration magnitudes and for other values of room return, and the results are presented in Figure 12.

Although the null depth is sensitive to very small movements of range components, do not interpret this to be a weakness peculiar to CW compact ranges. A similar sensitivity applies to all CW ranges, but with reasonable care, good performance can be achieved with both compact and conventional ranges.

V. PULSED REFLECTIVITY RANGE

In a pulsed reflectivity range, the return from the target can be range-gated, and return from unwanted objects can be rejected. For example, assume that we have a compact range with a 12-foot focal length located in a room that is about 36 feet long, 20 feet wide, and 17 feet high. If a short-pulsed signal is transmitted and received by the feed, the returned signal would be as indicated in the symbolic A-scope display of Figure 13. Note that most return from the room occurs within the first 25 feet of range. The main exception is the back wall return at about 42 feet.

This is a very simple analysis of how a pulsed system would perform on a compact range, but it indicates that satisfactory performance probably could be obtained if the receiver recovers fast enough to detect the target about 30 to 40 feet beyond the feed horn. The analysis neglects multiple reflections within the room, but such reflections are expected to be small.

The receiver recovery problem is serious but probably within the state-of-the-art; both the skirts of energy on the transmitted pulse must be very low and the receiver must recover quickly. In the example above (see Figure 13), the target is about 35 feet beyond the feed horn. If we allow the equivalent of about 10 to 15 "free-space" feet of transmission line between the transmitter/receiver and the feed horn, the target return will be received about 90 to 100 nanoseconds after the transmitted pulse.

In the previous section, we estimated that the return power from a 1 m^2 target would be about -70 dB with respect to the transmitted power. If we want to measure a -40 dBsm target, the receiver sensitivity must be considerably better than -110 dB with respect to the transmitted pulse within 90 to 100 nanoseconds.

VI. CONCLUDING REMARKS

It has been demonstrated through approximate arguments that familiar far-field equations can be used with compact ranges. For coupling between the feed (source antenna) and the test antenna, we have the Friis equation:

$$P_{rcv} = \left(\frac{\lambda}{4\pi R_o}\right)^2 G_f \, G_{aut} \, P_o \quad . \tag{41}$$

For backscatter measurements, we have the radar equation

$$P_{rcv} = \frac{G_f^{\,2} \, \sigma \lambda^2}{(4\pi)^3 \, R_o^{\,4}} \, P_o \quad . \tag{42}$$

In the above equations, R_{rcv} is the received power, P_o is the power accepted by the feed horn, λ is the wavelength, σ is the radar cross-section, G_{aut} is the gain of the antenna under test, G_f is the gain of the feed horn in the direction of the principal ray that passes through the center of the test zone, and R_o is the distance from the feed horn to the point where the principal ray strikes the reflector.

In the course of the arguments, it was demonstrated that a compact range can be considered to be an angle filter. The solid angle passband $\Delta\Omega$ is

$$\Delta\Omega \equiv \left(\frac{a}{R_o}\right)^2 \quad , \tag{43}$$

where a is the dimension of the feed horn aperture and R_o is as defined above.

In a CW reflectivity range, the achievable null depth is sensitive to movements of range components. The most sensitive component should be the feed horn. Vibrations of the feed will introduce a disturbing (null filling) signal. For axial vibrations having a peak-to-peak excursion of $2\,\Delta\ell$, the power level in the disturbing signal is

$$\Delta P = (4\pi)^2 \left(\frac{\Delta\ell}{\lambda}\right)^2 P_3 \quad , \tag{44}$$

where P_3 is the power level of the room return.

In a pulsed reflectivity range, the return from unwanted objects can be rejected; however, there is a receiver recovery problem due to the short distances involved on a compact range. Although the recovery problem is serious, it is likely that a solution is available with current state-of-the-art components.

REFERENCES

1. R. C. Johnson, H. A. Ecker, and R. A. Moore, "Compact range techniques and measurements," IEEE transactions on Antennas and Propagation, Vol. AP-17, pp. 568-576, September 1969.
2. R. C. Johnson, H. A. Ecker, and J. S. Hollis, "Determination of far-field antenna patterns from near-field measurements," Proceedings of the IEEE., Vol. 61, pp. 1668-1694, December 1973.
3. R. C. Johnson and D. W. Hess, "Performance of a compact antenna range," Digest of the AP-S International Symposium, pp. 349-352, 2-4 June, 1975.
4. D. W. Hess, F. G. Willwerth, and R. C. Johnson, "Compact range improvements and performance at 30GHz," Digest of the AP-S International Symposium, pp. 264-267, 20-22 June 1977.
5. D. G. Bodnar, C. P. Burns, R. C. Johnson, and J. W. Cofer, "Compact range study for RATSCAT," Final technical Report, Contract F29601-77-C-0051, Georgia Institute of Technology, January 1978.

APPENDIX I
IDEALIZED FEED HORN

In the course of discussion within this paper it is convenient to make certain oversimplifying assumptions about the feed horn of the compact range. This appendix develops the ideas that describe this impractical but useful concept.

In order to design a compact range one must break with past traditional practice followed in designing far field antennas. The ideal compact range would have a test zone just as large as the dimension of the offset reflector used. Furthermore, the power density of the planar wave would be uniform throughout the test zone. The requirement of having a large test zone with uniform illumination implies that one wishes to use a feed whose pattern is uniform over the sector of solid angle intercepted by the reflector at the focal point and which is zero outside this solid angle. In achieving this ideal configuration one finds in practice that the pattern of the feed horn has much less taper at the edges of the reflector than one would have if he were designing an offset reflector antenna for far field use. Neglecting the differential loss along the various ray paths from the focal point to the reflector, one may take then as his ideal feed, a horn with a pattern that is constant over a sector of solid angle, equal to its beamwidth.

The directivity of an antenna at the peak of its pattern is given by the ratio of the peak radiation intensity to the average radiation intensity for the entire pattern. For the sector shaped feed horn, then, the peak directivity is given by

$$D_f = \frac{\left(\frac{dP}{d\Omega}\right)_{pk}}{P_t/4\pi} = \frac{P_t/\Delta\theta\cdot\Delta\phi}{P_t/4\pi} \qquad (I,1)$$

$$= \frac{4\pi}{\Delta\theta\cdot\Delta\phi}$$

In these expressions P_t is the total power transmitted and $\Delta\theta$ and $\Delta\phi$ are the beamwidths in θ and ϕ. When $\Delta\theta$ and $\Delta\phi$ are nearly equal the denominator is simply $(\Delta\theta)^2$. One may convert this into an expression for the gain of the feed horn by making the further idealization that the horn is lossless and

therefore has an efficiency of unity. Therefore, for a feed horn with efficiency equal to unity and having equal beamwidths, the expression for the gain in

$$G_f = \frac{4\Pi}{(\Delta\theta)^2} \tag{I.2}$$

Now relate this expression to the dimensions at the aperture of the feed by utilizing the conventional relationship between gain and effective area and the conventional approximation for the beamwidth of an antenna.

The effective area is therefore

$$A^f_{eff} = (\lambda^2/4\pi)G_f = \frac{\lambda^2}{(\Delta\theta)^2} \tag{I.3}$$

The beamwidth is given by

$$\Delta\theta = \lambda/a \tag{I.4}$$

where a is the dimension of the feed. Therefore

$$A^f_{eff} = a^2 \tag{I.5}$$

for this idealized feed horn and its gain is

$$G_f = \frac{4\pi a^2}{\lambda^2} \quad . \tag{I.6}$$

APPENDIX II
COMPACT RANGE GEOMETRY

The design of compact ranges based on paraboloidal reflectors typically utilized an offset feed horn in order to achieve a clear aperture for illumination. A sample profile view of a range is illustrated in the accompanying Figure II.1. The primary parameters which control the operations of the reflector as a compact range are its focal length f and its outside dimension D. A secondary parameter is also very important for the discussion of this paper; it is the distance R_o from the focal point F to the point Q_o where the principal ray strikes the surface of the reflector.

The distance R_o can be easily computed from the geometry of the configuration. The equation of the paraboloidal surface is simply

$$4fx = r^2 \equiv (y^2 + z^2) \qquad \text{(II.1)}$$

where the x axis is taken to be the axis of the paraboloid and r is the cylindrical radius. The principal ray from the focus to the center of the test zone is drawn in the centerplane of the range, which may be taken to be the x-y plane. In this plane the equation of the surface is simply

$$y^2 = 4fx \qquad \text{(II.2)}$$

Devote the coordinates of the point Q_o in the xy plane as x_o, y_o). Assume that the test zone of the range is centered on the aperture of the offset paraboloid; this gives the result that $y_o = D/2$

$$y_o = D/2 \quad . \qquad \text{(II.3)}$$

The x-coordinate of the point Q_o is then given by

$$x_o = \frac{y_o^2}{4f} = \frac{(D/2)^2}{4f} = \frac{1}{16}\frac{D^2}{f} \qquad \text{(II.4)}$$

The distance R_o is also given by a simple application of analytical geometry;

from the Pythagorean Theorem one has

$$R_o = [y_o^2+(f-x_o)^2]^{1/2} \tag{II.5}$$

Substitution from II.2 and expression gives

$$\begin{aligned} R_o &= [4fx_o + (f^2 - 2fx_o + x_o^2)]^{1/2} \\ &= [f^2 + 2fx_o + x_o^2]^{1/2} \end{aligned} \tag{II.6}$$

$$R_o = f + x_o \tag{II.7}$$

Combining II.4 and II.7 then gives readily the following expression for the Secondary Parameter R_o in terms of f and D:

$$R_o = f + \frac{1}{16}\frac{D^2}{f} \tag{II.8}$$

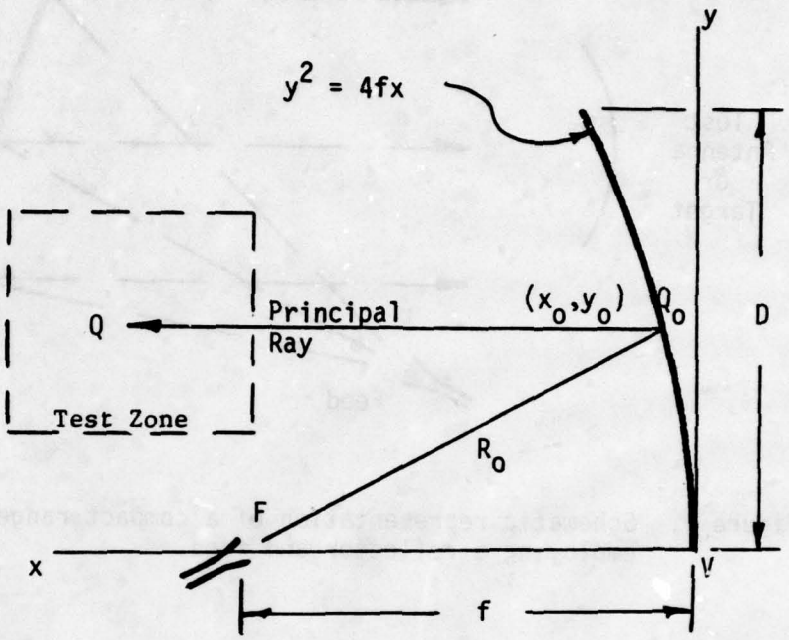

R_o = Length of line segment FQ_o

f = Length of line segment FV

D = Aperture dimension of the paraboloid

Figure II.1. The distance R_o from the focal point to the reflector along the principal ray is given by

$$R_o = f + \frac{1}{16}\frac{D^2}{f} \quad .$$

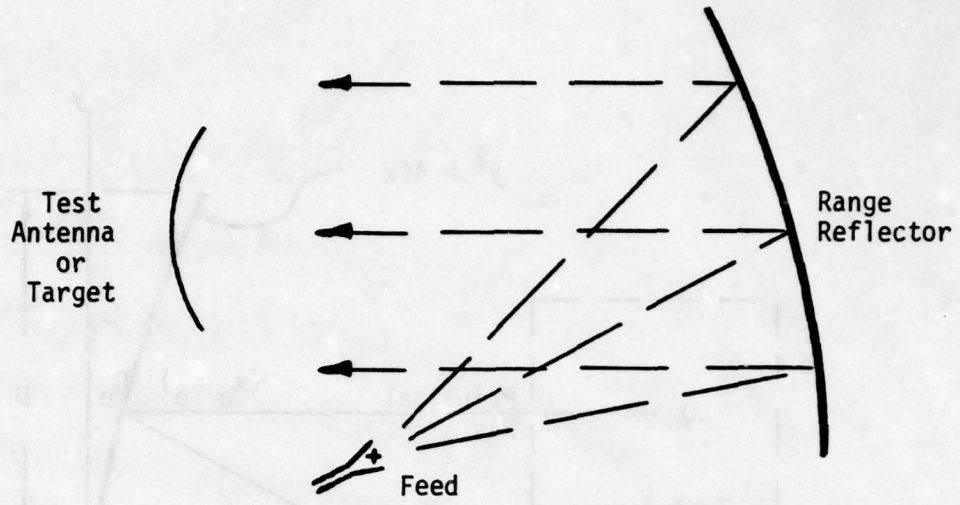

Figure 1. Schematic representation of a compact range employing a reflector and feed.

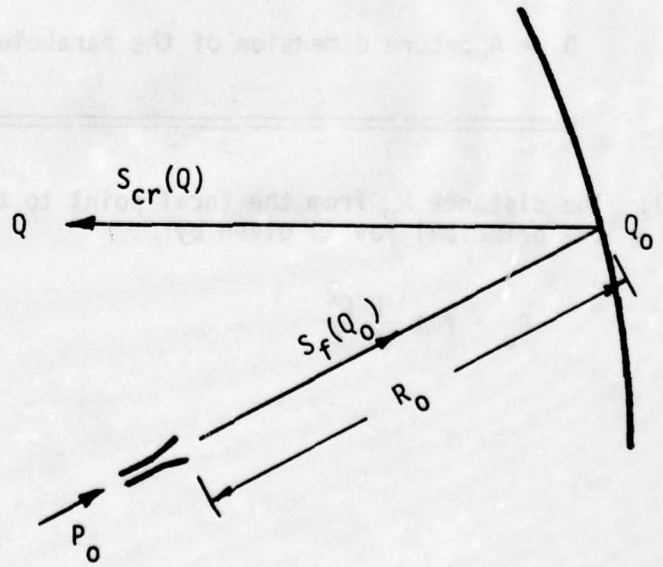

Figure 2. Power density relationships with the feed transmitting.

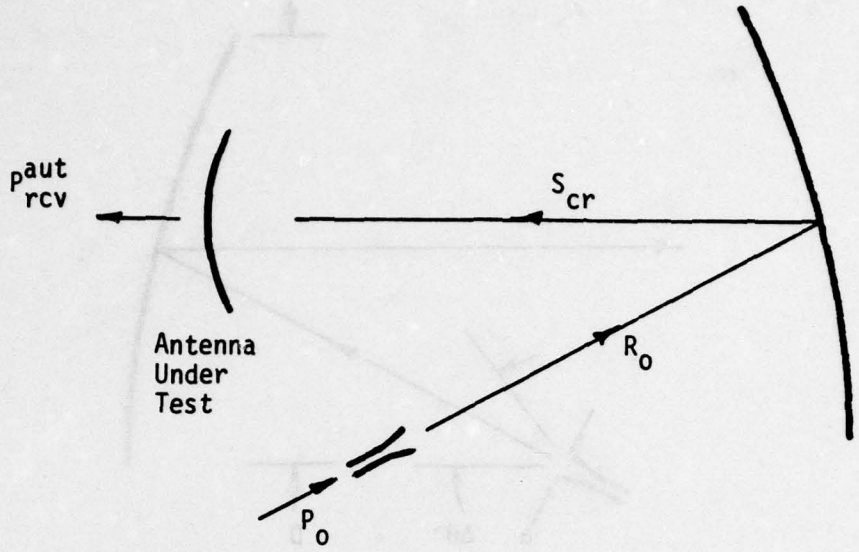

Figure 3. Port-to-port power transfer from feed to the antenna under test.

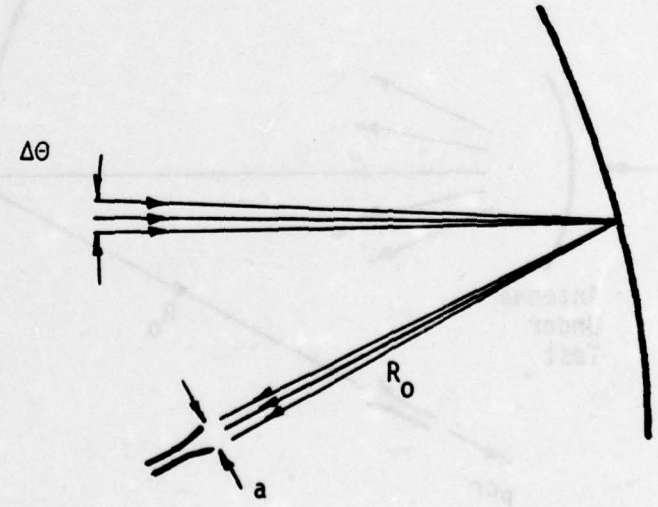

Figure 4. Ray diagram used to estimate the passband of the compact range angle filter.

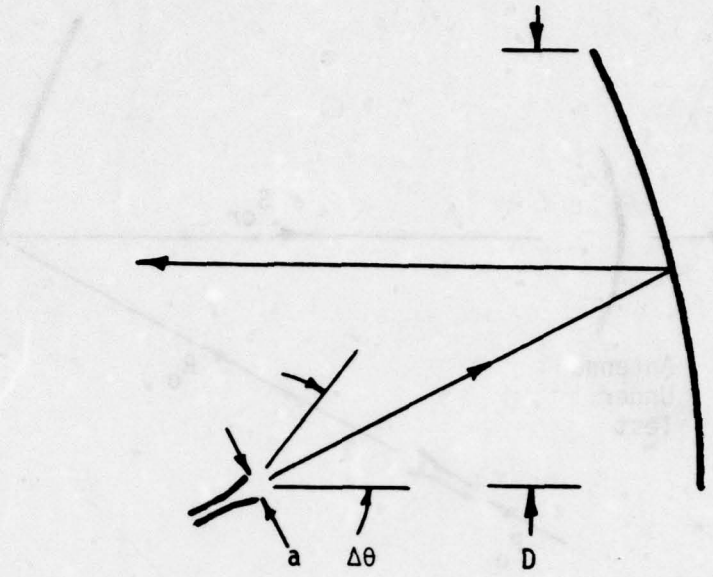

Figure 5. Feed-reflector antenna configuration used to estimate the angle filter passband from consideration of the beamwidth.

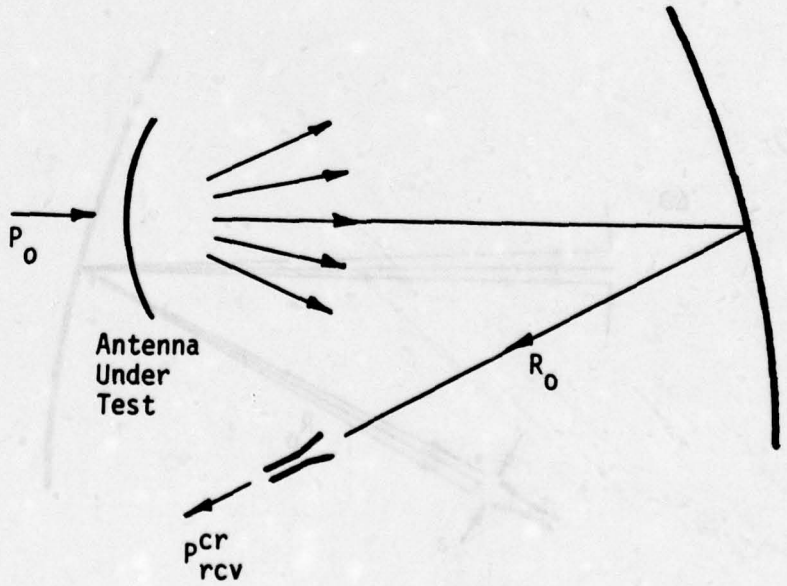

Figure 6. Port to port power transfer from the antenna under test to the compact range feed.

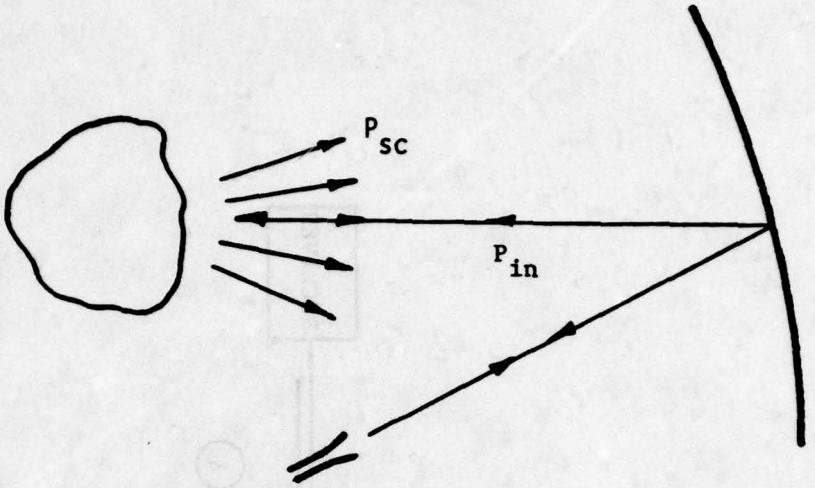

Figure 7. Schematic diagram of incident and scattered plane waves in a compact range radar cross section measurement.

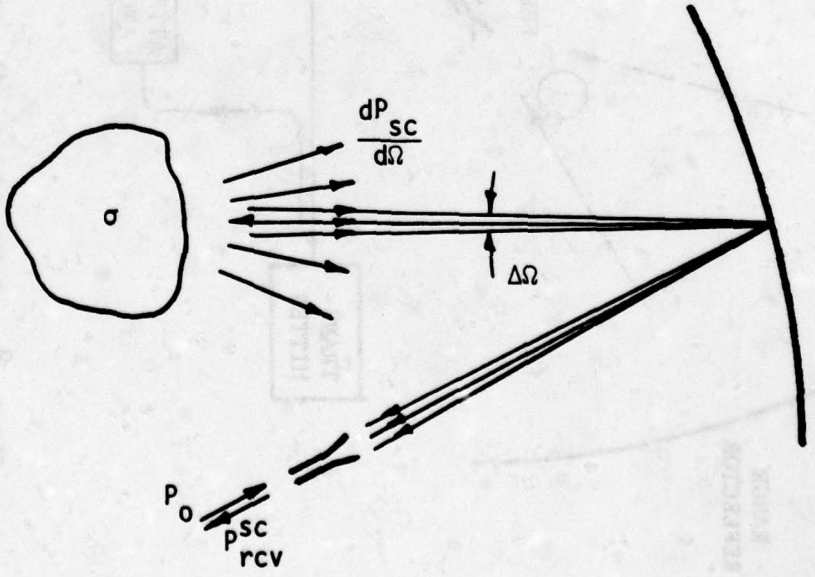

Figure 8. Schematic diagram of compact range angle filter operation in radar cross section measurement.

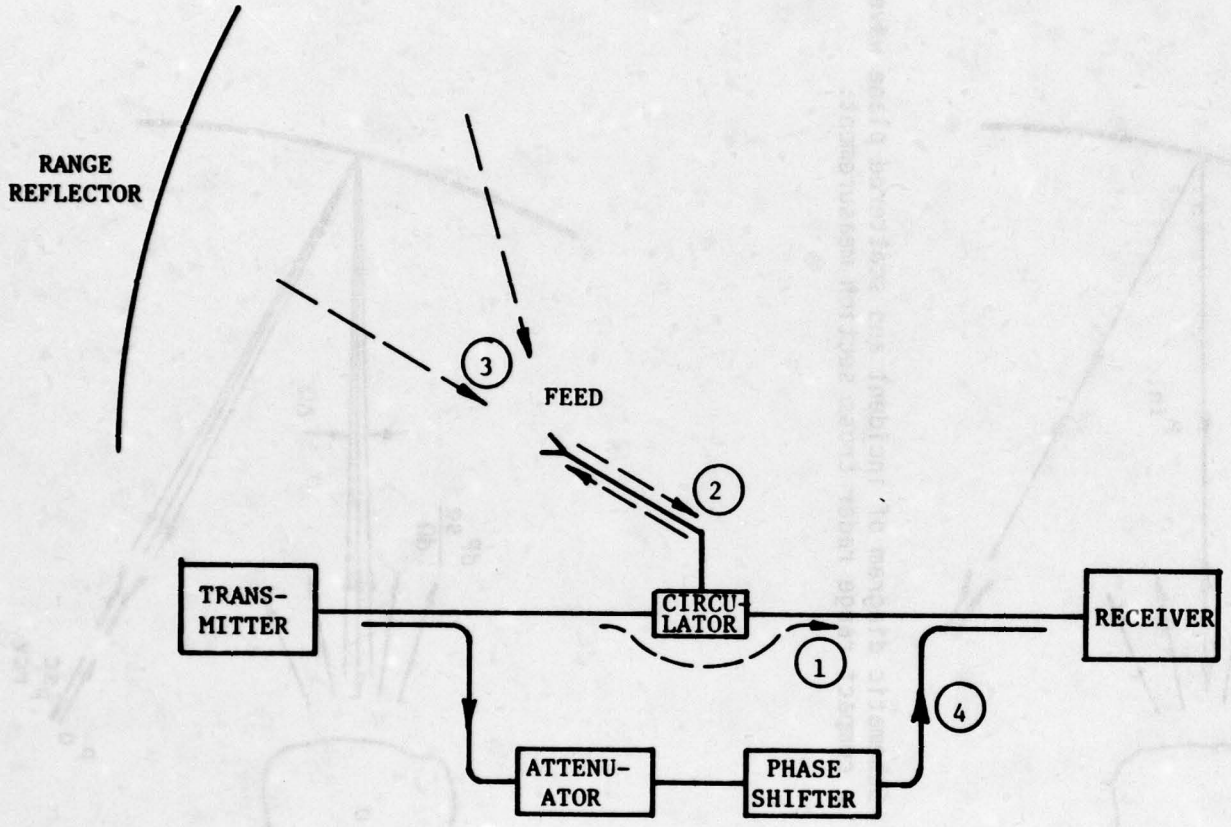

Figure 9. Schematic drawing of a CW compact reflectivity range illustrating the three main signals that must be nulled out by a fourth signal coupled directly from the transmitter.

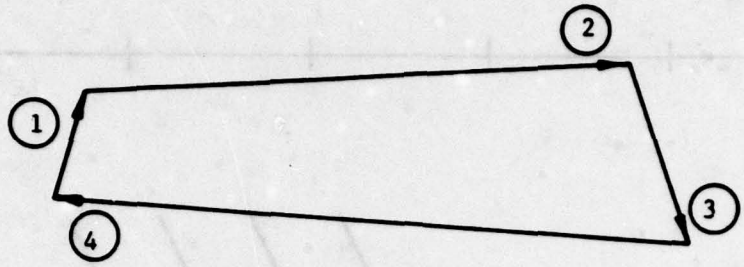

Figure 10. Phasor representation of the four signals indicated in Figure 9. The magnitudes and phases of the first three phasors have been chosen arbitrarily; the magnitude and phase of the fourth phasor is adjusted so that it terminates at the origin of phasor 1 (thus, producing a null signal).

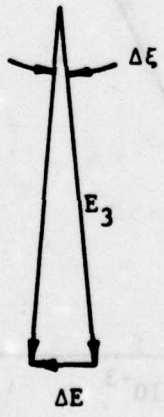

Figure 11. Phasor diagram illustrating a change of phase in the room-return signal and the generation of a disturbing signal which replaces the null.

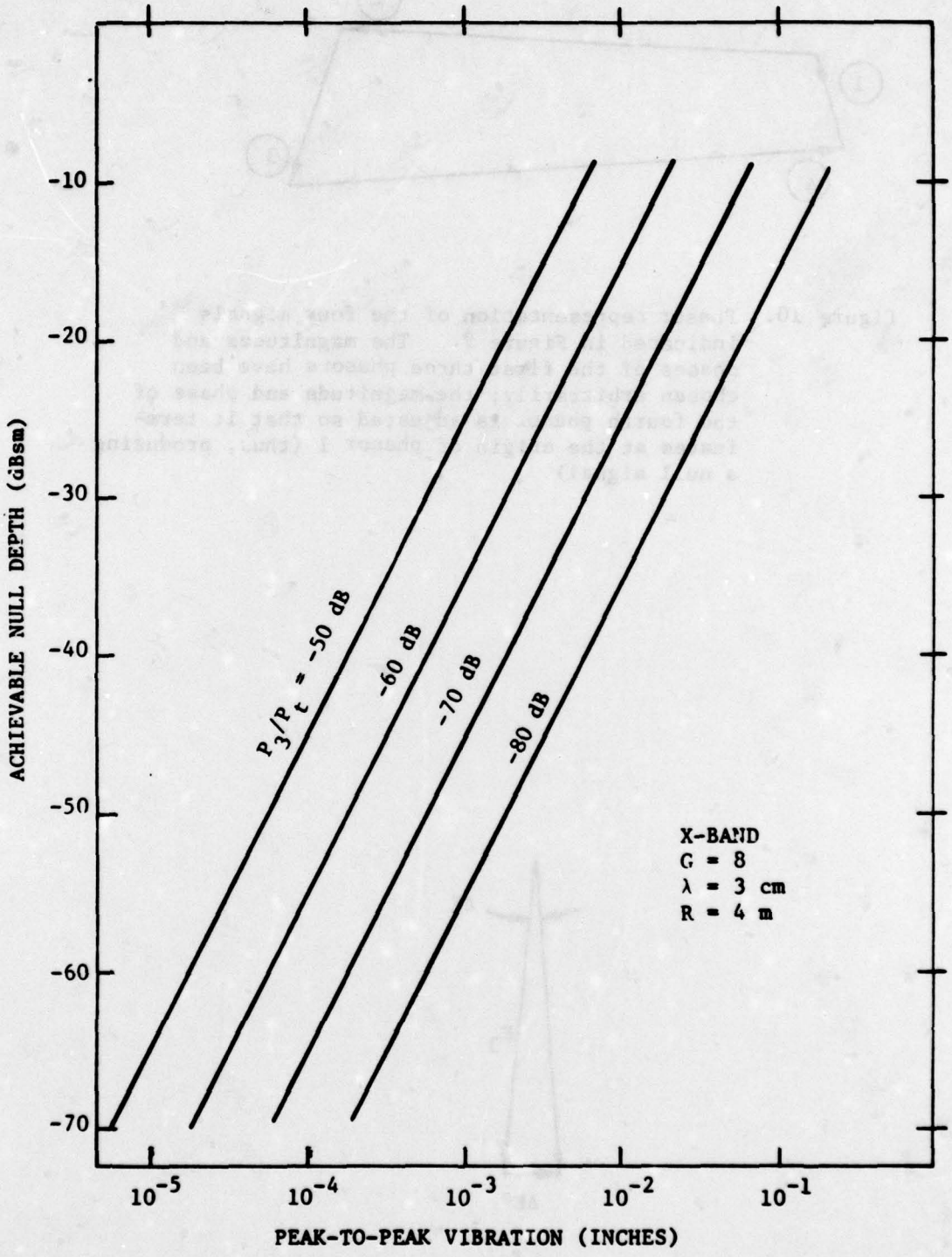

Figure 12. Achievable null depth versus peak-to-peak vibrations of the feed for various ratios of return to transmitted power at X-band.

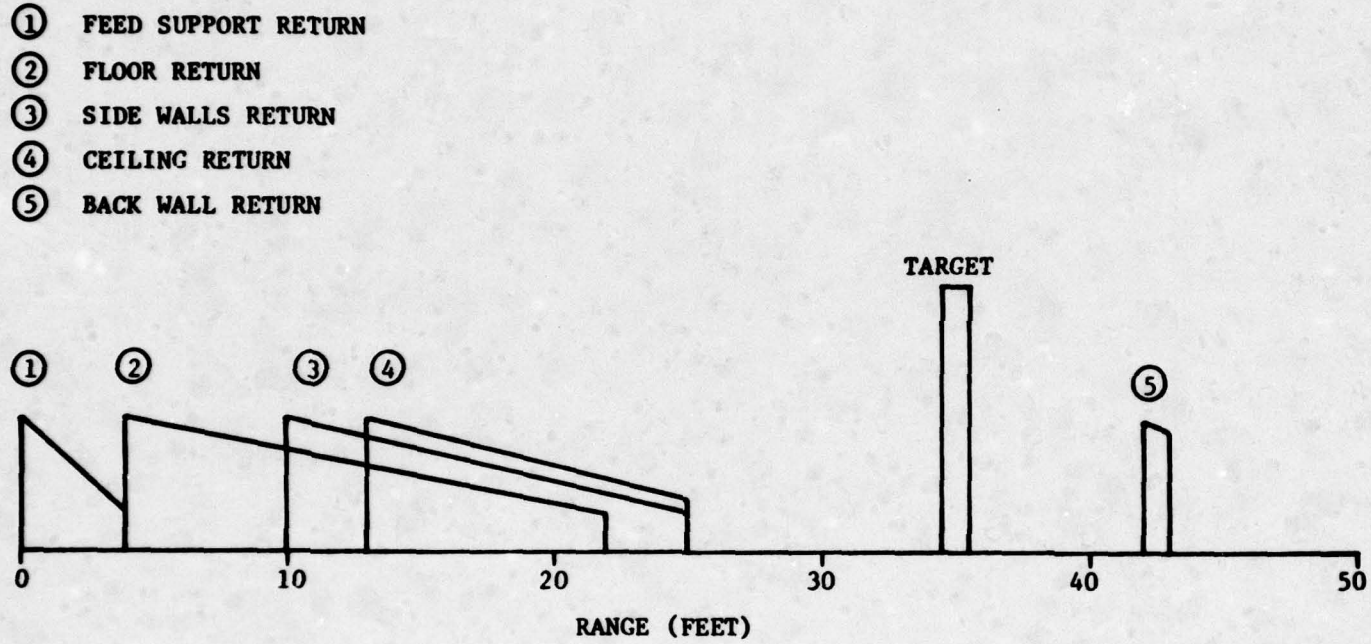

Figure 13. Symbolic A-scope display for a short-pulsed radar on a compact reflectivity range. Range is indicated as distance from the feed.

University of Illinois
Antenna Applications Symposium
September 1979

A SAFE TEST METHOD FOR EFFECTIVE RADIATED POWER MEASUREMENT

BY GEORGE J. MONSER
RAYTHEON COMPANY
GOLETA, CA. 93017

A SAFE TEST METHOD FOR EFFECTIVE RADIATED POWER MEASUREMENT

BY GEORGE MONSER

SUMMARY

A peak sampling-technique is described for use in safely measuring radiated power for both CW and pulse systems. Measurement error for the reported tests is estimated at about ±1 dB, however, with additional effort the error can probably be reduced to about ± 1/2 dB.

1.0 INTRODUCTION

Concurrent with an increased military need for achieving higher power transmitters there was created a need for developing safe test methods which are reliable and adaptable to various transmitter modes of operation. In addition, the test method must be accurate and repeatable with minimum hazards to operating and other personnel.

Consider what constitutes a safe microwave exposure level. The US standard is 10 milli-watts per square centimeter. However, in other countries 1 milli-watt per square centimeter is commonly used.

Using 1 mw/sq. cm power density as safe, we can readily calculate the nearest approach point (range) to the transmitter:

$$P.D. = P_T G_T / 4\pi R^2 \quad \ldots\ldots\ldots\ldots\ldots (1)$$

Where $P_T G_T$ = the effective radiated power

And R = the range (distance) from the transmitter.

Table I gives the results of such calculation for various levels of radiated power in a free-space environment such as an anechoic chamber. For outdoor test sites, where multipath is likely, the tabulated distances should be doubled.

The calculation on page 1 presumes that the transmitter will be radiating cw or average power. It is also important to avoid exposure to high peak powers typified by pulsed radar systems. However, this aspect is not addressed here primarily because the test method was developed for use in testing modulated cw systems.

The typical transmitter to be tested consists of an N-element array with each element powered by a power amplifier (TWT). A principal mode of operation consists of gating the transmitter ON followed by quiescent periods.

Figure 1 illustrates the mode of operation. The core or kernel of the test method is also illustrated. For example, if the on/off times were 50/50 then the average power level would be 50% of the CW level. However, if the on to off time is 1/100, then the average power level would be 1% of the cw level. Again referring to Table I, it may be observed how the safe distance improves with a reduction in duty cycle.

2.0 THE TEST METHOD

Application of the test method is best illustrated by example. First consider the test set-up shown in Figure 2. The primary steps in making a radiated power measurement follows:

1. A calibrated signal level is established using a gain-standard horn with known input power. This may be accomplished by

measuring power to be delivered to the horn with a power meter and the signal set for CW (PIN Modulator OFF but in the line). Next, the PIN Modulator is energized and set to approximately 3% (not critical).

At the receiving end the pick-up horn delivers power to the crystal video receiver (CVR) detector via the tuned filter path where pulse detection occurs. Next, the sampling gate is positioned within the detected pulse window and a sample of the pulse amplitude taken. Finally, the sampled voltage level is fed to the chopper-stabilized recorder amplifier for subsequent recording.

Suppose 1 watt (+30 dBm) were delivered to a 22.8 dB gain standard. Then the recorded level would correspond to +52.8 dBm.

2. Next, following identical power-set steps, the system under test is energized. For this particular system it was estimated prior to test that the system was capable of radiating 20 kilowatts of power (i.e. +73 dBm). Thus it is expected that the recorder level would exceed the calibrated (standard) setting by approximately 20 dB.

For differences greater than 20 dB the calibrated step-attenuator ahead of the CVR detector requires re-setting the received level within the transfer curve for the CVR used in the tests (Figure 3).

Figure 4 shows a cluster of beams recorded for the test transmitter. As indicated in the figure the beam power for Beam no. 4 is approximately +73 dBm or 20 kilowatts.

Accuracy for a particular measurement is estimated to be about ±1 dB determined by combining known errors in RSS fashion. Contributing errors were; CVR non-linearity ±1/4 dB, step attenuator accuracy ±1/4 dB (each), gain standard power set ±1/2 dB, gain standard ±1/2 dB, and siting errors ±1/2 dB.

During the tests it was found that a particular value could be repeated on different days within 1 dB. Also the measured value was verified by CW test and found to agree within 1 dB.

3.0 CONCLUDING REMARKS

A measurement technique has been presented for safely testing transmitters capable of high effective radiated power utilizing pulse-modulated CW signal emission. With some adaption the basic procedures can be extended to cover other test applications.

G. J. Monser

G. J. Monser

TABLE I

SAFE DISTANCE FROM CW TRANSMITTER [1]

AVERAGE POWER IN KILO-WATTS	SAFE DISTANCE IN FEET
1.0	9.2
10.0	29.0
100.0	91.7
1000.0	289.8

1. BASED ON FREE-SPACE TRANSMISSION 1 MILLI-WATT PER SQUARE CENTIMETER AS A SAFE EXPOSURE LEVEL FOR SHORT PERIODS OF EXPOSURE.

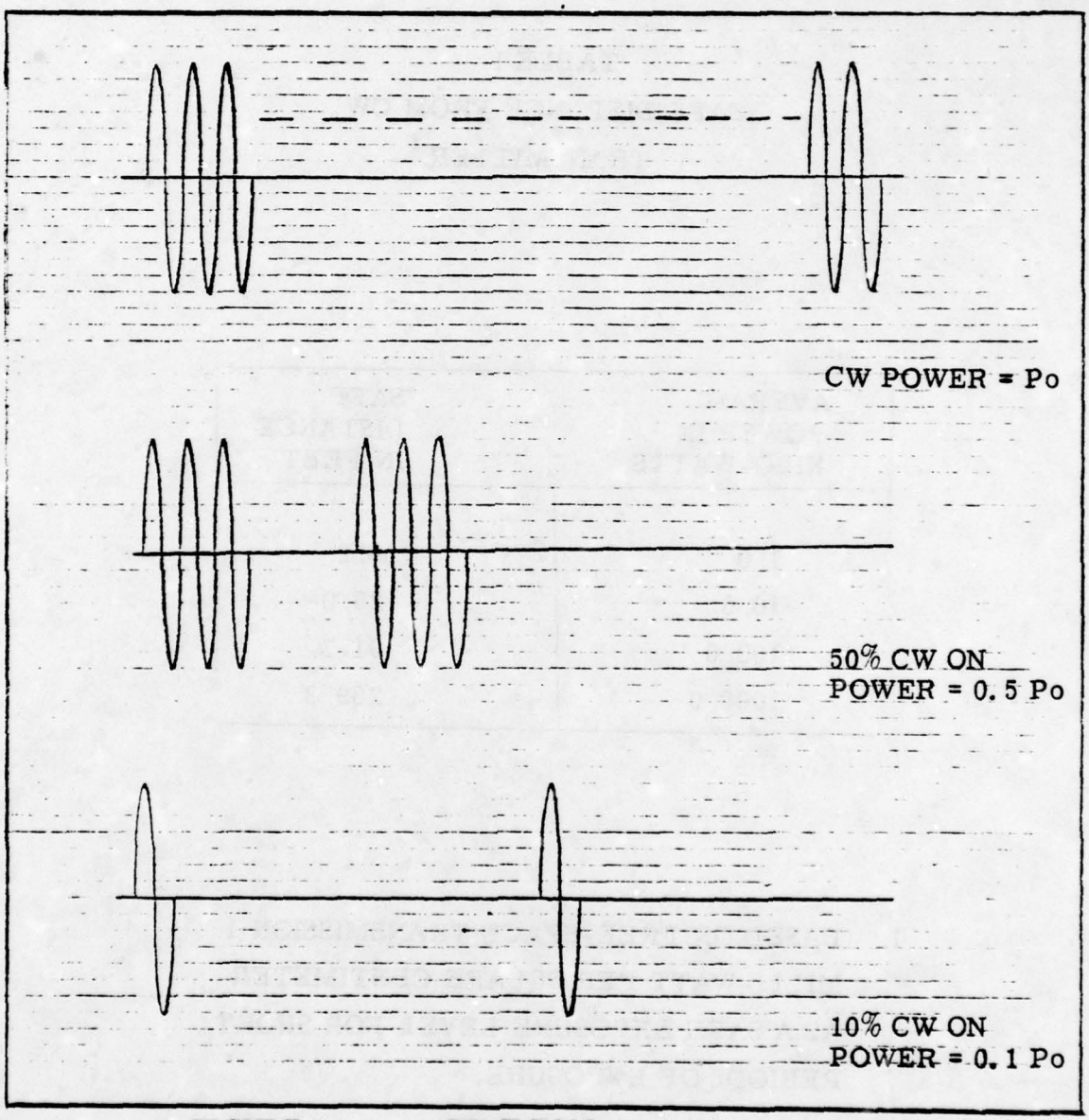

FIGURE 1 CW SIGNAL
VARIOUS ON PERIODS
(ILLUSTRATIVE)

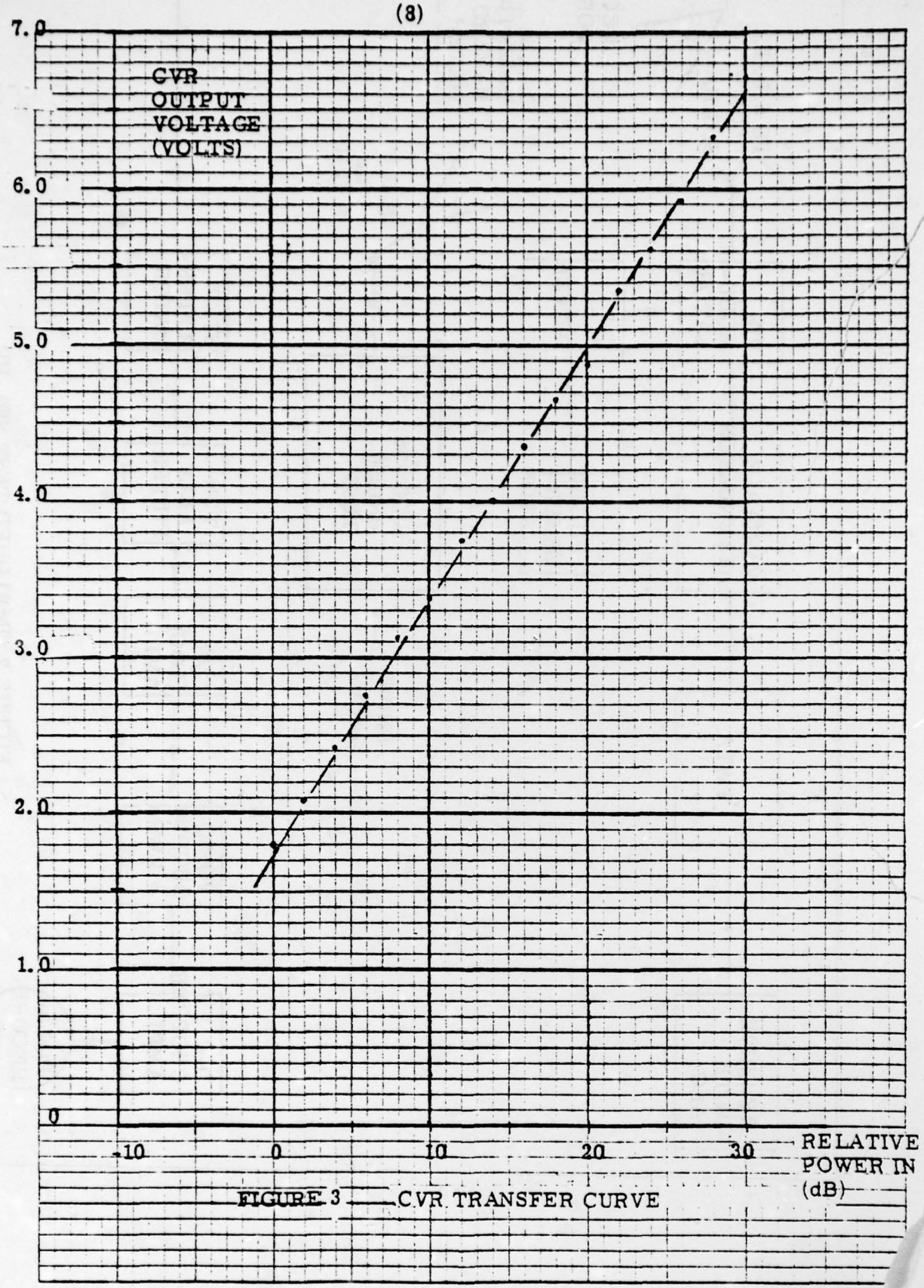

FIGURE 3 CVR TRANSFER CURVE

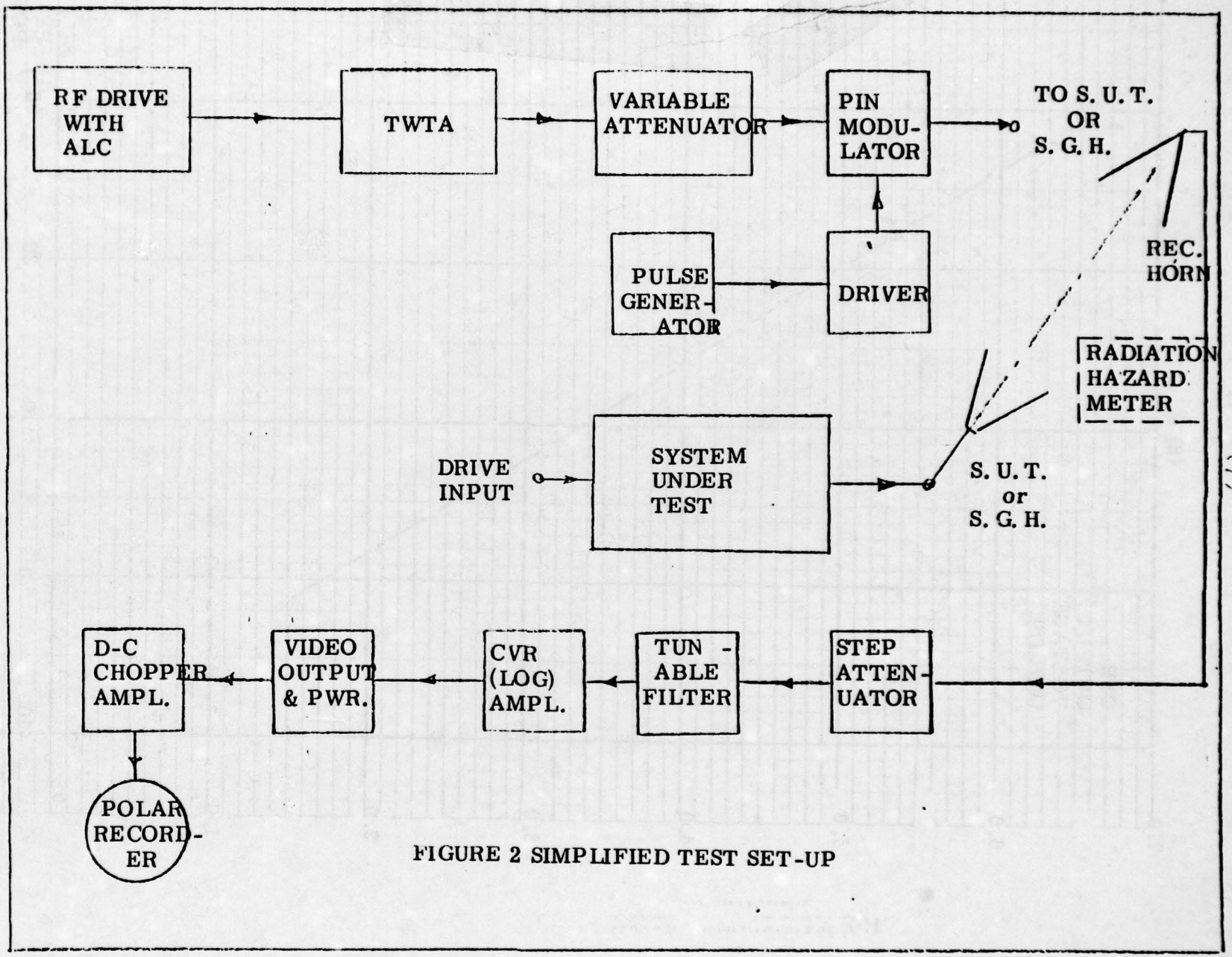

FIGURE 2 SIMPLIFIED TEST SET-UP

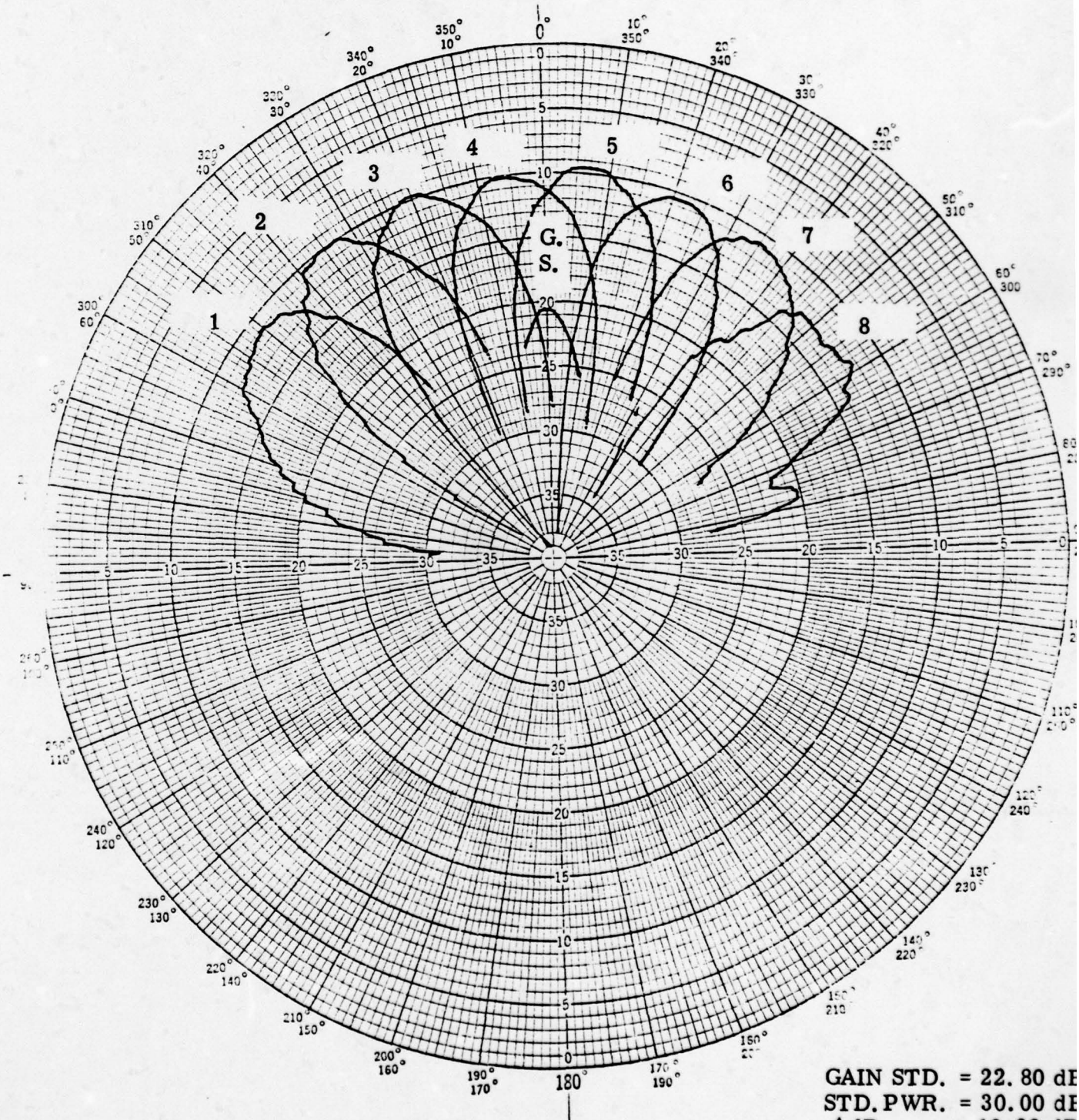

FIGURE 4 BEAM NO. 4
RADIATED POWER

GAIN STD. = 22.80 dB
STD. PWR. = 30.00 dB
ΔdB = 10.00 dB
ΔdB_4 = 10.50 dB
ERP = 73.30 dB_r

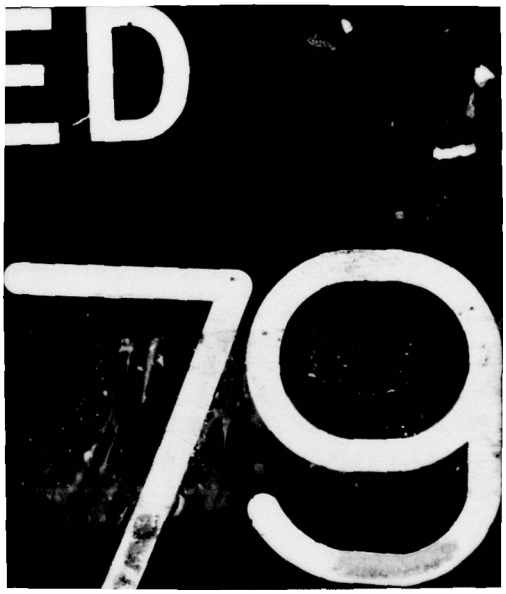
ED
79